



TECHNISCHE
UNIVERSITÄT
WIEN

Vienna University of Technology

Dissertation

Chemical Tailoring of Metal Oxide Nanoparticle Surfaces to Control Structure and Properties of Polymer Nanocomposites

ausgeführt zum Zwecke der Erlangung des akademischen Grades eines
Doktors der technischen Wissenschaften

unter der Leitung von

Univ.-Prof. Dipl.-Chem. Dr. Guido KICKELBICK

eingereicht an der Technischen Universität Wien
Fakultät für Technische Chemie

von

Dipl.-Ing. Bernhard FEICHTENSCHLAGER

Matr.Nr. 0325769

Flurschützstraße 15/26
1120 Wien

Wien, 26.07.2011

für Viktoria

In der Regel folgt auf Wenn

Erst ein So und dann ein Denn.

Wilhelm Busch

Danksagung

Großer Dank gilt meinem Betreuer Prof. Guido Kickelbick. Er gab mir die Möglichkeit an einem sehr aktuellen und breitgefächerten Thema wissenschaftlich zu arbeiten, förderte die Entstehung, und ermöglichte die Umsetzung meiner eigenen neuen Idee. Danke für die vielen Gestaltungs-Freiheiten. Dadurch konnte ich mich wissenschaftlich weiter entwickeln. Auch konnte ich viel über das Zusammenarbeiten in einem Projekt-Team lernen. Weiterer Dank gilt meinem Betreuer für seine große Geduld beim Korrekturlesen meiner Manuskripte und dieser Arbeit und für sein Verständnis!

Ich möchte mich sehr bei meinen Projekt-Partnern und Kollegen Silvia Pabisch (Uni Wien), Prof. Herwig Peterlik (Uni Wien), Muhammad Sajjad (TU Wien) und Dr. Thomas Koch (TU Wien) bedanken, für ihr Engagement und die gute Zusammenarbeit im Projekt, in dessen Zuge diese Arbeit abgefasst wurde. Dem Fonds zur Förderung der wissenschaftlichen Forschung Österreichs (FWF, Projekt Nr. P20693) sei für die finanzielle Unterstützung dieser Arbeit gedankt. Dank gilt Prof. Schubert für seine Unterstützung am Institut für Materialchemie.

Viel Dank kommt meinen Kollegen, Mitarbeitern und Freunden am Institut für Materialchemie an der TU Wien zu, da ich mich die letzten 4 Jahre an diesem Institut nicht zuletzt wegen ihnen sehr wohl gefühlt habe: Angelika für viele Unterhaltungen über Alles; Aparna, Christian Mau., Christian Mar., Christine, die seit dem ersten Tag an der Uni meine Kollegin und gute Freundin ist; Christoph L. für seine fachliche Kompetenz; Christoph R., mein Lehrmeister; Claudia, Denisa für viel Phosphonatchemie; Denise, Gregor der Unabhängige, ich rechne ihn unserem Institut zu; Harald, Hongzhi, Jakob der mein bester Freund hier am Institut geworden ist und mir bei allen möglichen Dingen so oft geholfen hat, aber vor allem sehr viel auf guten Humor hält; Jingxia, Jasmin, Maia, Majka, Marco vor allem für den großen Spaß aber auch für seine gute Kollegialität und seine angenehme Art; Matthias, Melitta, Michael, Mirka, Mohsin für gute Kollegenschaft und die Offenbarung vieler neuer Sichtweisen; Philipp, Ralf, Robert L., Robert P., Rupali, Rupert, Sarah, Simas, Sorin, Stefan, Stephan, Sven für Mittagsspaziergänge und Van An, meine langjährige gute Kollegin, unter anderem für viel gemeinsamen Tratsch und die großzügige Auflockerung der Arbeitsatmosphäre.

Ich möchte mich auch bei meinen Kollegen und Mitarbeitern aus Saarbrücken bedanken, die mir während meines Gastaufenthalts viel Unterstützung boten, aber auch den Schmah nicht eintrocknen ließen: Dank gilt vor allem Eric für den Mauch, Florian der sich gut auskennt, Holger, Jonas dem Joghurtmacher, Julia die sagt was sie denkt, Kilian für den deutschen Spaß, Matthias für seine Gastfreundlichkeit, Olli für seine Hilfsbereitschaft und Frühstücksgleichgesinntheit, Robert für Ruhe und Kulinarik, Tom für das Durchlöten und Susanne dafür, dass alles reibungslos geklappt hat.

Dank gilt Dr. Berthold Stöger, Christine Artner und Dr. Robert Haberkorn für Messungen und Kompetenz am Röntgendiffraktometer. Bedanken möchte ich mich bei Dr. Johannes Bernardi, Dr. Michael Stöger-Pollach und Karin Whitmore, von der Universitären Serviceeinrichtung für Transmissionselektronenmikroskopie der TU Wien, für ihre Hilfe bei meinen Messungen und ihre Geduld dabei. Bedanken möchte ich mich bei Anders Henriksson für Ellipsometrie und IR Messungen und den vielen Spaß den wir abseits der Arbeit hatten. Großer Dank gilt Dr. Michael Puchberger für NMR Messungen und die Hilfe bei Planung und Auswertung der Experimente aber vor allem für die erheiternden Tai-Chi Unterrichtsstunden. Bedanken möchte ich mich bei Stephan Abermann, dass er ZrO₂ beschichtete Siliziumwafer zur Verfügung gestellt hat. Weiterer Dank gilt Prof. Gernot Friedbacher (TU Wien) und Matthias Lessel (Uni Saarbrücken) für AFM Messungen und die guten Unterhaltungen dabei. Dank geht an Elisabeth Eitenberger für SEM und EDX Messungen und ebenfalls kurzweilige Unterhaltungen.

Ich danke Viktoria und meinen lieben Kollegen Angelika, Christian, Jakob, Jasmin, Marco, Sarah, Sven und Van An für das Korrekturlesen dieser Arbeit.

Dank gilt meinen Freunden Hannes und Gerald für die notwendige Nicht-Chemie in meinem Leben und ihr Verständnis, dass ich wegen dieser Arbeit so oft mal dies oder das zu tun hatte. Danke an meinen Bruder Arnold für den vielen Spaß, den nur Eingeweihte verstehen.

Großer Dank gilt meinen Eltern, die mir Schule, Studium und Leben ermöglichten und mir immer ein starker Rückhalt waren und sind. Sie standen immer hinter meinen Entscheidungen und unterstützten sie. Danke.

Vielen Dank, liebste Viktoria, dass Du mit mir diese Zeit meines Lebens gemeinsam durchschritten hast und Dich mit mir gefreut und mich getröstet hast. Danke für Deine Liebe und Deine Geduld!

Danke!!

Kurzfassung

Anorganisch-organische Nanokomposite stellen eine Kombination von anorganischen- mit organischen Komponenten auf nanoskaliger (1-100 nm) Ebene dar. Der hohe Anteil an Grenzfläche in diesen Materialien verleiht ihnen einzigartige Materialeigenschaften, wie zum Beispiel stark verbesserte mechanische Eigenschaften, im Vergleich zu klassischen Polymerwerkstoffen oder Kompositen. Diese Kombination ermöglicht weiterhin den Zusammenschluss der Eigenschaften anorganischer Materialien (z.B. Keramiken) mit denen organischer Materialien (z.B. Polymere), wobei die Transparenz einer Polymermatrix erhalten bleiben kann, wenn die anorganischen Nano-Objekte kleinere Dimensionen als die Lichtwellenlänge aufweisen. Allerdings sind meist beide Komponenten inhärent inkompatibel. Deshalb ist die systematische Anpassung der Grenzfläche durch chemische Oberflächenmodifizierung der anorganischen Komponente eine große Herausforderung. Die systematische Untersuchung des Einflusses der organischen Oberflächenmodifizierung von Metalloxid-Nanopartikeln auf ihr Dispersionsverhalten sowie auf die Struktur und mechanischen Eigenschaften von Nanokompositen war Gegenstand dieser Arbeit.

Dazu wurden SiO_2 (sphärisch, amorph) und ZrO_2 (nanokristallin) Nanopartikel in unterschiedlichen Größen hergestellt. Die ZrO_2 Nanopartikel wurden mit Organophosphor-Kupplungsreagentien und die SiO_2 Nanopartikel mit Trialkoxysilanen, mit unterschiedlichen organischen Resten (inerte und polymerisierbare Gruppen, etc.), oberflächenmodifiziert und charakterisiert. Der Einfluss der Art der organischen Oberflächenmodifizierung auf das Dispergierverhalten in organischen Flüssigkeiten wurde untersucht. Des Weiteren wurden Studien zur Struktur von selbstanordnenden Monolagen aus langen Alkylketten auf Nanopartikeloberflächen durchgeführt. Es konnte gezeigt werden, dass der Ordnungsgrad der Alkylketten stark von der nanoskopischen Struktur der Partikel abhängt und mit dem Agglomerations- und Dispergierverhalten selbiger korreliert. Ein Ansatz zur Steuerung dieses Ordnungsphänomens durch gemischte Oberflächenmodifizierung konnte erfolgreich angewandt werden. Des Weiteren wurden auch alternative Oberflächenmodifizierungen wie etwa Polydimethylsiloxane verwendet, was stark verändertes Dispergierverhalten zur Folge hatte. Aus den erhaltenen oberflächenfunktionalisierten Nanobausteinen wurden durch *in situ* Polymerisations- und Aushärteverfahren Polymethylmethacrylat-, Polystyrol- und Epoxidharz- Nanokomposite hergestellt. Die Struktur dieser Materialien wurde mittels Röntgen-Kleinwinkel-Streuung und Elektronenmikroskopie untersucht. Mechanische Kennzahlen wurden durch z.B. dynamisch mechanische Verfahren und *Vickers* Tests ermittelt. Die Ergebnisse wurden mit der chemischen Struktur der Oberflächenmodifizierung verglichen um Struktur-Wirkungsbeziehungen zu erhalten. Daraus ergab sich, dass die wichtigsten Voraussetzungen für homogene Materialien mit verbesserten mechanischen Eigenschaften die Grenzflächen-Anpassung und -Adhäsion sind. In dieser Arbeit wird gezeigt, wie die makroskopischen Materialeigenschaften von Polymer Nanokompositen über die Beschaffenheit ihrer inneren Grenzfläche kontrolliert beeinflusst werden können, um die systematische Entwicklung zukünftiger neuer Nanomaterialien zu erleichtern.

Abstract

Inorganic-organic nanocomposites result from a combination of inorganic and organic compounds, usually polymers, in one material with a heterogeneous structure on the nanoscale (1-100 nm dimensions). The high interfacial area in these materials is responsible for unique properties such as superior mechanical strength as compared to pure polymers or classical composite materials. Furthermore, properties can be generated which are located in between those of inorganic (ceramic) and organic (polymer) materials, maintaining transparency of the polymer matrix if the inorganic nano-objects are smaller than the wavelength of light. However, in inorganic-organic nanocomposites, the mixed compounds are often inherently incompatible. Consequently, the systematic tailoring of the interface via tuning the surface of the inorganic compound by applying an organic surface modification, is a great challenge. The systematic study of the impact of a surface modification of metal oxide inorganic nanoparticles on their dispersion behavior, materials structure and macroscopic mechanical properties of polymer nanocomposites was the topic of this work.

A full multiscale approach, starting from molecular precursors and resulting in nanocomposite materials, was applied in this work. SiO₂ (spherical, amorphous) and ZrO₂ (nano crystalline) nanoparticles with different particle sizes were synthesized. The ZrO₂ nanoparticles were surface modified with organophosphorus coupling agents and the SiO₂ with trialkoxysilanes, containing various organic moieties (inert groups and polymerizable groups, etc.) and characterized with respect to their chemical structure and grafting density. The influence of the organic moiety on the dispersion behavior in organic media was tested. Furthermore, studies on the self-assembled-monolayer behavior of long alkyl chain modified nanoparticles were carried out. Thereby, it was concluded that the alkyl chain ordering strongly depends on the nanoscopic curvature of the particles and influences nanopowder agglomeration and dispersion behavior. A mixed monolayer approach, to tune monolayer ordering and thus the nanopowder agglomeration behavior, was taken. Furthermore, alternative poly(dimethyl siloxane) based organic surface groups were introduced via a grafting *from* and a grafting *onto* approach, which resulted in significantly altered dispersion behavior of the nanoparticles. Primarily, the *in situ* polymerization / curing method was applied, utilizing different types of nanoparticles with systematically varied organic surface groups synthesizing poly(methyl methacrylate)- polystyrol- and epoxy resin nanocomposites with different amounts of inorganic nanofiller. The structural properties of the materials were determined via small angle X-ray scattering and transmission electron microscopy. Mechanical characteristics were measured by methods such as dynamic mechanical analyses and *Vickers* hardness tests. The results were correlated with the chemical surface modification and structure-property relations were generated. In conclusion, for the preparation of homogeneous nanomaterials and the achievement of strong mechanical reinforcement, interfacial compatibility and interfacial adhesion are crucial factors. This work demonstrates how the macroscopic properties of polymer nanocomposites can be controlled on a molecular level by various ways to facilitate a systematic development of novel polymer nanocomposites in the future.

Parts of this work have been published

Tuning the Self-Assembled Monolayer Formation on Nanoparticle Surfaces showing different Curvature: Comparison of Spherical Silica Particles with Plane-Crystal-Shaped Zirconia Particles; Bernhard Feichtenschlager, Christoph J. Lomoschitz and Guido Kickelbick: Journal of Colloid and Interface Science (2011), 360 (1), 15 - 25.

Index of Abbreviations

General Abbreviations

AG	anchor group
FG	functional group
IEP	isoelectric point
NP	nanoparticle
M/I	monomer-to-initiator
M_n	number average molecular weight
M_w	mass average molecular weight
PDI	polydispersity index
ROP	ring opening polymerization
SAM	self-assembled monolayer
wt	weight
at	atom

Chemicals and Substances

AIBN	2,2'-azobis(2-methylpropionitrile)
BFDGE	bisphenol-F-diglycidylether
Bu	butyl
C_n	linear aliphatic hydrocarbon chain with n carbon atoms

D ₃	hexamethylcyclotrisiloxane
DBPO	dibenzoyl peroxide
DEG	diethylene glycol
DETA	diethylene triamine
DMSO	dimethyl sulfoxide
Et	ethyl
GLYEO	glycidoxypropyl trimethoxysilane
M	metal atom
Me	methyl
MCPBA	meta-chloro perbenzoic acid
MMA	methyl methacrylate
PA	phosphoric acid
PDMS	poly(dimethyl siloxane)
PEO	poly(ethylene oxide)
PMMA	poly(methyl methacrylate)
PPA	phosphonic acid
Pr	propyl
PS	polystyrene
PTFE	polytetrafluoroethylene
R	organic moiety
TEOS	tetraethyl orthosilicate
TMS	trimethoxysilane
TMeS	trimethylsilyl
THF	tetrahydrofuran

Instrumental Techniques

AFM	atomic force microscopy
ALD	atomic layer deposition
ATR	attenuated total reflection
BET	<i>Brunauer, Emmett, Teller</i>
BJH	<i>Barrett, Joyner, Halenda</i>
CP	cross polarization
DEPT	distortionless enhancement by polarization transfer
DLS	dynamic light scattering
DMA	dynamic mechanical (thermo)analysis
DSC	differential scanning calorimetry
EDX	energy dispersive X-ray spectroscopy
FEG	field emission gun
FT	Fourier transform
GPC	gel permeation chromatography
HPDEC	high power decoupling
HRTEM	high resolution transmission electron microscopy
IR	infrared
IRRAS	infrared reflectance absorption spectroscopy
MAS	magic angle spinning
MS	mass spectrometry
NMR	nuclear magnetic resonance

pXRD	powder X-ray diffraction
rms	root mean square
SAED	selected area electron diffraction
SANS	small angle neutron scattering
SAXS	small angle X-ray scattering
SEM	scanning electron microscopy
SP	single pulse
TEM	transmission electron microscopy
TG	thermogravimetry
TGA	thermogravimetric analysis
UV	ultraviolet
VIS	visible
WAXS	wide angle X-ray scattering
XRD	X-ray diffraction

Spectroscopy Abbreviations

b	broad
d	doublet
m	multiplet
q	quartet
s	singlet
t	triplet
tert	tertiary

Table of Contents

1	Introduction	1
1.1	Inorganic-organic nanocomposites.....	3
1.2	Generation of inorganic nanostructures	8
1.3	Metal oxide nanoparticles	8
1.4	Chemical nanoparticle surface engineering / interface engineering	11
1.4.1	Organosilane coupling agents	15
1.4.2	Organophosphorus coupling agents	18
1.4.3	Self-assembled-monolayers on nanoparticle surfaces.....	21
1.4.4	The role of functional end groups	26
1.4.5	Polysiloxane modified nanoparticles	27
1.4.6	Polymer shell modified nanoparticles	29
1.5	Polymer matrices in this work: What is the state of the art in polymer nanocomposites research?	30
1.5.1	Poly(methyl methacrylate)	31
1.5.2	Polystyrene	34
1.5.3	Epoxy resins	36
1.6	Structure property relations	41
2	Research Goals	43
3	Results and Discussion	47
3.1	Nanoparticle surface engineering.....	47
3.1.1	Nanoparticle model systems.....	47
3.1.1.1	ZrO ₂ nanoparticles	47
3.1.1.2	SiO ₂ nanoparticles	58
3.1.1.3	Characterization of the prepared nanoparticles applying small-angle-X-ray scattering (SAXS), theory and experimental results	61
3.1.1.4	A comparison of the determined size values applying various size measuring methods.....	66
3.1.2	Anchoring of coupling agents to the nanoparticle surfaces	72
3.1.2.1	Organophosphorus coupling agents on ZrO ₂	73

3.1.2.2	Trialkoxysilane coupling agents on SiO ₂	85
3.1.2.3	Grafting densities of organic molecules at oxidic surfaces.....	93
3.1.3	Hydrophobic nanoparticle surface modifications, self-assembled-monolayers on nanoparticles.....	98
3.1.3.1	Alkyl chain ordering in self-assembled-monolayers on ZrO ₂ nanocrystals.....	100
3.1.3.2	Alkyl chain ordering in self-assembled-monolayers on SiO ₂ spheres .	104
3.1.3.3	Mixed SAM formation on ZrO ₂ surface to control the alkyl chain ordering	107
3.1.3.4	Control of alkyl chain ordering on SiO ₂ surface via mixed monolayer approach	111
3.1.3.5	Comparison of SAM-formation on SiO ₂ nanospheres / ZrO ₂ nanocrystals	113
3.1.3.6	The influence of mixed SAM on ZrO ₂ nanocrystals on particle agglomeration and powder redispersibility	115
3.1.3.7	Model experiments on macroscopical substrates.....	133
3.1.3.8	Conclusions: alkyl chains on nanoparticle surfaces.....	138
3.1.4	Hydrophilic Nanoparticle Surface Modifications	138
3.1.5	Polysiloxane grafted nanoparticles.....	141
3.1.5.1	Polysiloxane grafting- <i>onto</i> nanoparticle surface.....	143
3.1.5.2	Polysiloxane grafting <i>from</i> ZrO ₂ Nanoparticle Surface	164
3.1.6	Polymer shell nanoparticles	178
3.1.7	Comparison of different nanoparticle surface modifications.....	183
3.2	Nanocomposites, interface engineering	195
3.2.1	Thermoplasts as matrices: polystyrene (PS)	196
3.2.1.1	<i>In situ</i> bulk polymerization and characterization of the polymer matrix	196
3.2.1.2	PS nanocomposites from molecular modified nanoparticles.....	197
3.2.1.3	PS nanocomposites from PS shell nanoparticles	199
3.2.2	Thermoplasts as matrices: poly(methyl methacrylate) (PMMA).....	208
3.2.3	Crosslinked polymers as matrices: epoxy resin nanocomposites.....	217
3.2.4	Surface chemistry and interface chemistry	228
3.2.5	Structure property relations.....	229
3.2.5.1	Interface chemistry – dispersion structure (SAXS).....	229

3.2.5.2	Interface chemistry – mechanical properties.....	245
3.2.5.3	Dispersion structure (SAXS) – mechanical properties	257
4	Experimental Section.....	260
4.1	Materials.....	260
4.2	Analytical techniques	261
4.2.1	Nuclear magnetic resonance spectroscopy (NMR).....	261
4.2.2	Fourier transform infrared spectroscopy (FT-IR)	261
4.2.3	Elemental analysis.....	261
4.2.4	Gel permeation chromatography (GPC)	262
4.2.5	Thermogravimetric analysis (TGA).....	262
4.2.6	Differential scanning calorimetry (DSC).....	262
4.2.7	pH measurement.....	263
4.2.8	Zeta potential measurement	263
4.2.9	Dynamic light scattering (DLS)	263
4.2.10	Transmission electron microscopy (TEM).....	264
4.2.11	Ultramicrotomy	264
4.2.12	Scanning electron microscopy (SEM) and energy dispersive X-ray spectroscopy (EDX)	264
4.2.13	Atomic force microscopy (AFM).....	264
4.2.14	Small angle X-ray scattering (SAXS)	265
4.2.15	Powder X-ray diffraction (pXRD)	265
4.2.16	Nitrogen sorption experiments	266
4.2.17	Water uptake experiments.....	266
4.2.18	Ellipsometry	266
4.2.19	Contact angle measurements.....	267
4.2.20	Optical transmittance measurements (UV-VIS)	267
4.3	Mechanical tests	267
4.3.1	Dynamic mechanical thermoanalysis (DMA).....	267
4.3.2	Hardness	268
4.4	Preparation of nanoparticles.....	268
4.4.1	Preparation of small ZrO ₂ nanoparticles	268
4.4.2	Preparation of large ZrO ₂ nanoparticles.....	269
4.4.3	Preparation of SiO ₂ particles with various sizes	269

4.5	Syntheses of coupling agents	271
4.5.1	Preparation of alkyl spacer / no spacer based coupling agents	271
4.5.1.1	Preparation of dodecylphosphonic acid (DPPA)	271
4.5.1.2	Synthesis of 1-pyryl phosphonic acid (PhPPA)	271
4.5.1.3	Preparation of 3-(2,3,-dihydroxypropoxy) propylphosphonic acid (Diol-PPA)	272
4.5.1.4	Synthesis of oxiran-2-ylmethylphosphonic acid (Ep-PPA)	273
4.5.1.5	Synthesis of 2-Methacryloyloxy-1-ethylphosphonic acid (MA-C2-PPA).	274
4.5.1.6	Synthesis of 1-Methacryloyloxy decyl-10-phosphoric acid monoester (MA-C10-PA)	275
4.5.1.7	Synthesis of 2-bromoethylphosphonic acid (Br-C2-PPA)	275
4.5.1.8	Preparation of 10-(trimethoxysilyl)decyl methacrylate (MA-C10-TMS)..	276
4.5.1.9	Synthesis of 3-(trimethoxysilyl)propyl 4-cyano-4-((2-cyanopropan-2-yl)diazenyl) pentanoate (Azo-TMS)	277
4.5.2	Preparation of diethylene glycol chain coupling agents.....	280
4.5.2.1	Preparation of the allyl ether of diethylene glycol monomethyl ether. 280	
4.5.2.2	Synthesis of 1-(3-diethylene glycol monomethyl ether) propoxyphosphonic acid dimethyl ester.....	280
4.5.2.3	Synthesis of 1-(3-diethylene glycol monomethyl ether) propoxyphosphonic acid (DEG-PPA).....	281
4.5.2.4	Synthesis of 1-(3-diethylene glycol mono methylether) propoxy trimethoxysilane (DEG-TMS)	282
4.5.3	Syntheses of polysiloxane spacer chain coupling agents	282
4.5.3.1	Synthesis of α -(1-ethylphosphonic acid), ω - ⁿ Bu-poly(dimethyl siloxane) (ⁿ Bu-PDMS-PPA)	282
4.5.3.2	Allyl-lithium initiated ring opening living anionic polymerization procedure using hexamethylcyclotrisiloxane as monomer	284
4.5.3.3	Preparation of α -(1-propyl-3-trimethoxysilyl), ω -trimethylsilyl- poly(dimethyl siloxane) (TMeS-PDMS-TMS)	287
4.5.3.4	Preparation of α -(1-propyl-3-(phosphono)), ω -allyl-poly(dimethyl siloxane) (allyl-PDMS-PPA)	287
4.6	Nanoparticle surface modification	289
4.6.1	ZrO ₂ nanoparticle surface modification	289

4.6.2	SiO ₂ nanoparticle surface modification.....	289
4.6.3	PDMS grafting <i>from</i> experiments	290
4.6.3.1	Model reaction: lithiation and trimethylsilyl-termination.....	290
4.6.3.2	PDMS grafting <i>from</i> Br-C2-PPA@ZrO ₂ nanoparticles.....	291
4.6.4	Polystyrene grafted nanoparticles (PS@SiO ₂).....	292
4.7	Experiments using wafer substrates	293
4.8	Preparation of nanocomposite materials	293
4.8.1	Polystyrene (PS) nanocomposites	293
4.8.1.1	PS materials via <i>in situ</i> -polymerization	293
4.8.1.2	PS materials via solution compounding.....	294
4.8.1.3	PS materials via melt extrusion.....	294
4.8.2	Poly(methyl methacrylate) (PMMA) nanocomposites	295
4.8.3	Epoxy resin nanocomposites.....	296
5	Summary.....	297
6	Bibliography.....	309

1 Introduction

The continuous advancement in technology and engineering demands the supply with novel and more sophisticated materials because traditional materials often do not fulfill the desired requirements.^[1] Especially, high mechanical strength at low weight is a prerequisite for materials in high performance engineering and construction parts (e.g. automotive parts, airplane, etc.).^[2] When a new construction part is designed, usually the material for its production is selected by this criterion. Figure 1 gives an overview on the mechanical strength of traditional materials, depending on their density.^[3] The question mark inserted in the diagram shows the technological materials gap for light weight engineering materials where research and development is in challenged to develop new materials. Advanced composite materials seem to be a promising materials class for to achieve the desired properties.^[4]

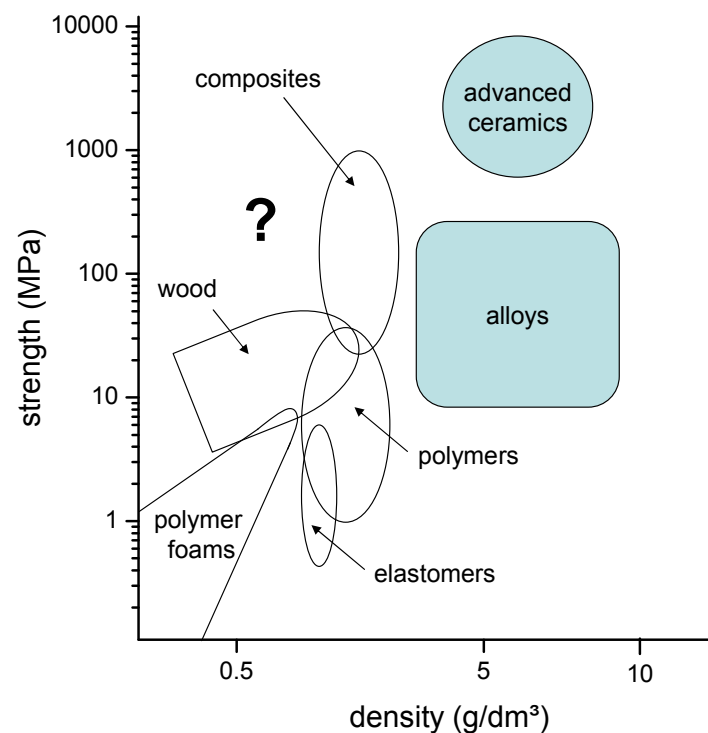


Figure 1. Strength of materials as a function of density, according to *Carraher* and *Seymour*.^[3]

Traditional composites, very often a combination of hard inorganic and soft organic compounds, such as glass fiber reinforced polymers,^[5] carbon fiber reinforced polymers^[6] or powder filler containing plastics^[7] show a high mechanical strength at a low density.^[8] A composite material is a composition consisting of two or more different compounds which are combined together in a macro- or micro phase separated system to obtain enhanced materials properties.^[8] The material class of composites is rather old, possibly the first composite was the combination of straw and mud.^[9] However, also nature has been applying composite technology for a long time, e.g. wood or bones can be considered to belong to that materials

class. In bones, for example the combination of structured apatite and biopolymer can be found, which results in unique mechanical properties.^[10, 11] Via the combination of a hard inorganic part and a soft organic matrix materials can be generated, showing properties that lie in between those classes.^[8] However, for classical inorganic-organic composites a relatively high amount of inorganic compound, e.g. powder filler, is required to obtain significant effects of reinforcement of a polymer matrix (up to 40 wt% inorganic filler is usually needed).^[8] As common inorganic compounds have a relatively higher density compared to common organic matrix materials, higher content of inorganic components is undesirable in terms of light weight materials. The use of carbon fiber, which reveals a lower density, is limited as the production of such composite materials is not possible via common methods such as melt extrusion or injection molding. Furthermore, the strength of such materials shows strong anisotropic behavior.^[5] The situation is different for particle filled composites. In most cases they can be processed like common polymeric materials via extrusion or injection molding.^[7] However, a new class of composite materials allows overcoming the problem of high filler amounts needed for significant reinforcement: nanocomposites. These materials consist of compounds where at least one dimension is confined in the nanometer range (1-100 nm^[1]).^[1, 12, 13] This causes a high interfacial region in the material, which allows unique energy and stress transfer. Thus, less filler amount as for traditional composites is needed (usually < 1-5 wt%^[14]) to obtain the desired strong mechanical reinforcement effect.^[12, 14]

For these reasons, the relatively new field of nanocomposites research is very topical and became of great interest within the last two decades in the scientific community, see Figure 2. This recent development within the last years has also to do with the parallel development of novel analytical techniques for nanocomposites characterization. In this emerging field of research, many possibilities and chances but also questions are raised, which this work will also deal with.

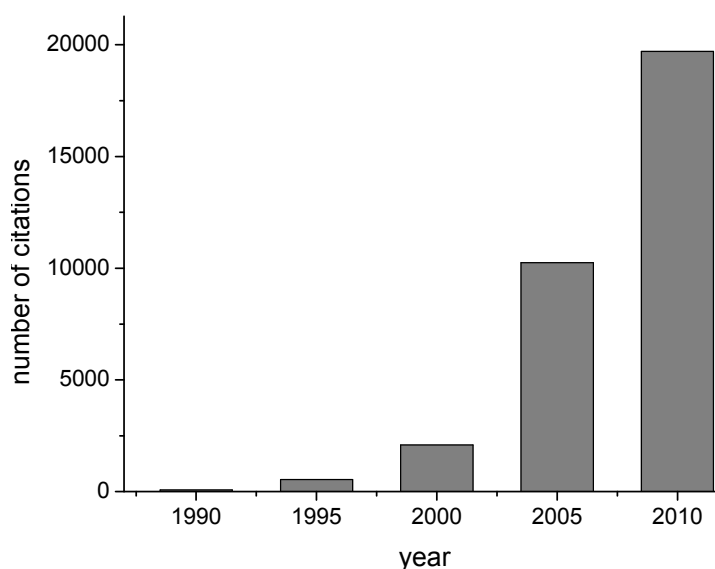


Figure 2. Number of citations according to *Scifinder-Database* (accessed April 11th 2011) which contain the concept of "nanocomposites".

1.1 Inorganic-organic nanocomposites

In the preparation of inorganic-organic nanocomposites, the inorganic compounds can be *in situ* generated within the organic matrix or incorporated after their preparation, via the building block approach. The building block approach is most widespread because of the lower complexity of the process, compared to the controlled *in situ* generation of nanoobjects. This approach will thus also be applied in this work.^[1]

Furthermore, there are three basic types of (inorganic) nanostructures of nano building blocks which can be incorporated into a polymer matrix, classified by their dimensionality:^[1]

- Nano-objects confined in one dimension, sheet like structures, e.g. clays^[15] and layered silicates (montmorillonite,^[16] talc,^[17] kaolinite,^[18] mica,^[19] etc.), graphite,^[20] other oxidic materials (titanates,^[21, 22] etc.).
- Nano-objects confined in two dimensions, e.g. nanotubes (carbon nanotubes,^[23] natural mineral nanotubes^[24]), nanorods,^[25] nanowires^[26] and nanofibers.^[27]
- Nano-objects with three dimensional confinement (low aspect ratio, quasi isotropically shaped nanoparticles): metal particles^[28, 29], (transition and main group) metal oxide particles (e.g. SiO₂,^[30-33] Al₂O₃,^[34] TiO₂,^[35-37] ZrO₂,^[36, 38, 39] Fe₂O₃,^[40, 41] Fe₃O₄,^[42] ZnO,^[43] etc.), other metal chalcogenide particles,^[44, 45] etc. The shape of such nanoobjects (e.g. faceted,^[43, 46] spherical^[47] or irregular,^[31, 38] etc.) depends typically on the structural chemical nature of the particles (crystalline, amorphous, polycrystalline).

The use of one- and two- nano-dimensional fillers can have several advantages concerning mechanical strength (fiber reinforcement effect, etc.^[8]) and manufacturing (easy availability of natural clay minerals^[48, 49]). However, the three nano-dimensional building blocks are the only type of nanofiller, which enable the production of transparent materials. In addition, nano-objects with higher aspect ratios are generally more difficult to disperse (stacking phenomena, etc.).^[50] For nano-objects, confined in three dimensions, no scattering losses during light transmission through the nanocomposite material are present, when they are homogeneously dispersed within the matrix material.^[51] Furthermore, the mechanical properties of nanocomposites prepared from nanoparticles can be considered to show isotropic behavior. In contrast, anisotropic fillers often show stronger reinforcement in a preferred direction.^[7]

In a typical particulate filler containing inorganic-organic nanocomposite material, inorganic nanoparticles need to be homogeneously dispersed in a polymer matrix. Often the different compounds are incompatible with each other and show much higher attractive forces to the same components compared to the intercomponent force. Therefore specific methods, such as high energy input or chemical surface tailoring, are necessary to form a homogeneous dispersion. Figure 3 shows the two basic types of nanoparticle interaction with the surrounding matrix, which has great influence on the final materials properties.^[1, 52] The materials are divided into two types: One type of materials show only a physical interaction

between particles and matrix (Figure 3a), whereas in the other systems the nano building blocks are strongly chemically linked with the matrix via covalent bonds (Figure 3b).^[1] The division in these types of nanocomposite materials is in analogy to the classification of hybrid materials classes (including blends, covalently linked homogeneous dispersed systems, interpenetrating networks and linked networks).^[1] Hybrid materials, in general, are a class of materials where different compounds (inorganic molecular structures^[53, 54], inorganic clusters^[55, 56]) and an organic polymer are homogeneously mixed together on molecular level, to generate novel materials properties. This concept is the same for nanocomposites, with the only difference that the size of the incorporated object is in the range of 1-100 nm. The transition between hybrid materials (molecular level) to nanocomposites (nanoscale level) can be considered gradual.^[1]

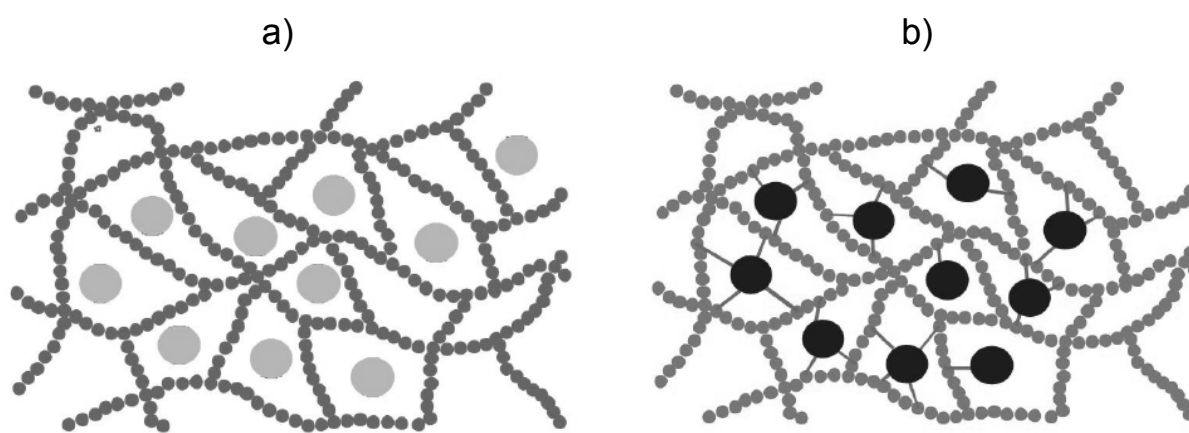


Figure 3. Scheme of a cross section of an inorganic nanoparticle containing polymer nanocomposite. The dark grey system represents the polymer chains and the light grey and black system the nanoparticles. In principle, such materials can be divided into two different types: a) only physical interaction is present between the inorganic and the organic compounds. b) strong chemical interaction between the compounds via covalent bonds is present.^[1]

The schemes in Figure 3 make also clear that for the achievement of a homogeneous dispersion state not only requirements on part of the particles have to be fulfilled, but also on part of the polymer matrix. A certain ratio between nanoparticle size and size of polymer chains is a requirement for the possibility to obtain homogeneous dispersions. The dimensions of the polymer chains from the matrix must exceed the dimensions of the nano-objects to a certain degree to enable a surrounding of the embedded particles with the matrix polymer and thus prevent particle agglomeration.^[36, 57, 58] This fact points out the unique situation which exists for such materials, namely that the gyration radii of nanoparticle and polymer chain coils or domains are within the same size range. This condition very often leads to unexpected and unique properties of the final materials such as overproportionally strong mechanical reinforcement.^[50, 59]

For the preparation of inorganic-organic nanocomposites, basically, three different methods are applied for pre-generated nanoparticles:^[1]

- Melt compounding: The nanoparticles are incorporated into the polymer matrix by mixing them with a polymer melt.^[60, 61] Afterwards, specimen for research or engineering parts can be produced via injection molding^[60] or extrusion.^[61] The advantage of this approach, when applied in research, is that it is close to typical industrial processes^[62] and also high throughput screening is possible via automation.^[61]
- Solution compounding: In this case, the nanoparticles are mixed together with a polymer solution and the solvent is evaporated to obtain the nanocomposite material.^[63, 64] An advantage of this process, compared to melt compounding conditions, is that it is a very gentle processing method where mild thermal and chemical conditions are possible (low temperatures, inert solvents). Therefore, very often the nano-dispersion quality is higher as compared to melt compounding technologies.^[63]
- *In situ* polymerization / *in situ* curing: A stable dispersion of nanoparticles in a monomer is generated. Then, polymerization is carried out and thus the organic matrix is formed around the nanoparticles.^[36, 37, 65] This is the only process which allows the preparation of materials where particles and matrix are chemically linked together via the matrix polymer chains grafting-*through* the building block surface, when the latter contains polymerizable groups.^[66]

Another process for the preparation of inorganic-organic nanocomposites is the *in situ* generation of inorganic nanoparticles in a crosslinked polymer matrix.^[67]

As mentioned, inorganic-organic nanocomposites can show over-proportionally enhanced mechanical properties and transparency under the given conditions. In addition to the enhancement of mechanical strength, the incorporation of inorganic nanoparticles into a polymer material can be used to introduce functional properties which are not available from the polymers. Examples for such functionalities, which have been introduced into polymer matrices via nanoparticles are:

- Magnetic properties due to incorporation of magnetic nanoparticles (Fe_3O_4 ^[68] or Fe^[69] nanoparticles)
- Fluorescence (Eu doped YVO_4 ^[70], lanthanide doped CeF_3 ^[71] nanoparticles)
- High refractive index materials (e.g. ZrO_2 nanoparticles in epoxy resins^[39] or polyacrylates^[72], ZnO in PMMA^[43])
- Tuning of electric and dielectric properties (e.g. BaTiO_3 ^[73])
- Tuning of thermomechanical or thermal degradation properties (SiO_2 ^[74], ZrO_2 ^[75]), or the incorporation of flame retardant nanoparticles to induce changes in the oxidative degradation mechanism of the polymer (e.g. MgAl layered double hydroxide^[76])
- Tuning of gas barrier properties (e.g. montmorillonite^[77])
- Size dependent properties of the nanoparticles can be exploited: Small nanoparticles can show different properties than the corresponding bulk material. Examples are

changes in the band gap structure of semiconductors (e.g. 5-9 nm CdSe showing quantum size related luminescence, "quantum dots"^[45]) or altered magnetic properties (e.g. superparamagnetism of 3.5 nm γ -Fe₂O₃^[78]), etc.).

Usually, small amounts (often less than 1-5 wt%^[14]) of nanofiller are required to obtain significant effects on the desired mechanical properties. These small filler contents allow an easy processing of the materials similar to common polymers (extrusion, injection molding, hot pressing, etc.), which is a great advantage of this materials class.

As noted, nanoparticles show a higher reinforcement effect when applied as filler in polymers, which is related to their small size.^[1, 14, 50] Figure 4 illustrates two typical examples for a nanosize related mechanical reinforcement effect. For instance, significantly lower mechanical reinforcement is obtained by using the same filler amount of micron-sized compound.

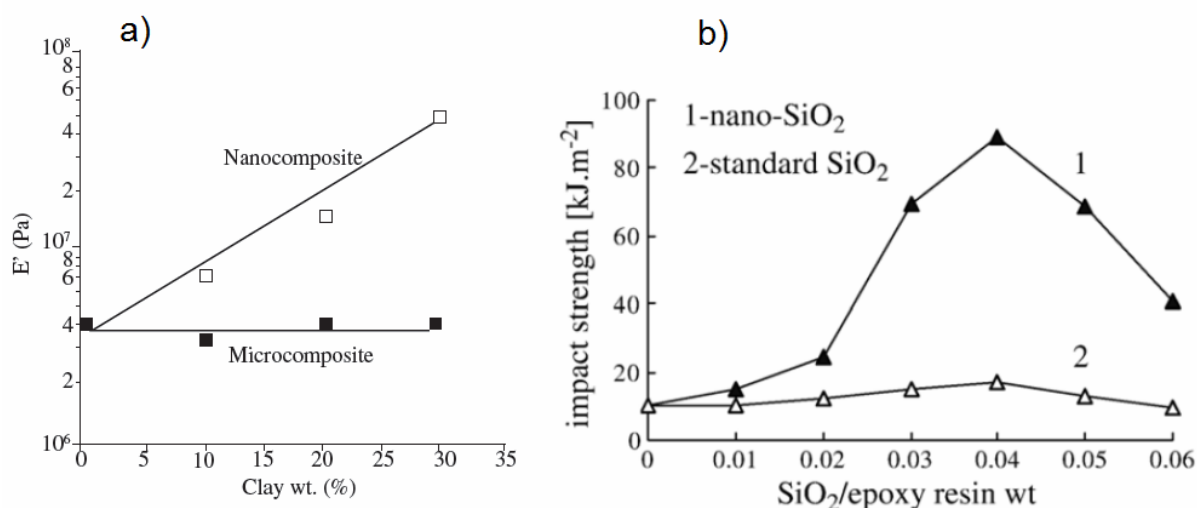


Figure 4. Two typical examples for "nano" effects on mechanical properties in inorganic-organic nanocomposites from literature. a) Exfoliated clay (nanocomposite) in styrene-butadiene-styrene block copolymers shows significant higher increase in plateau modulus with increasing filler amount at 258°C (E'), compared to non nanostructured clay filler.^[79] b) 30-40 nm diameter SiO₂ particles show a significantly higher increase in impact strength with increasing filler degree in an epoxy resin, compared to standard SiO₂ filler (3 μm diameter).^[32]

Following effects can be held responsible for this unique behavior of nanoparticle filled polymeric materials: ^[1, 47, 50, 80]

- Inorganic nanoparticles show a higher hardness than the surrounding polymer which enhances e.g. hardness (indentation)^[47] and scratch resistance^[81] of the materials due to a large number of such particles (at a comparable to traditional composites, low weight fraction) being homogeneously dispersed in the polymer matrix. Precisely,

nanoparticles offer a large number of obstacles towards materials deformation at low filler content because of their small dimensions.^[14]

- At the same volume fraction of filler the inter-particle distances are significantly lower for nanoparticles as for compared microcomposites, which alters the stress transfer in the material.^[47]
- Generally, the structure of the polymer in the interface region is different from the bulk structure of the pure polymer (mostly showing enhanced mechanical strength^[82]) due to the surface tension and polymer chain adsorption.^[50, 80] In homogeneous nanocomposites the volume fraction of such interfacial polymer layers in relation to the volume fraction of bulk polymer can be significantly high because of the high surface-to-volume ratio of nanoparticles.^[50, 80] Such effects usually play a role for particles with a size below 100 nm.^[50] Significant changes in mechanical properties are the result of this interphase polymer fraction.^[80, 83, 84]
- The unique situation is present that the nanoparticle and the polymer chain coil gyration radii are in the same size dimension.^[50, 59]
- The high interface area in general and thus the high interface energy within the material, in particular, can alter the energy and stress transfer within the nanocomposite material significantly.^[14] Surface-to-volume ratio of the filler and excluded volume interactions (e.g. the configurational entropy of polymer chains can be a driving force to push filler particles) are the most important factors.^[50]

A homogeneous dispersion of particles within the matrix is required,^[13, 14] as larger agglomerates or aggregates (the classification of these terms is given in continuative literature^[85]) of particles would behave like micron sized particles, showing no nano-related reinforcement effects.

A few examples of the current state of the art in research on nano-reinforcement of polymers are listed below:

- Polyester / TiO₂ nanocomposites show improved fracture toughness and tensile strength.^[86]
- Epoxy resin / SiC nanocomposites reveal improved tribological properties.^[87]
- Poly(methyl methacrylate) (PMMA) / CaCO₃ nanocomposites display high abrasion resistance and enhanced thermomechanical properties.^[88]
- Epoxy resin / ZrO₂ nanocomposites show improved tensile modulus and altered fracture mechanisms.^[38]
- Cyanate polyester / SiO₂ nanocomposites exhibit enhanced dynamical mechanical and thermomechanical properties.^[89]

- PMMA / SiO₂ nanocomposites show improved stiffness, hardness and fracture toughness.^[47]

A plethora of various other material combinations is described in the recent literature.^[14, 50, 80] A few types of polymer nanocomposites containing clay-, mica, and carbon nanotubes filler are already commercially available.^[62]

1.2 Generation of inorganic nanostructures

There are two, fundamentally different, approaches existing to the generation of nanostructures and thus for the preparation of nanostructured materials in general.^[12] A *top-down* approach where the nanostructure is generated, starting from a macroscopic structure, is lithography.^[90] To obtain nanopowders via a top-down approach, milling of a micron sized powder in a high energy ball mill^[91, 92] or by attrition milling or grinding^[93] is applied. This approach is limited to small amounts of material in the case of lithographic methods and, generally, high energy effort is needed to generate a nanostructure from a macroscopic structure. Furthermore, broad size distributions and defect rich surfaces are the result of mechanically treated samples. The second approach to nanostructure generation is the *bottom-up* technique. In this process the nanostructure is formed starting from molecular compounds by intentionally exploiting the natural tendency of matter, especially energy rich small units, to self assemble or react to larger aggregates.^[62] The required energy for the nanostructure generation is provided by the chemical and physical energy of the system itself and the structure formation proceeds via self organization of the matter. However, the difficulty is to find the right initial conditions and to control these processes to achieve the desired nanostructure.^[62] The great advantage of a *bottom-up* approach, compared to a *top-down* approach, is the facileness of generating nanostructures and the much lower energy effort which is required.^[62] For instance, nature forms nanostructured materials with a *bottom-up* approach (e.g. lipid bilayers in cells,^[94] bones^[10]). The incorporation of nanoparticles, prepared from molecular compounds into a polymer matrix (also prepared from molecular compounds) in a controlled way, here in this work, represents a *bottom-up* approach.^[62] The systematic control of these processes for the preparation of particulate nanostructures, building up materials from molecules, is one of the major topics of this work.

1.3 Metal oxide nanoparticles

In this work, metal oxide nanoparticles are used as fillers in polymer nanocomposites to study structural and mechanical effects related to nanofiller incorporation. The major reasons for the use of metal oxide nanoparticles are:

- Metal oxide inorganic compounds, main group metal oxides such as SiO₂ or Al₂O₃ as well as many transition metal oxides, are the most prevalently used (nano)fillers for polymer nanocomposites and thus their chemistry is well established.^[12, 14]

- Most of the common metal oxide nanoparticles (Al_2O_3 , CeO_2 , Co_3O_4 , TiO_2 , SiO_2 , Fe_3O_4 , WO_3 , etc.) show low toxicity.^[95] Furthermore, the most oxidic materials are chemically relatively inert (especially towards oxidation reactions, when the metals are in high oxidation states).
- Metal oxide materials often show high hardness and mechanical strength, which are typical properties of ceramic materials. These properties can be partially transferred to a composite material when the particles are incorporated into a polymer matrix, which is typically softer.^[14]
- Common metal oxides (oxides of Al, Ti, Zr, Si, etc.) do not show light absorption in the wavelength region of the visual light, which is important in terms of transparent nanocomposites. In contrast, there are other filler materials such as for example carbon nanotubes, which can induce strong reinforcement effects.^[96] However, their light absorption properties are often responsible for a low light transmission through nanocomposite materials.^[96, 97]

The metal oxides SiO_2 and ZrO_2 have been selected as materials for nanoparticle model systems in this work. A major reason for this selection was that two chemically complementary systems can be studied by using ZrO_2 and SiO_2 . As it will be discussed in the following chapter, the surface chemistry of these metal oxides is different.^[98, 99] The results from this work with regard to the surface chemistry of ZrO_2 should be transferable to many other transition metal oxides (e.g. TiO_2 , Fe_3O_4 , etc.) and the results for SiO_2 should be transferable to main group metal oxides (e.g. Al_2O_3 , SnO_2 etc.).^[100]

There are several further reasons why especially these two oxides are studied within this work:

All modifications of ZrO_2 show relatively high hardness (6.1-7.3 GPa (*Vickers*) for the monoclinic phase, 6.2-8.7 GPa (*Vickers*) for the stabilized tetragonal phase,^[101] a stabilized high temperature cubic ZrO_2 phase can reveal *Vickers* hardness values up to 10.5 GPa^[102]), a relatively high refractive index ($n_{589\text{ nm}} = 2.1$ ^[103]) and UV luminescence^[104] ZrO_2 is used as a white pigment^[105] but does not show photocatalytic abilities such as anatase- TiO_2 ^[106] which could lead to degradation of the surrounding polymer matrix. Si oxides have high natural abundance and nature creates Si based materials through biomineralization.^[107] Furthermore, the chemistry of SiO_2 is very well established, also for the corresponding silica nanoparticles. For instance, silica based nanopowders are the widely used in technological applications.^[12]

As regards the preparation of metal oxide nanoparticles there are several general possibilities for a *bottom-up* synthesis. The most common approaches^[108] particularly for the preparation of SiO_2 and ZrO_2 nanoparticles, are listed below:

- Spray pyrolysis or flame spray pyrolysis: In a typical procedure, a solution containing a molecular precursor or a liquid reactant is sprayed into a hot zone, containing a

reaction gas, e.g. O_2 , where the nanoparticles are formed. The particle size of the prepared nanoparticles can be controlled by the droplet size^[109] and/or nucleation rate. For example, typical commercial processes apply such methods, e.g. within the Aerosil process, where a spray aerosol from a mixture of chlorosilanes is combusted in oxyhydrogen gas to give pyrogenic nanosized SiO_2 ("fumed silica").^[110] However, an attribute of this approach is that the (primary) nanoparticles within the yielded powder are very often irreversibly aggregated.^[111] An example for the spray pyrolytic synthesis of ZrO_2 nanoparticles is the combustion of an aerosol of Zr-n-propoxide in alcoholic solution.^[112]

- Sol gel process (hydrolytic or non-hydrolytic):^[113] A typical hydrolytic sol-gel-route towards SiO_2 nanoparticles is the well-established *Stöber*-process.^[114] Amorphous spherical SiO_2 nanoparticles with a narrow size distribution are prepared by a controlled hydrolysis of tetraethylorthosilicate and silanol-condensation under basic conditions at room temperature. The particle size can be adjusted from ~ 7 nm diameter, stabilized primary particles,^[115] to typically 50-700 nm diameter^[116] and up to ~ 7 μm diameter micron sized spheres (e.g. via electrolyte addition)^[117] by variation of the reaction conditions. Applying a conventional non-hydrolytic sol gel route, uniform ZrO_2 nanoparticles can be prepared by a controlled condensation reaction of Zr-alkoxides with benzyl alcohol.^[118] Sol-gel-process occurs at mild temperatures, yielding well dispersed, highly uniform, nanoparticles.
- Microemulsion-method: In this process nanosized micelles with typical diameters around 50 nm are stabilized by surfactant molecules and used as nano-reactors in which nanoparticles can be formed. The nanoparticle size is controlled by the emulsion droplet size. For example, ZrO_2 nanoparticles were prepared from a $ZrOCl_2$ precursor in a 1-butanol in iso-octane emulsion, stabilized with several additives.^[119] For the preparation of amorphous SiO_2 nanoparticles, the application of a microemulsion method is also possible,^[120] however less prominent than the *Stöber* method allows the facile preparation of SiO_2 nanoparticles with various sizes. Microemulsion methods are typically low temperature processes resulting in mostly spherical (depending on the micelle shape) nanoparticles.
- Hydrothermal synthesis: With this method nanoparticles are prepared from an aqueous precursor solution at elevated temperatures, mostly under isochoric conditions in an autoclave, by controlling nucleation rate and growth rate of the prepared metal oxide phase. This is e.g. achieved via decomposition or hydrolysis and condensation of a precursor salt. For example, ZrO_2 nanoparticles in form of single nanocrystals or polycrystalline systems were prepared by hydrothermal treatment of Zr-precursor salt solutions (e.g. Zr-oxychloride, Zr-acetate).^[121, 122] Furthermore, additives can be used to adjust the surface tension within the reaction mixture and thus influence shape, size and type of crystalline phase of the prepared nanoparticles.^[123, 124] Hydrothermally prepared nanoparticles are in most cases crystalline and thus faceted. This can be of advantage because very often specific functional properties of metal oxides are related to their crystallinity. Furthermore, a hydrothermal process can also be used to treat

already prepared amorphous nanoparticles, e.g. from sol gel process or microemulsion process, for a transformation into a crystalline phase without irreversible aggregation "sintering". It is, for example, possible to transform amorphous SiO₂ nanoparticles into SiO₂ nanocrystals by applying such hydrothermal aging processes.^[125]

Dependent on the applied particle synthesis method, the surface termination is different (e.g. OH-groups, acetate groups, etc.).

In this work, amorphous spherical SiO₂ nanoparticles, prepared via a sol-gel process, act as an appropriate and efficient model system to study particle related chemical, structural and mechanical effects of polymer nanocomposites due to their controllable size and uniform morphology. ZrO₂ nanoparticles will be prepared via a hydrothermal route in this work to yield crystalline (hard) nanoparticles with specific crystal facet shape.

A few examples of recent literature studies point out the advantage of using especially SiO₂ and ZrO₂ nanoparticles in polymer nanocomposites:

- ZrO₂ is used in dental materials because of its high hardness and good tribological properties, e.g. ZrO₂ nanoparticles are applied in research in methacrylate monomer based dental filling formulations, where they result in enhanced mechanical strength of the materials.^[126]
- *Harada et al.* have prepared mechanically reinforced, transparent, high refractive index epoxy resin nanocomposites by incorporating ZrO₂ particles.^[39, 127]
- Uniform SiO₂ nanospheres are a perfect model system to investigate nanofiller effects in research. Applying such particles, it was possible to correlate the interfacial polymer chain conformation with bulk material properties.^[128, 129]
- The typical structure of fumed SiO₂ fillers can be intentionally exploited with regard to tune rheological properties of polymeric materials.^[31]

1.4 Chemical nanoparticle surface engineering / interface engineering

The surface of inorganic nanoparticles has to be adapted to their environment for two basic reasons:

Nanoparticles exhibit a high surface energy. Thus, the tendency to agglomeration or aggregation is very high and has to be prevented by surface engineering.^[100] This means that the interactions between the particles have to be decreased and the interactions between particle and environment have to be increased. In the case of inorganic-organic nanocomposites, where the two components such as hydrophilic ceramics and hydrophobic plastics are inherent incompatible, surface tailoring is necessary to decrease agglomeration to obtain good mechanical materials properties.^[14]

Nanoparticles often show high chemical reactivity. Consequently, surface tailoring is necessary to avoid chemical reactions with their environment.^[100] This is particularly the case

for metal nanoparticles which can undergo redox-processes.^[100] On the other side, in the case of metal oxide nanoparticles, e.g. photocatalytic active TiO₂ anatase particles, parts of the environment need to be protected towards the reaction with the particles to avoid degradation of the matrix.^[130] Nanoparticle surface engineering is thus used to change the surface energy of the nanoparticles.^[131]

A third reason, why targeted surface tailoring is of great interest to current research is the possibility to tune the self-assembly characteristics of nanoparticles via their surface properties.^[132-134]

In the present work the greatest attention will be paid to the dispersion stabilization of nanoparticles. This phenomenon is strongly connected to the assembly behavior of nanoparticles. Nanoparticle dispersions can be stabilized by two fundamental methods: electrostatic and steric stabilization.^[135] Electrostatic stabilization is achieved by introduction of surface charge, which generates repulsive inter-particle forces and thus stabilizes nanoparticle dispersions and prevent agglomeration.^[100, 136] Within the concept of steric stabilization of nanoparticles, moieties are introduced to the nanoparticle surface, which promote particle dispersion due to the steric structure of the surface attached moiety, generating steric repulsive forces.^[100, 136]

The chemical surface engineering of nanoparticles is commonly carried out utilizing coupling agents. This approach has been well investigated for macroscopic model substrates in research for many types of coupling agents and is well established in application. Examples are interphase compatibilizer for (powder) fillers in plastics^[137] or the tuning of physical properties of surfaces, e.g. tuning of wetting or corrosion protection.^[138] Especially within the relatively new field of the preparation of inorganic organic polymer nanocomposites the use of coupling agents is of great importance and interest.^[13, 139]

Figure 5 shows a schematic sketch of a coupling agent molecule. Such organic molecules consist of an anchor group, which allows a stable attachment of the organic moiety of this molecule to an inorganic surface. Examples for typical anchor groups are given in Table 1 and will be discussed below. The organic moiety consists of an inert spacer (in most cases alkyl chains) and an end group. The end group can be chemically inert (e.g. CH₃) or functional and thus allow further chemical reactions.^[100] As an example, in polymer composite chemistry, polymerizable end groups, such as methacrylates or vinyl groups, allow a covalent linkage between the particle and a polymer during an *in situ* polymerization (grafting *through*^[66]) or initiator groups are used for grafting-*from* reactions.^[140] Also amino- or epoxide groups are used as end groups and enable a strong bonding of inorganic compounds to organic matrices and promote interfacial adhesion.^[13] In principle, any type of end-functionality can be applied to tailor the surface of nanoparticles, e.g. ionic groups,^[135] photoluminescent groups,^[141] a second other anchor group,^[142] transition metal complexes,^[143] etc. The probably most applied type of coupling agents consist of a trialkoxysilane anchor group. Examples for these so-called silane coupling agents are MEMO (3-methacryloyloxypropyl trimethoxysilane), GLYEO (3-glycidoxypropyl triethoxysilane), or APTS (3-aminopropyltriethoxysilane).^[13]

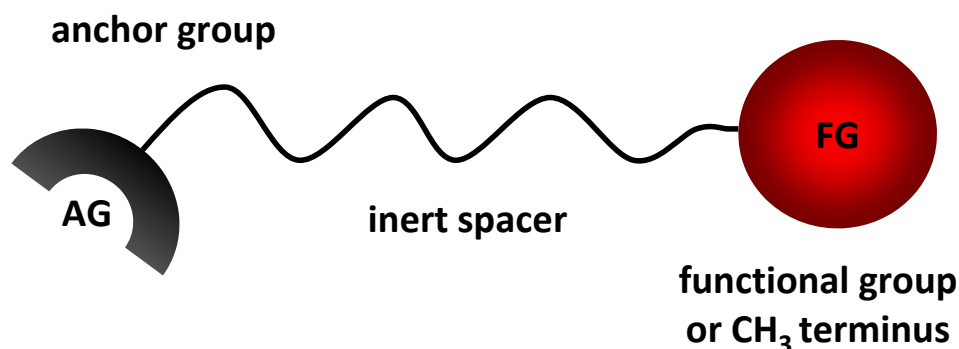


Figure 5. Schematic representation of a coupling agent molecule.

A variety of anchor groups (e.g. alkoxy- and chloro silanes,^[144-148] phosphonic acids,^[98, 149] sulfonic acids,^[133] etc.) are applied in coupling agent chemistry and technology, allowing different strength of interaction to the surface of various inorganic compounds. Table 1 shows examples for typical anchor groups and the corresponding substrates (metal and metal oxides) which show high affinity to these groups.

Table 1. Examples for different coupling agent anchor groups and typical substrates which show high affinity to these groups (R, R'...organic moiety of coupling agent including spacer and optional functional end group).

anchor group class	anchor group structure	substrate examples	substrate class	examples for application / research interest, remarks
organosilane	$\begin{array}{c} \text{R}-\text{Si}-\text{X} \\ \quad \\ \text{X} \quad \text{X} \end{array} \quad / \quad \begin{array}{c} \text{R}-\text{Si}-\text{CH}_3 \\ \quad \\ \text{CH}_3 \quad \text{X} \end{array}$ <p style="text-align: center;">-X ... -Cl, -O-alkyl</p>	SiO_2 , ^[144-148] Al_2O_3 , ^[150] SnO_2 ^[151]	main group metal oxide	composite technology, chromatography, membrane technology surface wetting tuning, very stable
phosphonic acid / phosphate	$\begin{array}{c} \text{O} \\ \\ \text{R}-\text{P}-\text{OH} \\ \\ \text{OH} \end{array} \quad / \quad \begin{array}{c} \text{O} \\ \\ \text{R}-\text{O}-\text{P}-\text{OH} \\ \\ \text{OH} \end{array}$	TiO_2 , ^[149] ZrO_2 , ^[98, 152, 153] Ta_2O_5 , ^[154] Y_2O_3 , ^[155] Fe_3O_4 , ^[156] BaTiO_3 , ^[157] $\text{Ca}_5(\text{PO}_4)_3(\text{OH})$ ^[158]	transition metal oxide, earth alkali metal ions	dental composites, self-assembled monolayer protection of surfaces, very stable
carboxylic acid (carboxylate)	$\begin{array}{c} \text{O} \\ \\ \text{R}-\text{C}-\text{OH} \end{array}$	AlOOH , ^[159] AgO , ^[138] Al_2O_3 ^[138]	metal oxide	natural fatty acids can be used, self-assembled monolayer protection of

				surfaces, lack of stability
sulfonic acid / sulfate	$\text{R}-\text{S}(\text{O})_2\text{OH} \quad / \quad \text{R}-\text{O}-\text{S}(\text{O})_2\text{OH}$	$\text{SiO}_2^{[133]}$ $\text{Fe}_2\text{O}_3^{[160]}$	metal oxide	surface property tuning, lack of stability
amine (ammonium)	$\text{R}-\text{NH}_2$	$\text{SiO}_2^{[133]}$ $\text{Pd}^{[161]}$	metal and metal oxide	surface property tuning, stabilization of nanoparticle dispersions, lack of stability
oligomers and polymers, e.g. poly- and oligo-ethylene glycol	$\text{R}-[\text{O}-\text{CH}_2-\text{CH}_2-\text{O}]_n-\text{R}'$	$\text{SiO}_2^{[116]}$ $\text{Al}_2\text{O}_3^{[162]}$ $\text{Fe}_3\text{O}_4^{[163]}$	metal oxide	stabilization of nanoparticle dispersions, technologically very important, lack of stability of these weakly binding nonionic surfactants
thiol	$\text{R}-\text{SH}$	$\text{Au}^{[164]}$ $\text{Ag}^{[13]}$ $\text{Cu}^{[165]}$	(noble) metals	nanoparticle passivation, very stable

Besides the mentioned anchor groups from Table 1, there are a plethora of other possible functional groups which can be used as anchor groups when strong (and selective) interactions with surfaces are required. The examples from Table 1 are the most common ones. Other types of agents which can be used in surface tailoring are polymeric surface modifications, which will be discussed in a separate chapter (1.4.6).

In most cases the process of surface modification using coupling agents is very simple. The coupling agent molecules are adsorbed from a solution to the inorganic surface, if their affinity to this surface is high enough. In many cases covalent bonds are formed (e.g. organosilanes@ $\text{SiO}_2^{[166]}$) or electrostatic interaction (e.g. alkylammonium@charged mineral layers^[48]) is present between the inorganic surface and the anchor group.

Another approach to increase the interaction between the matrix and the inorganic moiety is to adapt the polymer matrix.^[67, 167] However, this method alters the overall properties of the organic moiety. Some polymer matrices, e.g. poly(hydroxyethyl methacrylate),^[168] show inherently good compatibility with metal oxide surfaces. As most industrially applied plastics are hydrophobic, particle surface modification is necessary in most cases.

For many technological applications it is required to chemically tailor the surface of metal oxide nanoparticles so that nanoparticle powders can be easily (by low energy and low shear

force) (re)dispersed in organic media. A method to obtain such systems is to use coupling agents and vary their organic moiety systematically in order to obtain high compatibility between the inorganic and the organic compound and thus homogeneous nanomaterials. (Re)dispersible, modified, dry nanopowders are highly desired in terms of industrial application as the use of comparable stabilized nanoparticle dispersions implicates the carriage of the dispersion medium as ballast, which has to be transported and removed within the processing. Such nanopowders are very often deagglomerated via ultrasound^[169] or high shear force application (high pressure nozzle or rotor stator homogenizer^[170]) and thus dispersed in the desired dispersion medium, which proceeds best if the interaction between medium and particle surface is maximized and the interaction between the particles is minimized. If the compatibility is good enough, the compounds are theoretically miscible by gentle mixing.^[65] This is a highly desirable situation and represents the challenge in chemical surface/interface tailoring. Furthermore, coupling agents are also necessary to end cap surface hydroxyl-groups (surface termination^[171]) which may lead to inter-particle condensation^[172] and thus to the formation of irreversible aggregates which reduces the (re)dispersibility of the powders.

However, the chemical surface modification in order to tune the nanoparticle surface energy does not only change the dispersion properties (e.g. in monomers,^[75] polymer solution^[173] or polymer melt^[174]) of nanoparticles, but also the interface properties in final nanocomposite materials.^[52] The change of interfacial properties within polymer nanocomposites can significantly alter their mechanical properties (as discussed above, these materials include a high interfacial area) and this is also topic of this work.

1.4.1 Organosilane coupling agents

Silane coupling agents are the most popular class of coupling agents and have been widely used in application and research for the past decades.^[175] Organochlorosilanes and organoalkoxysilanes (basically methoxy- and ethoxy silanes) are the most commonly applied functionalities.^[147]

The most attractive substrate for modification with organosilane coupling agents is SiO₂, due to the strong covalent bonds (Si-O-Si) which are formed between the coupling agent and the SiO₂ surface. The attachment of reactive silane coupling agents to a metal oxide surface, e.g. SiO₂, requires surface hydroxyl groups,^[113] which are present at the surface of common metal oxide nanoparticle powders. In case of silica the density of these groups is typically 2.2 – 4.8 OH groups per nm².^[176]

By the use of chlorosilanes, the molecules are (partially) hydrolyzed to form silanol groups via a distinct amount of water,^[144] present in the reaction mixture, or adsorbed at the SiO₂ surface.^[177] Via a condensation reaction between the coupling agent silanol groups and the surface silanol groups, Si-O-Si bonds are formed and the coupling agent molecule is attached to the oxidic surface.^[147, 177] For alkoxysilanes, in principle, an analogous mechanism can be assumed. Under non-aqueous conditions the alkoxide (or other precursors) condensates directly under cleavage of alcohol molecules. Which kind of mechanism takes place, depends

on the reaction conditions, primarily water and catalyst content.^[178] Another proposed mechanism is the binding of the coupling agent to the surface on hydrophobic siloxane regions by a ring opening mechanism involving the Si-O-Si three membered ring which terminates these regions at silica surfaces.^[179]

Silane coupling agents are also applied for surface modification of transition metal oxides. However, there are cases where the Si-O-M bond is not very stable towards hydrolysis.^[180] This is one important reason why traditional silane coupling agents are nowadays successively replaced by organophosphorus coupling agents in many applications.^[181] *Mutin et al.* have shown that even selective surface modification of a mixture of transition metal oxide (TiO₂) and SiO₂ is possible.^[99]

Commonly, trifunctional (R-SiX₃) or monofunctional (dimethyl: R-Si(CH₃)₂X) silane coupling agents are applied. The trifunctional silanes have the advantage that they form more dense surface layers. A steric demand of 21-25 Å² of one surface bond trifunctional silane molecule can be assumed on perfect metal oxide surfaces with no defects and hydroxyl termination,^[147] which results in a maximum grafting density of ~4.3-4.8 molecules/nm² for one monolayer of trifunctional organosilanes, given that the organic moiety is smaller than the anchor group and a dense packing is allowed. This commonly reachable on usual oxidic powder samples.^[182] Trifunctional organosilanes samples have the disadvantage that their adsorption is more difficult to control. The reason is that multilayer and network formation can occur when trifunctional molecules are applied, which is not the case for monofunctional alkyldimethylsilanes. However, the latter form less dense surface (mono) layers because of the steric demand of the methyl groups at the silicon atom,^[182] allowing no full coverage and leaving more surface OH-groups unreacted.^[171] As this is usually disadvantageous in terms of providing maximum surface property change and maximum functionality, trifunctional coupling agents will be applied in the present work.

Alkoxide groups are usually methoxy- or ethoxy groups. The methoxy group is more reactive towards hydrolysis compared to the ethoxy group.^[113]

The structure of organic layers on metal oxide substrates, formed via the attachment of trifunctional organosilane coupling agents, is rather complex and indistinct. Figure 6 shows the most popular proposed structures that are usually formed.

Very often lateral cross condensation (Figure 6a) stabilizes the organosilane surface layer.^[144] Usually, in average one or less bonds of the coupling agent molecule to the surface is formed. The dense structure is stabilized by a polycondensed lateral network, which is proposed to be already formed (partially) in solution via self-assembly of organosilane molecules and then adsorbed to the oxidic surface. The mechanism where such oligomeric species are adsorbed on the surface is called *liquid-condensed-mechanism*.^[183] The other extreme case is the random adsorption of single molecules which is called *liquid-expanded-mechanism*.^[183] A combined presence of both mechanisms is considerable in typical surface modification procedures. Which mechanism is predominant depends on the reaction conditions.^[183] Different surface layer structures are the result of the different mechanisms.

Certainly, the structure additionally depends on the nature of the organic moiety of the coupling agent (Figure 6b). For small groups also multidentate (bi- to tridentate) binding modes are proposed.^[171] Additionally, a possible functional side group may affect the overall trialkoxysilane grafting reaction.^[178, 184]

The ability of these trifunctional molecules to form various structures often leads to indistinct multilayer type structures where, for example, polycondensed organosilane chains dangle from the surface (Figure 6c).^[185] A very popular structure, frequently evidenced via ²⁹Si NMR, is a ladder type arrangement of coupling agent molecules (Figure 6d).^[166]

Additionally, non-reacted silanol groups of the coupling agent molecule can form hydrogen bonds to the substrate.^[146, 186] Furthermore, for each here discussed binding situation residual surface silanol groups are possible even at high grafting density of coupling agent molecules (see Figure 6).^[144, 166]

A mixture of different organosilane surface structures can be assumed to be present on an organosilane modified SiO₂ nanoparticle surface. The fact that SiO₂ nanoparticle surfaces are non-ideal surfaces complicates the analyses of the products. On real surfaces, the amount of Si-OH groups per Si-surface atom can vary (resulting in siloxane terminated regions, free silanols, geminal silanols) and thus the organic coupling agent layer structure, whereas ideal surfaces would have a distinct surface OH structure.^[187]

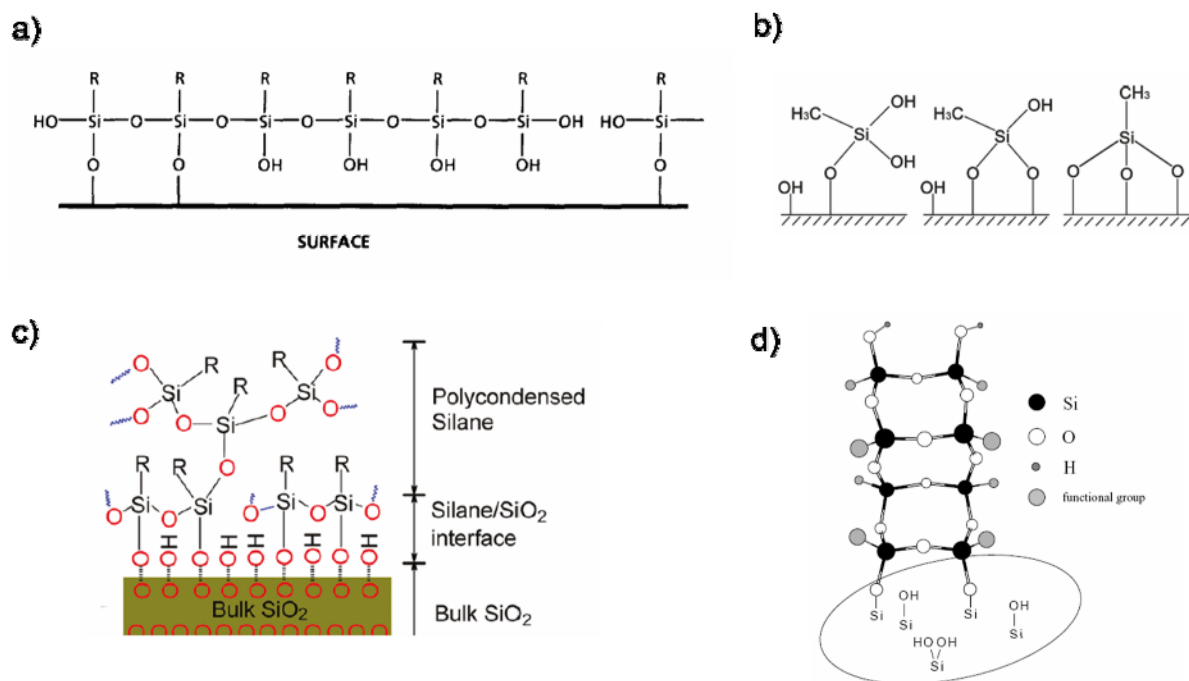


Figure 6. Frequently described structures of silane coupling agent layers from tridentate molecules, bond to hydrophilic SiO₂ surfaces (R...organic moiety). a) lateral cross condensed monolayer (R here: long alkyl chains),^[144] b) mono- bi- and tridentate binding modes of small methylsilane molecules,^[171] c) polycondensed organosilane (multi)layer^[185], d) usual ladder type structure of organosilane surface layer.^[166] The drawings were adapted from literature cited.

For the surface modification of SiO₂ nanoparticles with silane coupling agents, generally, three different approaches are applied:

- The *post*-modification approach, where a SiO₂ nanopowder is treated with silane coupling agents. A common method is to reflux the nanopowder dispersions in a non-polar, non-protic medium, such as toluene, with organotrichlorosilanes in the presence of traces of water,^[145] or the treatment of SiO₂ nanopowders with alkoxy silanes in polar protic media, such as alcohols, often by using a basic catalyst.^[186, 188] The *post*-modification approach can have the disadvantage that, as the nanopowder is isolated before surface treatment, irreversible aggregation phenomena can reduce the dispersibility of the powder.
- The *in situ*-modification approach where the particle formation and surface modification proceed in one step. *Van Blaaderen* and *Vrij* established a method in which they perform a sol-gel process from mixtures of tetraethylorthosilicate and a trifunctional coupling agent to directly produce modified nanoparticles in one pot. However, due to the presence of additional parameters (coupling agent type and concentration), the sol-gel process is more difficult to control and the particle densities vary as organic compounds can be incorporated into the particle bulk.^[189]
- A quasi *in situ*-modification, where particle formation and functionalization is performed in one pot, but in two different chronologically separated steps. First the particle colloid is generated and then the coupling agent is added to the colloidal dispersion. This procedure allows a better control of both processes and their results (particle size and coupling agent grafting density) but with the advantage, compared to the *post*-modification approach that the nanoparticles are not isolated as a powder. Thus, the dispersibility of the particles is not as likely to be affected by aggregation via silanol condensation as compared to a *post*-modification approach.^[116, 148]

The variation of the organic moiety at the inorganic surface is possible because of the plethora of commercially available organosilane coupling agents. If the requested function is commercially not available the silane coupling agent can also easily be synthesized via a hydrosilation reaction of an unsaturated bond with trialkoxysilane.

1.4.2 Organophosphorus coupling agents

Organophosphorus coupling agents allow the formation of strong covalent bonds to many transition metal oxides.^[149, 190, 191] Two major advantages, compared to traditional silane coupling agents, make this coupling agent class interesting for many applications: Firstly, these reagents do not undergo homo-condensation reactions under the usual synthetic conditions, which results in structurally more defined organic surface layers.^[149] Secondly, these molecules interact exclusively with the surface hydroxyl groups or coordinative unsaturated metal atom centers.^[181]

One of the few limitations of the application of organophosphorus coupling agents is the surface modification of silica substrates, as the P-O-Si-bond is not stable towards

hydrolysis.^[99, 192] However, for SiO₂ the chemistry of silane coupling agents is very well established and in this case superior. Thus, these two complementary classes, organophosphorus and silane coupling agents, cover the application range for almost every possible metal oxide substrate to obtain strong attachment of organic groups.^[99]

The chemical structures of the most important anchor groups of common organophosphorus coupling agents for the modification of metal oxide substrates are shown in Figure 7. The phosphoric acid derivatives (Figure 7a) and the organophosphonic acids (Figure 7b) are the best surface modifying agents for metal oxide surfaces, resulting in the strongest attachment and thus, most widely applied.^[181] As listed in Table 1, these molecules form stable surface modifications on many transition metal oxide substrates such as TiO₂,^[149] ZrO₂,^[98, 152, 153] Y₂O₃,^[155] Fe₃O₄,^[156] and many other. Thus, they can be used to modify almost every metal oxide nanoparticle but also oxidized metal substrates.^[193] Besides these two major anchor group types, also phosphinic acids^[149] (Figure 7c) and phosphine oxides^[194] can be applied (Figure 7d) as coupling agent anchor groups for the modification of nanoparticles.

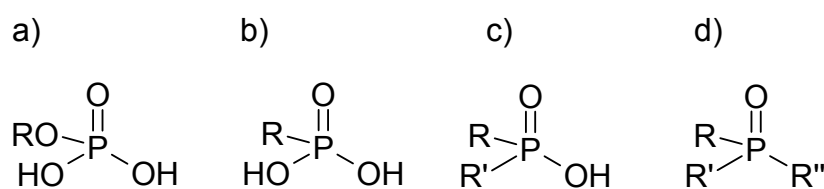


Figure 7. Prevalent anchor groups of organophosphorus coupling agents (R, R', R'' ... organic moiety): a) phosphoric acid (monoester), b) phosphonic acid, c) phosphinic acid, d) phosphine oxide.

As phosphonic and phosphoric acids show similar reactivity and surface bonding behavior,^[192, 195] the surface anchoring of phosphonic acids on metal oxides will be discussed exclusively further on in this chapter.

The binding of the phosphonic acid group to the metal oxide surface proceeds via a condensation reaction of M-OH with P-OH under cleavage of H₂O and formation of stable P-O-M-bonds. This reaction is catalyzed by the presence of protons. Furthermore, the P=O groups can form additional coordinative bonds to *Lewis* acidic metal centers.^[181]

The selective surface reaction and the high reactivity of these molecules (specific reaction and no homo-condensation) improve the process of nanoparticle surface modification significantly and allow very mild conditions. In a typical surface modification process,^[149] a coupling agent solution is added to a nanoparticle dispersion and the coupling agent molecules are strongly chemisorbed from the solution to the nanoparticle surface within minutes at room temperature.^[196, 197]

Since hydrothermally prepared metal oxide nanoparticles usually contain high amounts of OH surface groups,^[198] these organophosphorus coupling agents are highly appropriate for the modification of hydrothermally prepared ZrO₂ nanoparticles. Furthermore, the surface

coverage of phosphonic acids on metal oxide surfaces can be rather high, comparable to trifunctional silane molecules. For example, when $\sim 24 \text{ \AA}^2$ steric demand of one phosphonic acid molecule can be assumed, which is given on perfect metal oxide surfaces with no defects and hydroxyl termination,^[149] a maximum grafting density of $\sim 4.3\text{-}4.8$ molecules/nm² for one monolayer on real powder samples can be achieved. This assumption is, of course, only possible when the organic moiety is smaller than the anchor group and a dense packing of the surface bond molecules is allowed.^[182]

The chemical structure of metal oxide surface bond phosphonic acid molecules has been studied best for the system of TiO₂, which will be discussed in this chapter. Similarities in chemical reactivity between TiO₂ and ZrO₂ allow for a general treatment of both oxides in the same context.^[181] However, the type of predominant binding situation of the organophosphonates (bidentate, monodentate, etc.) can vary when chemically more different substrates as Ti and Zr oxides (e.g. oxides of Mn, Ni, Mo, Cr, Fe) are applied.^[193]

Due to their multidentate character, phosphonic acids (and alkylphosphoric acids), various binding situations are possible. Experiments with cluster model systems^[199] and FT-IR^[149] as well as ¹⁷O-^[190] and ³¹P NMR^[149] studies allowed conclusions on the predominant binding situations. The presence of (a) monodentate, (b, c) bridging bidentate, (d) bridging tridentate, (e) chelating bidentate, (f-h) additional hydrogen-bonding interactions, is proposed by *Mutin et al.* (Figure 8).^[190]

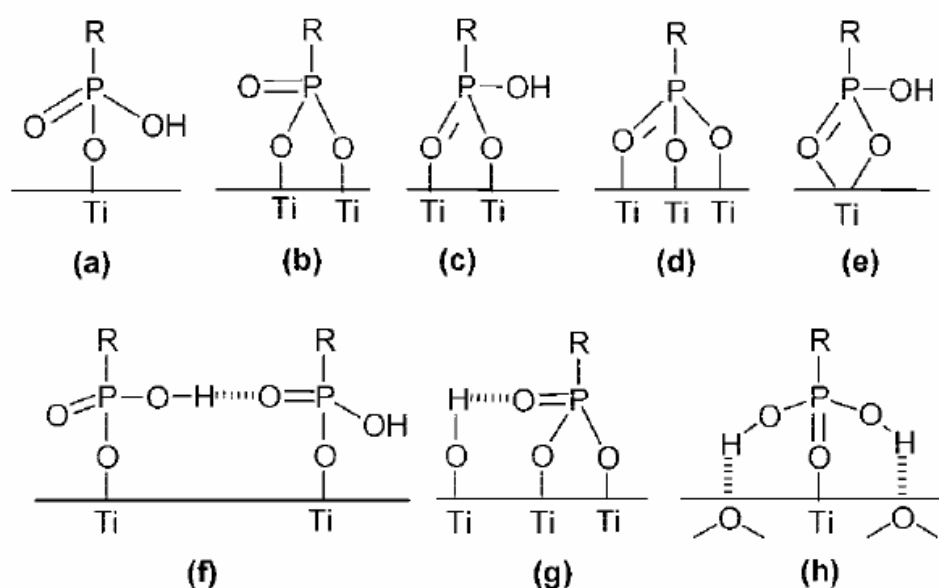


Figure 8. Schematic illustration of various binding modes of organophosphonic acids on TiO₂ according to *Mutin et al.*: (a) monodentate, (b, c) bridging bidentate, (d) bridging tridentate, (e) chelating bidentate, (f-h) additional hydrogen-bonding interactions.

Due to the possibility of these organophosphorus molecules of the formation of more than one stable covalent bond to metal oxide surfaces, these molecules are very often superior to other coupling agents, e.g. such as carboxylic acids or sulfates and sulfonates.^[155, 193] In

nanocomposite research, it has been demonstrated by *Agostiano et al.*, where phosphonic acids were compared with carboxylic acids. Both systems consisted of a long alkyl chain moiety with similar chain length and were applied for the preparation of TiO₂ / PMMA nanocomposites.^[35] Phosphonic acids showed much stronger binding properties to the TiO₂ surface as the previously surface bond carboxylic acids were replaced by them. In the case of the application of phosphonic acids, they could obtain much more homogeneous nanomaterials.^[35] Currently, the relatively new field of the application of phosphonic acids in inorganic-organic nanocomposites is increasing for this reason. Some examples of the current research are given below:

- dodecyl phosphonic acid @ TiO₂ in PMMA^[35]
- t-butyl phosphonic acid @ ZnO in PMMA^[43]
- n-octyl phosphonic acid @ TiO₂ or ZrO₂ in PMMA^[36]

In topical research, often only simple alkyl groups are applied as an organic moiety of organophosphorus coupling agents, to provide organophilicity to metal oxide surfaces for interfacial compatibilization (see listing above). Since the synthetic chemistry of organophosphorus compounds is well established, starting from the beginning of the 20th century,^[200] the variation of the organic moiety is possible applying well known reaction procedures such as the *Arbuzov* reaction,^[201] the *Michaelis-Becker* reaction^[202] or a radical addition of allyl-R molecules to H-P(OR')₃ molecules^[203] in analogy to hydrosilation reactions.

1.4.3 Self-assembled-monolayers on nanoparticle surfaces

To increase the compatibility of the, often hydrophilic, inorganic surface (metal oxide nanoparticles) with hydrophobic media such as solvents or polymers, in most cases long alkyl chain spacer coupling agents are applied as an organic moiety for coupling agents. It has been known for many years that such long alkyl chain coupling agents can form self-assembled monolayers (SAMs) on flat substrates.^[138, 147]

The highly ordered monolayers are two-dimensional structures that form spontaneously on the surfaces of various compounds and elements.^[147] Long alkyl chain SAMs (surface bond via e.g. silane,^[147] thiol^[164] or phosphonic acid^[197] anchor groups) are typically packings of alkyl chains, where the alkyl chains interact with neighbored ones via (lateral) *van der Waals* interaction forces, which stabilizes the SAM structure. The high quantity of interactions makes such long alkyl chain SAMs thermodynamically very stable, even though *van der Waals* forces are weak compared to other chemical interactions.^[138, 147] Thus, the longer the alkyl chains, the more ordered is the resulting SAM structure.^[204] For phosphonic acids on oxide surfaces, C8-alkyl chains form rather non ordered liquid like structures, C12-chains form moderately ordered structures and C16, C18 and longer chains form highly crystalline

well ordered SAM systems.^[205] In well ordered SAM systems, usually the surface bond alkyl chains are in all-trans configuration^[206] which allows a maximum grafting density.^[98] These facts are visualized in the scheme in Figure 9 at the example of alkylphosphoric acids @ TiO₂.^[207]

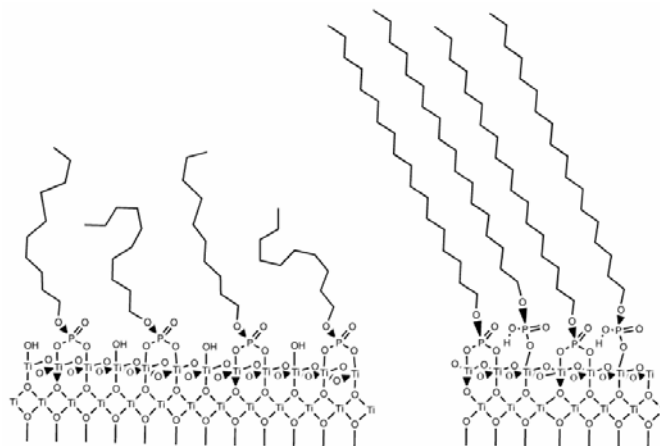


Figure 9. Structure of alkyl-phosphoric acid SAMs on TiO₂ according to *Spencer et al.*: Longer alkyl chains form dense, more ordered SAM structures (right), compared to shorter chains (left).^[207]

Two extreme types of growth mechanism of such alkyl SAMs are proposed: An island-like growth and a homogeneous growth (random attachment of single molecules) of SAMs (Figure 10).^[147, 183] Generally, as proposed by *Fadeev* and *Helmy*, trifunctional silanes tend to island-like growth whereas phosphonic acids tend to homogeneous growth. Both result in comparably high, maximum grafting density values (4.3-4.8 groups/nm²), when long alkyl chains are applied.^[182] As the self-assembly process is a thermodynamically driven process, the temperature plays also an important role in the SAM formation: At higher temperatures an island type growth mechanism dominates in most cases.^[183, 208]

The growth kinetics of typical SAMs is very fast. *Whitesides et al.* extensively investigated the growth of alkylthiol SAMs on gold substrates and proposed two growth steps. First, a monolayer is adsorbed very fast (within seconds to minutes) and then the defects in the SAM are healed within a slower step (several hours) to give highly ordered, densely packed SAMs.^[209] For phosphonic acid SAM growth on flat oxidic substrates, atomic force microscopy investigations in several studies in literature revealed similar time scales for the growth kinetics.^[196, 197]

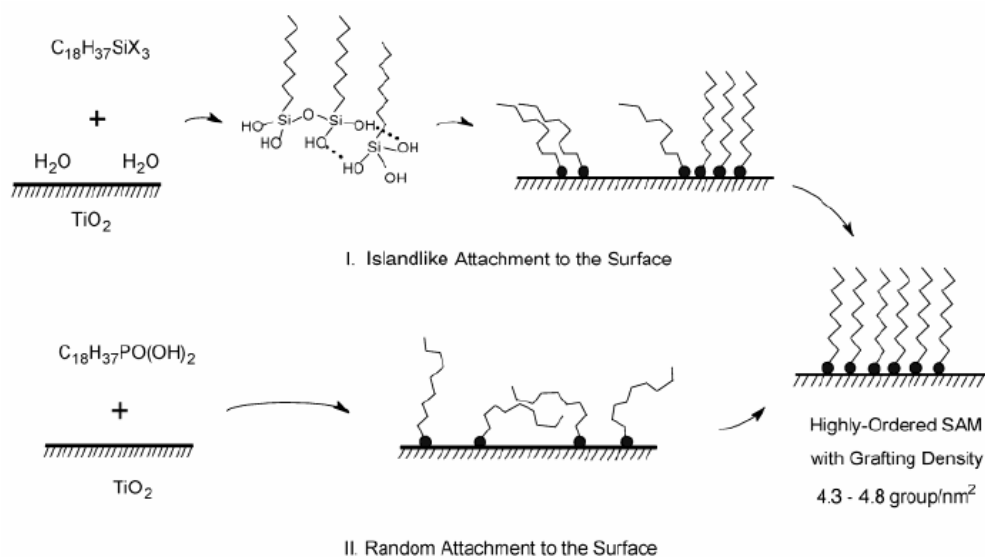


Figure 10. Two, fundamentally different, mechanisms of (dense) SAM formation, according to *Fadeev and Helmy: Island growth versus homogeneous growth* (random attachment of single molecules) for the example of C18 phosphonic acids and -trichlorosilanes on TiO₂.^[182]

This SAM effect, as it is known on flat substrates, is also described for nanoparticles in literature^[210-213] as it seems to play an important role in the preparation of homogeneous dispersions of hydrophobized nanoparticles. As discussed above, long alkyl chains are highly useful surface compatibilizers, as they provide high hydrophobicity but also allow a higher grafting density due to the SAM effect, which is desirable in terms of homogeneous inorganic-organic nano-dispersions. However, another effect described in literature, is connected to the application of long alkyl SAMs @ nanoparticles, which negatively affect the dispersion quality. Alkyl-bilayers between different particles can be formed,^[214-216] leading to a formation of nanoparticle assemblies and thermodynamically very stable agglomerates.^[213, 217, 218] These agglomerates are difficult to break via common methods (e.g. ultrasound) which is undesirable in terms of homogeneous nanomaterials. *Lennox et al.* proposed, for example, already in the year 1997 the existence of such an inter-particle "zipper" effect from their investigations of alkylthiols on gold nanocrystals (Figure 11). Nowadays, with the preparation of homogeneous inorganic-organic-nanocomposites by re-dispersing hydrophobic nanopowders in organic media, this phenomenon has become an actual topic, which is also of great technological importance and interest. This strong assembly phenomenon is very often intentionally exploited in nanoparticle self-assembly,^[133, 218, 219] but unwanted when homogeneous nanocomposites should be prepared.

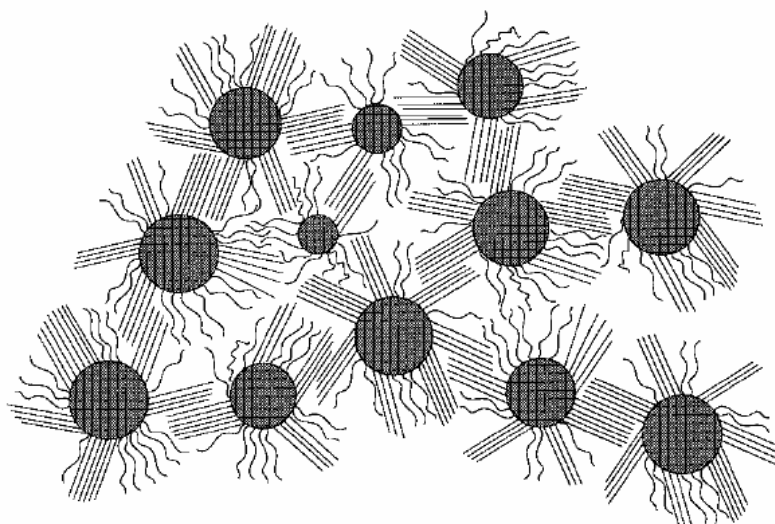


Figure 11. Schematic two-dimensional representation of agglomerates of long alkyl chain modified nanoparticles in a dry nanoparticle powder, according to *Lennox et al.* who investigated alkylthiols@Au nanocrystals.^[220]

Furthermore, other important issues arise when SAMs at nanoparticles are investigated: Nanoparticles exhibit a relatively high surface energy and their surface shows a nanoscopic curvature. These differences of nanoscopic structures compared to macroscopically flat substrates and their impact on the SAM structure are not negligible:

Due to the high surface energy, for very small nanoparticles and clusters (showing higher surface energy as larger objects), a strong intercalation of chains can occur to compensate the high surface curvature. For example long alkyl chains on gold nanoparticles/clusters with 2 nm diameter^[220] are highly ordered, and hydrocarbon- as well as fluorocarbon-chains on 4 nm zirconia nanoparticles are stronger ordered than on 20 nm zirconia particles.^[213]

On the other hand, it has been found that a strong nanoscopic curvature does not allow a dense SAM formation for geometrical reasons (Figure 12).^[221-223] According to a study from *Batteas et al.* long alkyl chains are not able to form well ordered SAMs on strongly curved, spherical, small, nanoparticles, for geometrical reasons particularly when the dimensions of coupling agents are in the range of the dimensions of the nanoparticle.^[222]

Thus, strong ordered SAMs on plane crystal facets of nanoparticles and even on small facets of clusters have been observed in several studies.^[160, 211, 213, 224]

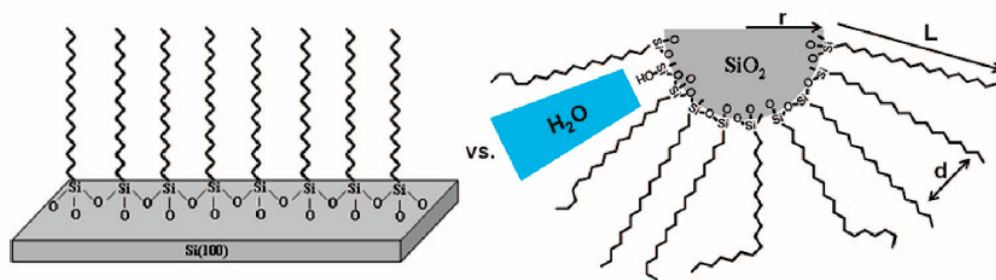


Figure 12. Long alkyl SAMs show higher chain ordering on flat substrates (left), compared to substrates with strong curvature, e.g. spherical nanoparticles, (right). Scheme from *Batteas et al.*^[222]

Furthermore, for nanoparticles where a strong SAM ordering formation occurs major questions are how the thermodynamic driving force for such surface-aggregates can be reduced and how their formation affects the nanoparticle agglomeration behavior.

A possible method, which can be used to study the influence of self-assembled monolayer formation on particle agglomeration behavior and to intentionally tune the long alkyl chain ordering, is the disordering of the surface bond long alkyl chains by co-adsorbing a disturbing molecule to form a mixed monolayer. This approach was already investigated for macroscopic substrates in literature, e.g. to tune the surface wettability, by using mixed monolayers of different alkanethiols on a gold surface to decrease the overall alkyl chain ordering in the surface layer.^[164, 225-230] However, only little is known for the functionalization of metal oxide surfaces, e.g. the formation of mixed phosphonic acid monolayers.^[231] The idea in this work is to explore, whether such a method is transferable to nanoscopic facets of transition metal oxide nanoparticles. Furthermore, it is an intention to evaluate how the alkyl chain surface ordering is connected to the particle agglomeration behavior. Up to now, the mixed surface modification of nanoparticles has been investigated basically for mixed alkyl thiols on gold nanoparticles, e.g. as emulsion stabilizing agent,^[212, 232] to control the spacing between deposited particles,^[233] to fine-tune a certain physical surface property,^[234] or to dilute a surface bond functionality for biological applications.^[235] For technologically highly relevant, transition metal oxide nanoparticles like ZrO_2 (ceramics, nanocomposites) little is known about such phenomena. SAM@transition metal oxide nanoparticles have been reported to play a significant role for tuning the dispersion behavior of the particles^[156] but knowledge about the underlying principles is lacking currently. Furthermore, literature reports mainly short n -alkyl chain coupling agents as disordering co-coupling agents.^[225, 229] However, no systematic studies on different organic moieties for the use as co-coupling agent molecules in mixed monolayers, such as aromatic systems or iso-alkanes, and their influence on the ordering of the particle surface long alkyl SAM has been carried out until yet. This will thus be investigated within the scope of this work. Primarily, dodecyl chains will be applied, as these long alkyl chain self-assemblies are non-crystalline at room temperature.^[205, 236] Contrary to the usually applied octadecyl coupling agents, the tendency of these molecules to form very strong inter-particle bilayers is already reduced, but the molecules already provide certain hydrophobicity.

Commonly, the structures of SAMs on macroscopic substrates are investigated via atomic force microscopy, in combination with contact angle measurement and ellipsometry.^[237] For the structural characterization of SAMs@nanoparticles, usually spectroscopic methods are applied (FT-IR^[238] and ¹³C NMR^[205]) which allow to investigate the SAM ordering degree via monitoring of the number of gauche defects in the long alkyl chains.

Besides mixed monolayer formation the use of alternative, non-alkyl chain spacers, to overcome the "zipper" effect, will also be investigated in this work.

As discussed within this chapter, the spacer part of the coupling agent molecule can play an important role for the manufacturing of homogeneous nanodispersions. In the following chapter, the role of the optional functional end group will be explained.

1.4.4 The role of functional end groups

The variation of the organic moiety of coupling agent molecules (and thus of the properties of the surface of organically modified nanoparticles) in the scope of polymer nanocomposite preparation, in order to tune the particle-matrix interaction, has two basic aims:

- (i) Providing organophilicity (in most cases hydrophobicity) to the surface to enhance the dispersion quality.^[64]
- (ii) Enhancing the interfacial adhesion between inorganic and organic compound to guarantee mechanical stability of the nanocomposite material (e.g. avoiding a pull-out of the nanoparticles at failure).^[52]

Besides *van der Waals* interactions via the (alkyl) spacers, optional functional end groups can provide additional possibilities of interaction and thus enable interface compatibilization and adhesion. Table 2 lists possible types of interactions with different strength between inorganic and organic moieties. Covalent bonds between matrix and particles can be formed during *in situ* nanocomposite preparation processes when polymerizable end groups are applied, as discussed in chapter 1.1.

Table 2. Types of interaction which can be obtained between an inorganic and an organic moiety ^[1] using surface modifiers under variation of the organic moiety / functional end group of coupling agents.

interaction type	interaction strength (kJ / mol)	interaction range	examples of organic moieties on nanoparticles
<i>van der Waals</i>	~50	short, nonselective, non directional	alkyl chains, ^[220] fluoroalkyl ^[213]
hydrogen bonding	5-65	short, selective, directional	carboxylates (end group) ^[239]
coordination bonding	50-200	short, directional	bipyridines ^[143]
ionic	50-250	long, nonselective	ammonium, carboxylate ^[234]
covalent	~350	short, irreversible	epoxide, ^[32] methacrylate ^[75] (during <i>in situ</i> polymerization)

Thus, spacer and functional end group of coupling agent molecules are both of great importance for the systematic interface tuning of inorganic/organic interfaces in polymer nanocomposites.

1.4.5 Polysiloxane modified nanoparticles

Polysiloxanes are highly chemical inert and thermally stable polymers.^[240] The most popular class of polysiloxane compounds in application and research are poly(dimethyl siloxane)s (PDMS).^[240] Linear PDMS chains are hydrophobic^[241] and highly flexible,^[242] compared to alkyl chains. Because of the high chain flexibility (low conformational change barrier) PDMS chains are in liquid state at room temperature and far below^[243] whereas long alkyl chains tend to crystallize, as discussed in the previous chapter. Therefore different surface properties can be expected when PDMS chains are applied for surface modification of nanoparticles, leading to different interfacial properties in nanomaterials. However, very little is known in literature about such PDMS interfacial tuned nanomaterial systems up to now, especially about how the interfacial properties affect macroscopical materials properties of thus prepared nanocomposites. Consequently, studies on this topic are carried out within this work to get more insight in an alternative spacer based type of surface modification, which is supposed to offer larger perspectives in systematic chemical surface tuning of nanoparticles.

Linear (poly)siloxane chains form elastomers when crosslinked. Recently, many developments in the field of inorganic nanoparticle filled polysiloxane elastomers have been carried out, offering new perspectives in elastomers technology, e.g. for tire-, biomedical-, aerospace- and electrostrictive elastomer nanocomposite applications.^[244]

However, only a few examples are given where PDMS chains have been used in common polymer nanocomposites or for nanoparticle surface modification:

- *Zhao and Samulski* systematically combined polysiloxanes with common polymers, such as polystyrene or poly(methyl methacrylate) (PMMA), and inorganic layered silicates. They obtained materials with high thermal stability and significantly altered mechanical properties, compared to combinations without PDMS.^[245]
- *Rogalski et al.* coated the surface of highly porous silica with linear and branched PDMS. They applied this system for the immobilization of catalysts. Thereby, the flexibility of PDMS chains could be exploited, which resulted in excellent wetting and diffusion properties at the interface.^[246]
- *Yuen et al.* applied PDMS for the surface functionalization of Ag nanoparticles. They reported excellent reduction of agglomeration of the ~4 nm diameter nanoparticles due to the application of PDMS.^[247]
- *Ganachaud et al.* applied PDMS modified alumina nanoparticles in PMMA nanocomposites and obtained excellent thermal stability and flame retardant properties, superior compared to PMMA materials with alkyl based surface modifications.^[248]

Still, none of the approaches described in literature so far applies a system, in analogy to alkyl chain coupling agents, consisting of an anchor group, a spacer chain and a functional (e.g. polymerizable end group). Other types of silicone coupling agents are already well known. Mostly α,ω -diol-PDMS molecules were used for the surface modification of SiO_2 ,^[249] but also novel bis-phosphonic acid PDMS molecules were applied.^[248] However, applying such bis-anchor group molecules is not appropriate for the use as a coupling agent in polymer nanocomposites in analogy to alkyl chain coupling agents, as the possibility of the introduction of a polymerizable group is not given.

Therefore, in this work, a synthetic pathway to PDMS (and oligomeric siloxane) molecules will be developed, which bear an anchor group on one chain terminus and a functional group on the other terminus.

The major reasons for establishing this new class of coupling agent molecules within the scope of this work are:

- (i) Applying flexible PDMS spacer based coupling agents to hydrophobize surfaces could be another possible solution to avoid alkyl chain intercalation leading to strong particle agglomeration ("zipper" effect).

(ii) Unique (mechanical) material properties are expected from PDMS modified nanoparticle filled polymer matrices by building a soft interfacial region between polymer matrix and inorganic nanoparticle.

(iii) PDMS spacer chains offer different surface properties compared to classical alkyl based molecules. For the application in silicone elastomer materials, e.g. polysiloxane nanocomposites,^[244] a PDMS modification is considered to result in interfacial fit a better than for alkyl based systems.

(iv) New functional, well-defined, silicone layers have high potential in applications in the field of microelectronics, lithography, as well as coating technology.

(v) Besides the major coupling agent function of such bifunctional telechelic molecules, another interesting application of heterotelechelic PDMS molecules would be in the field of PDMS block copolymers, when these novel molecules are used as macro-initiators.

Furthermore, within the scope of the preparation of PDMS modified nanoparticles in this work, also a *surface-grafting from* route will be developed. Investigations on PDMS chain modified nanoparticles should establish a new class of coupling agents plus generate materials with uniquely altered materials properties.

1.4.6 Polymer shell modified nanoparticles

The preparation of inorganic particles with a grafted polymer shell has been investigated intensively in several studies in literature.^[140, 250-252] The use of such nanoparticle systems is expected to be advantageous in many applications, such as coatings and film formation^[252] as well as assembly applications,^[253] rheological fluids, paints, etc.^[140, 251] The idea behind the formation of such materials is the following: If a polymer shell of the same polymer type as the matrix in which the particles are incorporated is used, the interfacial match within the material is assumed to be very high because of the chemical and structural similarity of surface modification and matrix.

It is known from studies in literature that polymer grafted nanoparticles show excellent dispersion stabilization properties and are expected to be superior to nanoparticles, modified with molecular coupling agents in specific cases. For example, *Lennox et al.* have demonstrated that gold nanoparticles with covalently attached polymer chains show high dispersion stability, superior to shorter chain modified nanoparticles.^[128] Additionally, of course, strong surface bond polymers show better thermal and chemical stability, compared to common systems where polymer chains are only adsorbed on the nanoparticle surface.

However, when polymer shell nanoparticles are applied in nanocomposites preparation an additional phenomenon has to be taken into account: The length of the polymer chains forming the particle shell must exceed the polymer chain length of the matrix material to thermodynamically promote a homogeneous mixing of the compounds by allowing a penetration of matrix chains into the particle core. This is described theoretically in literature

as a wetting phenomenon (small polymer brushes versus flexible behavior of longer chains).^[128, 254] Only a few experiments, where polymer shell nanoparticles have been incorporated into polymer matrices, have been presented up to now in literature studies. Besides some fundamental investigations on the mixing behavior, there is a lack of technological studies and investigations of materials properties of such nanocomposite systems. One example from *Jestin et al.* confirms the assumptions on the polymer chain length ratio between matrix and particle bond chains in polymer nanocomposite materials, as discussed above. The authors of the study applied polystyrene shell nanoparticles in polystyrene matrices and found via TEM measurements that highly homogeneous nanocomposites can be obtained when the molecular weight of the matrix chains exceeds the molecular weight of the chains at the particles.^[128]

The preparation of well-defined polymer shell nanoparticles is commonly carried out via controlled grafting of (linear) polymer chains *from* the nanoparticle surface.^[140, 250, 252, 255]

Prucker and *Rühe* developed one of the first controlled polymer surface grafting reactions *from* inorganic particles. They modified the surface of SiO₂ with azo-initiator molecules and grafted with polystyrene in a simple free radical polymerization approach.^[255, 256]

Moreover, *Kickelbick* and *Holzinger* established synthetic routes to a variety of polymer shell metal oxide nanoparticles, such as the oxides of Fe, Ti, Zr, Zn, etc. They built a well-defined PMMA shell around the (initiator modified) nanoparticles by a controlled living radical polymerization approach.^[140, 250]

1.5 Polymer matrices in this work: What is the state of the art in polymer nanocomposites research?

How can interfaces of polymer nanocomposites be tailored to tune macroscopic materials properties systematically? From the plethora of different polymers three polymer matrices for nanocomposites preparation are investigated within this work: The common thermoplasts poly(methyl methacrylate) (PMMA), polystyrene (PS), and a crosslinked epoxy resin system. These three systems are all non crystalline, which eases studying fundamental relations in nanocomposites properties, as the parameter of crystallinity, which strongly affects mechanical materials properties, does not have to be taken into account.^[257]

In the following sub-chapters the general properties and applications of the applied matrix systems, will be discussed. Examples of nanocomposites (especially containing SiO₂ and ZrO₂ nanoparticles) will be given to introduce the current state of the art in nanocomposites research. Advantageous effects of such nanocomposite materials, compared to the neat matrix systems, will be discussed. However, these examples from literature only point out a few advantageous effects of nanocomposites, very often without discussing the general relations between the synthetic parameters (especially surface chemistry) and the observed materials properties.

1.5.1 Poly(methyl methacrylate)

Poly(methyl methacrylate) (PMMA) is an optically clear thermoplastic material with good mechanical properties (tensile strength 48-76 MPa, fracture toughness $1.2-1.8 \text{ MPa}\cdot\text{m}^{1/2}$) and high weatherability. Thus, the major application of PMMA can be found in the replacement of glass. Common PMMA consists of $\sim 75\%$ atactic and $\sim 25\%$ syndiotactic polymer and is usually amorphous.^[257]

The incorporation of particulate nanofillers into PMMA can additionally enhance the mechanical properties of the material. For example, *Lach et al.* incorporated spherical SiO_2 nanoparticles with an average diameter of 26 nm into a PMMA matrix via a solution compounding approach. They obtained homogeneous nanomaterials. However at higher filler percentage (10 wt%), slight agglomeration of the nanoparticles was observed (Figure 13, left). The result of various mechanical tests was that several mechanical properties, such as elastic modulus, *Vickers* hardness and fracture toughness were significantly improved (up to +20%) in the nanocomposite. These reinforcement effects were optimal around 10 wt% inorganic nanofiller. At higher percentages, e.g. 20 wt%, the increase in fracture toughness was less and also other mechanical properties did not increase proportionally to increasing nanofiller content (Figure 13, left). The authors claim that they obtained mechanical properties, superior to any other commercially available PMMA material or PMMA composite material.^[47]

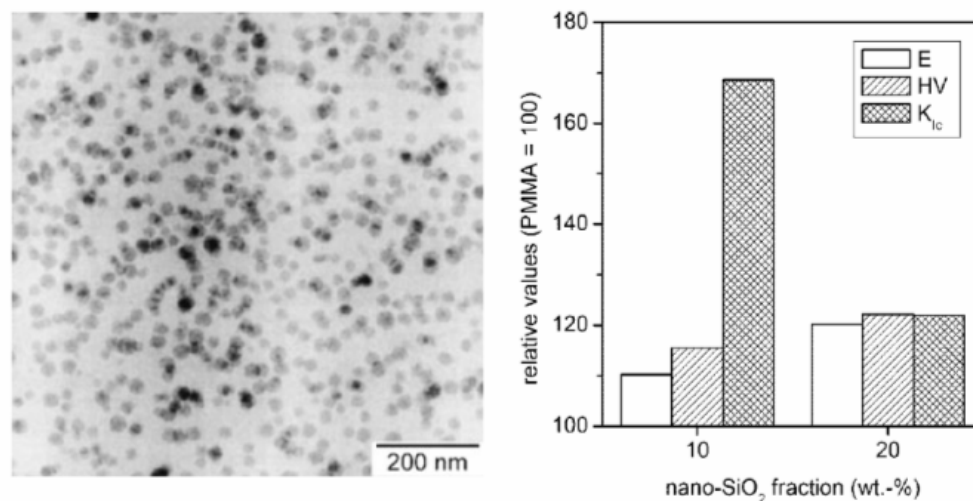


Figure 13. Investigations from *Lach et al.* on mechanical properties of SiO_2 nanoparticle filled PMMA nanocomposites: left image: TEM image of an ultra thin section of 10 wt% SiO_2 nanoparticle containing polymer sample. Right image: Summary on mechanical properties (relative to the neat PMMA matrix) of PMMA/ SiO_2 nanocomposites at different filler degrees. E...elastic modulus, HV...*Vickers* hardness, K_{IC} ...fracture toughness.

In another study, *Hub et al.* investigated the dynamical mechanical properties of PMMA nanocomposites, containing 14 nm diameter SiO_2 particles, prepared via *in situ* polymerization. They could observe a drastic increase in storage modulus (mechanical energy

uptake) of the material due to the incorporation of 8 wt% nanoparticles, by +60%, while the T_g did not change.^[258]

Jeremic et al. incorporated TiO₂ nanoparticles with a diameter of 4.5 nm into PMMA and observed a drastic increase in thermal stability of the nanocomposite materials compared to the neat polymer. The thermal decomposition temperature increased from 325°C to 380°C (differential thermogram peak) due to a change in the oxidative decomposition mechanism. To reach a proper homogeneity, they applied ascorbic acid palmitate as a coupling agent.^[37]

Most studies on PMMA nanocomposites (see also above) describe that mechanical reinforcement effects show a maximum at (higher) filler degrees around ~10 wt%. However, by using already low filler amounts significant effects can be observed in many cases (due to the high generated interfacial area). For example, *Schadler et al.* investigated the thermomechanical behavior of highly homogeneous (shown via microscopic methods) PMMA / alumina (39 nm diameter particles) nanocomposites. They observed a change in T_g due to the polymer interphase fraction already at filler concentrations slightly larger than 0.5 wt%. At higher loadings (5 wt% and 10 wt%), they obtained a plateau in the T_g change indicating that the maximum reinforcement effect is reached. They discuss in their work that due to the incorporation of nanoparticles in PMMA the T_g can both, increase or decrease. The reason for that is a complex combination of possible effects induced by nanoparticle incorporation.^[34]

Many positive effects on mechanical reinforcement of PMMA with metal oxide nanoparticles have been reported in literature recently and this combination of matter seems to be promising in research and application. However, a recent study by *Cangialosi et al.* on PMMA, filled with 8.9 wt% submicron silica spheres, modified with alkyl-moieties, prepared via *in situ* polymerization revealed that the physical aging of particle containing PMMA material accelerates compared to the neat matrix material. They concluded that accelerated aging is a general property of PMMA/SiO₂ nanocomposites. Therefore, taking positive and negative effects resulting from the incorporation of nanoparticles into PMMA into account, optimum conditions for the use of such materials (filler degree, application field, chemistry at interface, etc.) have to be found.^[259]

Furthermore, most of the results in the studies on mechanical reinforcement effects of PMMA with nanofillers in literature can be expected to result from both, micro- and nanofiller effects, as agglomerates of nanoparticles cannot be excluded. This explains the usually high filler degree which is required to obtain significant mechanical reinforcement effects, see examples above.

Agglomeration further plays an important role for optical transparent properties of PMMA nanocomposites containing particulate metal oxide nanofillers. *Wegner et al.* demonstrated this fact at the system of 22 nm diameter ZnO nanoparticles in PMMA. They showed that due to agglomeration of nanoparticles, which occurs at higher filler degrees, optical transparency decreases dramatically. Furthermore, they showed that chemical surface modification of the nanoparticles is the key to reduce agglomeration and improve the transparency of the

material. They applied alkyl moiety nanoparticle surface modifications to obtain transparent nanocomposite films.^[43]

A plethora of studies on metal oxide nanoparticle-filled PMMA has been published during the last years, showing increased mechanical properties. The most popular property changes have been described in the examples above. However, these research highlights are mostly application-based and show single effects. Less is known on general effects which arise due to the interface chemistry of such promising materials. In most of the presented studies in current literature, no chemical interface tailoring has been applied or studied. For this reason, in many cases agglomeration was accepted or a homogeneous dispersion was created by energy affording procedures. In some cases, the surface of the applied nanoparticles was modified with simple, non-functional alkyl moiety based systems to obtain better homogeneity within the materials. For example, *Wegner et al.* have demonstrated in another study that the homogeneity of PMMA / ZrO₂ nanocomposites, prepared via *in situ* polymerization, can be improved by using such simple coupling agent molecules. However, they still observed moderate agglomeration via transmission electron microscopy.^[36]

Nonetheless, a few examples have been recently shown in literature where the dispersion quality of PMMA nanocomposites could be highly improved by chemical surface tailoring of nano-building blocks, using more sophisticated coupling agent molecules.

In a systematic study on *in situ* polymerized SiO₂ / PMMA nanocomposites (particulate 20 nm diameter filler) by *Shipp et al.*, it could be observed that methacrylate end-functionalized nanoparticles (prepared by using silane coupling agents) result in highly homogeneous nanomaterials. They assume that these observations are, to a high degree, the result of surface grafting *through* (copolymerization of particle surface groups with monomer), as they found PMMA polymer chains tethered to the nanoparticles after the *in situ* polymerization reaction.^[30]

These results have been confirmed by *Aleksic et al.* They have demonstrated on a system of methacrylate functionalized (via silane coupling agents) SiO₂ nanofiller (Degussa Aerosil) that the more methacrylate groups are present on the inorganic surface the better is the homogeneity of the nanocomposite material.^[260]

Zhou et al. succeeded in the preparation of highly homogeneous ZrO₂ nanoparticle (3.8 nm crystals, up to 7 wt%) containing PMMA via an *in situ* polymerization approach by the use of 2-hydroxyethyl methacrylate as a coupling agent. They obtained homogeneous, transparent dispersions of particles in the monomer at room temperature which were, however, destabilized at elevated temperatures. As a possible reason for this destabilization phenomenon the relatively weak bonding (they expect only hydrogen bonding to take place) between the coupling agent and the ZrO₂ surface is discussed in the work of *Zhou et al.*^[75] Therefore, the synthetic conditions have to be adapted to obtain homogeneous nanomaterials. A possible solution for this problem would be the use of more stable attached polymerizable groups (e.g. via phosphonic acid anchor groups).

Generally, from these few examples on functional group-modified filler nanocomposites it can be assumed that the structural similarity of monomer/polymer and surface modification as well as the possibility to form covalent bonds between particle and polymer matrix is highly advantageous for the preparation of homogeneous nanocomposites. However, only a few systematic studies are known, where e.g. different surface modifications are compared and the influence on the dispersion quality is investigated. Similarly, not very much is known about the effect of the presence of polymerizable surface groups on mechanical properties on the final materials. Generally, the discussed effects of structural similarity and polymerizability of surface modification on nanocomposite homogeneity can also be assumed to be valid for other *in situ* polymerized nanocomposite systems and thus also for the other two mentioned polymer types, namely polystyrene and epoxy resins.

1.5.2 Polystyrene

Polystyrene (PS) is an optically clear, thermoplastic, rigid material. Common PS is atactic and amorphous and one of the most widely used low-cost plastics. Prominent applications of PS can be found in the fields of packaging industry, PS foams, construction, automotive, electronics, housewares, etc. Common PS shows a tensile strength at break of 30-60 MPa, but the material is usually relatively brittle. Moreover, PS is not very resistant towards chemicals and e.g. well soluble in almost any organic solvent.^[261] However, PS is rather widespread in application and research. Furthermore it is easy to prepare and study and because of its reproducibility in synthesis and low complexity in thermomechanical behavior (no crystallization phenomena, high conversion and thus no *post* polymerization occurs, etc.) one of the most frequently studied polymer matrices in literature in order to derive general relations in fundamental nanocomposites research.^[57, 58, 254] This is the major reason why PS has been selected to be applied in the present work.

Most literature studies on nano-reinforced PS deal with organoclay systems,^[262, 263] but in the present work, particulate fillers are investigated and thus discussed in the introductory part. A few examples on typical mechanical reinforcement effects, which have been investigated for particulate metal oxide nanofilled PS in a plethora of studies in literature, are given below to demonstrate the state of the art in PS nanocomposite research:

In a recent study by *Fu et al.*, crosslinked PS nanocomposites prepared via *in situ* polymerization including different metal oxide nanofillers have been investigated with respect to mechanical reinforcement. They applied alumina and silica fillers as well as clays. In the study it is reported that already a significant mechanical reinforcement can be observed for relatively low content of nanofiller (0.5 wt%). The highest reinforcement effect could be obtained for clay sheets and Al₂O₃ (~80 nm diameter) nanoparticle-filled system. In both of these cases the *Young's* modulus could be increased by more than 100%. By the use of any type of filler also the *Vickers* hardness increased significantly. Furthermore, they showed that the PS nanocomposites exhibit good shape memory properties by recovery tests.^[264]

Jestin et al. incorporated 5.2 nm diameter SiO₂ nanoparticles into a PS matrix, via solution compounding. They obtained high reinforcement effects and could further show that the

structure of particle aggregates has a huge impact on the rheological behavior of the nanocomposite material.^[265]

Schadler et al. have studied the effect of the interface on thermal properties of 20 nm diameter SiO₂ nanoparticle filled PS prepared via solution compounding. They have shown that the T_g is a function of the interparticle spacing, as T_g is a function of the thickness of the PS film. According to their study T_g decreases for very low interparticle spacing (distances in the lower nano range, < 100 nm). Therefore, when higher filler percentages are applied the thermomechanical properties can decrease and thus an optimum filler amount has to be found.^[266] *Kontou and Antholis*, for example, have studied PS nanocomposites including 16 nm SiO₂ nanoparticle and found a 4 wt% fraction to be optimal for the enhancement of thermomechanical properties.^[267]

For PS / metal oxide nanocomposites more studies on chemical tailoring of the interface (using coupling agents) are known, compared to PMMA nanocomposites. One reason for this fact might be that because of the relatively non-polar nature of PS there is stronger need for a surface modification of the inorganic compound for their use in a PS matrix to obtain homogeneous nanocomposites.

In this context *Lee et al.* carried out an interesting study in which they systematically varied the organic surface group, introduced via silane coupling agent, on submicron SiO₂ particles (130-149 nm diameter) and studied the influence of the surface group type on the dispersion quality of the particles in a PS matrix (solution compounding). Among other organic moieties they introduced methyl-, dodecyl-, octadecyl- and phenyl- moieties at the SiO₂ surface. They observed, via microscopic investigations of the prepared nanocomposite materials that the application of unmodified particles resulted in the lowest dispersion quality and agglomerates in the millimeter size range were obtained. The poor homogeneity is undesired in terms of interface area generation within the material. However, when they applied very hydrophobic surface modifications (dodecyl- or octadecyl) the homogeneity of the prepared nanocomposites was better as compared to less hydrophobic modifications.

Also for the application of the phenyl group for surface modification, they could obtain lower agglomeration due to the structural and chemical similarity of phenyl groups and PS chains.^[64]

In another study *Bateman et al.* investigated the influence of the organic surface group on montmorillonite in PS clay nanocomposites. They compared dodecyl groups with alkyl-styryl- and alkyl-ethylbenzyl- groups and concluded that the structural similarity of surface group and polymer, as well as polymerizability of the end group, are important in terms of the preparation of homogeneous nanocomposites, when *in situ* polymerization is applied.^[263]

For PS nanocomposites even a few studies on the influence of the organic surface group of the inorganic compound on the mechanical properties of the materials exists in recent literature:

Ruan et al. applied unmodified and poly(dodecafluoroheptyl acrylate) surface modified silica nanoparticles (Aerosil 200) in a melt compounding process to obtain PS nanocomposites.

They carried out tensile tests and observed that only when surface modified nanoparticles were applied a reinforcement effect could be observed, whereas the tensile strength for the unmodified filler material was even poor compared to the neat matrix. They explain these observations to be a result of increased homogeneity due to minimization of particle / particle interaction and enhancement of particle / matrix interaction.^[268]

These few examples of studies on chemical interface tailoring in PS nanocomposites show similar relationships like the previously discussed PMMA nanocomposites. The more structurally and chemically similar the organic surface group to the polymer / monomer is, the more homogeneous are the resulting materials. Furthermore, polymerizable groups are advantageous for homogeneity when molecular coupling agents are applied for the surface tailoring of the inorganic compound. Additionally, when polymeric surface modifications are applied, the grafted polymer chain length is important.

1.5.3 Epoxy resins

To study also thermoset polymer matrices for polymer nanocomposites, epoxy resins will be investigated in this work. From a structural chemical point of view, epoxy resins are complex (amorphous) crosslinked organic network systems, contrary to the thermoplastic, non-crosslinked linear polymer chain containing PMMA and PS matrices, which will also be applied in this work.

A variety of different formulations, very often containing bisphenol-A or bisphenol-F based monomer compounds and amine- or anhydride- curing agents in different ratios, is utilized in various applications to obtain tailor-made materials properties.^[269] The major resin types are classified into diglycidyl ether based compounds, novolaks, peracid resins, hydantoin resins, etc.^[270]

Epoxy resins show a wide range of properties, depending on their formulation and processing parameters. Typical properties of epoxy resins are high chemical and weathering resistance, toughness and durability. Epoxy resins exhibit optical transparency when adequate formulation and curing parameters are selected. They show good electrical and thermal insulation properties and better mechanical properties than most other castable plastics. For example, the tensile strength at break can be 30-90 MPa and up to 340 MPa for reinforced bisphenol molding compounds. A typical value for fracture toughness is $0.6 \text{ J} \cdot \text{cm}^{-1} \cdot \text{m}^{1/2}$.^[270]

Epoxy resins are also very widespread in their use as coatings due to their excellent adhesion properties on many surfaces, or applied as adhesives themselves (e.g. application as a structural glue). Therefore, the major application fields of epoxy resins can be found in protective coatings (automotive industry, etc.) and encapsulations of electric and electronic devices. Epoxy resins are also used in construction, e.g. for flooring and paving. When epoxy resins are applied as engineering materials they are often filled with a second compound (e.g. glass fiber, cotton, mineral powders, etc.) to tune their mechanical properties.^[270]

Due to the widespread property and application range of these materials, especially filled epoxy resins have been of great scientific and application interest, already for the last 50 to 40

years.^[4] Within the last few years, epoxy resin science and technology has been focusing especially on nanofilled materials. This is, on one hand, interesting in terms of mechanical materials reinforcement, as it has been discussed in the previous chapters. On the other hand, especially for epoxy resin coating applications, the optical transparent properties of such reinforced materials can be retained, which is possible when nanoparticles (three nano-dimensions) are applied as a filler and homogeneously dispersed within the matrix, as discussed above.

In situ curing is, from a technological point of view, the most important method for manufacturing epoxy resin composites and nanocomposites. In this regard, attention has to be paid to the fact that nanofiller content very often changes curing kinetics^[74] and final matrix properties (crosslinking degree)^[271] within such complex curing mixtures.

Many studies in literature research point out that high mechanical reinforcement can be obtained when metal oxide nanofillers are incorporated into epoxy resins. The best investigated systems are organoclay filled thermosets.^[48, 272]

Zhao and Luo have investigated the mechanical properties of SiO₂ nanoparticle containing anhydride-cured epoxy resin nanocomposites. They observed significant mechanical reinforcement already at 1 wt% filler content. For example, tensile tests revealed that elastic modulus and tensile strength increased due to the incorporation of nanoparticles. However, also depending on the type of curing agent, the nanoparticle filled materials exhibited brittle fracture behavior. Therefore, an optimum between strength and ductility has to be found by variation of the filler degree.^[33]

Zheng et al. investigated thermal-mechanical properties of anhydride-cured commercial epoxy formulations, filled with 20 nm diameter SiO₂ nanoparticles. They observed slight changes in the curing kinetics of the resin due to chemical reactions of the curing mixture with surface OH groups of the SiO₂ nanoparticles during the curing process, which also affected the glass transition temperatures of the materials. Besides these effects, the nanoparticle filled epoxy resin matrices showed significant enhancement of both, flexural strength and fracture toughness. In their study as well as in many other studies the mechanical properties increased with increasing filler amount to reach an optimum (here at 3 wt%) and decrease for higher amounts due to higher agglomeration of the nanoparticles at higher volume fractions.^[74]

Taylor et al. have studied the mechanical properties of 20 nm SiO₂ nanoparticle-containing, anhydride-cured epoxy resin nanocomposites. They could achieve a simultaneous, continuous enhancement of three mechanical property parameters with increasing filler amount. For example the 20.2 wt% nanofiller containing polymer exhibited an elastic modulus of 3.85 GPa (2.96 GPa for neat matrix), a stress-intensity factor of 1.42 MPa·m^{1/2} (0.59 MPa·m^{1/2} for the neat matrix) and a fracture energy of 461 J/m² (103 J/m² for the neat matrix). These significantly large changes could be achieved because the nanoparticles were highly dispersed within the polymer matrix even at high filler contents of 20.2 wt%. The T_g of the material changed by a few °C with different filler amounts but was not expected to impact the described mechanical properties significantly in the described study.^[273]

When clay is used as filler, typically the fracture behavior of the material is significantly altered.^[15, 272] In a study from *Hoa et al.* it was observed on an example of a montmorillonite filled, amine-cured, epoxy resin that the critical stress intensity factor and the critical strain energy release rate were increased by a factor of 2.2 and 5.8 due to the incorporation of 3 wt% nanofiller. They reported a drastic improvement of fracture toughness, caused by the sheet structure of the dispersed organoclay.^[272] This is an advantage of clay fillers compared to particulate fillers. However, by applying clay, no transparent materials can be obtained because the dispersed clay sheets do not show nanostructures in all three dimensions, which is a necessary condition for randomly dispersed objects to obtain transparent materials, see previous chapters.

Furthermore, nanofillers can significantly alter the glass transition temperatures T_g of the final material. *Sun et al.* have demonstrated that this is a nano-related phenomenon, by applying nanoparticles with 100 nm diameter and micron sized SiO_2 particles with 3 μm diameter to prepare epoxy resin nanocomposites by *in situ* curing of a bisphenol A type formulation with an anhydride. For 20 wt% particle containing samples they observed a decrease in T_g by 23°C (compared to the neat matrix) whereas no significant change was observed for the micron size filler containing sample. The authors explain this effects by the high interfacial area which is generated when nanoparticles were used, which causes significant changes in thermal relaxation mechanisms. They describe that the T_g change with nanofiller incorporation is highly related to formulation and processing parameters. Dependent on these parameters, both an increase and a decrease of the values for T_g is possible.^[274] *Chen and Morgan* observed a similar behavior for a different bisphenol F type resin. The T_g s decreased with increasing nanofiller (13 nm SiO_2 particles) amount.^[65]

Many other studies in literature reported similar reinforcement effects and alteration of thermomechanical properties, which makes epoxy resin nanocomposites worth to study. Only a few studies from literature are known where ZrO_2 nanoparticles have been used for fillers in epoxy resins. However, the results from these studies appear highly promising in the scope of development of new materials:

Medina et al. incorporated ZrO_2 nanoparticles (pyrolytically prepared) with a 12 nm average size into a bisphenol-A type formulation via *in situ* curing. They report a significant increase in the complex moduli from dynamical experiments, an increase in tensile strength and fracture toughness, as well as an increase in T_g due to the incorporation of ZrO_2 nanoparticles. They report an opaque appearance of the materials, which is expected to be the result of the presence of agglomerates/aggregates within the material, even though high shear forces (via milling) were applied in the compounding process.^[38]

However, not only from a mechanical property point of view the application of ZrO_2 nanoparticles in epoxy resins is promising. Optical properties, e.g. the refractive index of the nanocomposite, can be tuned via the incorporation of ZrO_2 into an epoxy resin, while the transparent properties can be retained if the particles are homogeneously dispersed in the polymer matrix. This is particularly interesting for epoxy resin materials in terms of coating applications.

For example, *Imai et al.* prepared transparent epoxy resin films (50-80 μm thickness) with high refractive indices by the incorporation of 5 nm sized ZrO_2 nanoparticles (hydrothermally prepared). The refractive indices at 486 nm, 589 nm and 656 nm could thus be increased by more than 0.05 units.^[275] *Harada et al.* report an increase in the refractive index at 589.3 nm from 1.583 to 1.622 due to the incorporation of 18.4 wt%, *in situ* generated ZrO_2 nanoparticles in an amine cured epoxy resin system. The *Abbe* number was thus decreased from 34.2 to 27.6.^[39, 127]

When the nanoparticles show good interaction with the polymer matrix, high dispersion quality is possible, enabling high filler degrees and thus more significant properties changes. Generally, epoxy resins represent a more polar matrix, compared to PMMA or PS. Therefore, it is possible to disperse unmodified metal oxide nanoparticles within this polymer matrix in specific cases, as a few examples from literature have shown. However, in most cases, agglomeration is reported when unmodified particles are used and thus coupling agents are applied to further enhance the interfacial compatibility and adhesion. A typical example is the use of GLYEO (see chapter 1.4). Several studies from literature point out the importance of chemical surface modification of the nanofiller to obtain well-dispersed systems which exhibit strong mechanical reinforcement:

For example, *Li et al.* applied γ -glycidoxypropyl trimethoxysilane-modified 30-40 nm diameter SiO_2 nanoparticles for the preparation of amine-cured epoxy resins. Via FT-IR spectroscopy they showed that the nanoparticles had been chemically linked to the surrounding epoxy resin via their surface epoxide groups during the curing procedure. Due to the incorporation of only 4 wt% surface modified nanofiller, the impact strength of the material could be increased from 9.9 kJ/m^2 to 89.2 kJ/m^2 . An analogous composition, where micron sized SiO_2 filler (3 μm size) has been used, resulted in impact strength of just 17.1 kJ/m^2 . These results point out the superiority of nanofillers to larger filler objects, if they can be homogeneously dispersed, which was accomplished in the discussed study from literature via coupling agents.^[32]

A model system of polyhedral oligomeric silsesquioxanes (POSS), to investigate on the copolymerization of inorganic nano-compounds with epoxy resins, has been applied by *Chiu et al.* They reported (from investigations via spectroscopic methods) that these nano-objects were linked to the resin matrix via surface isocyanate groups, which resulted in highly homogeneous networks showing increased glass transition temperatures and enhanced flame resistance.^[276] These results showed that surface modification with linkable groups can be a way to overcome a possible T_g depression with increasing filler amount, as described earlier in this chapter. In another study by *Laine et al.* who applied POSS, it was shown that also epoxide end group surface modifications are highly appropriate for the formation of homogeneous nanomaterials.^[277]

These highlights from literature point out the importance of chemical surface tailoring (mostly by investigating one single system of surface modification). However, there is a lack of systematic knowledge. For organoclay systems more systematic studies are existing, which

show the influence of various organic surface groups at the inorganic component on the final materials properties.^[48]

In a systematic study by *Mascia et al.*, coupling agents with epoxide-, amino- and thiol-groups were applied for the preparation of epoxy-silica nanocomposites. They showed that the variation of these functionalities resulted in a change of thermomechanical properties. It was concluded that via the variation of the coupling agent the attraction forces between particle and matrix can be tuned, which causes different mechanical properties.^[53]

For particulate nanofiller containing epoxy resins there is a lack of studies in literature on the variation of the organic surface groups at the nanoparticles to tailor particle dispersion and mechanical properties. One comparative study has been published by *Kim et al.* who modified the surface of submicron SiO₂ particles with epoxide- amino- and isocyanate groups and applied these systems, as well as unmodified particles, within the preparation of epoxy resin nanocomposites. They point out that the degree of Si-OH (present on the surface of the non modified SiO₂) substitution is important to obtain significant effects. Furthermore, they conclude from their studies that the surface group has an impact on the overall curing reaction, where the amino group modified particle system led to the highest curing reaction heat. Microscopy studies revealed that the best dispersion quality could be obtained for amino- and epoxide modified particles, whereas for unmodified and isocyanate group modified systems, strong agglomeration / aggregation could be observed. Moreover, microscopic investigations on the fractured surface of these materials revealed that different surface groups led to different interfacial adhesion between the inorganic and the organic compound. While the interfacial adhesion for the amino- and the epoxide- systems was good, it was poor for the unmodified and the isocyanate modified samples and a "pull-out" of the particles from the matrix could be observed in the micrographs, see Figure 14.^[52]

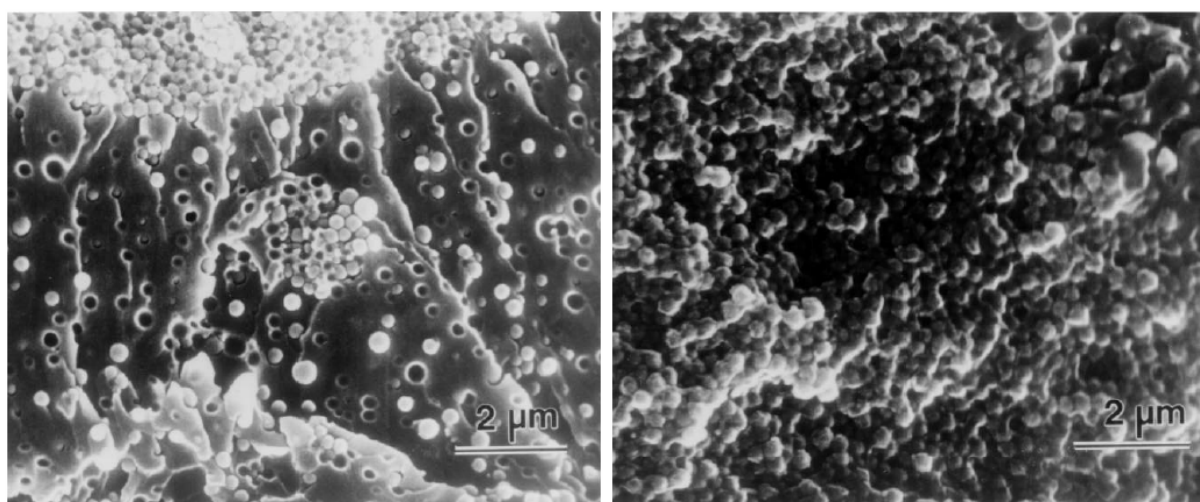


Figure 14. Scanning electron micrographs of fractured SiO₂ nano-sphere filled epoxy resin nanocomposites from a study by *Kim et al.* Left image: unmodified SiO₂ leads to stronger agglomeration and "pull-out" of particles, Right image: epoxide group modified SiO₂ nanoparticles result in lower agglomeration and stronger interfacial adhesion.^[52]

These results point out the high importance of the use of (appropriate) coupling agents for the preparation of metal oxide-filled epoxy resin nanocomposites in terms of dispersibility (transparency, mechanical properties) and interfacial adhesion (mechanical properties). The studies from literature, which have been discussed in this chapter, show a similar influence of the type of surface modification on materials properties as already discussed for the PMMA and PS system in the previous chapters: Organic surface groups which are structurally similar (miscible) to the matrix and which can form covalent bonds to the matrix during the *in situ* curing or polymerization reaction are positively influencing the dispersion quality and interfacial adhesion.

1.6 Structure property relations

For the systematic development of novel polymer nanocomposite materials, the research and the gain in knowledge on structure property relations is of high importance. By applying the approach of chemical interface tailoring it is primarily necessary to know how the structure and type of the chemical surface modification of the nanofiller affects the dispersion structure and the mechanical materials properties of the final nanocomposite material. However, also the size and chemical nature of the nanofiller are important parameters. Within the presentation of the state of the art in research for metal oxide nanoparticle-filled PMMA, PS and epoxy resin nanocomposites in chapter 1.5, the discussed examples from literature already indicate a few relations:

Interface chemistry – Dispersion structure:

High dispersion quality is promoted by the following structural properties of the surface modification:

- chemical similarity to the matrix (miscibility): e.g. hydrophobic long alkyl chains are good for application in hydrophobic polymers such as PS.
- linkable group: If the functional end group can allow strong interactions with the matrix, the dispersion quality is enhanced.

Dispersion structure – Mechanical properties:

High reinforcement effects can be obtained for:

- well-dispersed systems (due to chemical similarity of surface with matrix and linkable groups)
- aggregation alters the rheological behavior

Interface chemistry – Mechanical properties:

- strong interfacial adhesion due to use of linkable group leads to high reinforcement

Such structure property relations are usually generated via the variation of one parameter (e.g. coupling agent end group) and preparation of a series of nanocomposites, containing different filler amounts to quantify the observed effects (changes of mechanical properties, thermal properties, transparent properties, etc.). The results can then be correlated with the dispersion structure of the material. To derive information on the dispersion structure of nanocomposites, the following methods are applied in modern research:

In many studies on the dispersion structure of polymer nanocomposites, microscopic imaging techniques, such as transmission electron microscopy (TEM) of ultra thin cuts,^[80, 128, 265, 266] scanning electron microscopy (SEM)^[52, 278] of fracture surfaces, or AFM (nano-mechanical mapping)^[279] are applied. Visual light microscopic methods are applied for the investigation on larger agglomerates.^[64]

Besides these imaging techniques, scattering techniques are the most widespread applied method for dispersion structure investigations in nanocomposites in systematic studies, having the advantage that the probe volume and thus the statistical accuracy of the method, is usually much higher.^[280] A common and widespread scattering method is SAXS (small angle X-ray scattering).^[173, 265, 280] Thereby, an X-ray beam is scattered at the nanocomposite sample. The scattered X-rays include structural information from the material as the different compounds within nanocomposites have different scattering abilities, depending on their electron density. Through various mathematical models it is possible to derive information on the structure of the nanocomposite probe from the thus generated scattering image. Complex models allow to deduce information on the size and shape of the incorporated nanoobjects (also of polydisperse systems, resulting in distribution functions) as well as agglomerate size and structure (and distribution) of regular ordered or disordered systems.^[280] Another scattering method, which allows to gain similar structural information as from SAXS, is SANS (small angle neutron scattering). SANS is based on the interaction of cold neutrons with matter (elastic scattering) and is also frequently applied in nanocomposite structure investigation. An advantage of SANS compared to SAXS is that neutrons interact strongly also with lighter elements (as neutrons are scattered at the atomic nuclei), e.g. hydrogen atoms, which is not possible with SAXS. This can be advantageous for the investigation of organic structures.^[129, 265]

The, thus generated systematic knowledge on the relations between chemical surface properties of nanoparticles, interface properties in nanocomposites, as well as dispersion quality and mechanical properties of the materials, should help to systematically tailor the interface of nanocomposites to tune the macroscopic materials properties.

2 Research Goals

The aim of this work was the preparation of metal oxide (ZrO_2 and SiO_2) nanoparticle containing polymer nanocomposites by applying a multiscale approach. The materials had to be prepared by a *bottom-up* synthesis starting from molecular precursors. This approach should allow to control and optimize every step and coordinate the different synthetic processes within the nanocomposite preparation - from the nanoparticle synthesis, their surface modification, to their incorporation into polymer matrices. The properties of the thus prepared materials, their dispersion structure, optical transparency and mechanical properties then had to be investigated in dependence of the applied synthetic parameters for the development of structure-property relations. A main focus lies on the chemical surface modification of the nanoparticles and its impact on structural and mechanical properties of the final nanocomposite materials. The idea behind is to control the macroscopic materials' properties on a molecular level. Novel nanocomposites should be prepared and investigated and fundamental aspects had to be investigated within the studies to improve the future development of surface modifications for inorganic-organic nanocomposites. Besides these scientific goals, an important technological goal was the optimization of the organic surface modification of metal oxide nanoparticles in order to obtain nanopowders, which are dispersible in organic systems (solvents, monomers, polymers) with low energy effort. To reach the primary goals of this work, the following points had to be accomplished:

Synthesis of SiO_2 and ZrO_2 nanoparticles

Synthetic routes for SiO_2 and ZrO_2 nanoparticles had to be selected, which allowed a precise control of the particle size and size distribution. Nanoparticle powders with two different particle sizes, one with equivalent diameter in the lower nanorange and one powder with particles with a size in the upper nanorange had to be prepared for each chemical type of nanoparticles, which was necessary to study particle size related effects. This size tuning should be achieved by variation of the synthetic conditions. Furthermore, different particle size determining methods had to be applied and compared in order to find out which method is the most applicable in terms of facileness and which method gives the most reliable results with regard to the true particle size.

Preparation of novel coupling agents

In the scope of systematical chemical surface tailoring of metal oxide nanoparticle surfaces, novel phosphonic and phosphoric acid, as well as trimethoxysilane coupling agents, had to be prepared. End groups (e.g. $-\text{CH}_3$, methacrylate-, styryl-, epoxy-, diol-, etc.) and the alkyl spacer chain length (0 to 12 carbon atoms) of the coupling agents had to be varied systematically. Great attention had to be paid to the development of phosphonic acid coupling agents, analogous to the more established silane coupling agents, for a better applicability for transition metal oxide surface modification.

Anchoring of coupling agents to the nanoparticle surface

The prepared metal oxide nanoparticles had to be surface modified with known and novel coupling agents in order to achieve a strong, stable attachment of the organic moiety to the inorganic surface. Organophosphorus coupling agents had to be applied for the surface modification of ZrO₂ and organotrialkoxysilane molecules for SiO₂. The binding mode of these molecules at the nanoparticle surface had to be investigated via FT-IR and NMR spectroscopy. The grafting density (surface coverage) of these molecules at the nanoparticle surface, as well as the thermal stability of the attached molecules, had to be investigated because of the high importance of these parameters during the preparation of nanocomposites.

Investigations of self-assembled monolayer formation at nanoparticle surfaces

Investigations on the self-assembled-monolayer (SAM) formation at nanoparticle surfaces were carried out and effects of the nanoscopic curvature have been studied. The investigations focused on how the surface ordering can be tuned and how the alkyl chain ordering affects agglomeration and dispersion behavior of modified metal oxide nanopowders. These studies are of great interest with regard to the optimization of the (re)dispersibility of inorganic nanoparticle powders in hydrophobic organic media.

Investigations on alternative surface modifications

Synthetic routes for coupling agent containing spacer chains alternative to alkyls had to be developed, as they may offer a new perspective in surface engineering. In this context polydimethylsiloxane (PDMS) and oligo(ethylene glycol) systems had also to be examined. Within these studies a modular synthesis of PDMS chain coupling agents had to be developed consisting of α,ω -heterotelechelic PDMS molecules with variable chain length. Furthermore, a PDMS grafting *from* approach was examined as an alternative route. In addition, polystyrene shell nanoparticles should be prepared for the application in nanocomposites.

Investigations on the dispersibility of organically surface modified nanoparticles

The dispersibility of the obtained organically modified metal oxide nanoparticles had to be investigated in organic media, such as solvents and monomers, in order to predict the degree of compatibilization between inorganic and organic compounds. Furthermore, the influence of the organic surface modification on physical surface properties of the nanoparticles, such as hydrophobicity, had to be investigated.

Preparation of polymer nanocomposites

Polymer nanocomposites had to be prepared by using poly(methyl methacrylate) (PMMA), polystyrene (PS) and a bisphenol-F-based epoxy resin. The effect of the kind of surface modification of SiO₂ and ZrO₂ nanoparticles as well as the variation of the particle size had to be examined. An additional important parameter to consider is the amount of filler in the polymer matrix. Methods to prepare PMMA-, PS- and epoxy resin nanocomposites via *in situ* polymerization / curing were optimized in order to obtain reproducible results and a structure-property-relationship for materials properties. Furthermore, also solution compounding and melt compounding methods for nanocomposite preparation had to be tested for selected examples, for a technological outlook. Typical characteristics such as the thermal stability and the glass transition temperature were measured.

Investigation of the optical properties of the prepared materials

The optical transparency of the prepared nanocomposite materials, depending on filler degree and surface modification of the particles, had to be analyzed via UV and visible light spectrometry and demonstrated via optical photographs. A technological goal was to achieve to produce transparent polymer films.

Investigations on the dispersion structure of the prepared materials

The dispersion structure of the prepared nanocomposites, namely the degree of agglomeration of the nanoparticles within the material, depending on particle type, size, surface modification and filler degree, had to be investigated by applying small angle X-ray scattering and transmission electron microscopy methods.

Investigations of the mechanical properties of the polymer nanocomposites

Mechanical properties of the prepared nanocomposites had to be measured. For that purpose, hardness tests and dynamical mechanical (thermo)analyses had to be carried out.

Development of structure property relations

The obtained results from the material characterization on the dispersion structure and optical and mechanical properties of the prepared nanocomposites had to be correlated with other important parameters within the nanocomposite preparation, such as nanoparticle surface modification (type of functional end group, spacer type and chain length), particle nature, particle size and filler content. Based on these correlations, structure property relations had to be generated.

The following points are of highest interest and had to be investigated in terms of structure and property change:

- Influence of the chemical particle nature (SiO_2 versus harder ZrO_2) on both properties (structure and mechanical behavior).
- Influence of the particle size on both properties.
- Influence of the surface-SAM structure on both properties.
- The use and influence of alternative coupling agent spacers (polysiloxane, oligo ethylene glycol) on both properties.
- The use of coupling agent end groups which allow a particle-matrix-interaction in between weak *van der Waals* and strong covalent interaction. The influence of particle-matrix-interaction strength on both properties.
- (How) can chemical changes, done only at the interface of the materials, induce a change of the overall macroscopic properties of the material?

3 Results and Discussion

3.1 Nanoparticle surface engineering

This part of the work will focus on the tuning of nanoparticle surface properties applying chemical methods to minimize inter-particle interactions and to maximize particle-environment interaction for their use in polymer nanocomposite materials. The primary goal the development of methods that allow a precise tuning of physical surface properties to yield particle powders which can be easily and homogeneously (re)dispersed in organic media such as solvents or polymer matrices. The highest attention will thus be paid to the influence of the (inert) spacer group in the coupling agent molecule on the nanoparticle dispersion behavior. The further role of possible functional end groups in terms of linking to a polymer matrix will be examined in chapter 3.2.

3.1.1 Nanoparticle model systems

In order to investigate the adsorption of various coupling agents and the related effects such as self-assembly phenomena on nanoscale surfaces, two different nanoparticle model systems were synthesized: spherical amorphous SiO₂ nanoparticles on the one hand and plane facet shaped crystalline ZrO₂ particles on the other hand. The particles were prepared in different sizes to correlate the self-assembly behavior with their nanoscopic curvature, but also to investigate the influence of particle nature, size and shape on structural and mechanical properties of nanocomposites (chapter 3.2) with regard to structure-property-relationship development.

3.1.1.1 ZrO₂ nanoparticles

ZrO₂ nanoparticles have been prepared applying hydrothermal syntheses. Nanoparticle powders of two different particle sizes, one with equivalent diameter in the lower nanorange, "ZrO₂ small", (the nanorange is here specified to be from 1-100 nm) and one powder from particles in the upper nanorange, "ZrO₂ large" were prepared varying the synthetic conditions. Applying a literature known procedure utilizing the decomposition of a concentrated zirconium oxychloride solution small ZrO₂ nanoparticles were prepared under acidic conditions.^[122] Using a zirconium-acetate precursor solution ZrO₂ nanoparticle powders consisting of larger particles were synthesized also under acidic conditions.^[121]

Homogeneous aqueous dispersions of the nanoparticle powders were drop-cast on carbon coated copper grids and investigated via TEM. Figure 15 shows the recorded TEM micrographs. The insert in the images, representing the corresponding selected area electron diffraction patterns (SAED) reveal a crystalline structure by the presence of sharp diffraction rings for both, the small and large ZrO₂ nanoparticles. Both nanoparticle systems show a homogeneous distribution of particle size and shape and the particles are slightly

agglomerated on the TEM-grid because of the applied drop-casting and the subsequent drying process within the sample preparation. The small ZrO_2 nanoparticles (Figure 15a) show uniform rice like grains, an average aspect ratio of approximately 2, and a spherical equivalent diameter of 6.0 ± 0.6 nm (from 100 particles). The large ZrO_2 nanoparticles (Figure 15b) reveal uniform particles of random shape (aspect ratio ~ 1) with a rough and bumpy particle surface and a spherical equivalent diameter of 38.1 ± 2.8 nm (from 100 particles).

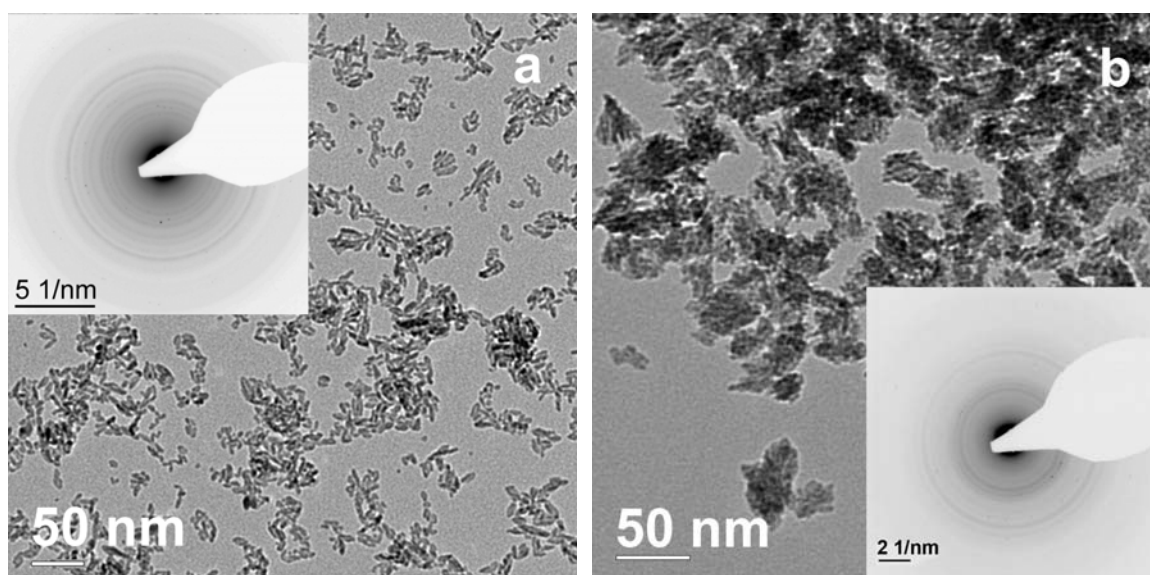


Figure 15. Representative TEM images and SAED patterns of (a) small ZrO_2 nanoparticles and (b) large ZrO_2 nanoparticles.

As the ZrO_2 nanoparticles, especially the small ZrO_2 nanoparticles, which are applied in the self-assembled-monolayer studies will be from special interest concerning their morphology, high resolution TEM (HRTEM) images have been recorded. Figure 16 shows HRTEM micrographs of small ZrO_2 nanoparticles with an overview in the left image and a detail of a representative nanoparticle in the right image. Applying the phase-contrast method it could be observed that each nanoparticle consists of one single crystalline domain. Such a single crystal particle is visible from a perpendicular view on the $[100]$ axis in Figure 16 having a smaller neighbored particle below.

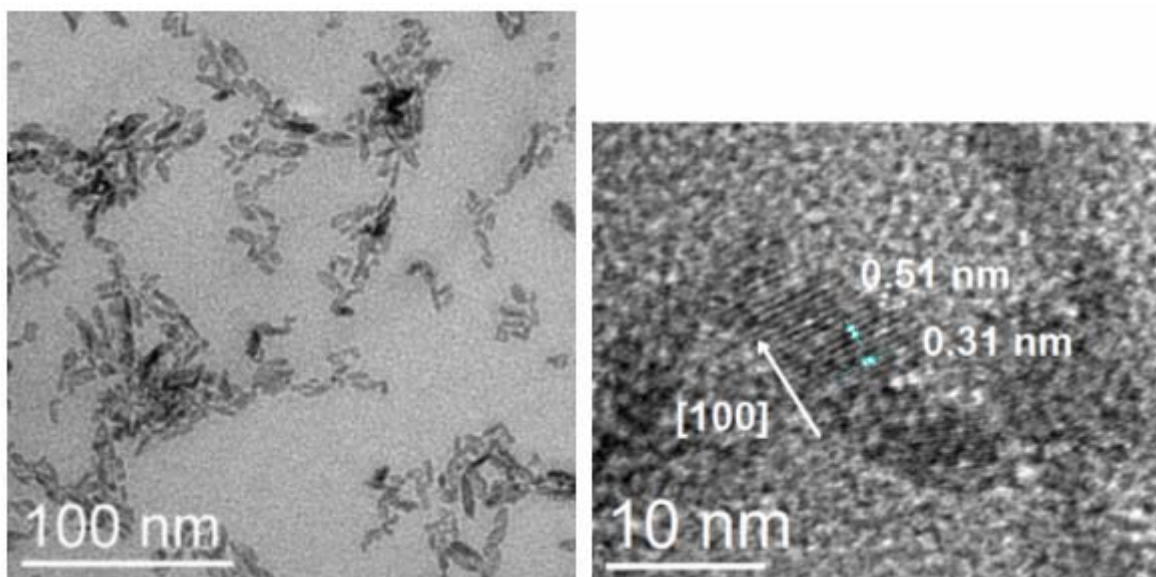


Figure 16. HRTEM micrograph of small ZrO_2 nanoparticles: left image: overview, right image: detail.

A HRTEM-image of a representative large ZrO_2 nanoparticles is shown in Figure 17. From the orientation of the lattice planes in the crystalline domains and the space between the grains it can be concluded that the large ZrO_2 nanoparticles are aggregates of smaller ZrO_2 grains. These polycrystalline nanoparticles further exhibit a porous structure.

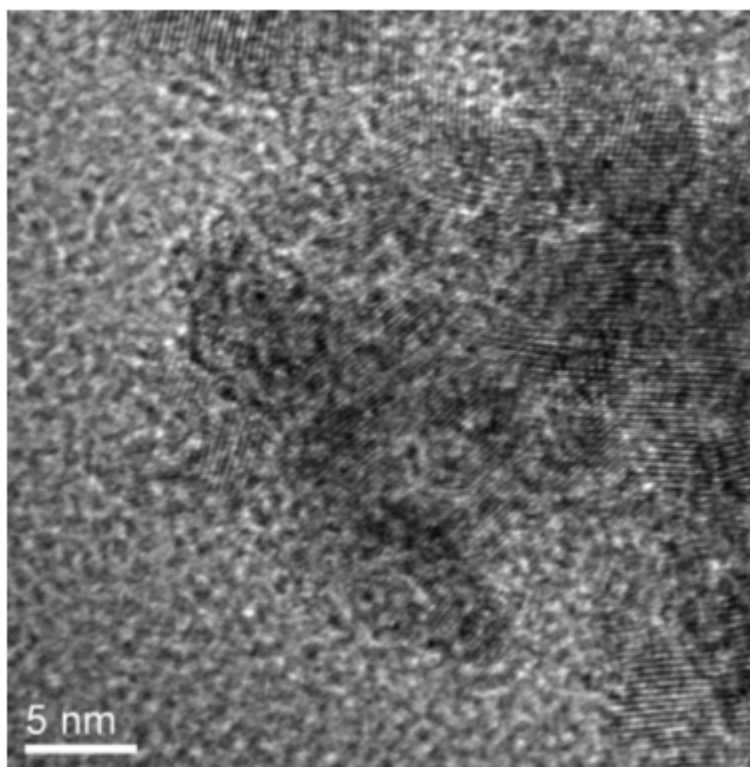


Figure 17. Representative HRTEM micrograph of a large ZrO_2 nanoparticle showing the crystallites aggregated to form the particle.

For both, small and large ZrO_2 , nanoparticle systems only crystalline domains could be observed by HRTEM.

The nanoparticle samples in powder form were also investigated applying a scanning electron microscope (SEM) with a field emission gun (FEG-SEM). Figure 18 left shows the image of a small nanoparticle powder sample and in Figure 18 right a representative micrograph of a large ZrO_2 nanoparticle sample is presented. Both nanoparticle powders exhibit the presence of very uniform particles being randomly agglomerated. From these powder samples, EDX analyses have been carried out and revealed just the presence of Zr, O and traces of C in both samples (from the carbon coating which had to be applied to make the powder conductive) and additionally only in the case of the small particle sample, 3 wt% Cl were detected. This detected amount of chlorine may origin from Cl^- anions, adsorbed to the positively charged ZrO_2 surface. This is very likely as the usually ZrO_2 surfaces carry a positive charge under acidic conditions^[281-283] and a chloride precursor has been used for their preparation.

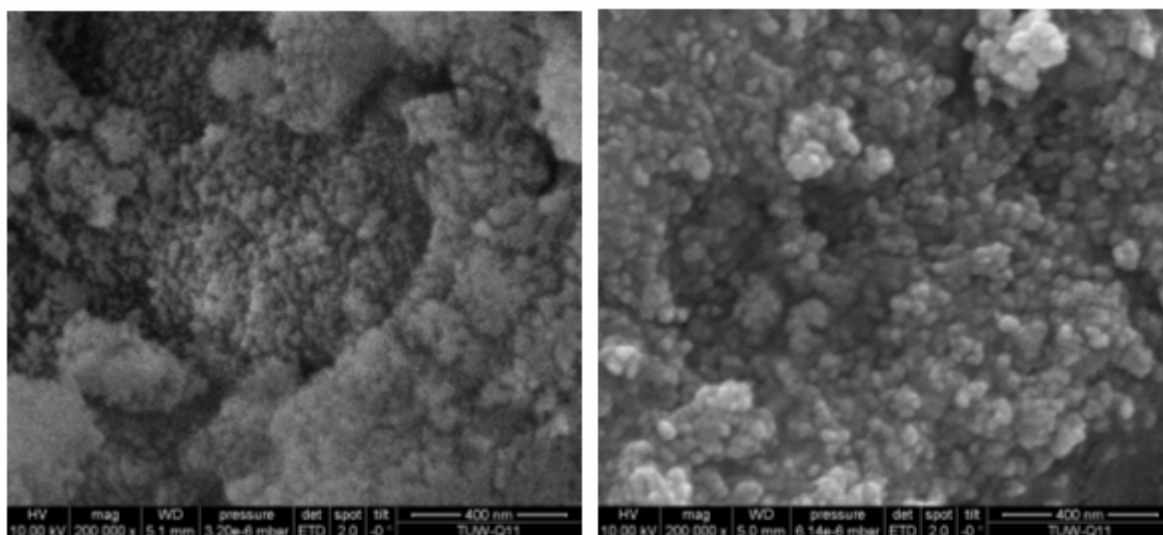


Figure 18. FEG-SEM images of ZrO_2 nanopowders: left image: small ZrO_2 nanoparticles, right image: large ZrO_2 nanoparticles.

Furthermore, for the chemical and structural characterization of the prepared nanopowders the, powder-X-ray diffractograms (pXRD) have been recorded. *Rietveld* refinement (revealed the presence of phase pure monoclinic ZrO_2 (*Baddeleyite*) in both nanoparticle samples. The pXRD-patterns of small and large ZrO_2 nanoparticle powders are depicted in Figure 19, including the reflexes of a reference material from the powder diffraction database for the monoclinic ZrO_2 phase *Baddeleyite*. From the width of the most intense (-1, 1, 1) reflex, crystallite sizes of 5 nm for the small ZrO_2 nanoparticles and 3 nm for the large ZrO_2 nanoparticles could be calculated applying the *Debye-Scherrer* relation (Eq. 9), chapter 4.2.15). By showing an average particle size of ~6 nm spherical equivalent diameter in TEM, the assumption is plausible that the small nanoparticles are single crystals as observed in the HRTEM-images. In this case the crystallite size can be seen as a number for the total particle size.

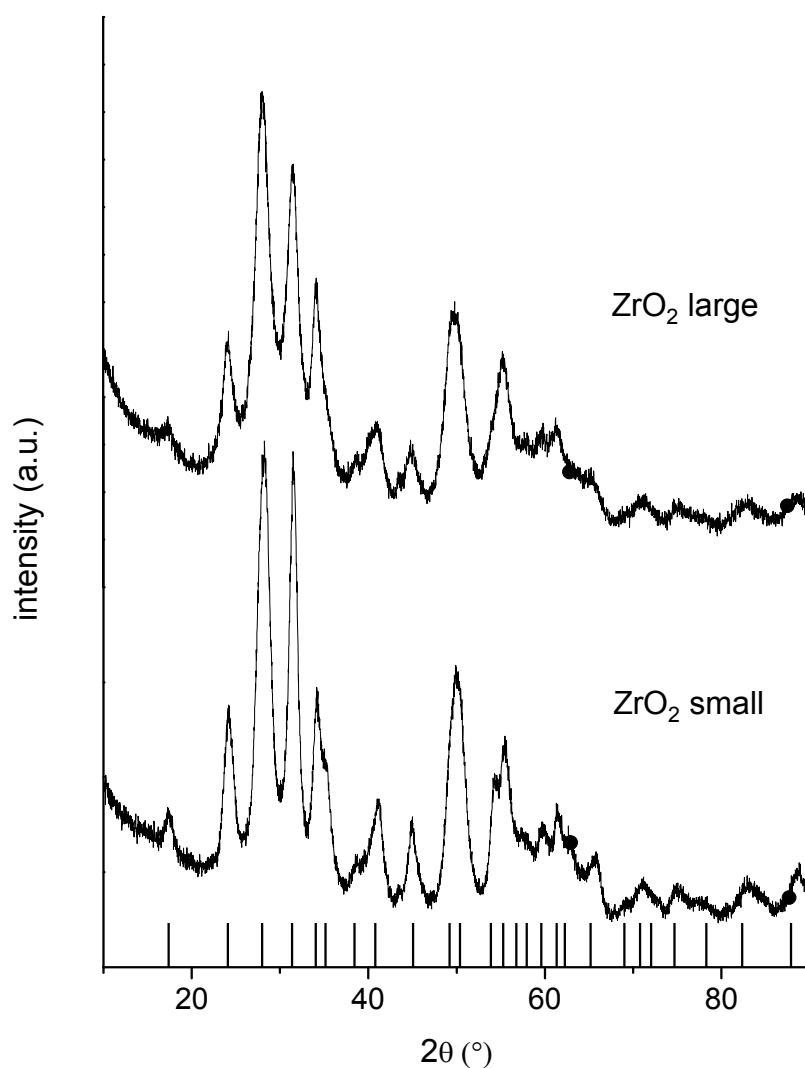


Figure 19. Powder X-ray diffractograms of large and small ZrO₂ nanoparticles; A comparison pattern for *Baddeleyite* from the powder diffraction file database (pdf Nr. 01-0750) is shown below.

However, this assumption in the case of the large ZrO₂ nanoparticle would be senseless. The particle size of large ZrO₂ nanoparticles from TEM of 70 nm is far higher than the crystallite size of only 3 nm. As already discussed from the HRTEM micrograph, these particles are polycrystalline – the results from pXRD confirm this assumption.

For the determination of the surface area and for porosity measurement of the prepared ZrO₂ nanopowders, nitrogen sorption measurements at 77K have been carried out. The resulting adsorption-desorption-isotherms are shown in Figure 20 for the small nanoparticle sample and in Figure 22 for the large nanoparticle powder sample. Generally, the hysteresis between the adsorption and desorption curves in the isothermal plots can be assigned to capillary condensation in the pores of the powder. The size, slope and shape of the hysteresis loops include information on the type of porosity (macro/meso/micro) and also on a quantitative

number of the size and on the shape of the pores. For the interpretation of the hysteresis curves, the IUPAC classification of nitrogen sorption isotherms has been used.^[284] According to this classification, the isotherm for the small ZrO₂ nanoparticle sample was of type IV with a H1 hysteresis. Thus it can be concluded that only mesopores are present, whereas the presence of micro- or macropores can be ruled out. The *Barrett–Joyner–Halenda* (BJH) plot of the pore size distribution (Figure 21) showing a small uniform peak below 5 nm also confirms that. These mesopores result from the packing of the particles (the random packing is visible in the FEG-SEM-image in Figure 18). As no micropores are observed, it seems to be a proper assumption that the particles are dense and non-porous, which is in good agreement with results from TEM and pXRD. For the large ZrO₂ particles the situation is different. The isotherm type can be classified to be between II and IV which is an indication that both, different types of mesopores and possibly also macropores are present in the powder sample. Also the hysteresis is not from uniform or distinct classifiable shape (H2 mixed with H3). This fact is again well illustrated by the BJH-plot in Figure 23. A broad, bimodal pore size distribution with pore sizes ranging from 5 nm to 50 nm, could be calculated. The specific surface area was calculated from the sorption isotherms according to *Brunauer, Emmett and Teller* (BET).^[285]

For the calculation of the specific surface area, a demand of 0.162 nm² per N₂ molecule, adsorbed to the surface of the powder sample was assumed. Thus, specific surface areas of 140 ±2 m²/g for the small nanoparticle powder sample and 171 ±2 m²/g for the large nanoparticle sample could be calculated. The fact that the larger particles show a higher surface area compared to the smaller particles, which are considered to be solid non porous crystals, indicates that the large particles are porous. Hence, two types of porosity are present in the large ZrO₂ nanoparticle powder sample. Assuming that one type of porosity is created by the space between the randomly packed particles, the other type must be related to the inner porosity of the complex shaped nanoparticles. The large ZrO₂ nanoparticles are aggregates of small crystallites, as concluded from HRTEM and pXRD investigations. The assumption regarding porosity can be confirmed by the HRTEM image (Figure 17) of this sample in which free space between the grains can be observed. The broader pore size distribution may also result partially from the more irregular shape of the larger nanoparticles (HRTEM, Figure 17).

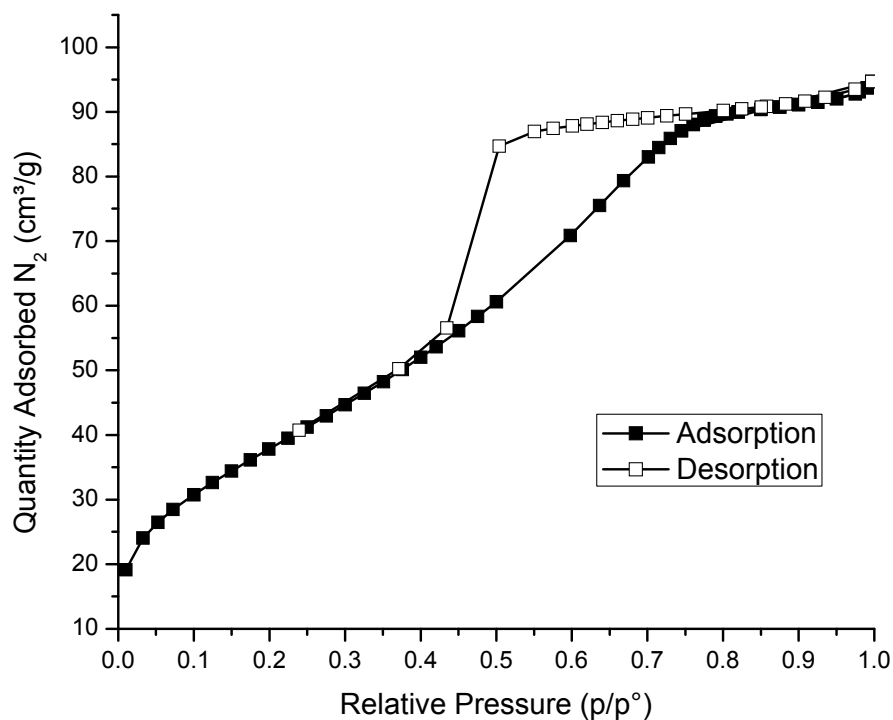


Figure 20. Nitrogen sorption isotherms (77K) of the ZrO₂ small nanoparticle powder sample.

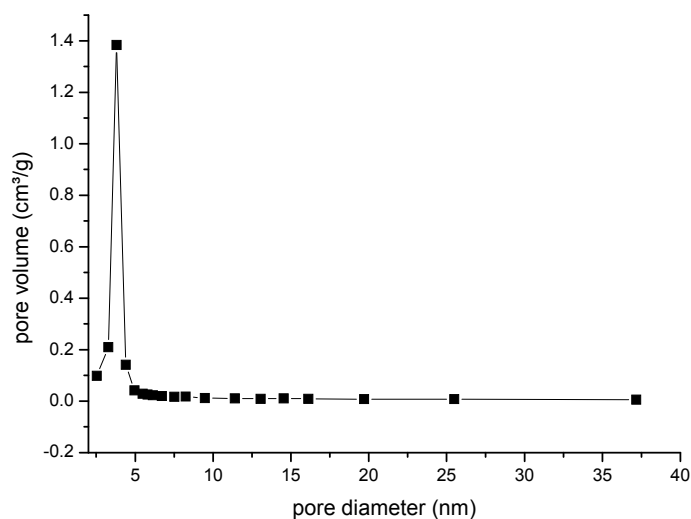


Figure 21. BJH plot from the nitrogen sorption experiment at the ZrO₂ small sample representing the pore distribution in the nanopowder.

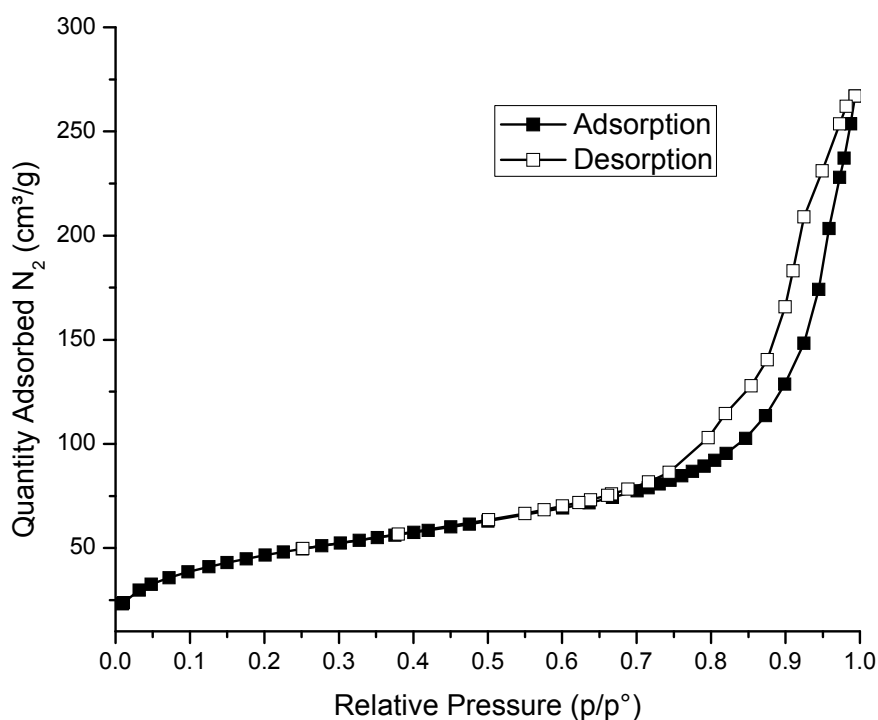


Figure 22. Nitrogen sorption isotherms (77K) of the ZrO₂ large nanoparticle powder sample.

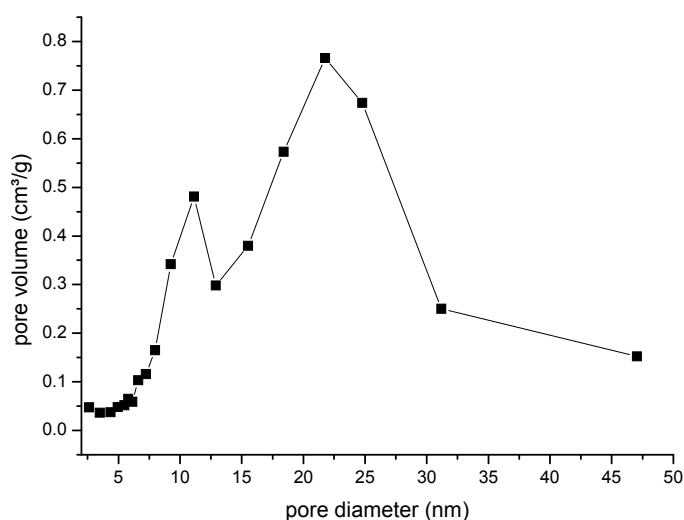


Figure 23. BJH plot from the nitrogen sorption experiment at the ZrO₂ small sample representing the pore distribution in the nanopowder.

With the very rough assumption of a cylindrical shape with an aspect ratio of ~ 2 in the case of the non porous small ZrO₂ nanoparticle system, it was possible to calculate a particle size of 19 nm (spherical equivalent diameter for reasons of comparison with other methods such as DLS) from the specific surface area of 140 m²/g, via the laws of geometry and assuming a

density of 5.7 g/cm^3 (monoclinic ZrO_2). However, for the large ZrO_2 sample this does not make sense as the particles are porous. A diameter of 16 nm would be the result assuming a spherical shape of the particles. This would be in contradiction to all previous reported results. As a conclusion the small crystal shaped ZrO_2 nanoparticles are non-porous and will be used in the following SAM-studies as they are a more reliable model system compared to the porous, irregular shaped ZrO_2 nanoparticles. However, both systems are well-defined and uniform and will thus be applied in surface functionalization studies and for the preparation of nanocomposite samples.

The prepared nanopowders in their agglomerated state are easily redispersible in water (the deagglomeration takes place when powder is added to water and stirred) which makes further characterization methods applicable, such as routine light scattering experiments. Such stable ZrO_2 nanopowder dispersions in water are electrostatically stabilized.^[281, 282] A series of 5 g/L aqueous particle dispersions was prepared and investigated with respect to pH stability (pH was adjusted using NaOH and HCl) and isoelectric point (IEP) to examine the stability of these dispersions and thus to ensure the existence of single dispersed nanoparticles in the dispersion medium. This knowledge is crucial for later applied dynamic light scattering (DLS) experiments. It has to be ensured that the pH of the dispersion is different from the pH at the IEP of the particle systems to guarantee a well dispersed, electrostatically stabilized system.^[281, 282] Furthermore the dispersion stability is from general interest because during the following surface functionalization reaction the pH conditions may vary (different coupling agents can have different pKa values) but a high dispersion quality has to be guaranteed within this process. As a first basic experiment, the dispersion stability at different pH was examined in order to set the working range for the zeta potential measurements. The pH was adjusted with HCl and NaOH until a destabilization of the colloid could be observed by a change of the optical appearance of the dispersion from transparent to opaque followed by sedimentation. Samples outside the stability range (and the allowed pH range of the instrument, which should be not lower than $\text{pH} = 1.5$ because of electrode corrosion etc.) were not used for the zeta potential measurement as the sedimentation occurred too fast to get reproducible reliable results from these unstable dispersion. The small ZrO_2 nanoparticle dispersions were stable between $\text{pH} = 0.58 - 6.9$ and after an instable region about 1 pH unit again up to $\text{pH} = 10.04$. The large particle dispersions were stable between $\text{pH} = 0.46 - 7.1$ and after an instable region about 1 pH unit again up to $\text{pH} = 12.82$. In the mentioned stability regions no change of the dispersion quality could be observed for several weeks. The zeta potential of a series of dispersions with different pH in this determined stable region was measured for both systems (small and large particles) and the zeta potential versus the pH value is plotted in Figure 24. The IEP is given at the value for $\text{zeta} = 0 \text{ mV}$ per definition, this is the point at a certain pH where the particles are effectively neutral in the liquid continuum and thus the electrostatic stabilization is not given at this point. For our systems (Figure 24) the particles reveal a positive effective charge in the acidic pH-region ($\text{pH} = 1.7 - 6.9$ for the small particles and $\text{pH} = 1.5 - 7.1$) and a negative effective charge in the basic pH-region, beyond the IEP, ($\text{pH} = 11.1$ for the small nanoparticles and $\text{pH} = 11.2$ for the large nanoparticles). Between $\text{pH} = 6.9$ and 11.1 for the small nanoparticle system and $\text{pH} = 7.1$

and 11.2 for the large particle system a zero crossing of the zeta/pH curve takes place and thus the IEP lies between these values. Unfortunately, between these points no further data points could be measured because of the instability of the colloidal suspension. An interpolation of the zeta/pH curve reveals an IEP between 8 and 9, where the IEP of the small nanoparticle system is considered to be slightly lower than the IEP of the large nanoparticle system.

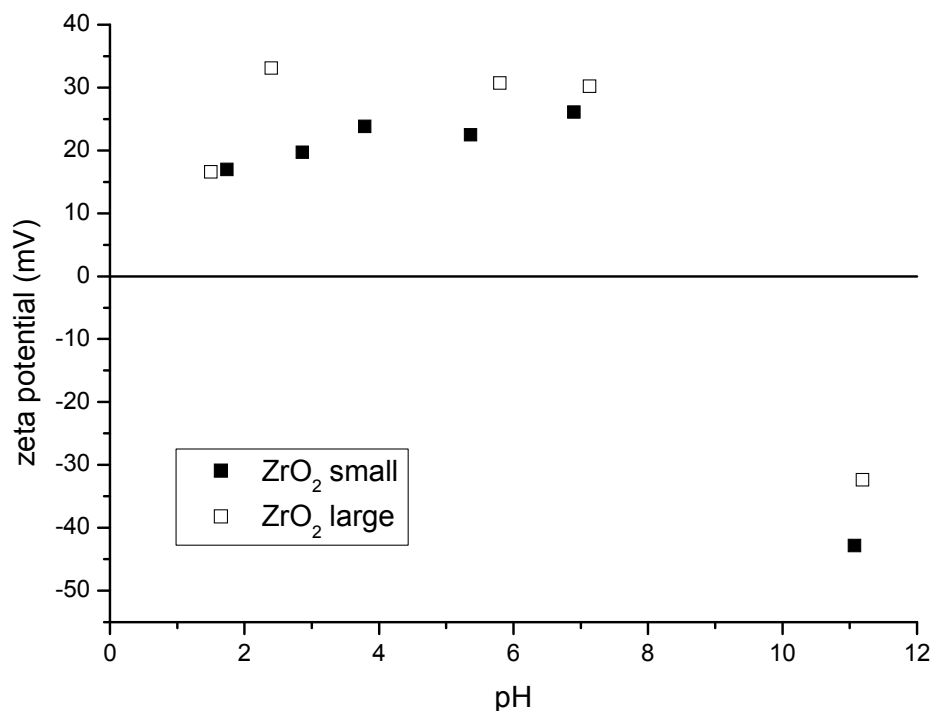


Figure 24. pH dependence of the zeta-potential of ZrO₂ small and large nanoparticle aqueous colloidal dispersions (5 g/L).

The IEP of these systems (pH = 8-9) is slightly higher than that of literature-reported zirconia surfaces (pH ~ 6).^[282, 283] However for nanoparticles the situation can be different: For instance, *Walther et al.* also report a higher IEP of pH = 8.2 for commercial ZrO₂ nanoparticle (yttrium stabilized tetragonal zirconia particles from Degussa with an average size of 100 nm) aqueous dispersions. Their results for the pH dependent colloid stability are in quite good confinement with the results of this work, regardless of structural and chemical differences of the used materials. *Walther et al.* further directly correlated zeta potential measurement with light scattering methods using dispersions of small ionic strength (0.001M NaClO₄), comparable conditions can be assumed for this present work. They found that the investigated systems are homogeneous colloidal dispersions due to electrostatic stabilization when a pH value is adjusted outside of the range of IEP-2 to IEP+2.^[281] Because of the similarity in the pH/zeta curve slopes of this experiments from literature to the here investigated systems, the comparison of these two different systems is considered as warrantable. The dispersions (5 g/L) reveal a pH of 2.7 in the case of small ZrO₂ nanoparticles and 4.5 in the case of large ZrO₂ nanoparticles without the addition of any additional acid or base which is far below the IEP (pH between 8-9). This evidences that the nanoparticle dispersions from this present work

are, for electrostatic reasons, stable enough to allow further precise measurements (dynamic light scattering). Consequently, these homogeneous and stable colloidal dispersions are appropriate to be used in further modification reactions (where the pH will be adjusted to 2.5). The modifying agent molecules have proper access to the particle surface due to the well dispersed particles.

Dynamic light scattering (DLS) experiments were carried out to yield a better representation of the whole particle collective on a larger average in form of particle size distributions. For the DLS measurements, the dispersions were further diluted by a factor of 50 (concentration ~ 0.1 mg/mL) to reduce multiple particle scattering. The resulting particle size distributions are plotted mass weighted for the small and large ZrO₂ nanoparticle dispersions in Figure 25. Only one peak resulting from the scattering at the nanoparticles is visible. No signals corresponding to sizes >100 nm were observed and thus the presence of larger agglomerates can be ruled out. Hence, the high colloidal dispersion quality and thus the good redispersibility of both synthesized nanopowders is demonstrated by these experiments. The applied calculation model gives spherical equivalent diameter values but even though the particles are non spherical (anisotropical ZrO₂ small and irregular isotropical ZrO₂ large) this approximation can be justified by the quality of the results. As a number for the particle size, the peak values have been taken with the full width at half maximum as deviation. According to this procedure, from the mass weighted distribution, which is more feasible to demonstrate the overall quality of the samples, a value of 22 ± 7 nm diameter for the small nanoparticles and 66 ± 19 nm diameter for the large nanoparticles was calculated. From the number weighted distribution, which is better to compare with other number weighted particle size determining methods such as TEM or SAXS, a value of 18 ± 4 nm diameter for the small nanoparticles and 54 ± 11 nm diameter for the large nanoparticles was calculated. The difference between the number weighted and mass weighted derived values are assumed to result from the particle size distributions and from irregularity of the particle shape. Though the number weighted sizes are systematically higher as the values derived from the TEM measurements, a good correlation between the numbers could be obtained. These differences will be discussed in more detail in chapter 3.1.1.4. However, the particle size and distributions for both nanoparticle systems are considered to be sufficiently different from each other to observe significant size effects for further experiments. The very facile and routine method of DLS will nevertheless be applied to indicate a value as a representation for the particle size.

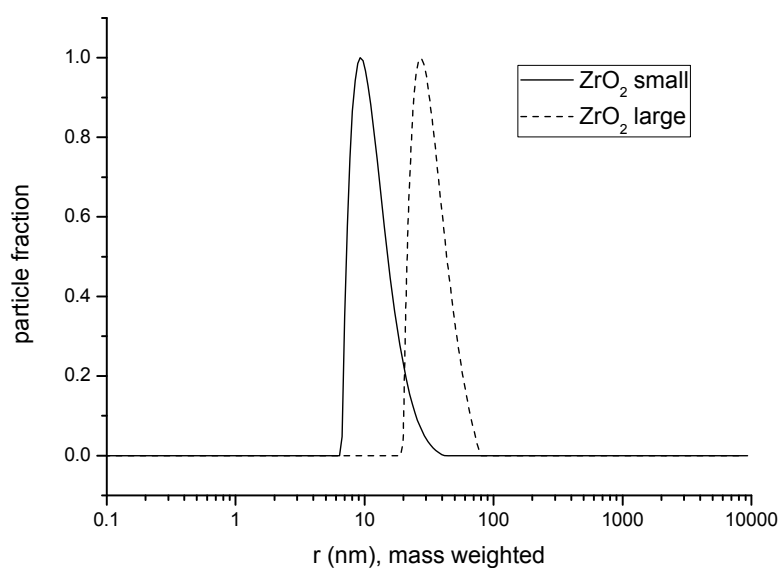


Figure 25. Particle size distributions (mass weighted) from dynamic light scattering (DLS) experiments of aqueous ZrO₂ nanopowder dispersions.

3.1.1.2 SiO₂ nanoparticles

SiO₂ nanoparticles were used as model systems to study characteristic effects in nanocomposite materials related to surface chemistry (sample names SiO₂ small and SiO₂ large) and to study the SAM-formation at the particle surface (sample names SiO₂ nano, SiO₂ micron1 and SiO₂ micron2) have been prepared applying the *Stöber*-process.^[114] The SiO₂ small nanoparticles in the lower nanorange^[286] as well as the SiO₂ large nanoparticles in the upper nanorange^[287] were prepared adapting the method described by *Stöber et al.* according to literature known procedures as cited. By systematic variation of the reaction conditions of the applied literature approach^[287] the other samples such as SiO₂ nano, SiO₂ micron1, and SiO₂ micron2 have been prepared. The parameters for these syntheses and the obtained particle sizes from DLS are listed in Table 3. Applying DLS measurements to calculate spherical equivalent diameters seems to be an appropriate particle size determining technique as the *Stöber* particles reveal spherical shape.^[114] The DLS measurements were carried out directly from the reaction mixture, which was a stable colloidal dispersion in all cases, diluted with the reaction solvent to yield a particle concentration of ~0.1 mg/mL. The resulting particle size distribution are shown in Figure 26. The mass weighted particle size distributions are unimodal and show the absence of a significant amount of larger aggregates or agglomerates in the samples. Furthermore, very narrow distribution functions are observed and comparing the size distribution of the nanoparticle samples (diameter from number weighted distribution vs. diameter from mass weighted distribution) with the difference of these values for the ZrO₂ samples from chapter 3.1.1.1, these particle systems seem much more uniform. It is considered that this is due to the spherical shape of the particles and thus

the sphere-approximation is better applicable within the mathematical autocorrelation curve fitting.

Table 3. SiO₂ particle samples with various sizes (from DLS), depending on the listed parameters applied in the *Stöber* process (100 mL solvent was used for each reaction).

Sample	H ₂ O [mL]	TEOS [mL]	NH ₄ OH conc. [mL]	Solvent	Particle diam. (DLS) m.w. [nm]	Particle diam. (DLS) n.w. [nm]
SiO ₂ small	2.00	10.5	0.05	methanol	9.4 ± 2.7	7.8 ± 2.3
SiO ₂ large	2.00	4.0	3.3	ethanol	72 ± 19	64 ± 13
SiO ₂ nano	2.00	4.0	3.0	ethanol	46 ± 10	40 ± 7
SiO ₂ micron1	2.00	6.0	12.0	ethanol	390 ± 80	380 ± 23
SiO ₂ micron2	0.00	6.0	12.0	ethanol	680 ± 55	480 ± 39

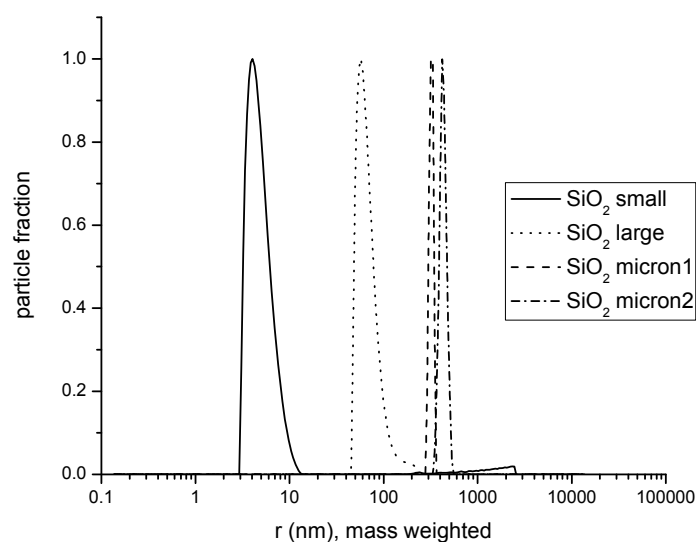


Figure 26. Particle size distributions (mass weighted) from DLS experiments with SiO₂ nanoparticles of various sizes, dispersed in methanol (small) and ethanol (all others).

Powder X-ray diffraction revealed that the particles are X-ray amorphous. Additionally the SAED applying TEM showed the features of an amorphous material. TEM-micrographs have been recorded after drop-casting the particle sols onto carbon coated copper grids to investigate the shape of the prepared SiO₂ particles. Images of the SiO₂ small and large

nanoparticles as well as one example for a (sub)micron sized particle are shown in Figure 27. All particles are spherical which justifies the assumptions made for the DLS experiments and further eases the modeling of particle size determining data (such as SAXS, N₂ sorption experiments, etc.). The samples SiO₂ large and SiO₂ micron reveal a smooth surface with low roughness. For the small SiO₂ nanoparticle sample the maximal resolution of TEM and also the contrast was too poor to draw a conclusion about the surface morphology. Even the particles themselves were difficult to image because of the low z-contrast and the lower contrast for this amorphous material compared to crystalline materials such as ZrO₂ (diffraction contrast). This will be the reason why in the later nanocomposite investigation, no images of small SiO₂ nanoparticle containing samples will be shown.

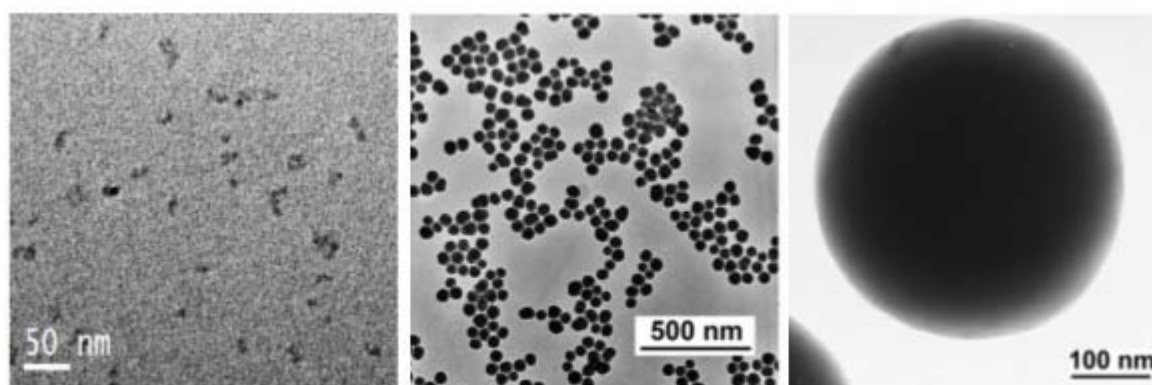


Figure 27. Representative TEM images of small SiO₂ (left) nanoparticles, large SiO₂ nanoparticles (middle) and as an example one micron sized SiO₂ particle sample "SiO₂ micron2" (right).

A diameter of 6.8 ± 1.3 nm for the small SiO₂ nanoparticles and a diameter of 60.8 ± 1.6 for the large SiO₂ nanoparticles has been determined from TEM images (measuring 100 particles each). These results are in better agreement with the DLS-derived results (7.8 nm and 64 nm) compared to the results obtained for ZrO₂ in chapter chapter 3.1.1.1. The model of spherical equivalent diameter seems to be highly applicable in this case.

From the dried and washed powders, FEG-SEM-images have been recorded showing the random sphere packing of the SiO₂ nanospheres resulting in a porous structure (Figure 28). These powders have been used for nitrogen sorption experiments at 77K. According to IUPAC,^[284] the hysteresis curves of the sorption isotherms can be classified as follows: An isotherm type IV with a H1 hysteresis can be attributed to the curves of the smaller nanoparticles and IV/II isotherms with a H1/H2 hysteresis to the curves of the large nanoparticles. Together with the BJH- pore size distribution, mainly 3.5 nm pores for the small system and 12 nm pores for the large system, peak values, it could be concluded that the measured pores represent only the space between the particles in the packing. Thus, the nanoparticles are considered to be dense spheres with no significant inner (micro)porosity.

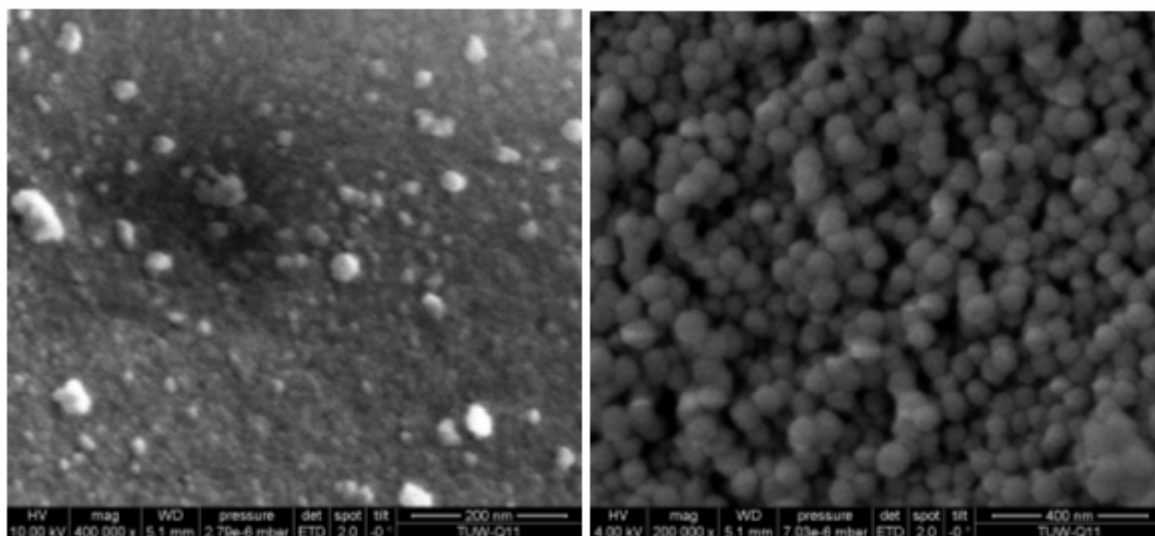


Figure 28. FEG-SEM images of SiO₂ nanopowders: left image: small SiO₂ nanoparticles, right image: large SiO₂ nanoparticles.

Applying the BET model, assuming a demand of 0.162 nm² per adsorbed N₂ molecule, specific surface areas of 710.6 m²/g for the small SiO₂ nanospheres and 76.2 m²/g for the large SiO₂ nanospheres could be calculated from the nitrogen sorption data. The fact that the particles are spherical and dense justifies the calculation of particle diameters from the measured specific surface areas. For the small SiO₂ nanoparticles a diameter of 4.0 ± 0.4 nm and for the large SiO₂ nanoparticles a diameter of 36 ± 4 nm could be obtained from the specific surface area via the geometrical law and assuming a density of 2.2 g/cm³ for the amorphous SiO₂. The fact that these particle size values are the smallest obtained diameter values, compared to methods such as DLS or TEM, can be due to the fact that the surface area is in total larger because of surface roughness of the nanoparticles which is not resolvable in TEM for the here used nanoparticles. However in the case of the large SiO₂ sample a small second shoulder in the BJH distribution could be observed (but not quantified) which would be an indication for this assumption. This can be due to the fractal microstructure of *Stöber* particles where in literature even inner porosity of the particles has been observed.^[288]

In general, all in this work applied SiO₂ nanoparticles, prepared via the well-established *Stöber* method, are very uniform in size and shape which makes the appropriate model systems for further experiments.

3.1.1.3 Characterization of the prepared nanoparticles applying small-angle-X-ray scattering (SAXS), theory and experimental results

Small-angle-X-ray scattering (SAXS) is a versatile method to characterize weakly ordered systems of objects with dimensions in the nanometer range such as inorganic-organic hybrid materials.^[280] For that reason the prepared nanoparticle powders (small and large ZrO₂/SiO₂ nanoparticles) have been investigated via SAXS applying literature known mathematical models to describe the materials and calculate their dimensions. One big advantage of SAXS

compared to imaging techniques such as SEM or TEM is a much higher probe volume (usually in the mm³ range, compared to a typical nm³ range in TEM and SEM being a surface analysis technique). Thus the SAXS derived results are highly representative for the whole ensemble of nanoparticles in a macroscopic sample. Secondly, not only particle size information can be gained from SAXS, but also structural information can be derived from SAXS experimental data, such as distances between particles, possible ordering effects and particle packing. This makes this method very important for the characterization of the nanocomposite materials in this work. Therefore it is also of high importance to characterize the prepared SiO₂ and ZrO₂ particles via SAXS methods and compare the results with routine particle analysis methods such as DLS as carried out in the previous chapters, where particle size values can be directly measured from the reaction solution.

In contrast to DLS, SAXS directly probes differences in electron densities which has the particular advantage that sample features which could falsify the result, such as a hydrodynamic shell in aqueous dispersion, does not impact the results. In this work, the scattering intensity $I(q)$ versus the q -vector, derived from the scattering experiment, represents the dataset which is used for all calculations.^[289, 290] Scattering intensities of weakly ordered structures are generally described by the product of form factor and structure factor, $I(q) = I_0 V_0^2 \cdot P(q) \cdot S(q)$, with q being the absolute value of the scattering vector, V_0^2 the volume of the particle to the second power, $S(q)$ the structure factor and $P(q)$ the form factor. The factor I_0 contains experimental parameters such as the scattering contrast, the beam intensity and additional variables depending on the experimental setup. For the calculation of the particle size from the SAXS profile two different models have been used and will be compared in this chapter. For spherical particles with a Gaussian size distribution, the form factor is well known as (Eq. 1).^[280]

$$P(q) \propto \int dR \cdot R^6 \exp\left(-\frac{1}{2} \frac{(R-r)^2}{\sigma^2}\right) \left(3 \frac{\sin(qR) - qR \cos(qR)}{(qR)^3}\right)^2 \quad \text{Eq. 1}$$

In the hard-sphere model, the *Percus-Yevick* approximation^[291] (Eq. 2) delivers a structure factor for weakly agglomerated/aggregated systems, such as expected for the nanocomposite materials investigated in this work. It describes the interference of the scattering of particles applying two parameters, a hard-sphere radius R_{HS} and a mean hard-sphere volume fraction η ^[292, 293]

$$S(q) = \frac{1}{1 + 24\eta G(2qR_{HS}) / (2qR_{HS})} \quad \text{Eq. 2}$$

with the function $G(2qR_{HS})$ being defined by Kinning and Thomas.^[292] The hard-sphere diameter $2R_{HS}$ gives information on the correlation distance of particles within a cluster, aggregate or agglomerate and the hard-sphere volume fraction η on the probability to find particles in vicinity to each other. Different from Eq. 1, a unified equation for the form factor has been proposed by *Beaucage*.^[294-296] In this model, the scattering intensity $I(q)$ includes a form factor consisting of a *Guinier* like regime, which means an average structural size is

described in terms of radius of gyration, and a limited power law regime, which characterizes a mass or a surface fractal. The *Beaucage* mode is here formulated (Eq. 3)^[297] for an arbitrary number of hierarchical levels n

$$I(q) = \sum_{i=1}^n \left(G_i \exp\left(\frac{-q^2 R_{gi}^2}{3}\right) + B_i \left[\frac{(\text{erf}(qR_{gi}/\sqrt{6}))^3}{q} \right]^{p_i} \right) S(q) \quad \text{Eq. 3}$$

while G_i and B_i are the numerical prefactors, p_i are referred to as *Porod* exponents, R_{gi} are the gyration radii and $\text{erf}(x)$ is the error function. The particle radius r_{SAXS} of spherical particles is obtained by $r_{SAXS} = R_{gi} \sqrt{5/3}$. For a lognormal distribution of the size of particles with $p_i = 4$, a sharp interface, the ratio B/G allows the calculation of the polydispersity index (PDI).^[298] From the PDI and the expected value (the mean) $\langle R_{gi} \rangle$, the standard deviation s.d. (Eq. 4) of the distribution is obtained by

$$\sigma = \left(\frac{\ln PDI}{12} \right)^{1/2} \quad \text{and} \quad \text{s.d.} = \langle R_{gi} \rangle (\exp(\sigma^2) - 1)^{1/2} \quad \text{Eq. 4}$$

An overview on the different theoretical models is discussed in the literature.^[293] However, the method is limited to particles smaller than 80 nm diameter for common laboratory SAXS instruments, because for larger objects the signal from the scattering feature (at the particles) interferes too much with the intense signal from the primary X-ray-beam. This is one reason why the particle sizes for ZrO₂ large and SiO₂ large were adjusted to be <80 nm in this work. Figure 29 shows the intensity profiles (scattering curves) from the SAXS experiments at small and large ZrO₂ and SiO₂ nanoparticle powder samples. Thereby, the features, basically shoulders (e.g. for small SiO₂ visible at $q \sim 0.8$), of the scattering curves between $0.1 \text{ nm}^{-1} < q < 10 \text{ nm}^{-1}$ result from the scattering at the particles as an obstacle in the X-ray beam. In the case of the ZrO₂ particles, the visible peak at $q = 12.3 \text{ nm}^{-1}$ results from the diffraction at the (100) atomar planes and thus from the crystalline chemical structure in the bulk of the ZrO₂ material, see powder-X-ray-diffraction (pXRD) results. To calculate the nanoparticle dimensions, the datapoints from the measured SAXS curves (Figure 29) were fitted with the corresponding mathematical function. Also the fitting curves, applying the Gaussian distribution model (Eq. 1), are drawn in the diagrams in Figure 29. All SAXS curves from the particle powders, discussed in this chapter, were fitted with both, the Gaussian distribution model (Eq. 1) and the *Beaucage* model applying a lognormal distribution function (Eq. 3) where no significant difference in the results for the particle size could be obtained, even not for the more complex structured and irregular shaped, large ZrO₂ nanoparticle powder system, see Table 4. Therefore, for reasons of easiness, for all further investigations, the SAXS curves were fitted applying the Gaussian model resulting in the particle diameters d_{SAXS} .^[289, 290]

Nevertheless we want to discuss a comparison of the two fitting models using the example of large ZrO₂ nanoparticle with the results for the calculated diameters given in Table 4. In this specific case the two levels of hierarchy, which means two different characteristic sizes in the sample (named d_1 and d_2), are visible from the scattering curves in form of two characteristic

bumps and were therefore fitted applying a system with includes two different radii of gyration, precisely a bimodal size distribution. Thereby, d_1 and d_{SAXS} represent the size of the whole particle which is an aggregate of smaller crystallites and d_2 represents the dimensions of the crystallites. In the scattering curves, this smaller dimension of the inner particle structure can be observed in form of the maximum of a bump at high q -values, corresponding to a short range order of these small units with a typical distance of 2.0-3.2 nm (depending on the applied model), which is in high coincidence with the crystallite size of 2.9 nm as obtained from pXRD. This further confirms the fact that the large ZrO_2 nanoparticles are polycrystalline. On the other hand, for small ZrO_2 particles only one size dimension could be detected applying SAXS which is a clear indication for the single crystallinity (as assumed from HRTEM and pXRD) of these samples.

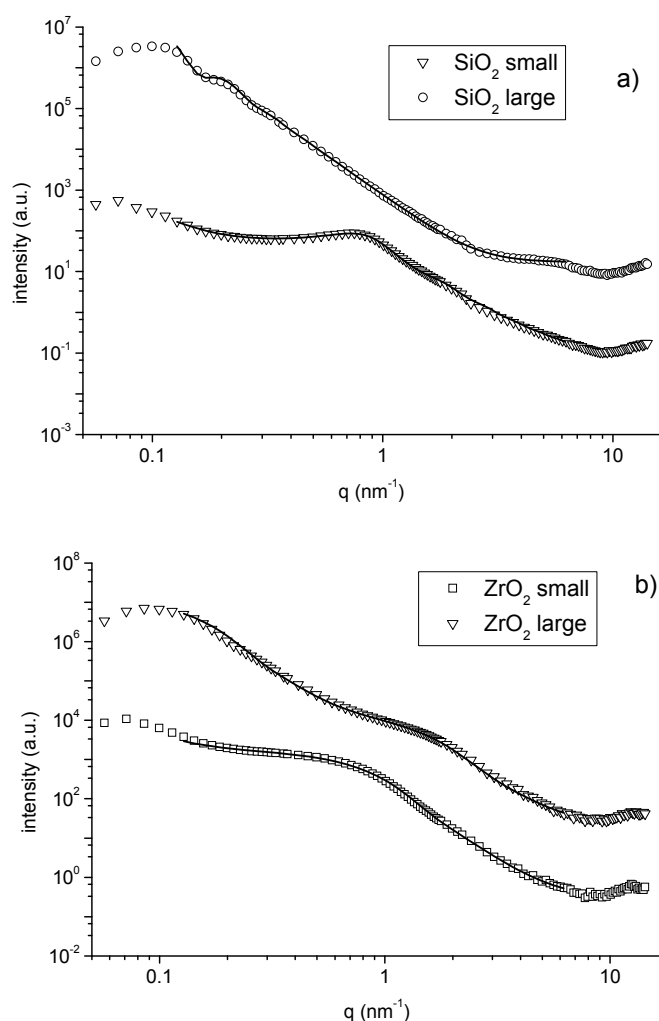


Figure 29. Intensity profiles from SAXS experiments at SiO₂ (a) and ZrO₂ (b) nanoparticle powders. $I(q)$ (symbols) and fitting curves (solid lines) using the form factor for spherical particles and a Gaussian size distribution are plotted in the diagrams. The profiles are shifted vertically for better visibility of the curves.

Further aspects on the consistency and structure of the nanoparticle powders have to be considered and discussed at this point. From the results of the fitting of the scattering curves it can be seen that SiO₂ nanoparticles exhibit a higher tendency to agglomerate than ZrO₂

nanoparticles, which can also be concluded from the more pronounced peak-like maximum in the scattering curve in particular for the small SiO₂ sample (Figure 29a). This short range order is generated by a stronger particle-particle interaction, a more dense packing of the particles, and leads to a higher numerical value for the volume fraction η in the hard-sphere model (Eq. 2). The higher the hard sphere volume fraction, the higher is the probability to find a neighbor particle in the vicinity of a nanoparticle. Strong agglomeration of small *Stöber* particles is a common issue described in literature which makes the characterization of single particles difficult.^[299] Enthalpy, surface energy minimization, is usually responsible for the strong agglomeration of small nanoparticles, which is a crucial parameter to be tuned for the dispersion of nanoparticles in organic systems.^[58] Namely, the agglomeration of SiO₂ nanoparticles reduces the surface and leads to a gain in enthalpy. The described effect is less pronounced in case of ZrO₂ particles, which is deduced from the smaller hard sphere volume factor and thus a lower tendency to agglomerate. This can be on one hand due to the fact that spheres can be more densely packed than irregular shaped objects. Also the different effective surface charge of the different particles may play a role where for ZrO₂, which is assumed to carry a stronger surface charge in the powder as SiO₂ in this work (from simple chemical nature reasons and taking the production process into account), this higher surface charge would usually lead to more loose agglomerates, because of repulsive forces, compared to less charged surfaces. In literature, the degree of agglomeration from metal oxide nanopowders dried from a solution is described as an interplay of various thermodynamical factors with coulomb interactions playing the major role for charged surfaces and electrostatic repulsion avoiding a dense agglomerate formation.^[300] Furthermore in this specific case the surface silanol (Si-OH) groups of two different of these sol gel derived SiO₂ particles can condensate to form interparticle covalent bonds if the particles are not surface modified, as it is the case for the powder samples in this chapter. This may also play a role within the phenomenon of closer packing of the SiO₂ spheres (for the ZrO₂ prepared under hydrothermal conditions it is considered to be not the case that the Zr-OH group react with each other^[301]). These hard sphere volume fraction as a value for the particle agglomeration will further play a crucial role in the investigation on modified nanopowders and nanocomposite materials, the topic of this work. It should be also noted that the wiggles in the SAXS intensities of the large SiO₂ particles towards very low q -values (Figure 29a) origin from the oscillating form factor of the spheres. This is a phenomenon, being observed in the case of very narrow size distributions,^[302] which confirms the good quality of the prepared *Stöber* particle powders.

Table 4. Particle diameters (nm) from SAXS of large ZrO₂ nanoparticles calculated with two Gaussian functions and the model of *Beaucage* for multiple levels of hierarchy. d_{SAXS} and $d_{1, \text{BEAUCAGE}}$ represent the particle size of the whole particle aggregate (large feature) and the d_2 values represent the inner crystallites in the particle.

d_{SAXS}	d_2, GAUSS	$d_1, \text{BEAUCAGE}$	$d_2, \text{BEAUCAGE}$
33.8	2.0	34.1	3.2

Finally, all particle diameters calculated from SAXS data are listed in Table 6. As previously discussed, the diameters d_{SAXS} from now on, including the data from Table 6 are calculated applying the Gaussian distribution model ($d_{\text{GAUSSIAN}} = d_{\text{SAXS}}$) as the difference between the two fitting models is not significant. In the case of the SiO_2 nanoparticles the diameter values of 4.0 nm and 52 nm are good comparable with the previously applied particle size determining methods (DLS, TEM) which can be related to the high match of model and real particle nature for the nanospheres. The situation is different for the crystal shaped and irregular shaped ZrO_2 nanoparticles. The values calculated from SAXS experiments are significantly different from the measured diameters by other methods. This fact will be discussed in detail in the following chapter 3.1.1.4 for a better understanding of its causes.

Table 5. Particle diameters from SAXS, calculated applying a Gaussian distribution function.

sample	d_{SAXS}
SiO_2 small	4.0 ±1.2
SiO_2 large	52.0 ±8.8
ZrO_2 small	4.4 ±1.2
ZrO_2 large	33.8 ±11.0

3.1.1.4 A comparison of the determined size values applying various size measuring methods

As discussed in the chapters 3.1.1.1 and 3.1.1.2, when applying different techniques of particle size determination (DLS, TEM, nitrogen sorption, powder-X-ray-diffraction (pXRD), SAXS) for the ZrO_2 and SiO_2 nanoparticles resulted in different values for the particle diameter. The question is: Which values represent the true particle size best and which effects are responsible for the differences in the size values comparing different techniques. Furthermore, the validity and significance of applied methods may differ for each particle system. But also the probability to measure fast and easy is considered as a quality factor which a particle size measurement technique should consist of, if it is routinely applied in the development of new nanoparticle based nanocomposite materials, as it is the case in this work.

The particle diameters for SiO_2 and ZrO_2 small and large nanoparticles from all different applied techniques are compared in Table 6 and are depicted in Figure 30 for a better visual overview. At a first glance, the results of all presented experimental methods give a nearly perfect agreement for the SiO_2 nanoparticle system whereas a considerable discrepancy of the results obtained by DLS, nitrogen sorption and pXRD is observed for the ZrO_2 nanoparticles. In general, the values obtained from DLS are always higher than the sizes measured by the

other techniques, which are about twice the value of SAXS and TEM for the ZrO₂ large nanoparticles. For small ZrO₂ particles, the size from DLS exceeds the values from SAXS and TEM by even nearly a factor three. SAXS and TEM delivered nearly identical values for all types of nanoparticles, ZrO₂ and SiO₂. Taking only the statistical error into account, the standard error of the mean diameter is low for SAXS due to the large number of particles in the beam. The calculated diameters from pXRD measurements are in perfect agreement for small ZrO₂ nanoparticles, as they are highly crystalline single crystal particles, and reflect the crystallite size of the smaller subunits in case of the polycrystalline large ZrO₂ particles. Therefore, it does not make sense to use pXRD as a particle size determining method for the explored system. When particle diameters are calculated from the specific surface area, obtained by nitrogen sorption isotherms according to the BET model, the particle size results for the solid flat nanocrystals of the ZrO₂ small sample are in coincidence with the other values for particle size. This is not the case for the large ZrO₂ nanoparticles. An extreme difference to other calculated diameters can be observed, which is considered to be due to the irregularities in shape and surface roughness and due to a possible inner porosity of the particles (in contrary to the solid small crystals where this method gives coincident values). For that reason nitrogen sorption techniques cannot be applied to determine the particle size of the ZrO₂ large nanoparticles. In case of SiO₂ nanoparticles, the results from BET fit to the particle size obtained from other methods only for small nanoparticles, whereas a considerable deviation is observed for large nanoparticles. Any agglomeration or aggregation would cause a loss of surface area and would therefore lead to an (result falsifying) increase in the calculated particle size using the specific surface area. As the particle size of the large SiO₂, calculated from the BET surface area, are significantly lower than the values obtained by any other technique, a plausible explanation would be that surface roughness (which was not visible applying the other measurement techniques) is responsible for this differences. The phenomenon of rough *Stöber*-particle surfaces has its origin in the inner fractal ultrastructure of the particles and is described in literature for larger *Stöber*-particles.^[288] Especially when high H₂O/TEOS ratios have been applied in the *Stöber*-process, the surface roughness is very strongly pronounced and even visible using imaging techniques^[303] and in some cases even microporosity could be observed.^[288]

It has to be kept in mind that during the following discussions each of the different techniques reports a value for the mean diameter of nanoparticles. The advantage of TEM is that direct images are obtained, which enables not only the determination of a size but also the specific shape of particles and taking it into account when calculating a mean spherical equivalent diameter. However the particle sizes reported by TEM studies can be affected by several sources of falsification. Firstly, variations in the electron beam setup can cause relative errors up to 10%.^[304] Secondly, the sample preparation, namely, the drop casting followed by ultra evacuation can influence the whole sample so that the taken images do not represent the prepared nanopowder sample. Classing, which means size discrimination, (e.g. on the sample grid during the drying procedure) have to be considered. Anisotropic particles (e.g. the small ZrO₂ nanocrystals) are considered to orient preferentially on the sample grid, namely with their largest base side on the grid. These facts can lead to non representative images even

when the particles themselves are not physically or chemically changed. In general due to the high vacuum conditions applying TEM investigation the harsh drying may involve effects such as aggregation by capillary forces between the particles during drying. These effects can influence the structure and size of primary particles.^[305] For example, by placing the sample on a coated copper grid and evaporating the solvent, the nature of the particles can be changed. As an extreme example *D. J. Tobler et. al* showed that highly hydrous and open-structured SiO₂ particles can even collapse due to the dehydration and relaxation processes under high vacuum conditions.^[299] In our work no such high vacuum drying effects were observed, neither for SiO₂ nor ZrO₂ nanoparticles. This is evidenced by the perfect coincidence of the measured diameters from SAXS and TEM, where no difference in the values could be observed. In some cases also the interaction of electron beam and nanosample is not negligible and the nature of the particles, e.g. crystalline phase, may be changed. Such TEM-induced phenomena (common for organic materials) have been reported for metal oxide nanoparticles in literature.^[306] This can be excluded in the present work as shown by the results. However taking the good comparable results from SAXS and TEM into account, the TEM results are calculated from a much smaller statistical ensemble as from any other here applied technique ($\sim 10^2$ vs. $\sim 10^{12}$ particles) and therefore it is crucial to select a representative image applying TEM.

Thus SAXS gives an average diameter with high statistical accuracy. Even when the TEM-images are very representative and the mean size values coincide, the distribution function, and polydispersity of the powder sample, calculated from SAXS is in all cases more accurate as applying TEM. In almost all cases, when applying SAXS also the sample preparation is simpler compared to TEM and thus there are less possibilities to influence and falsify the final results. Furthermore, for SAXS no high vacuum conditions are needed. A disadvantage of SAXS, compared to direct imaging techniques however, is that no direct information on particle size and shape is obtained, and in most cases very sophisticated numerical methods have to be applied to extract the desired information. If the choice of the respective numerical approach is unambiguous – taking for example the additional information (approx. size and shape) obtained from other methods into account – the size as determined by SAXS can be considered an absolute measurement.^[304] With the exact knowledge of experimental parameters such as X-ray-detector resolution and X-ray wavelength, which is given here, it is a very precise method. Nonetheless, a considerable difficulty arises in the case of a short range order of the particles as it is the case for the agglomerated powder systems shown here, because this introduces an additional structure factor, which complicates the numerical approaches considerably and leads to an additional uncertainty. A high packing density of particles could lead to a slightly higher calculated radius of gyration R_g for a particle embedded in an agglomerate than the corresponding radius of gyration of a single particle.^[304] In this particular case, SiO₂ nanoparticles show a tendency to form denser agglomerates, therefore, this fact could possibly influence the calculated size of SiO₂ nanoparticles obtained from SAXS measurements. Another limitation in the accuracy of results from SAXS is that the calculation of the mean diameter from the radius of gyration depends on the shape of the particle, which is in a first approach assumed to be spherical, but strongly deviating shapes

lead to a further error source. However, one limitation is given by SAXS. Object sizes which exceed ~60 - 100 nm, depending on the experimental setup, cannot be measured via common laboratory SAXS instruments, because the scattering feature is in that case too strongly superposed with the primary X-ray-beam, to enable the calculation of distinct size values. For TEM such size limitations are not given.

Table 6. Comparison of particle size distribution determined by SAXS, DLS, TEM, BET and pXRD (in nm), DLS diameters origin from the number weighted particle size distribution.

sample	d_{SAXS}	d_{DLS}	d_{TEM}	d_{BET}	d_{XRD}
SiO ₂ small	4.0 ±1.2	7.8 ±2.3	6.8 ±1.3	4.0 ±0.4	-
SiO ₂ large	52.0 ±8.8	64.0 ±12.8	60.8 ±1.6	36.0 ±3.6	-
ZrO ₂ small	4.4 ±1.2	17.8 ±3.6	6.0 ±0.4	19.0 ±1.9	4.5
ZrO ₂ large	33.8 ±11.0	54.0 ±10.8	38.1 ±2.8	16.0 ±1.6*	2.9*

*...because of the porosity and polycrystallinity of ZrO₂ large, these values are not representative for the particle size

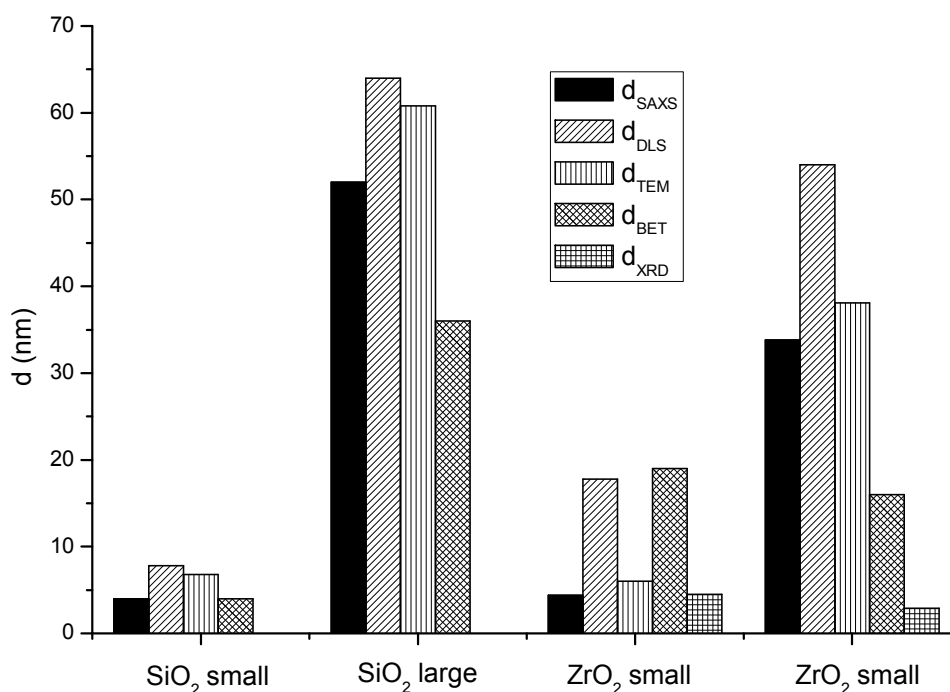


Figure 30. Comparison of particle size distribution determined by SAXS, DLS, TEM, BET and pXRD (in nm) for SiO₂ and ZrO₂ nanoparticles.

Comparing the highly accurate methods TEM and SAXS with DLS (photon correlation spectroscopy), the latter has the particular advantage that it is a simple method, e.g. applicable

directly from the reaction dispersion. This allows not only fast determination of particle size with comparable low effort in instrumentation and calculation, but has also the advantage that directly a size distribution function for the measured nanoparticle system can be obtained.^[307] This is in first approximation true if the measured sample is fitting properly to the model assumption of spherical particles, which means that they are isotropic and/or nearly spherically shaped. Nearly identical values were obtained for SiO₂ nanoparticles due to the proper shape of the nanoparticles. The DLS values were slightly higher for this system which can be explained by the solvodynamic shell around the particles in dispersion. However, for the ZrO₂ nanoparticles (large and small), the diameters determined by DLS were always considerably higher. This should lead to the conclusion that cautiousness is needed when interpreting the results of this measurement techniques by not directly comparing them with results from direct methods such as TEM and that the chemical nature of particles should not be neglected applying simple particle size determining methods. As mentioned, a higher particle size value from DLS can be attributed to the influence of the hydrodynamic shell of the particle which is again related to chemical (surface) properties of the particle. In dilute suspensions, concentration fluctuations relax only by *Brownian* motion of the nanoparticles characterized by the self-diffusion coefficient D (Eq. 5). Primarily time-dependent fluctuations of scattered coherent light are measured via this approach, which is represented by the decay of the autocorrelation function. This is caused by diffusive motion of the particles. The experimentally measured diffusion coefficients can be converted to a hydrodynamic radius via the *Stokes-Einstein* equation

$$D = \frac{k_B T}{6\pi\eta R_h} \quad \text{Eq. 5}$$

where k_B is *Boltzmann's* constant, T the temperature, η the viscosity of the suspension medium and R_h the hydrodynamic radius. This indirect particle size determining approach is only valid for systems of non-interacting particles and thus concentrated suspensions, where strong interparticle interaction can take place, have to be avoided.^[308] Furthermore, in DLS experiments, even a small amount of 1-2 vol% of larger particles can significantly change the DLS derived particle size distribution (e.g. only two neighboring particles can touch each other and being detected as one double sized particle), whereas SAXS measurements are less susceptible to the presence of such agglomerates.^[299] Needless to say that a particular advantage of SAXS compared to DLS is the ability of size determination, directly from powder samples. Dry nanoparticle powders have to be redispersed before measuring the size distribution with DLS. Thus, residual agglomerates can never be excluded, which then falsifies the overall measurement results.

Furthermore, the results for the particle size from DLS depend on the evaluation method (which is generally included in the instrument's standard software, in this case a $g^2(t)$ model), whether a mass-weighted or number-weighted particle size distribution is calculated, compare DLS results from 3.1.1.1 and 3.1.1.2, Table 3. Especially mass-weighted evaluation is very susceptible to larger particles or agglomerates of particles whereas number-weighted evaluation takes more account of the number of single particles at similar size and is less

influenced by agglomeration phenomena. For that reason this method is used for comparison with (unweighted) size distributions calculated from SAXS data. At this point it has to be mentioned again that the mass-weighted evaluation of the here investigated particle systems show monodispersity as it can be seen from the number weighted approach but with only a slightly broader distribution function, see Figure 25 chapter 3.1.1.1 and Figure 26 in chapter 3.1.1.2, which confirms the high quality of the measured samples. From SAXS, the diameter of the particle core (without any solvodynamic shell) is obtained, which perfectly coincides with the particle diameter in the case of the, as dense considered and only having a small surface roughness, SiO₂ spheres. Differently, the ZrO₂ nanoparticles are non spherical with nanoscopic edges and corners (crystal shaped and irregular shaped and porous), see chapter 3.1.1.1. This and the assumption of the higher surface charge and affinity to water molecules of ZrO₂ due to its chemical nature suggests a larger total hydrodynamic diameter for the latter. Concluding, the porous and irregular shape together with the enhanced hydrodynamic shell as a consequence of the larger coordination sphere of ZrO₂ might lead to a considerably higher diameter in DLS as compared to SAXS and TEM. This is plausible as dry powders were measured with the latter two methods. Another inaccuracy might arise from the complex particle shape itself, namely the deviation to the model assumptions, which can affect the numerical values obtained from DLS^[309] being still representative for the sample but false in absolute numbers. All these facts can and are assumed to be responsible for the much higher observed ZrO₂ particle sizes, calculated from DLS, compared to the other methods discussed up to now, whereas for the *Stöber* SiO₂ particles this is not the case.

The result for the particle sizes calculated from the specific surface area from N₂ sorption experiments (BET model) coincide with SAXS, TEM and DLS only for small SiO₂ nanoparticles as they are considered spherical and dense with no surface roughness with the surface of the powder sample being good accessible to N₂ molecules. These assumptions are obviously not the case for all the other samples which has already been discussed previously. Therefore, applying N₂ sorption experiments for particle size determination is very restricted to the model assumptions, more than the other methods discussed here. Furthermore, small nanoparticles lead to a high surface area and any mixture of particles of different size is dominated by the specific surface area of the small particles.^[310] This means that this method is more accurate for small nanoparticles.

The size determination via pXRD is only applicable to highly crystalline, monocrystalline nanoparticles, which is only the case for the small ZrO₂ nanoparticles. Therefore only for ZrO₂ small the diameter calculated from pXRD coincides with the other measurements techniques (SAXS, TEM). The SiO₂ nanoparticles are X-ray amorphous. The larger ZrO₂ nanoparticles polycrystalline and it is therefore clear that the measured diameter from pXRD reflects the size of the small crystallites and not the one of the nanoparticle as an aggregate of crystallites. In general, the importance of the sample crystallinity itself when pXRD is applied as a size measuring technique, has also to be pointed out: This method would also fail if an amorphous shell of unknown thickness would cover the crystalline core of the material, as it can be the case for small oxidic nanoparticles.^[311] HRTEM investigations would be needed to

clarify that. Therefore, when applying pXRD as a standard technique for particle size measurement, the nature of the sample has to be exactly known.

Concluding from all these discussions and considerations, DLS, SAXS, TEM, nitrogen sorption and pXRD (only for crystalline ZrO₂) experiments can be applied to determine particle size values of larger and smaller amorphous SiO₂ and crystalline ZrO₂ nanoparticles considering the necessity of a fit of model assumptions and particle nature. Therefore, the experimentator has to be very careful with the interpretation of the obtained results. The "real" size of the nanoparticles, especially the spherical SiO₂ particles which are easy to model, is most likely best represented by the direct methods of TEM and SAXS but also the results from the indirect DLS method seems to be valid in this case. Supposably, for the ZrO₂ samples, the results from SAXS and TEM also give the most representative values for the equivalent size of these particles. The DLS results seem to be not valid taking the absolute number but representative for the sample and keeping the reasons for the deviation in mind, this simple method can be applied in routine studies and the data can be correlated with earlier SAXS or TEM studies. Applying N₂ sorption or pXRD to determine nanoparticle sizes make sense only in specific cases where the investigated system has to be well known. For the mentioned reasons discussed in this chapter, mostly SAXS will be used to characterize the nanostructure of the materials investigated in this work (modified nanopowders, nanocomposites), but for reasons of simplicity (easiness and fastness of the measurements) the DLS spherical equivalent diameters from mass weighted distributions are reported as particle sizes in this work, keeping in mind that the "real" value is smaller in all cases. Generally, the values obtained from all the different measurement techniques should never be directly compared without sufficient specific knowledge on the investigated system.

Finally, considering the particle sizes from SAXS as best representative for the nanoparticles, comparing the small SiO₂ with the small ZrO₂ nanoparticles and also both large nanoparticle system, the sizes are sufficiently similar and ranged in the desired upper and lower nanoregion to give appropriate model systems for precise studies applying them in nanocomposite materials. The measured size strongly depends on the applied method.

3.1.2 Anchoring of coupling agents to the nanoparticle surfaces

In order to adapt the surface of the prepared inorganic nanoparticles to their environment it is modified applying coupling agents. This is necessary for studies on enhancing the compatibility of the inorganic nano objects with organic media, e.g. solvents, monomers, polymers. Investigations on self-assembled-monolayer formation and the properties of different modified nanopowders are carried out as well as studies on hydrophilic and hydrophobic nanocomposites. Thus a plethora of different organic groups need to be tethered to the nanoparticle surface. The ZrO₂ nanoparticle surfaces were functionalized applying organophosphorus coupling agents according to a standard procedure from *Guerrero et al.*^[149] Via this *post*-modification approach, the coupling agent molecules are adsorbed from a coupling agent solution to the suspended nanoparticle surface. The SiO₂ nanoparticles were

surface modified applying a method of *Philipse and Vrij*.^[148] A quasi *in situ* modification was used where the nanoparticle sol is directly treated with organosilane (organotrimethoxysilane) coupling agents.

The modified nanoparticles were investigated to answer the following questions:

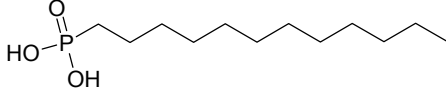
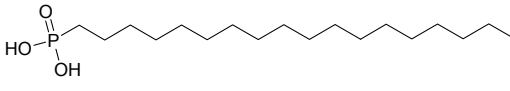
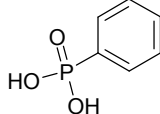
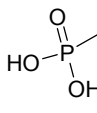
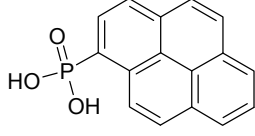
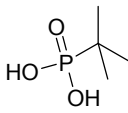
- Is each of the coupling agents attached to the nanoparticle surface with a high chemical stability?
- Can undesired chemical changes of the coupling agent functional end group during the functionalization procedure be excluded?
- Are the nanoparticles themselves affected by the functionalization procedure (e.g. growth, changes in size distribution)?
- What is the resulting grafting density?

3.1.2.1 Organophosphorus coupling agents on ZrO₂

Infrared spectroscopy has been applied as a facile routine method besides solid state NMR spectroscopy to prove the bonding of phosphorus coupling agents to the ZrO₂ surface. The P-O vibrational region shows the most important bands which give hints on the binding mode between 900 and 1300 cm⁻¹.

First, non-functional end group containing phosphonic acid coupling agents were used for the self-assembled-monolayer studies (Table 7). DPPA has been prepared from 1-bromododecane applying the *Arbuzov* reaction^[312, 313] and PyPPA from 1-bromododecane by a similar approach utilizing additionally nickel salts.^[314] The corresponding FT-IR spectra before and after attachment to the ZrO₂ surface are shown in Figure 36. Before the whole series of differently surface modified ZrO₂ nanoparticles will be discussed, the bonding of phosphorus coupling agents will be demonstrated here using the example of DPPA@ZrO₂. The FT-IR spectra of the reagent and of unmodified small and large ZrO₂ nanoparticles as well as of the modified nanopowders are shown in Figure 31. A detailed view of the P-O-vibrational range for bound and free DPPA can be seen in Figure 32. Generally, all spectra of modified powders have been recorded via transmission mode using KBr disks as matrix and the free coupling agents have been measured applying the ATR method.

Table 7. Phosphonic acid coupling agents used in the self-assembled-monolayer studies and also for composite materials preparation.

coupling agent formula	coupling agent name	abbreviation
	dodecyl phosphonic acid	DPPA
	octadecyl phosphonic acid	ODPPA
	phenyl phosphonic acid	PhPPA
	methyl phosphonic acid	MPPA
	1-pyryl phosphonic acid	PyPPA
	<i>tert</i> -butyl phosphonic acid	tBuPPA

In the FT-IR spectra (Figure 31 and Figure 32), the relative intensity of the P-OH bands, located between 940 and 1050 cm^{-1} and precisely 942 cm^{-1} for free DPPA, significantly decrease after modification because of deprotonation and formation of phosphorus-oxygen-metal bonds. Also a vanishing of the P=O vibration, between 1180 and 1280 cm^{-1} and precisely 1209 cm^{-1} for free DPPA, is noticed indicating a P-O-M bond to the metal oxide substrate. The P=O vibration is shifted to lower wavenumbers when binding to the metal oxide surface because of higher electron delocalization in this state.^[149, 190] The overall PO_3 signal of the free acids (between the P=O and the P-OH vibrational region, namely between 942 and 1209 cm^{-1} in this specific case) changes upon the attachment to ZrO_2 . Altogether, the overall PO_3 signal broadens and is also shifted in most cases to form one broad band between 1250 and 900 cm^{-1} (with a peak at 1065 cm^{-1} in the specific case), which is consistent with observations in literature, describing covalent bonding of phosphorus coupling agents.^[193, 236] Additionally the characteristic patterns from the organic moieties, e.g. C-H vibrations in the region between 2800-3000 cm^{-1} , e.g. for free DPPA, with highest intensity, the methylene CH vibration at 2954 cm^{-1} and 2917 cm^{-1} , of the coupling agent after the attachment confirm the successful modification. From the ZrO_2 bulk no significant vibrational modes are detectable

in the discussed spectral range in the case of small ZrO_2 nanoparticles. For the large ZrO_2 nanoparticles, weak signals at 1550 and 1458 cm^{-1} which can be assigned to $\text{C}=\text{O}$ bands from residual acetate groups, shifted due to coordination, can be observed which vanish after surface modification with the phosphonic acid. This is plausible as ZrO_2 large was prepared from acetate precursor and therefore acetate surface groups are expected to be present. However, most of them should be displaced by the stronger binding phosphonic acid groups. That also makes sense as organophosphorus coupling agents selectively bind to transition metal oxide substrates in the presence of carboxylic acids.^[315, 316] However, no significant difference in the spectra of the modified powders could be observed between small and large ZrO_2 nanoparticles. Therefore, in the further discussion only the IR and NMR spectra of modified small ZrO_2 nanoparticles are shown, representing also the large ZrO_2 nanoparticle system.

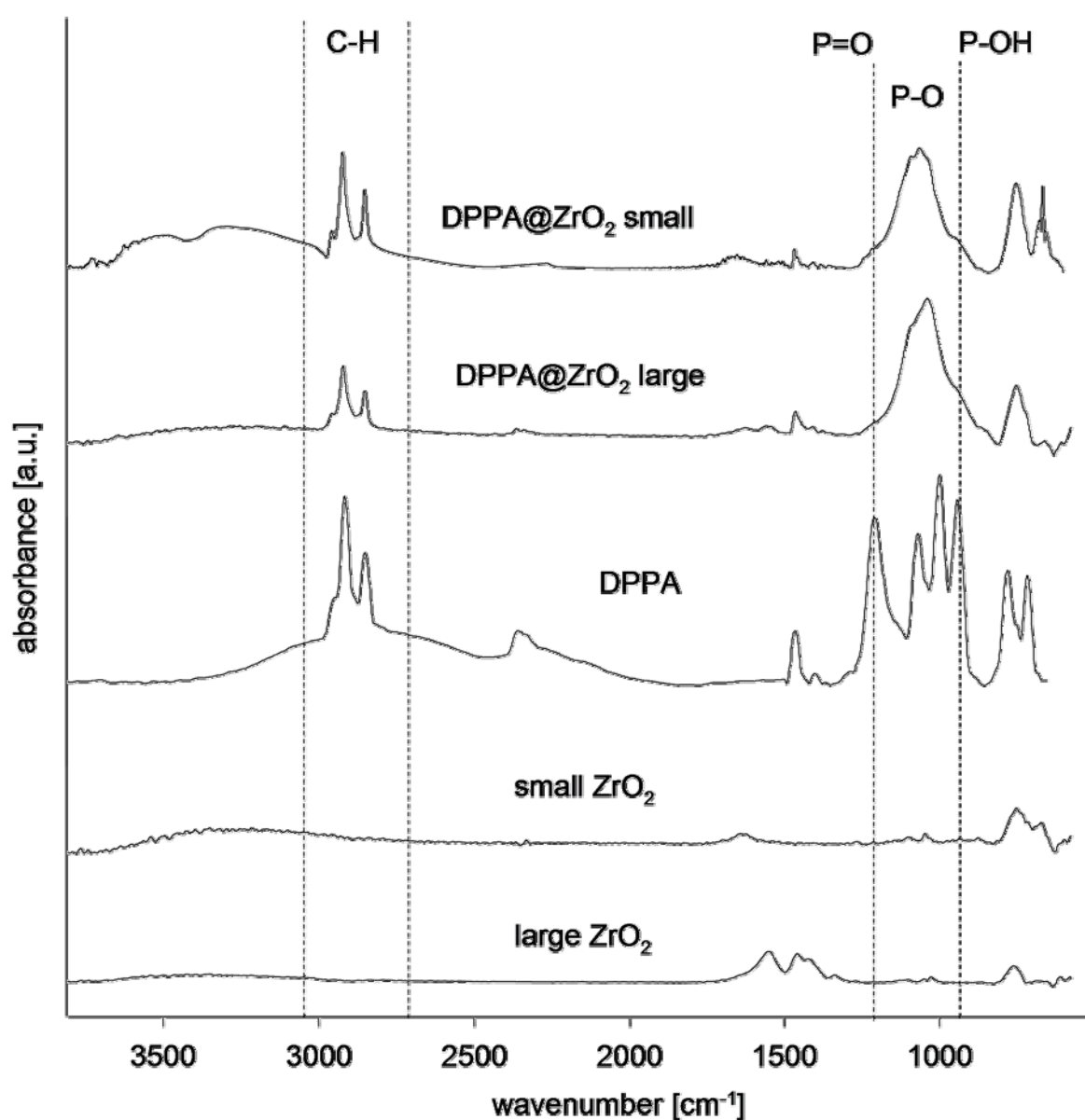


Figure 31. FT-IR spectra of unmodified ZrO_2 nanopowders, DPPA and DPPA@ZrO_2 nanopowders.

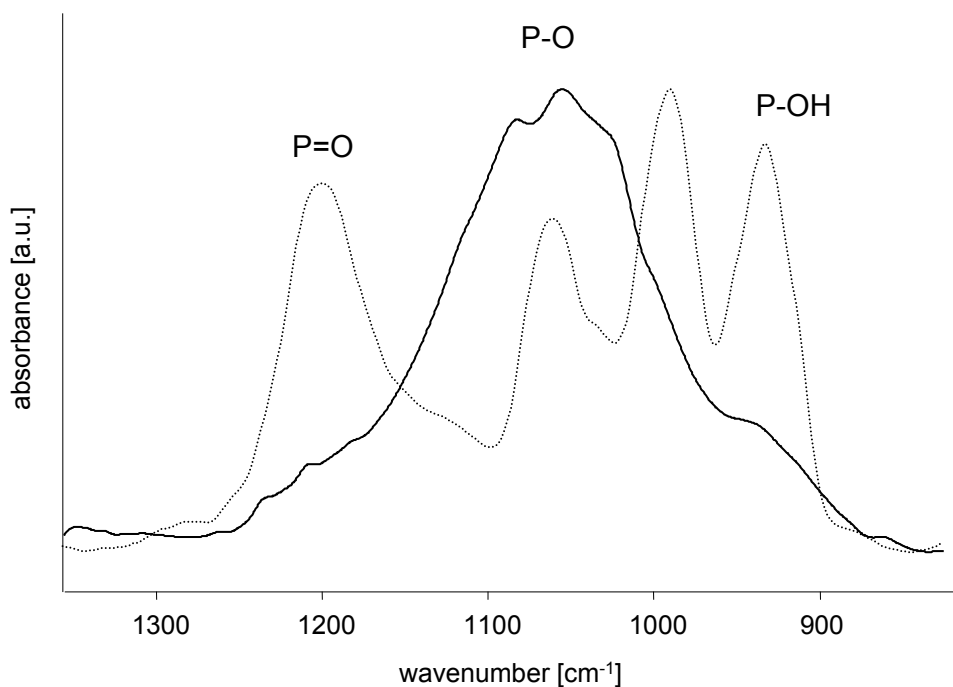


Figure 32. FT-IR spectra of DPPA (dotted line) and DPPA@ZrO₂ small (solid line), detail from the P-O vibrational region.

Concerning the several possible binding modes of the phosphonic acid group on the ZrO₂ surface, no conclusion can be drawn from the FT-IR-Spectra.^[190] Only the presence of weak binding modes where the P-OH or the P=O bonds are not strongly involved can be excluded. For a more detailed investigation ³¹P MAS solid state NMR spectrum of the DPPA@ZrO₂ sample has been recorded, which is shown in Figure 33. A highfield shift of the ³¹P nucleus after the functionalization of about 12.5 ppm indicates a covalent attachment of the anchor group to the zirconia surface. This fact is in agreement with literature, where high field shifts up to 30 ppm have been observed for very strong bonding.^[149, 236] The value observed here is comparatively lower, indicating the presence of a weaker binding mode, which means monodentate with intermolecular hydrogen bridges, which is theoretically strongly favored, and or bidentate binding modes.^[190] For comparison, only a weak interaction of surface with the P=O bond, which is common when phosphonates are only weakly adsorbed, would cause a lowfield shift.^[190] However, the obtained results exclude the significant presence of such a species because upfield shifts are detected which can be assigned to a bonding via the P-OH group. However, the NMR shift also depends on the O-P-O angle.^[190] The broadness and slight anisotropy of the signal indicates the presence of a variety of chemical species, respectively binding modes, attached to the surface. This is plausible as nanoparticle surfaces show many different sites of different geometry, surface energy, and chemical reactivity compared to simple molecular phosphonate compounds.^[317] That means that the presence of a mixture of different binding modes is very likely to be present. As a conclusion, neither from FT-IR nor solid state NMR spectra a distinct binding mode of phosphonic acid to ZrO₂ surface can be assigned in this case because of the chemical complexity of the system.^[149, 190, 236, 318] However, the amount of free acid groups is considered to be very low and strong attachment of the phosphonic acid to the ZrO₂ surface can be assumed.

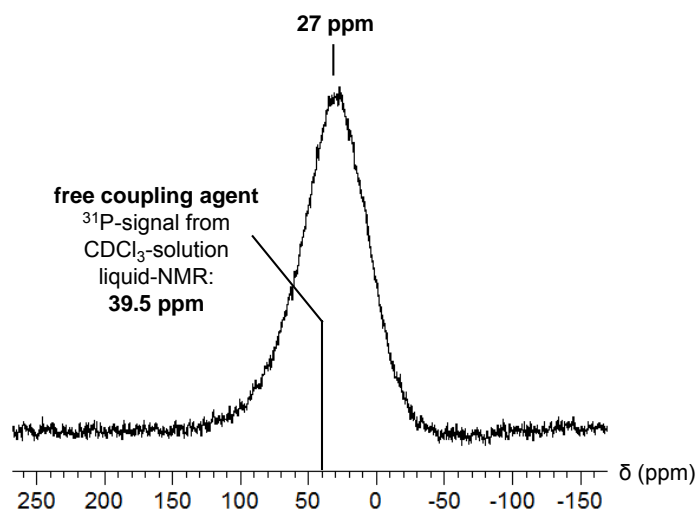


Figure 33. ^{31}P MAS NMR HPDEC spectrum of DPPA@ZrO₂ small.

Furthermore, the ^{13}C MAS NMR spectrum of DPPA@ZrO₂ confirms the presence of the alkyl chain on the particles by showing the specific resonances of the coupling molecules (Figure 34).

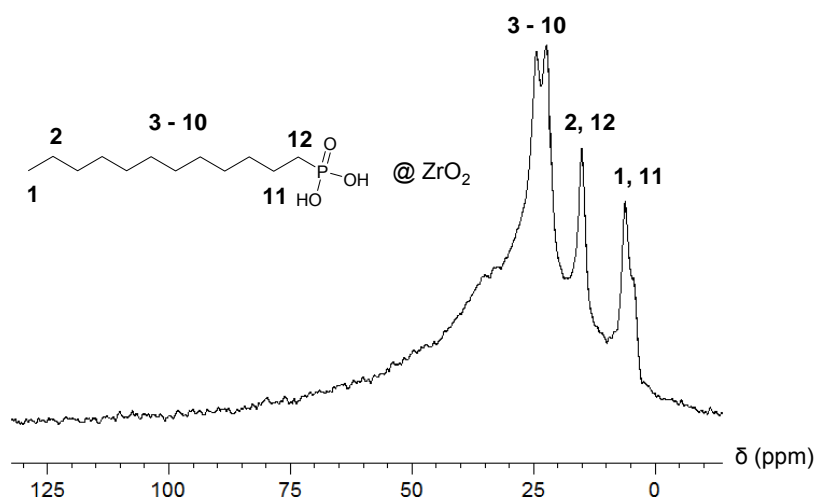


Figure 34. ^{13}C MAS-NMR CP spectrum of DPPA@ZrO₂ small.

Another phenomenon needs to be discussed as it was observed for PhPPA modified nanoparticles. The ^{31}P solid state NMR spectrum from Figure 35 shows one broader resonance at 14 ppm which results from the surface bond phosphonate species which was high field shifted for 11 ppm, which indicates a covalent attachment. However, a second resonance peak is visible at -3 ppm, which can be assigned to a bulk salt phase being a stoichiometric zirconiumphosphonate compound and is observed in literature for the attachment of PhPPA to ZrO₂^[121] or other phosphonic acids at metal oxides applying harsh reaction conditions, e.g. such as 100°C.^[149] That this phenomenon is not observed for DPPA in this studies is likely to be caused by the fact that PhPPA is more acidic than alkylphosphonic acids^[319, 320] and thus more reactive towards coordination to Zr atoms.

Higher pH values as the applied pH 2.5 during the reaction and shorter reaction time may avoid such bulk salt phases also in this case.^[195, 321] For some other modified ZrO₂ systems, this phenomenon has also been observed but in all cases the estimated amount of this salt phase is considered to be very low and not significantly affecting the further presented studies.

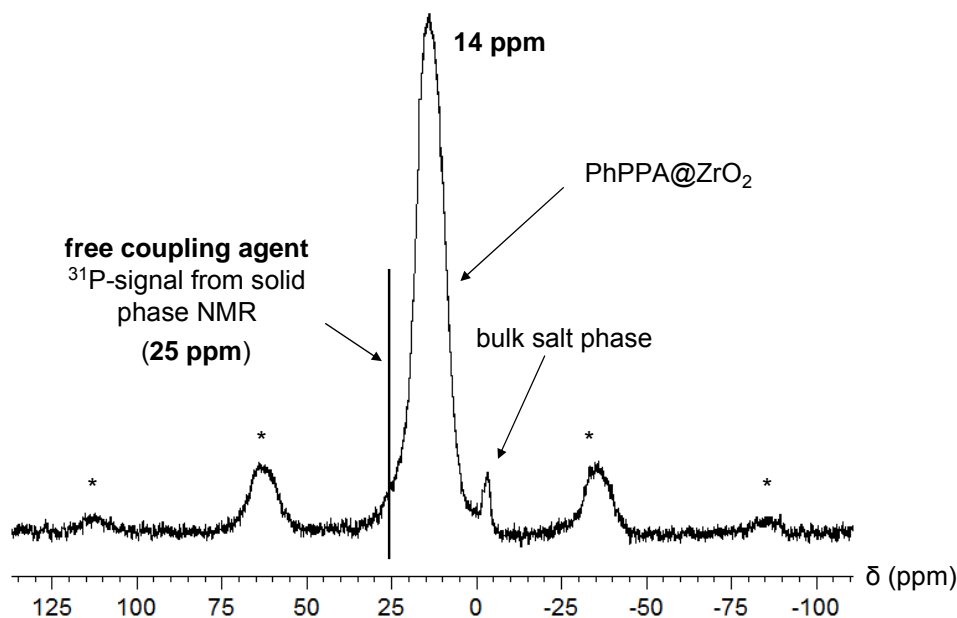


Figure 35. ³¹P MAS-NMR HPDEC spectrum of PhPPA@ZrO₂ small, the asterisk indicates side spinning bands.

The FT-IR spectroscopic study (Figure 36) revealed that the attachment of each phosphonic acid coupling agent molecule led to the formation of the characteristic broad band with its maximum around 1000 cm⁻¹ confirming a covalent bonding. Also the characteristic modes in the C-H vibrational region are present. In further studies this C-H modes will be investigated in detail. The very broad band between 3000 and 3500 cm⁻¹ in the spectra of MPPA@ZrO₂, PyPPA@ZrO₂ and tBuPPA@ZrO₂ most likely results from the vibrational modes of ZrO₂-surface OH groups.^[322] resulting from a non dense monolayer formation as well as strongly adsorbed water molecules.^[322] This is plausible as short chain alkyl chains do not form very dense monolayers.^[207] Coupling agents with sterically demanding moieties also led to a lower grafting density.^[323] However, this fact does not have an influence on the grafting density here in these studies as these coupling agents are always used as mixtures together with long alkyl chain coupling agents in further studies where then a complete coverage of the surface can be reported.

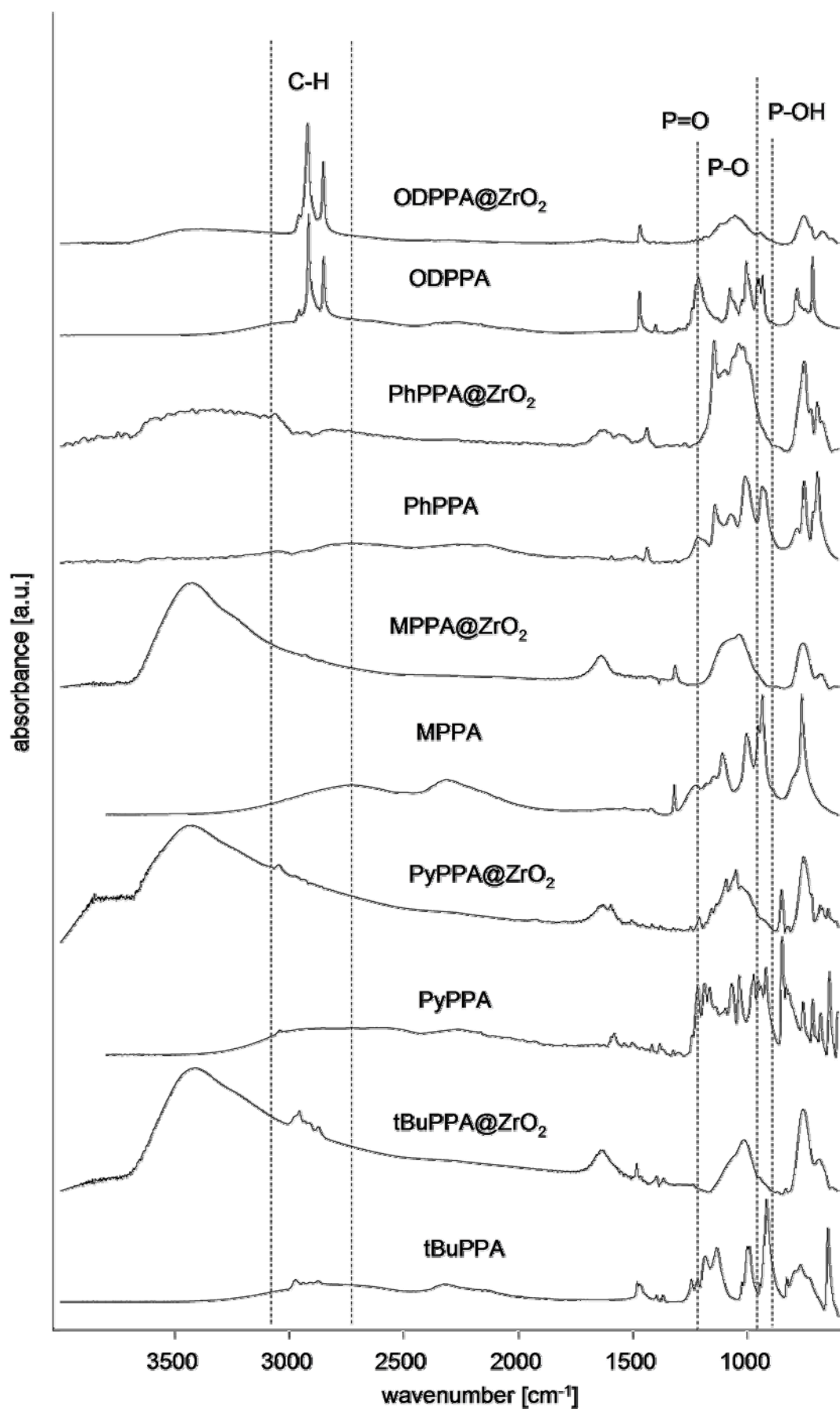
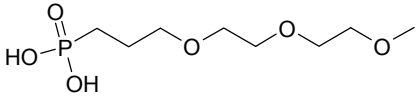
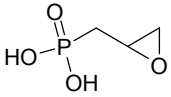
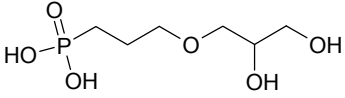


Figure 36. Comparison of FT-IR spectra of coupling agents used in the self-assembled-monolayer studies and the corresponding modified ZrO₂ nanopowders.

Table 8 lists the coupling agents used for the epoxy resin nanocomposite preparation. The organic moieties should allow different strength of interaction with the organic matrix which will be discussed in detail in following chapters. DEG-PPA and Diol-PPA have been prepared from the corresponding allyl ethers via radicalic addition to the P-H bond of dimethylphosphite according to a procedure described in literature.^[203] Ep-PPA was synthesized via oxidation of allyl phosphonic acid.

Table 8. Phosphonic acid coupling agents used for the surface modification of ZrO₂ for the preparation of epoxy resin nanocomposites.

coupling agent formula	coupling agent name	abbreviation
	1-(3-diethylene glycol monomethyl ether) propoxy phosphonic acid	DEG-PPA
	oxiran-2-ylmethyl phosphonic acid	Ep-PPA
	3-(2,3,-dihydroxypropoxy) propyl phosphonic acid	Diol-PPA

The FT-IR spectra of the free and surface bond phosphonic acids are shown in Figure 37. The formation of the characteristic broad P-O band around 1000 cm⁻¹ indicates covalent attachment of the molecules as well as the C-H vibrations from the introduced organic moiety. Special attention is given to the DEG-PPA@ZrO₂ nanoparticles because this novel system will be intensively studied in following chapters. Therefore, a ¹³C solid state NMR spectrum is shown in Figure 38 confirming the presence of the diethylene glycol monomethylether moiety on the nanoparticles.

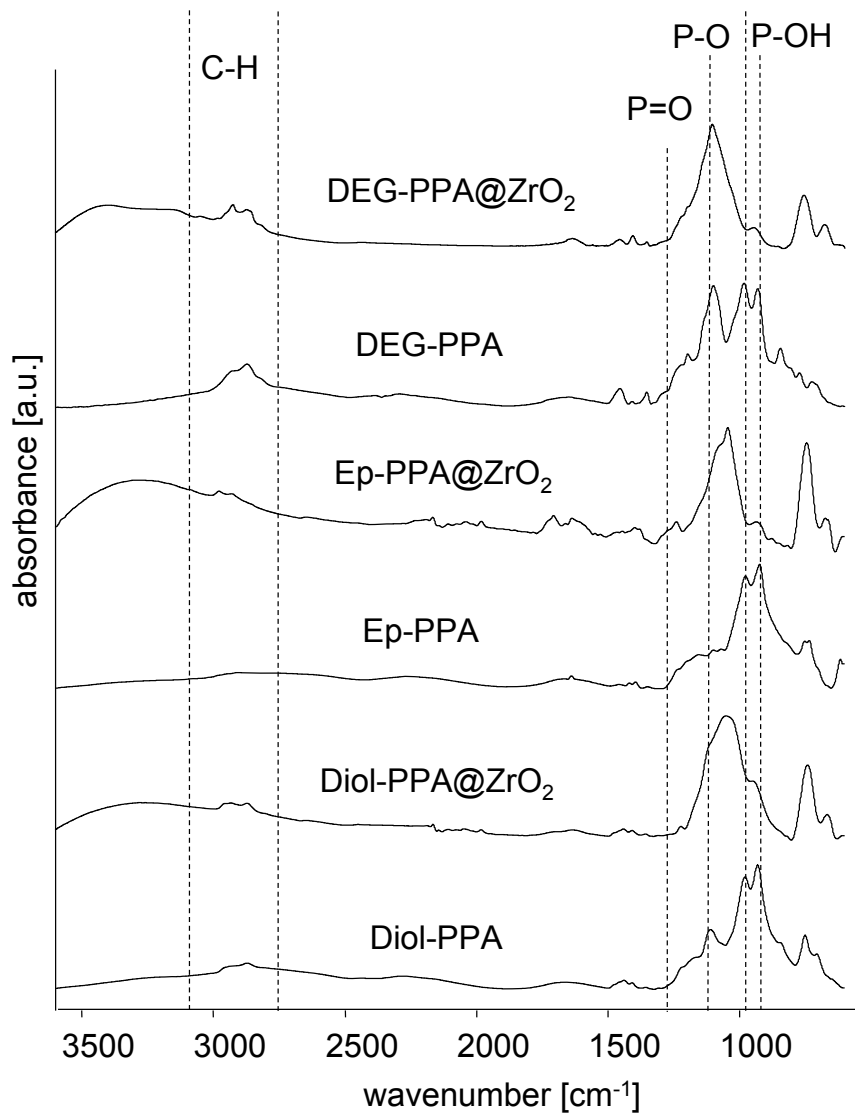


Figure 37. Comparison of FT-IR spectra of coupling agents and the corresponding modified ZrO_2 nanopowders, used for epoxy resin nanocomposite preparation.

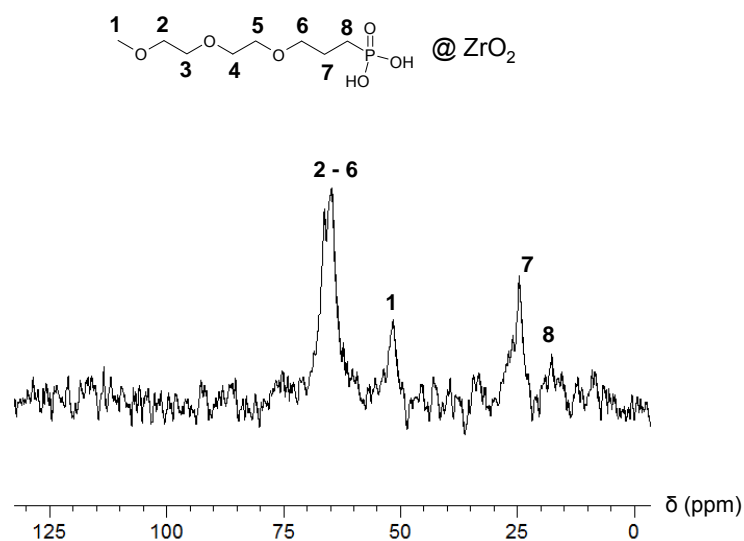
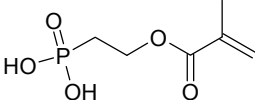
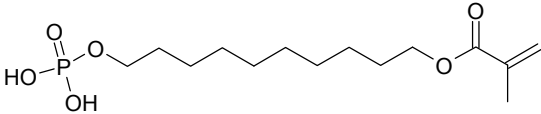


Figure 38. ^{13}C MAS-NMR CP spectrum of DEG-PPA@ ZrO_2 small.

For the preparation of PMMA nanocomposites, coupling agents bearing methacrylate end groups have been prepared and applied. MA-C2-PPA was prepared by a literature known procedure by first preparing a phosphonate with a terminal alcohol group via *Arbuzov* reaction of acetyl protected bromoethanol followed by deprotection and methacrylic acid ester formation.^[203] MA-C10-PA is the only used organophosphoric acid in this work. This specific system, including a phosphoric acid group, was chosen because of the facileness of the synthesis via phosphoric acid mono esterification using phosphoryl chloride and the terminal alcohol methacrylate derivative. Also this molecule is of high relevance in dental nanocomposites.^[324] The result of the attachment of these phosphoric acid monoester molecules is similar applying phosphonic acids.^[195, 325] The result is also a strong covalent grafting to the surface.

Table 9. Organophosphorus coupling agents used for the surface modification of ZrO₂ for the preparation of PMMA nanocomposites.

coupling agent formula	coupling agent name	abbreviation
	2-(methacryloyloxy)ethyl phosphonic acid	MA-C2-PPA
	10-(phosphonooxy)decyl methacrylate	MA-C10-PA

The FT-IR spectra of these methacrylate end group coupling agents, free and attached to the zirconia surface, are shown in Figure 39. For the phosphonic acid MA-C2-PPA, the attachment can be confirmed as discussed previously. However, also for the protic phosphoric acids the surface binding is similar to the binding of phosphonic acids as reported in literature, e.g. by *Paterson et al.* for various organophosphonic acids and phosphoric acid.^[326] Thereby, the IR-spectra of the surface modified system can be interpreted analogously. The formation of a broad band from the P-O vibration around 1000 cm⁻¹ and the vanishing of the P-OH and the P=O vibrational modes can be observed for the phosphoric acids. However, in both cases the P-O signals slightly overlap with the C-O-C vibrational modes around 1200 cm⁻¹ from the methacrylic ester group. The characteristic C-H vibrational bands from the alkyl chain methylene groups are visible. Furthermore, the bands of C=O (1690-1700 cm⁻¹) and C=C (around 1630 cm⁻¹) evidence that the methacryloyl group is still intact after the modification procedure and a chemical change, e.g. hydrolysis, under the functionalization reaction conditions is therefore excluded. The ³¹P solid state NMR spectrum in Figure 40 shows a very asymmetric peak, with at least two sharp shoulders, indicating a complex binding behavior as described for the phosphonic acids. A small overall highfield shift due to attachment of 3 ppm and the fact that the resonance peak shows a tailing towards high field ppm values, indicates

the strong interaction of the phosphoric acid group with the ZrO_2 surface.^[121] Here also the presence of a bulk phase, indicated by a peak at -20 ppm can be assumed, similar as reported in literature.^[121] The plausible reason for the formation of a salt phase for this sample can be found in the nature of monoesters of phosphoric acids which are more protic than comparable phosphonic acids. Analogous alkyl phosphonates did not show such a behavior in this work.^[320] However the amount of this by-product is not considered to affect further studies significantly.

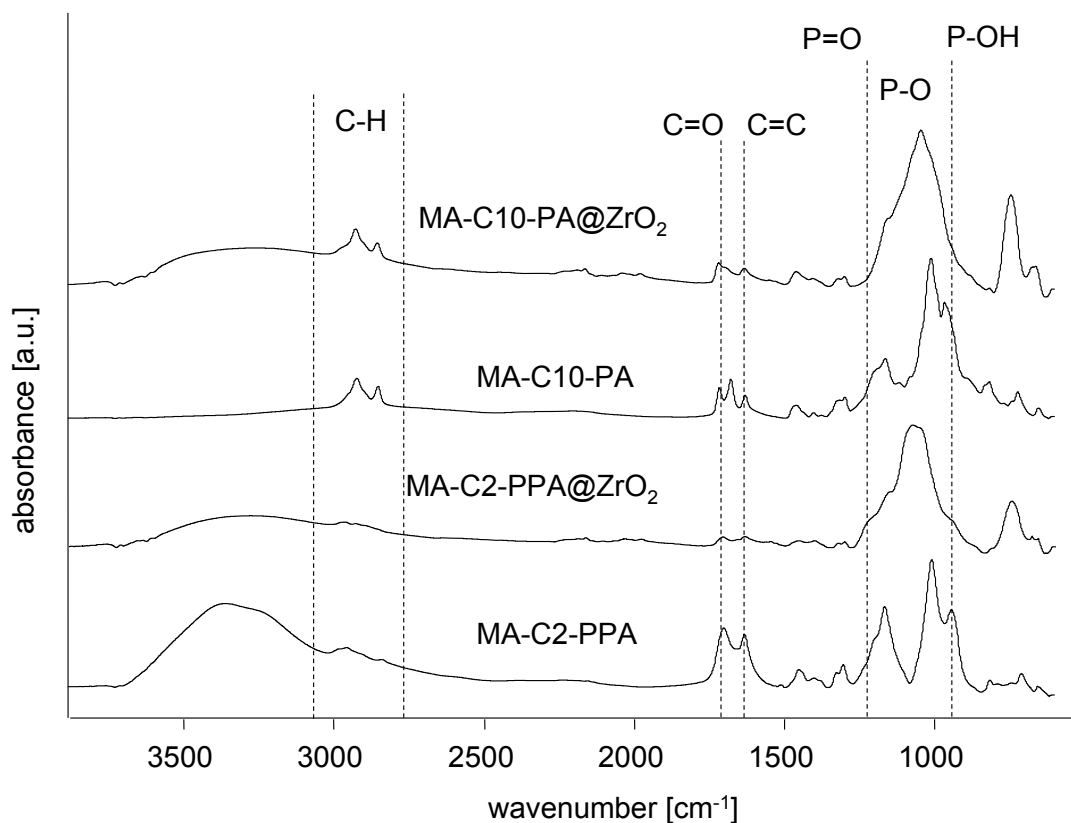


Figure 39. Comparison of FT-IR spectra of coupling agents and the corresponding modified ZrO_2 nanopowders, used for PMMA nanocomposite preparation.

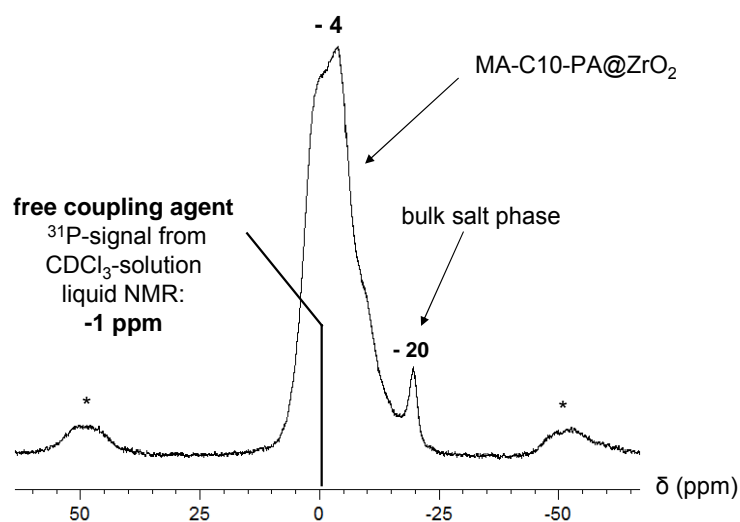


Figure 40. ^{31}P MAS-NMR HPDEC spectrum of MA-C10-PA@ZrO_2 small, the asterisk indicates side spinning bands.

Finally, the ^{13}C NMR spectrum (Figure 41) confirms that the methacrylate group is still present after the surface functionalization reaction and has not been degraded in the reaction process.

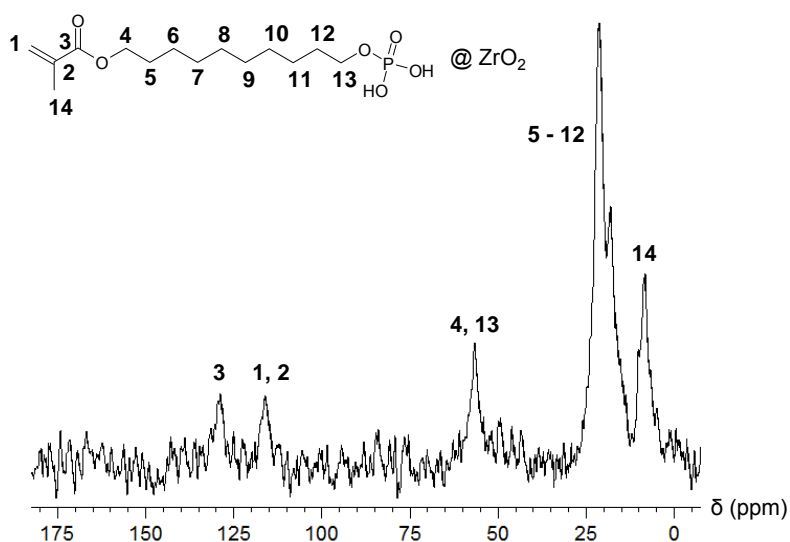


Figure 41. ^{13}C MAS-NMR CP spectrum of MA-C10-PA@ZrO₂ small.

A special alkylbromo end group phosphonic acid coupling agent (Table 10) was also prepared via selective *Arbuzov* reaction from 1,2-dibromoethane followed by isolation of the desired product via distillation according to a literature known procedure^[327] and hydrolysis of the phosphonate group via trimethylsilylbromide.^[203] This molecule Br-C2-PPA is applied in further studies to provide alkylbromo end groups at the ZrO₂ surface which are then lithiated and the particles then act as initiators for anionic ring opening polymerization reaction (see PDMS grafting *from* chapter, 3.1.5.2).

Table 10. Coupling agent used to introduce the initiator precursor for polysiloxane grafting *from* reaction experiments.

coupling agent formula	coupling agent name	abbreviation
	2-bromoethyl phosphonic acid	Br-C2-PPA

The FT-IR spectra in Figure 42 confirm the covalent attachment of this molecule to the ZrO₂ surface by the appearance of the characteristic broad band at 1000 cm⁻¹. Additionally elemental analysis of the modified particles reveals a bromine content of 5.3 wt% which is the evidence that the bromo end group is still intact after functionalization (and was not e.g. hydrolyzed).

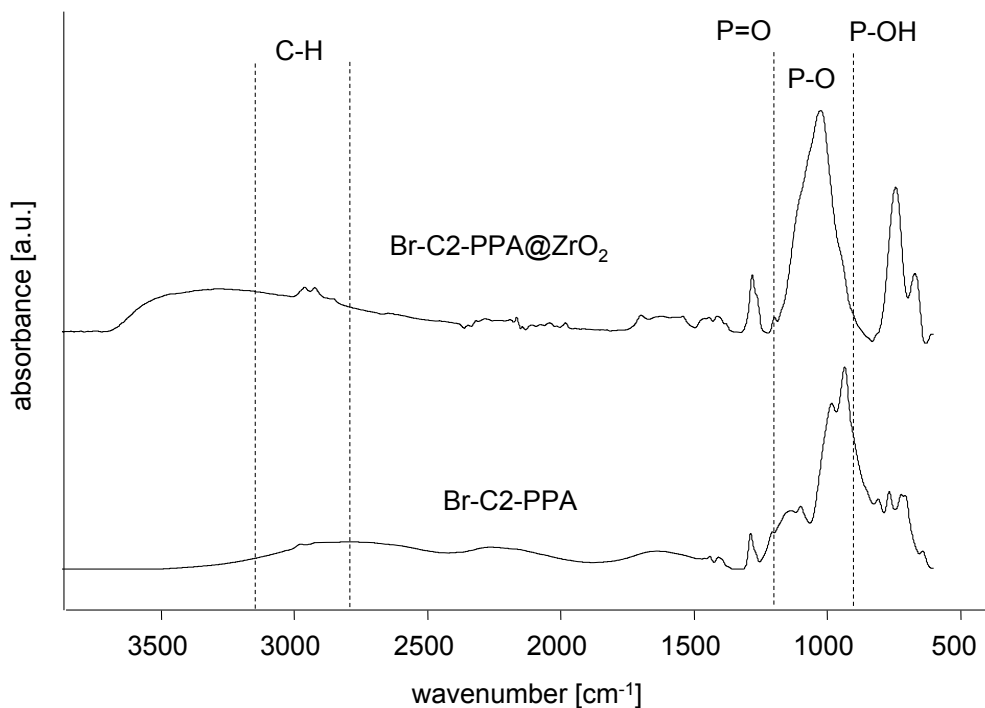


Figure 42. FT-IR spectra of Br-C2-PPA, free and bonded to the surface of ZrO₂ small.

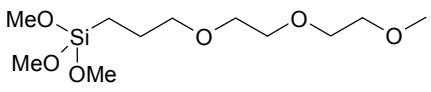
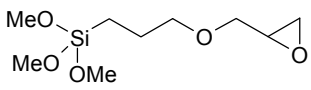
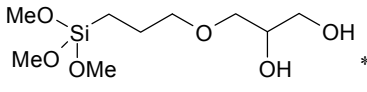
From this chapter it can be concluded that all coupling agents needed for the further studies are strongly bonded to the ZrO₂ surface and the functional end groups remain unchanged during the modification reactions and thus result in well-defined model systems for the following studies. The particles (namely the ZrO₂ bulk) themselves are in some cases (when stronger acid molecules are adsorbed) affected by the functionalization reaction where salt phases are formed. However, the reported amount is assumed to be not significantly high enough to affect the studies in this work and in TEM no change of the particles in size and shape can be reported for this case. An additional comparison via DLS whether the particles shrank due to salt phase formation (which is of course excluded already from the TEM results) or not cannot be made because due to hydrophobization the dispersion medium has to be changed. The novel class of poly (siloxane) spacer phosphonic acids and their binding to ZrO₂ surfaces will be later discussed in the corresponding chapter 3.1.5.1.

3.1.2.2 Trialkoxysilane coupling agents on SiO₂

As surface modifying reagents for SiO₂, trimethoxysilanes have exclusively been applied because of their higher reactivity towards hydrolysis to silanol groups followed by condensation to the particle surface^[178, 301] To prove the attachment of the trialkoxysilanes to the Stöber particles FT-IR and solid state NMR spectroscopic methods have been applied. Because of the small particles having a much higher surface-to-volume ratio and thus the signals from the surface modification are stronger, compared to the signals from the larger nanoparticles, all analyses are discussed here for the small SiO₂ nanoparticles exemplarily. The results were qualitatively the same for the other, larger particle systems.

Table 11 lists the silane coupling agents used in the preparation of epoxy resin nanocomposites, analogous to the organic moieties as applied for ZrO₂. The novel coupling agent DEG-TMS has been synthesised via hydrosilation reaction of trimethoxysilane and the allyl ether of the diethylene glycol monomethyl ether. The Diol-TMS reagent itself was not used for surface functionalization. This end group was prepared via acidic hydrolysis of the end groups of Gly-TMS@SiO₂ particles.

Table 11. Organotrimethoxysilanes for SiO₂ particle surface modification, applied in epoxy resin nanocomposites.

coupling agent formula	coupling agent name	abbreviation
	1-(3-diethylene glycol mono methylether) propoxy trimethoxysilane	DEG-TMS
	3-glycidoxy propyl trimethoxysilane	Gly-TMS
	-(2,3,-dihydroxypropoxy) propyl trimethoxysilane	Diol-TMS

*...not used as a free coupling agent, formed via post-hydrolysis of surface attached Gly-TMS

The FT-IR spectra of unmodified SiO₂ nanoparticles and modified nanoparticles for the use in epoxy resin nanocomposites are shown in Figure 43. However, the confirmation of the attachment of the trialkoxysilane applying this method is rather difficult compared to the described system of organophosphorus coupling agents on ZrO₂. The highly intense and broad band resulting from the Si-O-Si vibration around 1200 cm⁻¹ from the SiO₂ bulk of the particles superposes with the low quantity of Si-O-C modes which would indicate a covalent coupling agent attachment, as it also can be observed in literature for similar systems.^[188] However, the presence of the C-H vibrations resulting from the organic moieties (C-H vibrations in the region of 2800-3000 cm⁻¹) are indicating the presence of the organic moiety as the non modified blank system shows no significant C-H modes. The characteristic vibrational mode of the epoxide ring at 3050 cm⁻¹ was too weak to be detected.

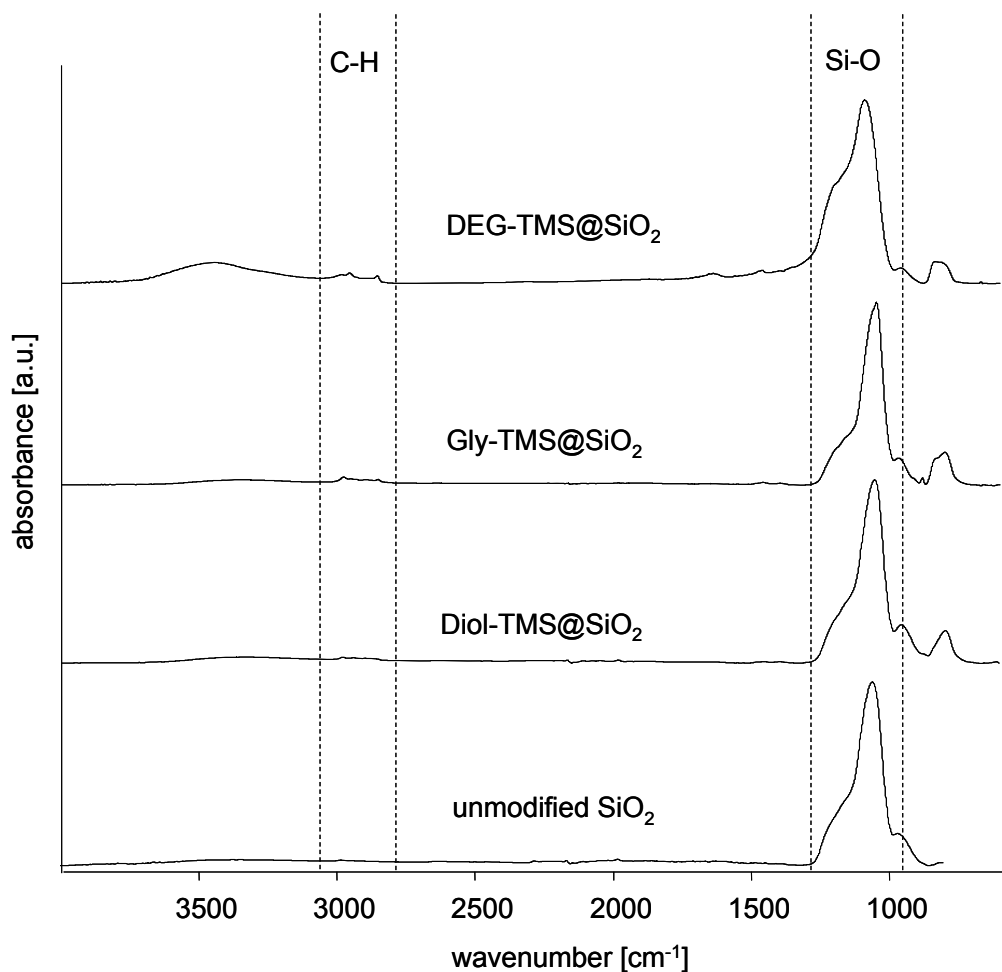


Figure 43. FT-IR spectra of silane coupling agent modified SiO_2 nanoparticles, used for epoxy resin nanocomposite preparation.

To further investigate on the success of the attachment of the trialkoxysilane to the nanoparticles, a ^{29}Si solid state NMR spectrum was recorded exemplarily for DEG-TMS@ SiO_2 (Figure 44). The signals from the Q-unit between -80 and -120 ppm result from the SiO_4 -units in the particle bulk. The signals between -55 and -70 ppm indicate the presence of T-units (RSiO_3), which would not be the case for unmodified particles, indicating the successful covalent attachment of the coupling agents. This spectrum appears exactly as reported in literature for similar organosilanes on the surface of *Stöber* particle systems.^[189] Concerning the binding mode, also some conclusions can be drawn. In general, the system of alkoxy silanes@ SiO_2 is less defined compared to the system of phosphonates@ ZrO_2 , because the molecules tend to homocondensate forming complex polycondensed layers at the SiO_2 surface.^[138, 185, 186] In addition to that also chemically different sites from the particles are again present. However, the results from the ^{29}Si NMR spectrum, where shifts for the T-units between -55 and -70 are observed, enable the exclusion of the presence of a significant amount of only monodentate bound species, as the shift would be in this case between -45 and -50 ppm. Thus, and because of the characteristic shape of these resonances, comparing this NMR data with literature data, a bidentate and or tridentate binding mode can be suggested where a ladder like T^3 arrangement of the coupling agent molecules at the SiO_2 nanoparticle

surface is very likely.^[166] Again no distinct characterization of binding modes is possible for this complex system. However, the ^{29}Si NMR data gives the evidence for the strong covalent attachment of the organosilane coupling agents to the SiO_2 nanoparticles.

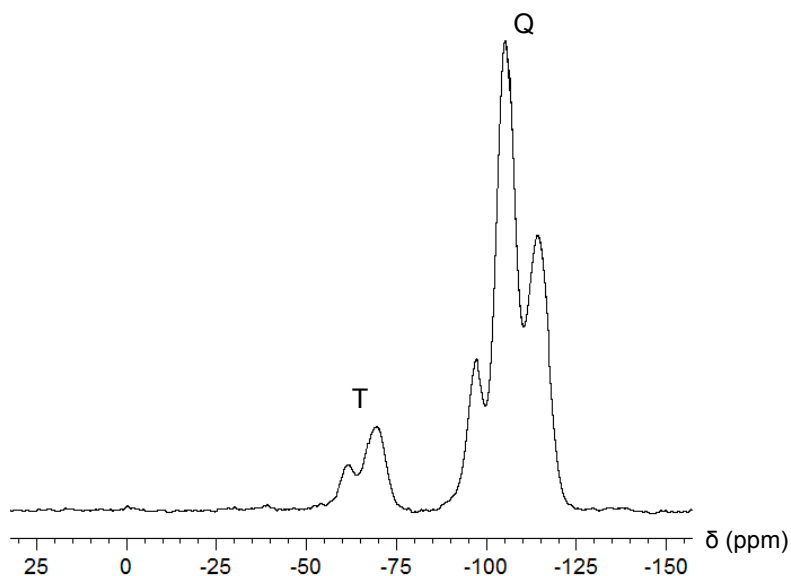


Figure 44. ^{29}Si -MAS-NMR CP spectrum of DEG-TMS@ SiO_2 small.

The ^{13}C solid state NMR spectrum of DEG-TMS@ SiO_2 evidences the presence of the diethylene glycol monomethylether chain on the nanoparticles by showing the characteristic peak pattern (Figure 45). The resonance peaks, marked by the asterisk are likely to result from a small amount of residual ethoxy groups, which remain unreacted during the *Stöber* process, from the bulk of the nanoparticles. This is a common phenomenon especially for smaller nanoparticles prepared under use of low amounts of ammonia.^[328]

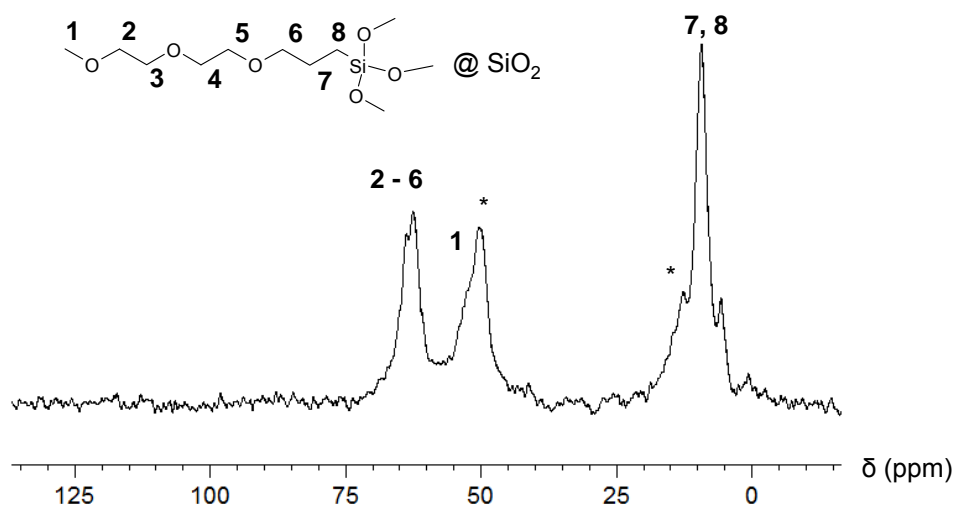


Figure 45. ^{13}C -MAS-NMR HPDEC spectrum of DEG-TMS@ SiO_2 small.

The organosilane coupling agents used for self-assembled-monolayer studies on SiO_2 nanoparticles are listed in Table 12 and coupling agents for the preparation of poly(methyl methacrylate) and polystyrene nanocomposites are listed in Table 13. The molecule MA-C10-

TMS has been synthesized applying a selective hydrosilation with trimethoxysilane and the corresponding decenyl ester of methacrylic acid. The chemical similarities with the end groups and the monomers of the mentioned thermoplasts should be noted here, they will be from importance in the following nanocomposite chapters.

Table 12. Organotrimethoxysilanes for SiO₂ particle surface modification, applied in self-assembled-monolayer studies and also in composite material preparation.

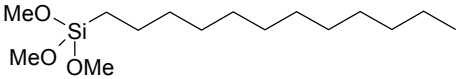
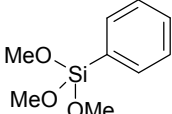
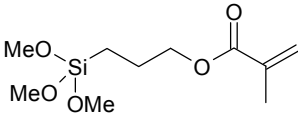
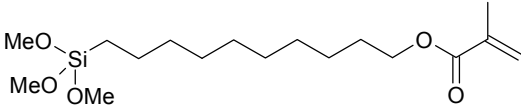
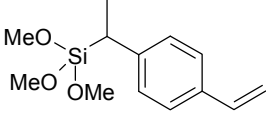
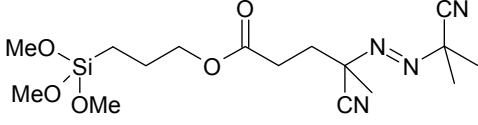
coupling agent formula	coupling agent name	abbreviation
	dodecyl trimethoxysilane	DTMS
	phenyl trimethoxysilane	PhTMS

Table 13. Organotrimethoxysilanes for SiO₂ particle surface modification, applied in thermoplasts nanocomposite preparation.

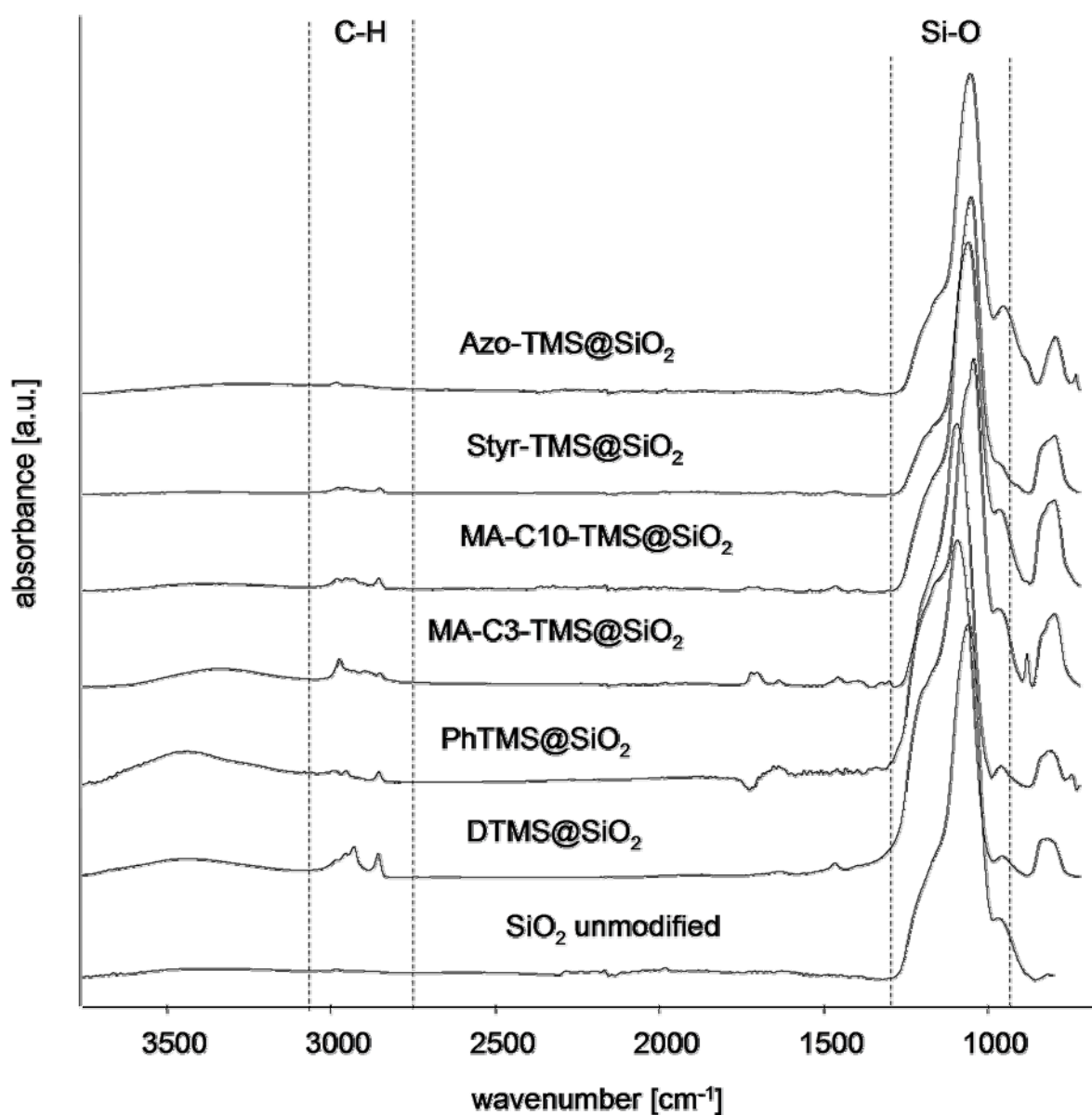
coupling agent formula	coupling agent name	abbreviation
	(3-methacryloyl)oxypropyl trimethoxysilane	MA-C3-TMS
	(10-methacryloyl)oxydecyl trimethoxysilane	MA-C10-TMS
	(1-(4-vinylphenyl)ethyl) trimethoxysilane	Styr-TMS

Finally, a coupling agent providing an initiator group for radical polymerization for the preparation of polystyrene grafted SiO₂ nanoparticles, is shown in Table 14. This reagent was prepared following a procedure by *Prucker and Rühle*^[255] by preparation of an asymmetric diazo molecule and finally hydrosilation with trimethoxysilane.

Table 14. Silane coupling agent for SiO₂ particle surface modification as initiator group for free radical polystyrene grafting.

coupling agent formula	coupling agent name	abbreviation
	3-(trimethoxysilyl)propyl 4-cyano-4-((2-cyanopropan-2-yl)diazenyl)pentanoate	Azo-TMS

The collected FT-IR spectra of this various reagents, attached to the SiO₂ surface are plotted in Figure 46. The increase in the intensities of the C-H stretching vibrations for the modified particles, compared to the unmodified ones, can again be seen as an evidence for successful modification.

**Figure 46.** FT-IR spectra of miscellaneous silane coupling agent modified SiO₂ nanoparticles, used for several studies.

Only in the case of Azo-TMS, the difference in C-H intensity was not significantly higher. However, results from thermal analysis (DSC and TGA) of the modified particles show an expeditious decomposition at 123°C (peak DSC, onset TGA: 102°C, each measurement performed with a heating rate of 10K/min) which is the evidence for the intact azo initiator group at the particle surface. Further Investigations on this system as well as solid state NMR spectra showing the diazo group signals will be discussed in the corresponding chapter 3.1.6.

Finally, the ^{13}C NMR spectrum of MA-C3-TMS@SiO₂ in Figure 47 confirms that the methacrylate group remains unchanged during the procedure of functionalization by the presence of the characteristic resonance signals, which was also the case for MA-C10-TMS.

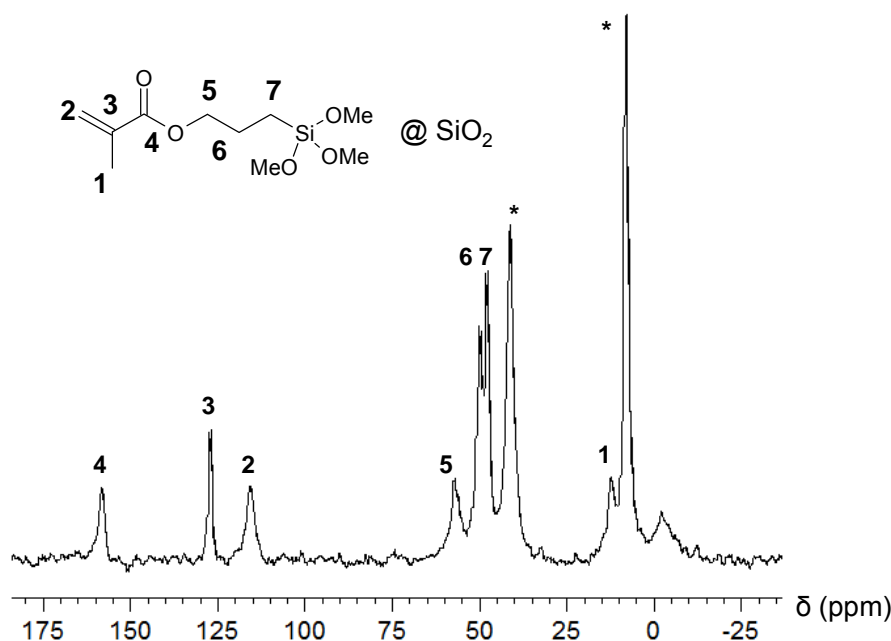


Figure 47. ^{13}C -MAS-NMR HPDEC of MA-C3-TMS@ SiO₂ small (* ... signals from ethoxy groups from particle bulk).

The chemical attachment of all used alkyl based silane coupling agents was shown in this chapter. Only the polysiloxane spacer based silane coupling agents will be discussed in a separate chapter.

The next point which has to be clarified is, whether the particles themselves (size and shape) have changed during the quasi *in situ* modification process. This is more likely here than for the analogous system of phosphonate on ZrO₂ where (when no bulk salt phase is formed) only molecular monolayers are adsorbed and the coupling agents do not tend to homocondensate^[181, 190] as the trialkoxy silane coupling agents, which usually can form polycondensed organosilane (multi)layers and thus the particle size can increase.^[185] Additionally, further homoreactions between specific coupling agent molecules, depending on the functional end group, can occur resulting in a larger particle size. For instance, *Riegel* and *Kiefer* have demonstrated applying FT-IR and Raman spectroscopy that epoxy end group bearing trimethoxysilanes can form homopolymers also via their epoxy-end group,^[184] which can lead to additional surface layer growth. Therefore as an extreme example, where the

highest particle size change can be expected, the Gly-TMS@SiO₂ small and large nanoparticle system, is inspected here. DLS experiments were carried out before and after the surface modification and the resulting mass weighted particle size distributions are shown in Figure 48. A slight increase in the particles size can be observed, precisely an increase by 3.6 nm in diameter (peak) for the small nanoparticles which corresponds to a 1.8 nm thick polycondensed organosilane layer and similar for the larger nanoparticles. However it is assumed that this fact does not significantly impact the following studies on particle size depending properties, as the diameters of both particle systems are still significantly different, one in the lower nanorange and one in the upper range. Also for all other systems, e.g. MA-C3-TMS@SiO₂, for the mentioned reasons, the particle growth during modification was much smaller and negligible. However, from DLS it has also to be considered that a change in diameter can result from a change in the hydrodynamic shell which has also to be taken into account when discussing the change in particle size here, as it may falsify the results. As a conclusion, where the ZrO₂ nanoparticles could in principle become smaller during the modification reactions, the SiO₂ nanoparticles can grow.

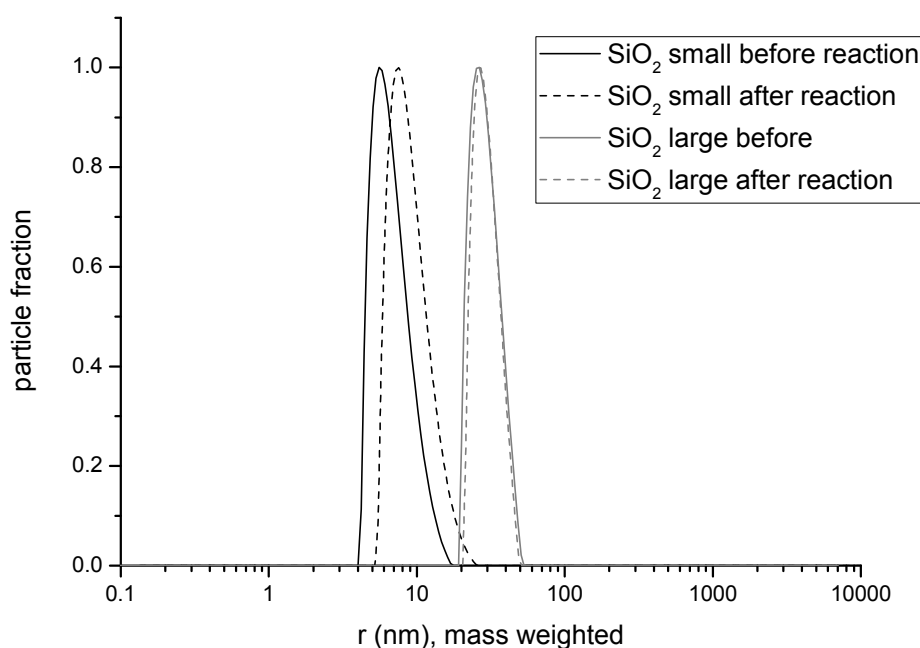


Figure 48. Particle size distributions from DLS (mass weighted) of SiO₂ small and SiO₂ large nanoparticles before and after the surface functionalization with MA-C3-TMS.

Finally, the modified SiO₂ particle model systems can be considered to be appropriate as the coupling agents are strongly chemically linked to the nanoparticle surface.

3.1.2.3 Grafting densities of organic molecules at oxidic surfaces

It is not only necessary for our studies to ensure a covalent grafting of coupling agent molecules to the nanoparticles but also to ensure a certain amount of adsorbed molecules. In order to obtain significant effects, the grafting density needs to exceed a certain value. Therefore, all modified nanoparticles which are used for nanocomposite preparation will be investigated in this chapter.

The grafting densities σ (molecules/nm²) were calculated using the formula (Eq. 6), which has been applied in literature for similar nanopowder systems.^[98, 329]

$$\sigma = \frac{\Delta_m}{M_R} \cdot \frac{1}{S_{BET}} \cdot N_A \cdot 10^{-18} \quad \text{Eq. 6}$$

where Δ_m is the mass loss from TGA in synthetic air between 200°C and 800°C (g/g) which is feasible because the onset of the thermal desorption for all used coupling agents was higher than 220°C, M_R is the molecular mass of the organic moiety (g/mol), S_{BET} is the N₂ surface area of the bare metal oxide sample (m²/g) and N_A is the *Avogadro* constant. The assumption is made that only the organic compounds are removed upon heating during the TGA analyses. This is plausible for SiO₂ as the anchor group of the attached silane results in a SiO₂ residue under the conditions applied for TGA investigations. *Fadeev et al.* have demonstrated for alkylsilanes on SiO₂ and phosphonic acids on ZrO₂ that the assumption a complete decomposition of the organic moiety is valid. The anchor-group residue remains on the inorganic substrate. Hence, this approach results in correct values for the grafting densities.^[329] Additionally, for modified ZrO₂ the assumption that only the organic residue is cleaved off was proven by the fact that pXRD analysis revealed the presence of Zr-phosphate-species in the residue, obtained after thermal treatment, and TGA coupled mass spectrometry (TG-MS) experiments did not show a desorption of the phosphonate species, only characteristic fragments (e.g. propyl cation) were observed in the decomposition offgas. These observations and the fact that the P-C-bond as well as the P-O-C-bond are the weakest chemical bonds in the whole system of organophosphorus coupling agent on metal oxide surface^[330, 331] also justify these assumptions. Therefore, the molecular mass of the anchor group should not be incorporated in the calculations in both cases (surface modified SiO₂ and ZrO₂). The calculation of grafting densities will be demonstrated by the example of DEG-PPA@ZrO₂ small as this is a novel system used for nanocomposite materials in this work. The thermograms of DEG-PPA@ZrO₂ small and unmodified ZrO₂ small are therefore presented in Figure 49. For the unmodified particles a continuous decrease in mass showing no decomposition step is observed, which can be related to the desorption of weaker and/or stronger surface bond water molecules. This is a common problem in nanoparticles research, also for SiO₂ nanoparticles, especially for small particle sizes.^[223] In the case of the large ZrO₂ particles also the inner surface is taken into account by using the S_{BET} specific surface area for the calculation. As the particles exhibit a dense, solid nature, the assumption that evaporated water can only originate from surface adsorbed layers is plausible. Therefore, the thermogram of the unmodified sample is not subtracted from the thermogram of the modified sample

before determining Δm , because in the modified system the surface sites where water can adsorb are blocked. This effect can be observed better for hydrophobic surface modifications e.g. for PhPPA and DPPA (Figure 50). Water adsorption could not be avoided even by drying the particles in high vacuum over P_2O_5 , because nanocurved objects, such as nanoparticles, own a higher surface energy than macroscopic surfaces,^[332] capillary condensation lowers the vapor pressure in nanopowders. In addition to that a condensation of the surface M-OH groups is also possible, releasing water molecules.^[176] The onset temperature for the decomposition step of DEG-PPA@ZrO₂ was determined to be 260°C from the thermogram and a mass loss of 11.8% was observed for this degradation step. These results from TGA are in agreement with results from elemental analysis. Thereby, 7.7% C, 1.7% H and 1.6% P (Analysis of free the DEG-PPA revealed 39.6% C 7.9% H, 12.8% O) could be found, which is equal to 11.9% organic residue mass and thus perfect concordance is given. Elemental analyses of random samples were all in agreement with results from TGA measurements Hence, the assumptions proposed above have been confirmed. Therefore, the molecular mass of the organic moiety $M = 162$ and the specific surface area $S_{BET} = 140$ were inserted in Eq. 6 and a grafting density of $\sigma = 3.1$ molecules/nm² was obtained for this system.

For the modified SiO₂ system the situation is different: Already the unmodified nanoparticles show a significant decomposition step at 230°C, very likely originating from the cleavage of residual alkoxide (EtO-) groups in the particle bulk.^[116] Therefore the mass loss of the unmodified particles, 7.4% for SiO₂ large and 5.0% for SiO₂ small, has to be taken into account for the calculation of Δm . This makes the interpretation and comparison of the results rather difficult.

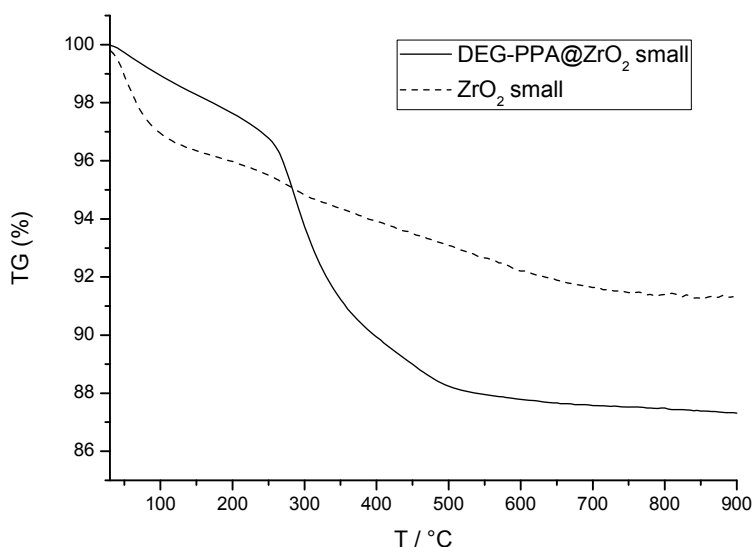


Figure 49. Thermogravimetric analysis curves (thermograms) for unmodified ZrO₂ small nanoparticle powder (dashed line) and for DEG-PPA@ZrO₂ small (solid line).

Exemplarily, TGA analyses of particles with hydrophobic surface modification (DPPA and PhPPA) are shown in Figure 50. The thermal stability (in air) with decomposition temperatures of 470°C for PhPPA and 260°C for DPPA (onsets) points out the quality of these systems for technological applications.

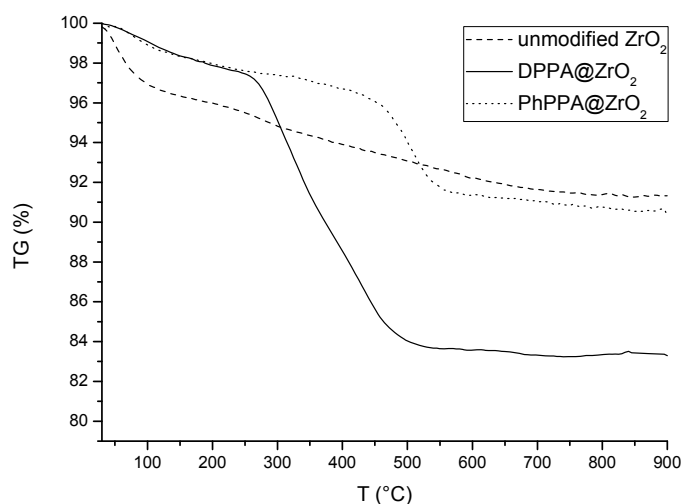


Figure 50. Thermogravimetric analysis curves for unmodified ZrO₂ small nanoparticle powder (dashed line), DPPA@ZrO₂ (solid line) and PhPPA@ZrO₂ (dotted line).

The thus calculated grafting densities for organophosphorus coupling agents on ZrO₂ are listed in Table 15. Generally, the values (except those marked with an asterisk), do not exceed 3.6 molecules per nm² for ZrO₂ large (and 3.4 for ZrO₂ small in case of the strong self-assembled monolayer forming ODPPA). The maximum grafting density for phosphonates at a plane metal oxide surface has been reported to be 4.2-4.8 molecules/nm² for the dense C18-monolayer in other studies in literature.^[182, 326] Assuming a theoretical demand of 24 Å² per anchor group, the surface would be covered to 100% in this case. The difference between the values obtained in the present work and in literature can be explained by the fact that *Fadeev et al.* assume a surface demand of N₂ molecules of 0.135 nm² for the calculation of the specific surface area from their nitrogen sorption experiments. Whereas in this work, a steric demand of 0.162 nm² is assumed which results in a higher specific surface area of the nanopowder and therefore the values, obtained for the grafting densities in this work, are lower by a factor of 0.83. However, also the variations in the morphology of a metal oxide nanoparticle surface compared to a macroscopically plane surface might be blamed for the relatively lower grafting densities. Nanoparticle surfaces exhibit a strong curvature with many defects and disordering phenomena. In addition many particles show an amorphous outer-shell-formation at their surface which has to be taken into account if the surface is compared with ideal crystal surfaces.^[311] Also the number of surface OH-groups, responsible for chemical bonding between organophosphorus anchor group and a nanoparticle surface at different oxidic nanoparticles, usually differs from the coordination site number on a perfect plane surface^[176] which has negative impact on the grafting density. It is known from

Tong et al. from ^{13}C NMR spectroscopical investigations of organothiols on gold nanocrystals that the different reactive sites such as edges, corners or terraces are responsible for a different structure of the adsorbed organic monolayer^[333] and thus influences the grafting density. Such organic moiety ordering related phenomena at nanoparticle surfaces will be discussed in chapter 3.1.3 in detail. Also a systematic error for all series has to be taken into account, namely how good the BET surface value represents the real surface area of the nanoparticles, which is accessible for the coupling agent molecules in the modification process. It is possible that the BET surface area underestimates the total accessible area, because during the nitrogen sorption measurement parts of the surface are non accessible for nitrogen molecules in the dried powder. In reaction dispersion, these surface parts might be accessible for the coupling agent which would result in higher values for grafting densities. However, this mentioned error is considered to be low and in the range of the measurement accuracy. PhPPA on ZrO_2 shows a maximum grafting density of approximately one molecule/ nm^2 (in ZrO_2 small), which is much lower than for the long alkyl chain DPPA molecules due to the lack of SAM formation in this case. They are still not forming perfect monolayers compared to the longer ODPPA system which shows a grafting density of 3.4 per nm^2 .^[207] These effects, concerning the correlation of SAM formation with grafting density, will be intensively discussed in the following chapter. The grafting densities of nanoparticles, modified with only MPPA, tBuPPA and PyPPA, are not presented because these molecules have only been used in the studies in combination with DPPA in mixed monolayers and will thus be discussed separately. In the case of MA-C10-PA@ ZrO_2 small, the comparatively lower grafting density is very likely to result from the fact that the steric demand of the organic moiety does not allow a dense monolayer formation as also observed in literature for bulky groups, even with a long chain spacer.^[323, 330, 334] This effect seems to be more drastic for the flat substrates applied in literature than for the irregular rough micron sized particles. All the other molecules seem to tend to form denser packed monolayer due to their chemical and physical nature. For the special case of Ep-PPA covering the ZrO_2 surface with 8.8 molecules/ nm^2 for ZrO_2 small and 5.7 molecules/ nm^2 for ZrO_2 large the presence of a partial bilayer or even multilayer is possible or at least it can be assumed that more molecules than possible anchoring sites are somehow bond to the nanoparticles. This is plausible keeping in mind the high reactivity of the Ep-PPA molecule's epoxide-end group and the acidic conditions during the reaction conditions, which would catalyze (possible) homo-(poly)addition reactions between the coupling agent molecules by their organic side chain. ^{13}C -MAS-NMR experiments indicated also what has been described in literature for various epoxide containing coupling agents,^[184] resulting in a higher organic load.

The general differences between the grafting densities for the larger and the smaller ZrO_2 nanoparticles are assumed to result from the different nature of substrate itself, especially the surface curvature which is flat for the small nanocrystals and rough for the larger polycrystalline system.

Table 15. Grafting densities in molecules per nm² at surface modified ZrO₂ nanoparticles calculated from TGA and nitrogen sorption data (for some studies only the small nanoparticles have been used).

coupling agent	grafting density at small nanoparticles [per nm²]	grafting density at large nanoparticles [per nm²]
DPPA	2.1	1.9
ODPPA	3.4	-
PhPPA	1.0	-
DEG-PPA	3.1	3.6
Diol-PPA	3.3	2.7
Ep-PPA	8.8*	5.7*
MA-C2-PPA	2.0	2.4
MA-C10-PA	1.5	2.6
Br-C2-PPA	2.3	-

Taking a closer look to the grafting densities for the trimethoxysilane modified silica particles, listed in Table 16, two general differences can be observed, compared to the ZrO₂ system. Firstly, the smaller nanoparticles generally show lower grafting densities. This can be explained by the strong curvature of these objects which are only a few nanometers in diameter. Hence, a dense attachment of the organic moieties, compared to flat substrates,^[222, 335] (also such as the small zirconia nanocrystal facets in this work), is not possible. This phenomenon will be investigated in detail in chapter 3.1.3. Secondly, this fact must also be the reason why sterically more demanding coupling agents (e.g. MA-C10-TMS, Azo-TMS) result in a lower surface coverage for the smaller nanoparticles.^[334] Also the different adsorbing and attaching mechanism for the alkoxy silane, which means lateral cross polymerization of the organosilane coupling agent molecules, has to be considered within the discussion of a steric SAM effect^[185, 186]. The attachment of molecules seems to be difficult for the smaller nanoparticles possibly due to a hindered cross-polymerization mechanism on these strong curved substrates, but might be no problem in the case of the larger nanoparticles. The general differences in the grafting densities of alkoxy silanes compared to organophosphorus coupling agents are ascribed to their different nature. Moreover, the values, obtained for SiO₂, are considered to exhibit less validity, because of possible systematical errors resulting from the fact that a comparatively high bulk mass loss has to be considered in the calculations of the grafting densities. The true surface coverage values are thus considered to be higher.

Table 16. Grafting densities in molecules per nm² at surface modified SiO₂ nanoparticles calculated from TGA and nitrogen sorption data.

coupling agent	grafting density at small nanoparticles [per nm ²]	grafting density at large nanoparticles [per nm ²]
DEG-TMS	0.7	2.1
Gly-TMS	1.0	1.8
Diol-TMS	0.9	1.5
DTMS	0.8	1.3
PhTMS	1.4	3.4
MA-C3-TMS	1.0	1.7
MA-C10-TMS	0.4	2.9
Styr-TMS	1.1	2.7
Azo-TMS	0.3	1.1

However, the validity of the absolute values as such is problematic as there are many sources of systematic errors which cannot be excluded (such as from S_{BET} or surface adsorbed water observed in the TGA and how these facts are handled in the calculation, as discussed) being integrated into the calculation and having a great impact on the results. Furthermore, several approximations had to be applied. Nevertheless, the obtained grafting density values can be applied for comparative investigations. Grafting densities of the novel PDMS-chain coupling agents, investigated in this work, are discussed in the corresponding chapter 3.1.5.1. As a conclusion, the grafting densities of the modified nanoparticles are considered to be high enough to observe significant effects in materials properties and materials structure and additionally another qualitative evidence for the successful attachment of the coupling agents to the nanoparticle surfaces has been adduced in this chapter.

3.1.3 Hydrophobic nanoparticle surface modifications, self-assembled-monolayers on nanoparticles

In many cases long alkyl chain spacer coupling agents are used to increase the compatibility of the often hydrophilic surface of metal oxide nanoparticles with hydrophobic media such as solvents or polymers, which plays a crucial role in the preparation of homogeneous nanocomposite materials. Since many years it is known that such long alkyl chains can form

self-assembled-monolayers (SAMs) on flat substrates.^[138, 147] This effect is also described for nanoparticles in literature^[210-213] and has to be discussed in this work because of its important role in the preparation of homogeneous dispersions of hydrophobized nanoparticles as it will be shown in this chapter. One question is whether there is a critical surface curvature, which leads to self-assembled-monolayer formation^[222] and how the thermodynamic driving force for such surface-aggregates can be reduced. One of the reasons why this becomes interesting is the formation of bilayers between different particles^[214-216] leading to the arrangement of particles and thus to thermodynamically very stable agglomerates,^[213, 217, 218] which are undesirable in terms of homogeneous nanomaterials. In this chapter the formation of self-assembled-monolayers (SAMs) dependent on the structure and curvature of the nanoparticle surface is investigated. The two different prepared nanoparticle systems were evaluated, namely (i) spherical amorphous silica nanoparticles and (ii) crystalline zirconia nanoparticles. Recently, a work on the effect of curvature on the SAM formation on the surface of silica particles was published, which showed a large effect of this parameter.^[222] The aim of this study is the extension of the previous work to transition metal oxide nanoparticles with a focus on non spherical crystalline systems, which often show planar crystal facets that mimic flat substrates on the macroscopic scale. Long alkyl chain alkoxy silanes were used for the silica surface-functionalization while molecules with phosphonate anchor groups were used for zirconia particles. Dodecyl alkyl chain containing coupling agents were selected because SAMs from these molecules are non-crystalline at room temperature^[205, 236] and therefore they less likely form very strong interparticle bilayers, which is desired by technological reasons (agglomeration via bilayer formation) in this work. This argument was proofed applying also a C18-phosphonic acid, which results in the formation of crystalline SAMs at plane surfaces below 50°C,^[205] as disordering/ordering effects should appear more significantly in this system. Also methods to overcome strong alkyl chain ordering phenomena in case of the model systems (i) and (ii) by mixed monolayer formation are investigated. The latter has been examined mostly for mixed alkyl thiols on gold nanoparticles for example as emulsion stabilizing agent^[212] or to control the spacing between deposited particles.^[233] The mixed-surface approach was also investigated in the presented work to study its effect on the formation of dispersions in organic media, for example to improve the deagglomeration behavior of nanoparticles in dispersions. *Prado et al.* have studied the coadsorption approach on macroscopic flat surfaces for organophosphorus mixed monolayer^[336] but this concept has not been applied to transition metal oxide colloids before. Finally, this mixed monolayer concept will be investigated in an extended study were different co-coupling agents are compared with respect to their power to disturb long alkyl chain ordering. Furthermore, small angle X-ray scattering experiments will be applied to gain information on the effect on powder agglomeration which is highly important. The goal is to obtain hydrophobic nanopowders which can be easily re-dispersed in organic solvents, monomers or hydrophobic polymer matrices. Some points have to be generally considered in the comparison of the ZrO₂ and the SiO₂ system. As mentioned before, the silane coupling agents also have an affinity to metal oxide surfaces, however the stability of Si-O-M bonds is in some cases low, e.g. against hydrolysis. Phosphonates show a much higher stability to metal oxide surfaces and are therefore quite often used as anchor groups.^[99, 180] The coupling agents which have been used

in these studies have been listed in Table 7 and Table 12. Silane coupling agents of the type R-SiX₃ covalently bind with a maximum of three Si-O-Si bonds but usually only one bond to the surface and a cross condensation of coupling agent molecules.^[144] Phosphonic acids covalently bind to many metal oxide surfaces detailed studies can be found in literature for titania surfaces.^[190] The binding mechanisms usually involve one to three M-O-P bonds and are expected to be similar for zirconia. In both cases the kinetics for the anchoring reactions for phosphonates@zirconia^[182] and alkoxy silanes@silica^[337] is very fast. Therefore a maximum possible surface coverage can be assumed for each performed modification reaction. The presented studies focus on C12 chains for technological reasons: The maximal chain ordering is not as high for C12 chains as for longer alkyl chains, non-crystalline surface-SAMs are obtained. C18 chain coupling agent molecules have just been used for demonstration issue to show the transferability of the observed effects to other systems. Besides covalently bound monolayers of the coupling agents additional physisorbed molecules can be excluded due to the intense washing steps after modifying the surface and because there was no spectroscopic evidence for physisorbed molecules by IR and solid state NMR. For reasons of complexness of these objects, the irregular shaped large ZrO₂ particles are not included in these studies.

3.1.3.1 Alkyl chain ordering in self-assembled-monolayers on ZrO₂ nanocrystals

The degree of ordering of the molecules on the surface of the nanoparticles has been investigated applying FT-IR spectroscopy. Following a method used for the detection of self-assembled-monolayers (SAM) a redshift of the long alkyl chain methylene group C-H-vibration indicates a higher ordering in the SAM and thus a more dense chain packing, due to a decrease of gauche defects.^[338, 339] The asymmetric C-H-stretching mode of the chain methylene unit is the most significant mode where the peak value is used to monitor the degree of chain ordering.^[182] This effect is related to a different sum of C-H binding energies in the system when more gauche defects are present in the alkyl chains, compared to an all-trans configuration.^[339-341]

The grafting density has been varied using different concentrations of the coupling agent DPPA in the reaction mixture. Table 17 lists the results, which are visualized in Figure 51, for the grafting densities at different coupling agent concentrations in the reaction solution calculated from mass loss from TGA and specific surface area from N₂ sorption measurements. The maximum grafting density was determined to be 2.1 molecules/nm² for DPPA@ZrO₂ and 3.4 for ODPPA@ZrO₂. The higher density of the C18-SAMs is the result of the higher ordering and the thus more closed packing. The maximum grafting density for phosphonates at a plane metal oxide surface has been reported to be 4.2-4.8 molecules/nm² for the dense C18-monolayer.^[182, 326] The difference in these values can be explained by the fact that *Fadeev et al.* assume a surface demand of N₂ molecules of 0.135 nm² for the calculation of the specific surface area from their nitrogen sorption experiments, whereas here a demand of 0.162 nm² is assumed according to the IUPAC convention,^[284] which results in a higher specific surface area of the nanopowder and therefore the here calculated values are lower by a factor of 0.83. Additionally, the difference in shape and chemical sites as well as errors due

to the determination of S_{BET} have to be considered. PhPPA shows a maximum grafting density of approximately 1 molecule/nm², which is much lower than for the long alkyl chain DPPA molecules due to the lack of tendency for SAM formation in this case.^[207]

Table 17. Variations of grafting-density on ZrO₂-nanoparticle surface using different coupling agent concentrations (DPPA or PhPPA) in the reaction mixture.

coupling agent conc. [mM]	DPPA@ZrO ₂	DPPA@ZrO ₂	PhPPA@ZrO ₂	PhPPA@ZrO ₂
	Δ_M [g/g]	σ [molecules/nm ²]	Δ_M [g/g]	σ [molecules/nm ²]
0.10	0.000	0.00	0.001	0.01
0.75	0.009	0.20	0.011	0.52
2.50	0.041	0.89	0.018	0.87
7.50	0.090	1.95	0.021	0.99
15.00	0.098	2.13	0.020	0.94

The correlation of coupling agent concentration and the resulting grafting density is shown in Figure 4 for DPPA@ZrO₂ and for PhPPA@ZrO₂.

The diagram reveals that with increasing coupling agent concentration the grafting density increases nearly linearly up to a certain level at a threshold of ~7.5 mM. Then, the surface seems to reach saturation (plateau for grafting density for PhPPA ~1 molecule/nm² and for DPPA ~2 molecules/nm²) for both coupling molecules where the PhPPA-titration-curve is more uncontrolled. The ostensible decrease for the PhPPA coverage at highest concentrations is not significant, the data point lays within the measurement error (~5%). In literature similar characteristics have been observed for bulky phosphorus coupling-agents attached to zirconia nanoparticle surfaces where the adsorption-isotherm shows *Langmuir*-characteristics.^[152] Figure 51 can therefore also be interpreted as an adsorption isotherm where every data point represents an equilibrium grafting density.

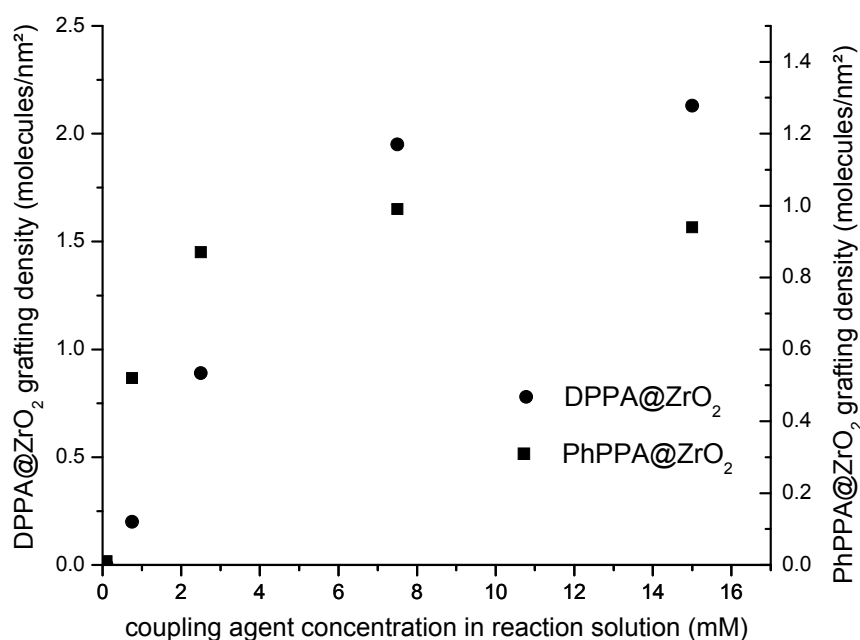


Figure 51. Effect of the coupling agent concentration (DPPA or PhPPA) in the reaction mixture on the zirconia nanoparticle surface coverage with DPPA or PhPPA.

The ordering degree of the dodecyl chains on the particle surface has been investigated via IR spectroscopy. The values (Table 18) for the asymmetric stretch vibration ν_{as} of the methylene-chain C-H-bond in Figure 52 visualize the observed shift to lower C-H wavenumbers for higher grafting densities. The lowest wavenumber in the investigated sample is 2922 cm^{-1} at maximum grafting density (highest ordering). This wavenumber is considerably higher than those of ideal SAMs reported in literature, e.g. C17-thiol@gold shows a C-H-wavenumber of 2917 cm^{-1} ^[204] and C18-organosiliconhydrides@zirconia 2916 cm^{-1} .^[98] Explanations for the differences in packing and the lower ordering in the case of these systems are the already mentioned differences between flat substrates and nanoparticles surfaces and the more dense packing of longer alkyl chains (C17 and C18 compared to C12) which is a common known phenomenon.^[207] Gao *et al.* have investigated the microcrystallinity of SAMs of alkylphosphonates with different chain length on ZrO₂. They have shown that below 50°C , where also the preparation steps are carried out, only alkyl chains longer than 16 C-atoms per chain form real crystalline surface SAM structures.^[205] C12-chains as applied in the present work form packings, but in a more disordered way. All chain methylene units can be in the all-*trans* configuration, but more disordered as in a crystal.^[236]

The results on the nanoscopic surface reveal that higher grafting density causes a higher ordering of the alkyl chains attached to the surface. Similar observations were made in literature for long alkyl chain trialkoxysilanes or phosphonic acids at micrometer powder surfaces of silica, titania, zirconia, hafnia^[98, 182, 207, 338] where greater flat surface areas compared to nanoparticles can occur. However no conclusion about the consistency of the

monolayers with different grafting densities can be drawn from the absolute values of C-H-shifts. Not fully covered surfaces can have the coupling agent randomly attached, which is more likely for phosphonates than for trialkoxysilanes^[182] because the trialkoxysilanes form preordered structures via cross-condensation of the anchor groups already in solution before they adsorb to the particle surface. They can form a number of small islands or a mixture of both.^[182]

Table 18. DPPA@ZrO₂ at different surface coverage: shift of chain-methylene-vibration ν_{as} due to higher grafting density.

surface coverage [molecules/nm ²]	ν_{as} [cm ⁻¹]
0.0*	2930.3
0.2	2928.4
0.9	2922.3
2.0	2922.0

*...not quantitatively detectable but observable in the infrared spectrum

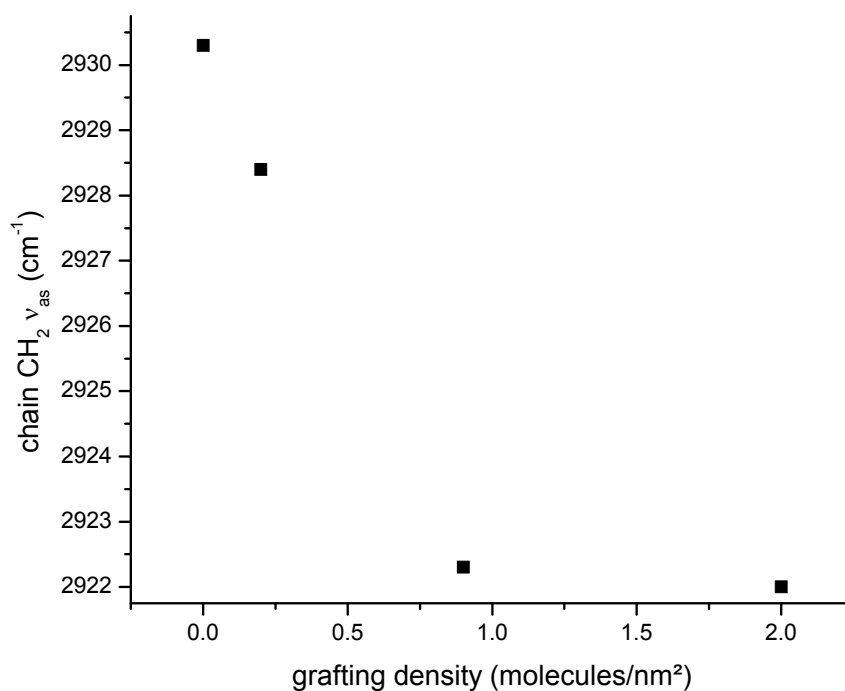


Figure 52. Different grafting densities of DPPA@ZrO₂, ν_{as} CH-wavenumber represents the ordering degree of the alkyl chains (chain packing).

It can be concluded from these results that a 7.5 mM concentration of DPPA leads to a dense SAM for this particle type. Below this concentration, as IR measurements indicate (Figure 51), lower ordered alkyl chain structures are formed at the surface.

Variation of the coupling agent concentration is a method to tune the SAM-formation on the surface (Figure 52 shows the different alkyl chain ordering states for different grafting densities). This is important because SAM-functionalized particles can interact with each other through bilayer formation. Such bilayers are thermodynamically very stable and therefore it is difficult to separate agglomerated particles showing this effect.

The average surface polarity of the nanoparticles could be tuned via this concentration-approach. However, in most cases the surface mostly needs to be fully covered with an endcapping molecule for chemical and physical reasons to avoid a direct contact of a reactive metal oxide surface with the organic compound in nanocomposite materials and thus avoiding a lack of interfacial adhesion between the inorganic and organic compound at the non-covered regions.

3.1.3.2 Alkyl chain ordering in self-assembled-monolayers on SiO₂ spheres

Small nanoparticle exhibit a strong curvature, which has to be considered discussing SAM formation. Contrary to the ZrO₂ nanocrystals the SiO₂ particles have a spherical nature and thus the nanoscopic curvature has an influence on the SAM-formation. *Jones et al.* have shown by modifying 7 nm, 12 nm and 40 nm diameter spherical Silica particles using different alkyl chain-length silane coupling agents ($n = 8, 10, 12, 18$) that the chain packing decreases for lower diameter particles due to the higher curvature which prevents a continuous parallel packing of the alkyl chains as it would be possible for plane substrates.^[222] Crystalline 22 nm (DLS, spherical equivalent) zirconia particles of similar size ranges show quite strong ordering phenomena in long-alkyl chain phosphonate interaction, based on the defined flat crystal facets of the nanocrystals.

SAM formation and disordering was proven applying SiO₂ samples with different sizes and thus variations in surface curvature. The surface functionalization was carried out using a two step process. First a *Stöber*-process was used to synthesize well-defined particles followed by a surface modification step with the silane coupling agent DTMS. Organophosphorus coupling agents could not be used in this case because they do not interact with silica surfaces by strong covalent bonds, like they do on metal oxides. Trialkoxysilane based coupling agents and not mono alkoxysilanes were used in surface-modifications, because the application of trifunctional silanes results in SAMs with grafting densities and chain ordering more comparable to the phosphonate systems than to monofunctional silane systems.^[98] Other reaction parameters, such as temperature and coupling agent concentration, were also chosen to be comparable with the phosphonate surface-modifications. The resulting grafting densities (~ 2 molecules/nm² at least for larger nanoparticles) were similar to those of the zirconia particles, however not exactly determinable by the method used for the zirconia nanoparticles because of the possible ultrastructure of *Stöber*-particles and possible residual surface-ethoxy groups from the preparation. These conditions are in contrast to common methods, used in

chlorosilane- or alkoxy silane-treatment of metal oxide surfaces in non-polar aprotic media, mostly at elevated temperatures.^[145, 177, 342, 343] SiO₂-particles with four different diameters have been prepared and surface-modified with DTMS. Table 19 lists the particle diameters and the corresponding methylene-C-H-vibration from IR-investigations. Compared to the value for C-H ν_{as} for C12@ hydroxylated Si(100) of 2920.9 cm⁻¹^[222] which should represent the maximum ordered C12 chain-packing of silica surfaces the alkyl chains at the nanoparticle surfaces are much less ordered showing a liquid like behavior. Also the C12 monolayer on a hydroxylated Si-wafer (flat macroscopic substrate) from the experiment shows less ordered structure compared to literature.^[222] The reason for this is considered to be that the reaction conditions, namely the used solvent water/methanol or water/ethanol, which leads to more disordered monolayers as non-polar media as used in literature for SAM-formations, e.g. also by *Jones et al.* using THF/cyclohexane or *n*-hexane. However these conditions were necessary to yield a sample, comparable to the functionalized ZrO₂ nanoparticle powders. Figure 53 shows the alkyl chain ordering at the nanoparticle surface in dependence on the particle size revealing the influence of the curvature on the SAM-formation.

Table 19. Dodecyl chain methylene C-H-vibration ν_{as} of DTMS@SiO₂ particles with different diameter and on a flat substrate.

d(DLS), m.w. [nm]	C-H ν_{as} [cm ⁻¹]
9	2929
46	2928
390	2927
680	2925
∞	2925

The ordering of C12 chains at the surface increases for higher particle diameters and thus for lower curvatures which was also shown by *Jones et al.* Their study was extended from nanoparticles to micron-sized particles and flat substrates. The 680 nm particles should already mimic the SAM formation on flat surfaces which can be concluded from a comparison of the C-H-stretching vibrations. The nanoparticles at 9 and 46 nm diameter follow the trend, observed by *Jones et al.* However the data points for the 390 and 680 nm diameter do not represent the same trend. A possible explanation for this is that *Stöber* particles, consist of a fractal particle structure by nature due to its preparation process^[305] (e.g. 3 nm close packed nanoparticles^[344]). For this reason, the outer surface is never totally flat, as *Szekerés et al.* showed by comparison of SAXS and BET data. For the trend in the diagram in Figure 9 this would mean that for higher nanoparticle diameters the "surface roughness" is lower than for the smaller nanoparticles which results in better ordered monolayers, whereas

for 9 nm the particle curvature resulting from the spherical diameter itself dominates the overall curvature. This differences can be explained by the variations in synthetic conditions of the large and small nanoparticles influencing the nucleation rate and thus the primary particle size.^[345] For example a higher water-content at the same ammonia concentration in the *Stöber*-process leads to a surface with higher roughness in electron micrographs.^[303] However this surface structure does not seem to play a role for the 680 nm particle as the same C12 methylene vibrational shifts are observed as for the atomic flat wafer substrate, which means that the 680 nm particles can be considered flat for the coupling agent molecules.

It is concluded that the curvature has a stronger influence on the ordering as expected. However, it is not so easy to determine a real curvature effect which is responsible for an alkyl chain disordering effect, a possible ultrastructure (surface roughness or smaller local radius) of the nanoparticles has to be taken into account. But it can be concluded that the smaller the overall surface curvature is the higher is the degree of ordering. Therefore the study shows an extension of the results previously reported in literature for small SiO₂ nanoparticles.^[222] The observations that the impact of SAM ordering for very small particle sizes of spherical nanoparticles is the highest for geometrical reasons has recently also been demonstrated by *Browne* and *Grzybowski* applying probe molecules where a change in pKa or redox behavior indicated these effect.^[221] The values for the methylene C-H for DTMS@SiO₂ nanoparticles of 2929-2928 cm⁻¹ indicate a nearly liquid like unordered surface-alkyl-chain-system.^[182] This is in contrast to 2925 cm⁻¹ for DTMS@SiO₂ micron sized particles, showing a more semicrystalline behavior. Such a semicrystalline structure can be described as a far more ordered structure than liquid alkyl chains, but with a not as densely packed SAM structure as it can be observed for C18 on planar and slightly curved silica.^[223] It can be considered that by using DTMS@SiO₂ nanoparticles in nanocomposites no possible zipper-effect will occur due to bilayer formation. Thus, approaches to avoid strong SAM formation, e.g. the later described co-modification with different coupling agents is not necessary for avoiding strong SAM-formation for smaller nanoparticles, having a size in the range of the investigated zirconia nanoparticles. The grafting densities have been investigated by thermal analysis and showed values of ~1.1 molecules/nm² for the 46 nm particles and ~1.7 molecules/nm² for the largest 680 nm diameter particles. TGA studies only reveal a limited precision due to the mass loss of remaining silane alkoxide groups. However there is a qualitative agreement with the observed ordering of the C12-chains: high chain ordering allows higher grafting densities. That such a SAM effect can play a role for larger nanospheres has been demonstrated by *Szekeress et al.* where significant particle assembly behavior of micron sized *Stöber* particles applying long alkyl chain surfactants could be observed.^[133]

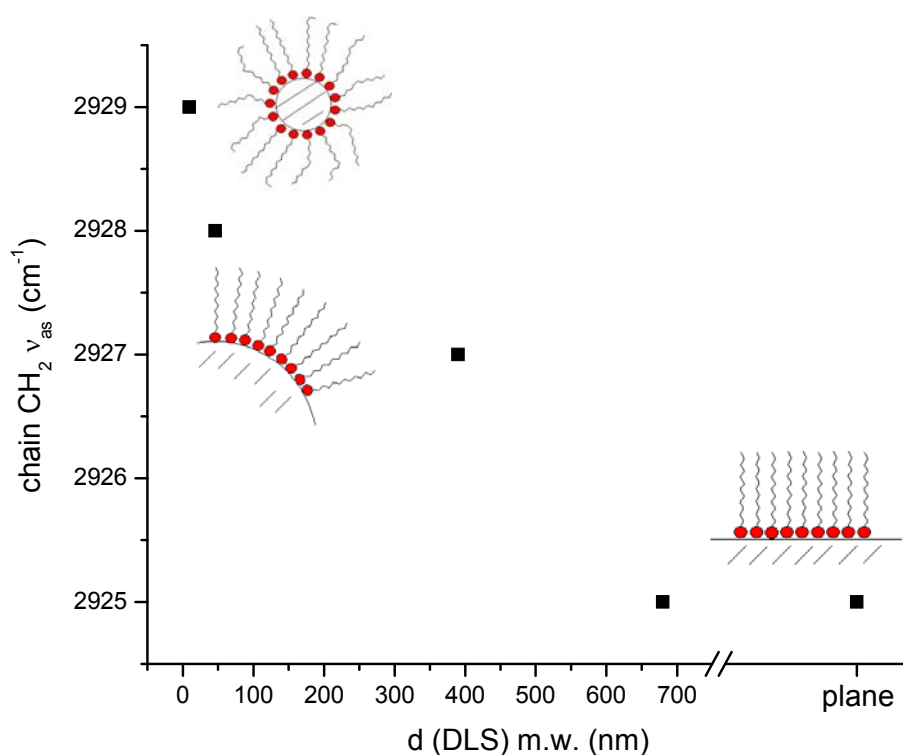


Figure 53. Methylene C-H-vibration ν_{as} of DTMS@SiO₂ representing alkyl chain ordering degree at different particle curvatures.

3.1.3.3 Mixed SAM formation on ZrO₂ surface to control the alkyl chain ordering

A method to tune the alkyl chain ordering while having a certain constant coverage of molecules on the nanoparticle surface is to mix two different coupling agents consisting of the same anchor group but showing organic rests of different chemical nature, such as a dodecyl chain and a phenyl group. The smaller organic rest can disturb the long-alkyl-chain-SAM formation process. This approach was investigated by mixing DPPA and PhPPA in certain ratios to give an altogether 7.5 mM solution of phosphonic acid coupling agents which represents the threshold-concentration for a dense monolayer formation. This concentration has been chosen to exclude a significant preferential adsorption and binding of one of the different coupling agents which would lead to higher surface concentrations of one type of molecule than desired. The reason for this approach is that phenylphosphonic acids are known to be more reactive than alkylphosphonic acids towards binding to metal oxide surfaces.^[190] Also it is known from literature that in a coupling agent mixture to form a mixed monolayer smaller molecules are faster adsorbed to the surface as *Offord* and *Griffin* have shown for mixed layers of homologous n-alkyltrimethoxysilanes on a plane silica surface.^[346] The mixture was then used for surface modification to prepare 10%, 30%, 50%, 70%, 90%, 100% DPPA@ZrO₂ where the difference to 100% is PhPPA. Because of working with 7.5 mM reagent concentrations it can be assumed that the PhPPA/DPPA ratio is the same in the reaction mixture and on the surface. ¹H NMR experiments in which the nanoparticles were

dissolved in HF and extracted with deuterated chloroform support this assumption. Integration of the NMR signals revealed that at a concentration of 7.5 mM the found ratio after surface degrafting represented in all cases the mixing ratio of the coupling agents in the solution before the reaction.

TGA analyses revealed that a total grafting density of 2.8 ± 0.6 molecules/nm² with a slight tendency to lower grafting densities with increasing PhPPA percentage was reached for the prepared mixed modified samples. The grafting density is higher than for the only DPPA-grafted particles. A possible explanation for this behavior is that the smaller more reactive PhPPA molecules bind to sites where DPPA cannot bind, e.g. defect sites.

FT-IR-spectroscopy was again used for the determination of the degree of ordering of the C12-alkyl chains in dependence of the mixture of molecules on the surface. Figure 54 shows the superimposed spectra for the C-H-stretching region and the corresponding values for the peak of the band are listed in Table 20. It reveals that with increasing PhPPA-concentration on the particle surface the methylene C-H-vibration (ν_{as} as example) shifts significantly to higher wavenumbers. Thus the ordering of the C12- chain which is non-crystalline but ordered in a way that more methylene-units are arranged in an all-*trans*-configuration, decreases (Figure 55). To verify the effectiveness of this approach also for crystalline SAM-systems, C18-chain-mixed-systems have also been tested by this method (see Table 20 and Figure 55).

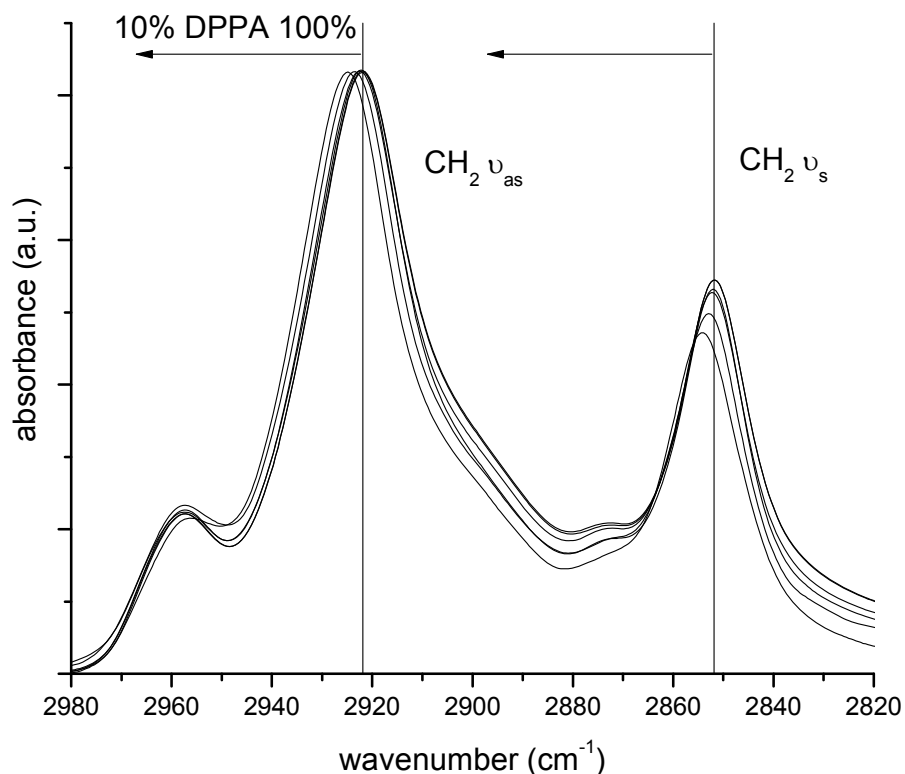


Figure 54. Infrared spectra of DPPA/PhPPA@ZrO₂: Methylene C-H shifts to higher wavenumber at increasing PhPPA surface concentration.

Table 20. Methylene C-H-vibration ν_{as} of the dodecyl-chain for different percentage of long alkyl chain coupling agent (rest PhPPA) at zirconia surface.

Mol% long alkyl coupling agent	DPPA ν_{as} [cm^{-1}]*	ODPPA ν_{as} [cm^{-1}]
100	2922.0 \pm 0.05	2919.3
90	2922.1 \pm 0.10	2919.4
70	2922.3 \pm 0.30	2920.3
50	2922.9 \pm 0.30	2921.1
30	2924.0 \pm 0.35	2922.2
10	2925.5 \pm 0.50	2923.4

*For demonstration, the error within the DPPA series was calculated from 6 values where the reaction has been repeated and measurements have been repeated 3 times each resulting in a measurement error <0.1 . The high reproducibility shows on this example the significance of the observed trends

Figure 55 shows an increase in alkyl chain ordering by increasing the percentage of long alkyl chain coupling agent in the mixed surface layer. This effect has qualitatively the same trend for C12 and C18, only the absolute values differ which means that the C12 systems are generally more disordered than the C18 system, which is crystalline at room temperature.^[205] Therefore this mixed monolayer alkyl chain disordering approach is applicable for crystalline ordered and medium ordered SAM systems. Scheme 1 visualizes the mixed SAM formation on the zirconia surface.

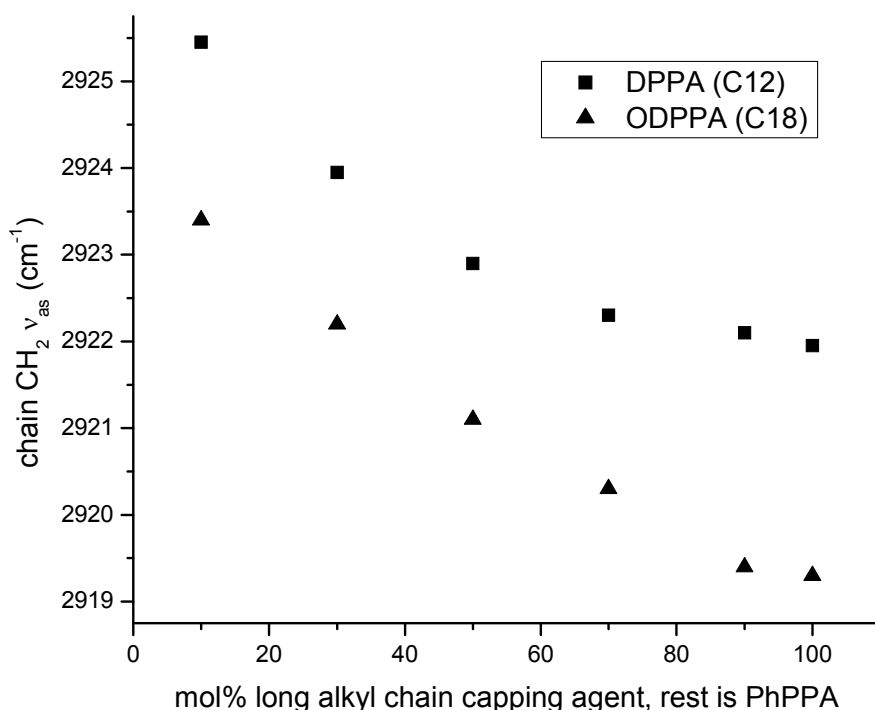
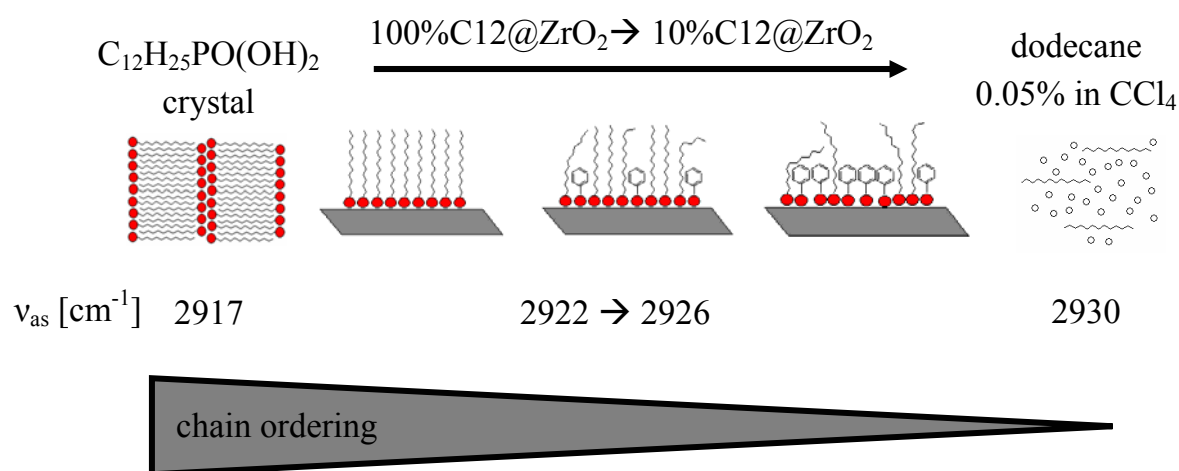


Figure 55. Methylene C-H-vibration ν_{as} of long alkyl chain-PPA@ZrO₂ representing the alkyl chain ordering degree at different percentages of DPPA or ODPPA (rest PhPPA).

The DPPA and ODPPA ordering curves in Figure 55 show two different regions, a flatter slope at higher long alkyl chain coupling agent concentrations and a linear steep slope in SAM ordering for high PhPPA concentrations. These two regions are most likely due to the concurrency of different SAM growth mechanisms. In a first step the attachment of the molecules occurs randomly all over the particle surface. In the second step an island type growth of ordered regions can be expected.^[347] But there is no information on the growth mechanism of this mixed coupling agent monolayer and as the IR peaks represent a statistical average over all attached species it is likely to be a combination of effects that leads to the shifts which makes the system rather complex and does not allow to distinguish between the mechanisms. However, it is clear that the PhPPA attachment to the surface can disturb the DPPA monolayer formation. This can be explained by adsorption of molecule by molecule which leads to a mixed surface layer where the PhPPA/DPPA molecules are randomly mixed, as observed for mixed alkyl thiols on gold with different chain length.^[229, 230] The second extremum, strong macroscopic island formation as discussed by *Bain and Whitesides*^[225, 227] and investigated by *Vercelli et al.*^[348] for strong interacting co-coupling agents is not very likely because there would be no effect on the disordering of the (amorphous) ordered C12 chains. A mechanism in between these extrema is likely to be existent, e.g. like octadecylphosphonic acid on mica forming islands in the nanometer range,^[197] or below. Also a pre-formation of coupling agent assemblies in solution by weak interactions before

adsorption to the surface is also possible in analogy to the covalently crosslinked structures of trialkoxysilanes. Driving forces for such a mechanism are chain-crystallization energy of long alkyl chains or π - π -interaction^[138, 147] for PhPPA. This is only possible if the compounds have a natural tendency to form preordered structures in solution before surface-attachment as it is observed in literature for functional long alkyl chain phosphonic acids.^[203]

Scheme 1. Schematic representation of different C₁₂-alkyl-chain-ordering-degrees at the zirconia nanoparticle surface and comparison with totally crystalline C₁₂-chains and high diluted unordered liquid C₁₂-chains.



3.1.3.4 Control of alkyl chain ordering on SiO₂ surface via mixed monolayer approach

The generality of this approach in breaking the order of SAM formation on particle surfaces by applying different surface coupling agents was tested by using the DTMS-modified micron-sized silica particles (680 nm diameter) as they show significant alkyl chain ordering. Mixing of PhTMS with DTMS in surface modification of the particles should lead to a decrease of ordering in the chain packing. The surface-functionalization method was similar as described for zirconia, the overall molar coupling agent concentration was kept constant while the ratio of DTMS/PhTMS was varied. The degree of alkyl chain ordering has been analyzed via FT-IR-spectroscopy and the methylene C-H shift for each percentage of C₁₂-chain@SiO₂ is listed in Table 21 and visualized in the diagram in Figure 56.

Table 21. Methylene C-H-vibration ν_{as} of dodecylchain for different percentage of DTMS (rest PhTMS) at 680 nm diameter silica particle surface.

mol% DTMS	C-H ν_{as} [cm^{-1}]
100	2924.8
90	2925.5
70	2926.9
30	2928.7
10	2930.2

The alkyl chain ordering of DTMS@SiO₂ decreases with increasing percentages of PhTMS with a similar trend as observed for the DPPA/PhPPA@ZrO₂ system. Comparison of the two systems (Figure 55 and Figure 56) revealed that in both cases a linear like trend for the decrease of ordering from 100%C12 to 10%C12 is observable with a total shift of $\sim 5 \text{ cm}^{-1}$. The wavenumber of the most disordered state for silica particles is $\sim 2930 \text{ cm}^{-1}$ and for zirconia $\sim 2925 \text{ cm}^{-1}$, which means that the chain-ordering in absolute is higher for the zirconia system. The entire ordering curve (Figure 56) is shifted to lower wavenumbers as compared to the zirconia system (Figure 55). A possible ultrastructure of the *Stöber*-particle-surface yielding in higher disordering may also be responsible for this fact. Also these two systems, phosphonates@ZrO₂ and trialkoxysilanes@SiO₂ are not completely comparable. For phosphonates the modification reaction is more represented by an adsorption of molecule by molecule whereas trialkoxysilanes adsorb pre-formed aggregates via self-condensation in solution. The latter effect is also seen as responsible for the quantitative differences in chain-ordering of these two systems. Nevertheless the effect of binding of a co-coupling agent shows qualitatively and quantitatively a similar effect regardless of the different curvatures and chemical surface properties of the particle systems and the chemical behavior of the different coupling agents.

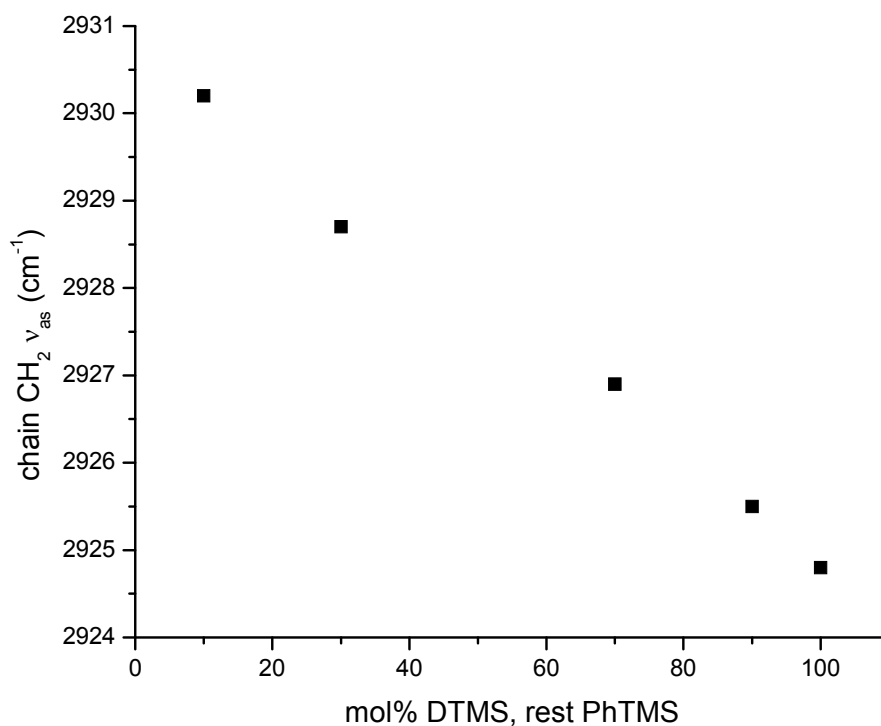


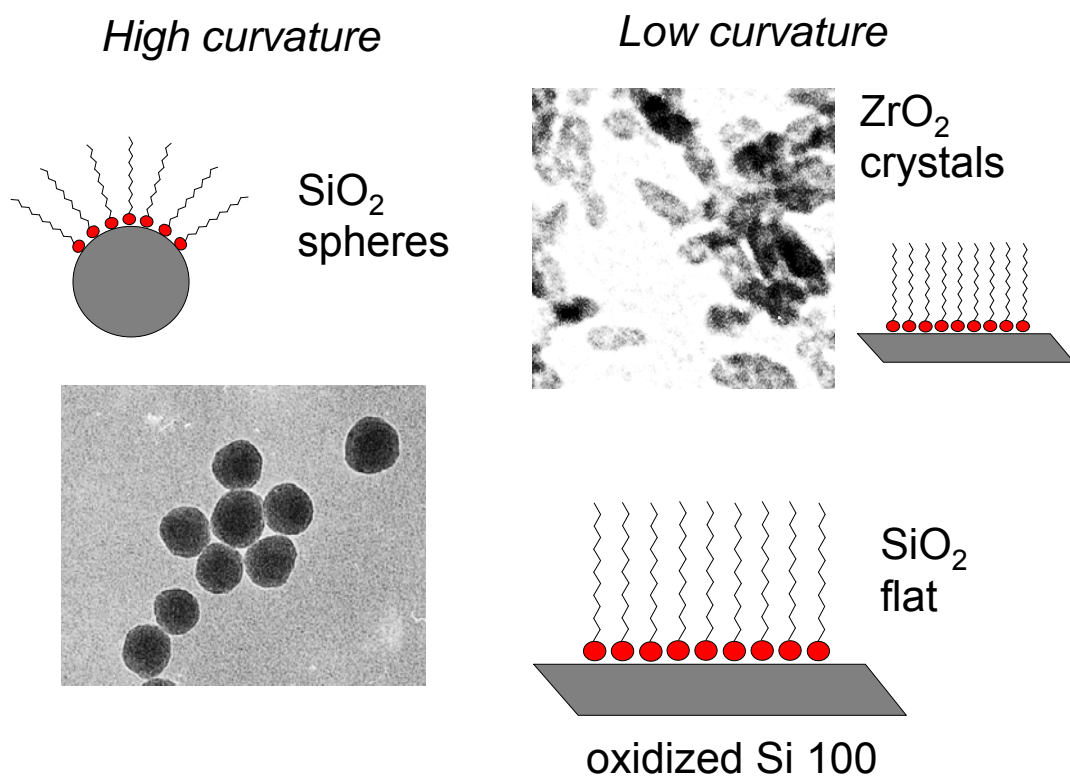
Figure 56. Methylene C-H-vibration of DTMS@SiO₂ 680 nm diameter representing alkyl chain ordering degree at different percentages of DTMS (rest PhTMS).

3.1.3.5 Comparison of SAM-formation on SiO₂ nanospheres / ZrO₂ nanocrystals

As a conclusion from the investigations on the SAM formation on the nanoparticle surfaces the ordering behavior of dodecyl chains on plane-crystal-shaped zirconia nanoparticles and on spherical silica particles with phosphonate or alkoxy silane anchor groups has been investigated. The CH-vibrations of the alkyl chain methylene units in FT-IR-studies were used to detect the degree of alkyl chain packing in the self-assembled-monolayer (SAM) of the surface-bonded long alkyl chain molecule. The highly ordered SAM can be responsible for significant changes in physical particle surface properties and influence the tendency of the particles to agglomerate via interparticle alkyl-chain-bilayer formation, and thus destabilization of nanoparticle dispersions, which is undesirable for many applications. This can be a problem for facets of larger size (upper nm range to macroscopic scale) as it is the case for zirconiumalkylphosphonate-films,^[313] because the stability of the alkyl bilayer is given by the number of *van der Waals* - interacting alkyl chains. However; this occurs also for very small nanoparticles, as described in literature: A strong intercalation of chains can occur to compensate the high surface curvature, e.g. long alkyl chains on 2 nm gold nanoparticles/clusters^[220] are highly ordered and hydrocarbon- as well as fluorocarbon-chains on 4 nm zirconia nanoparticles are stronger ordered than on 20 nm zirconia particles.^[213] It was shown that for SiO₂ particles in the lower nano range the SAM-effect does not play a

role, because of the particles' high curvature, which seems to be still high enough that chain intercalation does not increase because of surface energy compensation. Zirconia nanocrystals in the same size range but showing plane surfaces, form ordered SAMs of dodecylchains because the surface in these samples mimic flat ideal crystal surfaces which enhances a dense chain packing. Thus the nanoscopic curvature of the particles is crucial whether strong alkyl chain ordering occurs or not (Scheme 2), but however it was shown for both systems, silica and zirconia that mixed monolayer formation of long alkyl chains (dodecyl-moiety) with a small, disturbing, coupling agent (phenyl-moiety) at a certain total grafting density gives less ordered alkyl chains at the nanoparticle surface. This is important in terms of nanoparticle surface engineering where highly ordered surface-SAMs have to be avoided because of possible interparticle bilayer formation and thus the formation of thermodynamically very stable agglomerates of the nanoparticles in their application which is undesirable in many cases.

Scheme 2. Schematic representation of dodecyl chains adsorbed on zirconia/silica showing different nanoscopic curvature: Comparison of C12@ZrO₂ nanocrystals with C12@spherical SiO₂ nanoparticles in the same size range (middle nanoscale: 10-40 nm): zirconia nanoparticles show high ordered SAM due to plane crystal facets whereas spherical silica nanoparticles show no strong ordering of alkyl chains, however the coupling agent and its adsorption behavior are different in this systems, but for silica with low curvature also alkyl chain packing plays a significant role.



Nanoparticle-SAM effects stick to the rules of well investigated SAM-effects on macroscopic flat surfaces such as SiO₂ on Si wafers, except for the presence of ultrastructure with high

curvature, e.g. *Stöber*-particles or the high curvature of nanoparticle itself not allowing this analogous transferability. Although the systems of SiO₂ and ZrO₂ should not be compared directly because different surface modifying anchor groups are used with different adsorption behavior (e.g. pre-cross polymerization of alkoxysilanes). It is obvious that for both systems the nanoscopic curvature is important for the formed alkyl-surface-layer structure (Scheme 2) and co-adsorption of other coupling agents with different organic moieties yields in disorientation of long alkyl chains in both cases. This study shows on the basis of the investigated samples, spherical Silica and Zirconia crystals, where this type of materials cover a wide range in metal oxide nanoparticle technology that the nanoscopic curvature has impact on the surface-properties itself. Furthermore, by variation of the grafting density or by mixed SAM-formation at full surface coverage, the surface properties of metal oxide nanoparticles can be controlled on a molecular level.

3.1.3.6 The influence of mixed SAM on ZrO₂ nanocrystals on particle agglomeration and powder redispersibility

As a possible method to investigate the influence of self-assembled-monolayer formation on nanoparticle surfaces on the agglomeration of the particles and for the targeted disordering of the surface bond long alkyl chains by co-adsorbing, a ordering disturbing molecule (as shown previously) in order to form a mixed monolayer, is applied in these extended studies.

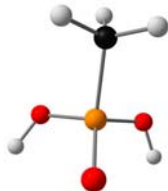
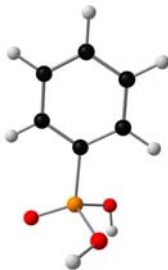
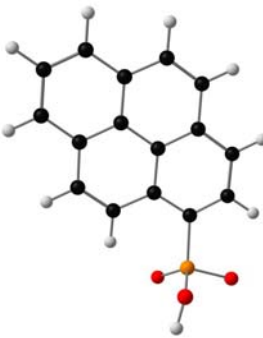
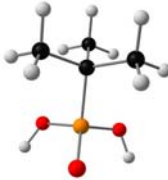
Such an approach, e.g. to tune the surface wettability, was already investigated for macroscopic substrates using mixed monolayers of different alkanethiols on gold surfaces to decrease the overall alkyl chain ordering in the surface layer.^[164, 225-230] Only little is known for the functionalization of metal oxide surfaces, e.g. by mixed phosphonic acid monolayers.^[336] The idea is to explore whether such a method is transferable to nanoscopic facets of transition metal oxide nanoparticles and how the mixed monolayer-formation affects their agglomeration behavior. A further intention is to evaluate how the alkyl chain surface ordering is connected to the particle agglomeration behavior. Up to now the mixed surface modification of nanoparticles has been investigated mostly for mixed alkyl thiols on gold nanoparticles e.g. as emulsion stabilizing agent,^[212, 232] to control the spacing between deposited particles,^[233] to finetune a certain physical surface property,^[234] or to dilute a surface bond functionality for biological applications.^[235] For technologically highly relevant transition metal oxide nanoparticles like ZrO₂ (ceramics, nanocomposites) nearly nothing is known about such phenomena until yet. SAM@transition metal oxide nanoparticles have been reported to play a significant role in tuning their dispersion behavior^[156] but knowledge about the underlying principles is currently lacking. A goal of this study is the production of surface modified nanoparticles which reveal reduced agglomeration through strong interparticle bilayers and thus easily redisperse in commonly used solvents. Literature reports mostly short chain *n*-alkyl coupling agents as disordering co-coupling agents.^[225, 229] However, no systematic studies of different organic moieties, such as aromatic systems or isoalkanes, and their influence on the ordering of the particle surface SAM was carried out until yet.





As model systems the ZrO₂ small single nanocrystals were used in combination with organophosphonate coupling agents. Dodecyl phosphonic acid was again selected as the self-assembling system is non-crystalline at room temperature.^[205, 236] Contrary to the behavior of commonly applied octadecyl coupling agents, the tendency of these dodecyl molecules to form strong interparticle bilayers is already reduced, but dodecyl moieties already provide certain hydrophobicity. In the previous work on the formation of crystalline SAMs it was shown that octadecyl phosphonic acid systems revealed qualitatively the same results concerning a possible SAM-disordering via coupling agent mixing as C12 coupling agents as shown in the previous chapters. Therefore transferability of the results obtained in this study is expected for other long alkyl chain systems. To gain more information on this interesting and technologically important phenomenon of mixed monolayer formation, which has been investigated for PhPPA as co coupling agent molecule in the previous chapters, the study has been extended. For co-adsorbing molecules methyl-, phenyl-, pyryl- and *tert*-butyl phosphonic acid was used in different mixing ratios with dodecyl phosphonic acid to vary steric (molecular) properties and physical properties (hydrophobicity) of the co-coupling agent. The monolayer formation and the agglomeration tendency were investigated applying FT-IR and small angle X-ray-scattering (SAXS) measurements.

Mixed SAM formation applying different co-coupling agents

Again, the ordering of the long alkyl chain was determined by means of FT-IR spectroscopy. In this study the concept of mixed monolayer formation was systematically extended to other organophosphonates (Table 22). Taking a closer look on these systematically selected probe molecules, from a structural point of view two aromatic molecules were used to study the influence of potentially occurring π - π stacking phenomena (pyryl- and phenylphosphonic acid) on the C12 chain ordering. In addition less and more sterically demanding phosphonic acids were used as co-adsorbing coupling agents (methyl- and isobutyl phosphonic acid).

Table 22. 3D Structure of different co-coupling agents, optimized structure gas phase (Gaussian, B3LYP/6-31G**).

abbreviation	coupling agent structure
MPPA	
PhPPA	
PyPPA	
tBuPPA	

H  C  O  P 

The functionalization reaction of the ZrO_2 nanoparticles with a mixture of coupling agents (DPPA and ordering disturbing coupling agent) to form a mixed monolayer on the nanoparticle surface was carried out analogous as described for the modification of TiO_2 with phosphonic acids.^[149] The coupling agents were mixed in a certain molar ratio, namely a series of 10 mol%, 30 mol%, 50 mol%, 70 mol% and 90 mol% DPPA, to give a total concentration of 7.5 mM which is the threshold concentration for a monolayer coverage within this specific system as discussed previously. Therefore a significant preferential addition of one of the coupling agents in the reaction mixture is excluded. For that reason one

can assume that the molar mixing ratios of DPPA with the co-coupling agent in the reaction solution and the molar mixing ratios at the nanoparticle surface after the modification reaction are identical.

The surface coverage values are 2.1 for pure DPPA, 2.7 ± 0.9 for DPPA/MPPA, 2.8 ± 0.6 for DPPA/PhPPA, 2.4 ± 0.2 for DPPA/PyPPA and 2.7 ± 0.6 molecules/nm² for DPPA/tBuPPA, with a slight tendency to lower grafting densities for higher co-coupling agent concentration within one series. All mixed monolayers reached a slightly higher surface coverage than a pure DPPA monolayer. A possible explanation for this behavior is that the co-capping molecules bind to sites where DPPA is not able to bind, such as sterically not approachable locations on the surface, e.g. on edges. However, for the bulky molecule PyPPA mixed with DPPA the lowest coverage compared to other mixed series is obtained, for steric reasons most likely. The surface coverage for all mixed series is in a comparable range which is assumed to be the maximum reachable coverage for each of the mixed systems. The thermogravimetric analyses curves of the DPPA/PyPPA (Figure 57) confirm the assumption made previously that the molar ratio of coupling agents in the reaction mixture is the same at the nanoparticle surface after the functionalization reaction. This is possible because the mass loss due to thermal degradation of the different bond capping molecules occurs at sufficiently different temperatures (onset DPPA@ZrO₂-decomposition-step: 273°C, PyPPA@ZrO₂: 470°C) so that a mass loss for one type of molecule can be detected, which was not the case for all other sample series. The composition can be estimated from the diagram in Figure 57 applying Eq. 6 using 198 g/mol for the pyryl residue and 168 g/mol for the dodecyl residue to calculate mol% from the wt% composition obtained by the TGA measurements. For the sample containing 10 mol% DPPA and 90 mol% PyPPA in the reaction mixture, 11 mol% DPPA and 89 mol% PyPPA could be found at the particle surface by this thermogravimetric method. For the other mixing ratios a similar trend can be observed (Figure 57) however a calculation is not possible because the DPPA-degradation is not finished when the PyPPA-degradation already starts during the thermal program. This prove via TGA is not possible for mixed monolayers with other co-capping-molecules as the decomposition step occurs at similar temperatures when the DPPA@ZrO₂ decomposition takes place. However, it is assumed that the recovery of the mixing ratio remains the same for the other series for the mentioned reasons of working at a threshold coverage concentration during the functionalization reaction.

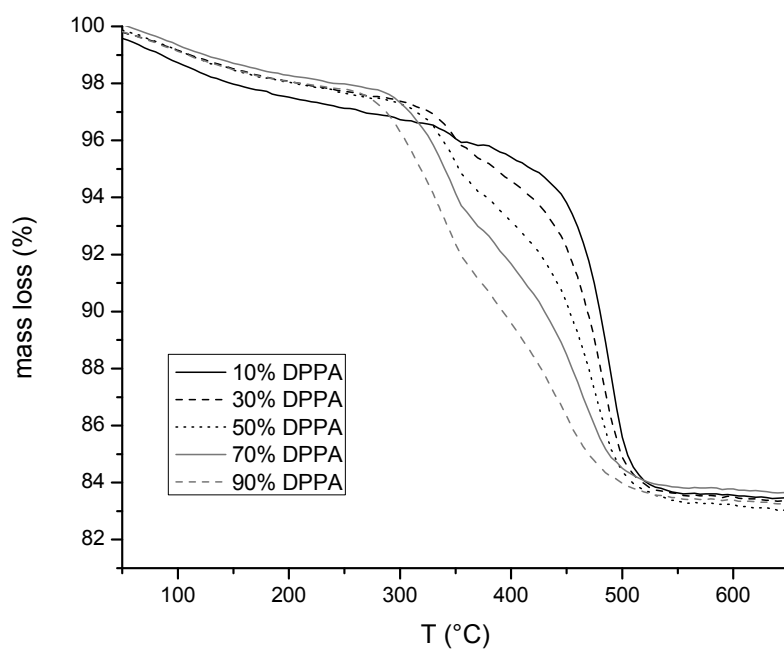


Figure 57. Thermogravimetric analyses curves of mixed modified nanoparticle powders DPPA/PyPPA in different molar ratios.

Investigation on the structure of the mixed SAM

The degree of ordering of the surface DPPA molecules was investigated applying FT-IR spectroscopy. Self-assembled-monolayers formation was detected via a shift of the long alkyl chain methylene group C-H-vibrations to lower wavenumbers with decreasing number of gauche defects in the alkyl chain. This indicates a higher ordering and thus a more dense chain packing in the SAM^[338, 339] with the asymmetrical CH-stretching mode being the most sensitive and significant.^[182] The nanoparticles with mixed coverage applying DPPA and another molecule disturbing the degree of ordering in different molar ratios were investigated with FT-IR-spectroscopy. Four sample series were obtained with MPPA, PhPPA, PyPPA and tBuPPA as co coupling agent. The IR-spectra of the C-H-stretching region are shown in Figure 54 in the previous part of this work and in Figure 59. The wavenumbers of the asymmetric methylene C-H-stretching mode for the dodecyl-chain in the SAM for every molar percentage of a certain disturbing coupling agent are listed in Table 23 and the shifts are summarized in Figure 59 for a better overview.

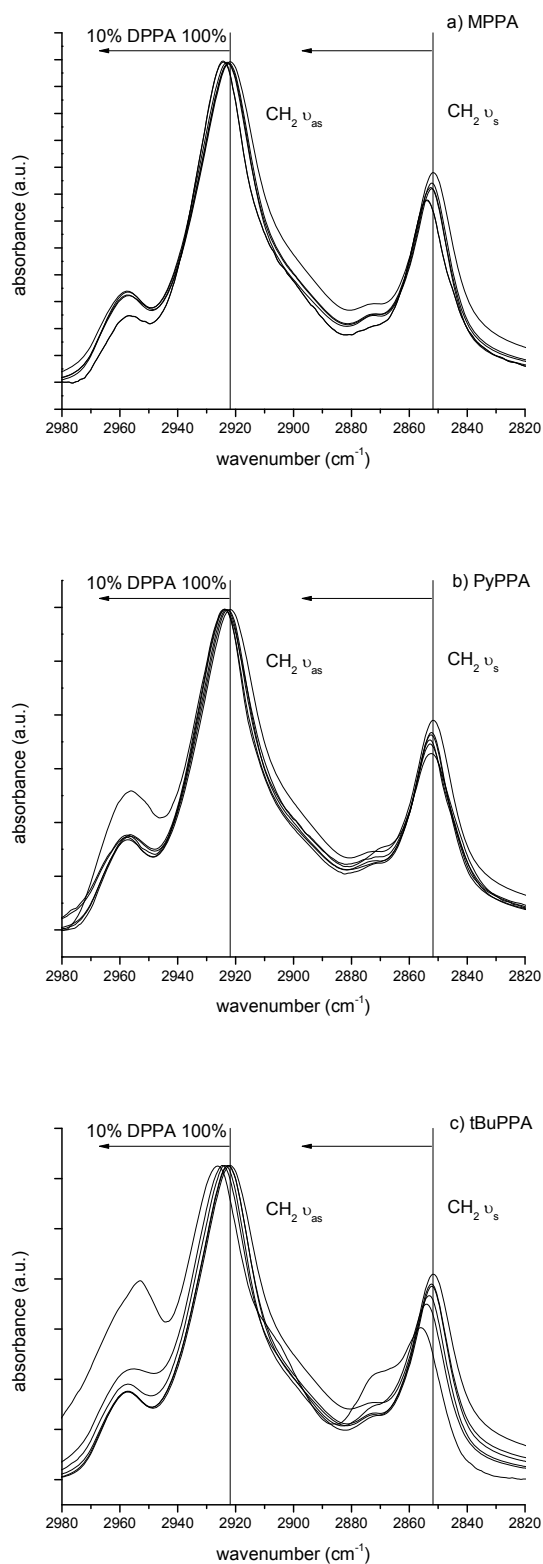


Figure 58. Infrared spectra of DPPA mixed with a) MPPA, b) PyPPA and c) tBuPPA @ZrO₂: Methylene C-H shifts to higher wavenumber at increasing co-coupling agent surface concentration. This is indicated by the arrows, going from right (highest DPPA-content) to left (lowest DPPA content) which means that the peak curve for the 100% DPPA-sample is the right one and the 10% DPPA sample is the left one.

Table 23. Methylene C-H-vibration ν_{as} of the dodecyl-chain for different percentage of co-coupling agent at the ZrO_2 nanoparticle surface.

Mol% DPPA	rest MPPA ν_{as} [cm^{-1}]	rest PhPPA* ν_{as} [cm^{-1}]	rest PyPPA ν_{as} [cm^{-1}]	rest tBuPPA ν_{as} [cm^{-1}]
100	2921.9	2921.9	2921.9	2921.9
90	2922.6	2922.0	2922.7	2922.6
70	2923.4	2922.0	2923.1	2922.6
50	2923.1	2922.6	2923.7	2923.7
30	2923.0	2923.6	2923.8	2924.6
10	2924.4	2924.9	2924.1	2926.3

*... This series has been successfully reproduced with a $< 0.5\text{ cm}^{-1}$ and in average 0.3 cm^{-1} random error (standard deviation)

The FT-IR investigations Figure 59 reveal that for each type of disturbing molecule (MPPA, PhPPA, PyPPA, tBuPPA), the ordering of dodecyl chains decreases with increasing percentage of these co-coupling agents. This is indicated by the shift of its methylene vibrational bands to higher wavenumbers. Even though all different molecules disturb the alkyl chain ordering with increasing molar percentage, the slope of the curves that are yielded from this effect and the absolute vibrational values are different. All four curves consist of an approximately linear area in the middle mixing ratio, which means a content of co-coupling agent of 30-70%. At lower and higher percentages, the behavior is different so that the whole array of curves appears sigmoidal-shaped. This results from the fact that the molecules tBuPPA and PyPPA lead to a relatively high disordering already at low co-molecule percentages, and molecules like also tBuPPA and PhPPA show a, compared to a linear trend, relatively larger disordering increase in the higher co-molecule percentage region. It also appears that every curve has a kind of plateau, like MPPA between 70 and 50 mol%.

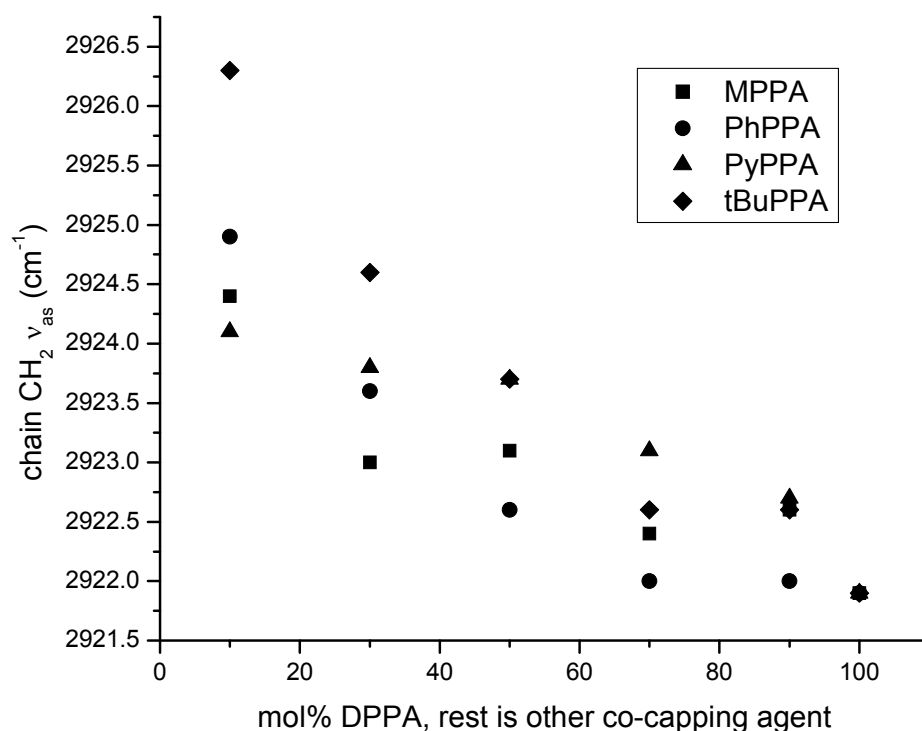


Figure 59. Methylene C-H-vibration ν_{as} of DPPA@ZrO₂ representing the alkyl chain ordering degree at different percentages of DPPA in the mixed monolayer at the nanoparticle surface, the rest to 100% coverage is the coupling agent mentioned in the diagram.

A first conclusion concerning the maximum reachable absolute values of disordering from the FT-IR-experiments (Figure 59) is that bulky molecules like tBuPPA have a higher effect on disturbing the alkyl-monolayer-ordering as smaller molecules such as MPPA. However the form of the curve in Figure 4 can only be explained by identifying the structure of each mixed monolayer. Two structure types are considered to be present within these mixed monolayer as it is also known from literature for non-fully covered long alkyl chain monolayers.^[98, 197, 347] One type can be described as a random mixture of the different molecules to form a collective monolayers analogous to not completely covered substrates, which was already observed for C18 phosphonates^[182] and organosilane coupling agents.^[98] In another type the molecules form island structures, as e.g. observed in literature for octadecylphosphonic acids on mica,^[197] where regimes of collectives of the same molecules are covering the surface in an alternate way. This has been intensely investigated for mixed monolayers of thiols on gold surfaces. *Laipis et al.* discuss completely mixed regimes and divide island type regimes additionally into micro- and macro-phase-separated systems.^[230] As known from literature a formation of preordered structures in solutions which can then adsorb to the nanoparticle surface can have an influence on this behavior. This was observed for phosphonates and silanes.^[182, 203] Of course every gradual mixture of these extreme cases is expected to exist for the systems, investigated in this work. Also, a lower tendency to strong island formation is

expected within the investigated systems because the C12-chains used in these studies do not show the same extremely high ordering tendency as C18-chains do.^[207] The formed structures are considered to be depending on the mixing ratio and the type of the co-adsorbed molecule. The latter can be reduced to a model which says that island growth is preferred if the interactions between molecules are more favored compared to interactions between two different molecules to a certain degree. Examples for such higher interaction forces can be the sum *van der Waals* interactions over a long chain, π - π -interactions of extended aromatic systems, strong polar or ionic interaction or hydrogen bonds, etc.^[138, 147]

Using these structural models the difference in the ordering behavior with different mixing ratio using different molecules can be explained in the following way. Small and weak interacting molecules such as MPPA show a linear like behavior because of the presence of a randomly mixed SAM (no high island-formation tendency of this molecule) for all data points. Additionally, as *Offord* and *Griffin* have suggested for mixed organosilane-surface layers, the longer alkyl chains can form ordered structures around these small molecules (e.g. short alkyl chains in mixed thiol@gold systems^[225-227, 229]) with the chain packing being not dramatically effected at lower disturbing molecule surface concentration.^[346] This would not be the case for the sterically far more demanding molecule, tBu-PPA. This can explain the fact that this molecule leads to a sharp increase in disordering at higher molar ratios. The larger but planar molecule PyPPA does not show a very strong increase in disordering of alkyl chains with increasing mixing ratio PyPPA/DPPA. However the slope of this series-curve at lower concentrations is the highest compared to all other molecules. This can be explained by randomly mixed monolayers at low concentrations where the bulky molecules can effectively disturb the C12-SAM-formation and changing to an island like regime for higher concentrations of PyPPA where C12-chains can be still medium-ordered in DPPA@ZrO₂ island regions. This phenomenon was already discussed by *Laibinis et al.* for mixed monolayers of alkylthiols with different chain length on gold. They showed that the ordering disturbing is most effective for randomly mixed systems.^[230] Analogously *Prado et al.* showed if C8 and C18 chain phosphonates are mixed a complete molecular homogeneous layer is formed where the chains above the length 8 carbon-atoms are expected to be unordered.^[336] Whereas *Vercelli et al.* have evidenced a close packed island structure via cyclic voltammetry for a system where hexylferrocenyl phosphonic acid and dodecyl phosphonic acid were adsorbed to ITO.^[348] This is very likely to happen also in the investigated DPPA/PyPPA mixed layers at higher PyPPA concentrations because strong π - π -interactions between two neighboring PyPPA molecules is energetically beneficial. Finally, the PhPPA-molecule represents a mixture of all these effects.

Up to now, mostly the effect of mixing alkyl chain coupling agents of different chain length on the long alkyl chain ordering has been investigated.^[164, 225-230] It was demonstrated that a variety of non alkyl chain moieties can also be applied for this disordering approach, even on the facets of small nanoparticles, where in most of the investigated cases random mixture is expected because of the high effectiveness of disturbing the ordering by the co-coupling agent.

Agglomeration behavior of mixed monolayer modified nanoparticles

The agglomeration behavior of the mixed monolayer endcapped nanoparticle powders was studied via small angle X-ray scattering (SAXS) using the following model to describe the agglomerated particle system, based on the theory explained in chapter 1.3, with some specifications: In this chapter, exclusively, the *Beaucage* model has been applied for the curve fitting because of the possibility of a more accurate consideration that the particles undergo a distribution. Thereby, the scattering intensity $I(q)$ according to *Beaucage*^[294-296] describes two functions. One function is based on *Guinier's* law and the other on the structurally limited power law (Eq. 3, chapter 3.1.1.3), formulated for one hierarchical level. For weak agglomerates, the structure function $S(q)$ ^[292, 293], Eq. 2 (chapter 3.1.1.3), describes the interference of the scattering of particles. Two additional parameters are used within this function, the hard-sphere radius R_{HS} , which gives the correlation of the interparticle distance within an agglomerate cluster, and a mean hard-sphere volume fraction η , which gives the probability to find neighbored particles. $S(q)$ s were calculated with the *Percus-Yevick* approximation (Eq. 2, chapter 3.1.1.3).^[291] Curve fitting was performed by the software Mathematica™. Therefore, η is a numerical value describing the degree of agglomeration of the modified zirconia nanoparticles – the higher η , the stronger the agglomeration.

Figure 60 shows the scattering curves of the four different mixed surface layer nanoparticle powders, for each different disturbing co-capping molecule one diagram. Qualitatively observable from these scattering curves is already the trend that the shoulder around $q = 1 \text{ nm}^{-1}$, representing the nanoparticle dimension, is more pronounced with an increased packing of particles per volume fraction. The peak between $q = 10$ and $q = 15 \text{ nm}^{-1}$ originates from the diffraction at the ZrO_2 crystal planes. The hard sphere volume fraction η as a numerical parameter calculated from the scattering curves for the degree of agglomeration and is listed in Table 24 for all series with different co-capping molecules.

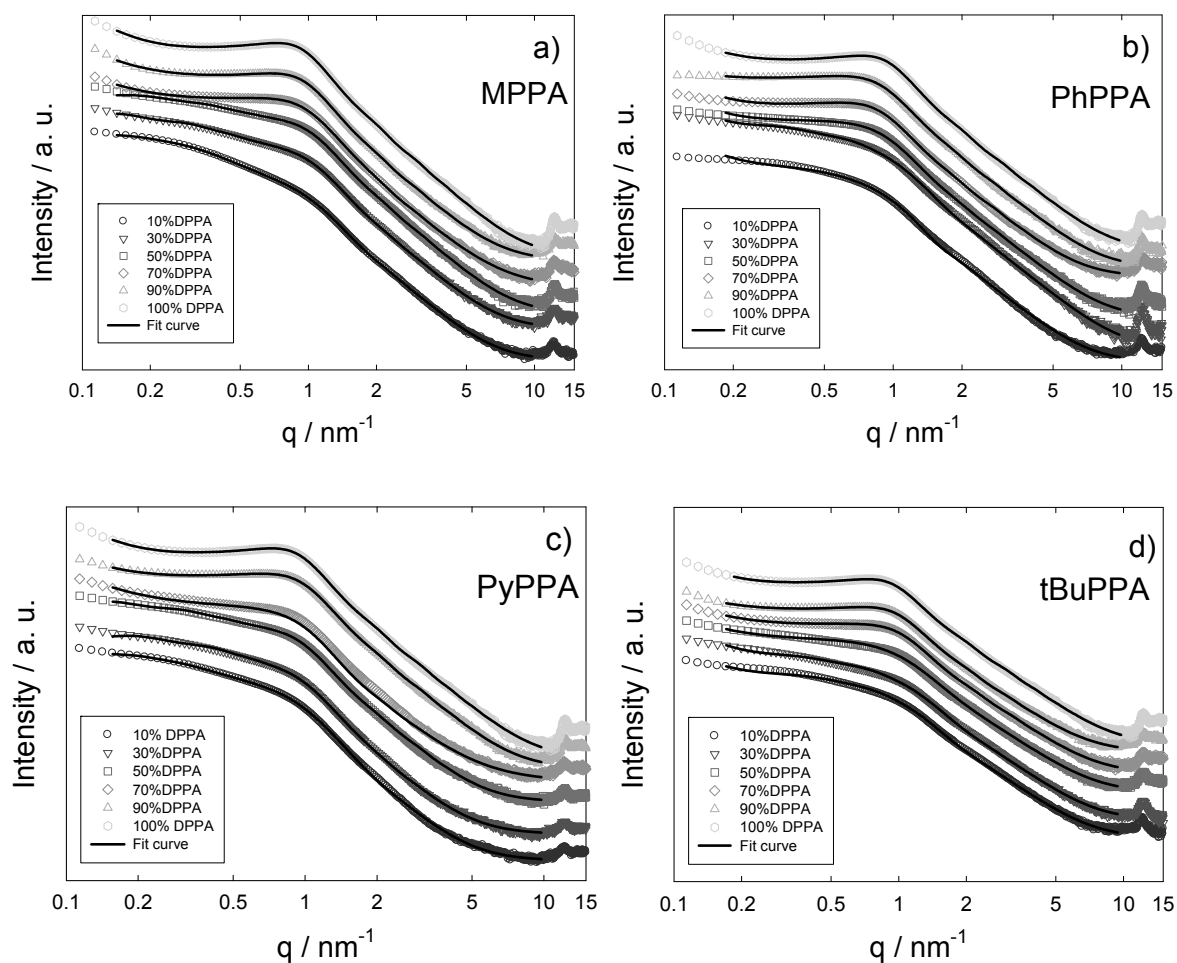


Figure 60. Scattering intensities from SAXS measurements for a) MPPA, b) PhPPA, c) PyPPA and d) tBuPPA @ZrO₂.

Table 24. Hard sphere volume fraction η of ZrO₂ nanoparticle powders with different percentage of co-coupling agent at the surface.

Mol% DPPA	rest MPPA η	rest PhPPA η	rest PyPPA η	rest tBuPPA η
100	0.128	0.128	0.128	0.128
90	0.116	0.105	0.112	0.117
70	0.096	0.107	0.082	0.103
50	0.097	0.079	0.104	0.050
30	0.078	0.055	0.100	0.049
10	0.036	0.035	0.050	0.040
0	0.025	0.025	0.025	0.026

For a simplified discussion the values from Table 24 are plotted in the diagram in Figure 61. The agglomeration of the nanocrystals decreases, nearly one order of magnitude, with increasing concentration of co-coupling agent, regardless of, which coupling agent was used (Figure 61). The trend for this behavior is, in average, linear-like for all different molecules but different for different mixed SAM systems. The behavior at very low and very high mixing ratios is very similar for every co-molecule series whereas at a 1:1-mixing ratio the characteristics of each series differ the most. At 50% co-coupling agent addition, tBuPPA leads to the most effective avoidance of agglomeration, followed by PhPPA. PyPPA and MPPA do not show this strong effect. At a low concentration of the co-coupling agent, tBuPPA is the most effective agglomeration decreasing molecule.

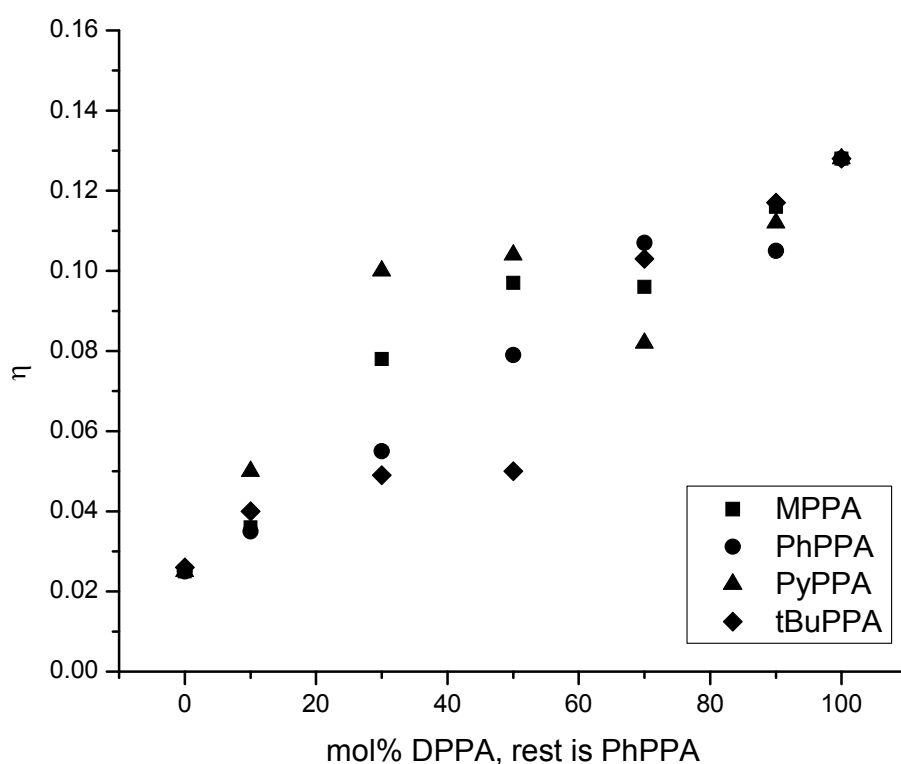


Figure 61. Hard sphere volume fraction η representing the agglomeration of the mixed modified zirconia nanoparticles using different coupling agents for mixed monolayer formation at the nanoparticle surface applied in various mixing ratios, the rest to 100% coverage in the diagrams axis of abscissae is the coupling agent mentioned in the diagram legend.

The TEM-images of agglomerates of 100% DPPA@ZrO₂ powder (Figure 62) demonstrates how the nanopowder agglomerates look like at a η -value of 0.13. The crystals are closely packed and approximate 1-2 nm spacing between the particles is visible which may origin from the interparticle bilayers (Scheme 3). Mixed modified particles are less agglomerated in the macroscopic powder assembly and thus considered to be easier deagglomerated using

common approaches like soft ultrasound, which is of high technological relevance and will be shown later in this work.

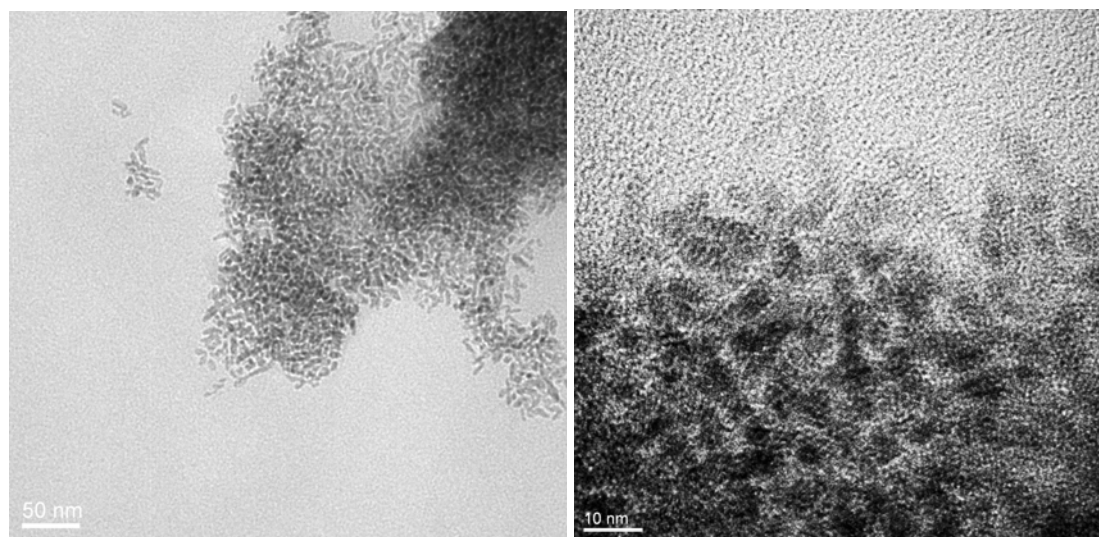
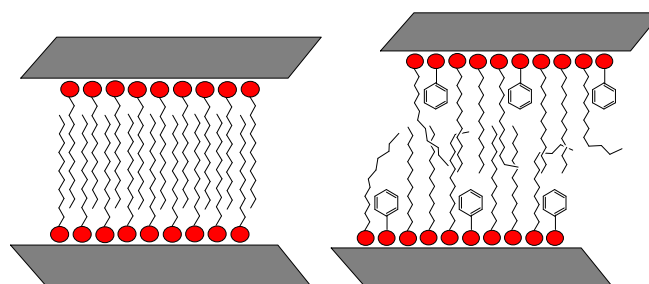


Figure 62. TEM-Images of agglomerates of 100% DPPA@ZrO₂ nanocrystals, right: detail.

Of course, the total physical surface-properties (e.g. wettability with different solvents, hydrophobicity) also change with co-adsorbing other molecules compared to a 100% long alkyl chain layer. Therefore an optimum has to be found.

Scheme 3. Schematic drawing of two particle facets in particle agglomerates of 100% DPPA@ZrO₂ (left) and mixed modified particles (right).



The fact that nanoparticles with higher content of long alkyl chains at the surface are more strongly agglomerated can be explained by the so called "zipper"-effect of the surface bound long alkyl chains, forming a bilayer-structure between two particles (Scheme 3) resulting in a close packed system where the agglomerates are difficult to break. This occurs even for, usually at room temperature non crystalline, but ordered C12 chains.^[205] The hypothesis that a decreasing alkyl-chain-"zipper-effect" is responsible for a decrease in agglomeration with the formation of a mixed monolayer, is also supported by the observed fact that the particles modified with 100% co-coupling agent all show nearly the same agglomeration behavior. Regardless of the steric demand of the used coupling agent (MPPA or PyPPA), the η values

are the same at this point. Therefore it can be excluded that the observed hard sphere volume fraction change results just from different distances of the particles in the agglomerates. It seems that a general property is changed, which is the strength of the interaction between two crystal facets of two different particles "zipped" together. This effect has been investigated in detail for (non mixed) alkanethiols of different chain length on Au-clusters by *Terrill et al.*^[216] They show a correlation between the degree of chain packing and particle agglomeration behavior using DSC, SAXS and AFM-data concluding that a zipper-effect can also be strong for smaller particles because of their tendency for surface energy minimization. This effect is also described for gold-nanoparticles with a surface area of approx. 100 m²/g by *Badia et al.*^[220, 224] where they describe an agglomeration structure in which the interparticle alkyl chains are highly ordered compared to the dangling chains which are not participating in the "zipper". For larger facets this effect is considered, as shown in this work, also to be very strong, because over larger facets, the number of interacting alkyl chains is higher. The next issue to discuss is why the trend of a decreasing "zipper-effect" is different for the different used molecules. The difference in the hard sphere volume fraction to a linear trend and also the difference between the various series is the highest at a 50% mixing ratio. A linear like trend would be expected for a total randomly mixed surface layer. The explanation for these differences can again be found by taking two mixing regimes (island like and randomly mixed) into account, where molecules like PyPPA more tend to an island-like-SAM and molecules like tBuPPA more tend to a randomly mixed layer.

Up to now, this "zipper-effect" has been investigated in literature mostly for thiols@gold-nanoparticles,^[216, 220, 224] less is known for oxidic nanopowders. One example is from *Sahoo et al.*^[156] where they attached hexadecyl phosphonic to magnetite nanoparticles. For metal oxide systems, a mixed modification approach is mostly used to tune nanoparticle surface properties like polarity by mixing two different molecules.^[336] It is possible, using this facile mixing approach, to finetune the surface SAM ordering and thus the agglomeration behavior, not only via different mixing ratios but also using different co-adsorbents, physically all from non-polar nature.

Correlation of surface SAM-ordering and particle agglomeration behavior and Conclusions

Can the molecular parameter, namely the gauche-defects observed by IR, and the macroscopic parameter, namely particles per volume unit as investigated by SAXS be correlated? Their correlation is plotted in Figure 63. The different series all follow a general trend: With decreasing wavenumber, this means less gauche defects due to higher ordering in the surface-SAM, the agglomeration of the particles increases. This means that these phenomena are connected together underlining the "zipper effect"-theory of an interparticle bilayer formation. However, some data points do not show a strong correlation. The PyPPA displays higher agglomeration even at higher alkyl-disordering. This may origin from strong interaction of pyrene molecules within the bilayer, e.g. pyrene moieties from one particle strongly interact with others on the neighbor-particle which is very likely to occur due to the high tendency for strong π - π -interaction in such systems. Also the tBuPPA series seems to fall

out of the scheme at the point of very high disordering (2926.3 cm^{-1}). The agglomeration there is nearly the same as for the other molecules at this mixing ratio, which means that at a certain point of disordering or alkyl chain dilution, the agglomeration behavior stays the same, there is no zipper effect and thus further disordering of the alkyl chains does not further reduce the particle packing.

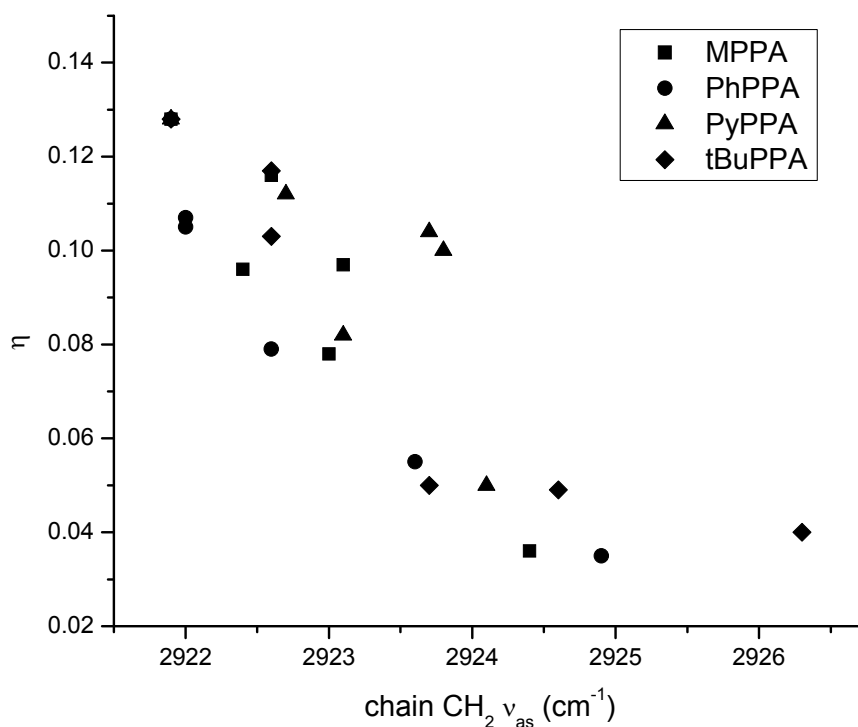


Figure 63. Correlation of hard sphere volume fraction η from SAXS and attached DPPA-methylene chain asymmetric vibration from FT-IR of mixed modified ZrO_2 nanoparticle powders.

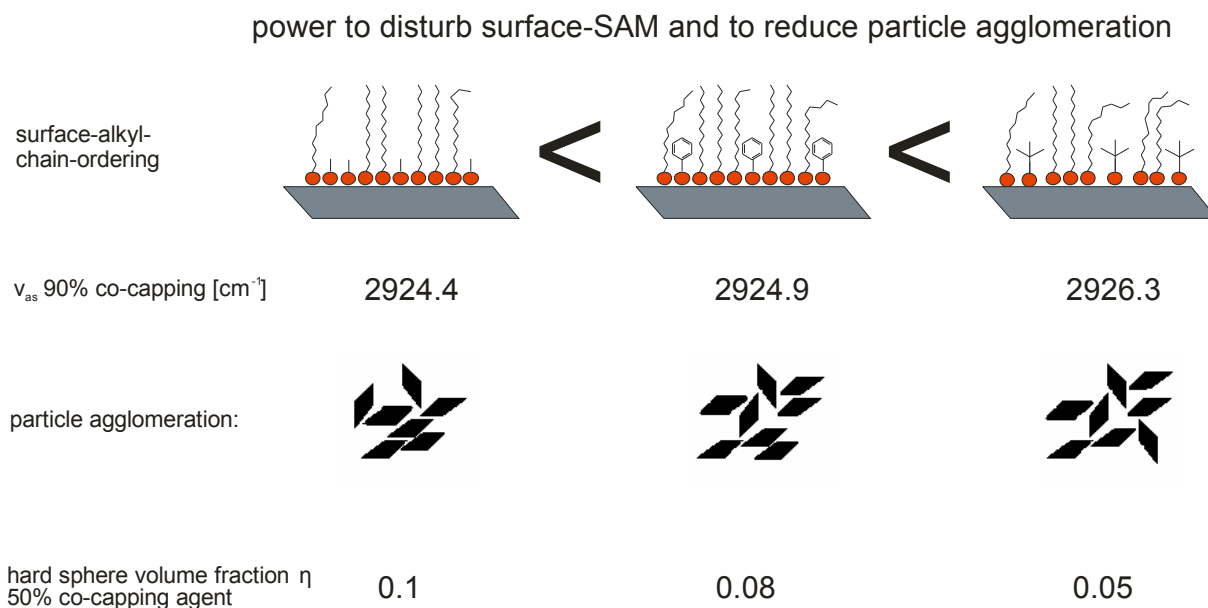
Up to now, in literature, such concepts of mixed monolayer formations to tune physical surface properties have been basically described for thiols of different alkyl chain length on planar gold surfaces.^[164, 225-228, 230] It could be learned from these systems and introduced this mixed modifying approach to oxidic nanoparticle technology using not only different mixing ratios but also various co-capping molecules. It is concluded from this chapter that by this approach that the macroscopical phenomenon of agglomeration behavior of this alkyl chain modified nanoparticles is strongly influenced by the nanoscopic phenomenon of surface ordering which can be controlled on a molecular level.

As a conclusion the ordering of dodecyl chains in mixed monolayers of phosphonic acid coupling agents on zirconia nanocrystal(facet)s, prepared by a co-adsorbing approach has been investigated. Different phosphonic acid co-capping molecules to disturb the long alkyl

chain ordering have been studied, namely the small methyl-, the bulky but planar pyryl-, the sterically demanding *tert*-butyl- and the intermediate phenyl-moiety. In FT-IR-studies, the C-H vibrational modes of the dodecyl-chain-methylene-units were used to detect the degree of alkyl chain packing in the self-assembled-monolayer (SAM) via a blueshift with increasing gauche defects. The SAM, consisting of 100% dodecyl-chains showed moderate ordering, not totally crystalline as it would be the case for C18, as expected and desired in terms of dispersibility behavior of the nanoparticles, but far more ordered than in a liquid state. With increasing amount of adsorbed co-coupling agent, the ordering of the dodecylchains decreased significantly. This effect was quantitatively different for different co-adsorbed molecules (Scheme 4). Some moieties as the small methyl-group showed less power for disordering and bulky moieties like *tert*-butyl gave the absolute highest chain disordering. Why this trend is not same with the mixing ratio for all molecules and linear like, can be explained by the presence and interplay of different regimes of ordering and disordering within the mixed SAM: The two extrema of a randomly mixed monolayer and an island-like layer, where the two different molecules are phase separated, have to be taken into account. This effect of deviation from the expected linear-like trend is considered to be very strong for molecules such as pyrene phosphonic acid, having the tendency to homo-interact given by the natural π -electron rich molecular structure. For this reason, this bulky molecule has less influence on the alkyl chain ordering degree over the major part of the mixing ratio ranges, e.g. compared to the smaller phenyl-coupling agent.

The agglomeration behavior of the prepared mixed modified, nanoparticle powder series has been studied with small angle x-ray scattering (SAXS), calculating a hard sphere volume fraction number from the scattering curves as a value for the density of nanoparticle packing. From this study, it could be deduced that with increasing degree of co-coupling agent within one series the particle agglomeration decreased over nearly one order of magnitude, and thus the redispersibility properties as it will be shown in the following chapter, of the nanoparticle powders are improved (Scheme 4). For all different co-coupling agent molecule series, a good correlation between the agglomeration behavior of the nanoparticles and the degree of ordering of the surface bond long alkyl chains could be found. From this it can be concluded that for the investigated system a stronger alkyl chain ordering causes higher agglomeration of the particles. This can be explained by a "zipper-effect" where the nanoparticles agglomerate via alkyl-bilayers between their crystal facets (Scheme 3). Except for the pyrene-residue, this correlation was weaker, which can be due to a competing pyrene-pyrene-interparticle-bilayer-formation at the pyrene island regions leading to more agglomeration.

Scheme 4. Surface SAM-disordering and mixed modified particle agglomeration behavior depends on the nature of the organic moiety of the used co-coupling agent.



These results point out that the well known chemistry of mixed monolayer formation on macroscopic substrates can be applied to nanoscopic (metal oxide) crystal facets resulting in tunable physical surface properties, which has not been reported yet. Up to now there was also less knowledge about the "zipper-effect" between, technologically highly relevant metal oxide nanoparticles (nanocomposites, ceramics). Most studies deal with thiols on gold nanoparticles. With the current study it is shown how surface tuning on molecular level impacts nanoscopic surface ordering properties and thus the macroscopical phenomenon of particle agglomeration behavior. The next step would be to apply this knowledge to inorganic-organic-nanocomposite technology with the additional parameter of a polymer matrix.

Additionally from an analytical point of view, taking the correlation between SAM-ordering and particle agglomeration into account, characterize SAMs at nanoparticles can be characterized by two fundamentally different methods: Nanoparticles can be used as probes for SAM-investigations by applying an indirect method (SAXS) which detects features of the particles itself and allows a conclusion on the SAM-structure via the correlation with the direct method of FT-IR-Spectroscopy where the molecular surface structure is directly probed. Thereby it is astonishing that the non-spectroscopic approach (SAXS) shows comparable sensitivity to the spectroscopic approach (FT-IR).

Redispersibility of mixed modified nanoparticle powders in organic media

As discussed above, the mixed monolayer formation at the nanoparticles that prevents interparticle bilayer-formation should enhance the dispersibility in organic solvents (the deagglomeration properties). To demonstrate this, the system of mixed monolayer modified ZrO_2 , using PhPPA and DPPA, has been taken. This, for many applications of nanoparticles

desirable effect, has been investigated by dispersing the nanoparticles in an organic solvent (*n*-hexane) using the same procedure which is applied when nanoparticles are dispersed in monomers for nanocomposite syntheses via *in situ* polymerization.^[13, 36, 349] A simple ultrasonic bath (treatment for 30 min) was used for dispersing the dry nanoparticle powder in the solvent to give 0.5 g/L dispersions. The dispersions were allowed to set for 1 h and then the quality of the dispersions was evaluated by DLS-measurements. Figure 64 shows the size distribution, derived from DLS-measurements, of mixed modified nanoparticles containing 90% and 70% DPPA as well as 100% DPPA. The distribution function is shown surface weighted as the interface region is crucial in inorganic-organic nanocomposites. Each measured distribution is bimodal with the peak at lower radii representing the single nanoparticles (see also Figure 25) and most likely agglomerates of a few nanoparticles in the case of the 100% DPPA modified nanoparticles. The 100% DPPA-system shows the largest size distribution in case of small radii and larger agglomerates (around 0.5 micrometer), which is a strong indication for agglomeration in suspension. The peak at lower radii sharpens for the particles with 90% DPPA and 70% DPPA. In addition, the peak for the larger agglomerates shifts to lower radii and narrows, which can be due to decrease of agglomerate and also change of the hydrodynamic behavior of the different modified particles. In the case of 70% again a slight broadening of this second peak is observable and for the 50% system (not shown), the dispersion quality again decreases dramatically showing huge agglomerate peaks. This is considered to be due to the fact that DPPA is the major molecule that hydrophobizes the surface and thus enhances the interaction with the non-polar solvent. If the surface is only partially covered with DPPA (rest PhPPA), the dispersion quality is as poor as for the analogous system with 100% PhPPA in *n*-hexane.

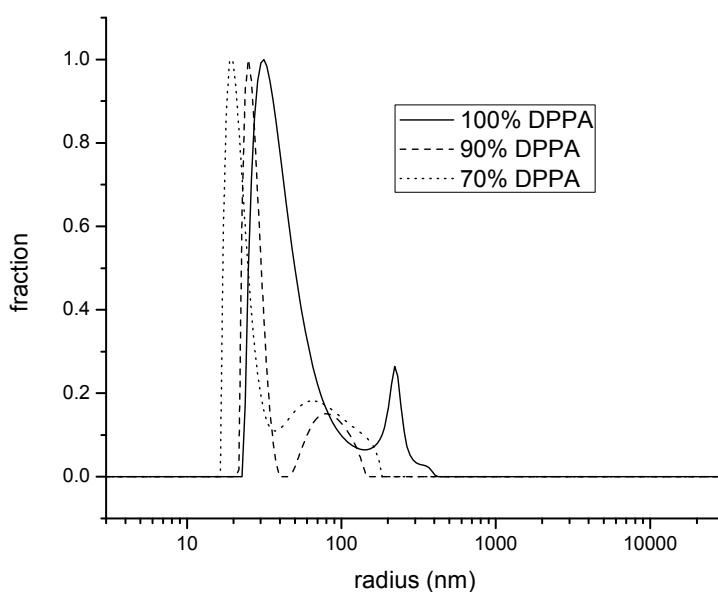


Figure 64. Surface weighted size distribution of mixed modified ZrO_2 nanoparticles (from DLS-measurements), dispersed in *n*-hexane via ultrasonic treatment.

Thus, there is an optimum in dispersibility for a PhPPA-content of 10-30%. This fact is likely to originate from the described agglomeration effect by interparticle alkyl bilayer formation. The alkyl chain ordering, see C-H-shifts from Figure 55, is already affected at PhPPA contents of 10-30% which may result in better deagglomeration properties, because agglomerates from more oriented alkyl chain systems are more stable^[216, 220] and therefore more difficult to break. This effect of chain ordering (packing) on dispersion behavior is plausible as *Sahoo et al.* described that disordered monolayers like oleic acid monolayers on nanoparticles compared to monolayers of hexadecane phosphonic acid show better dispersibility where the latter form bilayer structures.^[156]

The hypothesis that the surface alkyl ordering affects the dispersibility is also justifiable because one would expect, in an alkane medium like *n*-hexane that the particles are better dispersible if the DPPA content increases since the alkyl chains of the solvent better interact with the dodecylchains than with phenyl-residues. This incompatibility may be the reason for a decrease of dispersibility at higher PhPPA contents (50%). However the liquid *n*-hexane molecules can better interact with more liquid (disordered) surface alkylchains than with stronger ordered systems,^[156] which would explain the observed dispersibility optimum.

In literature, gold nanoparticles have been modified with binary mixtures of alkylthiols to tune interparticle spacing of particle deposits^[233] and *Kubowicz et al.*^[212] use a mixed monolayer formation approach by *Glogowski et al.*^[232] via ligand exchange to finetune the wettability properties of gold particles to optimize the stability of oil-in-water emulsions. Similar mechanisms are expected to be responsible for their results. However, no alkyl chain ordering has been studied in their work. Usually there is a strong correlation of wettability and alkyl chain packing.^[350]

Applying this mixed monolayer approach, an improvement of the dispersion quality of the C12 modified ZrO₂ nanoparticles in hexane by disturbing the C12 chain ordering while maintaining full nanoparticle surface coverage could be reported. The C18 (ODPPA) modified nanoparticles did not give stable dispersions applying this approach.

Also it can be concluded that more loose agglomerated powder (shown by SAXS) achieved via systematic surface tailoring results in a better redispersibility (shown by DLS) of the nanoparticles and in more stable dispersions in organic media.

3.1.3.7 Model experiments on macroscopical substrates

Experiments were carried out to assess the transferability of the facile mixed monolayer approach. This is on one hand interesting to proof the generality of this approach. On the other hand simple methods for SAM and surface property characterization such as contact angle measurements, which strongly correlate with the alkyl chain ordering on plane substrates, are accessible using plane (wafer) substrates.^[226, 228-230, 350] Furthermore, a wafer system could act as a model system for the nanocrystal facets of ZrO₂ to allow the prediction of surface properties of the mixed modified particles when novel surface modification mixtures will be applied.

First, a simple model substrate has been applied for the SiO₂ system. Oxidized Si(100) wafer with a thickness of 13.1 ± 0.4 Å of the SiO₂ surface layer determined by ellipsometry were modified under the same conditions as used for the particle modification. These are however not the optimal conditions to form well ordered SAMs on plane wafers. Non-polar solvents such as n-alkanes are more appropriate for the formation of non-polar dense SAMs^[351-353] but also some well ordered systems have been reported using polar media.^[192] However these conditions are applied here for reasons of comparability. AFM measurements revealed a root mean square (rms) surface roughness of 0.081 nm (from three 1x1 μm areas) which is very smooth on an atomic level. Again, different mixing ratios have been applied for this system and contact angles of water droplets have been measured, also depending on the reaction time, which have been measured (Figure 65). No change in contact angle was observed after 96 h and the reaction can be considered complete. The unusual slow kinetics can be explained by a relatively poor self-assembly tendency under these conditions. However, after 24 h the contact angles were only a few degrees lower and thus the surface is already nearly fully covered which justifies the shorter reaction times (48h instead of 96h) in case of the nanoparticle systems. A decrease of the contact angle with increasing percentage of co-coupling agent PhTMS is clearly visible (Figure 65). It is excluded that this decrease of contact angle only corresponds to the fact that a certain percentage of PhTMS, which gives less hydrophobic surfaces even at full coverage compared to DTMS, is responsible for the observed trend. The reason is that in this case the mixing law could be applied which would lead to a linear decrease of contact angle, but in this case the shape of the curve is similar as observed in literature when alkyl chain coupling agents are applied and alkyl chain ordering is correlated with contact angle data.^[226, 228, 350] Thus it can be assumed that the observed decrease of water contact angle with decreasing DTMS coupling agent percentage results from a less ordered SAM structure in the mixed system in addition to the hydrophobicity decrease because of PhTMS adsorption. It has to be considered that the disordered SAM structure after such a long reaction time does not represent an ideal monolayer structure. Reports in literature describe a complex multilayer structure of low ordered trifunctional alkylsilane, when they have been chemisorbed to oxidic surfaces within several days. This is due to many possible side reactions such as vertical polymerization or attachment without self-assembly.^[354] No direct correlation between chain ordering and contact angle, applying via FT-IR reflectance absorption spectroscopy (IRRAS) methods, could be achieved, primarily because of the low signal intensities of such not fully ordered C12 chain systems when IRRAS is applied.

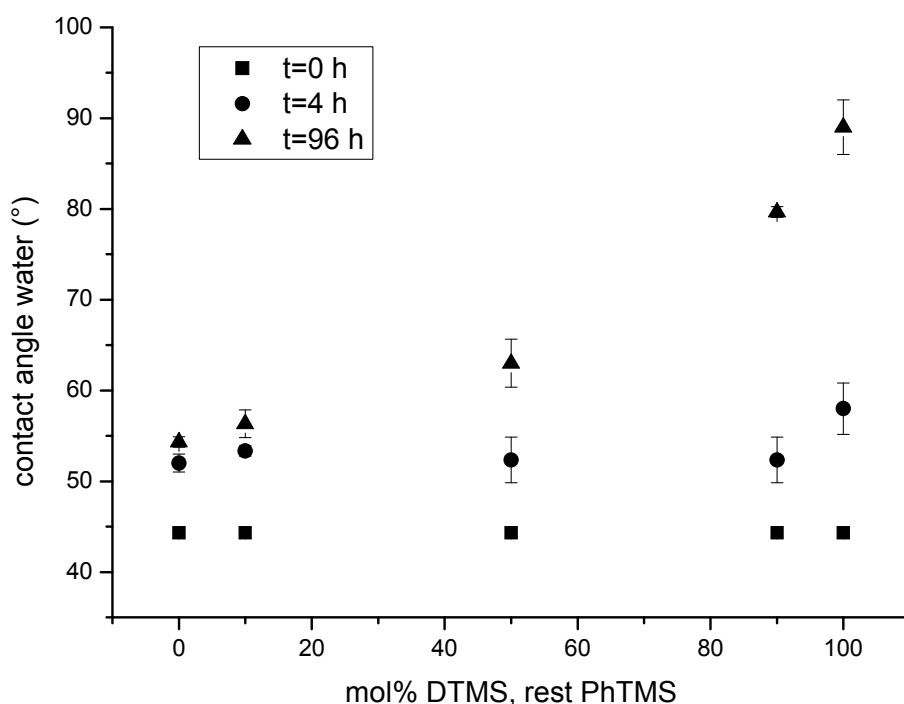


Figure 65. Water contact angle on mixed trimethoxysilane modified oxidized Si(100) wafer depending on the mixing degree, at different reaction times.

Atomic force microscopy (AFM) measurements of surface roughness (again from three 1x1 μm areas) of selected samples additionally gave information on the structure of these mixed SAMs. The 100% DTMS sample exhibits a rms roughness of 0.087 ± 0.002 nm which indicates a relatively densely packed system where 100% PhTMS resulted in a rms roughness of 0.12 ± 0.016 nm. Interestingly, a 50% / 50% mixed monolayer exhibited a rms roughness of 0.140 ± 0.012 nm which is significantly higher as both non mixed system. This is an indication for the presence of a relatively homogeneous and randomly mixed monolayer, as no islands in the micro and nanoregion could be observed in the corresponding AFM-images.

For ZrO_2 model substrates, ZrO_2 was deposited on a Si(100) wafer via atomic layer deposition (ALD) by a procedure from literature^[355] followed by thermal annealing at 600°C and activation of the surface with HCl. EDX measurements revealed the presence of 66.5 at% oxygen and 33.5 at% zirconium in the sample which confirms the successful deposition of ZrO_2 . Also IRRAS measurements revealed a characteristic Zr-O-Zr vibrational resonance around 760 cm^{-1} .^[356] Ellipsometry measurements resulted in an average thickness of this zirconium oxide layer of 8.5 ± 0.5 nm. Additional AFM measurements (Figure 66) revealed a rms roughness of 0.40 nm which is rather high compared to smooth Si-wafers. The surface structure, bumps with 15 to 20 nm diameter (comparable to the dimension of the small ZrO_2 nanoparticle system), can be seen in Figure 66. The relatively rough surface structure of this model substrate does not allow AFM studies concerning the SAM structure (island or randomly mixed), only conclusions on the average roughness are allowed. Nonetheless it is

expected to be an appropriate model system for contact angle measurements for comparison with the small ZrO_2 nanoparticle powders, although chemical surface properties may differ in these systems derived from ALD and hydrothermally synthesized.

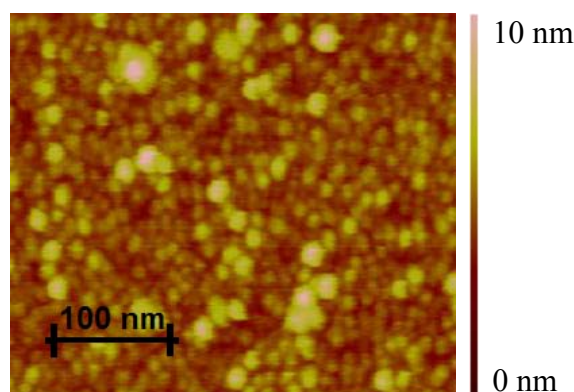


Figure 66. AFM image showing the surface roughness of ZrO_2 deposited on a Si(100) wafer.

The surface modification reaction was carried out under the exactly analogous conditions as applied for the small nanocrystals, for reasons of comparison. Again contact angle measurements were performed, depositing water droplets on the wafer substrates (Figure 67) resulted in significantly different contact angles.

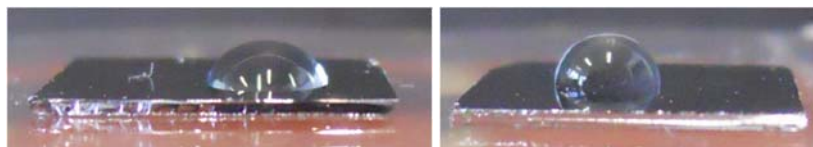


Figure 67. Water droplets on modified ZrO_2 , deposited on a Si(100) wafer. left photograph: PhPPA@ ZrO_2 , right photograph DPPA@ ZrO_2 .

This time, for a direct comparison of the wafer substrate model system with the nanoparticle system, the modified ZrO_2 small nanoparticle powders were pressed to pellets with 13 mm diameter under a load of 8 tons. AFM measurements revealed a considerable rms roughness of this pellets of 280 nm in average for all measured samples. A contact angle of the unmodified powder ($\sim 15^\circ$) could not be measured precisely because the water droplet was sucked into the substrate, which was not the case for all hydrophobized samples. The contact angles of water at different mixed SAM @ wafer substrate and also pressed nanoparticle powders are plotted in Figure 68. Generally the contact angles for high DPPA containing samples are significantly higher than for the analogous SiO_2 systems, which is in coincidence with the results obtained for the chain ordering on the nanoparticle surfaces in the previous chapters. Again with decreasing amount of co-coupling agent (PhPPA) the contact angle increases until the surface is highly hydrophobic, which occurred in both cases the pellets and the wafer substrates. A correlation between these two systems can be assumed. However, the point at 50% / 50% mixing ratio is significantly higher for the powder pellets and lies outside the assumed trend. This could be explained by roughness effects of the mixed SAM due to island formation, which however remains as a hypothesis because it cannot be proven completely. However, even, if no precise information on the SAM structure can be derived

from AFM measurements of the wafer substrates because of the rough quality, the 50% / 50% mixed sample was also by a factor of 2 rougher in AFM than the other pure monolayer samples, also on a level of 50x50 nm scanning. Thus macroscopic phase separation of the different coupling agents can also be excluded. Again, the 100% Ph covered samples show much lower contact angles as the 100% C12 system for ZrO_2 (Figure 67). The trend is similar to SiO_2 even though the systems are chemically different. Also again, no perfect linear trend is observed here and the fact that the change in contact angle results only from the mixing of both compounds can be ruled out as already discussed in detail for the SiO_2 system. Hence, a correlation between chain ordering and contact angle can here also be assumed. The difference in the absolute values for the contact angle is assumed to derive its origin from the different surface roughness values of the wafer substrate (0.4 nm) compared with the roughness of the pellets (280 nm). It is not assumed to be an effect related to the different chemical nature or differing surface coverage as the mixing behavior appears very similar from the contact angle trend in Figure 68. These assumptions are plausible as roughness plays a general role in influencing the contact angle and can have tremendous impact on it.^[357, 358] Generally a rougher surface with a roughness in a certain dimension in submicron and nanorange^[357] results in a higher contact angle.^[359] Again, it was not possible to correlate these results from the wafer with IR data because of the weak signal intensity for these mixed non-ordered systems in IRRAS. However, for the particles, the existence of a correlation of contact angle with alkyl chain ordering can be seen when Figure 55 (asymmetric C-H methylene vibration versus mixing ratio) and Figure 68 (contact angle versus mixing ratio) are compared.

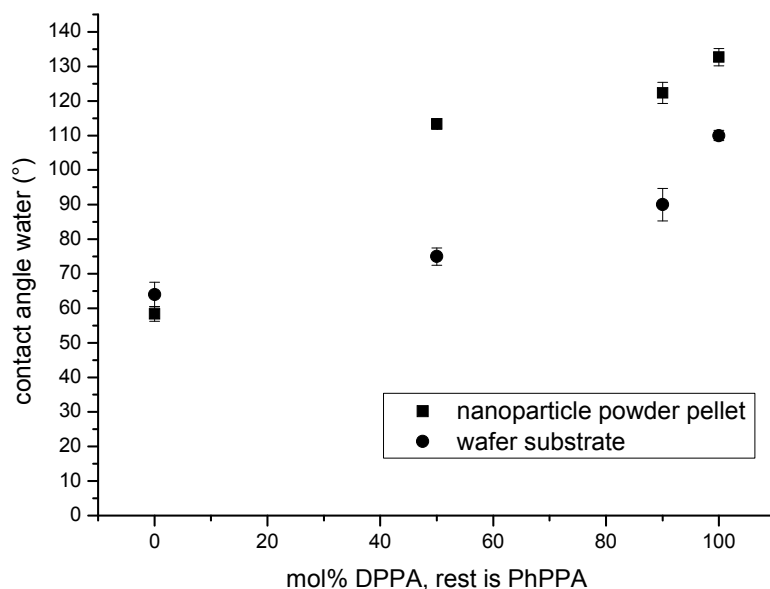


Figure 68. Water contact angle on mixed modified ZrO_2 : Nanoparticle powder pellets and $ZrO_2@Si(100)$ wafer substrate.

As a conclusion from this chapter, simple experiments on wafer substrates can be used to extrapolate the properties studied on nanocrystal facets with regard of surface modification. Contact angle measurements give quick information on physical surface properties and the

preparation of the samples is simple. The wafer and nanoparticle systems are comparable concerning mixed monolayer formation behavior. As a rule of thumb, for ZrO_2 the contact angles for such mixed SAM systems can be estimated from the wafer experiments to the particle powder pellets by multiplying the wafer value by 1.25. By these experiments complementary surface characterization data is available: FT-IR gives more intense signals for modified nanoparticles (high surface/volume ratio) and is less sensitive for macroscopic substrates, whereas contact angle measurement is a typical method applied for macroscopic surface property determination and can be easily applied for the wafer system. Also, the generality of the concept of mixed monolayer formation for the metal oxide surfaces could be proven here.

3.1.3.8 Conclusions: alkyl chains on nanoparticle surfaces

To summarize with the results on hydrophobic SAMs on nanoparticle surfaces the following statements can be made:

- The SAM formation characteristics, namely the dense packing of alkyl chains, strongly depend on the nanoscopic curvature. Generally the more crystalline the substrate is the more crystalline is the SAM.
- The ordering of long alkyl chains on nanoparticles can be tuned via mixed monolayer formation.
- The agglomeration of nanopowders directly correlates with the alkyl chain ordering and can be tuned via mixed SAM formation.
- Weaker agglomerated powders, attained via mixed SAM approach, show significantly better redispersibility in organic media.
- Simple wafer substrates can be used to predict or estimate SAM formation properties on nanoparticles.

It was shown that nanoscopic properties affect macroscopic properties and that both can be controlled on a molecular level. As an outlook, the next step is to investigate the influence of the agglomeration behavior of these systems on the dispersion quality in the final nanocomposite materials, which will be discussed in chapter 3.2.

3.1.4 Hydrophilic Nanoparticle Surface Modifications

Many polymer matrices show hydrophobic properties. Thus, the application of hydrophobic surface modifications and related scientific issues have been investigated in the present work up to now. However, hydrophilic polymers such as epoxy resins but also non crosslinked acrylate based polymers^[167, 360] give a better interfacial fit with hydrophilic surfaces. This has been reported in literature for epoxy resins with ZrO_2 and SiO_2 .^[38, 65] Thus, a novel type of coupling agent spacer chain is introduced in this chapter. Trialkoxysilanes and phosphonic acids with diethylene glycol spacer / moiety (Table 8 and Table 11 – DEG-PPA and DEG-TMS) are applied. The diethylene glycol (DEG) moiety should allow an enhanced physical

interaction between the modified particle surface and the hydrophilic organic matrix as DEG and matrix both are polar and (oligo)ethylene glycols are highly miscible with epoxy resins.^[361] It is a well established procedure to adsorb poly(ethylene glycol) (=PEG=PEO) chains (without further functional groups) to particle surfaces to tailor the surface properties of inorganic nanosubstrates.^[116, 362, 363] However, the approach introduced in this work has the advantage that the chain is strongly covalently bond to the substrate via the anchor group at one chain end. Thus, the system is well-defined as compared to randomly adsorbed chains, and the surface modification is considered to be more stable towards detachment. Of course, unmodified metal oxide nanoparticle surfaces are also hydrophilic but the particles are mostly strongly agglomerated or even aggregated (because of their reactive surface M-OH groups) and thus the powders are easier to handle when the particles are endcapped.^[100]

Considering the relatively high grafting densities reached with these molecules (>3 molecules/nm² for ZrO₂), one can speak of hydrophilic SAMs in this case, with grafting density results similar to the different approach done by *Luzinov et al.* where PEO grafting-*from* was applied to stabilize nanoparticle dispersions.^[364] Also other typical hydrophilic SAM forming approaches, applied to tune surface properties, comparable to this approach, use short alkyl spacer between the surface and the oligo(ethylene glycol) chain to further enhance the dense packing of the organic molecules.^[365, 366] However, *Lennox et al.* also observed a strong brush-like SAM formation with high grafting densities of PEO on gold nanocrystals without any additional alkyl-segment,^[210] and the here investigated ZrO₂ nanocrystals are assumed to behave similarly allowing a strong packing of the DEG chains at the crystal facets.

The redispersibility of these systems has been tested by short (1 min) ultrasound treatment of the particles in organic solvents and were allowed to settle for also just a short time (15 min). Thereby, the particles could easily be dispersed in ethanol and ethyl acetate where no sedimentation was observed. The ZrO₂ particles were not dispersible in these hydrophilic organic media before surface modification (the electrostatic stabilization of neat nanoparticles needs protic media). More hydrophobic dispersion media (e.g. toluene) also led to unstable dispersions. As an example, Figure 69 shows the particle size distribution of DEG-PPA@ZrO₂ small nanoparticles in ethyl acetate. The unimodal distribution shows a peak maximum around the same region where it could be found for the unmodified homogeneously dispersed particles in water (22 nm diameter, mass weighted, peak). The absence of peaks in the higher radius region points out the high quality and homogeneity of the dispersion. Ethyl acetate as a moderately polar, organic solvent is considered to be a good model dispersion medium from which can be concluded that the particles are with high probability well-dispersible also in comparable polar aprotic media (e.g. the epoxy resin monomers). Similar results have been obtained for the DEG modified SiO₂ nanoparticle systems.

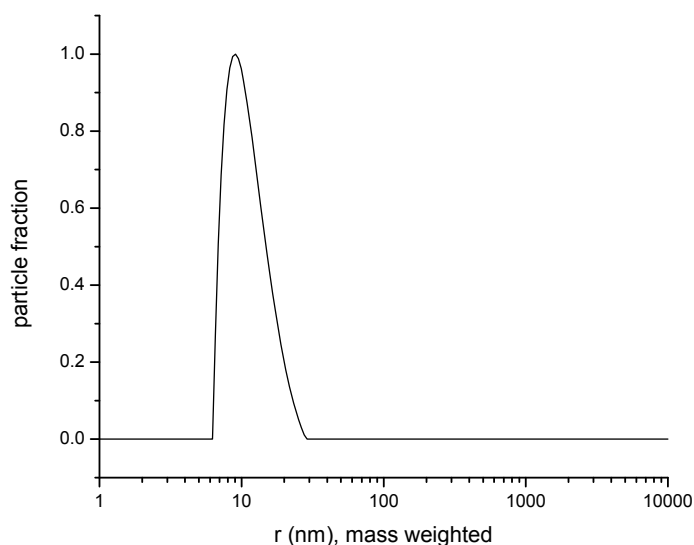


Figure 69. Particle size distribution from DLS of DEG-PPA@ZrO₂ small nanoparticles dispersion in ethyl acetate.

The contact angle of water at the DEG-PPA modified ZrO₂ wafer substrate was $36.0 \pm 2.5^\circ$ which is medium hydrophilic. The CH₃ end group of the densely packed DEG SAM is considered to be responsible for this rather high contact angle compared to hydrophilic PEG-SAMs from literature where e.g. also hydrophilic OH end groups instead of the here used methylether group were applied resulting in lower water contact angles of 25 to 28°.^[366]

An issue when working with hydrophilic modifications is the water uptake of the modified surface which can influence the mechanical properties when hydrophilic polymers are applied.^[271] Inorganic fillers with a potential high water uptake can influence this behavior.^[272] A change of the water uptake / swelling behavior in the final epoxy resin material is possible and this is studied in the nanocomposite chapters in detail. For this reasons, water uptake experiments have been carried out where dry powders (dried in 1 mbar over P₂O₅ at 25°C until the weight remained constant) were exposed to 100% relative moisture at 25°C until weight equilibria were reached. Unmodified, hydrophobic, and hydrophilic surface modifications were studied for the case of ZrO₂ small nanoparticles. The thus obtained maximum water uptake abilities of these modified powders are visualized in Figure 70. The hydrophilic unmodified and DEG-PPA modified particles absorbed significantly higher amounts of water than the hydrophobic systems modified with DPPA and PhPPA. This makes sense as poly- and oligo(ethylene glycol)s are hygroscopic. The fact that water is also taken up by these systems can be partially related to the fact that the SAM is not perfectly dense in the case of PhPPA and DPPA (see chapter 3.1.2.3). On the other hand the effect of higher water uptake of hydrophilic nanoparticles is exploited in membrane technology where e.g. poly(styrene sulfonic acid) grafted TiO₂ nanoparticles are applied to systematically enhance the water absorbing properties of membranes.^[367]

For these reasons the here used nanoparticles had to be dried and kept under dry conditions to achieve reproducible conditions for nanocomposite preparations.

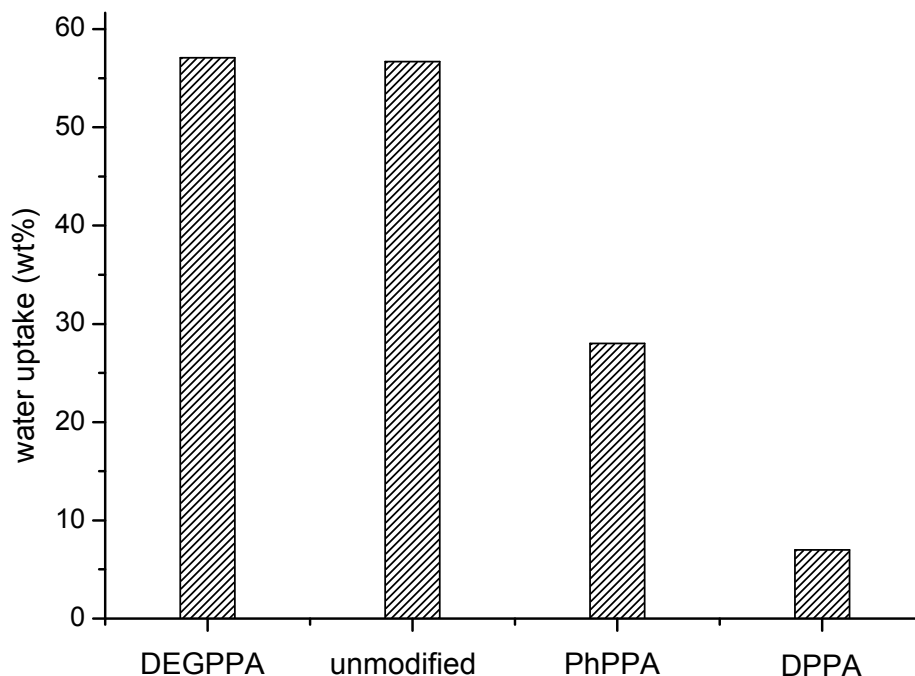


Figure 70. Water uptake behavior of unmodified and modified ZrO_2 (small) nanoparticles: A comparison of hydrophilic with hydrophobic surface modifications.

3.1.5 Polysiloxane grafted nanoparticles

As an alternative to alkyl chain modified nanoparticles poly(dimethylsiloxane) (PDMS) chain modified nanoparticles (with comparable chain length as used for the alkyl chain grafted particles) are introduced and investigated within this chapter. There are some major reasons why these systems are of great interest and thus worth studying.

(i) Applying PDMS spacer based coupling agents to hydrophobize surfaces could be another possible solution to avoid alkyl chain intercalation leading to strong particle agglomeration. As these PDMS systems are very flexible and do not show a tendency to crystallize as it can be observed for long alkyl chains.^[242]

(ii) Unique (mechanical) material properties are expected through the use of PDMS-grafted nanoparticles as filler in common polymer matrices by building a soft interfacial region between polymer matrix and inorganic nanoparticle, which will be studied in chapter 3.2.5.2. Up to now there is little known about related systems in literature. About the use of PDMS chains to build up hybrid materials, there is some knowledge and the results are promising.^[245, 368, 369]

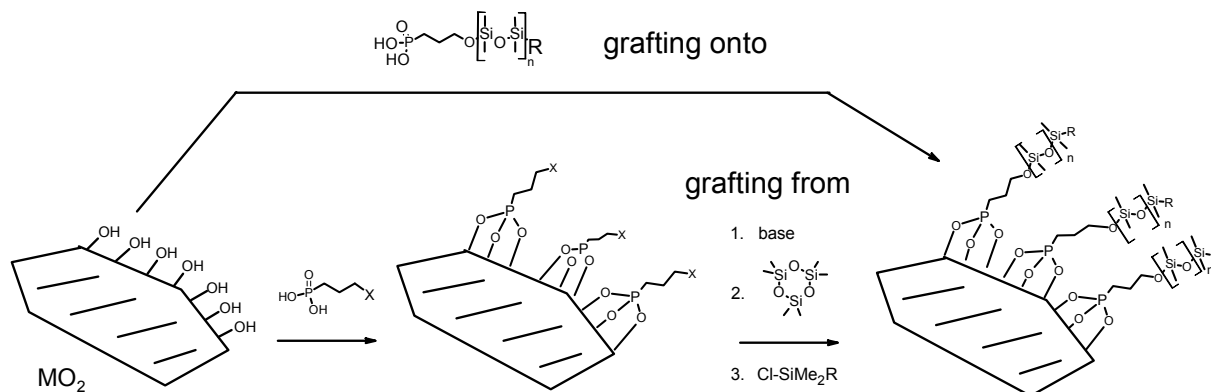
(iii) PDMS spacer chains offer different surface properties. For the application in silicone elastomers this modification is considered to result in a better interfacial fit than alkyl based systems.

The concept for these new coupling agents is the same as for the commonly used alkyl analogs. The nanoparticle surface is tailored by attachment of the organic chain via an anchor group on one chain end and also the introduction of a functional group (e.g. polymerizable groups) is done on the other end of a PDMS chain. The PDMS chain should also be from variable and selectively tunable length. Here, two different concepts in the synthesis of these systems (Scheme 5) are applied. In both cases an anionic ring opening polymerization (ROP) is used to build up a PDMS spacer with a selected chain length, which is possible by varying the ratio between monomer and initiator (M/I).

A grafting-*onto* approach will be applied in which a polymeric coupling agent is directly attached to a metal oxide nanoparticle surface. A drawback of this method is the difficult synthesis of these molecules particularly if they should also contain polymerizable end groups. Furthermore, the kinetics and the maximum surface coverage degree adsorbing such molecules is expected to be unfavorable compared to small or strong SAM forming coupling agent molecules.

Additionally, a grafting-*from* approach will be applied, which has not been described in literature before in this way. Here, initiator-molecules or initiator precursors (in this case alkyl bromo end groups which are then lithiated) are attached to the nanoparticle surface and a ring opening polymerization (ROP) is started from the particle surface. One advantage of this approach is that functional end groups can be easily introduced by quenching the polymerization with a certain reagent (e.g. trimethylchlorosilane). The adsorption of small initiator molecules should allow a high degree of coverage, which is shown in the course of these studies and the variation of the M/I-ratio should allow the production of any desired chain length, when the process can be controlled. However, the system is more difficult to study than a comparable grafting-*onto* approach where the defined molecule, which is adsorbed, is exactly known and characterized before. These grafting-*from* studies are basically carried out on small ZrO₂ nanocrystals which are well-defined and have been intensively studied applying other surface modifications (Scheme 5). The SiO₂ system will be investigated and discussed for reasons of proving the generality of the application of such PDMS systems.

Scheme 5. Possible strategies for the preparation of covalent attached PDMS chains on metal oxide nanoparticles. X = initiator generating end group (Br), reagent = ${}^n\text{BuLi}$, R = optional functional end group or CH_3 group, M = Zr.



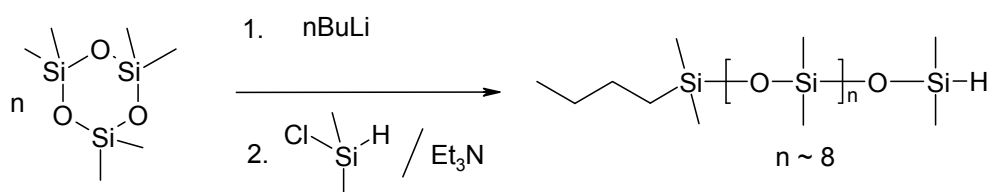
3.1.5.1 Polysiloxane grafting-onto nanoparticle surface

Applying this approach, first oligomeric siloxane coupling agents are prepared and then adsorbed onto the nanoparticle surface by the usual procedure. Simple systems of the type anchor group-PDMS-(alkyl)- CH_3 are studied first without any functional end group to have a less complex system to study and gain general information on these novel systems of coupling agents. Then polymerizable double bonds are introduced as functional end groups demanding a new synthesis pathway to guarantee a modularity (while still enabling a variable PDMS chain length preparation) of this approach.

PDMS-chain coupling agents for ZrO_2 surface modification

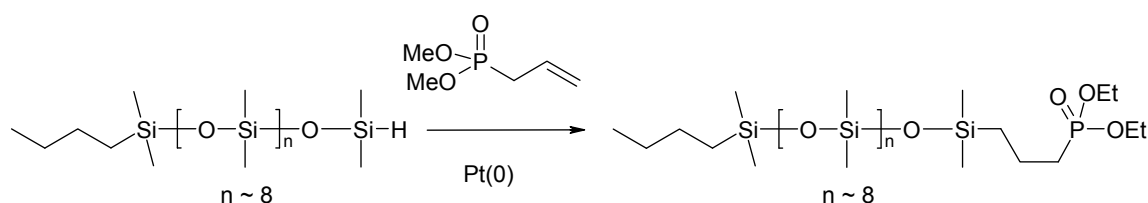
For the preparation of the simple, nonfunctional PDMS chain coupling agent of the type ${}^n\text{Bu}$ -PDMS-PPA. The polymer chain was prepared first via ${}^n\text{BuLi}$ initiated ROP (according to literature known procedures^[370, 371]) of hexamethylcyclotrisiloxane (D_3) and introduction of a Si-H group via the appropriate quenching agent ($\text{Cl-SiH}(\text{CH}_3)_2$) (Scheme 6). The ${}^n\text{Bu}$ group was selected as end group because this molecule will be compared later with the same molecule, but bearing the allyl-end group, which has about the same length (4 C atoms and 3 C atoms).

Scheme 6. ${}^n\text{BuLi}$ initiated living anionic ROP for the preparation of non-functional PDMS chain phosphonic acid coupling agents with adjustable chain length.



The ratio of M/I was tuned so that GPC measurement revealed a molecular mass of $M_n = 850$ g/mol, which is equal to ~ 2.5 D_3 units ($n \sim 8$), and has been also confirmed via ^1H NMR measurements. Furthermore, a low polydispersity index (PDI) of 1.2 was obtained. The phosphonate group was then introduced via a hydrosilylation reaction of the H-polymer and allyl phosphonic acid diethylester (Scheme 7). The phosphonate was finally hydrolyzed via the silylester method (reaction with trimethylsilyl bromide followed by addition of MeOH and H_2O) to give the final coupling agent. This product exhibited no change in the molecular weight during the reaction steps showing also a PDI of 1.2. Therefore, this system can be regarded as a well-defined molecular coupling agent.

Scheme 7. Introducing the phosphonate group on one chain terminus of the ^nBu -PDMS-H polymer.



The surface modification was carried out by the usual procedure with the only difference being that vigorous stirring and shaking was needed to homogenize the reaction mixture. It is noted that also different dispersions and more non-polar organic media did not lead to better modification conditions regarding the resulting surface coverage, which will be discussed later in this chapter. The FT-IR spectra of the coupling agent, free and attached to the ZrO_2 surface, confirm the successful attachment by the presence of the characteristic vibrational bands (Figure 71). Unfortunately for all these types of molecules the characteristic PO_3 modes which show the covalent bonding of the phosphonic acid group to the metal oxide surface are superimposed with the signal of the Si-O-Si vibrational modes from the PDMS chain (around 1020 and 1090 cm^{-1}). However peak deconvolution exhibited the typical broad PO_3 mode confirming the surface bonding. The intense washing steps did not remove the coupling agents confirms the strong bonding to the surface. In the modified nanopowder, a characteristic very broad band between 3500 cm^{-1} and 3000 cm^{-1} indicates the presence of residual surface OH groups and / or stronger surface adsorbed water molecules which is an indication for a not very high surface coverage.

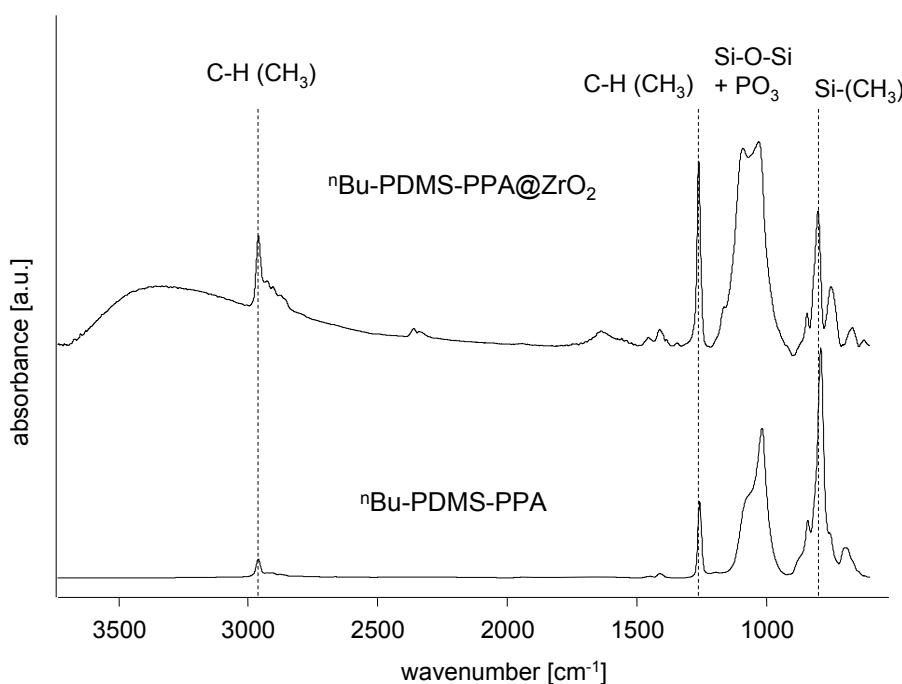


Figure 71. FT-IR spectra of ${}^n\text{Bu-PDMS-PPA}@$ small ZrO_2 nanoparticles and free coupling agent for comparison.

Furthermore, the presence of the characteristic resonances in the ${}^{13}\text{C}$ and the ${}^{29}\text{Si}$ solid state NMR spectra (Figure 72) confirm the presence of the PDMS chains at the nanoparticle surface. It should be remarked that due to the experimental method of cross polarization (CP) the integrals of the resonances cannot be compared. This is for example the reason why the resonance peak of the M unit in the ${}^{29}\text{Si}$ NMR spectrum appears significantly more intense as expected because of faster relaxation of M-nuclei compared to the D-nuclei. ${}^{31}\text{P}$ NMR again confirmed the covalent attachment of this oligomeric PDMS molecule via the phosphonic acid group by a typical high field shift from 37 ppm to 24 ppm due to surface adsorption.

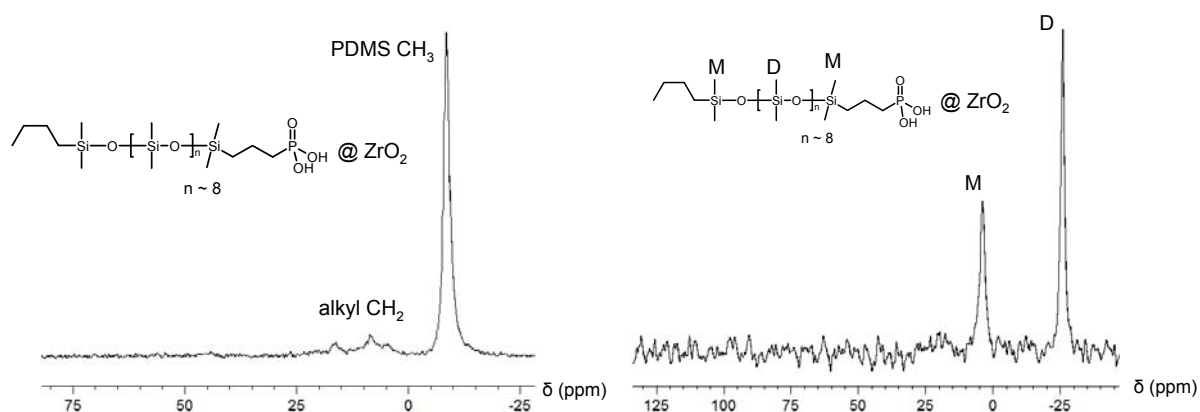


Figure 72. Solid state NMR spectra of ${}^n\text{Bu-PDMS-PPA}@ZrO_2$. Left: ${}^{13}\text{C}$ -CP-spectrum, right: ${}^{29}\text{Si}$ -CP spectrum.

The grafting density of these molecules on the ZrO_2 surface was first calculated from TGA mass loss and the surface area calculated from N_2 sorption experiments applying Eq. 6 resulting in 0.7 molecules/ nm^2 . This value is quite low compared to grafting densities of 3.4 molecules/ nm^2 reached for dense alkyl SAMs ($\text{ODPPA}@ZrO_2$) (see chapter 3.1.2.3). The

assumption that the TGA mass loss results from the thermal degradation and removal of the PDMS chain is very plausible since thermal degradation behavior of linear PDMS occurs via chain scissoring and evaporation of the thus generated smaller siloxane species.^[372] Even for crosslinked PDMS rubber, usually no significant residual mass can be observed in the TGA.^[373] Furthermore, TG-FTIR measurements revealed characteristic spectra by analysis of the offgas during the TGA measurement at 300-330°C under oxygen atmosphere. Vibrational bands at 1027 and 1086 cm⁻¹ (Si-O-Si) as well as bands at 815 and 2264 cm⁻¹ (from Si(CH₃)₂) can be assigned to siloxane degradation products. The thermal degradation behavior is similar to that reported in literature for pure trimethylsilyl end-functional PDMS chains. However for the pure and high molecular weight systems, higher thermal stabilities are commonly observed.^[372] Discussing this fact, it should be kept in mind that the whole PDMS chain is surface linked via C-P-O bond and for such systems thermal degradation temperatures around 300°C are usual, as observed in this work. From elemental analysis, a grafting density of 0.6 molecules/nm² was calculated. This result is in good agreement with the results obtained from TGA (0.7 molecules/nm²).

Another approach has been additionally used to investigate the validity of the value of the grafting density of this novel system. Single pulse (SP) ²⁹Si solid state NMR experiments are applied which allow an integration of the ²⁹Si signals and thus a quantitative detection of the different Si-species in the material. Therefore, a certain amount of a standard substance (octakis(trimethylsiloxy)silsesquioxane, Q₈M₈) was added to the sample, homogenized, and a spectrum was recorded (Figure 73). The spectrum shows the characteristic signals for the M unit of the standard and the sample from the D unit of the sample and from the Q unit of the standard substance. Via comparison of the integrals of the peaks from D(sample) and Q(standard), knowing the exact amounts of standard (10.08 mg standard, 179.14 mg sample), molecular weight of the adsorbed coupling agent (850 g/mol, from GPC) and standard (1130 g/mol), and specific surface area of 140 m²/g, a surface coverage of 0.7 molecules/nm² could be calculated. This is in very good agreement with the surface coverage determined via TGA mass loss and the value calculated from elemental analysis of 0.6 /nm². This correlation of the values obtained by three different methods can be seen as a proof of validity of the usual TGA method for grafting density determination for such systems. Furthermore, it is as well a proof for the quality of the solid state SP-NMR method under these conditions (30° pulse and 6 min relaxation delay time), which will thus be further applied in following studies.

These low obtained grafting density values are in agreement with the fact that in the FT-IR spectrum (Figure 71) OH-vibrations from non covered surface regions are visible. The use of other reaction systems for surface modifications, e.g. a toluene/methanol mixture and a toluene/methanol/water mixture, giving homogeneous emulsion, resulted in the same surface coverage values. Therefore, the assumption that adsorption is hindered due to inhomogeneities can be excluded. Furthermore, adsorption kinetics are ruled out to be responsible for these results because the experiments were tested also for 2 weeks reaction time (phosphonates usually adsorb within minutes to form a dense monolayer under the applied conditions^[374] and such an extreme difference in kinetics is not expected even for

because of the high importance of the interfacial area in nanomaterials. For the distribution in ethanol large agglomerates are observed, in methyl methacrylate (MMA) less agglomeration and in toluene no detectable agglomeration is observed. The later result can be explained by the fact that PDMS leads to hydrophobization of the surface, which is exploited in literature for the preparation of superhydrophobic surfaces in combination with additional patterning of the surface.^[241, 375] Thus good dispersibility in this non-polar medium is expected, which also explains the poor dispersibility in the polar medium of ethanol. For clarification, *Nakade* and *Ogawa* have modified titania coated ZnO nanoparticles with PDMS which resulted in a good dispersibility in siloxanes and rather poor dispersibility in hydrophilic alcohols (the particles were floating on the solvent). This is in agreement with the here obtained results.^[368] However, usually one would expect a higher agglomeration of the PDMS modified particles for the moderately polar MMA dispersions as well. Due to the fact that the surface coverage is very low, the remaining polar surface groups (OH) which are present on the surface (Scheme 8) are likely responsible for the good dispersion behavior in MMA. This would indicate that the lower grafting density is an advantage in this case if the systems are used in PMMA nanocomposite preparation (see following chapters) by *in situ* polymerization from MMA dispersions. The difference of the peak position in the distributions between toluene and MMA (the peak of the EtOH system is considered to result only from larger agglomerates, not from single particles) can be explained by the presence of different solvodynamic shells of ⁿBu-PDMS-PPA@ZrO₂ in those different liquids. In the case of methyl methacrylate as a moderately polar medium the PDMS chains tethered to the surface may collapse (in literature a denser arrangement of PDMS chains at incompatible interfaces is proposed^[376]) and form more dense coils on the surface resulting in lower solvodynamic radii. On the other hand the interaction of the PDMS chains with toluene is assumed to be better as reported in literature for non immobilized PDMS^[242] and the PDMS-chains point away from the particle surface into the solvent continuum. Furthermore, in ⁿhexane and hexamethyldisiloxane good dispersibility could be observed, concluding that the system can be dispersed in non-polar and moderately polar media. A major difference of the here discussed system to literature known behavior of PDMS is given by the fact that the PDMS chain is immobilized on one chain terminus. *Hartmann* and *Kremer* report a significant increase in the alpha-relaxation (glass transition) of PDMS chains in thin films comparable to the described system (<15 nm) when the chains are attached to the surface compared to free PDMS molecules.^[377] This means that the ordering in the surface layer increases. This effect could also be observed in a certain degree for the here discussed, nanoscopic crystal facet, system by a shift in the glass transition temperature T_g (DSC, peak maxima) from -130°C to -121°C due to attachment, which is conform with the studies carried out in literature for macroscopic surfaces. However, the here described state is still very unordered. The T_g is very low and no crystallization phenomena could be observed. Such chain ordering and movement effects are strongly dependent on the applied solvent, as *Auroy et al.* have demonstrated. There, they applied ²H NMR techniques proposing that poor solvents for PDMS like MeOH lead to a squeezing effect of the PDMS structure.^[378] Thus the PDMS layer structure is a plausible reason for the different solvodynamic shell size, observed in different organic media.

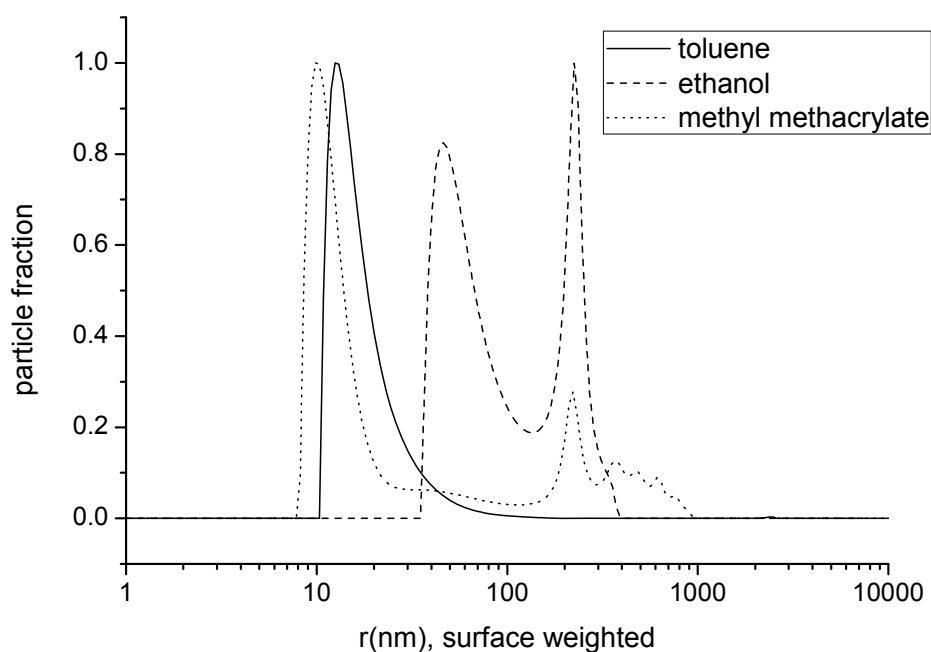


Figure 74. Surface weighted particle size distributions (DLS) of ${}^n\text{Bu-PDMS-PPA@ZrO}_2$ small nanoparticles representing the dispersion quality in different dispersion media.

Figure 75 shows a comparison of dispersions of DPPA@ZrO_2 and ${}^n\text{Bu-PDMS-PPA@ZrO}_2$ small nanoparticles in toluene, where in the first case agglomeration can be observed and in the second case not. This points out that by applying PDMS-spacer-based coupling agents, the alkyl chain zipper effect can be avoided. Thus, the adsorption of PDMS chain systems is an additional method to avoid the zipper effect, besides mixed alkyl monolayer formation.

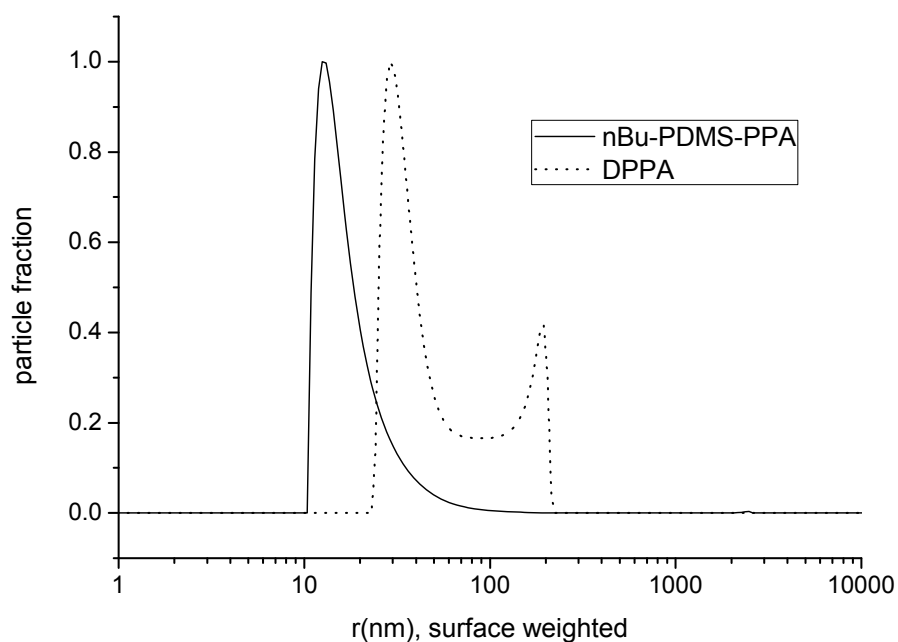
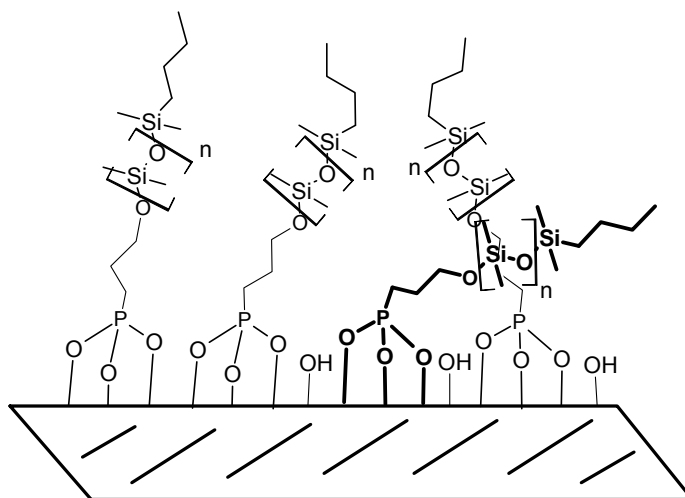


Figure 75. Comparison of particle size distributions (DLS) of ${}^n\text{Bu-PDMS-PPA@ZrO}_2$ and DPPA@ZrO_2 small nanoparticles in toluene.

Scheme 8. Schematic representation of PDMS chains anchored to ZrO_2 nanocrystals resulting in unordered systems, due to the flexibility of the PDMS chains, and leaving residual surface OH groups



As a conclusion, PDMS chain coupling agents result in low surface coverage, but this effect can be advantageous within the preparation of PMMA nanocomposites. Relatively homogeneous nanocomposites could be achieved, while usually PDMS and PMMA are not miscible on a molecular level and macroscopic phase separation occurs.^[245, 379] This is on one hand unfavorable for the here applied systems but on the other hand exploited in self-assembly of diblock copolymers of such systems.^[380] Generally, the prepared ${}^n\text{Bu-PDMS-PPA@ZrO}_2$ system is organophilic. Furthermore, the novel particle system is dispersible in a many organic solvents which can be used for other compounding approaches.

PDMS-chain coupling agents for SiO_2 surface modification

To prove the applicability of these PDMS-spacer coupling agents also for the quasi-*in situ*-functionalization of SiO_2 nanoparticles, the analogous trimethoxysilane coupling agent of the type (trimethylsilyl-) TMeS-PDMS-TMS has been prepared. The reason why the methyl-group has been selected is an expected better comparison of these molecules when attached to *Stöber* particles with the other methyl-end group molecules (see chapter 3.1.7). However, it is more difficult to introduce this methyl group instead of a ${}^n\text{Bu}$ group, which will be discussed in detail in the next chapter. The molecular weight of the PDMS molecule was $M_n = 810 \text{ g/mol}$ (GPC, PDI = 1.2), which is equal to $n \sim 8$ chain segments. The modification reaction was carried out by the usual procedure as applied for alkyl-chain coupling agents, where in case of the larger nanoparticles phase separation occurred in ethanol. This was an indication of the successful attachment of the PDMS chains. The linkage of this novel coupling agent molecule to the silica surface could be confirmed via FT-IR spectroscopy and solid state NMR spectroscopy. The characteristic bands from the PDMS chain in the IR spectra were strongly superposed by the signals from the bulk and are therefore not shown. However, the ${}^{13}\text{C}$ solid state NMR (Figure 76 left) shows the characteristic resonance peaks for the methyl group from the PDMS chain and the alkyl CH_2 groups. Signals marked with asterisk originate from residual ethoxy groups from the bulk of the particles. The ${}^{29}\text{Si}$ NMR

spectrum shows, besides the large signal from the Q unit from the particle bulk, the characteristic D-unit from the PDMS chain. The intensities of the other expected signals (M from the chain end) were too low, they can only be made out in the noise of the spectrum.

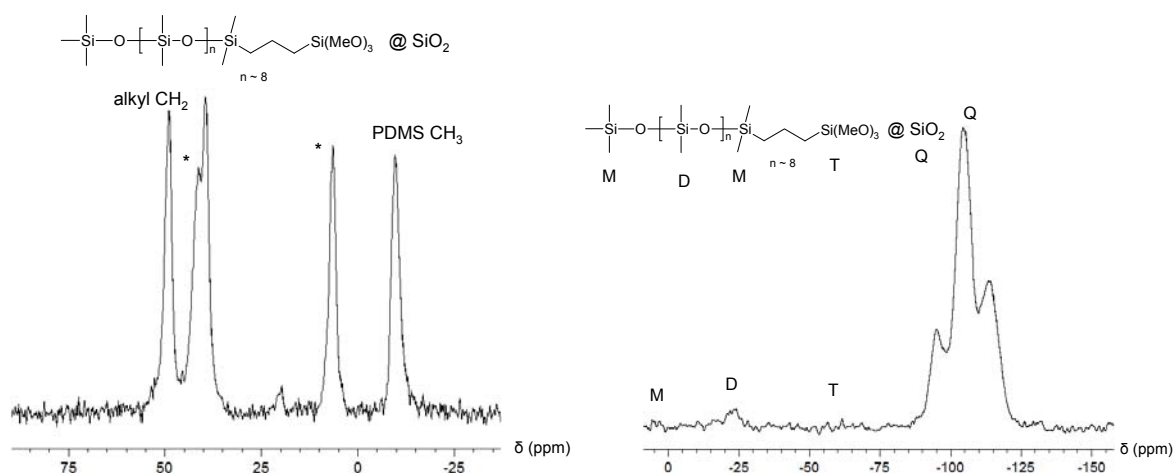


Figure 76. Solid state NMR spectra of TMeS-PDMS-TMS@SiO₂ small nanoparticles. Left: ¹³C-CP-spectrum, right: ²⁹Si-CP spectrum.

TGA analyses revealed a relatively low surface coverage of 0.9 molecules/nm² for the large *Stöber* particles. The same reasons may be responsible for this as described previously for the ZrO₂ system, the steric conformation of PDMS chains. For comparison, *Dutta* and *Green* showed that grafted -OH end-functional PDMS molecules *onto* 100 nm diameter *Stöber* particles. The result was a grafting density of only 0.17 chains/nm². The discussed effect of chain flexibility was held responsible for this result. They used approximately a 10-fold chain length than applied in the present work, which explains the much lower grafting density as obtained in the present work as longer chains can have more different conformations than shorter chains.^[249] This fact was further the reason that in the present work no longer PDMS chains via grafting *onto* approach have been applied. For the small nanoparticles with strong curvature, the coverage was even only 0.3 molecules/nm². Therefore, drastic dispersibility changes of the small nanoparticles could not be observed in that case, whereas the dispersion properties of the large nanoparticles changed significantly, comparable to the ZrO₂ nanoparticles. They were dispersible in moderately non-polar solvents only, e.g. MMA, which is advantageous. However, they were not dispersible in media like ethyl acetate or more polar solvents. This is demonstrated by the particle size distributions from the dispersions from DLS (Figure 77). Furthermore, in strong non-polar solvents, such as ⁿhexane, the dispersion properties were poor as compared to the ZrO₂ system. This may originate from irreversible aggregation phenomena of the silica particles via residual surface silanol groups, which does not occur for ZrO₂.^[301]

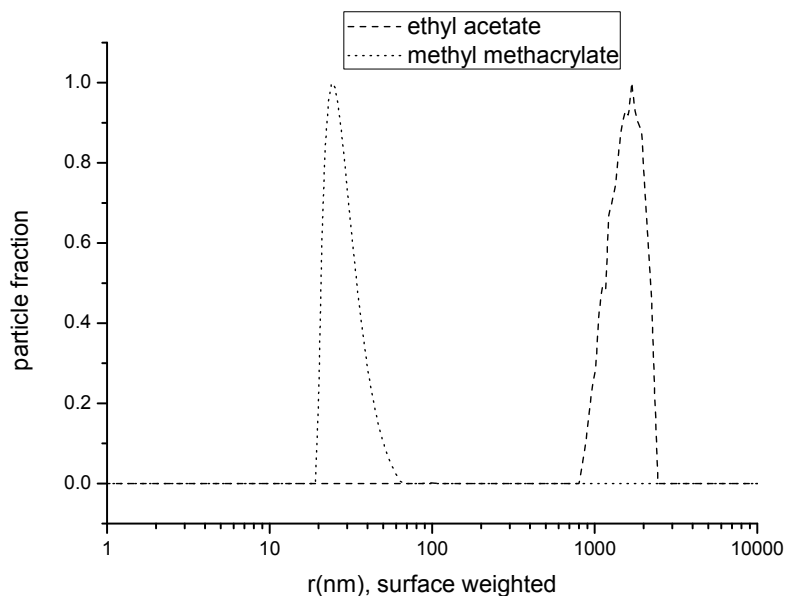


Figure 77. Surface weighted particle size distributions (DLS) of TMeS-PDMS-TMS@SiO₂ large nanoparticles representing the dispersion quality when different dispersion media are applied.

Generally, the analogous system of trimethoxysilanes is applicable to *Stöber* particles which results in significant physical surface property change (hydrophobicity).

Asymmetric, telechelic PDMS as a precursor for polysiloxane-spacer functional coupling agents

This chapter deals with the issue of the preparation of asymmetric telechelic molecules from the type X-PDMS-Y, where the PDMS chain should be variable in length to achieve a modular and tunable system. Why is there any need for such novel systems? One reason, which was already discussed in the previous chapters is: By application of the ROP approach using ⁿBuLi as an initiator, the possibility to introduce an anchor group on one chain side is given. However, the other terminus contains a non-functional and non-transformable ⁿBu group. Introducing PDMS spacer chain coupling agents in analogy to alkyl spacer molecules, the synthesis must also allow the incorporation of a functional group on the other chain end to tune the interface properties nanocomposite materials. Thus, X-PDMS-Y should be provided in analogy to the commonly used X-alkyl-Y coupling agent molecules. Although, there are also other general reasons why this new class of polymer molecules is of great interest. New functional and well-defined silicone layers have high potential in applications in the field of microelectronics and lithography technology. Furthermore, surface coating technology can profit from this novel class of coupling agents. Functional silicone monolayer coatings can introduce new properties to surfaces exploiting additionally the properties of PDMS such as water repellency, high thermal and chemical stability and biocompatibility. In such processes only very little amount of coating material is needed.^[381-383] Besides the major coupling agent

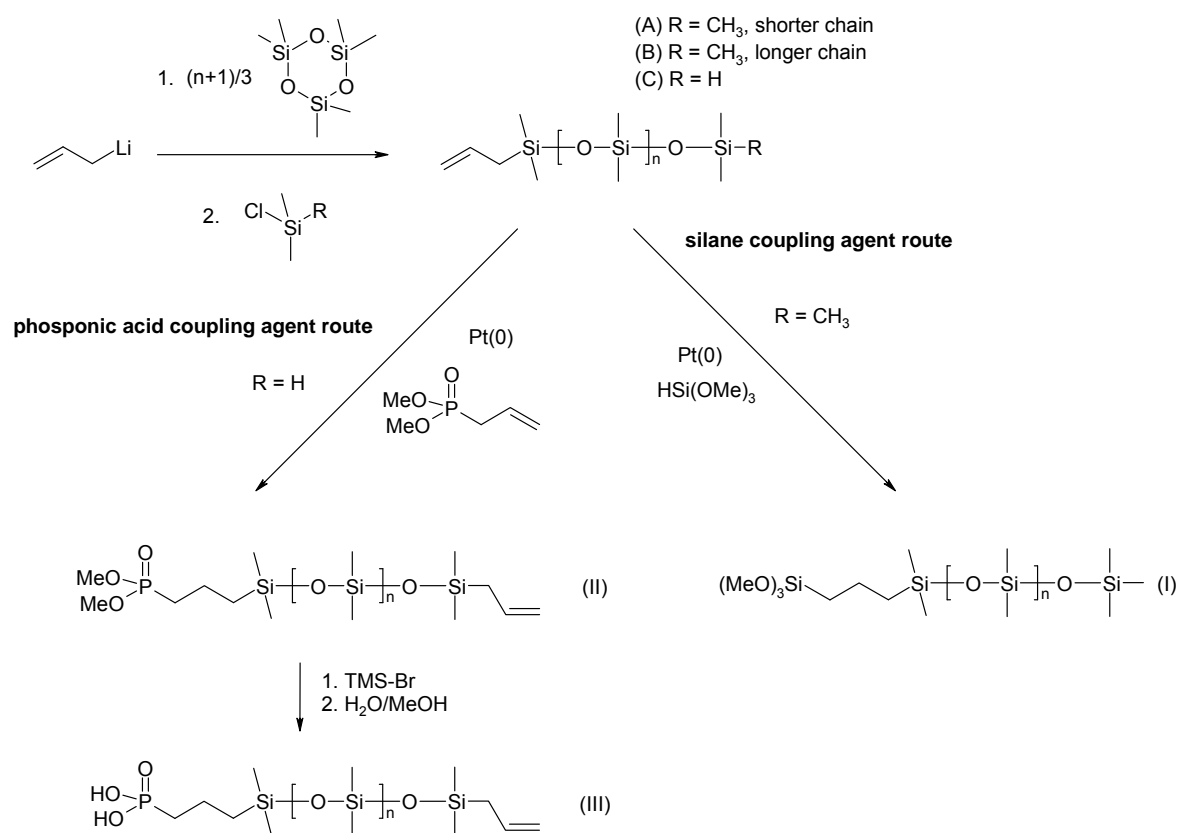
function of such bifunctional telechelic molecules another interesting application of X-PDMS-Y type heterotelechelic molecules would be in the field of blockcopolymers of PDMS with other polymers. Such systems are widespread and used in the form of diblock-(AB)^[384] or triblock-copolymers from the type ABA^[385] of PDMS with other polysiloxanes or polyolefines in self-assembly applications.^[370, 386] The application of the new class of X-PDMS-Y functional molecules in this research field would provide more controlled and facilitated approaches to more complex systems such as triblockcopolymers of the type ABC and open a wide spectral window in self-assembly. In the present studies, X should be a trimethoxysilane or phosphonic acid anchor group and Y a polymerizable double bond for *in situ* polymerization processes. The PDMS spacer should be tunable in length, analogous to the alkyl-coupling agent systems. The functional group should be of moderate reactivity towards its environment but easily transformable to any other functional group. Therefore, a synthetic approach to α,ω -bifunctional, heterotelechelic PDMS had to be developed because up to now there is no existing applicable synthetic route. As shown in the previous chapters, the method of living anionic ring opening polymerization reactions of cyclic siloxanes, such as D₃, is a facile route to obtain variable spacer chain PDMS through the variation of monomer/initiator-ratio. Furthermore, a functional end group can be introduced by the variation of the polymerization terminating quenching agent.^[370, 371, 386, 387] As mentioned before, common approaches use organolithium-compounds as initiators, mostly simple molecules like ⁿbutyl lithium^[370, 371, 386, 387]. However, via such approaches only one terminal functionality can be introduced, only end-functional systems of diblockcopolymers of the AB type are the result, e.g. when one block is used as a macroinitiator.^[370, 380, 384, 388] This is one type of telechelic functional PDMS which is reported in literature. Especially for siloxane type coupling agents which bind to metal oxide surfaces, the examples in literature up to now are very rare.^[247, 389] Another type is a, homotelechelic, difunctional molecule of the type X-PDMS-X having two equal functional end groups.^[390, 391] However, the goal is to synthesize bifunctional, heterotelechelic, type of PDMS, which is necessary for this work. Therefore, it was decided to use allyl lithium as an initiator, because the olefinic group allows various further functionalizations via addition reactions, e.g. such as hydrosilation reactions.^[390, 391] Furthermore, the allyl-group is not expected to be destroyed during in the quite harsh conditions (strong basic, alkyl-alkali-metal-species) where the polymerization is carried out. After that, the second functional end group can be easily introduced within the selected route, by quenching the ROP with a certain reagent of the type Cl(CH₃)₂Si-Y. Therefore, the following issues which are important in this context had to be proven within this work: Firstly, the possibility of using allyl-Li as initiator for ROP of D₃ had to be tested in order to yield products with predictable molecular weight. A special focus thereby was on the selectivity of the preparation of only terminal olefinic end groups as it is known from literature that the *Chameleon* behavior of allyl-Li can lead to isomers.^[392] This is of high importance in terms of further functionalization reactions such as hydrosilation. Secondly, by yielding an oligomeric or polymeric molecule of the type allyl-PDMS-Y, a route had to be proven, where the termini can be selectively addressed and the groups can be transferred to give the desired molecule of a coupling agent containing a desired functional linking and anchor group. These issues will be investigated and discussed in this chapter for the selected

systems of trimethoxysilane or phosphonic acid anchor groups with spacer chain length of approximately 8-10 siloxane units for nonfunctional end groups (trimethylsilyl-) and polymerizable olefinic end groups (allyl-).

Synthetic Route

The chosen synthetic route for the preparation of poly(dimethylsiloxane)s (PDMS) with variable chain length and two different terminal functional groups for the use as functional coupling agents, is presented in Scheme 9. The basic steps is an allyl-Li- initiated living anionic ring opening polymerization (ROP) of D₃ which allows the variation of the chain length through the reaction conditions, mainly by the monomer/initiator ratio. Afterwards, the allyl-terminus can be used for further modifications. Through the variation of the quenching agent, a second group can be introduced at the other terminus. Starting from these variable reaction products, the termini need to be selectively addressed. Here, two examples for this general approach are presented: The molecules TMeS-PDMS-TMS as an example for silane coupling agents, which has been used in the previous chapter, and a phosphonic acid molecule, allyl-PDMS-PPA have been prepared.

Scheme 9. Synthetic route to PDMS with variable chain length and two different functional groups at its termini for the use as functional coupling agents.



The allyl-groups have been chosen because they are one of a few reactive groups which are not destroyed by the harsh conditions of metal-organic species in the reaction solution. The phosphonate route (introduction of allyl phosphonate via hydrosilylation at the Si-H group) has been selected, because the *vice versa* approach of radically adding a P-H-bond to the allyl-

terminus was unsuccessful. Disappearing of the Si-H bond on the other terminus could be observed via IR-spectroscopy. This can be explained by the reactivity of silane bonds (Si-H) towards radicals, resulting in homolytic bond cleavage. However, in principle the analogous approach to silane coupling agents by using allyl trimethoxysilane is conceivable. The key element for the whole approach is the first step of the allyl-Li-initiated ROP. For this reason, this first reaction will be investigated in detail.

The allyl-Li-initiated living anionic ROP of D₃

Firstly, the major questions on this synthetic approach are: Is an allyl-Li-initiated ROP of D₃ possible? If so, which are the optimal conditions and how good is the quality of the living behavior of this reaction? The last point is indispensable for a molecular weight tuning by variation of the monomer/initiator (M/I) ratio. Secondly, if the reaction is successful it is highly important which type of regioisomer of the allyl-terminus is yielded (e.g. terminal or internal etc.). This issue is crucial in terms of further reactions with the olefinic bond, such as hydrosilation reactions, which only proceeds satisfactorily for terminal olefinic systems, in most cases.

To clarify these points model reactions have been performed using high concentrations of D₃ up to more than 1000 g/L. These conditions have been selected to reduce the possible side reaction of the dissolved Li-species with the solvent (THF) molecules, which is an at room temperature competing reaction. However, THF is needed as a polar molecule to separate the Li-ions from the growing chain/initiator moieties, to generally allow a ROP. Two different reactions using two different (M/I) ratios were performed and the molecular weight of the obtained products was determined using gel permeation chromatography (GPC). Table 25 lists the theoretical molecular weight and the experimentally determined molecular weight, calculated from the chromatograms shown in Figure 78, of the Product, A (M/I = 3), and the Product, B (M/I = 6) (Table 25). The comparison of the values for the molecular weight from Table 25 (M_n = number weighted molecular weight, determined by GPC) are slightly higher than the theoretical predicted values (M theoret., calculated from the M/I-ratio assuming a living character of the polymerization reaction) for both, sample A and B. This can be explained by the fact that not all initiator molecules in the reaction solution led to a polymerization reaction, because they are quenched by the side reaction of allyl-Li with THF. This is a well known and common problem which is present for organolithium compounds at room temperature. This side reaction was tried to be reduced as much as possible by using low solvent/monomer ratios. However, the molecular weight is well predictable. Together with the low polydispersity index (PDI) this indicates a living character of this polymerization reaction, as it is the case for common alkyl-lithium initiated cyclic trisiloxane-ring opening-polymerization reactions.^[370, 388]

Table 25. Experimentally determined (GPC) (M_n) and calculated molecular weights (M theoret.) of product A, (M/I) = 3 and product B, (M/I) = 6.

Product	(M/I)	M_n (GPC)	M theoret.	PDI (GPC)
A	3	810	560	1.2
B	6	1820	1230	1.2

Figure 78 shows the corresponding chromatograms which were consulted for the molecular weight calculations in Table 25. The rather broad molecular weight distributions can be explained by the fact that at room temperature already thermal equilibria play a role within the ROP mechanism. Together with side reactions such as single chain segment subtraction and addition where aggregation plays a crucial role,^[393, 394] this explains the visibility of chain length with non integral number values of D_3 multiples in the chromatogram for product A. However, a polydispersity index of 1.2 stands for a rather defined product, as compared to PDMS prepared by common methods such as condensation reactions of chlorosilanes yielding in a broad mixture of different chain length products.^[243]

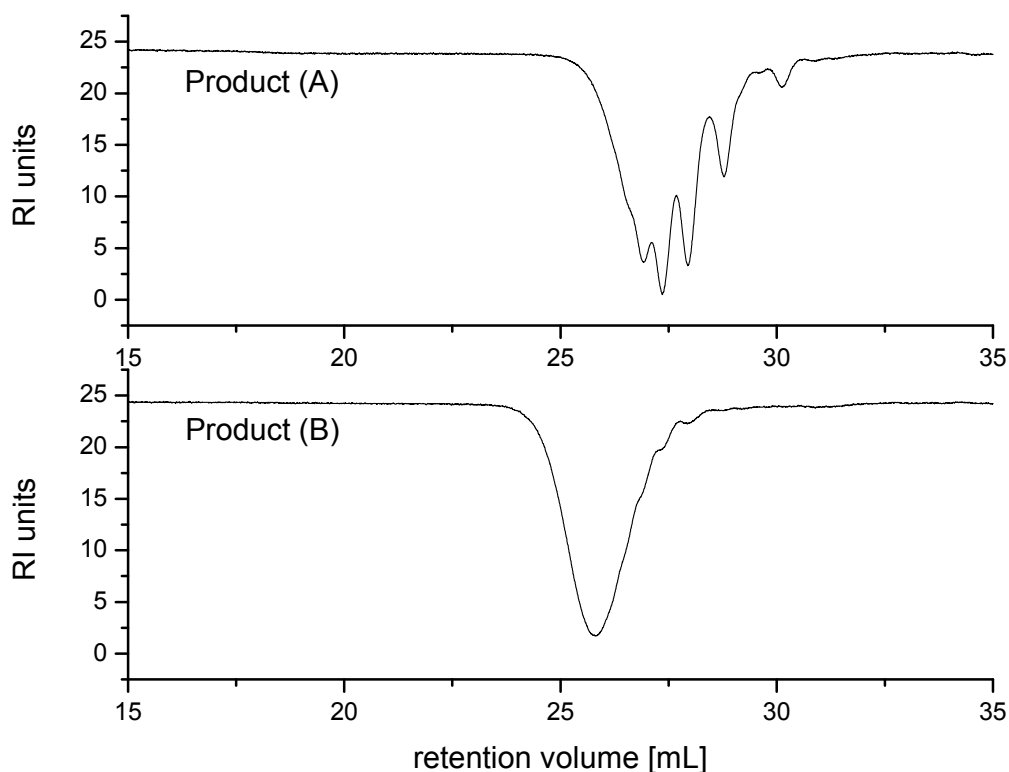


Figure 78. Gel permeation chromatograms of product A, (M/I = 3) and product B, (M/I = 6), signal from refractive index detector, flow: 1 mL/min toluene.

For further investigations on the living character and the applicability of the allyl-Li-initiated reaction, a kinetic experiment using a M/I ratio of 6 was carried out. Samples were taken at

different times, quenched with trimethylchlorosilane and analyzed via GPC. The corresponding plot is shown in Figure 79. A linear increase in molecular weight with increasing time indicates a strong living character of the reaction. This is consistent with the rather low PDI of 1.2 and the predictable molecular weight from M/I.^[380, 387] A chain growth rate constant of 8.5 g/(mol·min) for 25°C was calculated from the slope of the fitted line from the plot in Figure 79 (least square method) by assuming 1st order kinetics. Furthermore, the value of this rate points out that room temperature, and no lower temperature, is an appropriate condition for this reaction, because the chain growth reaction proceeds rather slow. Going to lower temperatures would slow the polymerization process further and decrease the solubility of the monomer, which is both undesired.

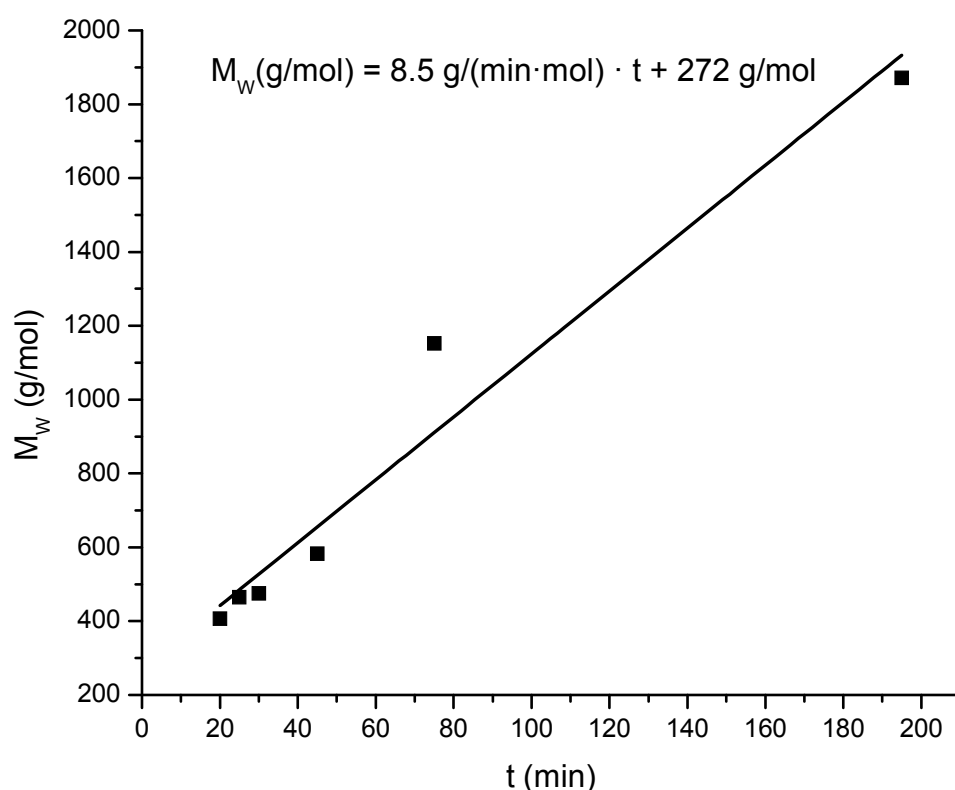


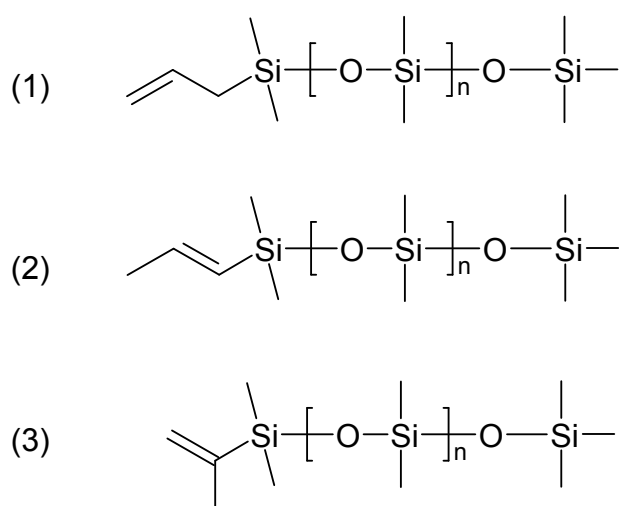
Figure 79. Kinetic plot and linear regression of allyl-Li-initiated ROP of D_3 , from GPC-measurements at different times after quenching with trimethylchlorosilane.

As the initiation and polymerization was successful, the question needs to be answered which type of product is yielded with respect to the configuration of the allyl-end group. In principle three different isomers as products are possible, see Scheme 10. These variations are given through the degree of regioselectivity of the initiation step into account, according to *Fraenkel et al.*,^[392] who described the so-called *Chameleon*-behavior of allyl-Li-compounds.

Fraenkel et al. explained this *Chameleon*-behavior of allyl-Li-compounds by the possible existence of three different species of allyl-Li in solution. Which species is predominant

depends on the polarity of the solvent, the nature of the counterion,^[395] concentration of the organometallic species and thus aggregation, as well as further factors such as other coordinating molecules (e.g. tetramethylethylenediamine^[396]). One extreme case is an allyl-anion with a separated ion pair and thus a free lithium cation, which is described in literature.^[397, 398] This would in principle not be appropriate for initiation or would lead to a variety of products by a possible migration of the Li on the allyl ((1)-(3), Scheme 10). Thus, low selectivity towards the desired product ((1) in Scheme 10) is expected. *Solomon et al.* for example described real η^3 -allyl-Li-complexes,^[399] or, as observed in other literature,^[392] a species with a terminal double bond and a covalent CH₂-Li-bond on the other terminus of the species. These species would theoretically lead to only the terminal double bond isomer ((1), Scheme 10). However, such an extreme case would not lead to good initiation properties, because a certain degree of deaggregation of the allyl- and the Li- species from the allyl-Li is thereby needed. The third, intermediate case between those two extremes, with only partial charges^[392] and no total ion separation would be favored therefore. However, in literature, all three types of allyl-lithium species are described and can be expected to be present.^[392] Therefore, a ¹³C NMR-DEPT experiment was carried out to clarify this regioselectivity-issue. This is not only important from a characterization and product-purification point of view, but is also of high practical synthetic relevance. The molecule with the terminal double bond ((1), Scheme 10) is the desired product because it eases further addition reactions to the double bond, such as the used hydrosilylation reactions. The hydrosilylation reaction would be hindered by the methyl groups of the isomers (2) and (3), Scheme 10, and in extreme cases suppressed if a bulky catalyst molecule like the *Karstedt's* catalyst, is used within this reaction.

Scheme 10. Possible regioisomers yielded from an allyl-Li-initiated ROP of D₃.



The ¹³C-DEPT-spectrum of product A in Figure 80 shows the presence of only product (1). A mixture of (1)-(3) can be excluded: The characteristic allyl carbon-resonances, 1, 2, 3, show a pattern which can only be assigned to a terminal allyl-group. This has also been proven via ²⁹Si 2D HPDEC NMR spectroscopy. For the longer chain Product B the same results were obtained but are not shown for reasons of clarity as the intensity of the allyl-nuclei-resonances is lower for this product.

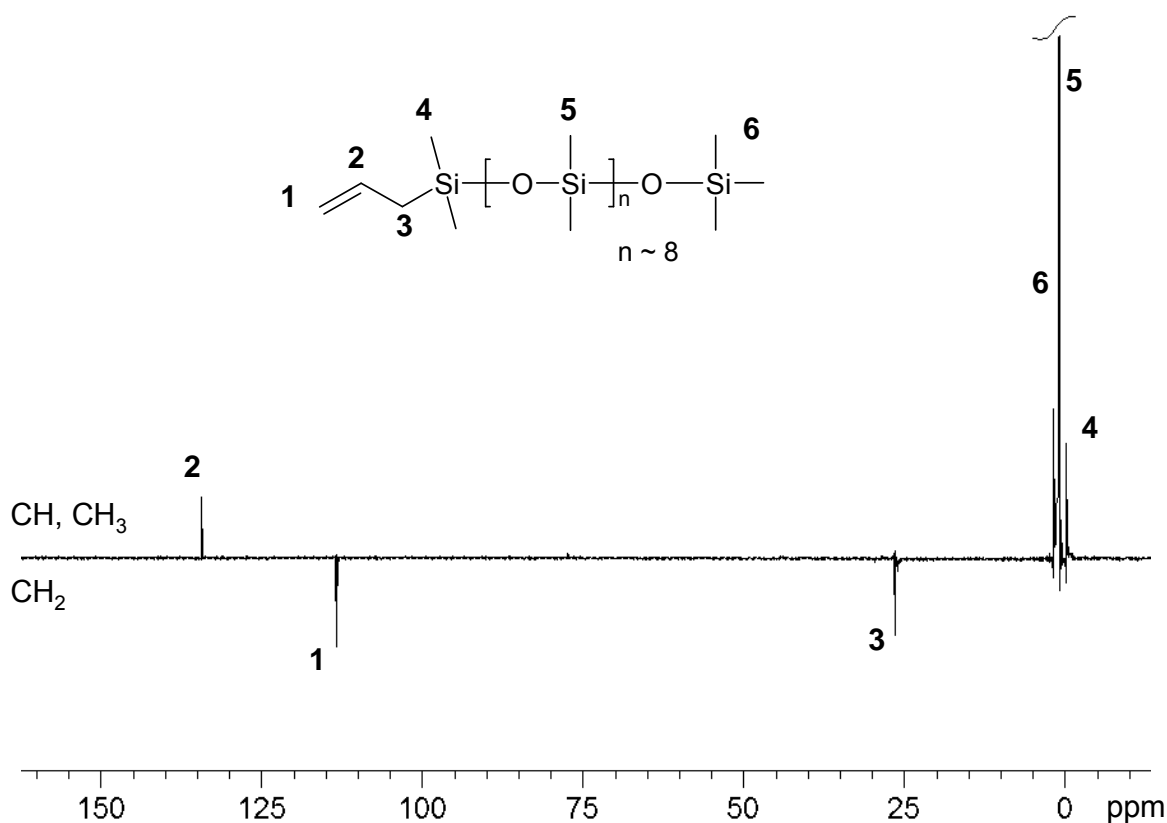


Figure 80. ^{13}C -DEPT NMR spectrum of product A, only showing the presence of the regioisomer (1) drawn in Scheme 10.

As a conclusion from these investigations, a highly selective allyl-Li initiated living ROP of hexamethylcyclotrisiloxane is possible, yielding polymer products with a terminal double bond on one terminus. This is a good starting point for further asymmetric terminal functionalization.

Preparation of non-functional coupling agents: TMeS-PDMS-TMS

As an example for the application of the allyl-PDMS, the, in the previous chapter used TMeS-PDMS-TMS molecule having a trimethoxysilane anchor group terminus and an inert trimethylsilyl terminus (Figure 76), has been prepared. This molecule was synthesized via hydrosilation of product A with trimethoxysilane $\text{HSi}(\text{OMe})_3$ using the *Karstedt's* catalyst. This product is not accessible via common ROP-approaches: An initiation with methyl-Li and quenching with an allyl-group introducing reagent, followed by a hydrosilation step would lead to the same product. However, the ROP initiation is not possible with methyl-Li in an appropriate way because of the higher ion association degree of methyl-Li and its relatively high reactivity towards undesired side reactions as compared to n -alkyl-Li. The reaction with the molecules from the required solvent THF limit the applicability of the methyl-Li compound. Furthermore, methyl-Li is known in literature to result only in a cleavage of cyclic

siloxanes, which proceeds under the here desired conditions.^[400] The analogous phosphonic acid coupling agent would also be easily accessible via this route by H-P addition of dimethylphosphite to the allyl-PDMS-TMS molecule, as known in literature for analogous substrates.^[203]

Introducing different functionalities at the termini of PDMS: The key molecule allyl-PDMS-H

For the access to bifunctional molecules of the type X-PDMS-Y, which are of greater interest in terms of interface engineering as monofunctional molecules, the allyl-Li initiated polymerization reaction was quenched with chlorodimethylsilane Cl-SiH(Me)₂ to introduce a reactive Si-H bond on the other terminus of the PDMS-chain. This functional group is also one of the few end groups which can on the one hand be introduced within the harsh synthetic conditions of the Li-initiated ROP and on the other hand provide enough selectivity towards further functionalization. Therefore, the analogous allyl-Li initiated ROP of D₃, as it was used for the preparation of product A, with a (M/I) of 3, was performed. The polymerization was quenched with chlorodimethylsilane to yield the product Allyl-PDMS-SiH (Product C). The molecular weight M_w, determined via GPC, was 605 g/mol, is in good agreement with the polymerization parameter of (M/I) = 3 (545 g/mol theoret.). The structure was confirmed via ¹H, ¹³C, ¹³-DEPT and ²⁹Si HPDEC 2D NMR methods. Furthermore, FT-IR measurements revealed the presence of the characteristic Si-H vibrational band at 910 cm⁻¹. The ¹H NMR-spectrum of product C (Figure 81) confirms the presence of the allyl-group (resonance signals 1-3) and the Si-H-group (resonance peak 7).

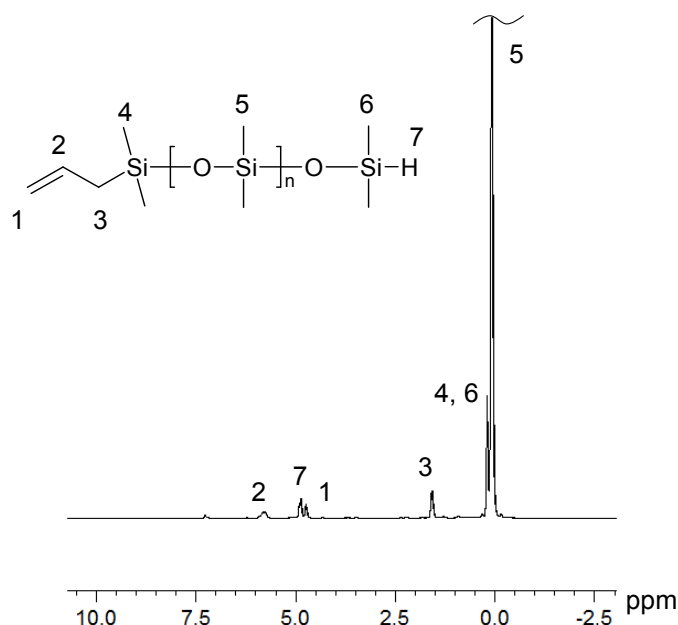


Figure 81. ¹H NMR-spectrum of "allyl-PDMS-H", Product C, showing the presence of the allyl group Si-H-group.

The described molecule, allyl-PDMS-H, represents the basis for further α,ω -different functional PDMS molecules in this work, such as coupling agents. The major issue in this

context is the selective addressing of the termini allyl- and SiH- in the following reaction steps. Thereby, e.g., via hydrosilation reaction of the Si-H-terminus and a functionalization of the allyl-terminus offers a variety of possibilities of chemical modifications via addition or epoxidation reactions followed by nucleophilic reactions.

An Example for selective addressing of the PDMS-termini for the preparation of coupling agents is allyl-PDMS-PPA, the polymerizable group containing analogon to the previously prepared ⁿBu-PDMS-PPA.

Here, the preparation of the type X-PDMS-Y molecule will be described, where X should be a polymerizable group (allyl) which can be linked to an organic moiety and Y represents an anchor group (phosphonic acid) which can bind to an inorganic moiety. By selective reactions on the termini the allyl-PDMS-SiH was further functionalized. The Si-H-terminal group was transferred into a phosphonic acid anchor group, as an example. A reaction pathway has been selected for the addition of the Si-H terminus of the polymeric molecule to the olefinic bond of allyl phosphonic acid dimethyl ester followed by hydrolysis of this phosphonic acid ester, see Scheme 9. The reverse approach of allyl-end group addition to a P-H-bond under maintenance of the Si-H group on the other end of the polymer chain, was not successful. However, a selectivity problem can arise within the hydrosilation reactions: Theoretically, the molecule could perform a self-addition where the Si-H terminus reacts with the allyl-terminus to form cyclic products. By choosing the reaction conditions of a high concentration and excess of allyl phosphonate, the formation of such cyclic by-products could be suppressed. This could be shown via ¹H and ¹³C NMR spectroscopic methods. A complete disappearance of the Si-H-band at 910 cm⁻¹ in the IR spectrum showed its full conversion. The product was further hydrolyzed via the silylester-method^[203] to give the final coupling agent molecule "phosphonic acid-PDMS-allyl" (allyl-PDMS-PPA). ¹H, ¹³C, ¹³C-DEPT, ³¹P and ²⁹Si HPDEC 2D NMR methods were used to confirm the structure shown in Figure 82. The ¹³C-DEPT NMR spectrum in Figure 82 further shows the presence of only one allyl group (signals 7-9) where in the ³¹P spectrum only one, for aliphatic phosphonic acids characteristic, peak at 37.0 ppm could be observed. These results evidence the bi-functional structure of the prepared molecule.

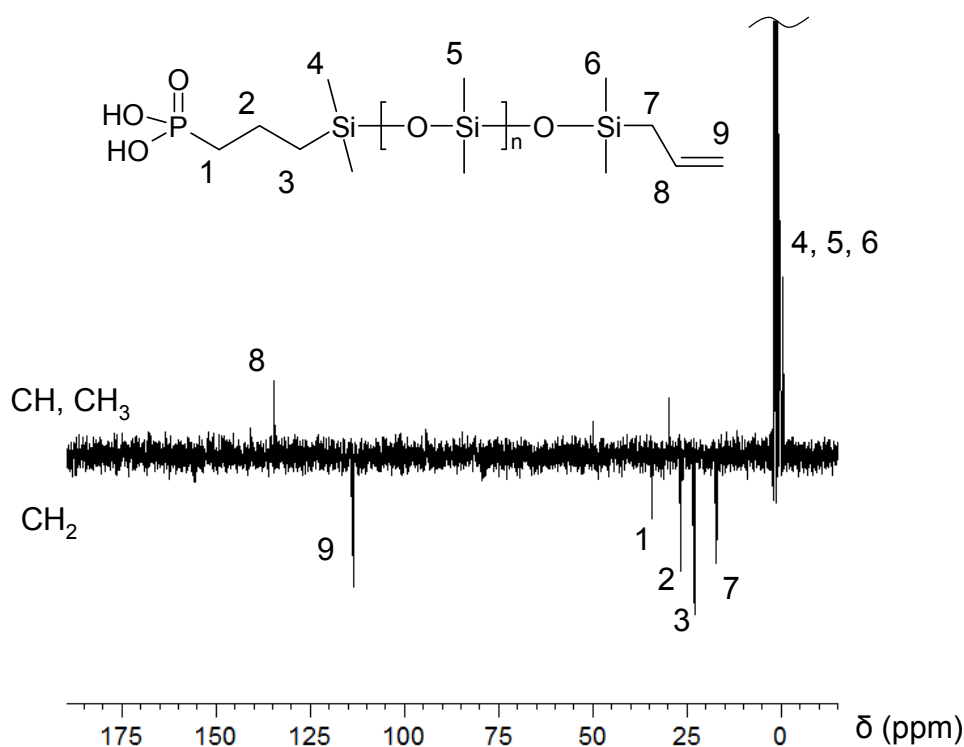


Figure 82. ^{13}C -DEPT NMR spectrum of allyl-PDMS-phosphonic acid.

The analogous alkoxy silane for the modification of silica substrates can be prepared following the same procedure but using allyl trimethoxysilane in the hydrosilation step. A possible selectivity problem within this step can be avoided when other functional end groups than the allyl group are desired: Then, the allyl-group should be addressed before the hydrosilation step. In principle, phosphonic acid-PDMS-allyl can be further functionalized at the allyl-end group, e.g. oxidized to form an epoxide.

Modification of small ZrO_2 nanoparticles with allyl-PDMS-PPA

The applied molecule consists of a PDMS chain with ~ 9 siloxane(Si-O)-units (GPC), an allyl group on one chain terminus and a phosphonic acid group on the other chain terminus. The functionalization reaction was carried out by the usual procedure. After intense cleaning steps, the nanoparticle powder was analyzed via FT-IR spectroscopy. The FT-IR spectra of unmodified ZrO_2 nanoparticles, ZrO_2 nanoparticles, surface modified with allyl-PDMS-phosphonic acid, and the free coupling agent allyl-PDMS-phosphonic acid are shown in Figure 83. Usually, for common alkyl based molecules, an attachment of the phosphonic acid group to a metal oxide surface can be monitored by the P-O vibrational bands in the characteristic region between $900\text{--}1250\text{ cm}^{-1}$. Relative intensities of the P-OH bands (900 and 950 cm^{-1}) significantly decrease after modification, because of a phosphorus-oxygen-metal bond formation and a decrease of the P=O vibration ($1200\text{--}1250\text{ cm}^{-1}$) is noticed indicating a coordinative bond to the metal oxide substrate.^[149, 190] However, in this specific case, the confirmation of the attachment was more difficult because of the superposition of this band region with the intense bands from the PDMS-chain at 1258 cm^{-1} (Si-C) and 1015 cm^{-1}

(Si-O). Nevertheless, due to the intense washing steps no signals would be obtained in the IR spectra after modification if no covalent bonds would have been formed. However this was not the case as Figure 83 shows.

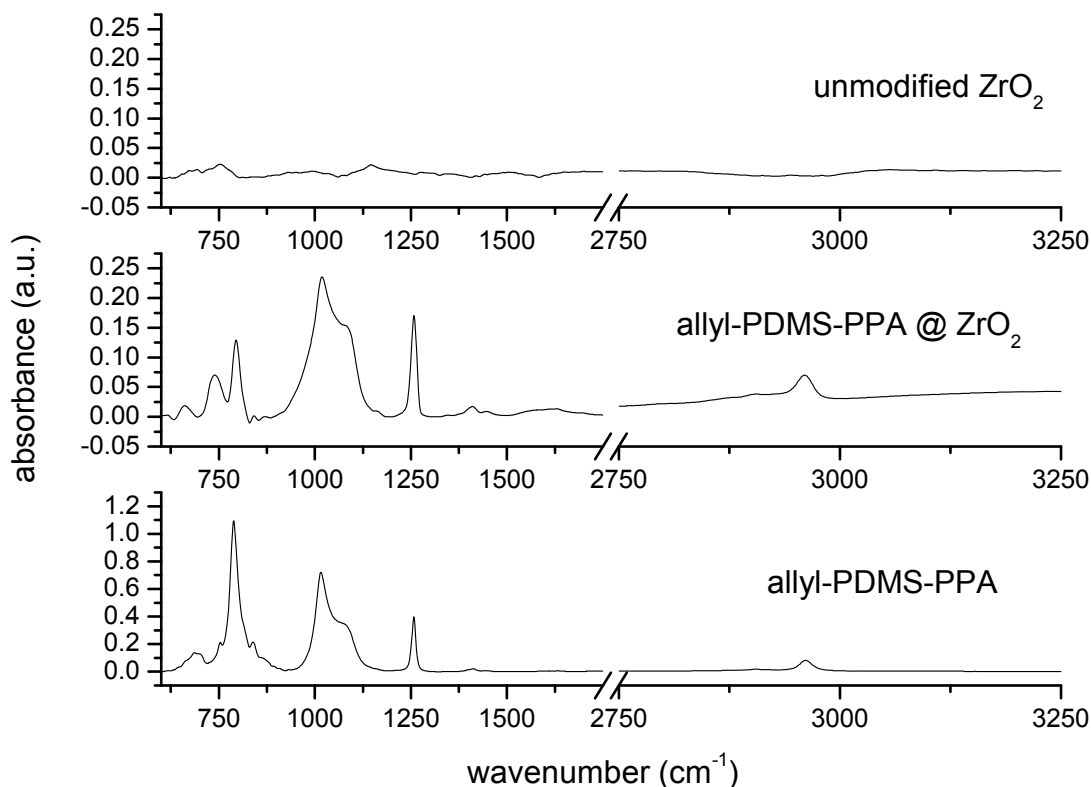


Figure 83. FT-IR spectra of unmodified small ZrO_2 nanoparticles, allyl-PDMS-PPA@ ZrO_2 nanoparticles and the free coupling agent allyl-PDMS-PPA.

To confirm the bonding of the coupling agent to the zirconia substrate, solid state NMR-spectra of the modified nanopowder were recorded. A shift of the phosphonic acid group in the ^{31}P spectra from 37.0 to 24.3 ppm due to the attachment to the zirconia surface^[149, 236] and the presence of no signal at 37.0 ppm in the solid state NMR spectra of the modified powder could be observed. This strongly indicates a covalent attachment of the phosphonic acid anchor group to the metal oxide surface.^[149] Figure 84 shows the ^{13}C solid state NMR spectra including a scheme of the surface attached molecule. The intensity of the resonance ((3) in Figure 84) of the CH_3 -group-C-atoms around 10 ppm is higher as compared to the other, rather weak, resonances, because the end groups are only a small part of the whole molecule. Nevertheless, all NMR signals confirm the presence of the described system. The resonances 1 and 2 at ~ 130 and ~ 110 ppm are associated with the presence of an intact allyl end group at the ZrO_2 surface, bond via PDMS-linker.

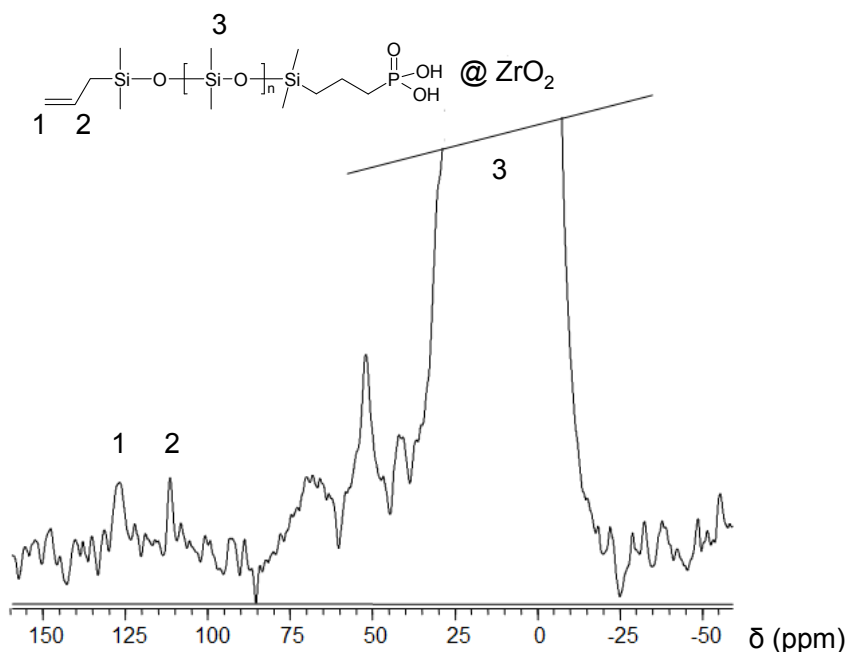


Figure 84. ^{13}C -MAS (CP) Solid state NMR spectrum of ZrO_2 nanoparticles, surface modified with allyl-PDMS-PPA.

TGA measurements revealed a grafting density of 0.6 molecules/ nm^2 , similar to the ^tBu end group system, described and discussed previously. Analogous dispersion behavior could also be observed as for the ^tBu -system. The modified particles were well-dispersible in non-polar solvents such as toluene and also in moderately polar solvents such as MMA. However, by the use of the allyl-PDMS-phosphonic acid for the modification of ZrO_2 , not only the surface properties could be changed but also a reactive double bond was introduced, which is connected to the particles via PDMS spacer.

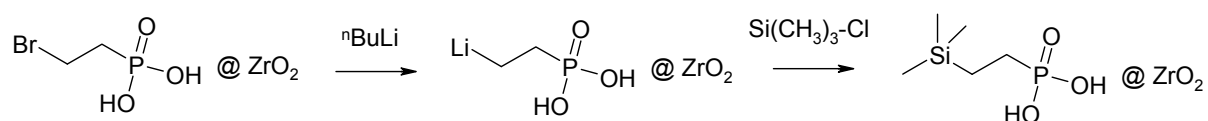
This chapter 3.1.5.1 has shown that the living anionic ring opening polymerization of hexamethylcyclotrisiloxane can be initiated by allyl-lithium resulting in α,ω -bifunctional heterotelechelic coupling agents of the type allyl-PDMS-X with a variable chain length. This is the key element in the preparation of functional PDMS chain spacer coupling agents in analogy to the widespread alkyl system in the present work. The applicability of this approach has been demonstrated for the preparation of trimethoxysilane and phosphonic acid coupling agents and their surface attachment to SiO_2 and ZrO_2 nanoparticles.

3.1.5.2 Polysiloxane grafting *from* ZrO_2 Nanoparticle Surface

A PDMS grafting *from* approach has been developed according to Scheme 5 where a dense monolayer of ethylbromo groups, attached to small ZrO_2 nanoparticles via phosphonate group, is lithiated in THF at -78°C . This should generate an organolithium species acting as initiator site for the ROP of D_3 to graft PDMS *from* the particle surface. This route has been selected, even though other experiments, applying OH-end groups, which are deprotonated via metal alkoxides and act as ROP initiator were successful. The reason is that by applying this approach, hydrolytically stable Si-C bonds are formed. No example for such an approach has been reported in literature up to now as far as known by the author. Furthermore, this

grafting *from* reaction promises a higher grafting density compared to the low grafting density values yielded by the grafting *onto* approach. Given the fact that every Br-group acts as initiating site, surface coverage values of 2.3 molecules/nm² (Br-C2-PPA@ZrO₂ small) could theoretically be yielded at a desired chain length, provided that it is possible to tune the process and steric effects of PDMS chains, due to chain conformational change should not show high impact on the final grafting density. However first, by attempting to apply such an approach of using the harsh conditions of organolithium compounds, the following points have to be ensured: It is important to exclude a reaction of the organo-Li-species with the phosphonate anchor group, which could result in undesired detachment of the surface modification and phosphonate Li-salt formation or even in reduction of the phosphorus species. The anchored phosphonate group should remain intact. Furthermore, it has to be ensured that the bromo group is lithiated. If the group is lithiated it should act as an initiator by opening the D₃ cyclic structure, which is then attached to the solid phase and starts the grafting reaction. It has to be investigated, whether these prerequisites are fulfilled under the given conditions. Therefore, a preliminary test experiment under exactly the same conditions as applied for the final polymerization experiment, was performed. The only difference was that after lithiation, the reaction mixture was directly quenched with trimethylchlorosilane (Scheme 11). It has to be noted that after the addition of an excess of ⁿBuLi, which was necessary because particle adsorbed water can never be excluded and cause an undesired quenching of the ROP, the excess was removed via centrifugation and washing with ⁿhexane under argon atmosphere using a *Schlenk*-equipment for the centrifuge to exclude any moisture after lithiation. This experiment gives a less complex model system which eases conclusions on the reactivity behavior of Br-C2-PPA@ZrO₂.

Scheme 11. Reaction scheme of preliminary test reaction to ensure the "survival" of the phosphonate anchoring during the organolithium initiated grafting *from* reaction.



Of course it is considered and accepted that the excess ⁿBuLi also reacts with non endcapped M-OH groups as well as residual P-OH groups (where also a grafting reaction can then in principle take place), given from the predominant binding mode (see chapter 3.1.2.3). However, such by-products are assumed to be washed off with water due to hydrolysis.

The FT-IR spectra of the thus prepared product showed no significant change in the PO₃ band around 1000 cm⁻¹. However, ³¹P solid state NMR investigations are more significant, because in the IR spectra the band could easily be superposed via Si-species modes. The characteristic vibrational modes from the CH₃ group could be observed as well as a broad OH peak (from M-OH), indicating an incomplete coverage (2.3 molecules/nm² of the educt is still no perfectly dense monolayer). The adsorption of silyl-species to the surface can be excluded as Zr-O-Si bonds are highly unstable towards hydrolysis^[180] and the intensive washing of the product

with water and other solvents. The presence of the M-OH vibrations is also an indication for this fact. For a significant statement on whether the anchoring of the phosphonate to ZrO_2 is still intact or not, the ^{31}P solid state NMR of Br-C2-PPA@ZrO_2 before and after the described test reaction is shown Figure 85. Both spectra, before and after the reaction, show the characteristic peak around 25 ppm which is assigned to the intact ZrO_2 bond anchor group, see chapter 3.1.2.3. The fact that the upper peak seems to tail, or to be tilted, results from a calculation procedure to suppress the side spinning bands which were stronger in this case. Ordered structures, such as the dense Br-C2 monolayer, tend to that effect, because such rigid systems introduce anisotropy effects in the NMR experiments contrary to mobile, flexible systems.^[401] However, if the phosphorus species would have been reduced, significant resonances in the lower (and negative) ppm region should be observed, but this was not the case. Furthermore, the presence of silylester-species which are expected between -9 to -30 ppm in the ^{31}P NMR^[402] or free acid groups which is expected at 35 ppm can be excluded. The negligible weak peak, superposed by the side spinning band at around -30 ppm, could originate from low quantities of such P-O-Si species. From these results, it is concluded that the anchor group remained unchanged, even under these harsh conditions. The relatively dense SAM can be held responsible for this fact, by shielding the anchor group from the reactive organolithium environment through inhibiting the diffusion of reactive species through the SAM to the anchor group. Such effects are applied in literature for protection of surfaces in reactive liquid media utilizing SAMs.^[403] The organic moiety is assumed to protect the anchor group to a certain degree in the dense SAM regions on the particle. Here, the C-Br bond as the most reactive bond in this system towards lithiation, preferentially reacts with the Li-species. M-OH groups which are considered to be present in non dense SAM regions, also preferentially react with the reactive Li-species. Of course, a partial cleavage of P-O-Zr bonds result in a larger amount of free P-OH as P-O-Si is also not stable towards hydrolysis.^[402] This could also be responsible for the change in the form of the peak after the grafting reaction in the ^{31}P NMR. However, the phosphonic acid groups would in this case still be anchored to the surface by a certain binding mode, or washed off. The later can be excluded, because the TGA data as well as elemental analysis results of this product, taking the new organic moiety after the reaction into account, revealed a surface coverage ~ 2.3 molecules/nm² after this test reaction. This can also be interpreted as a clue that every Br-group has been lithiated. This issue will be discussed later in detail.

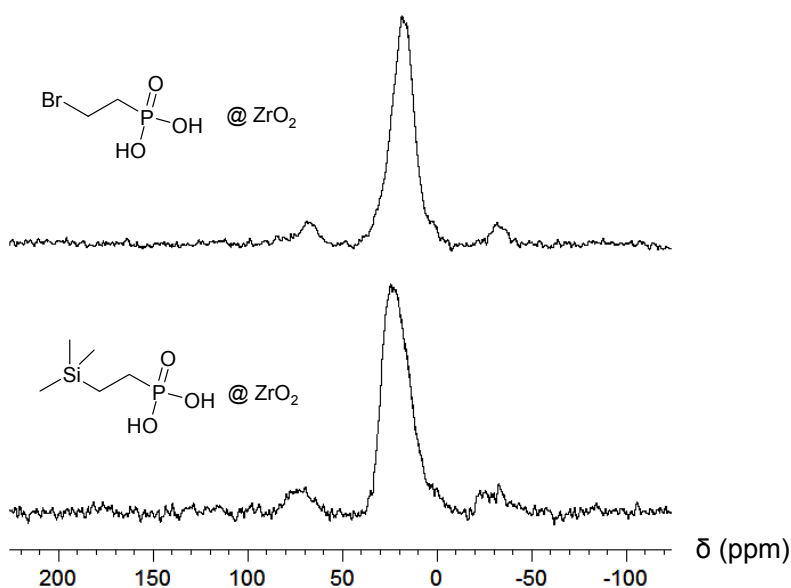


Figure 85. ^{31}P solid state NMR spectra (HPDEC) of Br-C2-PPA@ZrO₂ before and after the preliminary test reaction to ensure the survival of the intact phosphonate anchoring during the organolithium grafting *from* procedure.

The ^{13}C solid state NMR spectrum in Figure 86 shows the presence of the characteristic resonances of the product, such as CH_3Si . It should be noted that the intensities cannot be set into direct relation because the CP method was applied. They may vary depending on the movement of the attached chain and can be less for strong mobile moieties.^[404] However, as this is a very complex system of a solid phase synthesis – substrate, additional peaks in the CH_2 region in the spectrum indicate the presence of a by-product. This can be a butyl-alkoxide species or more likely surface adsorbed butanol which, was formed at the non-covered particle surface sites by reaction with $^n\text{BuLi}$ and surface adsorbed water or M-OH . It is well known that alcohols can adsorb to metal oxide surfaces,^[405] which can be even more distinctive for more reactive nanocrystals.^[406] Even the formation of an alkyl-alcohol SAM is possible.^[407] Most important is that no double bond species can be observed in the ^{13}C NMR spectrum, as it would be the case when Br is eliminated. Such an elimination reaction could also occur in this milieu as it is the typical reaction behavior of β -bromo phosphonic acids in strong basic aqueous media.^[408] However, this undesired side reaction pathway which would not lead to initiation of the ROP, is excluded from these results. The fact that after the reaction, no Br could be detected via EDX analysis confirms the assumption that every Br-group at the ZrO₂ particle surface was lithiated under the applied conditions.

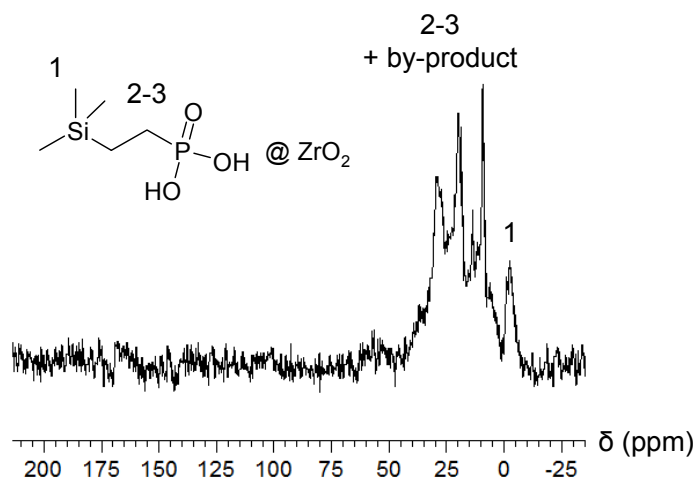


Figure 86. ^{13}C solid state NMR spectra (CP) of TMeS-C2-PPA@ZrO₂ after the test reaction which was carried out to ensure the survival of the intact phosphonate anchoring during the organolithium grafting *from* procedure.

If these generated alkyl-Li surface groups are able to open the D₃ ring, and thus initiate the ROP grafting *from* reaction under these conditions, has to be tested. If it is the case, further important for exploiting the advantage that this grafting *from* approach would be to answer the question: Can one assume that every of these surface attached groups initiate a ROP or are there too many side reactions? In this scope a second, molecular model reaction was performed, because such solid phase system are not applicable to quantitative analyses via usual liquid state ^1H NMR spectroscopy. Therefore, the phosphonic acid diethylester of Br-C2-PPA was reacted with 1 eq. $^n\text{BuLi}$, followed by the addition of exactly 1 eq. D₃ to investigate whether the adduct of the trisiloxane-C2-PPA diethylester has been formed. ^1H NMR spectroscopy revealed a full conversion of all alkyl-Br groups to the siloxane bond alkyl species by a shift of the CH₂CH₂Br resonance from 3.3 and 2.1 ppm to 1.4 and 1.2 ppm due to the formation of the CH₂CH₂Si group. No signal from the educt species could be detected in the spectrum. This is the evidence for the initiating properties of this system, as the D₃ cyclic compound was opened and attached quantitatively in this model system reaction. However, in this molecular model reaction, ^{31}P NMR spectroscopy gave the evidence of ester cleavage showing by an additional resonance around 18 ppm resulting from a P-Si, or more likely, Li-salt phosphonic acid monoester by-product which could be detected after this test reaction. This product could be the result of a possible side reaction of Li ions or scissored siloxane species, which are assumed to be present in such reactions.^[393] However, no reduction reaction or other degradation of the phosphonic acid (ester) group, or the molecule's backbone could be observed. Nonetheless, in the first, solid phase model system reaction, no effect of the reactive environment (Li-organic species) on the anchored organophosphorus species could be detected. It is assumed that the dense organic SAM protects the anchor group in this case, which is not the case in the molecular reaction.

All these discussed results from EDX, TGA, elemental analysis, NMR and FT-IR analyses from the model reactions allow the extrapolation to the grafting *from* reaction system with the conclusion that the initiation of D₃ ROP from the Br-surface groups is possible, under the given conditions. The anchored phosphonate is not affected by the reaction conditions. As

discussed for the preliminary test reaction, it is very likely that the organic SAM protects the anchor group from the reaction with the $^n\text{BuLi}$ -species. Additionally this first lithiation step is carried out at -78°C to slow down the chemical reactivity of these molecules. During the attachment of the first D_3 molecule, which is considered to proceed very fast,^[394] the relatively moderate chemical reactive environment of $\text{Si-O}^-\text{Li}^+$ species of the living chain ends, during the major duration of the reaction (days at room temperature), is not assumed to affect the organophosphorus anchoring.

As these studies argue for a successfully applicable grafting *from* reaction, reactions with different M/I ratios were carried out, in order to investigate the ability to tune the grafting chain length. The reactions were monitored via NMR spectroscopic methods and the products have been analyzed via the usual methods as applied for the grafting *onto* reactions. The reaction conditions were the same as described for the preliminary test reaction, using Br-C2-PPA@ZrO_2 , and the results for two samples where different M/I ratios have been applied are discussed here. For sample "E", a M/I ratio of 33 and for sample "F" a M/I ratio of 100 was used. The latter was already at the limits of solubilization of D_3 in THF, under the necessary conditions which were the application of low solvent amounts to avoid diffusion control of the reaction and thus the reduction of the reaction of Li-species with the solvent. The chemical equivalents of initiator groups were calculated from the known surface coverage of Br-C2-PPA@ZrO_2 , assuming that every surface group acts as an initiator site. The reaction was finally quenched with trimethylchlorosilane. The detailed discussions are carried out exemplarily for sample "F" in this chapter. The reaction progress of this reaction "F" was monitored via ^1H NMR. Samples have been taken at selected times and the particles were removed via filtration and centrifugation. The residual liquid phase was then prepared for the measurement and the concentration of siloxane species in the reaction mixture was calculated from the NMR experiments via integration of characteristic peaks and comparing the integral values of a known standard of diphenylether and siloxane species. The resulting concentration of siloxane species in solution (given as D_3 equivalents) during the monitoring time period is plotted in Figure 87. Two facts argue for a successful living ROP PDMS grafting from reaction: Firstly, the the concentration of siloxane species in the reaction mixture decreased, which means that the siloxane species is removed from the solution and attached to the particle surface. Secondly, the linearity of this trend of the decrease with $-14\text{g}/(\text{mol}\cdot\text{min})$ (from linear regression) indicates the living character of this reaction.^[370, 388] After 5 days the concentration did not change and the linear trend changed into a plateau around 1000 g/mol , which is very likely due to the presence molecular PDMS species which has been formed in the solution via unavoidable (but accepted) side reactions. This side reactions origin from initiating molecular species, very likely linear siloxanes which have been cleaved off and continue polymerization in solution. Such species could have been generated at other initiating sites (M-O^-) under these conditions in this complex system. The applied excess of $^n\text{BuLi}$ is responsible for these reactions, as discussed in the beginning of this chapter in detail. However the excess is necessary, because small amounts of e.g. surface adsorbed water can never be excluded, as mentioned. Such reactive species have to be overrun by $^n\text{BuLi}$ as they would significantly disturb the grafting reaction. On the other hand, different sites for possible

grafting not leading to stable attachments via Si-C bond are generated. However, the concentration decrease is assumed to derive its origin from the grafting *from* reaction, because possible molecular PDMS species are also detected by the NMR method to quantify the dissolved siloxane species and included in the plotted concentration values. This means that every siloxane species that cannot be detected via this method has been removed from the solution, including possible linear PDMS by-product species. Assuming that every Br-group led to a growing chain, after 5 days a molecular weight of the grafted PDMS of ~ 21000 g/mol is obtained, calculated from this concentration decrease. However, this assumption is not very proper and only gives an estimate, because under the given reaction conditions before hydrolysis it is assumed that also weakly attached or hydrolytically not stable attached PDMS, from initiation on other sites (free P-O⁻ or M-O⁻), are present at the particle surface. This is, however, excluded for the final samples as they are washed with water and organic solvents, where such weakly bond species are removed.

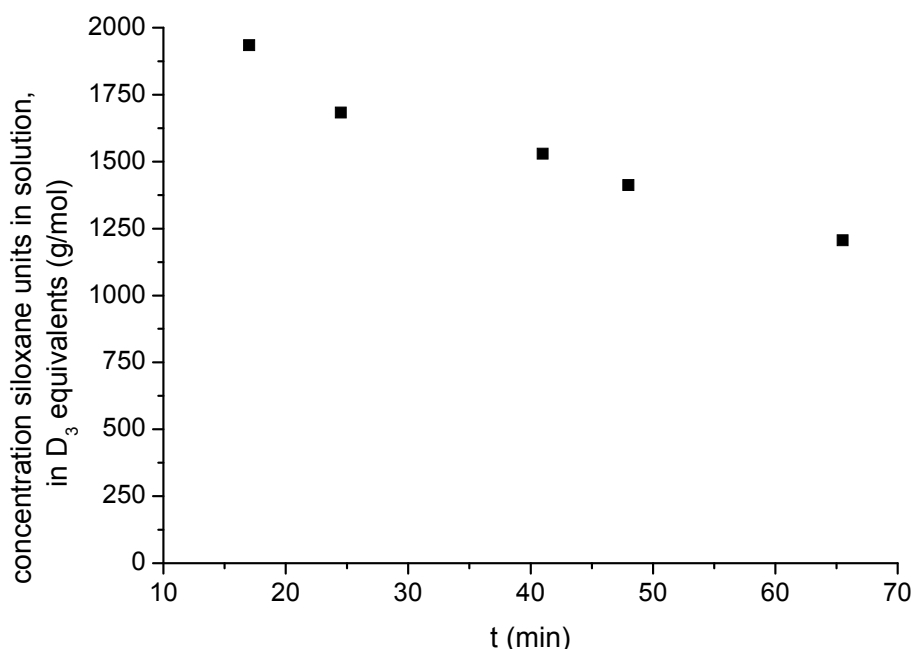


Figure 87. Removal of siloxane species (D₃) from the reaction solution during the grafting *from* reaction, observed via ¹H NMR using a diphenyl ether-standard solution (sample "F").

The assumption that every Br-atom is released from the surface, was proven by elemental analysis. This argues also for the assumption that at minimum a grafting density of 2.3 g/mol, from Br-C2-PPA@ZrO₂ before grafting, is present for the PDMS grafted product. For the unmodified ZrO₂ a Br-content of <0.1 wt% was detected, 5.3 wt% Br for the Br-C2-PPA@ZrO₂ before grafting and in the final product, after the grafting reaction, no Br (<0.1 wt%) could be detected. The washed nanopowders were further analyzed. The FT-IR spectrum of the system before grafting and the grafted sample "F" is shown in Figure 88. First, the presence of a PDMS chain in these nanopowder is confirmed by the characteristic vibrational modes at 1013 and 1090 (superposed by the PO₃ mode) cm⁻¹ from the Si-O-Si vibration from the chain backbone, as well as at 745 (Si-C valence) and 1259 cm⁻¹ (SiCH₃

deformation) and intense C-H vibrations from the methyl groups around 2900 cm^{-1} . The fact that these characteristic signals remained unchanged before and after the washing procedures confirm a (hydrolytically) stable attachment of the PDMS to the nanoparticles. However, this cannot be fully confirmed via FT-IR, because of the mentioned superposition of the PO_3 region with the Si-O-Si region around 1000 cm^{-1} . ^{31}P MAS NMR, which gave analogous results as shown for the preliminary trimethylsilyl product experiment, confirmed the intact phosphonate anchoring. Another observation could be made from the FT-IR spectrum of the PDMS grafted sample: The presence of M-OH surface groups from unmodified sites is indicated by a broad band between 4000 and 3000 cm^{-1} . This argues for the assumption made in the scope of the discussion of the kinetics experiment, (Figure 87) that PDMS species, attached to these sites, generated during the grafting reaction, disappear during the workup procedure and leave the original M-OH back on the surface. Therefore, the further analyses data and interpretation made from these powders, such as surface coverage or grafting chain length, is assumed to origin only from the desired products of C-Si linked PDMS and not from PDMS species which were generated on other sites. A drawback is that the variation of the M/I ratio does not allow a theoretical prediction of the molecular weight as for usual living polymerization reactions, because not excludable side reactions occur. It will be shown that via the M/I ratio, the chain length can be at least controlled to a certain extent. A possible solution to overcome these side reactions would be the use of coupling agents which fully cover the surface. A molecule such as Br-octadecyl-PPA, building up a dense crystalline monolayer, would be appropriate for this purpose. However, the homogeneous dispersion of the system in THF which is a prerequisite for this approach would not be possible anymore as it is known from preliminary dispersibility experiments for long alkyl chain modified nanoparticles, see chapters 3.1.2.3 and 3.1.3.

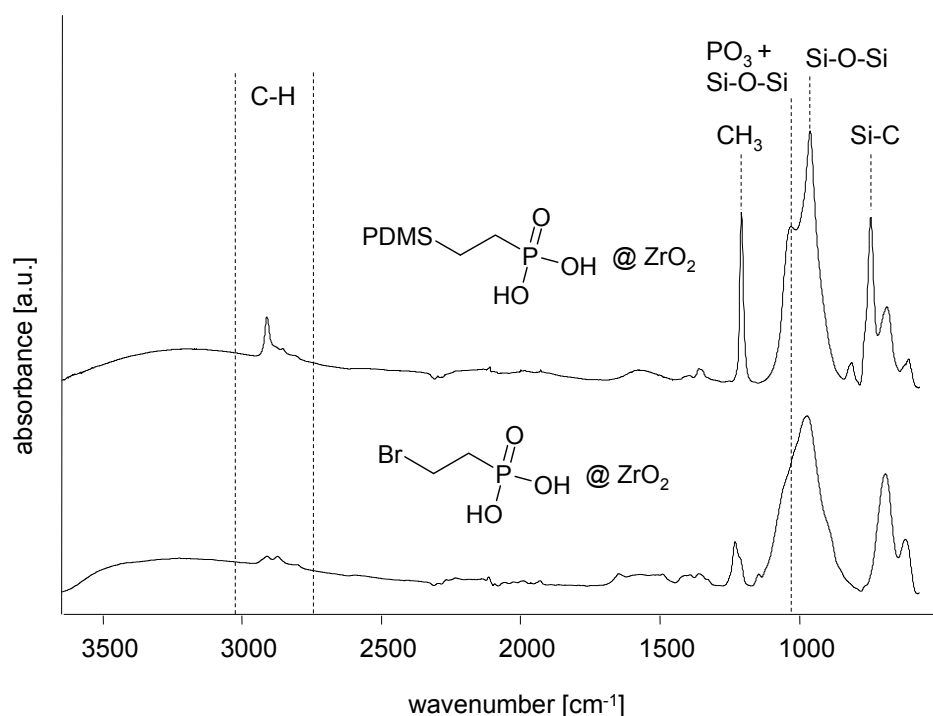


Figure 88. FT-IR spectra of Br-C2-PPA@ZrO₂ before and after the PDMS grafting *from* reaction (sample "F").

Furthermore, ^{13}C and ^{29}Si solid state NMR spectra of the powder (sample "F") have been recorded, applying the CP method (Figure 89). Again, the peak intensities do not represent the quantity of species due to the experimental method. In the ^{13}C NMR spectrum, the characteristic resonances from the CH_3 group from the PDMS chain around -2 ppm, as well as the resonances of the CH_2CH_2 residue, confirm the presence of the desired system. However, additional resonances from CH_2 groups (marked with asterisk) can be detected, which may origin from strongly adsorbed n butanol species, as discussed above for the test reaction. The ^{29}Si NMR spectrum further confirms this structure of $\text{PDMS}@Z\text{rO}_2$ showing the resonance from the D-unit of the PDMS chain at -22 ppm and the very weak signal from the trimethylsilyl terminus, the M unit, at +7.3 ppm. A broad second resonance from a M unit is also visible in the spectrum, possibly originating from small amounts of PDMS chains which were stronger adsorbed or are dissolved in the PDMS grafted layer and could not removed during the washing process.

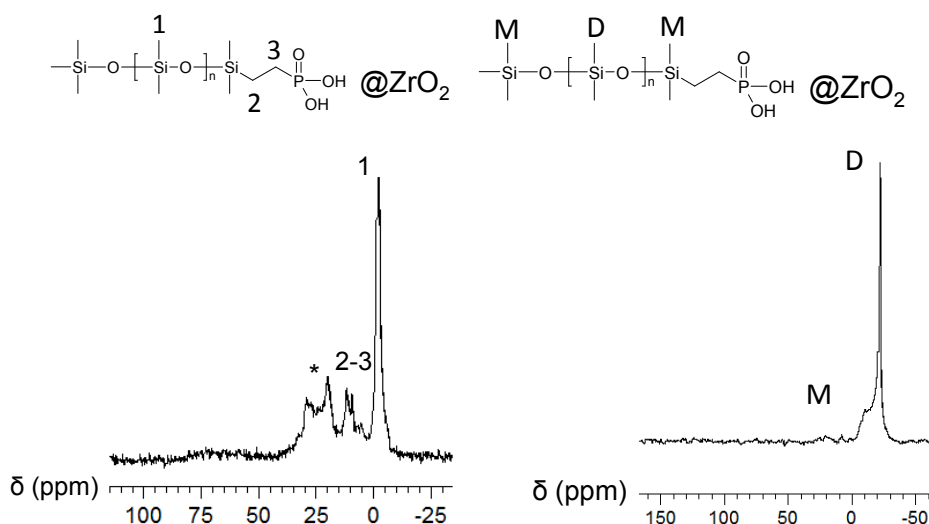


Figure 89. Solid state NMR spectra of PDMS grafted from ZrO_2 nanoparticles (sample "F").
left: ^{13}C (CP) spectrum, right: ^{29}Si (CP) spectrum.

Furthermore, both products, E and F, were analyzed via TGA coupled with FT-IR to, on the one hand to determine the amount of grafted organic substance. On the other hand the FT-IR analysis of the TGA offgas allows conclusions on the evaporated species and thus on the adsorbed species on the powder sample itself (Figure 90). The samples started to degrade at 190°C (onset) and the FT-IR spectrum from the offgas at 220°C (insert in Figure 90) shows the presence of organosiloxane species, by the characteristic vibrations at 1029 and 1080 cm^{-1} (Si-O-Si). Literature describes the thermal degradation products of PDMS to be basically cyclic siloxanes from D_3 to D_{11} ,^[409] cleaved off during the heating. Furthermore, some oxidation products (C=O vibrations between 1600 and 2000 cm^{-1}) and characteristic bands, assigned to $\text{Si}(\text{CH}_3)_2$ at 744 , 812 , 1298 cm^{-1} , as well as the C-H stretching vibrations around 2900 cm^{-1} confirm the presence of siloxane species. This degradation temperature is rather low compared to the thermal degradation via bond cleavage of pure long chain trimethylsilyl end group PDMS, which proceeds at 380°C under inert atmosphere.^[372] However, under

synthetic air, and even stronger expected for the here applied O₂ atmosphere, oxidative degradation mechanisms are also present which lower the thermal stability of the overall system.^[372] The organic residue which has been cleaved off, is assumed to be PDMS. Residual monomer for example can be excluded, because a comparison experiment with D₃ under the given conditions showed the complete removal of D₃ between 53°C and 80°C. In this temperature region, no significant mass loss can be observed in the product samples. Furthermore, this is a very complex, from a simple chemistry point of view "non pure" system, which can cause several possible additional degradation mechanisms. For example, zirconia or titania hybrid PDMS networks show degradation temperatures lower than 200°C due to changes in degradation mechanism.^[410] It has also to be considered that the breakage of the P-C- bond, which fixes the PDMS chains on the surface takes place between 180°-350°C, as it has been observed and discussed in this work previously. The overall system would change its consistency at these temperature, from PDMS-PPA@ZrO₂ to a phosphate covered ZrO₂ surrounded by loose PDMS chains, see also chapter 3.1.2.3.

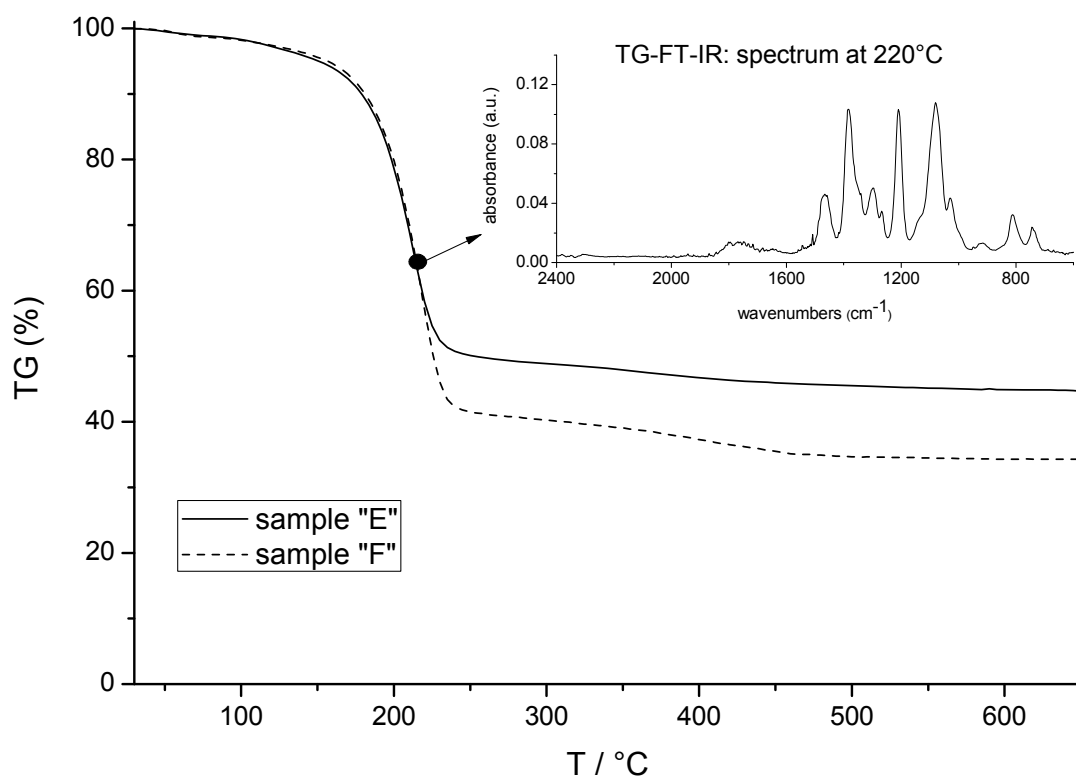


Figure 90. TG-FT-IR coupled analyses of the PDMS grafted from ZrO₂. The insert shows the IR spectrum of the TGA vapor of sample "F" at 220°C.

Another result from the TGA analysis is of high importance. Despite the fact that a exact theoretical prediction of the grafted chain length from M/I has been excluded, for the sample E (M/I = 33) a lower organic residue as for sample F (M/I = 100) was observed. Theoretically, sample "F" should reveal the three fold mass loss of sample "E" from TGA analysis which is not the case. However these results, lower massloss for lower M/I, indicate

that the grafting process can be controlled via the monomer concentration to a certain extent. This means that the variation of the monomer concentration results in different grafting chain length at given conditions (most important: suspension concentration), which makes this process also more flexible towards application. Furthermore, EDX analyses of these two samples (Figure 91) confirm this assumption by showing a Si/Zr ratio of 1.8/98.2 (wt%) for sample "E" and a Si/Zr ratio of 10.6/89.4 (wt%) for sample "F", for which the higher D_3 concentration has been used. This indicates the presence of significantly more amount of grafted PDMS species in the case of sample "F". Assuming that in both cases the same amount of grafting centers are present, which is plausible as the results could be reproduced, a higher D_3 concentration in the reaction mixture leads to longer PDMS grafted *from* chains. A major reason for this controllability of the grafting is considered to be the limiting through diffusion control of D_3 from the solution to the growing chains. Thereby, reactions from other sites (such as Zr-O⁻ surface groups) with cleavage and release of molecular growing PDMS chains cannot be excluded. This effect could also be observed by a viscosity increase in the reaction mixture and by the fact that a plateau concentration of siloxanes in the reaction mixture was observed after the end of the grafting procedure by ¹H NMR spectroscopy. These processes are competing with the desired reaction path. Thus, D_3 is not available for the latter reaction and in the end of the process diffusion control limits further chain growth. This is the most plausible suggestion for this observation. When working at higher D_3 concentrations, more PDMS can be generated in total, product and side products, in the case of sample "F". Further addition of D_3 during the reaction, to increase the grafted PDMS chain length is considered to be not reasonable, because the viscosity of the solution in the final state was already very high (because of free PDMS side product) and a test revealed that in this stage of the process D_3 is not sufficiently soluble anymore in the reaction mixture.

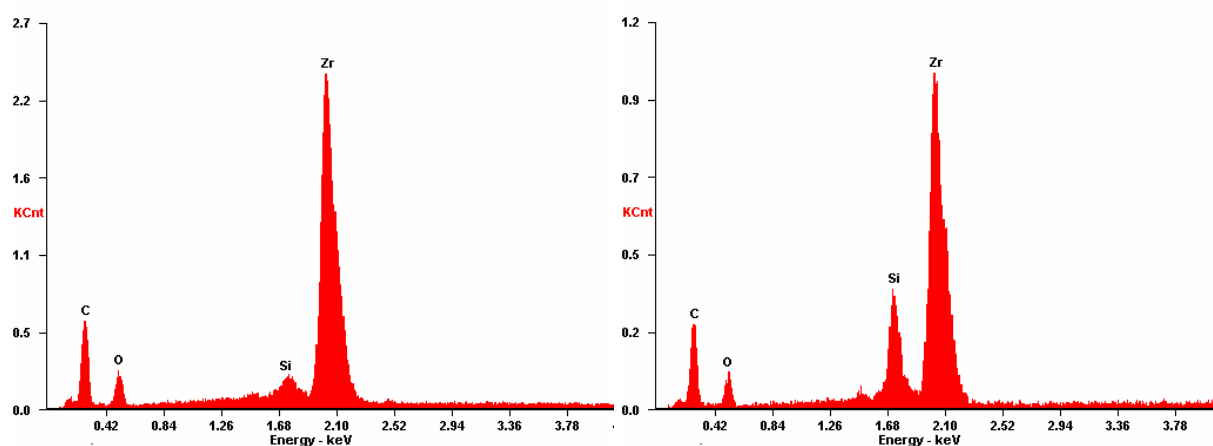


Figure 91. EDX spectra of PDMS grafted from zirconia powder samples, left spectrum sample "E", right spectrum sample "F".

As a detachment of the stable bond PDMS chains was not possible, e.g. by dissolving the particles with HF under keeping the PDMS intact or dissolving the particles in acetyl acetone, it was difficult to analyze the actual grafted chain length for this complex system. Via the assumption that 2.3 molecules/nm², the surface coverage before grafting, initiate the reaction, from TGA, elemental analyses and EDX, a grafting chain length can be estimated. From

TGA, the PDMS chains would reveal a molecular weight of 580 g/mol for sample "E" and 770 g/mol for sample "F", which would correspond to $n \sim 5$ and $n \sim 7$ siloxane units respectively. Elemental analysis would reveal 930 g/mol for sample E ($n \sim 9$) and 1160 g/mol ($n \sim 11$) for sample "F". From EDX, only 100 g/mol ($n \sim 1.5$) for sample "E" and only 390 g/mol for sample "F" ($n \sim 2-3$) could be estimated, which does not fit to the results obtained by TGA and elemental analyses. This can be due to the influence of the electron beam on this organically modified particles during the EDX analyses. Such an effect is used in electron beam lithography of PDMS materials, applying a usual SEM instrument as it has been utilized here.^[411] The results from EDX are therefore not considered for discussion. They should rather qualitatively demonstrate the presence of different amounts of Si-species in the different samples.

The calculation of the grafted chain length when assuming that every surface Br groups led to chain growth gives results in the range as obtained for the grafting *onto* approach in the previous chapters. However, theoretically from M/I, the chain length should be $33 \cdot 3 = 99$ siloxane units for sample "E" and $100 \cdot 3 = 300$ for sample "F". The obtained results are far lower, because of the mentioned difficulties of unavoidable side reactions, not because of the grafting reaction kinetics. The side reactions are assumed to proceed with a similar rate.

A more reliable value for the chain length can be obtained from SP ^{29}Si NMR-experiments as for this method no initial assumption has to be made, like assuming how much Br-sites act as initiator. The chain length can be directly calculated by the ratio of the peak integrals from the signals from the M terminus and the D chain segment, as described above and proven for the more defined grafted *onto* systems. By applying this method, a value of 1900 g/mol ($n \sim 18$) could be calculated for sample "F", which is assumed to be the best representation of the "true" average grafting chain length. Thus it could be shown that standard analysis procedures such as TGA, which were successfully applied for more defined systems of grafted *onto* samples, fail here and more sophisticated methods have to be applied. However, this value is still much lower than the theoretical value of 66000 g/mol (from M/I) or the value calculated for sample "F" from the D_3 loss from solution NMR experiments of 29000 g/mol. From this difference it can be estimated that half of the D_3 is used for molecular PDMS side reaction. Another majority is removed from the solution to graft *from* the particles and form a certain percentage of the desired Si-C bond PDMS species, which is stable towards the workup procedure and detected by measurements of the product powders.

Knowing the more valid value of 1900 g/mol from SP-NMR, the "real" grafting density of stable attached PDMS on ZrO_2 can be calculated from the TGA mass loss. Furthermore, it can be estimated how many of the Br-alkyl groups really initiated a chain growth. Thus, a grafting density of 1 molecules/ nm^2 could be calculated. However, this value has still to be taken as an estimation, since nothing about the molecular weight distribution of these molecules is known. Taking this result into account, it would mean that only one half of desired grafting reaction took place and the other Br sites did not lead to chain growth. However, this grafting density is still higher as obtained from the grafting *onto* approach and additionally twice the chain length under these assumptions. Applying this calculated grafting density for the calculation of the chain length from elemental analysis, a chain length of 2600 g/mol could be

obtained, which is assumed to be a more realistic than previous values. Contrary to that, from the results of the molecular preliminary study on the initiation quantity, it was expected that every Br-group leads to a grafting reaction. However, the solid phase particle system is much more complex and abruption reactions are considered to take place during the whole procedure, e.g. by adsorbed molecular species such as ${}^n\text{BuOH}$ (see ${}^{13}\text{C}$ NMR spectrum in Figure 89). Furthermore, steric reasons can also be responsible for this lower amount of initiating sites. Sterically demanding siloxane chains could disturb initiation processes at neighboring sites.

TEM investigation on the powder sample revealed no change of size and shape of the nanoparticles during this procedure, as expected. The PDMS grafting *from* reaction significantly changed the physical surface properties (hydrophobicity) of the nanoparticles as it is demonstrated by the photograph in Figure 92. The distributions of the nanoparticles between water and ${}^n\text{hexane}$ are shown in this photogtaph. Whereas the unmodified particles and the Br-C2-PPA modified ZrO_2 nanoparticles prefer to disperse in the aqueous phase, the particles after the grafting reactions are organophilic and prefer to disperse in the organic phase. These simple experiments additionally demonstrate the hydrolytically stable attachment of the PDMS chains to the nanoparticle surface and the success of the PDMS grafting *from* reaction.

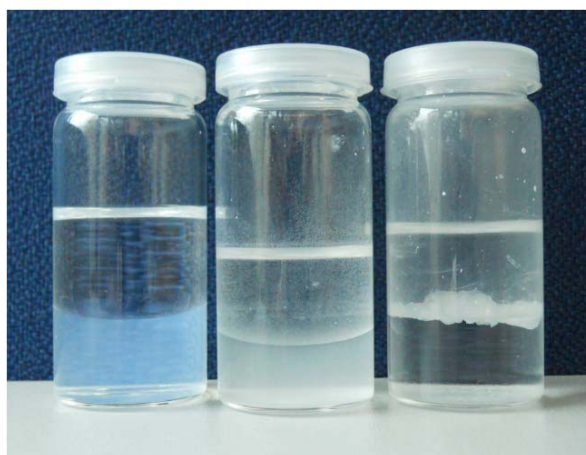


Figure 92. Photograph of nanoparticles distributed between ${}^n\text{hexane}$ (upper phase) and water. left: unmodified ZrO_2 , middle: Br-C2-PPA@ZrO_2 , right grafted from PDMS@ZrO_2 (sample "F").

Particle size distributions from DLS representing the dispersion quality of sample "F" in organic media further point out the organophilicity of the obtained product (Figure 93). Whereas the particles are well-dispersible in toluene, similarly to the particles from the grafting *onto* approach, they are not well-dispersed in THF and poorly dispersible in ethanol, as well as in MMA (not shown). This is very likely a result from the higher grafting density. Therefore the grafted *onto* nanoparticles, dispersible in MMA, will be used for the manufacturing of PMMA nanocomposites later in this work.

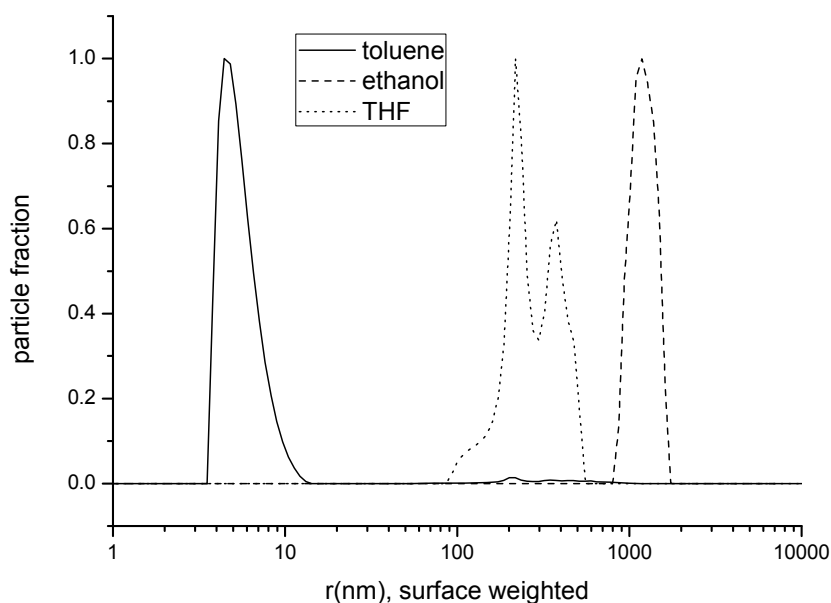


Figure 93. Particle size distributions representing the dispersion quality of PDMS grafted ZrO_2 nanoparticles, sample "F", in various organic media.

Altogether it can be concluded from this chapter that the PDMS grafting *from* reaction can be successfully applied by the described procedure and the molecular weight of the grafted PDMS can be controlled. However, a deviation from a theoretical predicted molecular weight of the PDMS from ROP has to be considered for this complex system. This points out the major disadvantage of this approach compared to the grafting *onto* procedure. Within the latter procedure, well-defined molecules are attached to the surface. However, the advantages of this particular approach, compared to the grafting *onto* approach, are a higher obtainable grafting density and longer grafted chains. A further advantage is that a desired functional side group (FG) can be easily introduced by quenching the polymerization reaction with silanes of the type $\text{Cl-Si}(\text{CH}_3)_2\text{-FG}$. Up to now, a comparable approach applying PDMS generating ROP grafting *from* reaction for inorganic surfaces has not been reported in literature as far as known to the author. Generally, it is expected that the difference of grafting densities of PDMS grafted *from* (higher grafting density) and *onto* (lower grafting density) products can be technologically exploited in nanocomposites preparation. Dispersibility experiments have shown this. The more polar because less densely grafted *onto* particles seem to be appropriate to be incorporated in moderately hydrophobic polymers, such as PMMA. The densely grafted *from* particles are expected to be applicable in PDMS based elastomer matrices, silicones, as a defined filler system.

3.1.6 Polymer shell nanoparticles

The topic of this chapter will be the modification of SiO₂ nanoparticles with a polymeric shell via a grafting *from* approach. The *Stöber* particles are good model systems for such an approach because of their sphericity and thus isotropic morphology, which eases the analysis of these, compared to usual small organic molecule modified particles, more complex systems. The SiO₂ nanoparticles were grafted with polystyrene (PS) applying a literature known approach from *Prucker* and *Rühe*.^[255, 256] They used an azo initiator silane coupling agent for the PS grafting *from* commercial Aerosil silica material. In the present studies, this approach is applied for the well-defined nanoparticle system. The idea behind is to build up an interface region in the final inorganic-organic nanocomposites which is structurally and chemically the same as the surrounding matrix. This should strongly enhance the interfacial compatibility and thus the dispersion quality in the final materials.^[128, 412] Especially of interest in the scope of this particular study is that such systems would thus offer a possibility for a low shear force mixing approach via simple methods such as solution compounding but also the technological important melt compounding in an extruder.^[412] Covalent linking end group containing molecular surface modifications are assumed to result in high dispersion quality. However thereby only an *in situ*-polymerization approach is reasonable because via this method a polymer chain tethering can happen during the polymerization reaction, a grafting *through*. This occurs more randomly and less controlled compared to a grafting *from* reaction which uses initiator surface functionalities instead of polymerizable functionalities.^[66] In this study, the polymeric shell is built up before the preparation of the final composite material, in a well-defined way. This, to the simple modification with non-macro molecules, alternative procedure should thus offer new possibilities for application of such novel nanocomposite materials. However, the preparation of such PS@SiO₂ is comparably rather intricate.

The grafting reaction was carried out from a dispersion of the azo initiator end group modified nanoparticles azo-TMS@SiO₂ in a mixture of toluene and styrene. As analyzed in chapter 3.1.2.2, the diazo group of this product decomposes at 123°C (DSC, peak value). This decomposition initiates a free radical polymerization under the applied conditions according to the procedure from literature.^[255] The by-product of free dissolved PS from thermal self initiation of styrene in the reaction mixture was removed completely via centrifugation. The removal was tested via precipitation of PS from the washing solution with MeOH. Exemplarily, the results are discussed for the SiO₂ large nanoparticle system because of a better visualization possibility with TEM. For the SiO₂ small system analogous results were obtained. The particles were only dried for the analyses during the whole procedure, beginning from the azo-TMS modified particles and ending up with PS@SiO₂. For further preparation steps they were kept as a wet powder, swollen in toluene, to guarantee optimal redispersibility of the system during all steps by avoiding stronger agglomeration / aggregation phenomena. In literature it has been observed that polymer shell nanoparticles form a stable macroscopic aggregate via the interaction / intercalation of the grafted polymer chains in form of a film when the solvent was removed from such a system.^[253, 413]

Figure 94 shows the FT-IR spectra of the initiator modified nanoparticles before and after the grafting reaction. The characteristic signals from the initiator group are too weak to be visible because of the lower surface-to-volume-ratio of this larger SiO₂ particle system, compared to smaller nanoparticles. Furthermore, a strong signal of the Si-O-Si band at 1053 cm⁻¹ from the particle bulk is predominant. However, the ¹³C solid state NMR spectrum confirms the presence of the diazo group (Figure 95). The PS grafted nanoparticles show characteristic vibrational bands at 727 and 694 cm⁻¹ from the aromatic C-H out-of-plane-ring bending vibration in the fingerprint region as well as the bands at 1453 and 1495 cm⁻¹ and 1604 cm⁻¹ from the skeletal (C=C) vibration of the aromatic system. Further characteristic bands can be assigned to the C-H vibration at 2921 cm⁻¹ from the aliphatic region and from the aromatic C-H between 3026 and 3085 cm⁻¹, which altogether confirm the success of the grafting reaction.

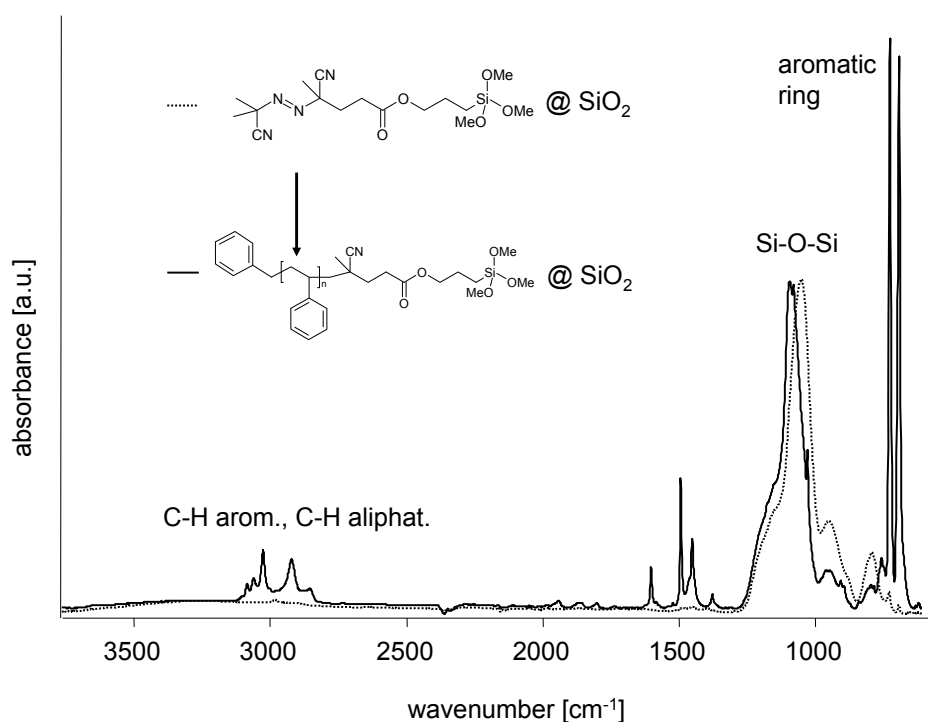


Figure 94. FT-IR spectra of azo initiator end group modified large SiO₂ nanoparticles before and after the polystyrene grafting *from* reaction.

The successful grafting is also confirmed by the ¹³C-solid state NMR spectra in Figure 95: Before the grafting reaction the characteristic resonance peaks from the initiator group are present and after the grafting the resonances from the PS shell are predominant.

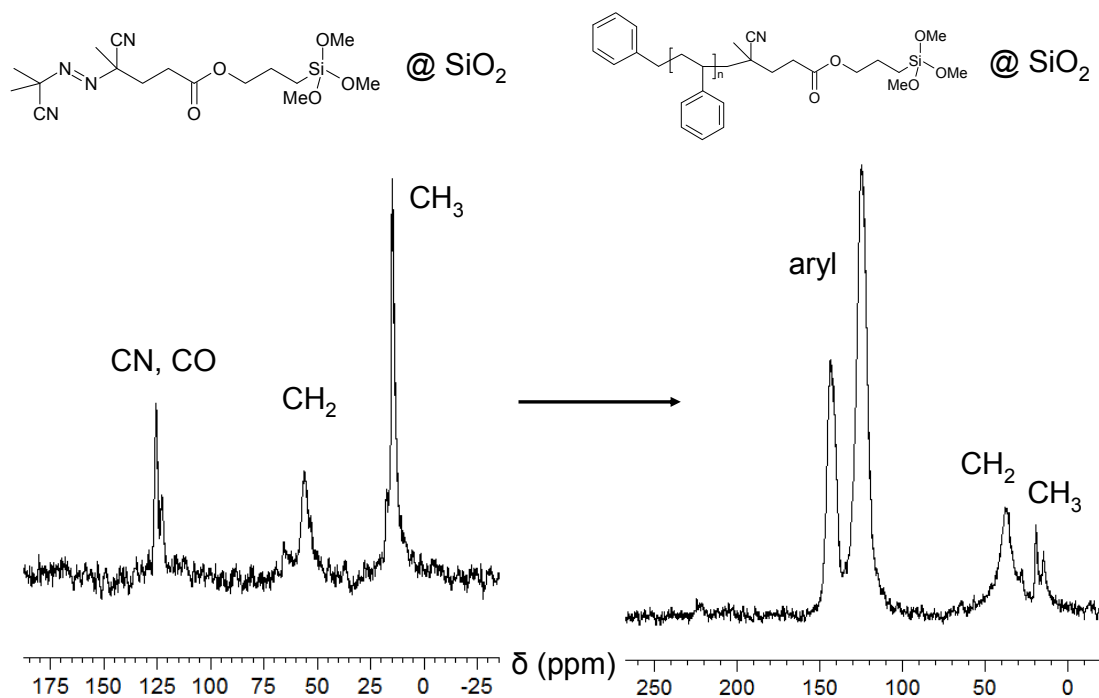


Figure 95. ^{13}C solid state NMR spectra (CP) of azo initiator end group modified large SiO_2 nanoparticles before and after the polystyrene grafting *from* reaction, showing the characteristic resonances which are marked in the spectra.

For an analysis of the molecular weight of the grafted chains, the PS chains have been detached and analyzed via GPC. This was possible by the hydrolysis of the ester-bond linkage, which was intentionally built into the initiator coupling agent molecule. The resulting molecular weight distribution, calculated from the refractive index detector signal for different retention volume, is depicted in Figure 96. From this distribution, the molecular weights of $M_n = 220000$ and M_w of 300000 were calculated. The determined PDI of 1.4 is rather low and confirms that the system is well-defined. These values are comparable to the results obtained for the Aerosil system in literature.^[255] However, the slight asymmetry of the molecular weight distribution is expected to be an effect related to the here applied *Stöber* particle system, as it was not obtained for Aerosil grafting.^[255] In an approach by *Jestin et al.*, who applied a more synthetically affording nitroxide initiated radical controlled polymerization (RCP) to graft PS from silica nanoparticles, very narrow molecular weight distributions were obtained, but the M_n was lower by a factor of 10. They found that the grafted chain length should be not much shorter than the molecular weight of the matrix where the nanoparticles have been incorporated into, if a highly homogeneous dispersion should be yielded.^[128] This effect is discussed later in detail in the sope of the results for the nanocomposite materials from this work in chapter 3.2.1. The here prepared system is appropriate for higher molecular weight matrices, which is favorable in plastics engineering technology as common PS plastics have higher molecular weight, typically M_n between 1500 and 3500 monomer units are used.^[414]

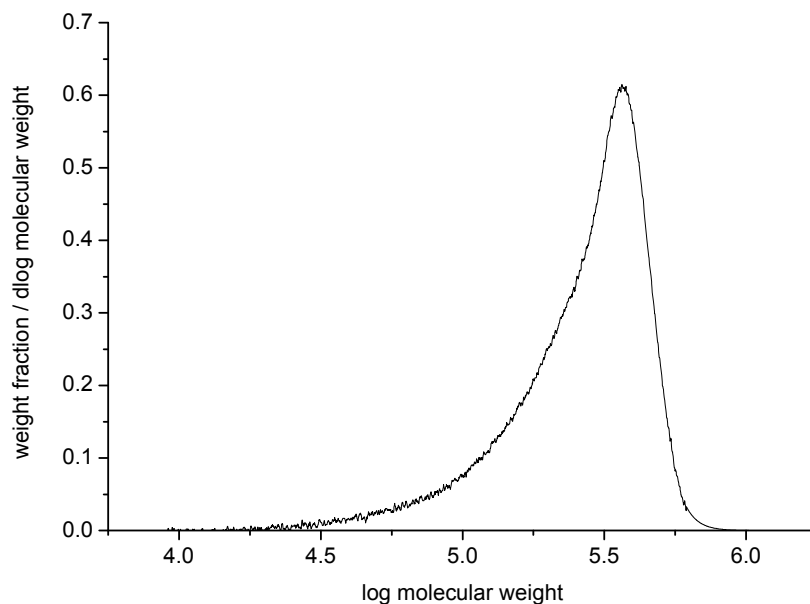


Figure 96. Molecular weight distribution from GPC of PS, grafted *from* azo-TMS@SiO₂ large, which was then detached for this analysis.

TGA analyses revealed an organic content of 53% in the nanopowder, which corresponds to the grafted high molecular weight polymer. Furthermore, a glass transition of the PS, attached to the nanoparticles, could be observed at 97°C (from peak) via DSC measurements. This points out the real core-shell character of these SiO₂ nanoparticles which have a polymer bulk layer of PS at their surface. For comparison, common bulk PS shows a glass transition at around 100°C.^[415] This PS shell can be observed in the transmission electron micrographs in Figure 97 which shows the nanoparticles, drop-cast on a coated copper grid. In the images, the SiO₂ core is visible with higher contrast and a typical corona from the PS shell, which collapsed in the high vacuum and was degraded by the electron beam, is also visible. This is a typical appearance of such organic shell systems in TEM.^[416] A shell thickness of approximately 20-50 nm can be estimated from TEM. The TEM micrographs further show that the nanoparticles can be dispersed as single particles or when they form small clusters during the evaporation of solvent, the inorganic cores do not touch and thus no irreversible aggregation of SiO₂ via surface silanol condensation is possible. These facts are highly desirable in terms of homogeneous nanomaterials and technological application.

Furthermore, atomic force micrographs (AFM-micrographs) have been recorded. A representative 3D-image of a PS@SiO₂ large nanoparticle is shown in Figure 98. From these images, taking also the phase contrast into account, which represents the softness of the investigated matter, a large soft polymer shell of ~50 nm thickness can be estimated. However, this value is difficult to determine via this technique as the large polymer shell spreads on the substrate. The hard SiO₂ core diameter is ~60 nm, which is visible from the height. These results are conform with the results, obtained by TEM.

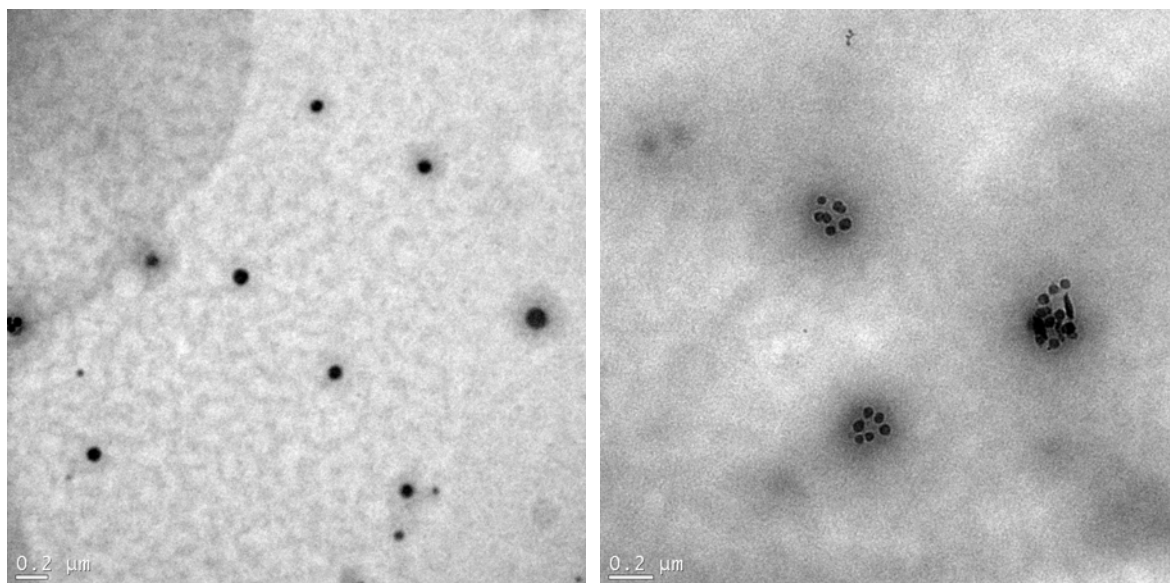


Figure 97. Representative TEM micrographs of PS@SiO₂ large nanoparticles, drop casted on a copper grid from toluene dispersion.

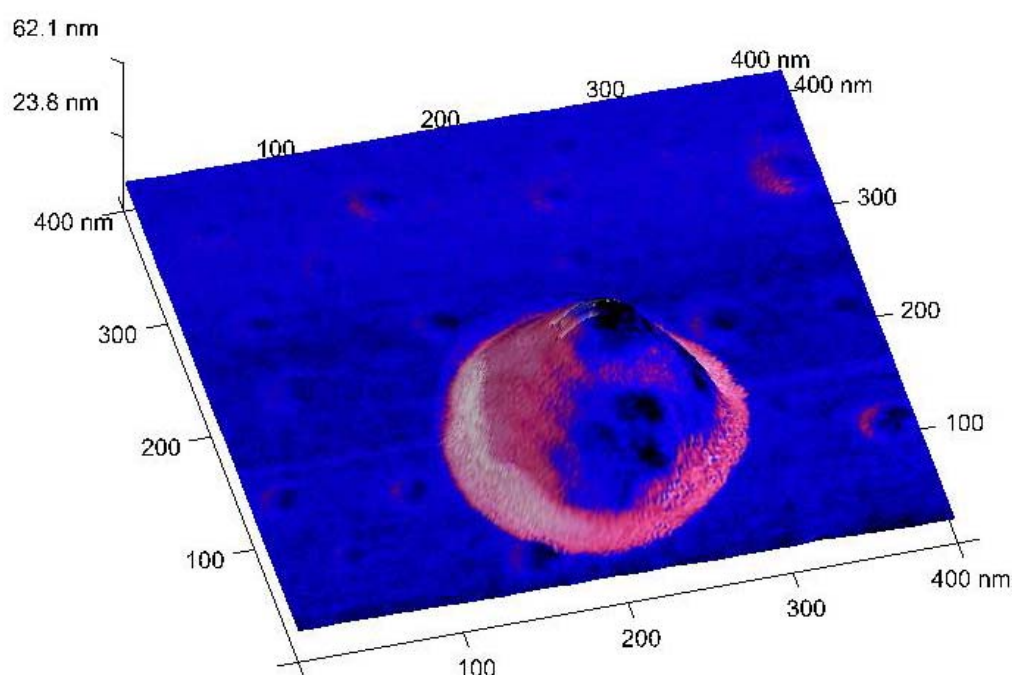


Figure 98. Three dimensional AFM image (tapping mode) of a PS@SiO₂ large nanoparticle (core diameter ~ 60 nm) on a Si (100) wafer. The coloration assigns the phase, where bright regions stand for softer matter and dark regions stand for harder matter.

Furthermore, the dispersion behavior of these PS@SiO₂ nanoparticles has been studied via DLS. The particle size distributions of the large SiO₂ nanoparticles in toluene before and after the PS grafting is shown in Figure 99. It has to be noted that the mass weighted particle size

distribution is very sensitive towards the presence of agglomerates in the dispersion. The particles before the grafting were rather poorly dispersible in toluene but highly dispersible after the grafting reaction. As the grafting reaction medium was toluene, the particles deagglomerated during the grafting process, which was clearly visible during the monitoring of the polymerization progress. The nanoparticles were also well-dispersible in THF, which will be important later, when solution compounding tests will be discussed. The PS grafting thus resulted in a gain in organophilicity of these inorganic particles.

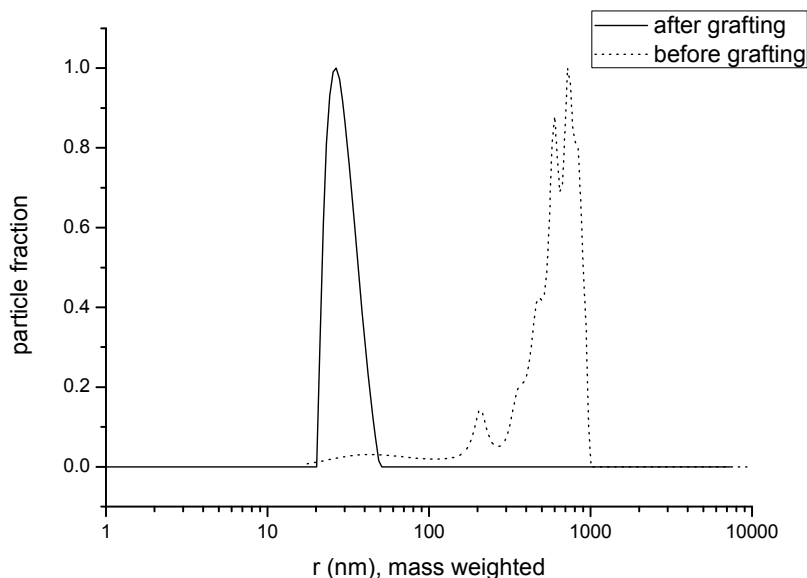


Figure 99. Mass weighted particle size distributions from DLS measurements of azo-TMS@SiO₂ large nanoparticles in toluene before and after the PS grafting *from* reaction.

The isolated dry powders showed a soft consistence and swelled in organic solvents. This surface modification, obtained by free radical grafting, is different from the complex living PDMS grafted system, not only from a chemical point of view also because as a real polymer bulk phase of PS is generated at the nanoparticle surface via this approach. Such a facile free radical polymerization grafting approach can also be carried out for transition metal oxide nanoparticles, as *Vaia et al.* have demonstrated recently by applying phosphonic acid anchor group initiator molecules to graft PS from TiO₂.^[253]

3.1.7 Comparison of different nanoparticle surface modifications

The previous chapters have shown different ways of organically modifying the prepared SiO₂ and ZrO₂ nanoparticles, resulting in different physical surface properties which has been shown by dispersibility experiments in various organic media. Thereby, alkyl modified nanoparticles were rather organophilic and dispersible in non-polar media when the chain "zipper effect" was reduced. Contrary to that, the DEG chain modified nanoparticles were rather hydrophilic and dispersible in polar organic media. The organophilicity of the PDMS modified nanoparticles depended strongly on the grafting density. Densely surface grafted

particles were well-dispersible only in non-polar media. Particles exhibiting a lower grafting density were also dispersible in moderately polar organic solvents, which is of advantage (PDMS-modifications used for PMMA nanocomposites, see chapter 3.2.2 and 0). The dispersibility of the modified nanoparticles (alkyl spacer and no spacer moieties), strongly depends on the nature of the end group as well as the spacer chain length, which determines the physical surface properties and will be discussed in this chapter in detail. The PS shell nanoparticles were best dispersible in toluene, an organic medium which is structurally very similar to the PS shell. A comparison of the dispersibilities with examples of typical organic dispersion media, (especially monomers are interesting in terms of nanocomposite preparation) is given in Table 26 for ZrO₂ and SiO₂ in average. The dispersion behavior of the analogous modified SiO₂ particles is generally similar but due to the lower surface coverage the usually hydrophobic alkyl and PDMS modified particles show slightly more affinity to polar media as compared to ZrO₂.

Table 26. The most important different chemical surface modifications studied in this work with remarks on the best dispersion media for each system.

surface modification organic moiety	dispersion medium
unmodified	H ₂ O (ZrO ₂), MeOH, EtOH
diethylene glycol	H ₂ O (ZrO ₂), MeOH, EtOH, ethyl acetate
long alkyl chain	styrene, toluene, ⁿ hexane
alkyl chain with polar methacrylate end group	ethyl acetate, MMA
PDMS chain	MMA, toluene, ⁿ hexane
PS polymer shell	styrene, toluene

To compare the physical surface properties of the nanoparticles with different surface modifications, reliable methods for comparison of the surface polarity had to be established. This should allow predictions of the interaction of the modified nanoparticles with their environment. The polarity, corresponding to the organophilicity in a reciprocal sense, of the nanoparticle surfaces depends on the overall nature of the organic moiety of the surface modification. Concretely it depends on the spacer chain (type and length) and on the functional end group. Via nitrogen sorption experiments the following propositions can be made: Applying the adsorption model from *Brunauer, Emmett and Teller*, a so called C_{BET} value, which can be calculated from the N₂ sorption isotherms, corresponds to the adsorption enthalpy of the nitrogen molecules, see Eq. 7.

$$C_{BET} = \frac{a_1 \cdot g}{b_1} \cdot e^{\frac{E_1 - E_L}{R \cdot T}} \quad \text{Eq. 7}$$

Thereby, a_1 and b_1 are constants for the first adsorbed layer and g is a constant taking all other adsorbed layers into account. E_1 is the heat of adsorption for the first gas layer physisorption, E_L the heat of liquefaction, R the *Rydberg* constant and T the temperature which is 77K in this case. This N_2 physisorption process is related to polar surface sites and the C_{BET} value is thus the larger, the more polar the surface of the investigated nanopowders is.^[285] The C_{BET} value is rather high for metal oxides (around 100 to 150) and lower for poor adsorbing non-polar surfaces of organic substrates like organically surface modified metal oxides (around 50 to 30 and less, depending on the modification type).^[121, 149, 158, 417] This effect of surface properties on the C_{BET} value has been intensively studied by *Amati* and *Kovats* who modeled the structure of the first adsorbed N_2 layer on polar and non-polar surfaces and confirmed the significance of the C_{BET} results from this approach.^[417] Thus, this method is appropriate for the systems investigated in this work. Random control samples within the studies in the present work further confirmed reproducibility and significance of the C_{BET} values and the fit function gave high correlation with the data points.

A comparison of the thus determined C_{BET} values of small ZrO_2 nanoparticles using meaningful examples of different surface modifications which have been studied in this work, is given in Figure 100. For reasons of comparison, only grafted *onto* samples are shown. The highest C_{BET} value was obtained, as expected, for the unmodified metal oxide ($C_{BET} = 79$) the lowest for PDMS modified ones ($C_{BET} = 5$). This C_{BET} value of 5 is rather low and represents a highly hydrophobic surface modification, as in literature values below 20 are reported to result from a very low surface polarity, e.g. for alkyl chain organosilane modifications.^[417] Even though the PDMS surface monolayer is not completely dense, this low C_{BET} is plausible as the PDMS chains can stick to the non covered parts of the surface when the chain structure collapses due to solvent removal. This results in the observed hydrophobicity effect for the dry powders in the N_2 sorption experiments, even when they are not completely covered. This is plausible as *Auroy et al.* have demonstrated: They found in 2H NMR studies that PDMS chains reveal an uniaxial symmetry, normal to the grafting plane with reorientational motions in good interacting solvents. In poor interacting media, such as air or an inappropriate solvent, the PDMS chains are squeezed.^[378] The C_{BET} value of 10 for the DPPA modified sample is also considerably low, which originates from the dense alkyl chain packing, shielding the ZrO_2 surface towards nitrogen adsorption. It has been shown that the alkyl chains are ordered and to a certain degree densely packed via FT-IR spectroscopy in chapter 3.1.3. *Lomoschitz et al.* have recently shown at the example of functional alkylphosphonic acids on ZrO_2 that the C_{BET} significantly correlates with the dense packing, respectively the ordering of the alkyl chains. Lower C_{BET} values could be obtained for more densely packed longer alkyl chain systems.^[330] The phenyl residue in the present work results in moderate polarity, which is comparable to the values obtained by *Guerrero et al.* for PhPPA@ TiO_2 .^[149] For the mixed monolayers of PhPPA and DPPA on ZrO_2 nanocrystals, which were studied in chapter 3.1.3.3, it was shown by investigation of random points (of different mixing ratio systems) that the C_{BET} value follows approximately the linear mixing law. For instance, for a DPPA / PhPPA ratio of 9:1, which was found to result in optimal dispersibility in organic solvents and is thus technologically most important, a C_{BET} of 14.5 could be calculated (100% DPPA: C_{BET}

= 10, 100% PhPPA: $C_{\text{BET}} = 40$). This result further confirms that the mixing ratio of coupling agents, present in the modification dispersion, is the same as the mixing ratio of attached coupling agents at the nanoparticle surface. It further points out that the overall surface polarity is also changed via the mixed SAM approach, where an optimum mixing degree for the desired application has to be found. The mixed SAM approach thus offers also the possibility for a targeted systematic adjustment of the surface polarity. The other C_{BET} values for the samples with functional end groups lie between the two extreme values for unmodified ZrO_2 and PDMS-PPA modified ZrO_2 . Hence, the surface polarity is tunable via functional end groups at the coupling agent terminus, indicating a high sensitivity of this method towards functional (polar) end groups. The latter assumption is clear when the DPPA and the MA-C10-PPA modified samples are compared. They have a similar alkyl chain length but the polar end group containing sample shows significantly higher surface polarity. Additional data which is not presented in this work e.g. for Diol-PPA ($C_{\text{BET}} = 45$) modification fits within this assumption. Only for the DEG-PPA modified samples, a significantly lower C_{BET} value as expected from such a polar molecule has been observed, $C_{\text{BET}} = 10$. This apparent contradiction to the previous assumption is ascribed to the formation of a rather dense DEG monolayer (seen previous studies in chapter 3.1.2.3). Hence, the methyl-terminated DEG molecules create a virtual surface of methyl groups in the dry powder which significantly affects the N_2 adsorption behavior. This assumption is reasonable as *Schreiber et al.* have demonstrated that methyl terminated oligo(ethylene glycol) (OEG) chains at surfaces, when forming a dense SAM, even do not allow water molecule immersion and penetration into the SAM. The methyl end groups represent the interface where the interaction with the environment takes place.^[418, 419] For a moderately dense OEG SAM, as presented by *Schreiber et al.*, the OEG chains can experience conformational changes. It has been observed that in air, the chains show a well ordered helical structure which shields the surface towards molecules. Upon the addition of water, a conformational change of the OEG residues can occur allowing the penetration of water molecules through the SAM. This could explain the different behavior of the system in the present work for liquid and solid interfaces as the (macroscopically flat gold substrate) system from literature was similar to the system described in the present work.^[418] Hence, the C_{BET} method is considered to be highly sensitive towards changes in the end group for the here discussed system. C_{BET} is thus not considered to be representative for the DEG moiety system to predict any dispersion behavior of the nanoparticles, etc. Through this comparative example (Figure 100) it has been demonstrated that via variation of surface modification the surface polarity of (dry) nanopowders can be well tailored systematically, e.g. by varying the spacer chain nature, by a mixing approach or by variation of the functional end groups. This is one requirement for the achievement of an interfacial fit in nanocomposites in this work. The polarity range reaching from polarities which would be appropriate for very polar environments such as epoxy resins to moderately polar or hydrophobic polymers such as PMMA or PS and to silicone rubbers is covered, leaving no gap in the row of surface polarities.

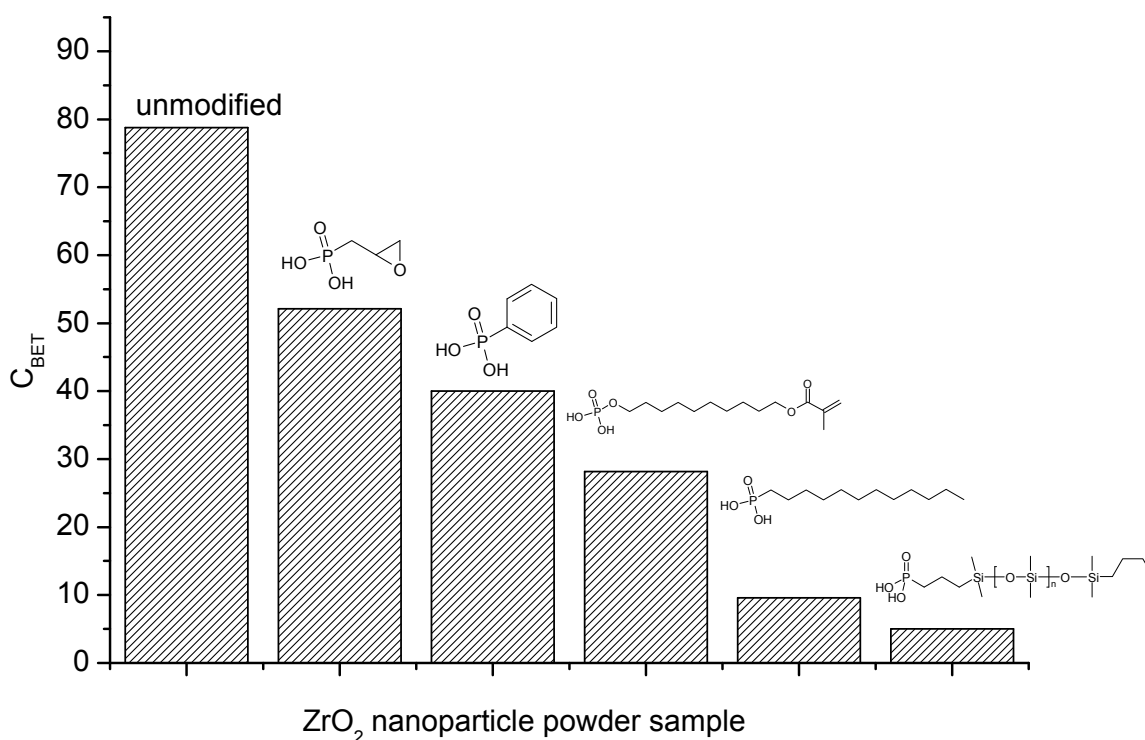


Figure 100. C_{BET} values calculated from N_2 sorption experiments on differently modified small ZrO_2 nanoparticles at 77K, representing the N_2 molecule adsorption enthalpy and thus being proportional to the surface polarity.

Similar experiments have been carried out for the analogous system of large SiO_2 nanoparticles, as they are more densely grafted than the small SiO_2 nanoparticles. The calculated C_{BET} values are visualized in Figure 101. Generally, the same trend is present here as observed for the ZrO_2 system. However the absolute C_{BET} values for the modified particles are higher and the trend is less strongly pronounced. This can be explained by the generally lower grafting densities at the SiO_2 powders, as investigated in chapter 3.1.2.3. This effect is attributed to the nanoscopic curvature and the difference in chemistry of trialkoxysilane and phosphonic acids. The PDMS grafted nanoparticles (grafting *onto*-approach) therefore even show a slightly higher or similar C_{BET} value compared to the C_{12} alkyl chain modified surfaces. The mixed monolayer modified, 680 nm diameter SiO_2 particles, which have been used as model system in the SAM chapter 3.1.3.4 because of their flatter curvature and thus higher grafting density, show also the applicability of the mixing law within the C_{BET} measurements. However, the results for these larger systems are less significant because of the relatively low surface area of these micron sized particle samples, compared to nanoparticles. Thus, it is considered that the C_{BET} method, applied to compare surface properties of these differently modified SiO_2 particles with lower grafting density is less applicable than for the more densely grafted ZrO_2 system.

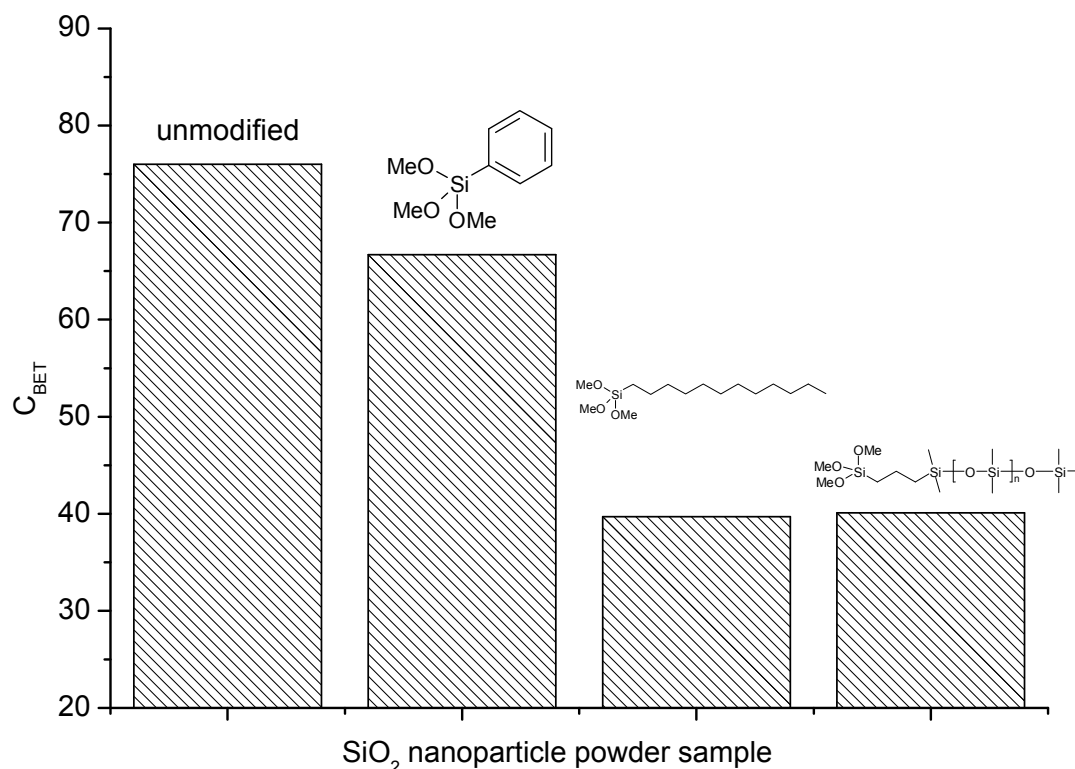


Figure 101. C_{BET} values calculated from N_2 sorption experiments on different modified large SiO_2 nanoparticles at 77K, representing the N_2 molecule adsorption enthalpy and thus being proportional to the surface polarity.

As the results obtained by adsorption of N_2 molecules to the surface of modified nanoparticles represent more the physical surface properties of the dry nanopowders, the solid-gas interface, contact angle measurements have been carried out. These experiments are assumed to be more representative for the wetting behavior of the SAM surfaces with liquids, the solid-liquid interface, in terms of surface polarity.^[164, 420, 421] Thus, contact angle measurements at a liquid-solid interface should allow a better understanding and prediction of dispersibility of the nanoparticles depending on their surface polarity. The higher the contact angle of water on the surface, the more hydrophobic is the surface, and thus less polar as the interaction with water molecules can be considered. Due to wetting, water contact angles are assumed to be more representative for the whole system of spacer and end group, whereas the C_{BET} method was mainly influenced by the end group.

Therefore, contact angle measurements on ZrO_2 model wafer substrates, as described in chapter 3.1.3.7, have been carried out. As it was demonstrated in this previous chapter, the results of these experiments represent the water contact angle behavior of the nanopowder surface and thus the physical surface properties wetting and polarity. The wafer model system is highly defined, easily accessible and more precisely measurable and can thus be used for prediction of nanoparticle wetting behavior. For SiO_2 in contrast, this comparison is less valid because the curvature and thus the SAM structure of a plane wafer compared to the applied nanospheres is too much different. As the small ZrO_2 nanocrystals exhibit plane facets, the assumption of comparability of wafer and nanocrystal surface is valid for the ZrO_2 system.

Contact angles of water on the various surface modified ZrO_2 wafer substrates are shown in Figure 102. DPPA gave the most hydrophobic surface due to the dense alkyl SAM, (see chapter 3.1.3) followed by the highly hydrophobic ${}^n\text{Bu}$ -PDMS-PPA system which is not densely grafted and thus less hydrophobic (see chapter 3.1.5). To demonstrate the representativity of these experiments towards the nanopowders, the water contact angle on a powder pellet of ${}^n\text{Bu}$ -PDMS-PPA@ ZrO_2 was measured. The water droplet exhibited a contact angle of $123^\circ \pm 1^\circ$ whereas for the same wafer sample a water contact angle of only $95^\circ \pm 2^\circ$ could be obtained. This indicates a discrepancy resulting from the different surface roughness of the measured substrates, as discussed in chapter 3.1.3.7. The most hydrophilic system, even more hydrophilic than the bare surface, is the DEG-PPA system. This is plausible and representative for the sample as the DEG-PPA modified powders were hygroscopic and dispersible in polar media, see chapter 3.1.4. The contact angles of the other samples were located between these extreme points and a similar trend is observed as for the C_{BET} values, including the mixed SAM particles (see chapter 3.1.3.7). Except for the DEG-PPA system for the mentioned reasons (methyl terminus induces virtual hydrophobicity), the situation was different. Furthermore, the water contact angles on this wafer model substrates correlate very well with the dispersion behavior of the ZrO_2 nanocrystals (from DLS particle size distributions). With increasing contact angle, the organophilicity increases, see also Table 26. Therefore, this facile method of applying wafer substrates and measuring water contact angles, (the modification, cleaning and measuring can be done within minutes) can be used for the prediction of nanocrystal surface properties and dispersibility when novel coupling agents have to be tested. Furthermore, the C_{BET} values allow predictions if the monolayer is dense enough or the compared modifications exhibit the same grafting densities. The variation of surface polarity can generally be achieved by variation of the end group.

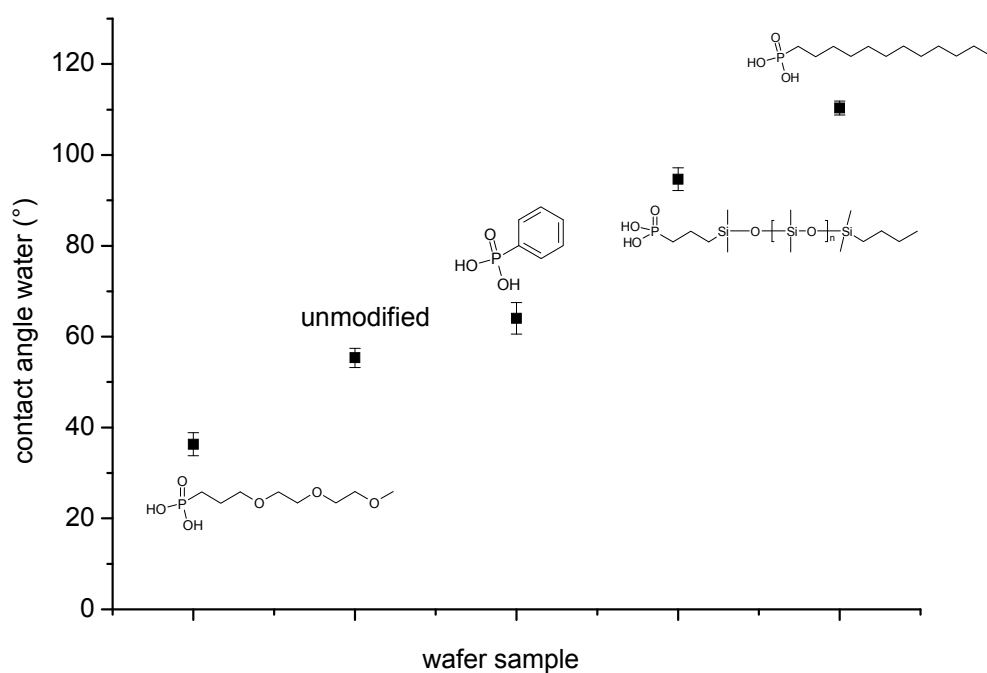


Figure 102. Water contact angles at surface modified ZrO_2 coated wafer substrates.

In a last experiment where the novel surface modification which have been presented in this work are compared, specifically the influence of the nature of the spacer chain on the nanoparticle agglomeration will be demonstrated. Three alternative inert spacers have been used in this work, alkyl-, oligo (ethylene glycol)- and poly (dimethyl siloxane) based systems. For the agglomeration behavior of nanoparticles, not only the nanoparticle surface polarity and the interaction of solvent molecules with the nanoparticle surface is highly important, but also the interparticle interaction is crucial, as it has been demonstrated during the discussion of the "zipper" effect of long alkyl chains in chapter 3.1.3: The interaction between particle and solvent must be higher or equal to the interaction between particle and particle, or close to this situation, when a homogeneous dispersion is aimed. However, even when agglomerates are present, they can differ in their form (densely packed or loose). These differences make them easier or harder to break when e.g. common ultrasonic methods are applied.^[169] Large three-dimensional (3D) agglomerates are considered to be difficult to break.

As model systems, large SiO₂ nanoparticles have been applied, owing to their isotropical shape which allows better conclusions from two-dimensional micrographs. The particles were modified with the three alternative organic chains (alkyl, DEG, PDMS), all with a comparable chain length and a methyl-terminus. Ultrasonicated dispersions of 2 g/L nanoparticles in ethyl acetate, a medium where all nanoparticles were at least moderately dispersible, have been prepared. After letting set some sediment if sedimentation occurred, they were drop cast on a carbon coated copper grid and the dispersion medium was evaporated. The TEM micrographs of the resulting nanoparticle assemblies are shown in Figure 103. It can be observed that the alkyl chain modified particles tend to form 3D-agglomerates by dense sphere packing, which is a common phenomenon for nanospheres which tend to minimize their surface energy. This is known in literature for spherical particles^[133] as well as for nanocrystals.^[219] However, the other two alternative spacer systems do not show the formation of three-dimensional agglomerates. In the case of the DEG-chain system, single dispersed nanoparticles are visible, owing to the good dispersibility of these systems in ethyl acetate. Nonetheless, also during the drying process no agglomerates seem to be formed. However, also for the organophilic PDMS system, showing similar moderat-to-poor dispersibility in ethyl acetate than the alkyl modified particles, no three-dimensional agglomerates could be observed. Only two-dimensional assemblies are present on the substrate, resulting from the solvent removal. Even in the case of PDMS modified particles, where it can be assumed that interparticle interaction dominates, no sphere packing can be observed. The intensity of the sphere packing observed for the alkyl modified particles is considered to be related to the "zipper effect", where the inter-particle bilayer formation is assumed to be still lower for these nanoparticles than for larger micron sized ones (see chapter 3.1.3). This sphere packing of alkyl chain modified nanoparticles is a well known effect which is used for purposeful assembly techniques of particles on substrates where additionally the solvent plays a crucial role in the alkyl chain nanoparticle assembly behavior.^[133, 218, 422] From the discussed experiments it can be concluded that the two alternative spacers are do not show such chain "zipping" behavior which would result in a poor dispersibility even in polarity-matching media. Not even the dense SAM of DEG moieties shows such an effect, because as demonstrated by contact angle

measurements in this chapter and by the water uptake experiments in chapter 3.1.4, the interaction of solvent molecules with the particle surface seems to dominate the inter-particle interaction. The fact that PDMS modified nanoparticles do not show 3D-agglomerates (in incompatible media) points out additional advantages connected to the application of PDMS spacer chains as an alternative to alkyl chains: On the one hand less grafting density is needed to obtain similar organophilicity as for alkyl chains. On the other hand the dense agglomerates of alkyl chains leads to the formation of stronger agglomerates than obtained for the PDMS systems. In the case of 3D-particle-packings each particle has more neighboring interactions, which makes these agglomerates difficult to break. Even for less compatible solvents, like EtOH no such packing phenomena have been observed for the PDMS modified nanoparticles.

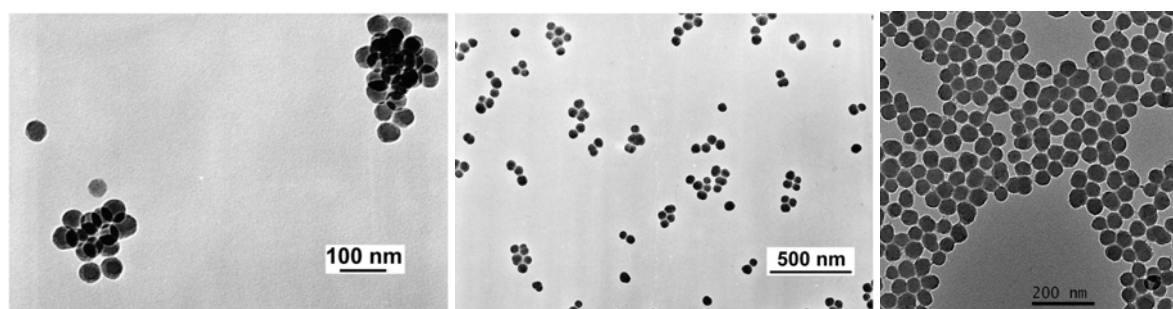


Figure 103. Assembly behavior of modified larger SiO_2 nanoparticles after drop casting from dispersion in ethyl acetate on a carbon coated copper grid, left: DTMS@SiO_2 , middle: DEG-TMS@SiO_2 , right: $\text{TMeS-PDMS-TMS@SiO}_2$.

Additionally, by drop casting $\text{TMeS-PDMS-TMS@SiO}_2$ nanosphere dispersions from ethyl acetate or ethanol, interesting assembly patterns (Figure 104) could be obtained, which are worth to be discussed in more detail at this point. A layer of SiO_2 spheres with round vacancies, holes, in a somehow regular arrangement can be observed. *Granick et al.* have obtained a highly regular pattern with regular holes in a particle layer. They intentionally applied so called hydrophobic triblock *Janus* particles where these colloids have three separated regions on their surface with different physical properties, e.g. caps are hydrophobic, equator is hydrophilic.^[132] The investigated system from this present work exhibits also hydrophilic and organophilic (PDMS) regions which could have led to similar self-assembling behavior forming a hole-pattern structure. However, the different regions on the particle surface for the studied sample are not as well-defined as in the literature example and thus the arrangement is also not very regular. This is one hypothesis. Another example in literature is given by *Lee et al.*^[423], where Au-nanoparticles showed a similar arrangement as observed in this work: They observed a nanoparticle mesh with more or less regular holes in the particle layer deposited on an OTS monolayer-covered substrate. They ascribe the pattern to a complex interplay of repulsive and attractive forces in the overall system. Generally, such nanoparticle assemblies, as e.g. yielded by drop casting methods, can be the result of a complex interplay of attractive and repulsive forces within the overall system of gas/liquid/solid.

Typical driving forces for intended nanoparticle assembly formation can be electrical fields (external or surface charges), magnetic fields, capillary forces (e.g. during drop-evaporation), gravitation or different mechanical forces^[134, 218] which are induced in a controlled way to get desired assemblies. This means that the assembly procedure itself has several optimization parameters. Typical methods for the generation of nanoparticle assemblies are "Drop Casting" which has been used for this present study or *Langmuir* methods and several more.^[134] For systems as used here in this work (1) Surface nature and (2) Solvent nature are the two most important parameters which balance particle attraction and repulsion to give assemblies.^[218, 422] Of course, the uniformity of size and shape of the particles, which is given for *Stöber*-particles, is thereby highly important. Furthermore, the nature of the material where the assembly is deposited plays a crucial role. In this specific case it can be assumed that an interplay of attraction and repulsion between particle and solvent and additionally a concentrating effect during the drying is responsible for the observed assembly pattern. Another hypothesis would be that the not fully grafted particles can still strongly interact with the polar solvents at the non covered surface sites and during drying the interparticle interaction is beginning to dominate. Then, at a certain concentration, drops of EtOH are trapped in the particle layer where the particles prefer to diffuse to agglomerate with other particles, forming the observed holes in the end. Such phenomena of nanoparticle arrangement forming a hole in a particle layer by solvent evaporation causing a dispersion concentrating process are described in literature as *coffee ring effect* for nanoparticle assemblies by drop casting of nanoparticle dispersions.^[424, 425] This effect provides another explanation for the observed self-assembly. In literature, the assembly behavior of PDMS modified nanoparticles is only little investigated. One example from *Koberstein et al.* shows that the spatial spacing of the nanoparticles can be controlled applying higher molecular weight PDMS.^[426] In this present study, for a medium such as hexamethyldisiloxane (M₂), in which the particles are well-dispersible and which is structurally highly compatible with the PDMS-chain (where EtOH or ethyl acetate is more compatible with the bare surface), no such assembly behavior has been observed. These unique assembly properties of the low densely grafted PDMS *Stöber* particles could be exploited by intention: This system could be promising, when applied in the upcoming science discipline of targeted systematic nanoparticle assembly formation.^[134, 218, 427] Structural patterning via such a *bottom-up* approach is done by the matter itself via self-assembling and the matter consists of simple nanoparticle building blocks which are easily accessible via well-established synthetic methods. Possible applications can be found in nearly every field where nanostructures are of advantage, like high performance catalysis,^[427] semiconductor patterning,^[134] 2D- and 3D networks for modeling elastic- and mechanical properties. Also for nanocomposite materials,^[134, 428] photonic crystals^[133] and more^[134] such self assembled structures might be interesting. A possible application for the here discussed system could be a nanopatterned rubber stamp, when additional crosslinkable end groups are used, which can be connected after the assembly via polymerization. When the assembly behavior is optimized, the structure of the arrangement of nanoparticles with PDMS shell could be utilized in the production of hierarchically structured surfaces by common technological methods.^[423] Such hierarchically structured inorganic moieties also play a role in nanocomposite technology, e.g. defined

fractal structured chain like nanoparticle assemblies, which are formed in a polymer matrix, can be used to tune the rheological behavior of the nanocomposite material.^[265]

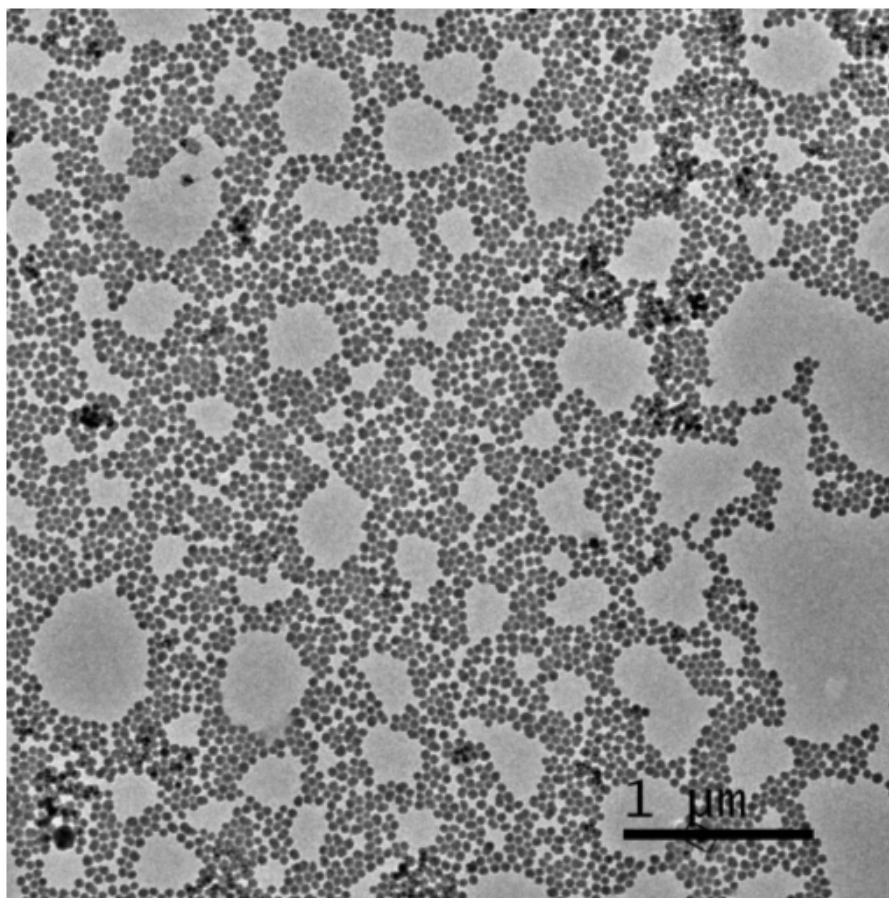


Figure 104. Representative micrograph of the assembly phenomenon of TMeS-PDMS-TMS@SiO₂ larger nanoparticles, drop casted from dispersion in ethyl acetate.

Nonetheless, in the present work agglomeration and assembly properties themselves are not of major interest. Principally, the investigation of related dispersibility effects and deagglomeration is carried out in order to avoid nanoparticle assembly. However, both phenomena are connected to each other and it is mainly the point of view that differs with regard to the discussion of assembly behavior or dispersibility.

Summing up the specific properties and effects related to the different surface modifications in the chapter 3.1, the following highlights of the studies have to be considered in the following chapter on nanocomposite materials:

- Steric effects from the organic moiety can result in lower surface coverage values if the moiety demands more space than the anchor group.
- Long alkyl chains result in dense monolayers, which are responsible for an undesired interparticle chain zipper effect, resulting in stronger agglomeration. This can be overcome by applying mixed monolayers or using alternative spacers (PDMS).
- Oligo(ethylene glycol) chains form dense monolayers that do not show a zipper effect behavior. These modifications result in hydrophilic, hygroscopic particle powders.
- PDMS chains do not form dense monolayers when grafted *onto* nanoparticle surfaces. This effect can be favorable when moderate polarity is required for the interfacial fit within polymer nanocomposites.
- PDMS grafted *from* nanoparticle surfaces can result in powders with higher grafting densities. These systems are, however, still much lower than for long alkyl SAMs. The steric demand of the PDMS chains may limit the dense grafting of PDMS generally.
- Polystyrene shell nanoparticles are surface-tailored to give a specific interfacial fit with the bulk polymer PS.

By a systematic variation of spacer nature, length and chain end group, it was possible to tune the nanoparticle surface properties and thus their compatibility with their environment resulting in different dispersion behavior. Thus, the investigated metal oxide nanoparticles can be surface-tailored to result in an interfacial fit within a whole palette of polymer matrices, reaching from hydrophilic epoxy resins to classical thermoplasts such as PS and PMMA to silicone elastomers. In this chapter 3.1 the systematic tailoring of the nanoparticle surfaces was investigated. In the next chapter 3.2, the surface tailoring approach will become an interface region tailoring approach, when the nanoparticles will be incorporated into a polymer matrix.

3.2 Nanocomposites, interface engineering

In this second part of this work, the chemically surface-tailored nanopowders, already investigated in the first part (chapter 3.1), will be applied as fillers for the preparation of polymer nanocomposites. It is of essential interest how the surface properties of the described nanoparticles influence the interface properties within different nanocomposites and thus the dispersion structure and the mechanical properties. Further on it will be examined how these properties are connected. The following chapters concentrate on the preparation of homogeneous nanocomposites, achieved by a systematic surface tailoring of the nanoparticles and thus an interface tailoring of the materials. The clue is to adapt the surface of the nanoparticles to allow a physical and chemical fit to the polymer matrix at the interface. This enables a homogeneous dispersion with low energy effort, applying low shear force mixing procedures. Theoretically, in the case of a perfect interfacial fit no energy affording mixing procedure would be necessary. When *in situ* polymerization is performed the material changes during the polymerization process from a nanoparticle-in-monomer dispersion to a nanoparticle-in-polymer dispersion. Similarly, the conditions also change when melt compounding or solution compounding would be applied. It is therefore interesting to see which dispersion behavior in polymer matrices can be deduced from dispersion experiments in organic solvents as performed in chapter 3.1. The major concern with respect to application in this case is the preparation of poly(methyl methacrylate) (PMMA) and epoxy resin nanocomposites. Polystyrene (PS) is applied as a simple matrix material to study interface related phenomena in inorganic-organic nanocomposites which are more difficult to investigate for the PMMA (polymerization reaction is more difficult to control) and epoxy resin systems (less defined because of a randomly crosslinked matrix systems). Thereby, PS has been selected as a matrix to study melt extrusion experiments by applying a laboratory extruder, which is important in terms of industrial application. This would not be possible for epoxy resins as they are crosslinked or PMMA because of the high melt viscosity. The latter makes PMMA, when filled with nanoparticles, not processable in a laboratory extrusion apparatus under usual working conditions. For these reasons, *in situ* polymerization or *in situ*-curing (in case of the epoxy resins) will be the most relevant method for nanocomposites preparation in research. Furthermore, the *in situ* process is the only method which allows a covalent linkage of matrix with particles via a grafting *through* reaction when the latter contain surface attached polymerizable organic end groups. In case of PMMA and epoxy resins *in situ* preparation would be also an industrial applicable method as these materials are prepared in particularly controlled processes to generate e.g. polymer films.

For this study, the chemically different modified nanoparticles from chapter 3.1 will be applied as nanofillers in the concentrations of 3 wt%, 5 wt% and 10 wt% to study filler degree related effects on structural and mechanical properties. Furthermore, larger and smaller nanoparticle systems will be compared to study size related effects on these properties. Firstly, as an introducing part in this chapter the preparation of the three different matrix based nanocomposites will be described. they will be characterized and discussed with regard to related effects such as optical transparence. Exemplarily, the materials will also be

analyzed via transmission electron microscopy (TEM) to give an outline on the chapter, discussing structural properties in detail. These properties dependent on the nanoparticle surface modification will then separately be discussed for the whole series of prepared materials applying SAXS. The latter method is more representative for the macroscopical material compared to TEM, as explained in chapter 3.1. Finally, the effect of nanoparticle surface modification on mechanical properties will be studied and correlations between interfacial chemistry, structure and properties will investigated. Surface engineering changes to interface engineering within this chapter.

3.2.1 Thermoplasts as matrices: polystyrene (PS)

This first chapter gives an outline on the issues and problems related to the preparation of polymer nanocomposites. As PS was found to give the most reproducible molecular weight distributions and is easy to prepare by having a full monomer conversion in *in situ* polymerization approaches, it represents a simple model system. To keep the system simple, the isotropical, spherical-shaped, SiO₂ nanoparticles (larger as well as smaller) have been exclusively applied here. The full correlation of chemical and structural effects from SAXS-data, will of course deal with all model particle systems. In this chapter only exemplarily the larger nanoparticles are applied, for two reasons: Firstly, because they are visible in TEM to investigate ultra microtome thin cuts of the materials, embedded in a polymer matrix, which is not the case for the smaller ones, contrast and resolution is insufficient. Secondly, these larger nano-objects make the optical properties of the system rather sensitive towards agglomeration, which is desirable in terms of homogeneity studies. This means, as it will be discussed in this chapter that optical transmittance is affected higher by agglomerates of larger particles than of smaller particles when the degree of agglomeration, respectively the agglomerate size (given by the number of particles in one agglomerate), is the same. Larger objects in the light beam cause more scattering and thus a higher degree of transmittance losses. Accordingly, optical transmission may be an indication for the homogeneity of the prepared materials.

3.2.1.1 *In situ* bulk polymerization and characterization of the polymer matrix

The polystyrene nanocomposites were prepared via free radical initiated *in situ* bulk polymerization, utilizing the thermal decomposition of dibenzoyl peroxide (DBPO) to initiate the reaction. By dispersing the nanoparticles in monomer via ultrasonification, followed by a temperature program treatment under stirring, the nanocomposite preparation process was carried out. The matrix material for the other nanocomposite preparation methods, solution compounding an melt compounding, was prepared analogously, for reasons of comparison. ¹H NMR measurements revealed a monomer conversion of ~100.0%, as no residual double bonds could be detected after the polymerization reactions. This was the case for blank matrix samples as well as for nanofiller containing samples. FT-IR measurements also confirmed the full conversion of monomer. The matrix component was then analyzed via GPC which resulted in molecular weights of $M_w = 66500 \pm 10000$ g/mol with a polydispersity index (PDI)

of ~1.8-2.0 in average for all prepared samples. A representative example for a typical obtained molecular weight distribution from GPC measurement is depicted in Figure 105. In this case, the mass weighted molecular weight M_w is 64000 g/mol and the PDI is 1.8.

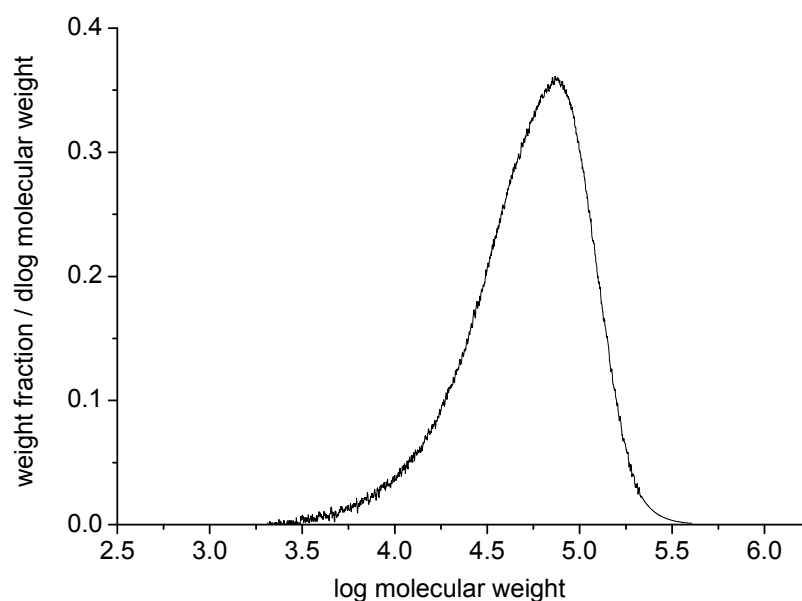


Figure 105. Molecular weight distribution from GPC of a typical PS matrix from *in situ* polymerization.

DSC measurements revealed glass transition temperatures T_g between 98-102°C, where the lower values have been obtained for high filler content samples when the particles did not contain surface bond polymerizable groups. This is considered to result from viscosity enhancement during the progress of polymerization, which affects the overall polymerization process. However, the differences in case of PS are considered negligible and the T_g values are in the range around 100°C which is typical for PS materials.^[415]

3.2.1.2 PS nanocomposites from molecular modified nanoparticles

First, SiO₂ nanoparticles, surface modified with different molecular coupling agents have been used in nanocomposite synthesis via *in situ* polymerization in the concentrations of 3, 5 and 10 wt%. DTMS-, PhTMS- and Styr-TMS- modified, as well as unmodified nanoparticles have been applied to study the effect of the organic group on homogeneity and transparency of the final nanomaterials. As concluded from prior dispersion experiments, all these modified particles are considered to be hydrophobic and thus fit to the hydrophobic PS matrix. However, this is not the only requirement for the preparation of homogeneous polymer nanocomposite materials, as it will be shown in the structural characterization (SAXS) chapter (0), where the full structure-interface chemistry correlations will be discussed in detail. In this chapter, only the strongest effects concerning dispersion quality will be highlighted. A typical sample series, as directly obtained from the polymerization process without further processing, is shown in the photograph in Figure 106. The samples consist of unmodified SiO₂ large nanoparticles in PS. The nanocomposites were yielded in form of disks with 2.4 cm diameter and 1.0 - 1.5 cm height. The materials shown in Figure 106 are non-

transparent and turbid. Smaller amounts of nanoparticles yielded opaque materials. This is the result of a insufficient interfacial match between the unmodified SiO_2 surface and polystyrene which led to agglomeration.



Figure 106. Photograph of *in situ* polymerized polystyrene SiO_2 (large, unmodified) nanocomposites, from left to right: upper row: blank matrix, 3 wt% and 5 wt% small SiO_2 , lower row: 10 wt % small SiO_2 , 3 wt%, 5 wt% and 10 wt % large SiO_2 nanoparticles content, captured stirring beads and some gas bubbles are also visible.

The TEM image of an ultra microtome thin cut of 5 wt% SiO_2 large nanoparticle containing PS, Figure 107 left, points out: Agglomerates or aggregates in the micron size range are the result of poor interfacial match and the cause of the materials turbidity. For comparison, when the same amount of nanoparticles, modified with an end group that is structurally very similar to the monomer (styryl-groups), is applied, single dispersed nanoparticles and thus homogeneous nanocomposites are the result (Figure 107 left). The other two chemical modifications, DTMS and PhTMS led to nanoparticle dispersion qualities in between these two extreme situations of unmodified and styryl- modified systems. Therefore, no representative TEM image could be found pointing out the actual dispersion situation in a valid way. SAXS investigations in following chapters will allow that precisely. The actual role of the end group (chemically similar, linking / non linking) will also be discussed in the structure-property chapter in more detail.

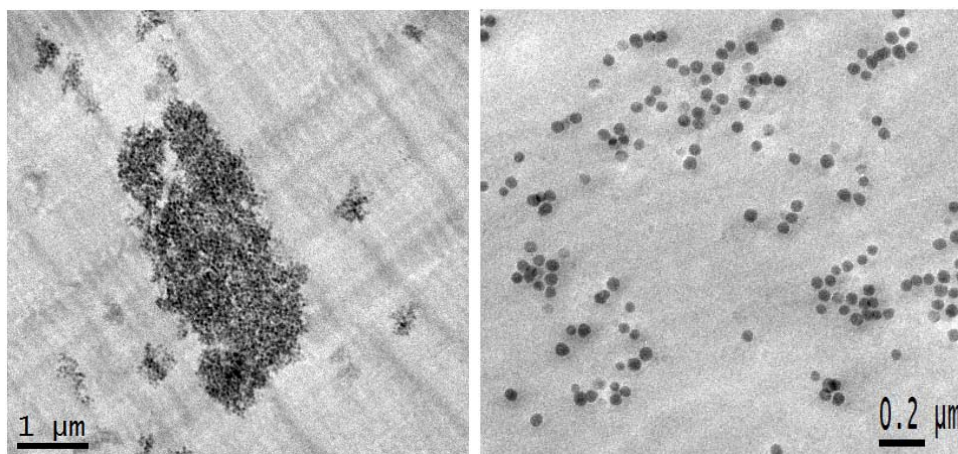


Figure 107. Representative TEM micrographs of ultra thin cuts (100-300 nm thickness) of 5 wt% unmodified SiO₂ large nanoparticles (left) and 5 wt% Styr-TMS@SiO₂ large nanoparticles (right) in PS, prepared via *in situ* bulk polymerization.

The observations made up to now match with the results given in literature and go one step further. In literature, one systematic study on the dispersion behavior of differently surface modified SiO₂ sub-micron *Stöber* particles in polystyrene has been carried out by *Lee et al.*, which is a comparable system as used in this present study. They could observe that unmodified nanoparticles led to the formation of large agglomerates and macroscopic phase separation occurred within the composite. When they applied surface modifications which are chemically similar to the matrix, such as phenyl-, or polymerizable groups, such as vinyl-, smaller agglomerates could be observed.^[64] In this work, both of these important parameters, chemical similarity and polymerizability of particle surface modifications, are combined through the use of styryl-groups. The result are almost single dispersed nanoparticles within the PS matrix.

3.2.1.3 PS nanocomposites from PS shell nanoparticles

As indicated by the results from the previous chapter, the more chemically similar the end groups on the inorganic nanoparticles, the more homogeneous is the final nanocomposite material when *in situ* polymerization is applied. Therefore, as a further step of interfacial matching, the PS grafted SiO₂ particles have been tested applying *in situ* polymerization. To obtain uniform sample specimen to allow precise investigations on transparency, the *in situ* polymerized samples have been compression molded to give exactly 0.25 mm thick plates. This is important when UV/VIS transmittance measurements should be compared. As a matter of the good chemical interface fit, the nanocomposites were rather homogeneous, which can be seen in the photograph in Figure 108. Photographs of the compression molded samples of PS@SiO₂ in PS nanocomposites are shown. For low filler content, the materials are transparent, for higher filler content, even for 10 wt%, they show good translucent properties. The TEM micrograph of an ultra thincut of the 5 wt% filler containing sample in Figure 109, shows the high dispersion quality of these interface-tailored nanomaterials. No significant difference in the dispersion quality before and after the hot pressing step could be observed.



Figure 108. Photograph of compression molded, *in situ* polymerized, PS@SiO₂ large in PS. Plates with a thickness of 0.25 mm, from left to right: upper row: blank matrix, 3 wt% filler, lower row: 5 wt% filler, 10 wt% filler.

Taking a closer look into the nanostructure of this sample by TEM, the material can be considered as disperse on a nanoscale (Figure 109). However on a macroscopic level, the nanoparticle concentration varies through the material. This seems to be a (technological) homogenization issue for the PS@SiO₂ and could not be observed for molecular modified SiO₂ systems.

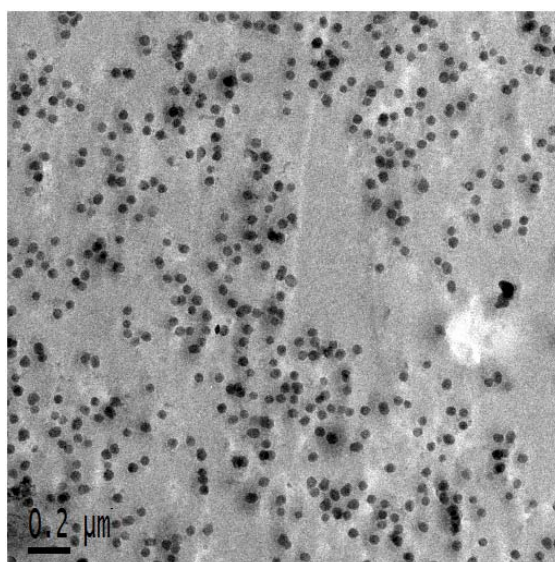


Figure 109. Representative TEM micrograph of ultra thin cuts of 5 wt% PS@SiO₂ large nanoparticles in PS, prepared via *in situ* bulk polymerization.

The investigation of optical transparencies of these nanocomposites, was carried out by UV/VIS-light transmittance measurements through the material, in the spectral range of 200 to 800 nm. The sample platelets prepared via hot pressing were used for this purpose. These

measurements do not only the characterization of the optical materials properties towards its application, the results also allow conclusions on the homogeneity of the materials. Agglomerates or aggregates are larger obstacles in the light beam and thus scatter light stronger according to *Rayleigh's* law, which is formulated in Eq. 8. It describes the increasing intensity of scattered light with increasing particle or agglomerate diameter within the nanocomposite material, which is responsible for non-transparency.^[51]

$$\frac{I}{I_0} = e^{-\left[\frac{3\phi_p \cdot x \cdot r^3}{4\lambda^4} \left(\frac{n_p}{n_m} - 1 \right) \right]} \quad \text{Eq. 8}$$

Thereby, I is intensity of the transmitted light and I_0 the intensity of the incident light. The transmittance T (%), as shown in the UV/VIS transmittance spectra, is the quotient of these intensities. The radius r is the radius of spherical particles scattering the incident light. n_p and n_m are representing the refractive index of the particles and the matrix, ϕ_p the volume fraction of the particles and x is the optical path length. In the experiment, the radius r only corresponds to the particle size if the nanoparticles are single dispersed. When agglomerates or aggregates are present, r also represents the agglomerate size. One important parameter which is crucial for transparent properties of such heterogeneous materials is the refractive index difference between particle and matrix. When $n_p \sim n_m$, the exponent in Eq. 8 is \sim zero, which means that the particle size does not affect the light scattering intensity. This situation is called index matching. Applying *Rayleigh's* law, it can be further deduced that the particle size has to be very small when transparent materials should be achieved. High differences of refractive indices require a particle diameter below 40 nm, when transparent materials should be prepared.^[51] This fact has been shown for various nanoparticle filled polymer nanocomposites within several experiments in literature.^[43, 51] For the materials described in this present work, the refractive index of the matrix n_m is $n_{589\text{nm}, 25^\circ\text{C}, \text{PS}} = 1.59-1.60$ ^[429] and the refractive index of the particles is $n_{546\text{nm}, 25^\circ\text{C}, \text{Stöber}} = 1.453$ ^[430] (the refractive index of typical *Stöber* particles). As the refractive index difference is not very high in this case, the condition of refractive index matching is nearly given. Thus, according to Eq. 8, the here applied larger nanoparticles with a diameter of approximately 60 nm diameter (TEM) result in transparent PS-nanocomposites. Therefore, when stronger scattering losses can be observed, these losses are considered to derive its origin from agglomeration. The UV/VIS transmittance spectra of the large PS@SiO₂ nanoparticle series in PS, 0.25 mm platelets containing different filler amounts, are shown in Figure 110. As the thickness of the specimen was the same, no normalization or calculation of extinction coefficients is necessary to compare the transmittance values directly compared. In the range of the visible light, from 400 to 800 nm, which is important in terms of application, an average transmittance value of $T_{\text{VIS}} = 92.1\%$ for the neat matrix of polystyrene could be calculated from the experiments. The fact that even the matrix material does not show 100% transmittance is considered to be due to reflection and scattering phenomena at the specimen-air interface due to surface roughness. However, the specimen are all comparable and show the same surface roughness due to their processing by using a polished metal stamp. Further, a self-light-absorption of the matrix has to be

considered. A slight darkening due to the hot pressing could be observed which leads to a lower optical transmittance. T_{VIS} for the 3 wt% containing sample was 90.3, 89.6 for 5 wt% and 86.8% for the 10 wt% filler containing sample. With a difference in transmittance of only a few percentages, the two samples with the lower filler content can be considered as transparent. This is caused by a relatively low refractive index difference in the material and the small size of the scattering objects. These results point out the homogeneity of these samples. However, for the 10 wt% filler containing sample, the appearance changes from transparent to translucent (see also photograph in Figure 108). It is a common phenomenon for such thermoplast nanocomposites that, in most cases the agglomerate size is higher for higher filler content. This phenomenon has also been experimentally observed for similar PS/SiO₂ nanocomposites in literature.^[266] Larger agglomeration is responsible for lower optical transmittance in higher filler containing materials.

The incorporation of unmodified nanoparticles led to non-transparent materials even at lower filler degrees. Nevertheless, these samples are still translucent due to the good refractive index matching with $T_{\text{VIS}} = 87\%$ for 5 wt% unmodified large SiO₂ particles. Even such small differences in T_{VIS} , as observed here for different filler degrees, are considered to be significant when refractive index matching is nearly given (Eq. 8). In literature, for materials where the refractive index difference is much higher, e.g. ZnO ($n_p \sim 2$) nanoparticles in PS, similar optical transmittance properties between 90 and 85%, as obtained in this work for the neat matrix and for the nanocomposites, could be observed. However, the particles needed to be well-dispersed in this case which was only obtained for low filler concentrations around 1 wt% in this literature study.^[431]

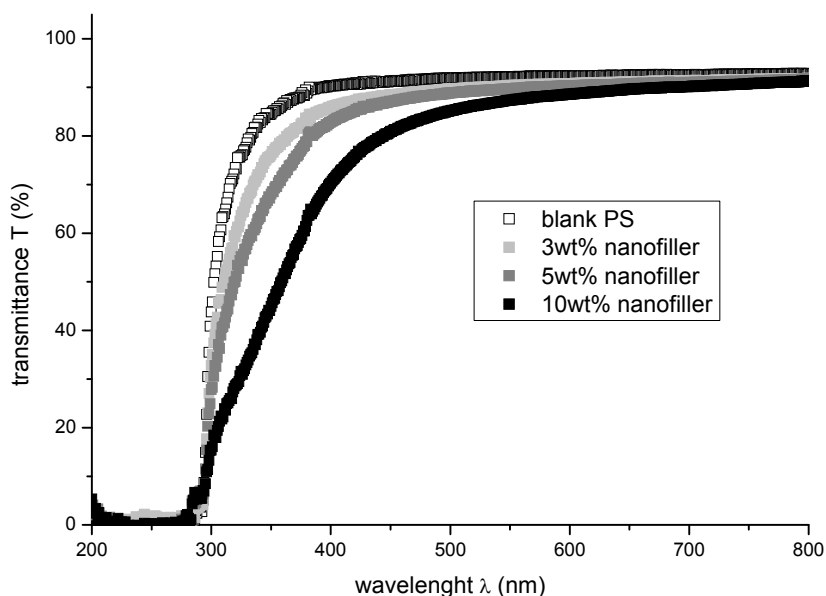


Figure 110. UV/VIS- transmittance spectra of 0.25 mm thick PS@SiO₂ in PS nanocomposites, prepared via *in situ* polymerization, and compression molded.

Generally, from the here observed results on homogeneity and the discussed literature, the following circumstances have to be considered when nanoparticles are applied within an

in situ bulk polymerization for the preparation of polymer nanocomposites. Even, when an interfacial match is given, which means that the nanoparticle surface modification is structurally very similar to the surrounding matrix system, inhomogeneities can occur. This can also be the case for the previously investigated molecular coupling agent modified particles. It has to be ensured that the polymer chains of the matrix are long enough to surround the particles, embedding them and sterically hindering the agglomeration. This seems to occur very well in the process of a surface grafting *through*, and is likely to be the case for the styryl- modified particles within this study. If the matrix polymer chains are too small, the particles tend to agglomerate.^[36] Precisely, following a general theory from literature for small (< 20 nm diameter) nanoparticles, the gyration radii of the polymer chains should have to exceed the effective nanoparticle diameter to allow a homogeneous dispersion by only thermodynamical driving forces.^[58] These requirements are considered to be fulfilled in the materials described in the present study because of the relatively high molecular weight of the applied matrix polymer. Additionally, when polymer shell nanoparticles are applied, a further requirement has to be fulfilled: The M_n of the matrix has to exceed the M_n of grafted chains to a certain degree. This phenomenon has been demonstrated in literature on a well-defined PS@SiO₂ in PS system, prepared via an affording nitroxide initiated polymerization. In this study in literature, it has been demonstrated that the ratio of molecular weights of matrix and grafted chains is crucial for the preparation of a homogeneous material, which is also according to the current theory. If M_n of the matrix is higher than M_n of grafted chains at the particles, the penetration of the shorter, free chains from the matrix into the grafted corona is facilitated. An entropic potential is built up which promotes the swelling of particle core with the surrounding matrix polymer, which is a highly favorable situation as thereby a homogeneous mixing is enabled. *Vice versa*, if M_n of the matrix is too small in relation to the M_n of the grafted chains, the latter are compressed and not wetted by the matrix. This effect can result in inhomogeneous materials.^[128] For the system of this present work, the M_n of the grafted chains from the particles is approximately three times higher than the M_n of the matrix. Thus, the described requirement is fulfilled, which can be observed by the good homogeneity of the prepared materials.

In conclusion this approach was suitable for the preparation of homogeneous polymer nanocomposites by two different means. The modification of SiO₂ particles with styryl-groups and with polystyrene chains resulted in homogeneous materials when *in situ* polymerization was applied. The use of core-shell particles makes the whole materials preparation process more affording. These particle systems can also be used for other preparation techniques such as melt- or solution-compounding, where the advantage of a surface grafting *through* could not be exploited.

Hence, other methods for the preparation of PS nanocomposites have been studied, solution compounding and melt extrusion, applying PS shell SiO₂ particles. The resulting materials were compared with materials where other surface modifications have been used. The idea within this study was to disperse the PS@SiO₂ nanoparticles in the PS matrix via a solution-compounding approach which should enable a facile mixing of PS with a higher content of

the particles. The resulting material with high particle content could then be used in form of a master batch for melt extrusion. Such technological considerations are of importance as *in situ* bulk polymerization can not easily be controlled on a larger scale. The solution compounding process was carried out using THF as a dispersion medium for the particles and also to dissolve the matrix-PS. THF was selected because from its chemical structure, it cannot be expected that the interaction of this solvent with one of the components is exceeding the particle/matrix interaction. The latter would affect the homogeneity of the final material. The components have been mixed applying magnetic stirring. After evaporation of the solvents, the nanocomposite material could be obtained. Small and large PS@SiO₂ nanoparticles with 3 wt%, 5 wt% and 10 wt% filler degree have been used. A TEM micrograph of an ultra thincut of a 5 wt% PS@SiO₂ large nanoparticles in PS, solution compounded, is shown in Figure 111. The presence of single dispersed particles and a nano-homogeneous system is thus confirmed.

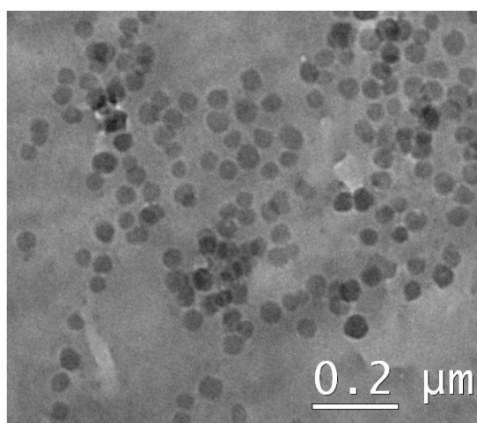


Figure 111. Representative TEM micrograph of ultra thincut of solution compounded 5 wt% PS@SiO₂ large in PS nanocomposite.

To investigate on the applicability of the described nano-solution-compounds for melt extrusion, they have been studied without further dilution with PS, for comparison reasons. Melt-compounded samples have been prepared by melting these compounds and mixing them in a laboratory extruder with counter rotating screws. To compare also different surface modifications, DTMS modified and unmodified particles have been applied within these extrusion experiments.

A temperature of 220° has been applied to the mixture in the extruder for 10 minutes. This is already close to the decomposition conditions but was necessary to lower the viscosity especially for the high filler content materials and make the materials processable. The detailed technical parameters are given in the experimental section of this work. The parameters such as rotating speed and temperature were selected, taking into account the limitation of temperature given by a strong darkening of the material at higher temperatures and the allowed pressure in the apparatus. The latter increased with increasing screw rotating speed, due to the addition of filler that enhanced the viscosity. Higher rotating speed introduces more shear force which is favorable in terms of homogeneous mixing, but thereby

the system pressure increases. Therefore, optimum working conditions had to be found. Photographs of the melt-compounded samples applying the PS@SiO₂ as obtained from the extruder, are shown in the photograph in Figure 112. Samples with higher filler content are more colored. This is considered to be due to degradation phenomena which occur when higher energy is put into the system. From literature it is well known that polystyrene shows significant degradation in extrusion processes, even at lower temperatures when high shear stress is present. Such thermal degradation results from oxidation or depolymerization reactions.^[432, 433]

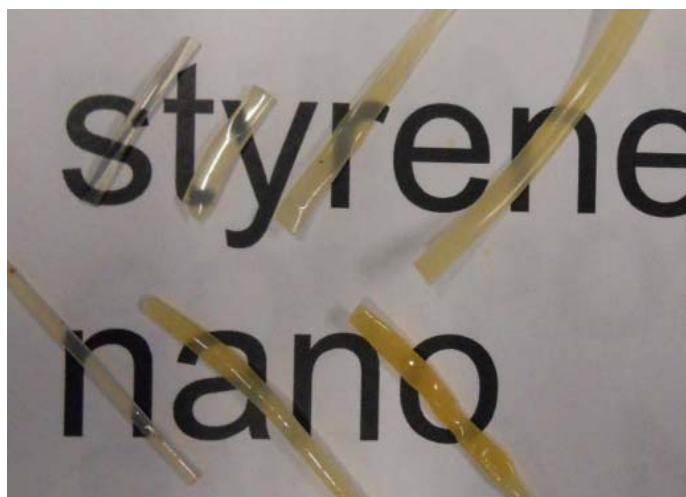


Figure 112. Photograph of extrudes samples of PS@SiO₂ in PS: from left to right: upper row: blank PS, 3 wt%, 5 wt% and 10 wt% large SiO₂ nanoparticle filler, lower row: 3 wt%, 5 wt% and 10 wt% small SiO₂ nanoparticle filler.

A TEM image of an ultra microtome thin cut of the 5 wt% PS@SiO₂ large containing sample after extrusion is shown in Figure 113. From TEM it is indicated that the agglomeration has slightly increased due to the melt processing, pointing out that polymer melts at high temperature behave differently than monomer suspensions or polymer solutions. It seems that de-mixing is thermodynamically favored under these conditions, which should not be the case, as discussed previously, if the PS shell is intact. Thus, it is considered that a partial degradation, e.g. via depolymerization or oxidation etc., of the PS shell is responsible for the slight increase in agglomerate formation. Basically, in this extrusion approach the mechanical forces are the driving forces for homogeneous mixing. Thus it was for example possible in a study in literature to use inorganic nanoparticles with large PS shell to incorporate them in poor compatible poly(ethylene terephthalate) (PET) and obtain homogeneous materials if they were pressed to thin layers by applying strong mechanical force.^[434] This means that systems which are appropriate for *in situ* polymerization or solution compounding are not necessarily optimal for melt-compounding and *vice versa*. Via melt extrusion, it can be possible to homogeneously mix non interfacial matching materials under appropriate rheological conditions. For example *Acierno et al.* were able to prepare homogeneous nanocomposites in a laboratory extruder by mixing unmodified Aerosil silica nanoparticles into polystyrene,

even though they observed a particle flocculation in the melt. This was possible, because they were able to introduce high shear forces.^[31]

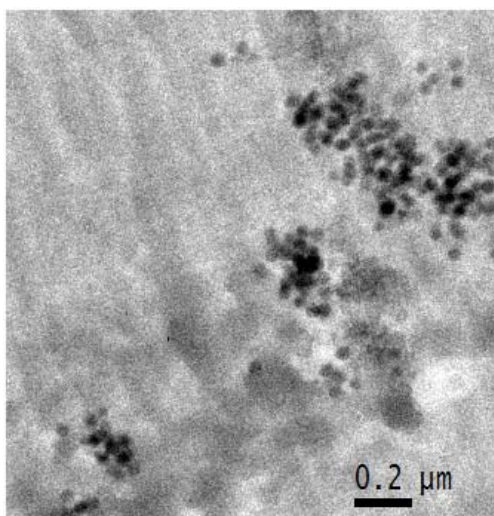


Figure 113. Representative TEM micrograph of ultra thin cut of extruded 5 wt% PS@SiO₂ large in PS nanocomposite sample.

Nevertheless, materials prepared in the present work are homogeneous enough to appear transparent, which can be seen in the photographs of the compression molded samples (0.25 mm thickness) in Figure 114: All composite samples contain 5 wt% SiO₂ large filler with different surface modifications. The details on the right side of the figure show that in case of unmodified SiO₂ large agglomerates in the mm range are present, already visible to the unaided eye. When PS@SiO₂ has been applied no such strong agglomeration is visible, also not for the DTMS modification.



Figure 114. Photograph of extruded 5 wt% SiO₂ large nanoparticles with different surface modification in PS, prepared via melt-extrusion and compression molded to 0.25 mm plates. The overview picture shows, from left to right, in the upper row: blank PS (also extruded), unmodified SiO₂ (detail right upper picture), lower row: DTMS@SiO₂, PS@SiO₂ (detail right lower picture).

A more detailed comparison of the effect of surface modification on transparency is given in the UV/VIS transmittance spectra in Figure 115. For a better comparison of the optical transmittance the curves are only shown between 400 and 800 nm light wavelength as in the UV region the materials are non-transparent. Again, because of the relatively good refractive index matching, the extinction is not very high even when agglomerates are present, for these reasons small differences ($\sim 1\%$) in transmittance have to be considered as significant according to Eq. 8. Generally, the transmittance values are slightly lower for all samples compared to the values obtained for *in situ* polymerized samples, because of a slight darkening during the extrusion process. The average transmittance values in the visual range T_{VIS} are 91.3% for the blank matrix, 87.3% for the neat SiO_2 , 89.4% for the DTMS modified and 88.6% for PS-grafted particles. It is clear that unmodified nanoparticles led to less transparent nanocomposite materials. The transmittance curve in the higher wavelength region for PS@ SiO_2 in PS shows similar transmittance values than the bare matrix. However, the transparency at lower wavelength, around 500-600 nm decreases faster with decreasing wavelength, because this sample contained more absorbing impurities due to degradation. Due to this transmittance behavior, the sample is considered to be homogeneous in terms of nanoparticle dispersion quality. Furthermore, the DTMS@ SiO_2 sample showed acceptable transparency over a wide spectral range and no macro-agglomerates.

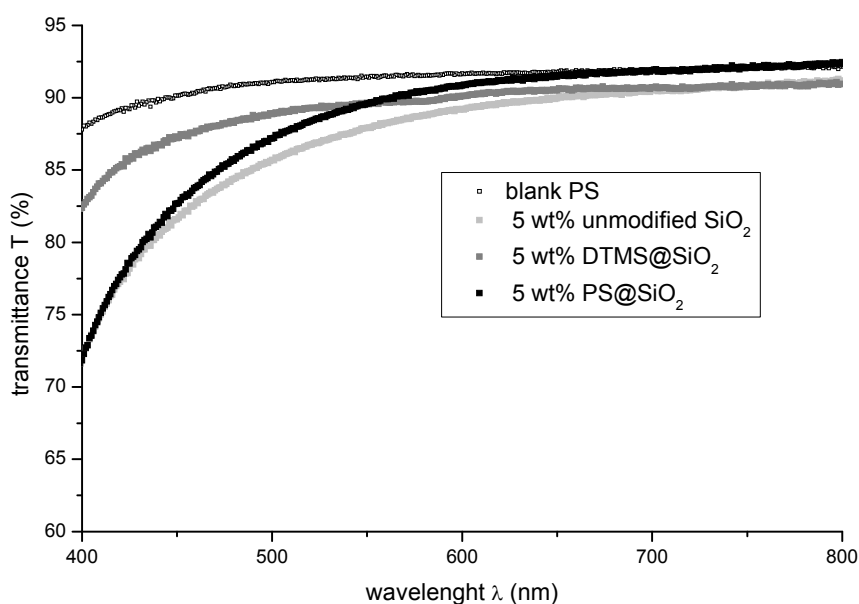


Figure 115. UV/VIS- transmittance spectra (visible light range is shown) of 0.25 mm thick 5 wt% differently surface modified large SiO_2 nanoparticle containing PS nanocomposites, prepared via melt extrusion, and compression molded.

Thus, it has been demonstrated that the prepared nanomaterials can be manufactured applying the technologically important process of melt extrusion, resulting in high optical transmittance values for the polymer nanocomposites, even when larger nanoparticles were applied. Furthermore it can be concluded that via dispersion experiments (DLS) in organic solvents or

monomer (e.g. styrene) only an indication is given, whether a prepared composite material (polystyrene) will be homogeneous (TEM) or not. Many additional parameters, given by the nature of polymer materials, have to be considered. It was shown how to produce homogeneous nanocomposites using surface modifications which are chemically similar to the matrix, under appropriate conditions.

The generality of the here made assumptions on interfacial matching will be proven applying other polymer matrices such as PMMA and crosslinked epoxy resins in more systematical and extended studies. Also ZrO₂ nanoparticles will be studied. Furthermore, the indications on the nanocomposites structure given by examples of TEM and UV/VIS measurements, will be proven in the structural-chemistry chapter when SAXS will be applied for different particle containing materials, which should allow a better comparison.

3.2.2 Thermoplasts as matrices: poly(methyl methacrylate) (PMMA)

This chapter will point out the issues associated with the preparation of PMMA nanocomposites, which are discussed for selected representative examples by TEM images and UV/VIS transparency results as well as by the optical appearance of the prepared materials. Through this, first assumptions on the influence of nanoparticle surface chemistry and, thus, nanocomposite interface chemistry on the dispersion structure, will be made. PMMA nanocomposite series including 3 wt%, 5 wt% and 10 wt% SiO₂ (small or large) or ZrO₂ (small or large) nanoparticles, as well as samples with 15 wt% filler content for selected examples, were previously prepared. Within this process the unmodified nanoparticles as well as the modifications DPPA, MA-C2-PPA, MA-C10-PA for ZrO₂ and DTMS, MA-C3-TMS and MA-C10-TMS for SiO₂ were applied. These types of chemical surface modifications have been selected for a further study of the influence of hydrophobicity and functional end group on the dispersion structure. Two different alkyl spacer chain lengths have been applied to introduce different hydrophobicity. By comparing samples with dodecyl and MA-decyl-moiety (similar chain length) the influence of the functional end group on the dispersion structure will be shown later on. The finally deduced structure-interface chemistry relations within the series of the samples prepared in this work are discussed by using SAXS derived results in a following chapter. Furthermore, the chemical characterization of the matrix material will be discussed. The spherical SiO₂ nanoparticle system is a widespread approach in the fields of materials chemistry and materials science as well as for the study of PMMA nanocomposites.^[30, 47] This is due to the fact that the nanospheres lead to a defined model system as well as to their relatively low refractive index difference. As will be proven in this chapter, transparent materials can more easily be prepared. It is more difficult to obtain transparent materials by applying ZrO₂ as compared to SiO₂ because of the higher refractive index difference within the material, as it will be demonstrated. This difficulty has to be overcome by interface-tailoring. The thus prepared ZrO₂ / PMMA system, as described in these studies, can be considered as a novel material.

All PMMA nanocomposites were prepared by *in situ* bulk polymerization of particle dispersions in monomer by making use of the free radical generating initiator azobis isobutyronitrile (AIBN), by applying a defined temperature program with a pre-polymerization step at 55°C and a final polymerization step at 80°C. Thereby, the monomer conversions were >99.1-99.5% (^1H NMR). Further on, small amounts of residual double bonds could be detected (NMR, FT-IR) in the products. This is a common problem occurring in the process of bulk polymerization of MMA, especially when inorganic fillers are incorporated additionally *in situ*.^[36] The presence of small amounts of oligomers may also contribute to the problem, which would further explain the variations in glass transition temperature T_g , that could be detected between 103 and 119 °C (the values scatter). The T_g values of common, atactic PMMA are usually in the range between 106 - 113°C, but they are distinct for a specific polymer system.^[435] Because these variations in conversion may affect mechanical properties, all samples were hot-pressed at 160°C before mechanical testing. After this treatment no residual double bonds or uniform T_g values could be detected. For all structural characterization methods (TEM, SAXS, etc.) these small differences in the matrix material can be considered to lead to no significant effect. The polymer system is defined with an average molecular weight of $M_w = 298000 \pm 70000$ g/mol with a PDI between 1.3 and 1.5, determined by GPC, for the prepared series. These are common values in industrial applications of PMMA.^[436] A representative molecular weight distribution from GPC with a M_w of 340000 g/mol and a PDI of 1.4 is shown in Figure 116. A slight peak tailing (towards lower M_w values) indicates the presence of a small amount of oligomer compounds. On grounds of this high molecular weight it is assumed that the requirement for homogeneous nanocomposites are given, as for the matrix side. The polymer chains of the matrix are long enough to surround the particles in a network, as discussed in detail for PS in the previous chapter, 3.2.1. From a structural point of view, all PMMA samples described in this work, as well as the PS samples from the previous chapter, were amorphous, which was the result of SAXS and wide angle X-ray scattering (WAXS) measurements.

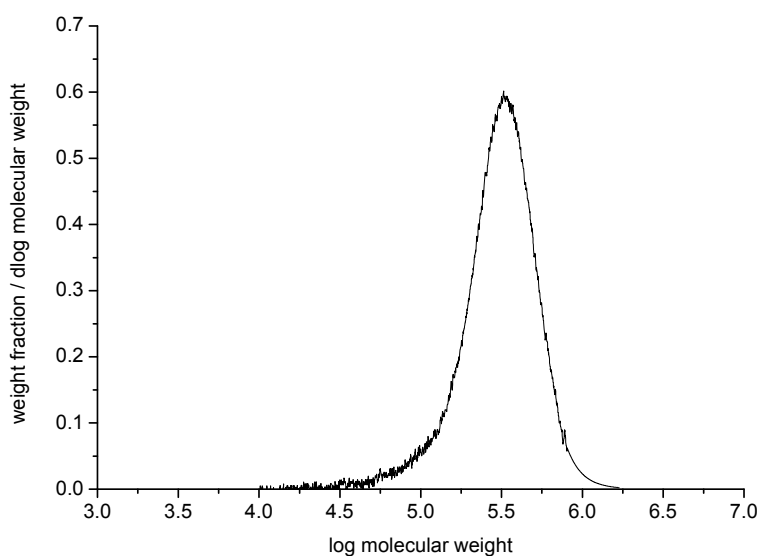


Figure 116. Molecular weight distribution from GPC of a typical PMMA matrix from *in situ* bulk polymerization.

In situ bulk polymerization yielded PMMA nanocomposite disks with a diameter of 2.4 cm and a height of ~1.0 cm. Figure 117 shows typical samples, filled with SiO₂ particles, in two different sizes and with different filler contents. Surface modification was applied and led to homogeneous nanocomposites, see later TEM investigations. Thereby, the samples, including particles with small sizes (~7 nm diameter from TEM), appear to be transparent even at the thickness of ~1 cm, according to Eq. 8., because they were not strongly agglomerated. As a matter of fact the larger nanoparticle containing samples (~60 nm diameter from TEM) were less transparent. The transparent properties in this case are also a result of the relatively good refractive index matching ($n_{546\text{nm}, 25^\circ\text{C}, \text{Stöber}} = 1.453^{[430]}$, $n_{\text{PMMA}} = 1.49^{[435]}$). For nanoparticle samples without appropriate surface modification, however, the materials appeared more turbid because of agglomeration.



Figure 117. Photograph of *in situ* polymerized PMMA / MA-C10-TMS@SiO₂ nanocomposites, from left to right: upper row: blank matrix, 3 wt% and 5 wt% small SiO₂, 10 wt % small SiO₂, lower row: 3 wt%, 5 wt% and 10 wt % large SiO₂ nanoparticle content.

With regard to the ZrO₂ nanocomposites, primarily the ZrO₂ large (38 nm diameter from TEM) system will be discussed here as the particle size effect on transparent properties can be more clearly demonstrated thereby, taking into consideration that the optical transparency is more sensitive towards the presence of larger nanoparticles. The photograph of selected ZrO₂ / PMMA nanocomposite samples in Figure 118 underlines how difficult it is to obtain transparent materials from ZrO₂. DPPA modified systems were completely non-transparent, they appeared to be white. MA-C10-PA, which was the most suitable modification in terms of homogeneity, the application of modified particles resulted in transparent materials but showed a strong typical *Rayleigh* scattering at the same time. This effect can be observed especially when the sample is illuminated (Figure 119). This phenomenon is due to the fact that the refractive index difference between the two compounds is rather high ($n_{589\text{ nm}, \text{ZrO}_2} = 2.1^{[103]}$, $n_{\text{PMMA}} = 1.49^{[435]}$). Therefore, at the average large particle size of ~38 nm diameter (TEM, only peak of distribution, which means also larger particles are present), according to Eq. 8, scattering intensity losses are higher for light transmittance. On the other side, high refractive index components, incorporated into a polymer matrix, can be used intentionally to tune the refractive index of the final composite materials if the particles are homogeneously dispersed: This is possible as the total refractive index is given as approximately the average

of n_p and n_m by a linear mixing law.^[43] Polymer nanocomposites with a higher refractive index than the blank matrix are thereby yielded.



Figure 118. Photographs of *in situ* polymerized PMMA / ZrO₂ nanocomposites, left image: 3 wt% and 5 wt% large DPPA@ZrO₂ filler content, right image: 5 wt% MA-C10-PA@ZrO₂ (sample contains captured gas bubbles).

From the optical appearance of the ZrO₂ / PMMA nanocomposites, in Figure 119, there are further indications for the material to be homogeneous even at high filler amounts of 15 wt% (apparently no percolation is given at this point, because in that case white samples would be expected). At the same time the material has a characteristic optical appearance due to *Rayleigh* scattering at the particles. The homogeneity of these ZrO₂ / PMMA samples will be further investigated with TEM and SAXS. A further investigation will also verify the indications stated in this part.



Figure 119. Photograph of PMMA nanocomposites with 5 wt% MA-C10-PA@ZrO₂ large (lying) and 15 wt% MA-C10-PA@ZrO₂ large (standing).

The influence of the interface chemistry on the dispersion structure on the nanoscale can already be presumed by taking a look at TEM-images of ultra microtome thin cuts of the prepared materials. In Figure 120, the dispersion quality of DTMS@SiO₂ and MA-C10-TMS@SiO₂ large nanoparticles (5 wt% filler each) can be seen. The structure of smaller SiO₂ nanoparticles containing samples could not be visualized in that quality by applying TEM. The reasons are explained in detail in chapter 3.1.1, but they will of course be discussed in the SAXS chapter. In contrast to MA-C10-TMS@SiO₂, where the particles are single dispersed in a homogeneous way in the matrix, the DTMS@SiO₂ particles form agglomerates that have a diameter of around 1 micrometer or smaller. These agglomerates are homogeneously distributed over the whole material and responsible for the optical non-transparency. This proves the importance of the functional end group for the achievement of homogeneous nanocomposites. Several effects are responsible for the good dispersion achieved in the methacrylate end group modified sample. As the methacrylate end group of MA-C10-

TMS@SiO₂ is structurally and chemically very similar to monomer and polymer, a good interfacial fit can be assumed. Thereby, the C10 chain provides hydrophobicity to the material. The dispersion quality can further be positively influenced by copolymerization with the particle end groups and the organic matrix. Additionally, due to the end groups steric demand, lower dense packing of the hydrophobic chains (as compared to the DTMS system) can be assumed. This helps to avoid the "zipper effect" (see chapter 3.1). All the effects investigated in the previous chapters of this work indicate that, for DTMS modifications, the inter-particle interaction dominates. For MA-C10-TMS, which is a molecule with similar alkyl chain length but having a methacrylate end group, the particle-matrix interaction is predominant, leading to a homogeneous distribution of the particles in PMMA.

Moreover, it is important to provide hydrophobicity as the application of unmodified nanoparticles resulted in very large agglomerates (above micron size) and are thus not shown in TEM images. Also, the shorter MA-C3-TMS modification led to larger agglomeration, deduced from the optical properties of these samples. These assumptions are plausible in the light of existing theories in literature about systems concerned with *in situ* polymerization of SiO₂ nanoparticles in PMMA. *Shipp et al.* incorporated commercial SiO₂ nanoparticles, modified with MA-C3-moiety, into PMMA ($M_n \sim 100000$, thus comparable with the here described system). By preparing a well-defined polymer system generating RAFT (reversible addition-fragmentation chain transfer) polymerization approach, they demonstrated that the polymer chains are grafted *through* the nanoparticle surface during the *in situ* polymerization. Through this they obtained much more homogeneous nanocomposites as was the case when they applied unmodified nanoparticles.^[30] Taking a look at the TEM images used in their work, the particles used for the MA-C10-TMS modification are agglomerated and not single dispersed, as it is the case in this present work. It is assumed, in this work, that the C10 chain brings a further improvement in dispersion quality by providing enough hydrophobicity to the particle surface. Yet, hydrophobicity is not the only important parameter, as could be demonstrated by the example of DTMS modified SiO₂. The profit gained by the use of methacrylate end groups at nanoparticle surfaces during the preparation on homogeneous PMMA nanocomposites, has also been demonstrated by *Schmidt et al.* They applied the MA-C3-moiety via organosilane anchor group also to Fe₃O₄ nanoparticles and held this specific end group responsible for the obtained good dispersion quality as compared to what quality they would have obtained when the same molecule without a methacrylate group would have been applied. Furthermore, they point out the importance of the use of the trimethoxysilane end group: They also used di- and monomethoxysilane end groups for surface modification to introduce the MA-C3 moiety, but the trifunctional anchor system gave the highest grafting density.^[42]

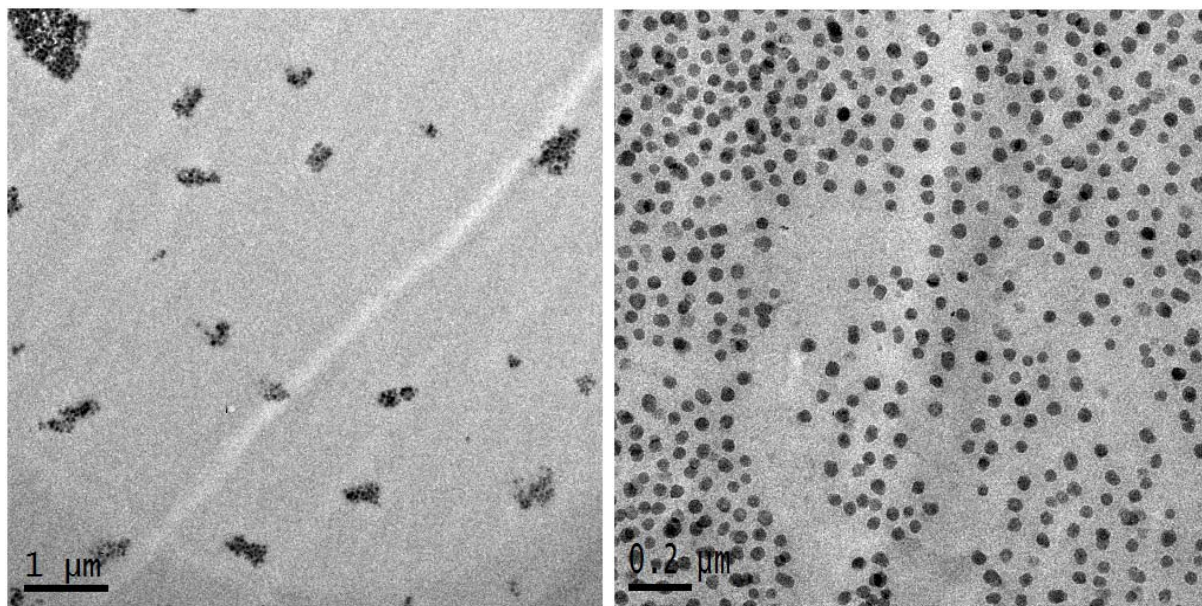


Figure 120. Representative TEM micrographs of ultra thin cuts ($\sim 100\text{-}300$ nm thickness) of PMMA / SiO₂ large nanoparticle nanocomposite, containing 5 wt% inorganic filler, left: DTMS@SiO₂, right: MA-C10-TMS@SiO₂.

An analogous behavior can be observed in Figure 121 in the ZrO₂ / PMMA system, where TEM images of the similar DPPA@ZrO₂ and MA-C10-PA@ZrO₂ in PMMA are compared. The application of only one long alkyl chain led to stronger agglomeration. In contrast, when an additional methacrylate end group was applied, the nanoparticles were homogeneously dispersed in the polymer matrix. The DPPA modified particles were even more strongly agglomerated as in the case of SiO₂. The crystal shape of ZrO₂ (also given for the smaller crystallites of ZrO₂ large here) and the resulting stronger SAM effect (inter-particle bilayers - "zipper effect") on the dispersibility may be responsible for that. The effects described for SiO₂ (influence of polymerizable group: structural similarity and grafting *through*) are considered to be responsible for these results. Again, the application of unmodified nanoparticles resulted in rather macroscopically inhomogeneous materials. In that case it was not deemed useful to investigate these materials with TEM. In general, the smaller ZrO₂ nanoparticles showed a similar behavior. These samples, as well as a comparison of long (C10) and short (C2) alkyl chain spacer modification, is discussed in detail in the SAXS part later in this work.

Nanozirconia / PMMA nanocomposites, prepared via *in situ* polymerization, are currently of great interest in materials research. For example *Li et al.* used calcined ZrO₂, containing low surface OH groups, and incorporated the particles without surface modification into PMMA. However, they do not show representative TEM images or other characterization results to visualize the quality of the nano-dispersion.^[46] Nonetheless, *Hu et al.* recently demonstrated that this surface treatment leads to homogeneous nanocomposites. They used a methacrylate modification for ZrO₂ nanoparticles, adsorbed to the ZrO₂ surface via alcohol group on the other alkyl chain end of the organic molecule.^[75] In the present studies, a more stable

attachment of the methacrylate moiety via phosphonic acid group is present. In this present work, as well as in the work of *Hu et al.*, the importance of this polymerizable end group, also with regard to the preparation of homogeneous ZrO_2 nanocomposites, was demonstrated. Long before the investigations carried out by *Hu et al.* and *Li et al.*, *Demir et al.* applied the simple ODPPA molecule for the surface modification of nano ZrO_2 and incorporated the particles into PMMA via *in situ* bulk polymerization. They obtained a rather agglomerated system (revealed by TEM), comparable to the DPPA system as also described in the present work.^[36] The results for $\text{DPPA}@ZrO_2$ revealed in this work are thus state of the art. The comparison of these literature examples make the advantage of the here described MA-C10-PA modification clear. When both, a longer alkyl chain and a methacrylate end group, are applied, the material is more homogeneous. This result was obtained by applying the simple procedure of redispersing a nanopowder in monomer with low mixing forces.

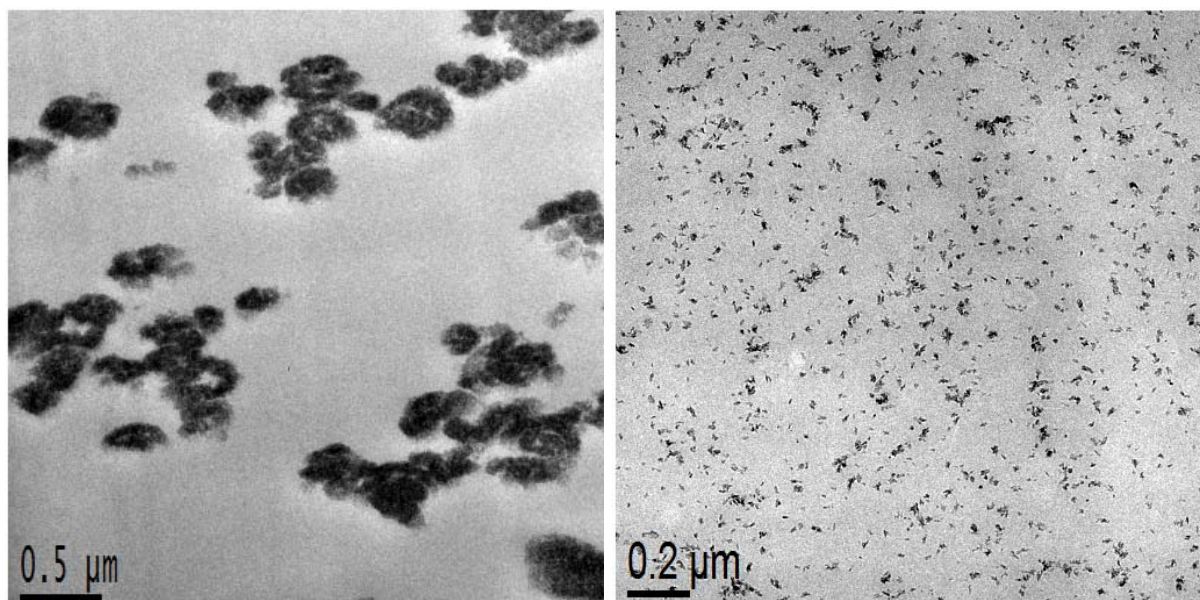


Figure 121. Representative TEM micrographs of ultra thin cuts ($\sim 100\text{-}300$ nm thickness) of PMMA / ZrO_2 large nanoparticle nanocomposite, containing 5 wt% inorganic filler, left: $\text{DPPA}@ZrO_2$, right: $\text{MA-C10-PA}@ZrO_2$, it has to be kept in mind that the average diameter of 38 nm (TEM) of the larger particles represents only the peak value of the size distribution of a certain broadness – this explains why much smaller particles can be observed here too.

The influence of surface modification on the transparent properties of the PMMA nanocomposites will be exemplarily shown by applying UV/VIS transmittance measurements for representative systems. The best transparent materials were obtained by applying small SiO_2 nanoparticles (~ 7 nm diameter, TEM), which is explained by *Rayleigh's* law, Eq. 8. An appropriate surface modification is crucial for transparency, which can be seen in Figure 122, a photograph of 0.25 mm thick nanocomposite plates (hot pressed at 150°C with 2 tons) containing unmodified and MA-C10-TMS modified nanoparticles. The sample including unmodified nanoparticles appears turbid due to the presence of agglomerates that are visible

to the unaided eye. This was not the case for the MA-C10 modified sample. These platelets were used for UV/VIS measurements. The resulting spectra are shown in Figure 123.



Figure 122. Photograph of hot pressed, 0.25 mm plates of PMMA nanocomposites for UV/VIS measurements, from left to right: blank PMMA, 5 wt% MA-C10-TMS@SiO₂ small, 5 wt% DTMS@SiO₂ small.

The samples containing 5 wt% nanoparticles show a similar transmittance behavior for the whole spectral range to the bare PMMA matrix. Unmodified particle PMMA with the same filler amount, however, causes higher light scattering losses. The average values for optical transmittance in the visible range (400-800 nm wavelength) T_{VIS} are 93.6% for blank PMMA, 92.8% for modified filler containing PMMA and 89.3% for unmodified filler containing PMMA. Due to the low refractive index difference, these differences in transmittance values are considered to be significantly representative for the dispersion quality of the nanoparticles.

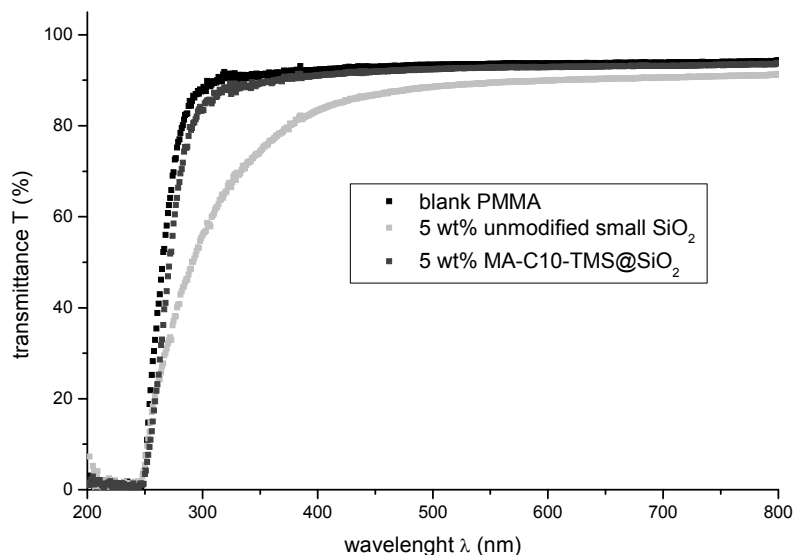


Figure 123. UV/VIS transmittance spectra of differently modified small SiO₂ nanoparticles in PMMA (0.25 mm platelets).

Also allyl-PDMS-PPA and ⁿBu-PDMS-PPA modified small ZrO₂ nanoparticles, incorporated in 3 wt%, 5 wt% and 10 wt% amount, have been used for the preparation of PMMA nanocomposites and will be analyzed with SAXS and mechanical tests in detail in the following chapters. As discussed in chapter 3.1.5, the particles were relatively well-

dispersible in the monomer, which does not stand in contradiction to the expected behavior: As PDMS and PMMA are immiscible on a molecular level,^[245, 379] macroscopical phase separation was expected to occur in the here described composite materials. However, the grafting density of the particles (0.6 molecules/nm²) was rather low so that the particles were partially hydrophilic. This explains the relatively good dispersion of the particles in the monomer, see chapter 3.1.5. As regards the polymer, the dispersion is not ideal, as can be seen in Figure 124, a TEM image of an ultra thincut of a 5 wt% allyl-PDMS-PPA@ZrO₂ small nanoparticle containing PMMA sample. Agglomeration can be observed to a certain degree and the system has slightly de-mixed during the polymerization reaction. However, the system can be considered nano-disperse, which is necessary for the mechanical tests. Further on, mechanical property effects will be discussed in respect of a successful unification of these three immiscible compounds. A high blending quality so that a hard ZrO₂ core is surrounded by a very soft PDMS shell which is incorporated in a moderately soft PMMA matrix is desired. The fact that the particles are not fully dense grafted is held responsible for the effect that no macroscopic de-mixing occurred. This is plausible, as it is more likely for low grafted systems that PMMA chains of the matrix penetrate the PDMS chains via the particles, forming a uniform material.

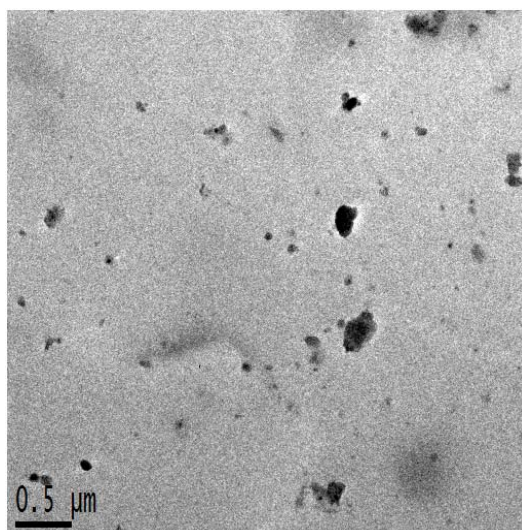


Figure 124. TEM micrograph of ultra thincut of 5 wt% allyl-PDMS-PPA@ZrO₂ small nanoparticles in PMMA.

To conclude on the prediction of dispersion quality in polymer matrix (TEM) from pre-experiments of dispersibility in monomer (DLS), the following statements can be made: In the case of the application of alkyl chain coupling agents, particles which were poorly dispersed in the monomer also led to poor dispersions in the final composite material. *Vice versa*, good dispersions in monomer led to good dispersions in the final polymer. For PDMS spacer coupling agents the situation was different: Good dispersion in MMA showed a slightly lower dispersion quality in the final PMMA material. This confirms the assumption that the crucial parameter for homogeneous nanocomposites is the interfacial match of particle with the matrix, not only of particle with the monomer, but the latter is a basic requirement.

Technologically, *in situ* prepared PMMA nanocomposites could be applied for transparent PMMA plates production. Extrusion experiments analogous to PS were not possible as the particle containing PMMA melt showed strong viscoelastic behavior. Thus, no homogeneous mixture could be obtained below the degradation temperature of the material by the utilization of a laboratory extruder. Not all materials prepared in this work via *in situ* polymerization considering every filler type and filler content were investigated with TEM due to the fact that each sample was measured with SAXS for structural investigations. The TEM images are only supposed to give a visual impression on how the nanoparticles are dispersed inside of the matrix. They should give an idea which dispersion state corresponds to a certain hard sphere volume fraction number, derived from SAXS.

3.2.3 Crosslinked polymers as matrices: epoxy resin nanocomposites

Crosslinked organic polymers, epoxy resins, were systematically studied in terms of interface engineering because of their great technological relevance, e.g. in coating applications. As a matrix system, an amine cured bisphenol-F based epoxy resin formulation (to yield better elastic properties of the final materials compared to bisphenol A based formulations) was applied by using an *in situ* curing approach. For a systematic study of the influence of specific organic surface modification on dispersion structure and mechanical properties, selected coupling agents have been applied. Molecules have been studied which provide differently strong interaction possibilities between particle and matrix. Furthermore, SiO₂ as well as the ZrO₂ nanoparticle systems were studied. Thereby, three different chemical types of organic moieties, attached to the inorganic particle surface, have been studied for the interface tailoring in the epoxy nanocomposites. The major goal in transparent nanocomposite preparation is to achieve a highly homogeneous dispersion of the particles in the matrix by enhancing the particle-matrix interaction. Therefore,

(ii) the widely used epoxide end groups which show excellent physical intermediating properties between inorganic-organic surfaces^[146] and covalently link the particles to the organic matrix^[53] as they can chemically react with the surrounding resin during the applied *in situ* curing approach, which may result in a higher dispersion quality,

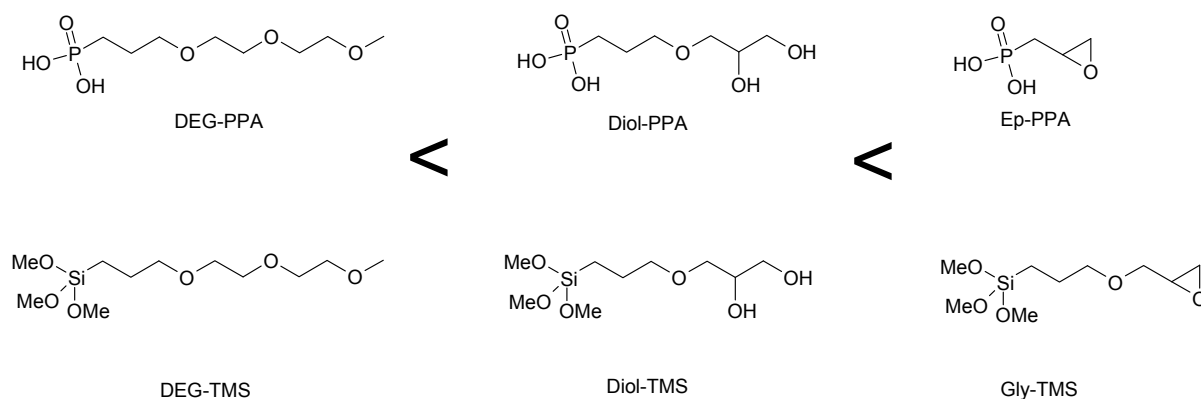
(iii) diol end groups as an less reactive analogon to the used epoxide end groups whereas the alcohol-end groups can also form a covalent bond to the epoxy resin during the reaction during the curing process. Interactions via hydrogen bonds with the polar organic component are also possible,^[276] resulting in a moderately strong interacting group (between DEG and epoxide),

(iv) and for comparison reasons, the easier available but, mostly not optimal dispersible system, non modified metal oxide nanoparticles which are in principle also equipped with the possibility to form stronger interactions between surface OH-groups and the resin^[437] as it is well known for layered silicate epoxide systems^[48]

were applied.

By applying these different surface modifications the possible interaction strength of the nanoparticle surface with the surrounding matrix could be varied from end groups that offer a strong (covalent) interaction at the interface (epoxy or OH- groups), to a medium strong interaction (e.g. hydrogen bonding via OH groups), and to weaker interactions (ethylene glycol derivatives, polar interactions) This is depicted in Scheme 12, where the applied coupling agents are lined-up by their possible interaction strength with the matrix compounds / monomers during the *in situ* curing approach.

Scheme 12. Possible interaction strength of particle surface with matrix for the studied different organic surface modifications.



The preparation of the nanocomposites was carried out via an *in situ* curing approach where the nanoparticles (3%, 5% and 10%) were dispersed in the molten monomer bisphenol-F-diglycidylether (BFDGE) applying only little shear force by magnetic stirring at 500 rpm for homogenization. Then the hardener was added, the aliphatic amine diethylenetriamine (DETA) which initiates the curing by nucleophilic attack of the amine group at the epoxy ring of the monomer. Finally, the reaction mixture was cast on an anti-adhesive coated metal plate and cured at 120°C. The formulation as well as the curing temperature program were selected according to standard procedures.^[269] The ratio between monomer and curing agent was selected in order to adjust the stoichiometrical ratio of BFDGE to DETA to 3.3, which is off stoichiometry giving an excess of epoxide groups, to obtain thermoset materials. By applying this procedure, 1.4 mm thick plates were obtained. During the curing procedure the following reactions of the nanoparticle surface with the reaction mixture are possible, and show an influence on the dispersion structure in the cured nanocomposite: Hydroxy groups from the nanoparticles surface can react with epoxides of the resin mixture but also epoxide groups from the nanoparticle surface can be attacked by the hardener molecule to form covalent bonds between the nanoparticles and the matrix. In the other cases at least strong polar interaction between particle and resin (DEG) or hydrogen-bond formation (OH) can occur and influence the later dispersion structure.

In general, the glass transition temperature (DSC and DMA) of all prepared materials was between 110°C and 90°C. The lowest values have been observed for silica containing samples. The thermal decomposition temperature for all samples was at 353 ±7°C (onset,

TGA). From this data it is concluded that the matrix properties, which means the curing behavior of the epoxy resin formulation, were not affected by the particle incorporation significantly. Yet, some trends in glass transition temperatures were observed, which will be discussed in the mechanical property-chapter.

Generally, the materials containing unmodified nanoparticles appeared translucent where some combinations of surface modifications and nanoparticle type appeared transparent, like DEG-PPA@ZrO₂ or Gly-TMS@SiO₂ in the epoxy resin, see Figure 125. Other surface modifications gave materials with an optical appearance between transparency and opaque. This already indicates that the application of an appropriate nanoparticle surface modification yields a higher dispersion quality in these materials. The effect of agglomeration due to the use of non optimal surface modifications on turbidity is, visually seen, much stronger for the ZrO₂ nanocomposites than for the SiO₂ containing materials. Again, this can be explained by the much higher refractive index difference between the two components in the ZrO₂ nanocomposite ($n_{589\text{ nm, ZrO}_2} = 2.1^{[103]}$, $n_{546\text{ nm, 25}^\circ\text{C, Stöber}} = 1.453^{[430]}$). The refractive index for common epoxy resins is between $n = 1.50$ and $1.56^{[438]}$ e.g. typically $n_{589\text{ nm, 20}^\circ\text{C, commercial}} = 1.56^{[439]}$ for a commercial bisphenol A based formulation. This difference leads to stronger light scattering losses when a light beam is transmitted through the material according to *Rayleigh's law*, Eq. 8, as discussed previously. In the case of SiO₂ the refractive index matching is very good. This means that also for rather agglomerated systems the materials appear transparent. In contrast, the transparency of the ZrO₂ system is highly sensitive towards the presence of agglomerates. This is visualized in the UV/VIS spectra in Figure 126. Here the good transparency yielding DEG-PPA@ZrO₂ small filled resins were compared to unmodified small ZrO₂ nanoparticles.

blank matrix



5% ZrO₂ unmodified



5% DEG-PPA@ZrO₂



5% larger SiO₂ unmodified



5% larger Gly-TMS@SiO₂



Figure 125. Photographs of nanocomposite plates containing (each 5 wt%) unmodified larger silica and zirconia nanoparticles leading to opaque materials as well as particles with appropriate surface modification leading to transparent materials.

The optical transmittance in the VIS range is significantly higher for the optimally modified nanoparticle containing materials. A transmittance 91.6% has been measured for the pristine polymer matrix. The incorporation of 5 wt% of unmodified ZrO₂ lowered the transmittance to 52%. A maximum improvement to 84% of a filled sample was achieved by DEG-PPA modification of the particles. For SiO₂ these effects on transparency were not as

tremendously. For 5 wt% larger SiO₂ unmodified particles T_{VIS} was 69% and 70% for the Gly- modified ones, even if TEM investigations show strong agglomeration for one case and high dispersion for the other case. This slight difference can be explained by the good matching of refractive index in the case of the SiO₂/epoxy material as compared to the ZrO₂/epoxy material. However, in the particle containing samples generally, slightly lower transmittances were recorded because of stronger embrowning (a common phenomenon for amine cured epoxy resins) of the materials and more bubble inclusion. This is very likely to be due to that fact that the curing reaction and also browning side reactions proceed faster in the presence of nanofiller in the curing formulation because the viscosity of the overall reaction mixture is enhanced. This is held responsible for the fact that even for the clear and transparent ZrO₂ materials (see photographs, Figure 125) the transmittance is lower than the matrix. This would also explain the steeper decrease of optical transmittance for nanoparticle filled epoxy resins, as compared to the matrix when going to lower wavelength in the UV/VIS transmittance spectra, Figure 126. However, in the case of thin film coating application this effect was not observed.

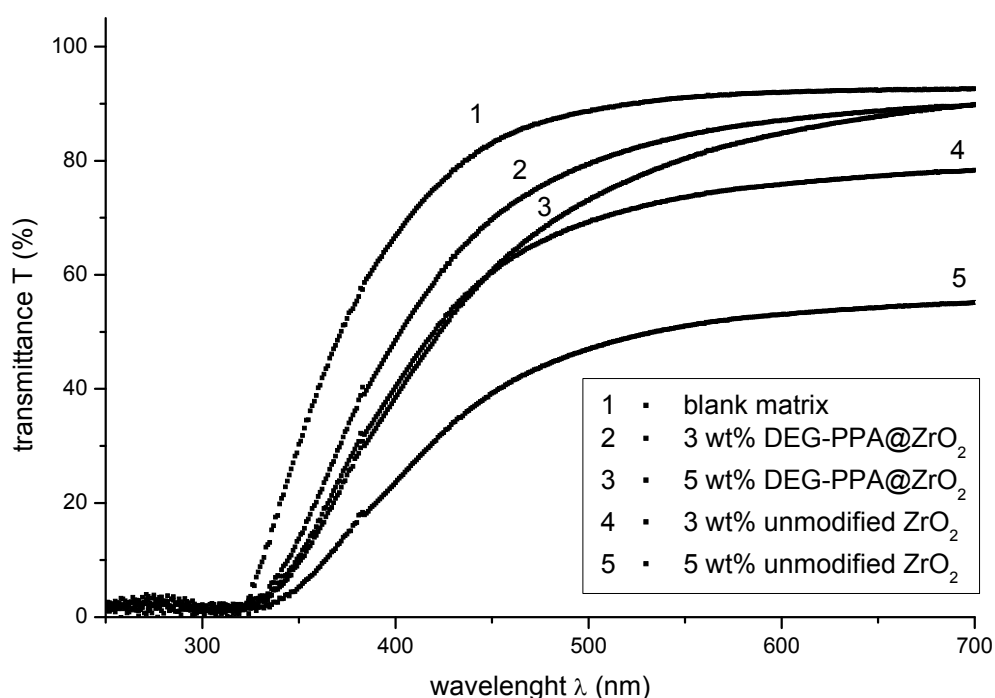


Figure 126. UV/VIS transmittance spectra of 1.4 mm thick epoxy resin nanocomposite plates, blank matrix and including small ZrO₂ nanoparticles in different percentages, with and without surface modification.

For a better insight into the dispersion structure, representative TEM-images of ultra microtome thincuts (100 to 300 nm thickness) of the nanocomposite materials containing 5 wt% nanoparticles with different surface modifications were recorded. Thereby, the systems containing ZrO₂ small and SiO₂ large nanoparticles, representing the dispersion behavior of these systems, will be exemplarily discussed. The ZrO₂ large system shows similar dispersion

behavior as also shown. Small SiO₂ nanoparticle containing materials are not discussed because of the poor quality of the TEM images. Figure 127 shows TEM micrographs of ZrO₂ / epoxy resin nanocomposites. Figure 128 shows TEM images of larger SiO₂ particles / epoxy resin nanocomposites, each with epoxy- diol- and diethylene glycol-interface tailoring as well as without surface modification. For the ZrO₂ nanocomposites the DEG- surface modification led to the best dispersion quality whereas the unmodified nanoparticles were slightly more agglomerated, which corresponds to the observed optical transparencies in Figure 125. The diol-modification lead to a formation of sub micron size particle agglomerates and finally use of epoxy end groups results in strongly phase separated materials. The SiO₂ nanocomposites do not follow this trend which has been observed for ZrO₂. The best results in terms of homogeneity could be observed for the epoxide end group modification, followed by the diol-modification. The degree of agglomeration was measured higher in the DEG modification and the highest in the unmodified systems.

A possible explanation for the high agglomeration in case of the epoxy modified ZrO₂ nanoparticles is the presence of a strong inter-particle interaction via co-linkage of surface epoxy group. This is very likely, even though the modification would chemically fit well to the matrix. For SiO₂ nanoparticles the opposite was the case. This different behavior may result from the fact that a strong interaction between the, crystal-shaped, ZrO₂ nanoparticles can occur. The possibility of irreversible inter-particle co-condensation can be considered to be higher for this higher plane contact areas than for the spherical SiO₂ particles which theoretically only contact each other via single points. Further, a highly homogeneous dispersion is observed and expected to derive from the compatibility of epoxide groups with the resin matrix. The presence of OH-groups on the particle surface, from the diol group from coupling agent as well as from the bare oxide surface, seems to allow a moderate interaction with the polymer, except in the case of SiO₂. Thus it is plausible that, at the synthetic conditions of amine-milieu at 120°C, a highly favored inter-particle silanol condensation (which is analogously not expected for ZrO₂) inhibits the formation of a homogeneous dispersion, even though the silanol groups show a good interaction with the epoxy resin matrices which has been reported in a previous study.^[437] This is another reason for the necessity of chemical surface tailoring of nanoparticles. SEM-investigations carried out by *Kang et al.* support this observation: When incorporated into an epoxy resin, unmodified *Stöber* particles showed high agglomeration compared to epoxide or amine modified nanoparticles^[52] that react immediately with the surrounding polymer environment to result in separated particles. Finally, the introduction of the DEG residue which provides good physical interaction with the epoxy resin matrix was less successful in the case of SiO₂ than for ZrO₂. Most likely, the dispersibility enhancement effect was not able to overcompensate for a possible inter-particle-co-condensation via residual surface silanol groups. It is assumed that, due to its spherical shape, in the described case the SiO₂ system sticks to the rule: The stronger the possible interaction between particle and matrix, excluding silanol condensation reactions, the more homogeneous the final material (covalent > H-bridges > polar-polar). For the ZrO₂ nanocrystals the opposite is the case as the inter-particle interaction predominates the particle-matrix interaction by applying strong interacting groups.

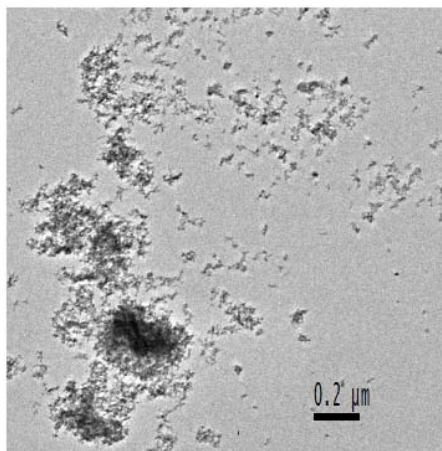
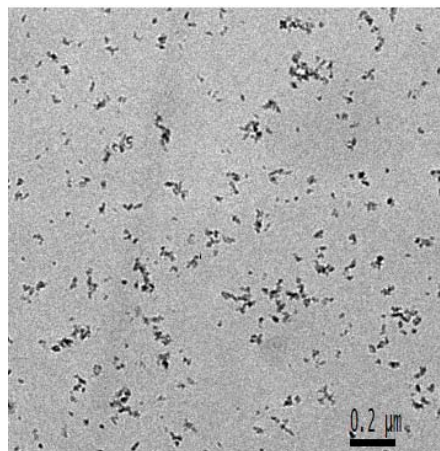
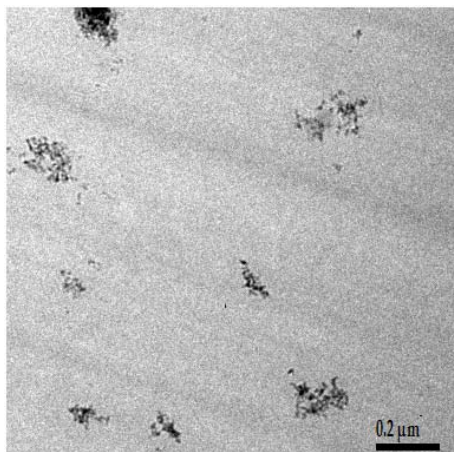
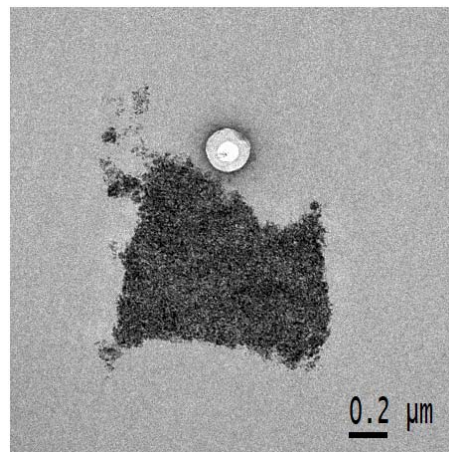
5% ZrO₂ unmodified5% DEG-PPA@ZrO₂5% Diol-PPA@ZrO₂5% Ep-PPA@ZrO₂

Figure 127. Representative TEM-images of ultra microtome thincuts (100-300 nm thickness) of 5 wt% ZrO₂ nanoparticle, with different surface modification, containing epoxy resin.

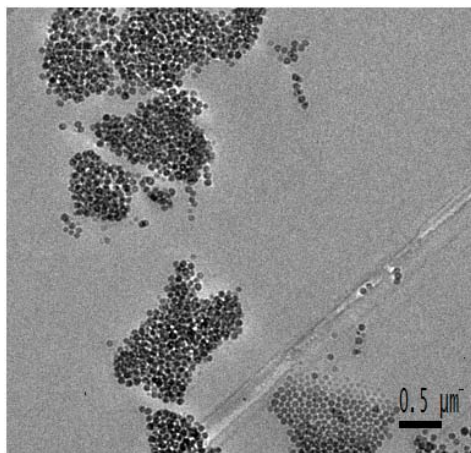
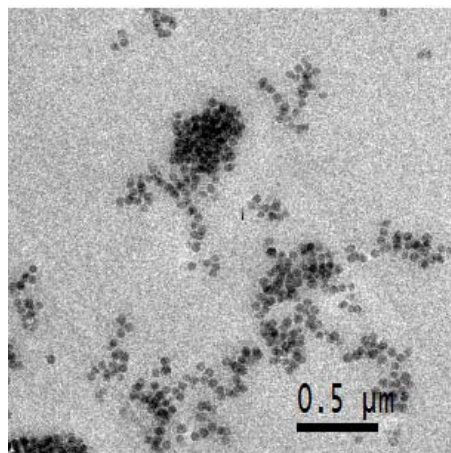
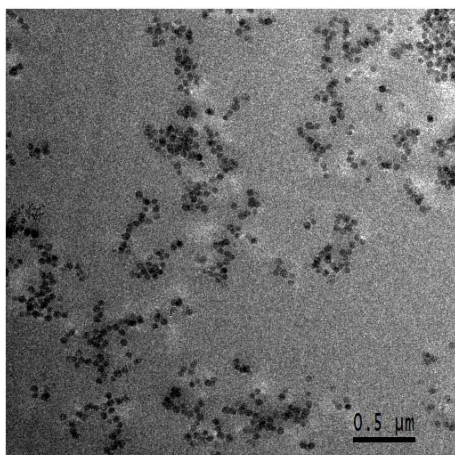
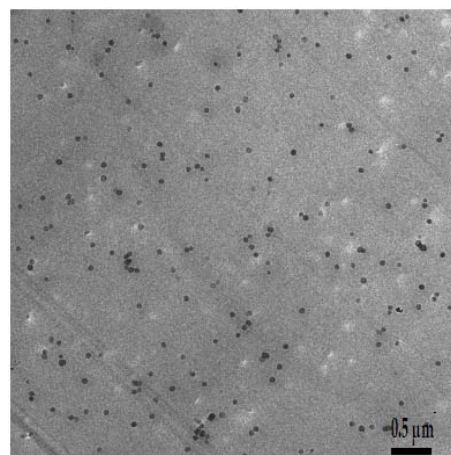
5% larger SiO₂ unmodified5% DEG-TMS@SiO₂5% Diol-TMS@SiO₂5% Gly-TMS@SiO₂

Figure 128. Representative TEM-images of ultra thincuts (100-300 nm thickness) of 5 wt% larger SiO₂ nanoparticle, with different surface modification, containing epoxy resins.

For demonstration purposes it is shown that when applying the optimum interface tailoring for SiO₂, and ZrO₂ respectively, also higher filler amounts lead to highly homogeneous nanocomposite materials. This can be seen by the TEM images for 10 wt% nanofiller containing materials in Figure 129.

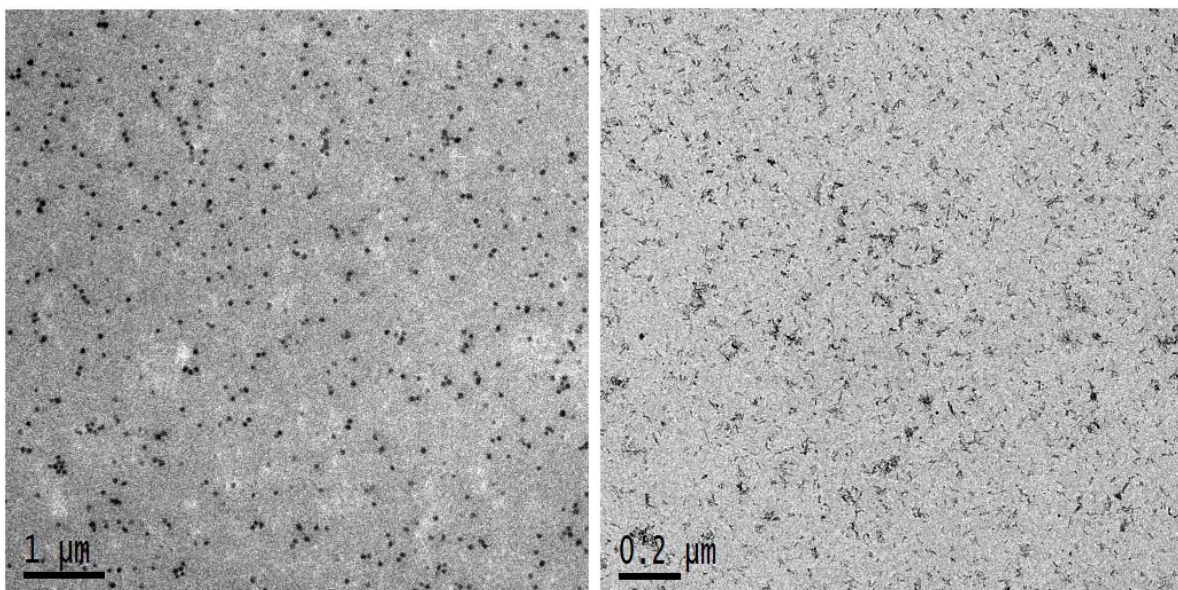


Figure 129. Representative TEM images of ultra thincut (~ 100 nm) of epoxy resin nanocomposites containing 10 wt% chemically surface-tailored nanofiller, left image: Gly-TMS@SiO₂ large nanoparticles, right image: DEG-PPA@ZrO₂ small nanoparticles.

The TEM-image in Figure 130 further demonstrates that the application of DEG-PPA as surface modifying agent also lead to the creation of homogeneous nanocomposites through the use of larger ZrO₂ nanoparticles.

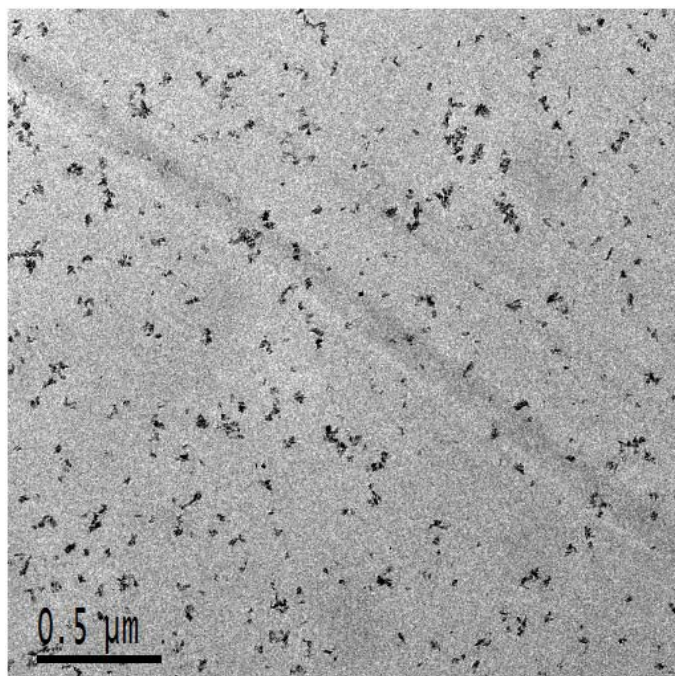


Figure 130. Representative TEM image of ultra thincut (~ 100 nm) of epoxy resin nanocomposites containing 5 wt% DEG-PPA@ZrO₂ large nanoparticle.

Within the course of applying DEG modified nanoparticles in epoxy resins, another important issue needs to be regarded. Epoxy resins show a specific water uptake as the matrix is hydrophilic even when no nanofiller is present. By following a standard procedure, the uptake of water is compared due to a storage of the materials in deionized water at increased temperatures was measured. The water uptake behavior can change if inorganic filler is incorporated. Furthermore, the water content of the materials can significantly influence their mechanical properties. For instance, construction parts can take up moisture from the air in application.^[271] Because the DEG modified nanoparticles showed hygroscopic behavior, as shown in water uptake experiments of modified nanopowders in chapter 3.1.4, it is expected that they influence the water uptake behavior of the final material to a certain degree.

The samples were dried and then immersed in water until mass stayed constant, which was given after 216 h, assigning the reached maximum uptake of water for each system. The water uptake of different DEG-PPA@ZrO₂ small nanoparticle filler percentage containing epoxy resins, is shown in Figure 131. A clear trend is visible: With increasing filler content, the water uptake of the overall material increases, by 2.8 wt% for the blank matrix and by 3.8 wt% for the 10 wt% filler containing material. This effect is considered to be significant and particle related, especially due to the hygroscopic surface of the DEG-modified particles. This assumption is reasonable because a comparison experiment with unmodified ZrO₂ nanoparticle containing materials showed no such trend. Unmodified ZrO₂ particle containing samples resulted in an average maximum water uptake of 3.0 ± 0.1 wt% for all samples from 3 wt% to 10 wt% filler content. In case of SiO₂ filled epoxy resins a similar phenomenon could not be observed. Well dispersed Gly-TMS systems, as well as unmodified systems with two different filler contents gave an average maximum water uptake of 3.0 ± 0.2 wt%. Taking these results into account the trend in Figure 131 may be considered significant.

Typical water uptake values for filler containing epoxy resin materials lie between 0.04 and 4 wt%^[440]. For instance, fumed silica filled bisphenol-F-based epoxy resin materials show a maximum water uptake of 2-3 wt%.^[271]

The trend in Figure 131 which seems to be linear for lower filler degrees and the increase in water uptake decreases for higher loadings. This is assumed to derive its origin from the following fact: In samples containing higher percentages of filler a smaller part of the interfacial area is available for water adsorption, as the particles are usually more agglomerated in materials with higher filler content. This trend appears to be a DEG-modification related effect. However, no conclusion can be drawn as to whether this effect originates from an interfacial swelling or from a lower crosslinking density of the matrix, which could be the result of the incorporation of these particle system.

Because of these water uptake phenomena and the fact that even the pristine material shows a high water uptake, the samples were stored under closed atmosphere conditions directly after curing. Afterwards they were tested via mechanical characterization methods to guarantee comparable and reproducible results. As for application objectives, such swelling phenomena are not considered to play a crucial role provided they remain controlled.

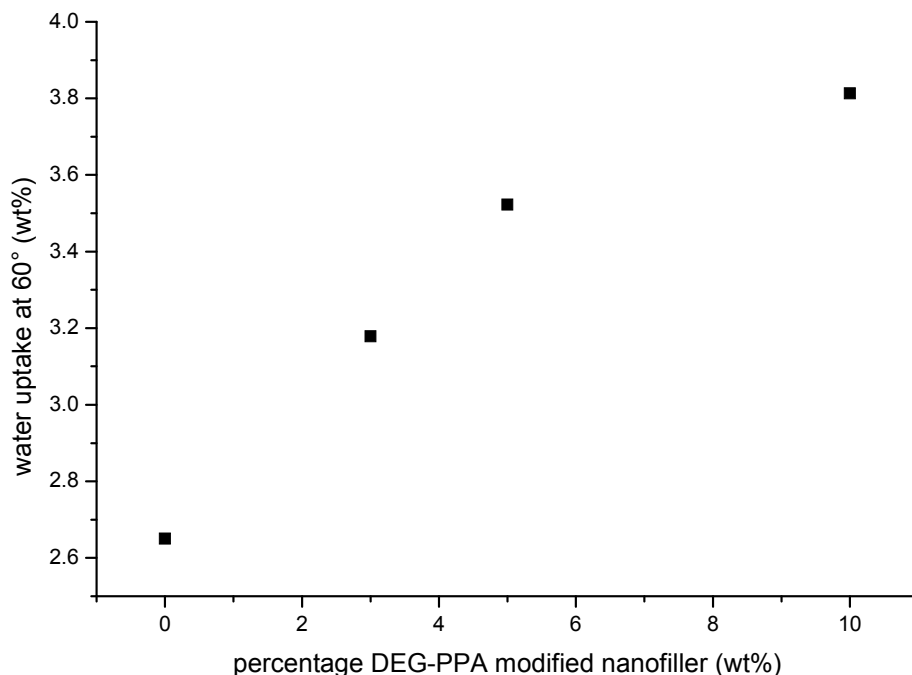


Figure 131. Water uptake at 60°C of epoxy resin nanocomposites with different filler amounts of DEG-PPA@ZrO₂ small nanoparticles.

Concerning application objectives, it has to be remarked that the covalent linkage of the DEG moiety to the particle surface via the phosphonate group is important with regard to the materials homogeneity. As discussed in chapter 3.1.4, during technological processes very often free DEG or PEO chains are applied for nanoparticle modification. This approach was tested under similar conditions by applying DEG and PEG400 as modifying reagents. The testing found non transparent materials. This leads to the assumption that due to the less stable attachment the modifying agent can diffuse into the reaction mixture, resulting in unmodified nanoparticles and thus in agglomerates.

Concludingly it may be stated that the dispersion quality is given by the interplay of several effects in this complex systems. On one hand, surface groups, like epoxides, allow a covalent interaction with the matrix and thus a better dispersion of the particles. On the other hand, homo-linkage between the particles may occur, resulting in agglomeration. When a maximum homogeneity should be reached via interface-tuning, predominantly the fact is important that the matrix-particle interaction has exceeded the particle-particle interaction. This effect can be seen in analogy to the copolymerization parameters in macromolecular chemistry. When polymerizable groups are present on the nanoparticle surface copolymerization occurs between particle and matrix. In this aspect, surface group as well as nanoparticle nature and shape are important for one reason: Via two crystal facets, as in the case of ZrO₂, the overall inter-particle interaction can become very high. This is due to the high contact area compared to the area which can be found when two spheres are in contact, as in the case of SiO₂. On one hand this may cause the effect that low interacting modifications, such as DEG for ZrO₂, give

an optimum homogeneity because the particle-matrix interaction is predominant. On the other hand, stronger interacting moieties lead to higher agglomeration because the particle-particle interaction dominates, as demonstrated in these studies. Additional SAXS studies will allow the discussion of the additional influence of the filler degree on the homogeneity and the assumptions made from TEM will be verified on a larger average.

3.2.4 Surface chemistry and interface chemistry

By the investigations carried out on differently surface modified nanoparticles, incorporated into different matrix systems by applying an *in situ* polymer formation process, the following conclusions on dispersion quality (from TEM and optical properties) can be drawn:

- The dispersion experiments of surface modified nanoparticles (analyzed via DLS in chapter 3.1) in liquid media, such as solvents and monomers, allow a rough estimation on the dispersion behavior in an organic matrix: If the nanoparticles are poorly dispersible in monomer compounds one can expect poor homogeneous nanocomposite materials. When the particles are well-dispersible in the monomer, however, homogeneous nanocomposites are likely to be obtained. Yet, this is no general rule: Specific requirements of the matrix condition, e.g. a certain molecular weight, need to be fulfilled as well.
- If the surface modification is similar to the matrix and monomer, in terms of chemical structure, the probability to obtain homogeneous nanocomposites is high.
- When applying thermoplasts within a radical polymerization approach, the application of polymerizable surface groups lead to more homogeneous materials as in the case of similar non polymerizable end groups. A surface grafting *through* effect of free polymer chains is held responsible for a substantial enhancement in the interfacial compatibility.
- Within the crosslinked epoxy resin system the situation was found to be rather complex: Various additional influencing parameters on the dispersion quality, such as the particle nature itself, were found to be relevant. For instance, groups which can covalently link matrix and particles, analogously to the thermoplasts system, can also link the particles more likely with each other in this system. In specific cases non polymerizable groups thus return optimum homogeneous materials. As a general rule, the matrix-particle interaction must be larger than the particle-particle interaction to obtain homogeneous nanomaterials. It is not merely the interfacial fit that plays an important role.

The assumptions stated here will be proven and investigated via SAXS in further detail within the following chapter on structure property relations.

3.2.5 Structure property relations

The overall goal of this chapter is to answer the question: How does the surface modification, a molecular structure, affect the nanostructure within the material and thus its macroscopic properties? These relations are of great interest in respect of systematical surface tailoring during the development of novel polymer nanocomposites and the prediction of their properties. Therefore, the type of chemical surface modification is correlated with the nanocomposite structure by applying macroscopical probe volumina. Surface chemistry is correlated with selected macroscopical mechanical surface properties. Concludingly, statements on the correlation of nanocomposite structure with mechanical properties will be made.

3.2.5.1 Interface chemistry – dispersion structure (SAXS)

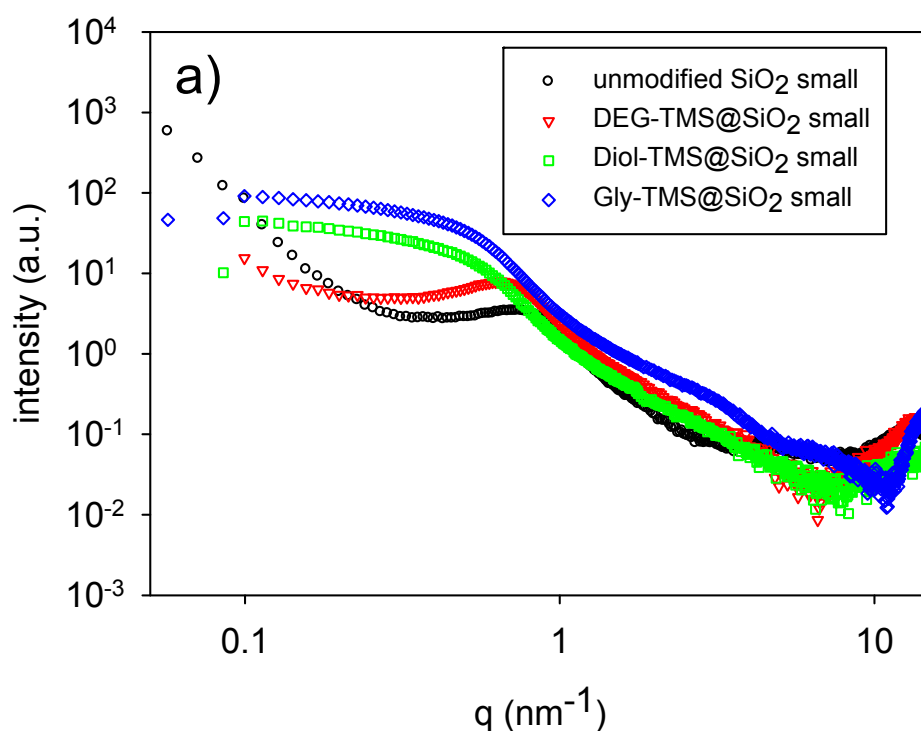
In this chapter a systematical correlation of parameters, such as surface modification type, particle nature, particle size and filler percentage, is carried out with regard to the agglomeration behavior of the particles in the investigated polymer matrices. As mentioned in previous chapters, SAXS is highly representative of the whole macroscopic material as the probe volume is in the mm^3 range, within which a large average of nanoparticles are responsible for the measured features. By way of comparison the discussed TEM-imaging of ultra thincuts only applies probe volumes in the nm^3 range. Additionally, SAXS allows the investigation of the small SiO_2 system, where no appropriate TEM images can be obtained because of the small particle size and the low contrast.

By applying SAXS, specific scattering curves are obtained in which the electron density of the inorganic nanoparticles and the polymer matrices (for the here applied components) is significantly different. Thus, signals and scattering features, resulting from nanoparticles only, can be detected and can further be set in relation to the study of agglomerated nanopowders in chapter 3.1.3.6. By applying the same theory as has been used for the study of powders (see chapter 3.1.3.6) for analysing the scattering curves, a certain hard sphere volume fraction value η can be calculated for each nanocomposite. This value is a number that represents the probability of finding neighbored particles in the direct vicinity of other particles. Simply speaking: The hard sphere volume η fraction represents the degree of agglomeration. It is the higher the more the particles are agglomerated and zero for single dispersed nanoparticles in the polymer matrix.

Up to now, by applying TEM, already a few relations between interface chemistry and nanocomposite structure have been recognized. These relations will be proven more precisely by applying SAXS. Yet, also the TEM images of the previous chapters are of high importance. They can be compared with the η values obtained for corresponding sample. This should give an idea which dispersion state is represented by a certain hard sphere volume fraction number. TEM provides better visualization, SAXS provides more representative values.

Epoxy resin nanocomposites

The epoxy resin nanocomposites, prepared in chapter 3.2.3, filled with 3, 5 and 10 wt% of differently surface modified (unmodified, diol-, DEG- and epoxide end groups) nanoparticles have been investigated via SAXS. The scattering curves with their corresponding fit curves, exemplarily for 5 wt% filler content, are shown in Figure 132. The systems of small and large SiO_2 nanoparticles and small ZrO_2 are investigated within this chapter. The SAXS-results for the large ZrO_2 nanoparticle containing materials are not shown. As these particles are of rather irregular shape, which decreases the representativeness of the SAXS-results, they are not discussed. However similar behavior as observed for ZrO_2 small nanoparticle containing materials has been observed. The scattering curves in Figure 132 (again) show characteristic features, as discussed in chapter 3.1.1.3. Shoulders (e.g. for small SiO_2 visible at $q \sim 0.8$), of the scattering curves between $0.1 \text{ nm}^{-1} < q < 10 \text{ nm}^{-1}$ result from the scattering of the X-ray beam at the particles. Already by taking a look on this scattering curves, statements on the dispersion quality (or *vice versa*, the particle dense packing) can be made. For instance in case of the small SiO_2 nanoparticles, the shoulder, respectively peak, at $q \sim 0.8$ which is the result of a particle dense packing. This phenomenon is very strong for unmodified nanoparticles and weak for glycidoxymodified nanoparticles, indicating their different dispersion behavior.



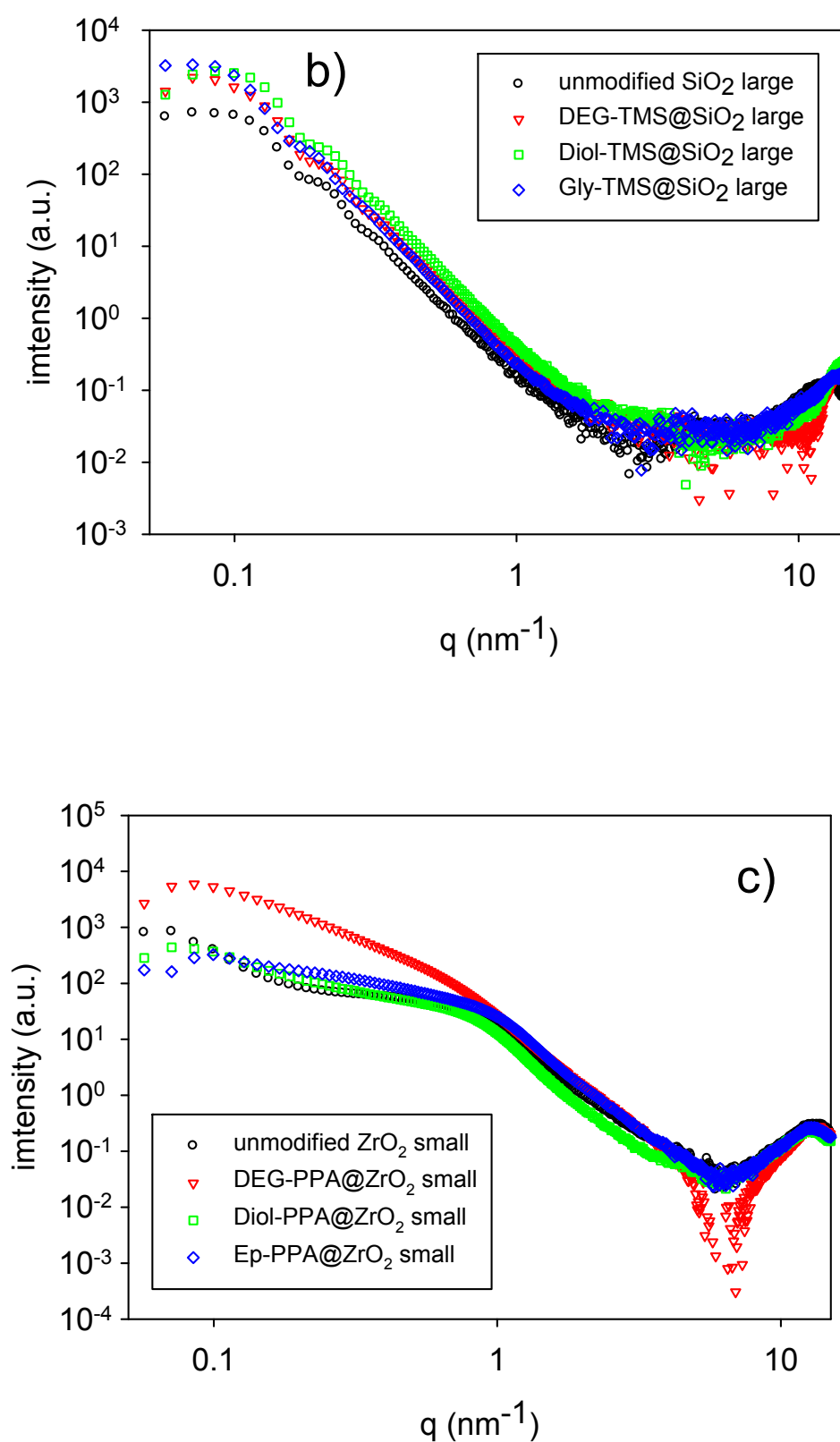


Figure 132. SAXS scattering curves, exemplarily shown for a 5 wt% inorganic nanofiller content of epoxy resin nanocomposites, a) small SiO_2 nanoparticle filler, b) large SiO_2 nanoparticle filler, c) small ZrO_2 nanoparticle filler.

From this scattering data, the hard sphere volume fraction values η , which represent the strength of agglomeration of the particles in the matrix, have been calculated and are listed in Table 27. The table visualizes the obtained results from SAXS corresponding to the observations made in TEM micrograph for all samples within one series of nanoparticle type and surface modification type. For higher observed agglomeration in TEM in the previous chapter, larger numbers of η have been obtained by SAXS. Namely, correlating interface chemistry and dispersion structure. Thus the following arguments can be advanced: For SiO₂ nanoparticle the strongest matrix interacting modification, Gly-TMS, lead to the lowest agglomeration, whereas weaker interacting modifications such as DEG and unmodified nanoparticles showed higher agglomeration degree. For ZrO₂ the matter was found to be *vice versa*: here for lower filler degrees, e.g. 3 and 5 wt% the dispersion quality decreases with increasing matrix interaction strength. Agglomeration is highest for epoxy < diol < unmodified (OH) < DEG. The reasons for this behavior have already been discussed in the corresponding chapter 3.2.3. The assumptions suggested on the relation between interface chemistry and dispersion structure are thus further proven by applying this method, which is representative for a much larger number of nanoparticles.

In general, the hard-sphere volume fraction is higher for silica than for zirconia nanoparticles. This seems to be due to a higher tendency of silica agglomeration as compared to zirconia agglomeration. The agglomeration of SiO₂ nanoparticles may also be supported by their perfect spherical shape (featuring a very narrow distribution) easing dense sphere packing or allowing to detect agglomeration with higher intensities in the corresponding scattering features. This is a common phenomenon occurring with uniform spherical silica particles, even if they are organically modified.^[133] Generally speaking, nanoparticles try to minimize their surface energy via agglomeration. This effect seems to be higher in the case of SiO₂. Enthalpy, which is commonly a crucial parameter for the dispersion of nanoparticles in polymer,^[58] may play an important role. This is also the reason why the η values for small SiO₂ nanoparticles are generally higher compared to the larger SiO₂ nanoparticles. Concludingly, SiO₂ nanoparticles can be more densely packed than irregular shaped ZrO₂ nanocrystals and thus, if agglomeration occurs, the η values are higher for the SiO₂ system.

Table 27. Hard sphere volume fraction values η for different percentages of surface modified SiO₂ and ZrO₂ nanoparticles in epoxy resin matrix, representing the particle agglomeration strength.

hard sphere volume fraction η from SAXS					
particle type	filler wt%	unmodified	DEG-PPA	EP-PPA	Diol-PPA
small ZrO ₂	3	0.045	0.001	0.097	0.073
	5	0.009	0.001	0.090	0.076
	10	0.008	0.020	0.090	0.049
filler wt% unmodified DEG-TMS Gly-TMS Diol-TMS					
small SiO ₂	3	0.132	0.145	0.060	0.025
	5	0.131	0.143	0.028	0.032
	10	0.121	0.144	0.036	0.042
large SiO ₂	3	0.174	0.160	0.148	0.099
	5	0.223	0.148	0.121	0.090
	10	0.156	0.188	0.079	0.110

For a better visualization of the values in Table 27 they are plotted in Figure 133, Figure 134 and Figure 135, which renders the discussions on agglomeration trends for each nanoparticle type series simpler. For the ZrO₂ nanoparticles (Figure 133) the agglomeration tendency from SAXS is the same as obtained from TEM. DEG-PPA modified particles give the best dispersion quality with η values close to zero which represents single dispersed particles (at 3 wt% and 5 wt%). Interestingly, for one type of modification the agglomeration can vary with increasing filler degree to lower or higher values, in some cases, even significantly. This is considered to be related to the interplay of two different counteractive phenomena. On one hand higher filler degree increases the viscosity which increases the shear force at the same stirring speed and thus breaks agglomerates (agglomerates collide and are thus broken, this is more likely at higher particle concentration). On the other hand, in thick suspensions the possibility for two particles to interact is higher. Thus, agglomerates can be formed when the inter-particle interaction dominates the particle matrix interaction. According to these assumptions, a study in literature on the shear thickening effect of silica nanoparticles in PEO underlines the complex viscosity changing behavior with suspension concentration. It could

be observed that the viscosity increases drastically for higher filler degrees over 7 %, depending on the nanoparticle size and polymer radius of gyration.^[441] Due to this result it was observed that in some cases the agglomeration curves showed a dispersion minima or a dispersion maxima. This was found to depend on the type of effect that is predominant and also on how good the matrix-particle interaction is in comparison to the particle-particle-interaction.

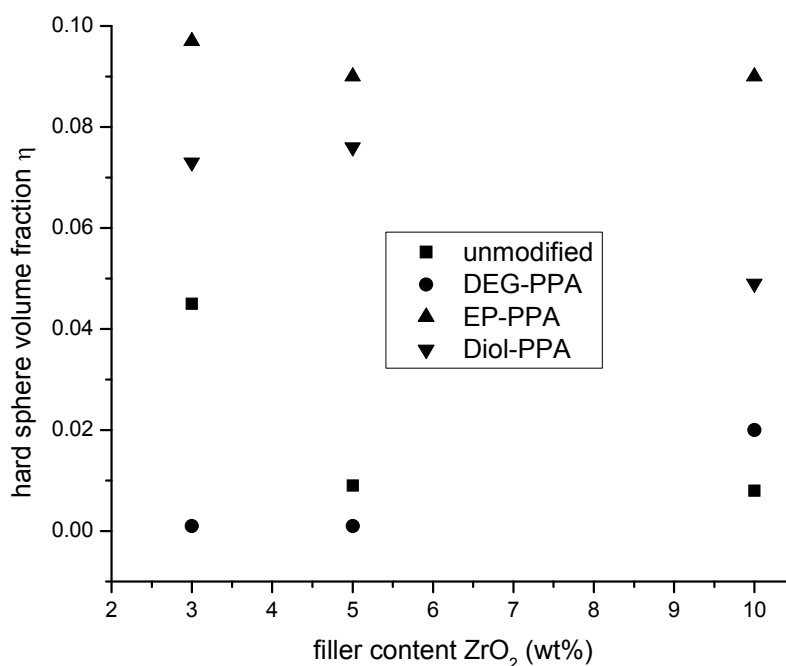


Figure 133. Hard sphere volume fraction of small ZrO₂ nanoparticles with different surface modifications and incorporated into the epoxy resin matrix with different percentages.

The observed agglomeration trend for small SiO₂ nanoparticles also follows this assumption. Gly- and Diol modification allows strong particle-particle interaction in an irreversible way (Gly). At first the hard sphere volume fraction η decreases when the reaction mixture is more concentrated but then it increases again. An optimum filler content for homogeneous nanocomposites lies below 10 wt%. Comparing the agglomeration trends for the small SiO₂ (Figure 134) to the trends observed for the large SiO₂ nanoparticle system (Figure 135), it can be concluded that the nanoparticle size also plays a crucial role in finding the optimum surface modification in order to yield maximum homogeneity. For instance, the Diol modification returns good homogeneities in case of the smaller particles, whereas more inhomogeneous materials are obtained for the larger particles. This may be related to particle curvature effects as observed for ZrO₂. A flatter structure allows more particle-particle interaction and thus results in stronger agglomeration. This behavior can also be observed for the strong interacting Gly-group and for lower filler degrees. As for higher filler degrees, the viscosity shear force effect, which was expected to be stronger pronounced for the larger particles, plays a crucial role and agglomeration decreases. This behavior indicates that the

matrix-particle interaction dominates the particle-particle interaction during the curing process. The trend for η within one modification for different filler percentages is different. This is assumed to derive its origin from the fact that differently sized particles result in different viscosities of the suspensions, changing the overall agglomeration behavior. In this context the relation between particle size and polymer domain size is important as well.^[441] The obtained data is considered to be the result of a complex interplay between the various described phenomena.

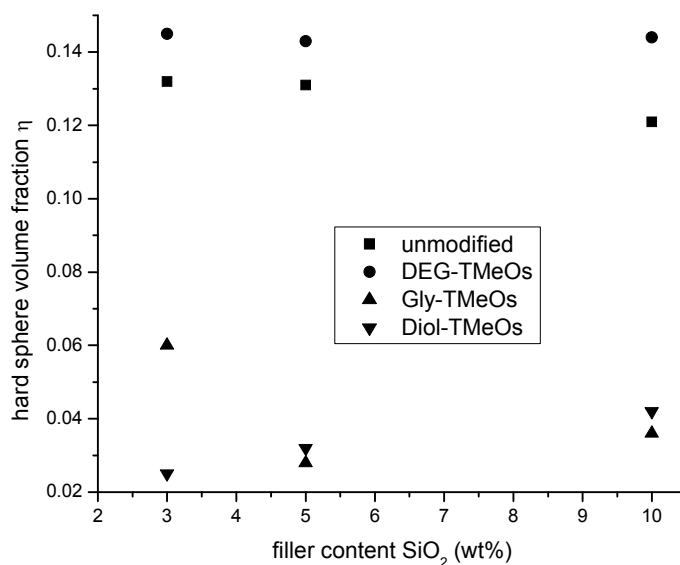


Figure 134. Hard sphere volume fraction of small SiO₂ nanoparticles with different surface modifications and incorporated into the epoxy resin matrix with different percentages.

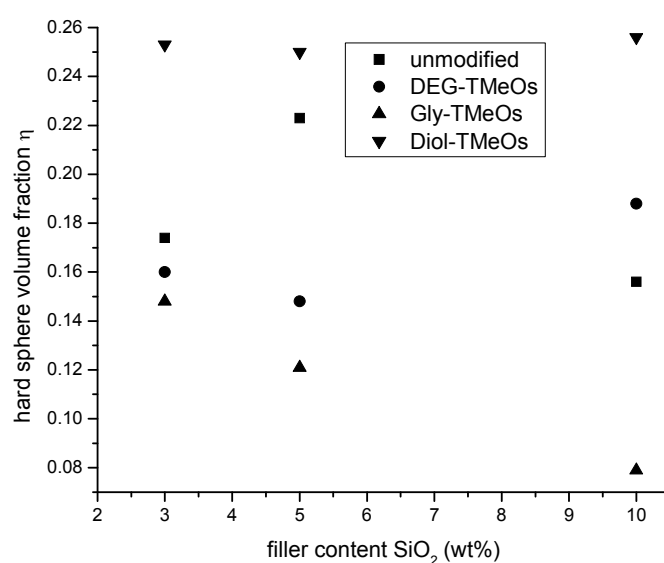


Figure 135. Hard sphere volume fraction of large SiO₂ nanoparticles with different surface modifications and incorporated into the epoxy resin matrix with different percentages.

For demonstration purposes, a highly incompatible surface modification was applied in the preparation of epoxy resin nanocomposites and further characterized by using SAXS. The novel surface modification of ⁿBu-PDMS-PPA is highly incompatible with the epoxy resin. When attached to ZrO₂ small nanoparticles and incorporated by 5 wt% into the matrix the highest hard sphere volume fraction value was obtained for this system, $\eta = 0.122$. By way of comparison, the same amount of the same particles with the best homogenizing surface modification gave $\eta = 0.009$, which is one order lower in magnitude and close to zero agglomeration.

In conclusion, the results gained from TEM concerning the relation between interface chemistry and structure, as shown and discussed in chapter 3.2.3, could be confirmed. Consequently, the dominance of the matrix/particle interaction to the particle/particle-interaction is crucial when homogeneous nanocomposites should be obtained. Additionally, suspension concentration effects can occur, which may lower the agglomeration when the viscosity increases. Thus, the shear forces increase at the same stirring speed and at the same time raise the probability that two particles get together and agglomerate. Again, these effects are expected to strongly depend on the nanoparticle nature, especially on their size. All of these influences on the dispersion quality of the nanocomposite material were observed and discussed in this study by comparing the different materials containing differently surface modified nanoparticle systems.

In consideration of the above stated effects the tuning of the dispersibility of metal oxide nanoparticles by applying organosilanes and organophosphonic acids to produce homogeneous nanocomposites via low shear force is possible. However, in each single case the optimum surface modification has to be found once again. The SAXS data presented in this work by means of comparison influenced the decision of selecting a surface modification for the preparation of novel nanocomposite systems.

Polystyrene nanocomposites

Polystyrene nanocomposites, containing SiO₂ nanofiller (3, 5 and 10 wt% content) with different molecular chemical surface groups, prepared via *in situ*-polymerization were also investigated via SAXS. The resulting hard sphere volume fraction values, exemplarily shown for small SiO₂ nanoparticles, are listed in Table 28 and plotted in Figure 136. The large SiO₂ nanoparticle system revealed similar behavior, but the absolute values are higher because of the uniform sphere system which gives stronger SAXS features when the particles are densely packed. The graphics in Figure 136 show that the filler degree has no significant impact on the dispersion quality within the investigated range in contrast to the previously investigated epoxy resins. The relatively low viscosity of the dispersion in styrene, before polymerization, compared to the viscous epoxy formulation (BFDGE melt) may be related to this fact. The application of the styryl-group resulted in the most homogeneous materials because of the structural similarity to the monomer and the possibility of copolymerization. The use of the, structurally similar, phenyl-group resulted in moderate homogeneity. The only-

hydrophobizing dodecyl-group resulted in the lowest dispersion quality. This serves to confirm the conclusions drawn from the study of TEM images in chapter 3.2.1.2. It appears that, for this defined low complex system of spherical nanoparticles and polymer matrix built up via radical bulk polymerization, the relations between surface groups and dispersion state are much simpler to describe as for a complex resin system. *Bateman et al.* recently investigated the influence of the organic surface group on PS clay nanocomposites by comparing dodecyl groups to alkyl-styryl- and alkyl-ethylbenzyl- groups. By relying on TEM and SAXS results, they also came to the conclusion that the structural similarity and polymerizability of the end group is important in terms of homogeneous nanocomposites when *in situ* polymerization is applied.^[263] These recent results, based on different inorganic systems of nano-sheets, point to the fact that the assumptions made in this work are not restricted to a spherical SiO₂ filler system but are of general nature.

Table 28. Hard sphere volume fraction from SAXS representing dispersion quality of small SiO₂ / polystyrene nanocomposites when different surface modifications were applied.

filler wt%	hard sphere volume fraction η from SAXS		
	DTMS	PhTMS	Styr-TMS
3	0.149	0.121	0.095
5	0.150	0.129	0.095
10	0.153	0.143	0.095

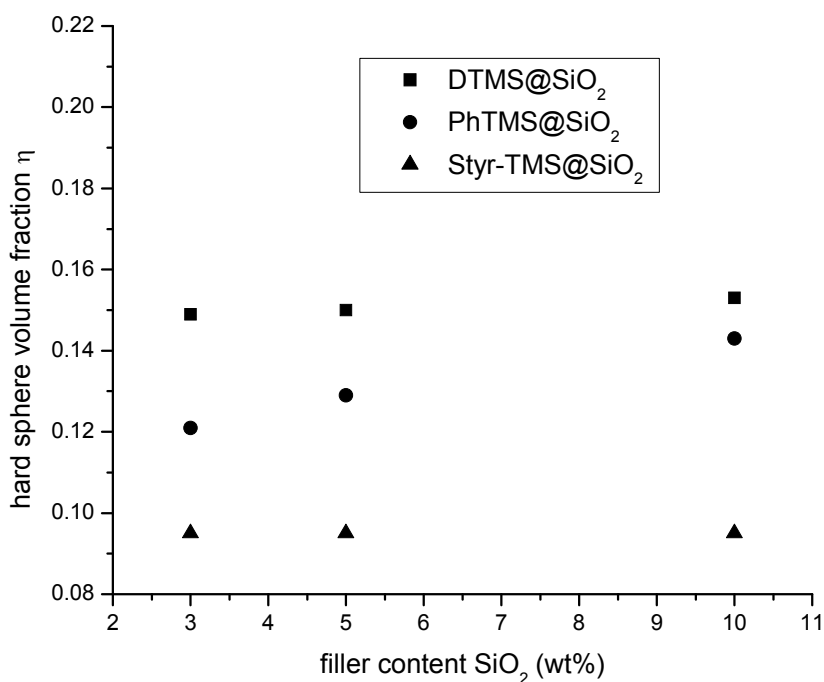


Figure 136. Hard sphere volume fraction from SAXS representing dispersion of quality small SiO₂ / polystyrene nanocomposites with different filler percentage and different surface modifications.

Also samples from melt compounding extrusion were investigated via SAXS. For 5 wt% large SiO₂ nanofiller content, e.g. when applying PS shell modified nanoparticles, a η value of 0.148 was obtained. Whereas for DTMS@SiO₂, a η of only 0.253 was obtained, which points to the fact that much stronger agglomeration phenomena are related to this system. Thus, the PS shell modification appears to be the most applicable surface modification for melt extrusion, in order to obtain nanoscale homogeneous materials. These observations confirm the assumptions made in chapter 3.2.1.3.

The system of PS@SiO₂ large nanoparticles were incorporated into a PS matrix within three different approaches. The hard sphere volume fractions from SAXS of 5 wt% filler containing samples are compared here. From the *in situ* polymerized sample, a value of 0.173 can be reported, characterizing a rather well dispersed system as the corresponding TEM-images in 3.2.1.3 are considered to show homogeneous dispersions (e.g. styryl- modification led to a value of 0.215 which is higher but considered as relatively homogeneous). As discussed above, the melt compounded sample showed a η of 0.148 and the solution compounded sample showed a η of only 0.030. This implies that in the latter case the particles are almost single dispersed. The high discrepancy between 0.148 and 0.030 further implies that η may not correlate in a linear relation with the agglomerate size and / or number, taking into consideration that it represents the probability of neighbored particles. This probability is e.g. still high for highly dispersed systems where only two or three particles are close together,

forming very small agglomerate structures. The value for η steeply decreases to zero when going from particle dimers to single dispersed nanoparticles. The reason why the highest dispersion quality could be obtained from such solution compounded material, can be found in a polymer chain - particle surface wetting phenomenon. The particle wetting with the polymer is considered to proceed better in polymer solution than in viscous melts (melt extrusion) or viscous reaction mixtures within bulk polymerization (*in situ*). Yet, as discussed above and also according to previous TEM investigations, all of the three PS@SiO₂ nanoparticle containing methods can be considered homogeneous with the solution compounded sample showing slightly better homogeneity. This is also implied by the η value of 0.030 for SiO₂ small in the solution compounded sample before melt extrusion, and a η of 0.050 after the extrusion process. However, in this case these SAXS-results can be falsified by the presence of the PS-shells around the particles, which would decrease the inter-particle distances within an agglomerate and give lower η values even for stronger agglomerated samples. That this is not the case here, can be seen in the TEM images in chapter 3.2.1. Further on, the SAXS method is not sensitive towards macro-inhomogeneities when the particles are well dispersed on a nanoscale, as demonstrated by the presence of nanoparticle rich and nanoparticle poor regions (see TEM images in chapter 3.2.1).

PMMA nanocomposites

The mixed monolayer (PhPPA/DPPA) modified, small ZrO₂ nanoparticles have been found in chapter 3.1.3 to be better dispersible in organic solvents as toluene, than pure DPPA modified systems. The reason for this is the avoidance of a strong inter-particle alkyl-bilayer, which would destabilize the dispersions (zipper-effect). These particles were also applied in the *in situ* nanocomposite preparation of PMMA nanocomposites, with a 5 wt% filler content, in order to prove whether this mixing approach can be applied to polymer nanocomposites. PMMA was selected as a matrix because PS might have falsified the results for homogeneity in terms of a zipper effect as it might favor the interaction which the phenyl groups from the mixed monolayer. Particles with 50%, 70% and 90% DPPA content at the surface (rest is PhPPA) were applied. The incorporation of lower DPPA content was not possible, as in that case the monomer dispersion was too unstable for appropriate processing. The prepared samples were investigated with SAXS. The resulting hard sphere volume fraction values are plotted in Figure 137. This figure shows that with decreasing DPPA content, the hard sphere volume fraction η , representing the agglomeration, decreases. This is agreeable to the results on mixed monolayer particle found in this work, up to now. As a major reason for the higher dispersion quality of lower DPPA containing samples, the better redispersibility of the powders, as shown in chapter 3.1.3, is held responsible. This small study confirms the applicability of the mixed-monolayer approach to tune particle dispersibility also for the final polymer nanocomposite material preparation.

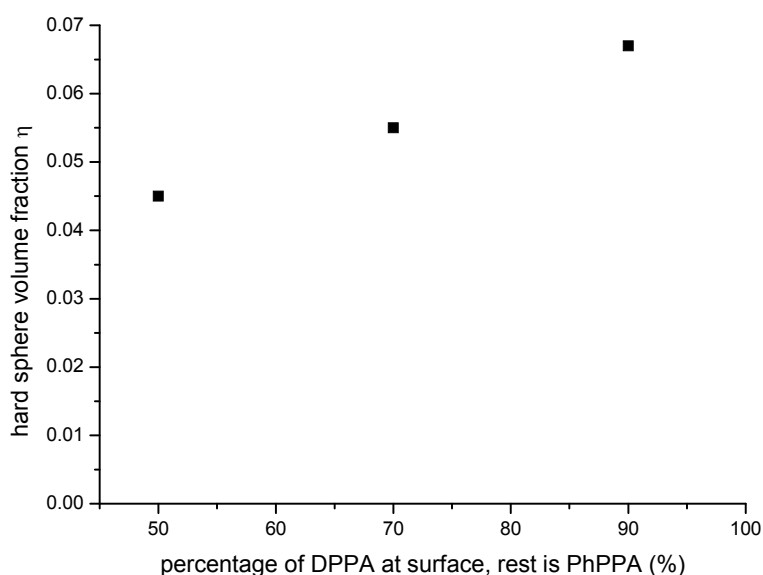


Figure 137. Hard sphere volume fraction from SAXS representing the agglomeration degree of 5 wt% mixed modified DPPA / PhPPA @ ZrO₂ small nanoparticles in PMMA matrix when different mixing degrees are applied.

Furthermore, the effect of the nature of the organic moiety of the surface modification on the homogeneity of nanocomposites was investigated via the SAXS method. This was especially for samples where when polymerizable end group containing coupling agents have been applied. The ZrO₂ small and large particle system were applied to investigate on particle size related effects. Furthermore, the small SiO₂ system with different surface modification and filler amounts of each particle type of 3, 5, and 10 wt% was investigated. Qualitatively similar results have been obtained for the larger SiO₂. The comparison of the two systems containing DTMS and MA-C10-TMS modified nanoparticles gives information on the influence of the polymerizable group and structural similarity of end group with matrix. Furthermore, the comparison of MA-C2- with MA-C10- modified particles allows to draw conclusions on the influence of the spacer chain length on the dispersion behavior. The measured hard sphere volume fraction values η for the nanocomposite systems are listed in Table 29. For a better discussion, η values of the ZrO₂ system are plotted in Figure 138. The values for the SiO₂ system are plotted in Figure 139. To the author's knowledge, a comparable study in literature has not been reported so far.

Table 29. Hard sphere volume fraction from SAXS representing dispersion quality of SiO₂ and ZrO₂ / PMMA nanocomposites when different surface modifications were applied.

		hard sphere volume fraction η from SAXS			
particle type	filler wt%	unmodified	DTMS	MA-C2-TMS	MA-C10-TMS
small SiO ₂	3	0.145	0.133	0.111	0.048
	5	0.122	0.143	0.113	0.029
	10	0.148	0.099	0.100	0.046
				MA-C2-PPA	MA-C10-PA
small ZrO ₂	3			0.074	0.108
	5			0.092	0.108
	10			0.091	0.124
large ZrO ₂	3			0.055	0.077
	5			0.077	0.089
	10			0.034	0.023

Examining Figure 138, the following statements can be made for ZrO₂ / PMMA nanocomposites. Generally, smaller nanoparticles are agglomerated in a much stronger way than larger nanoparticles. This is plausible as smaller nano-objects show a higher tendency to minimize their surface energy. In this specific case the plane crystal facets of ZrO₂ small nanoparticles can facilitate a particle arrangement via stacking, compared to the irregular shaped larger ZrO₂ nanoparticles. From the relatively low absolute η numbers of the whole sample series it can be concluded that the MA- end group, in general, is helpful for the preparation of homogeneous materials. This confirms the results previously gained from TEM. At higher filler amounts (10 wt%) the agglomeration of smaller nanoparticles increases and the agglomeration of the larger nanoparticles decreases. This effect derives its origin on one hand from a stronger tendency of ZrO₂ small nanocrystals to assembly when the concentration is high enough. On the other hand, reaction mixture viscosity effects can also play a role. This means that in one case, the suspension viscosity rises up to a value within the progress of the polymerization reaction so that the shear forces are enhanced at the same stirring speed, which consequently leads to a better homogenization. In all cases, except for the sample of 10 wt% ZrO₂ large nano filler in PMMA, the shorter spacer chain led to slightly

but significantly better dispersion quality than the same systems with a longer alkyl chain spacer. The reason for that can be that a possible advantage of an increased hydrophobicity, when the C₁₀ chain is applied is overran by the negative effect on dispersibility resulting from a stronger alkyl chain zipper effect when longer alkyl chains are used. The results presented in chapter 3.1 underline the validity of these explanations. The agglomeration via alkyl-chain-zipping seems to be more pronounced for the, crystal facet shaped, small ZrO₂ nanoparticles than for the irregular shaped larger nanoparticles. For the high filler containing 10 wt% ZrO₂ large sample the result that in that case the C₁₀ chain led to higher dispersibility is thus considered to be relevant.

As a conclusion to ZrO₂ / PMMA nanocomposites from SAXS results, the success of fine-tuning of the interface via spacer chain length variation in order to gain dispersion quality, is influenced by several other effects. These effects are assumed to be related to particle size and shape.

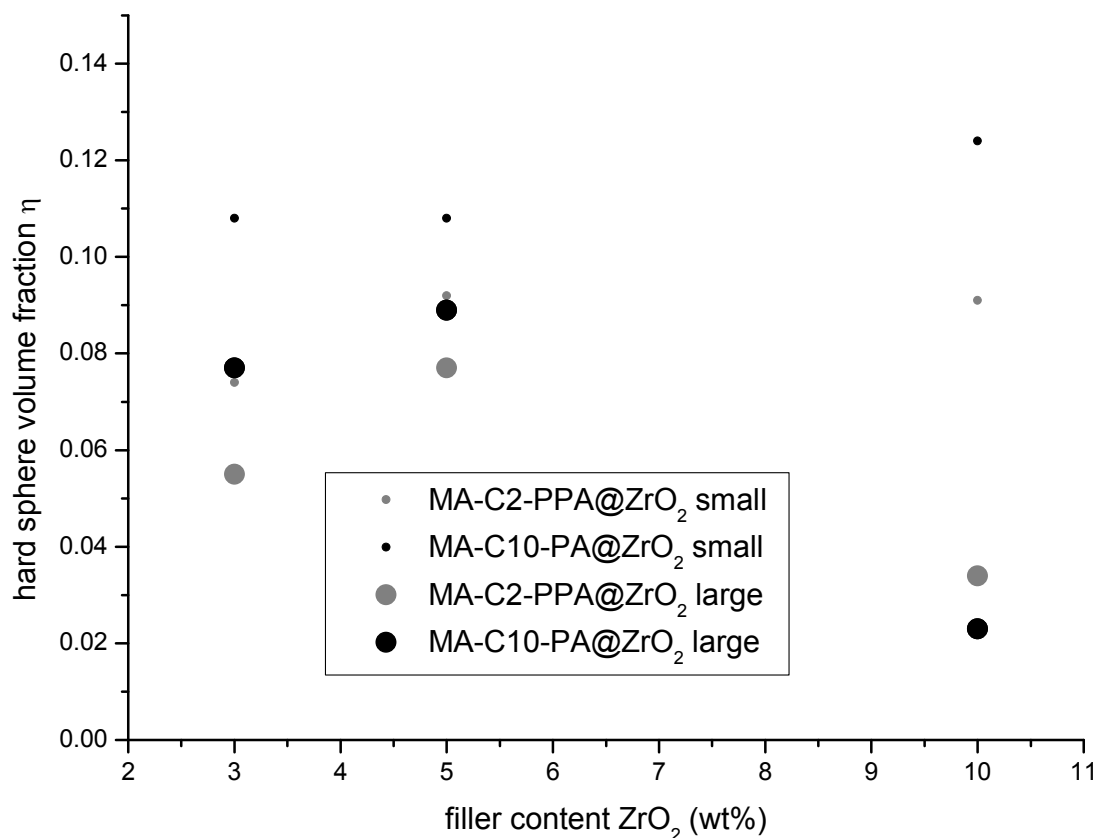


Figure 138. Hard sphere volume fraction from SAXS, representing dispersion of quality large and small ZrO₂ / PMMA nanocomposites with different filler percentage and different surface modifications.

For the uniformly, isotropically shaped SiO₂ sphere system, the relations between surface chemistry and dispersion structure seem to be less complex, see Figure 139. The sensitivity of

the applied SAXS method towards the presence of agglomerates (which then consist of uniform dense sphere packings) is thus considered to result in more significant results. As revealed by preliminary investigations in chapter 3.1.3, such small spherical nanoobjects (7 nm diameter, TEM) do not show long alkyl chain ordering because of their nano-curvature. The absence of a zipper effect can be expected.

Generally, as also observed for SiO₂ spheres in PS, the agglomeration degree seems to be independent of the filler degree within the investigated range of filler percentages, in this more simple model system. The lowest homogeneity was observed when unmodified nanoparticles were applied. A slight improvement in dispersion quality was noted when the system is modified with DTMS. Through the application of MA-C3-TMS, the dispersion quality was already improved and the application of MA-C10-TMS results in highly homogeneous nanocomposite materials (see also previous TEM-results).

Again structural similarity and polymerizability of end groups are responsible for an enhancement in homogeneity: The longer spacer chain helped to further improve the dispersion quality as no strong zipper effect can be assumed for these materials. *Aleksic et al.* applied an analogous system by using 7 nm SiO₂ nanoparticles (commercial) for *in situ* polymerization in MMA. Via this approach they pointed out the good dispersion quality when MA-C3-TMS is used as surface modification, showing the high importance of the functional end group in terms of dispersion quality.^[260] By applying MA-C10-TMS, the interfacial match within these systems could be further improved.

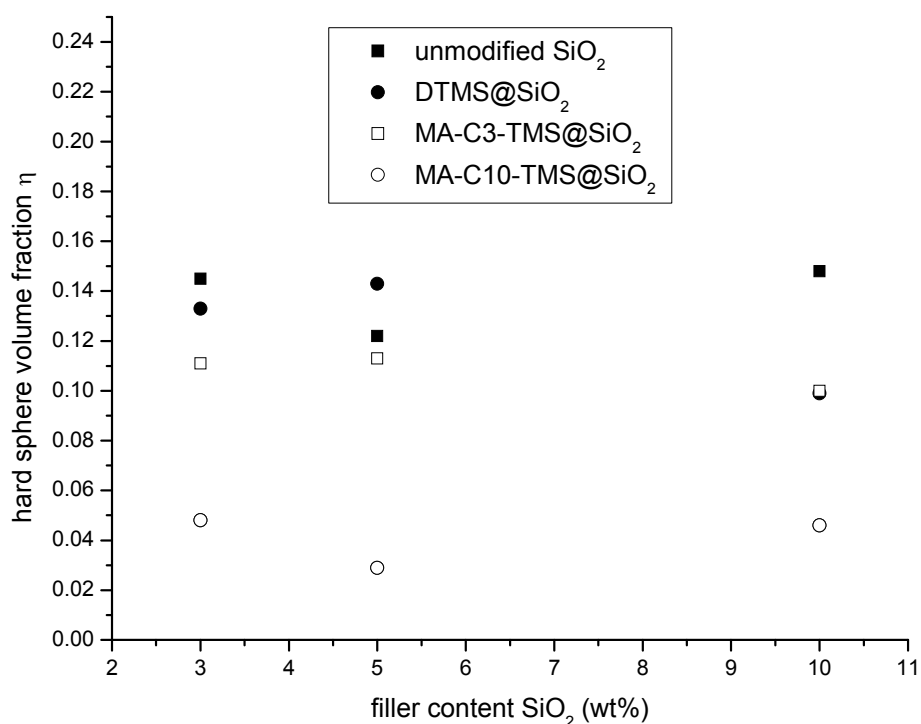


Figure 139. Hard sphere volume fraction from SAXS representing dispersion of quality small SiO₂ / PMMA nanocomposites with different filler percentage and different surface modifications.

Also, the PDMS-spacer modified ZrO_2 nanocrystals, with an allyl- and ^nBu end group, that were incorporated into PMMA, were investigated via SAXS. Through this, rather low agglomeration degrees, similar to both end groups, could be obtained. For instance, for 5 wt% ^nBu -PDMS-PPA@ ZrO_2 small in PMMA, a η of 0.058 and for allyl-PDMS-PPA@ ZrO_2 small a η of 0.040 could be obtained. These high homogeneity indicating results are related to the results obtained from TEM, in chapter 3.2.2. However, TEM indicates the presence of at least small agglomerates, whereas with SAXS, obtaining η close to zero, single dispersed nanoparticles would be expected. In that case, it was assumed that the presence of the PDMS-shell at the particle surface falsifies the SAXS values. Lower values are obtained because a PDMS region is present between the particles within the agglomerates that keep the particles in distance.

In summary it can be stated that: If the basic requirement of a polymer matrix with molecular weight in the appropriate range is fulfilled, the dispersion quality of the final nanocomposites mainly depends on the surface modification of the nanoparticles that determines the interfacial match. First of all, it must be guaranteed that the particles are dispersible in the monomer, which depends on the structural and chemical nature of the surface modification. Consequently, the following statements on the homogeneity of nanocomposites (and thus of the nanopowder re-dispersibility in polymer matrices) can be made.

- The functional end group is very important for the achievement of homogeneity because of its structural similarity to monomer and matrix, but also because it allows a polymer grafting *through* of the nanoparticle surface.
- The variation of the spacer chain additionally allows a fine-tuning of the dispersion behavior.
- For the low complex system of SiO_2 nanospheres, incorporated into the selected thermoplasts, the conditions are ideal with respect to high homogeneity, when a structurally similar polymerizable end group is present and a hydrophobicity providing long alkyl chain is applied as spacer.
- For the more complex ZrO_2 nanocrystal (crystals and irregular shaped) system, these arguments are also valid. However, due to other effects, such as the zipper effect or effects related to structure and nature of these nanoparticles, the relations as described for the simple SiO_2 system need not be exactly the same. In the case of a more complex system, as for ZrO_2 , this means that the fine-tuning of the dispersion quality has to be tailor made for each type of nanoparticle.

The present comparative study aims for a simplification of the future systematic development of novel polymer nanocomposite materials.

3.2.5.2 Interface chemistry – mechanical properties

In this chapter, the influence of the nanoparticle surface modification (and thus the interface properties within the prepared nanocomposites) in the previously introduced nanocomposites, on mechanical properties are discussed. This is done by using selected examples for epoxy resins, PS and PMMA, when significant and application relevant effects have been obtained. As mechanical characteristics, basically the hardness from *Vickers* indentation test are discussed. These values can be obtained also from smaller sample amounts, compared to larger specimen sizes needed for tensile or bending tests, but represent overall macroscopical mechanical materials properties.^[47, 442] Furthermore, the application of the *Vickers* test allows to characterize non homogeneous materials which include bubbles or a few larger agglomerates, which would not allow tests experiments like tensile tests, as these regions introduce predetermined failure points^[47, 442] In the indentation tests, these inhomogeneities can be systematically ignored during the measurement. Additionally data from dynamical mechanical thermoanalyses (DMA) will be discussed exemplarily to also demonstrate the dynamical stress behavior of prepared nanocomposites. When comparing these mechanical material characteristics, attention will be paid to the dependence of mechanical characteristics on the filler percentage. This comparison gives good indications on the quality of a nano-reinforcement effect of the polymer, a mechanical property enhancement induced by a large interfacial area in homogeneous nanocomposites.^[50, 443]

Epoxy resin nanocomposites

For a comparing overview on material property enhancement for different nanoparticle types and sizes as well as varying the filler amount, ZrO₂ and SiO₂ nanoparticles, modified with DEG moieties and incorporated into epoxy resins are discussed here. The reason, why the DEG-modified samples are discussed is that it is the only organic moiety within the studies from the present work, which gives homogeneous (in the case of ZrO₂) or at least moderate homogeneous (in the case of SiO₂) epoxy resin nanocomposites (see chapter 3.2.3). This is one of the basic requirements when significant results on obtained changes in mechanical properties should be measured. A comparison of the whole DEG modified series is given in the diagrams in Figure 140, where the hardness values are plotted for the mentioned, differently filled epoxy resin nanocomposites. The filler percentage is deliberately plotted as wt%, as this is an important parameter in the design of novel light weight engineering materials, and has the highest relevance towards application. However, it has to be considered that the same weight percentage filler represents a much lower particle filler volume for ZrO₂ than compared to SiO₂, because of the difference in the densities of these materials ($\rho(\text{SiO}_2) \sim 2.2 \text{ g/cm}^3$, $\rho(\text{ZrO}_2) \sim 5.7 \text{ g/cm}^3$). All *Vickers* impressions did not show cracks, which underlines the appropriate fracture toughness behavior of these materials.^[47, 442] The neat matrix showed a hardness of 0.163 GPa. By increasing filler amount, for all types of particles, the hardness increased. The highest increase was obtained by incorporating 10 wt% large SiO₂ nanoparticles, 0.234 GPa, and by incorporating 10 wt% large ZrO₂ nanoparticles, 0.232 GPa. This is an increase by ~44% in hardness, for both particle types. These results show that,

taking the densities of the nanoparticles into account, ZrO_2 gives a similar enhancement in hardness as SiO_2 (more than one half), but at lower volume percentage loadings, keeping the density difference in mind. On one hand these results show that the reinforcement of epoxy resin by ZrO_2 nanoparticles is much more effective than for SiO_2 nanoparticles. On the other hand, the gain in mechanical strength per mass of the material, which is an important criteria when these materials should be applied as construction engineering materials, is not higher than for SiO_2 as the reinforcing effect relative to the material weight is compensated by the higher density of ZrO_2 . That ZrO_2 is a very effective filler and qualified for enhancing mechanical properties, such as tensile strength properties in epoxy resin nanocomposites, was demonstrated by *Schlarb et al.*^[38] In the present work the effect of nanoparticle size was compared to the hardness. With respect to the results of this comparison the following statements can be made: For both types of particles (SiO_2 and ZrO_2), the hardness increases stronger in larger nanoparticles, with increasing filler amount. Due to the use of smaller nanoparticles, which introduce a larger interfacial area, a higher reinforcement effect than for larger nanoparticles would be expected. However, the opposite effect has been observed in this specific case. This phenomenon may be explained by the following effect: The DEG-modification allows high homogeneity due to good miscibility of DEG-moiety and matrix. The interaction of DEG and matrix is not considered to be very strong, when compared to a covalent linkage, etc. Thus, the interfacial adhesion between the inorganic and the organic components, which influences the possibility of movement of the nanoparticles within the matrix, shows a similarly low level of interaction. This means that the nanoparticles can be moved within the material if a certain stress is induced and if interfacial adhesion is low. A possible interpretation of the obtained results is that in the case of indentation experiments a high local stress is induced and the larger nanoparticles serve more effectively as obstacles towards the indenter than smaller nanoparticles that could be more easily moved within the matrix during the indentation progress. It is known from studies in literature that the interfacial properties significantly change the mobility of nanoparticles in a polymer, e.g. changing the migration behavior, which means particle movement is easier when low interfacial adhesion is present.^[444, 445] In particular, the relation between the size of the nanoparticle and polymer coil domains is considered to be a determining factor of the observed effect. When the particle size is in the domain range of the polymer coils or segments gyration radii (which is difficult to analyze in this crosslinked matrix system) a unique interaction behavior between the inorganic and organic part is expected^[57, 349] (e.g. it has already been observed in studies in literature that the filler particles are pushed into the matrix^[50]). This behavior manifests itself in an unexpected phenomenon of mechanical property change. As this behavior is also noted for the different systems of SiO_2 and ZrO_2 , it is assumed that it may be a general phenomenon for similar nanoparticles with low force particle-matrix interacting moiety, (such as DEG) where the particle can move within the matrix. When these results are compared to the results gained from the investigation of stronger (covalent) interacting organic moieties, another prove for this claim is given.

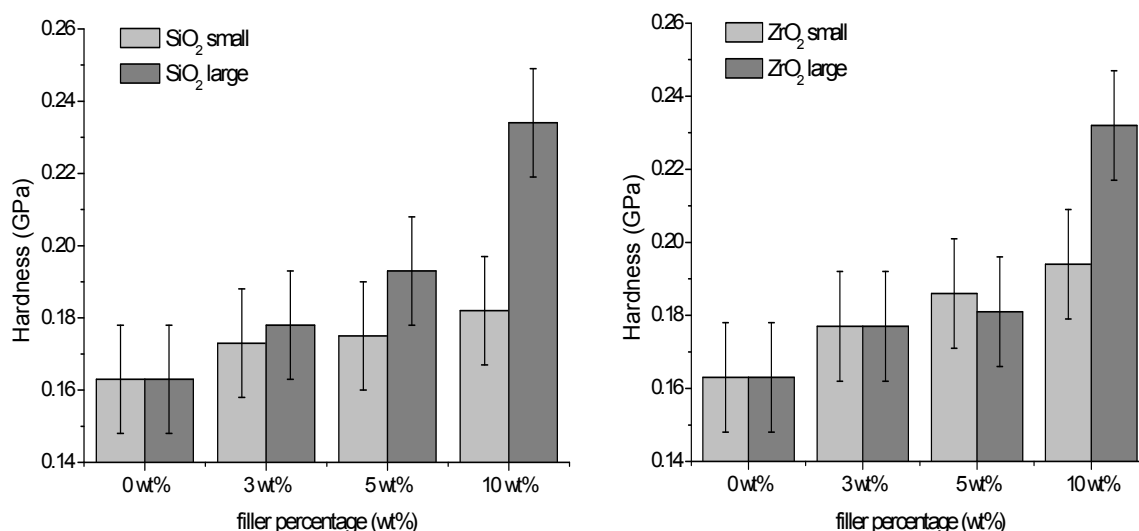


Figure 140. Hardness from *Vickers* test, converted into SI units via the geometrical parameters of the indenter, of epoxy resin nanocomposites including different DEG- modified nanoparticles with different particle sizes, left: SiO₂, right ZrO₂.

For further mechanical characterization of these systems DMA measurements have been carried out. The plateau moduli, depending on the filler degree when using different nanoparticles, are plotted in Figure 141. The plateau modulus increases by increasing particle load for every type of nanoparticles and is, in contrast to the hardness increase behavior, more pronounced for smaller nanoparticles. As for SiO₂, but not for ZrO₂, a similar trend can be observed with regard to hardness values can be observed. However, these results are not in contradiction to the results obtained from hardness in the considering a possible particle movement during the indentation. Through DMA it is observed that no such high local stress emerges. This result is very likely due to the effect of the increasing interfacial area on the (dynamic) mechanical energy uptake behavior. Further on, the plateau moduli for the lower volume fraction filled ZrO₂ nanocomposites are generally lower as for the comparable SiO₂ systems. Via this method the nano-filler effect can be more easily discussed from DMA results. The practically highly relevant hardness is determined by a complex interplay of parameters such as nanoparticle nature, flow behavior and interfacial adhesion, etc. The exact reasons for the materials' behavior in the DMA tests, as demonstrated in Figure 141, may derive from various origins. With increasing filler amount, the physical crosslinking and therefore the plateau modulus increases. However, additional chemical crosslinking of particle and matrix can be assumed to further increase the plateau moduli. This is assumed to proceed especially in the case of SiO₂ nanoparticles, where residual surface OH groups are expected also to be present after surface modification. The plateau modulus thus increases also with decreasing particle size because of the increase in interface area and thus the increase in crosslinking interaction. As a general reason for these effects, the unique situation at the interface can be seen as responsible, where the chain mobility of the polymer between matrix chains and interface is reduced, strengthening the material.^[14]

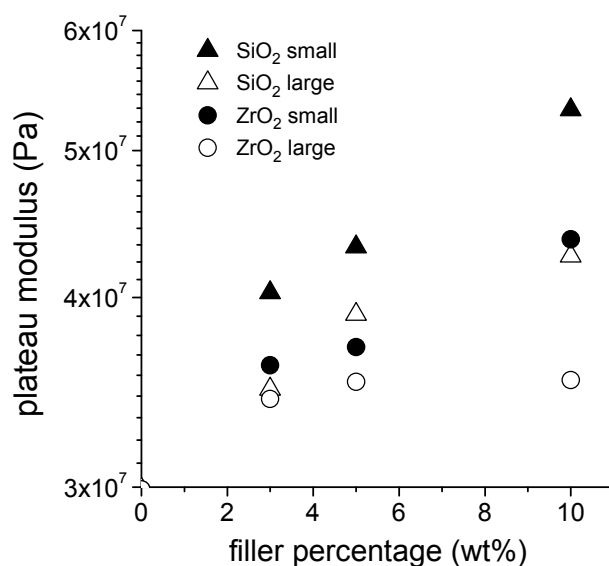


Figure 141. Plateau moduli from dynamic mechanical thermoanalysis (DMA) measurements at DEG- modified nanoparticle filled epoxy resin nanocomposites.

From DMA analyses, the glass transition temperatures T_g were monitored in view of the investigated series of materials. It showed that the T_g of the neat matrix was 113° and decreased slightly with increasing filler contents. This was also confirmed via DSC measurements. For instance, when small DEG-modified SiO_2 nanoparticles are incorporated the T_g is reduced to 105° . This effect can be related to the DEG moiety, (an effect similar to plasticizing) inducing disordering and softening within the material. Another possible explanation is that this effect relates to the matrix crosslinking density, if the latter is influenced during the *in situ* curing process. A decrease of crosslinking through the presence of nano-filler can be considered. Effects on the curing behavior of epoxy resins deriving from the presence of nanoparticles are well known in literature. It was shown, for instance, that SiO_2 nanoparticles influence the overall curing kinetics, especially when (residual) surface OH groups are present.^[74] These assumptions correspond to the observed higher probability of the nanocomposites for water uptake when they contain more DEG-modified nano-filler, as investigated in chapter 3.1.4. This fact, in combination with the though obtained results of hardness increase for the overall material, point out the strong reinforcement effect related to the nano-filler incorporation. Because a softening of the matrix system would be expected due to lower crosslinking density.

To compare the only-physical-particle-matrix-interaction-allowing DEG-modification with stronger interacting systems, the effect of the strong-chemical-interaction-allowing Gly-modified particle containing nanocomposites on hardness will be discussed. This discussion will be carried out for the SiO_2 system as the analogous ZrO_2 system could not be measured as it led to inhomogeneous materials which were inappropriate for measurements (see chapter 3.2.3). Figure 142 shows the hardness of epoxy resin nanocomposites, filled with Gly-TMS modified large and small SiO_2 nanoparticles, in dependence of the filler degree. To give a

better demonstration of the nature of the trend also composites including 15 wt% nano-filler are included in this study. Again, with increasing particle fraction the hardness increases. However, concerning the effect of the particle size, the situation for the stronger interacting modification of Gly- is *vice versa* as obtained for the weaker interacting DEG- system: Smaller nanoparticles result in higher reinforcement than larger nanoparticles (with 0.227 GPa hardness for Gly-TMS@SiO₂ small and only 0.182 GPa hardness for DEG-TMS@SiO₂). It appears that due to the crosslinking of particle with matrix the hypothesis of a nanoparticle movement during indentation is not applicable here. This would explain the obtained results where the smaller nanoparticles induce a higher interfacial area as larger particles, which in consequence is responsible for energy and stress uptake and the observed increase in hardness. This consideration, together with the fact that this nano-reinforcement effect reaches a plateau at a certain filler concentration (above ~ 5 wt%), is according to the accepted theory in literature. Theories in literature describe how the nano-filler degree can affect mechanical reinforcement when the material properties are basically determined by the interface region which is generated through homogeneous dispersion of small nanoparticles in polymer matrices.^[14, 50] Similar behavior, a first steep change of the property and then a flattening of the change, in the change of mechanical characteristics with filler degree could be observed in literature for comparable epoxy resin nanocomposite systems. The authors of these studies assumed it to be a nano-related phenomenon. For instance, *Fan et al.* report a similar behavior with impact strength and thermal properties of glycidoxypropyl modified SiO₂ nanoparticles, where for comparable micro-powders such behavior was not observed.^[32] Another study found similar behavior in impact strength enhancement for SiO₂ filled epoxy resins.^[74]

Interfacial adhesion is thus crucial for a nano-reinforcement effect as the nanoparticles are fixed e.g. via covalent bonds within the polymer. The system consequently behaves more rigid under high stress, contrary to a possible particle movement within the matrix when the particles are not strongly linked to the surrounding polymer. Further studies in relevant literature have shown that with increased crosslinking or even network formation of the inorganic part within silica/epoxy resin nanocomposites, thermo-mechanical properties are significantly higher increased as compared to less strongly particle-matrix-linked or lower network forming particle systems.^[53]

Additionally, the system of Gly-TMS@SiO₂ is much better dispersed (hard sphere volume fraction close to zero) than the analogous DEG-system. Thus, agglomerates are mostly excluded as indentation obstacles. This may give an explanation on why the larger nanoparticles (Gly-modified) do not result in a high reinforcement effect, as observed for the DEG modification.

The observed mechanical reinforcement effects within these studies on epoxy resin nanocomposites all seem to be related to the nanocomposite structure and interfacial adhesion. Yet, these two parameters cannot be tuned separately, as was demonstrated in the previous SAXS studies on the relation of interface chemistry and structure. The change in chemical modification always influences both parameters.

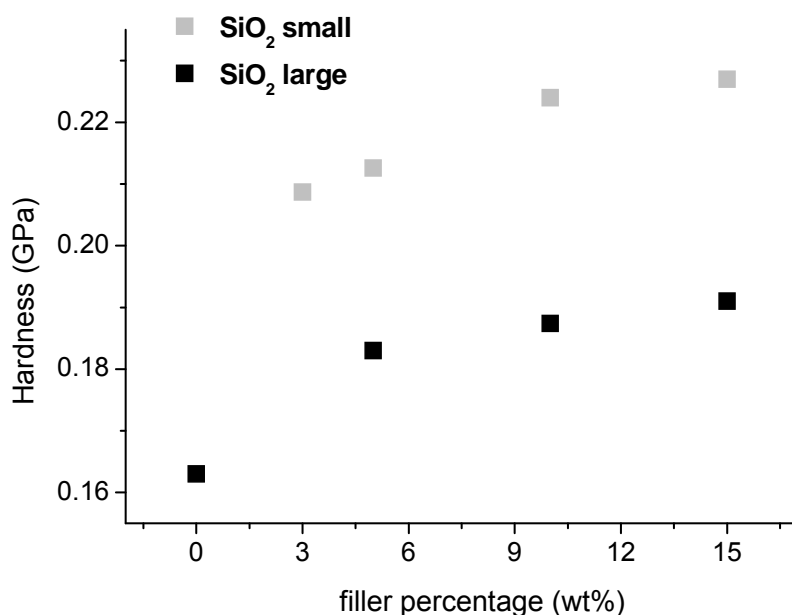


Figure 142. Hardness from *Vickers* test, converted into SI units via the geometrical parameters of the indenter, of epoxy resin nanocomposites including Gly-TMS modified SiO₂ nanoparticles with different particle sizes.

It was shown that by varying the surface functionality of the nanoparticles, and thus the interfacial adhesion and dispersion structure, for different systems (DEG-PPA@ZrO₂ large, DEG-TMS@SiO₂ large and Gly-TMS@SiO₂ small), similar reinforcement effects of epoxy resins can be obtained. Through this, the incorporation of smaller nano-objects may result in better optical transmittance properties (see chapter 3.2.1, 3.2.2 and 3.2.3).

Concludingly it may be stated that the tuning of the nanocomposite via chemical surface modification of the nanoparticles strongly affects the parameters of particle agglomeration. Furthermore, interfacial adhesion and both parameters significantly affect the mechanical properties depending on the nano-filler loading.

Polystyrene nanocomposites

For the correlation of mechanical properties and interfacial properties, polystyrene nanocomposites filled with SiO₂ nanoparticles were compared. In one case systems with an only physical matrix-particle interaction generating modification, DTMS, and in the other case SiO₂ nanoparticles modified with Styr-TMS. The Styr-TMS system allows a covalent linkage of matrix and particle during the *in situ* polymerization process. For a detailed investigation on the impact of the functional end group (polymerizable or not) on materials properties (hardness) only samples from *in situ* polymerization (not from other compounding techniques) were used. The results on the hardness of the investigated system are shown in

Figure 143. For each particle type, the hardness increases with increasing filler degree. Via different steepness and different maximum, reinforcement effects are obtained. The highest reinforcement effect could be obtained for 10 wt% Styryl-TMS@SiO₂ small in PS, resulting in a hardness of ~0.23 GPa, whereas the neat polymer matrix shows a hardness ~0.16 GPa.

The diagram in Figure 143 features the following general trends: The highest reinforcement effect (= increase in hardness with increasing filler percentage) is observed for crosslinkable Styr- group modified nanocomposites. The reinforcement thereby is higher than for only-physical-interacting DTMS modifications. Larger interfacial adhesion, when using Styr-TMS, as well as lower agglomeration, are assumed to be responsible for the differences. This can be set in relation to the effects reported in the previous chapter for the differently crosslinked epoxy resin materials. Furthermore, analogous to these previously discussed materials, the reinforcement effect depending on the filler degree has a characteristic slope: First a steep increase followed by a plateau region can be observed. This slope is more pronounced for smaller particles because of the higher generated interface for the case when interfacial adhesion and homogeneity are considered high (Styr-TMS for PS, Gly-TMS for epoxy resin). This characteristic slope relates to the accepted theory on nano-reinforcement effects.^[14, 50] The larger DTMS modified nanoparticles show a linear like reinforcement behavior, which is considered to be a traditional micro-or-macro-filler-effect. No nano-related specific effects, as they usually lead to an disproportionately high change of a selected material property. In literature such nano-reinforcement effects are e.g. observed for the change in *Young's* modulus with different filler degrees. A study in literature where micro-composites and nanocomposites are compared demonstrates this effect.^[14]

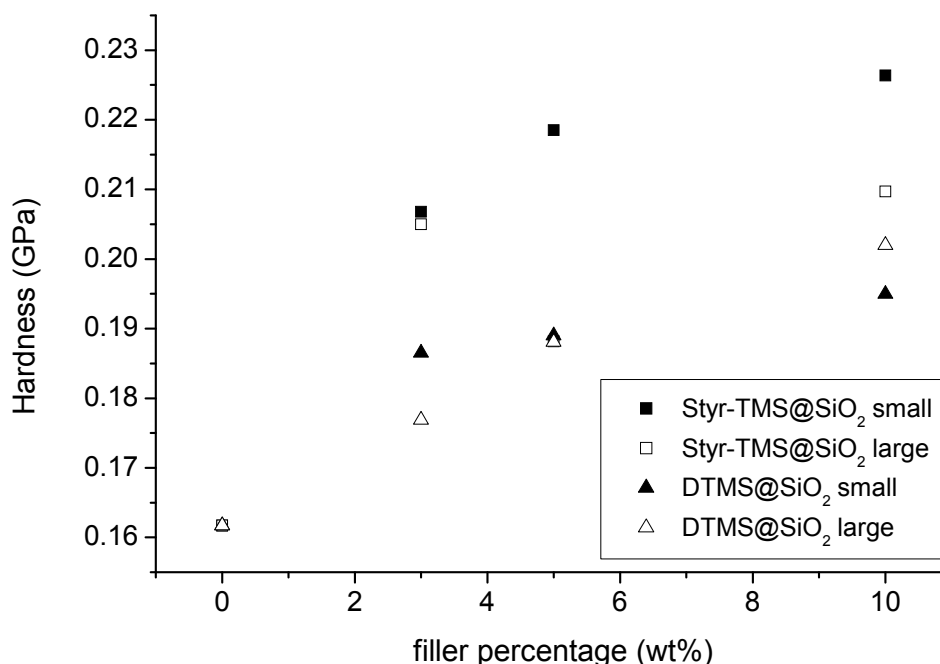


Figure 143. Hardness from *Vickers* test, converted into SI units via the geometrical parameters of the indenter, of PS nanocomposites including differently surface modified SiO₂ nanoparticles with different particle sizes.

The fundamental principles within nanocomposite reinforcement effects seem to be the same here, regardless whether a thermoplast matrix, such as PS, or a crosslinked epoxy resin is used. These principles are the generation of a high interfacial area that absorbs energy and reinforces the materials when appropriate interfacial adhesion is guaranteed. Via the interface chemistry, the nano-reinforcement effect can be generated and tuned.

PMMA nanocomposites

Comparing the simple system of monodisperse SiO₂ spheres, incorporated into PS, with the more complex system of irregular and / or crystal shaped ZrO₂ nanoparticles in PMMA, it is more difficult to come to a conclusion on the phenomenon which is responsible for the nano-reinforcement effect. The PMMA / ZrO₂ system with the best expected comparability of results on mechanical properties, is investigated here: Small and large ZrO₂ nanoparticles with different filler degrees, modified with MA-C2-PPA and MA-C10-PA, were incorporated into PMMA via *in situ* polymerization. These materials are rather similarly homogeneous and thus the complexity of the overall relations is reduced. The measured hardness values are plotted in Figure 144. Generally speaking, the hardness increases by increasing filler amount for every investigated system. For the larger ZrO₂ nanoparticles the reinforcement is the highest and results in a hardness of 0.283 GPa for 10% MA-C10-PA@ZrO₂ large nano-filler containing sample. Compared to the hardness of 0.198 of the neat matrix, this is an increase in hardness by 28%. For unmodified nanoparticles the effect was lower by 10%, which points out the importance of a polymerizable end group. There are only few examples in literature on PMMA/ZrO₂ nanoparticles where polymerizable groups were used as interface intermediating functionality. Even less is known on the mechanical behavior of such materials. One recent example, given by *Wu et al.*, shows that when hydroxyethyl methacrylate modified, 3.8 nm ZrO₂ nanoparticles, are incorporated into PMMA via *in situ* polymerization, the strength (from tensile tests) is enhanced.^[75] Together, the results on hardness increase gained from literature as well as the results found in this work emphasize the high reinforcement potential of ZrO₂ nanoparticles.

The effect that the reinforcement is generally through the use of ZrO₂ large nanoparticles than for the small ZrO₂ nanocrystals, even though interfacial adhesion is accepted to be similar in both systems, can be explained by their morphology (see chapter 3.1.1.1). In the previous investigations it was shown that the large ZrO₂ nanoparticles consist of a high nanoscopic surface roughness and inner porosity, which can introduce a higher interfacial region in the nanocomposite material and thus explain the higher observed reinforcement effect. The specific surface from N₂ sorption is higher for the rougher, larger nanoparticles. Therefore, the effect of particle morphology on mechanical properties in the final material is considered not to be negligible. This is in conformity with the current theory on interface phenomena.^[50] It is further held that the polymer interpenetrates the porous particles, which is desirable in terms of the mechanical reinforcement of the material. The linear like slope of the trend of the reinforcement effect is similar in all cases. These effects are considered to result from a

nano-reinforcement because of the high homogeneity of these samples and the observed high reinforcement effect at lower filler loadings. A characteristic plateau region for higher particle loadings is expected to be superposed by effects resulting from a larger number of agglomerates in the higher filler percentage region, micro-filler effects. This increase in agglomerate number with increasing filler degree (few agglomerates were then visible to the unaided eye) is also the reason why no further measurement points above 10 wt% filler degree were generated. Through this finding the assumption stated above is verified. Generally it has to be kept in mind that regarding the comparison of the reinforcement curves for different particle containing samples shown in this work are different because of the density difference of SiO_2 and ZrO_2 . For instance for PS/ SiO_2 (plateau observed) with PMMA/ ZrO_2 (no plateau observed) the particle volume fractions which are responsible for the interface generation differ because of the high density difference. The volume percentage is more than a factor two lower for ZrO_2 than for SiO_2 . This serves to explain the different slopes of the reinforcement curves where the hardness is plotted versus the wt% fraction.

Concerning the impact of surface modification on the reinforcement effect, the assumption can be made that in most cases there is no difference as to whether a short or a long spacer chain is used between particle surface and linking group. However, for higher interfacial areas (e.g. for 10% ZrO_2 large) a significant effect seems to come into play: the longer the alkyl chain, the better the mechanical property. This effect is very likely to correlate directly with the fact that the longer alkyl chain spacer resulted in better nano-homogeneity for this specific particle system, as was demonstrated via SAXS. In contrast, it is very likely that this effect is not directly related to the interface physical property (hydrophobic inter-region of assembled alkyl spacer chains). Concludingly, the reinforcement effect in this ZrO_2 /PMMA system is mainly determined by other parameters, such as particle morphology and presence of functional end group at the particle surface. The physical adaption of the interface, by varying the spacer chain length, allows a fine-tuning towards higher hardness values for a certain system.

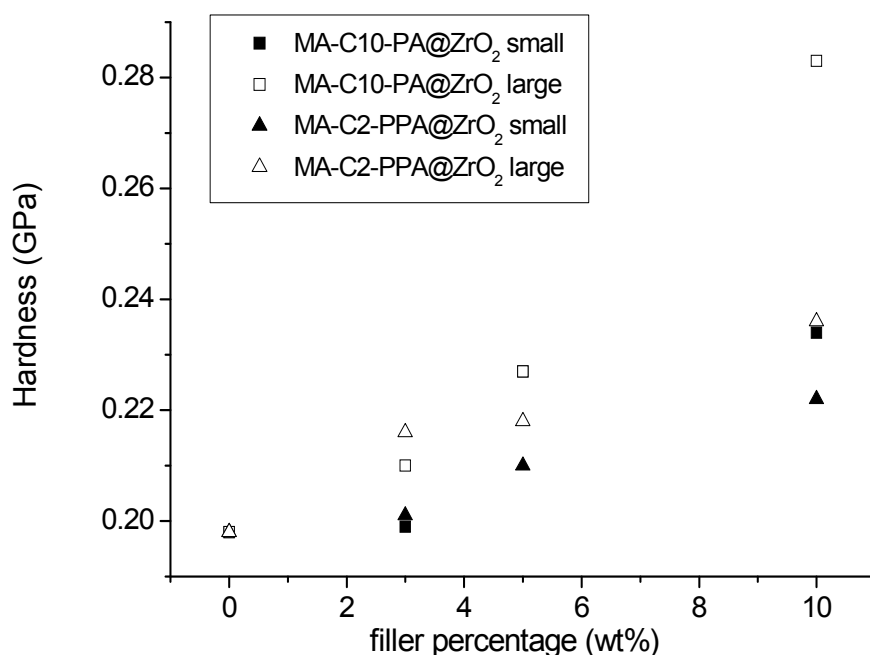


Figure 144. Hardness from *Vickers* test, converted into SI units via the geometrical parameters of the indenter, of PMMA nanocomposites including differently surface modified ZrO₂ nanoparticles with different particle sizes, the quality of the points at 10 wt% for the MA-C2-modification is not ensured because of a few macro-inhomogeneities.

Additionally, TGA measurements of the described ZrO₂/PMMA series revealed that in all cases the thermal degradation temperature shifted towards higher values, for more than 50°C for 10 wt% filler containing samples. This effect appears to relate to the crosslinking of particle and matrix, as in literature similar stability enhancement effects were observed for ZrO₂/PMMA nanocomposites when a polymerizable end group modification of the particles was applied.^[75] For an unmodified particle system, however, a different degradation behavior with comparably lower thermal stability was shown in another literature report.^[46]

For the use of SiO₂, modified with MA-C3-TMS and MA-C10-TMS molecules, qualitatively a similar reinforcement behavior as for the analogous ZrO₂ system, could be observed. The results are not plotted and discussed here in great detail because of the poor comparability of these results: the agglomeration degree was significantly different for different surface modifications. It has to be kept in mind that the "inorganic object", responsible for a reinforcement effect, is large in the case of strong agglomeration (i.e. equal to the agglomerate size) and small (i.e. equal the size of the particles) in the case of homogeneously dispersed nanoparticles. A rough comparison can be drawn between the ZrO₂ and SiO₂ system. The maximum hardness increase for SiO₂ (10 wt% MA-C10-TMS@SiO₂ small) was 18% whereas for ZrO₂ (10% MA-C10-PA@ZrO₂ large) a reinforcement by 28% could be obtained. Taking, furthermore, into account that the number of incorporated nanoparticles in the case of ZrO₂

was lower than for SiO₂ nanoparticles, it can be stated that ZrO₂ nanoparticles give a much stronger reinforcement for PMMA than SiO₂ nanoparticles.

Interesting (thermo)mechanical effects could be obtained when ⁿBu-PDMS-PPA and allyl-PDMS-PPA @ ZrO₂ small nanoparticles were incorporated into the PMMA matrix. As previous SAXS investigations showed, these materials are rather homogeneous, despite the immiscibility of PMMA and PDMS, because of the low PDMS grafting density (see chapters 3.1.5.1 and 3.2.2). Materials properties of these two particle samples, with the only difference being a polymerizable end group in case of the allyl-PDMS-PPA-modified system, were compared with regard to different filler degrees. As demonstrated by Figure 145, it could be observed that the glass transition temperature (T_g) significantly decreased by increasing filler amount for the polymerizable group containing sample. As for the ⁿBu moiety (which does not allow a covalent linkage of particle with matrix) sample, no significant change in T_g could be observed. A similar effect was also reported for the hardness in dependence of the nano-filler degree: Furthermore, a decrease in hardness with increasing filler degree could only be observed for the covalently linkable system (Figure 146). It can be assumed that the two effects of T_g change and hardness change bear relation to each other. This means that a softening of the material is reached by the incorporation of nanoparticles. This stands in contrast with the commonly observed effects of increasing hardness and increasing brittleness when hard objects, like metal oxide nanoparticles, are incorporated into a relatively soft polymer matrix.^[14] The trend for the change of both properties seems to be an interface related effect, because a reinforcement is already observable at low filler percentages and a plateau is reached for higher percentages. Literature describes one relevant system, where the components PDMS, PMMA and inorganic compound (namely clay) are combined to form a nano-material. In this case the PDMS is the continuous phase and PMMA shows a particle like microstructure. It was furthermore reported that via such a combination of compounds, mechanical characteristics like e.g. storage modulus, a number for the energy uptake of the overall system, are drastically changed. These results point out the high potential of such combinations.^[245] However systems which are comparable to the here described materials have been described in literature with respect to their mechanical properties up to now as far as known by the author. However, it is assumed that this softening effect results from the unique situation of flexible PDMS chains at the interface between PMMA and ZrO₂. The flexible PDMS chains allow a softening of the overall nanocomposite material. By comparing the ⁿBu group system to the allyl-group system, it also can be concluded that in order to achieve this effect, a strong linkage between ZrO₂-PDMS-PMMA is necessary. Only through this can the materials bulk properties be changed via the soft PDMS interface. This is plausible, as in PMMA with non-linked PDMS chains (ⁿBu end group), the PDMS chains can homo-agglomerate. It is assumed that thus PDMS domains are formed which lead to a different material stress transfer behavior, compared to the situation when the PDMS chains are linked (allyl end group) to PMMA and thus forced to interact with the polymer matrix. This is a possible explanation for the obtained results.

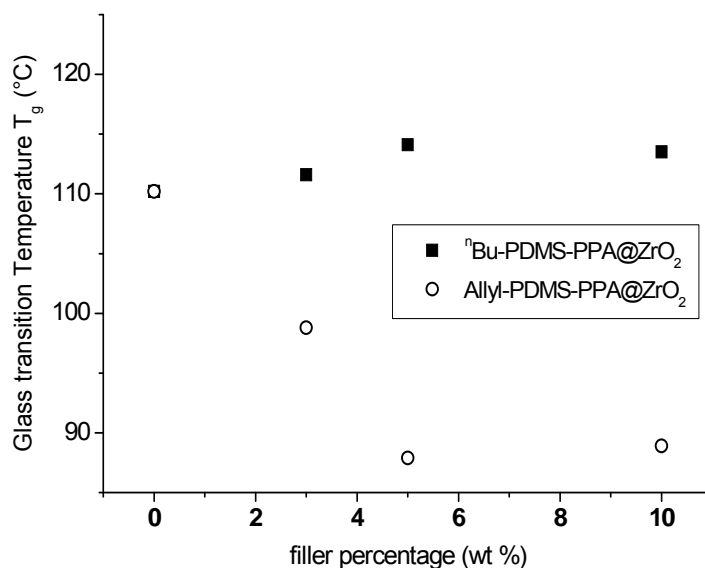


Figure 145. Glass transition temperatures T_g of PMMA nanocomposites including PDMS modified small ZrO_2 nanoparticles.

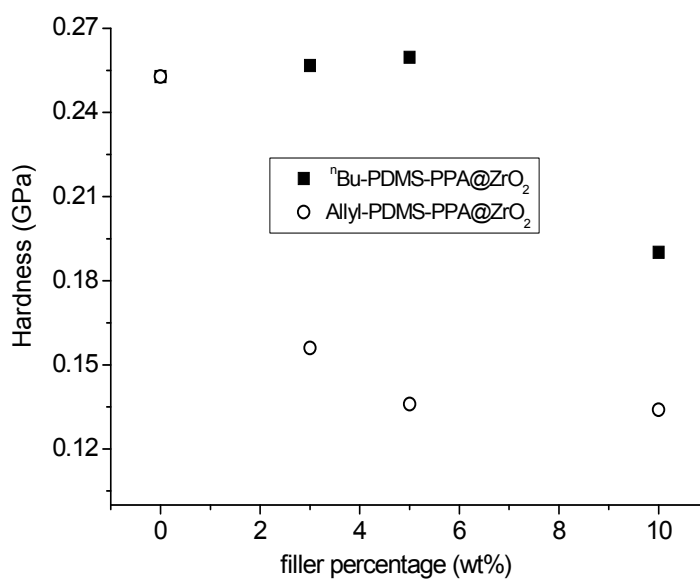


Figure 146. Hardness from *Vickers* test, converted into SI units via the geometrical parameters of the indenter, of PMMA nanocomposites including PDMS modified small ZrO_2 .

By using these nanoparticles to build a softer nanocomposite material, the toughness of the material is considered to be positively affected. Hence, a new possibility to tune mechanical properties of particle filled nanocomposites via chemical interface tailoring is presented here. The mechanical properties are already significantly altered at low filler degrees.

3.2.5.3 Dispersion structure (SAXS) – mechanical properties

The previous chapters discussed relations between surface chemistry and dispersion structure, as well as relations between surface chemistry and mechanical properties. The following conclusions on the relation of dispersion structure and mechanical properties can be drawn:

- Size of the nanoparticles: Smaller nanoparticles lead to stronger mechanical reinforcement effect (examples: Gly-TMS@SiO₂ in epoxy resin, SiO₂ in polystyrene).
- Morphology of nanoparticles: Rough, porous nanoparticles lead to stronger mechanical reinforcement (example: methacryloyl functionalized ZrO₂ in PMMA).
- Dispersion quality: Higher dispersion quality gives stronger reinforcement effects (general). The dispersion quality strongly depends on point 1 and 2 and the nature of chemical surface modification.
- The effects of point 1-3 are all considered to derive its origin from one effect: The higher the interfacial region in the material the higher the reinforcement effect.
- Requirement for point 1-3 is an appropriate interfacial adhesion within the nanocomposite material. For instance, when the interfacial adhesion can be considered as low, the particles could show stronger movement within the matrix under mechanical stress. Furthermore, larger particles show higher reinforcement effects (e.g. comparison of DEG- or Gly- modified SiO₂ nanoparticles in epoxy resins).

As it was shown, the nanocomposite dispersion structure is related to the nature of the chemical surface modification, the nature of the nanoparticle and the inorganic filler content. Furthermore, the investigated mechanical parameters (hardness) depend on these three parameters.

By keeping two parameters constant, particle nature and filler degree, which is the most reasonable way, the agglomeration (hard sphere volume fraction from SAXS) can be systematically varied via change of the chemical surface functionality in order to investigate its impact on the mechanical properties (hardness) of the nanocomposite material.

However, there is one major problem connected to this approach. When the hard sphere volume fraction η should be significantly changed via chemical surface modification, it cannot be achieved via only slight variations, tuning only hydrophobicity. To give substantially different η values, in one case a crosslinkable end group has to be applied, yielding in very high dispersion quality. In the other case, a hydrophobicity matching, but non crosslinkable group modification has to be applied to yield significantly lower dispersion quality, but still no macro-phase-separation as it would be the case for unmodified nanoparticles. However, by changing the surface functionality, also the interfacial adhesion within the composite can be changed, which has a direct impact on mechanical properties.

Nonetheless, for two selected examples, the hard sphere volume fraction (dispersion structure) are directly compared with the obtained hardness for different nano-filler contents. During the discussion it has to be kept in mind that different interfacial adhesion might be present for different dispersion structures as well, which may also lead to a mechanical properties change.

At the first example, small ZrO_2 nanoparticles, modified with DEG-PPA and Diol-PPA are discussed. The interfacial adhesion is not considered to be too much different for those systems, as both organic groups allow a weak (DEG) and moderate (Diol) particle-matrix interaction, in contrary if one would compare e.g. DEG-PPA (weak) with Ep-PPA (strongly covalent) modified systems. Thus, a comparison in terms of quality should be valid. This comparison is plotted in Figure 147. It is shown that the characteristics for reinforcement, depending on the filler percentage in the high η range, is different from the effect in the low η range. Stronger dispersed systems show a higher increase in hardness with nano-filler percentage and also higher absolute values for the hardness are obtained.

Following this interpretation, the diagram in Figure 147 can be divided into two parts: A high η range (larger agglomerates), where the materials behave like micro/macro-filled polymers and a low η range (single dispersed nanoparticles, interface determined properties), where the behavior can be related to nano-filler materials. This is plausible as the agglomerates, which are present in the high η region, behave like micron size particles. By dividing the diagram in these two regions, the presence of a transition region (moderate η) has to be assumed, where the reinforcement is related to both a nano-filler and a micro-filler effect. The data-point for 10 wt% Diol-PPA@ ZrO_2 in epoxy resin is considered to lie within this intermediate range. This assumption is conform with results from TEM. An explanation for the lower agglomeration at higher filler degrees can be due to higher present shear forces in the curing mixture due to a higher viscosity when higher filler degrees are possible (agglomerates collide and are thus broken, see previous discussions). These considerations explain the reinforcement behavior with the low η region as a region of steep increase in hardness and the high η region as a region of low increase in hardness with increasing filler percentage.

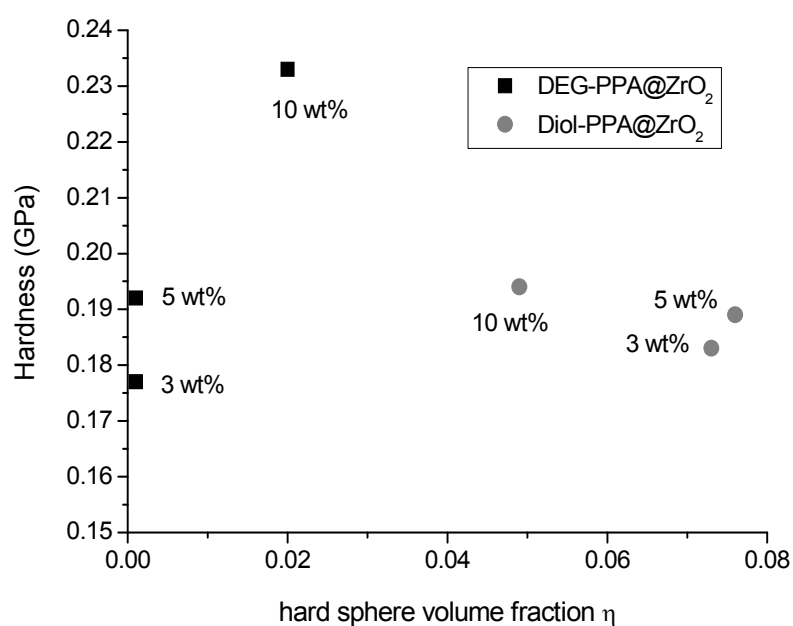


Figure 147. Correlation of agglomeration degree (hard sphere volume fraction from SAXS) with hardness of small ZrO_2 nanoparticle filled epoxy resin nanocomposites (3, 5 and 10 wt% filler content).

A similar behavior is observed for the different, simple thermoplast system of Styr-TMS@SiO₂ and DTMS@SiO₂ in polystyrene (Figure 148). Here, however, the impact on the interfacial adhesion on the mechanical behavior can not be neglected, as one group can covalently link particle and matrix and the other group can only allow physical interaction. Nonetheless, the discussed relation can be found: In the low η region the reinforcement effect is higher than in the higher η region.

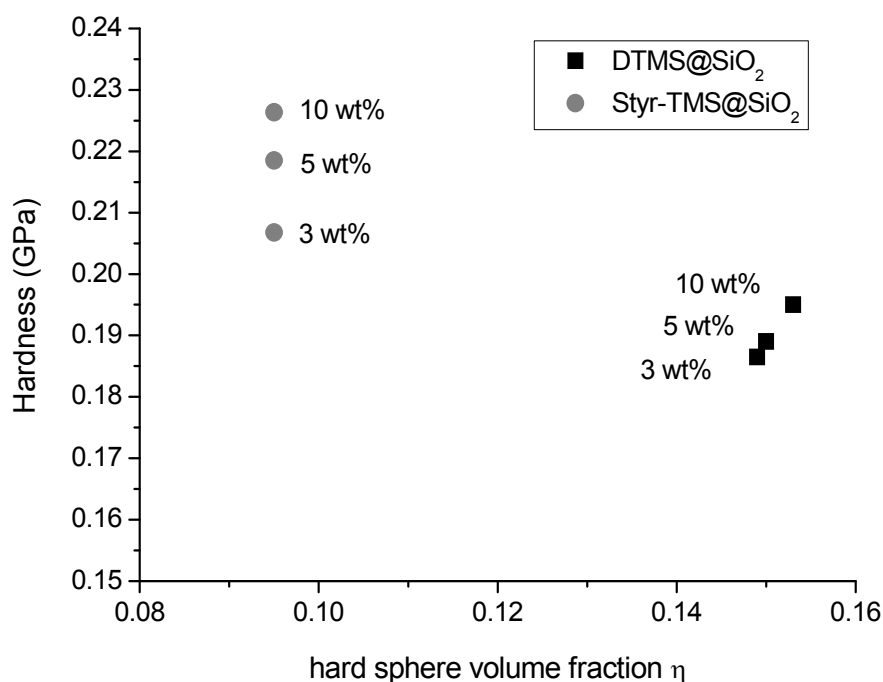


Figure 148. Correlation of agglomeration degree (hard sphere volume fraction from SAXS) with hardness of small SiO₂ nanoparticle filled PS nanocomposites (3, 5 and 10 wt% filler content).

Concludingly, the mechanical properties of the investigated nanocomposite materials (for thermoplasts as well as for crosslinked epoxy resins) are predominantly determined by the quantity of the interfacial region (depends on particle size, morphology, and dispersion quality) and the interfacial adhesion between the inorganic- and organic components. A chemical tailoring of the nanoparticle surface affects both of these crucial parameters.

4 Experimental Section

4.1 Materials

All chemicals used for syntheses (standard reagent grades) were obtained by commercial suppliers (Aldrich, Fluka, ABCR, Acros). Bisphenol-F-diglycidyl ether (BFDGE) was purchased from Organica Feinchemie GmbH. Phenyl phosphonic acid was recrystallized from acetonitrile. Hexamethylcyclotrisiloxane was dried by stirring the melt with finely crunched CaH_2 at 75°C under argon atmosphere and purified via re-sublimation at $60^\circ\text{C} / 30$ mbar. Diethylenetriamine was distilled before use. Triethylamine was dried by refluxing for 8 h over finely crunched CaH_2 followed by distillation and storage under argon atmosphere over a 4\AA molecular sieve. The monomers methyl methacrylate and styrene were filtered over a neutral Al_2O_3 column, degassed via three freeze-pump-thaw cycles, and kept under argon atmosphere, directly before use. All other chemicals were used as received. The *Karstedt's* catalyst was used in form of a 2.1-2.4% Pt containing solution in xylene (supplier ABCR).

The used solvents were from HPLC grade (Aldrich, Fluka, Acros). Methanol and dioxane were purified using a PureSolv (Innovative Technology inc.) solvent purification system and stored over a 4\AA molecular sieve under argon atmosphere. Water free tetrahydrofuran (THF) and toluene were prepared via a standard procedure by refluxing over sodium metal and distillation.^[446] Water was deionized via ion exchange columns.

Manipulations under inert atmosphere were carried out by standard *Schlenk* technique or in a glove box, using argon with the specification 5.0 as protective gas.

For experiments with a plane macroscopic SiO_2 substrate, a Si-wafer from Wacker Siltronic AG, fz, orientation 100, phosphorus doped, resistivity $\geq 4500 \Omega\cdot\text{cm}$ has been oxidized using the piranha-reagent. The thickness of the SiO_2 film was determined by ellipsometry, $13.7 \pm 0.3 \text{\AA}$.

For the preparation of flat macroscopic ZrO_2 substrates, a Si (100) wafer has been coated with ZrO_2 by atomic layer deposition (ALD) using 1x450 and 1x400 cycles at 200°C . This procedure, which is described in literature,^[355] was carried out by *S. Abermann* in the group of *E. Bertagnoli*, who kindly supported this substrate. The deposited layer was then annealed for 5 min at 600°C under argon-atmosphere. Ellipsometry revealed an average thickness of $8.5 \pm 0.5 \text{ nm}$ for the zirconium oxide layer and atomic force microscopy (AFM) measurements revealed a root mean square (rms) roughness of 0.35 nm (from the measurement of three $1 \times 1 \mu\text{m}$ areas).

4.2 Analytical techniques

4.2.1 Nuclear magnetic resonance spectroscopy (NMR)

Liquid state NMR spectra were recorded on a Bruker Avance 250 spectrometer (^1H at 250.13 MHz, ^{31}P at 101.26 MHz, ^{13}C at 62.80 MHz). ^{29}Si -spectra and ^{119}Sn -spectra have been recorded on a Bruker Avance DPX 300 spectrometer at 59.63 MHz (^{29}Si) and 111.91 MHz (^{119}Sn). The liquid state NMR instruments were equipped with a 5 mm broadband probe head and a z-gradient unit. 2D spectra (^{29}Si) were measured with Bruker standard pulse sequences. The used deuterated solvents were purchased from Eurisotop and Aldrich.

Solid state NMR spectra were recorded on a Bruker Avance DPX 300 instrument equipped with a 4 mm broad band MAS (Magic Angle Spinning) probe head operating at 75.40 MHz for ^{13}C , 59.6 MHz for ^{29}Si and at 121.39 MHz for ^{31}P . The ^{13}C spectra and ^{29}Si spectra were recorded with ramped CP/MAS (Cross Polarization and Magic Angle Spinning) and ^{31}P with HPDEC (high power decoupling) at a rotor frequency of usually 6-8 kHz.

The chemical shifts δ are given in ppm with the abbreviations for the signal multiplicities marked as s (singlet), bs (broad singlet), d (doublet), t (triplet), q (quartet) and m (multiplet)

4.2.2 Fourier transform infrared spectroscopy (FT-IR)

For characterization of synthetic products, Fourier transform infrared spectroscopy (FT-IR) measurements were performed on a Bruker Tensor 27 Spectrometer under ambient air conditions. For standard characterization of molecular compounds, the spectra were recorded in attenuated total reflection (ATR) mode (MicroFocusing MVP-QL with a ZnSe crystal) with 32 scans at a resolution of 2 cm^{-1} . For self-assembled-monolayer studies, the spectra have been recorded in transmission mode using KBr (Aldrich, IR grade) disks (1.3 mm diameter) as sample matrix ($\sim 1\text{ mg}$ sample, $\sim 100\text{ mg}$ KBr), with 64 scans at a resolution of 1 cm^{-1} .

For the investigation of plane wafer substrates, the IRRAS-method (infra red reflection absorption spectroscopy) has been applied, utilizing a Bruker Vertex 80 IR spectrometer under nitrogen atmosphere.

For thermogravimetric analysis – FT-IR coupled measurements (TG-FTIR), the spectra were recorded on a Bruker Vertex 70 with a TG-IR coupling gas cell device at 180°C . Details see chapter 4.2.5.

The used analysis software was OpusTM 4.0. The shown wavenumbers ν (cm^{-1}) have been taken from the peak values of the vibrational bands in the spectra by this software.

4.2.3 Elemental analysis

Elemental analysis was carried out at the Microanalytical Laboratory at the University of Vienna.

4.2.4 Gel permeation chromatography (GPC)

Gel permeation chromatography (GPC) also called size exclusion chromatography (SEC) measurements were performed using a Waters system including a 515 HPLC pump, a 717 autosampler, a 2410 differential refractive index detector and Styragel columns (GPC PHASE SDV 50/100/10E5A). Chromatograms were recorded at 40 °C at a flow rate of 1 ml/min applying linear polystyrene standards. Molecular weight analyses were carried out using the Viscotek Omniseq 4.5.6 software. For the measurement of poly (dimethyl siloxane) (PDMS) molecules, toluene was used as eluent and for all other measurements, tetrahydrofuran (THF) was used.

4.2.5 Thermogravimetric analysis (TGA)

Standard thermogravimetric analyses (TGA) for materials characterization were performed on a Netzsch Iris TG 209 C in a platinum crucible heating from 25°C to 900°C with a heating rate of 10°C/min under synthetic air at 25 ml/min gas flow. Initial masses were kept in the range of 10 mg. Correction curves were recorded under the same conditions and subtracted. Onset temperatures and mass losses of decomposition steps were analyzed with the Proteus analysis software (Netzsch) after subtraction of the measured correction curve. The functions determining the onset temperatures are standard methods to allow comparability. The onset temperature is defined by the intersection point of the tangent of the baseline and the tangent of the inflection point.

Thermogravimetric analyses coupled with mass spectrometry (TG-MS) measurements were performed on a TGA 2050 (TA instruments) TGA instrument, coupled with a Pfeifer Vakuum Thermostar mass spectrometer. The measurements were performed under nitrogen atmosphere with a flow rate of 25 ml/min and a heating rate of 10 K/min. The samples were measured in platinum crucibles with ~20 mg initial sample mass.

Thermogravimetric analyses coupled with FT-IR (TG-FTIR) measurements were carried out on a Netzsch Iris TG 209 F1 TG instrument, coupled with a Bruker Vertex 70 FT-IR spectrometer with a TG gas analysis cell, which was heated at 180°C. The transition line between the instruments (SiO₂ capillary) was heated at 180°C. The measurements were carried out under O₂ or N₂ atmosphere with 20 mL/min gas flow. The samples (~ 10 mg) were put in corundum crucibles and measured at a heating rate of 20 K/min.

4.2.6 Differential scanning calorimetry (DSC)

For analyses of molecular synthetic products or nanoparticles, DSC measurements were performed on a DSC823e from Mettler Toledo, with liquid nitrogen cooling for lower temperatures experiments. The polymer samples were filled into 40 µl aluminum crucibles. Measurements were carried out under N₂ atmosphere. The glass transition temperatures (T_g) were determined after a primal heating and cooling period to delete the thermal history of the samples. The heating and cooling cycle was repeated two times before analyzing the T_g with

the corresponding software from Mettler. For each measurement, a typical sample mass of ~4 mg was used and a heating rate of 10 K/min was applied.

For analyses of polymer nanocomposites, DSC thermograms were recorded with a TA Instrument DSC - Q2000 in a nitrogen gas flow of 50 mL/min with a heating rate of K/min. The T_g of the polymer materials was characterized as the midpoint of the change in specific heat from the DSC scans.

4.2.7 pH measurement

The measurement of pH values was done at 25°C utilizing a Mettler Toledo pH meter with glass electrode.

4.2.8 Zeta potential measurement

Zeta potential measurements have been performed on a PALS Zeta Potential Analyzer (equipped with a 660 nm wavelength laser) in water at 25°C. The suspension concentrations were 5.00 mg/mL. A voltage of 4.00 volts was applied with a field frequency of 2 Hz. For measurement, 10 cycles have been performed. Each measurement was repeated 5 times and the reported results represent the arithmetic average value of these 5 repeated measurements. For the data processing, the corresponding software (Ver. 3.54) has been used, applying the *Smoluchowski* model for the zeta-potential calculation.

4.2.9 Dynamic light scattering (DLS)

Dynamic light scattering (DLS) measurements were carried out by non-invasive backscattering on an ALV/CGS-3 Compact Goniometer System with an ALV/LSE-5003 correlator and multiple tau correlator at a wavelength of 632.8 nm (He-Ne Laser) at a 90° goniometer angle at 25°C. The dispersing media were purified before use with a syringe-filter (200 nm mesh).

DLS, also called photon correlation spectroscopy, primarily measures time-dependent fluctuations of scattered coherent light, which means the decay of the autocorrelation function, which is caused by diffusive motion of the particles. The experimentally measured diffusion coefficients can be converted to a solvodynamic radius via the *Stokes-Einstein* equation, see chapter 3.1.1.4, Eq. 5. These calculations were carried out using the corresponding software ALV-5000/E/EPP & ALV 60X0 by the analysis of the correlation-function via the $g_2(t)$ method to calculate the diffusion coefficients and applying the *Stokes-Einstein* equation (Eq. 5) for the calculation of the radii distributions. The obtained size distribution functions were then processed by a linearized mass-weighting (m.w.), surface-weighting (s.w.) or number-weighting (n.w.), applying the corresponding software.

The particle size values from DLS represent the value at maximum of the size distribution function and the deviation is represented by the full width at half maximum of the distribution function.

Dispersion behavior experiments (redispersibility and dispersion stability) were carried out under the following standard conditions. If not explicitly different conditions are mentioned, 0.5 g/L suspensions were prepared and homogenized by placing them in an USC 200-2600 ultrasonic cleaning bath from VWR for 30 min. The dispersions were then allowed to equilibrate for 1 h at 25°C and measured with DLS.

4.2.10 Transmission electron microscopy (TEM)

Transmission electron microscopy (TEM) images were recorded on a JEOL JEM-100CX and on a FEI TECNAI G20 transmission electron microscope. High resolution TEM images (HRTEM) were recorded on a FEI TECNAI F20 microscope. The instruments were provided by the University Center of Transmission Electron Microscopy, Vienna University of Technology.

For the investigation of nanoparticle powder samples, the powders were dispersed in the corresponding medium, applying ultrasound, and the dispersion was drop cast on a carbon coated copper mesh TEM grid. Also for ultramicrotome thin cuts (see chapter 4.2.11), these specimen carriers have been utilized.

4.2.11 Ultramicrotomy

Ultramicrotomy thin cuts for transmission electron microscopy (TEM) measurements were prepared on a Reichert-Jung Ultracut E with a 35° diamond knife. The epoxy resin samples were directly cut and the PMMA and PS samples were embedded in an epoxy resin before preparation of the cuts.

4.2.12 Scanning electron microscopy (SEM) and energy dispersive X-ray spectroscopy (EDX)

Scanning electron micrographs were recorded on a FEI Quanta 200 FEG instrument, equipped with a field emission tip cathode (FEG-SEM), at the University Center of Transmission Electron Microscopy, Vienna University of Technology.

Energy dispersive X-ray spectroscopy (EDX) was carried out on a FEI Quanta 200 Mk2 SEM microscope, with a tungsten filament electron gun, at 15 kV.

4.2.13 Atomic force microscopy (AFM)

Atomic force microscopy (AFM) for the investigation on plane wafer substrates was carried out at the Institute of Chemical Technologies and Analytics at the Vienna University of Technology, using a Nano-Scope III multimode SPM from Digital Instruments (VeecoMetrology Inc.). Measurements were conducted in tapping mode under ambient air using single-crystal silicon cantilevers (Arrow NC cantilevers, NanoWorld, spring constant 42 N/m, resonance frequency 285 kHz), and an E-scanner, operating at a scanning rate of

4 Hz. The data was evaluated with the NanoScope 6.10b20 software (Digital Instruments, Veeco Metrology Inc.).

Polymer shell nanoparticles have been investigated with AFM at the Saarland University Saarbrücken, Germany, at the experimental physics department in the group of *Prof. K. Jacobs*. The measurements were carried out on a Bruker MultiMode Scanning Probe Microscope, equipped with a Nanoscope IIIa controller, in tapping mode. For the measurements, the particles have been placed on a Si (100) wafer by spin coating using a 1 g/L particle dispersion in toluene.

4.2.14 Small angle X-ray scattering (SAXS)

Small angle X-ray scattering (SAXS) experiments as well as data processing and fitting was carried out by *S. Pabisch* from the Physics department of the University of Vienna, in the group of *Prof. H. Peterlik*.

The SAXS measurements were performed under vacuum conditions using a rotating anode X-ray generator with a pinhole camera (Nanostar, Bruker SAXS) with Cu K $_{\alpha}$ radiation monochromatized and collimated from crossed Goebel mirrors and a 2D position sensitive detector (Vantec 2000). The sample-to-detector distance was varied from 13 cm to 107 cm to cover a wide range of the scattering vector q from 0.1-15 nm $^{-1}$. All SAXS patterns were radially averaged and corrected for background scattering to obtain the scattering intensities in dependence on the scattering vector $q=4\pi/\lambda \sin\theta$, where 2θ is the scattering angle and $\lambda=0.1542$ nm the X-ray wavelength.

The data fitting was done utilizing the software MathematicaTM.

4.2.15 Powder X-ray diffraction (pXRD)

Powder X-ray diffraction (pXRD) measurements were carried out on a Philips X'Pert Pro instrument at CuK $_{\alpha}$ - radiation with a *Bragg-Brentano*-arrangement with an angle speed of 6°/min where the sample was carried on Si-single-crystal-wafers under ambient conditions. Crystallite size was calculated using the TOPAS software, via *Rietveld* refinement using 5 metric parameters. The average crystallite size D was determined from the broadening of the peaks by *Scherrer's* equation, Eq. 9,

$$D = 0.9\lambda /(\beta \cos \theta) \tag{Eq. 9}$$

where λ is the wavelength of the X-rays, θ the *Bragg* angle and β the calibrated breadth of a significantly intense diffraction peak (for ZrO $_2$ here the (1 1 1) reflection) at half-maximum intensity.

4.2.16 Nitrogen sorption experiments

Nitrogen sorption measurements were performed on a Micromeritics ASAP 2020 instrument at 77 K. The samples were degassed under vacuum at 60°C for at least 8 h prior to measurement. The surface area was calculated according to *Brunauer, Emmett and Teller* (BET).^[285] For the calculation of the specific surface area, S_{BET} , a demand of 0.162 nm² per N₂ molecule was assumed.

4.2.17 Water uptake experiments

For the measurement of the relative water uptake of nanopowders at room temperature, ~100 mg of each nanopowder sample were put in an open glass vessel and dried over water free CaCl₂ at 1 mbar until the weight remained constant (m_{start}). Then, the samples were placed in a desiccator over water at 25°C, to guarantee an equilibrium atmosphere. The masses of the samples were determined over the experiment period, and corrected with the determined value of water adsorption of an empty vessel, until they remained constant. This represented the end of the water uptake experiment (m_{end}).

The water uptake of epoxy resin nanocomposites was carried out following a literature known procedure for the determination of swelling degree of epoxy resins.^[271] Thereby, sample specimen with a thickness with the dimensions of 20.0 x 10.0 x 1.4 mm have been cut out of the prepared epoxy resin materials. The materials were dried at 60°C over P₂O₅ until their mass remained constant (m_{start}). Then, each sample was placed in a closed vessel and fully submerged in deionized water. These samples were kept in an oven at 60°C and for mass determination, removed quickly, wrapped 3 times with tissue, gravimetrically analyzed, and immediately put back into the experimental conditions. This procedure was repeated until the mass remained constant, which represented the end of the experiments (m_{end}).

The accuracy of the weighting instrument (Mettler Toledo) was 0.01 mg. The water uptake Δm was then calculated, applying the formula from Eq. 10.

$$\Delta m = \frac{m_{\text{end}} - m_{\text{start}}}{m_{\text{start}}} \cdot 100\% \quad \text{Eq. 10}$$

4.2.18 Ellipsometry

Ellipsometric measurements were performed on a SENTECH SE500adv instrument. Determination of the silicon oxide film thickness and the organic film thickness on the SiO₂ was based on a model of three layers (Si/SiO₂/air) and a four-phase model (Si/SiO₂/adsorbate/air), respectively. For the ZrO₂ film thickness the analogous model of three layers (Si/ZrO₂/air) and for the organic film thickness on ZrO₂ a four-phase model (Si/ZrO₂/adsorbate/air) was used to describe the system. A commercial software, based on the *McCrackin* algorithm,^[447] was used to calculate the film thickness from the measured

ellipsometric angles. For each sample, ten different spots were measured and the average value was determined.

4.2.19 Contact angle measurements

Water contact angle measurements have been performed on a Krüss G1023 contact angle measurement instrument, using deionized water.

4.2.20 Optical transmittance measurements (UV-VIS)

UV-VIS transmission measurements at nanocomposite films were carried out on a Perkin Elmer Lambda 35 UV/Vis spectrometer, operated with a 50 mm integrating sphere. The spectra were recorded from 200 to 800 nm with a data interval of 1 nm, a scan speed of 480 nm/min, a cycle time of 1 second and a slit width of 1 nm. The light source was changed at 326 nm.

For the preparation of 250 μm thick films, which were investigated by UV/Vis, a Specac high temperature constant thickness film maker with distance ring E was used. A Specac 15 ton press provided a maximum load of 2 tons.

4.3 Mechanical tests

Mechanical tests of nanocomposite materials have been carried out by collaborators, *T. Koch* and *M. Sajjad* in the group of *Prof. S. Seidler* at the Institute of Materials Science and Technology, Vienna University of Technology.

All thermoplast samples (poly(methyl methacrylate), PMMA and polystyrene, PS) have been hot pressed before mechanical tests were performed to get appropriate sample specimen with a uniform thermal history. PS samples were treated at 130°C for 20 min and PMMA samples were treated at 160°C for 20 min.

4.3.1 Dynamic mechanical thermoanalysis (DMA)

The dynamic mechanical properties were measured using a TA Instruments DMA 2980 instrument, operated in the tensile mode at an oscillation frequency of 1.0 Hz. Data was collected from 25°C to 170°C at a scanning rate of 2 °C/min. A dynamic strain of 0.1 % was imposed to measure the dynamic modulus in the linear viscoelastic regime. DMA specimens were prepared from the films with nominal dimensions 15 mm (length) \times 1 mm (thickness) \times 3 mm (width). A minimum of three specimens of each composition were tested. The data processing was performed utilizing the corresponding instrument software to calculate T_g values and moduli.

4.3.2 Hardness

A *Vickers* tester (small-load hardness) was used to evaluate hardness with a square-based pyramid diamond indenter with an angle of 136° between the opposite faces at the vertex, which was pressed into the surface of the test piece using a small force of 9.8 N. The test force was maintained for 30 s. After the force had been removed, the diagonal lengths of the indents (*Vickers* marks) were measured and the arithmetic mean, d , was calculated. The *Vickers* hardness number, HV , is given by Eq. 11,

$$HV = c \cdot \frac{F}{S} \quad \text{Eq. 11}$$

where c is a constant, F is the test force and S is the surface area of indentation. For the applied instrument, via including the geometrical parameters, Eq. 11 can be expressed as Eq. 12.

$$HV = 0.102 \cdot 2F \cdot \frac{\sin(136^\circ/2)}{d^2} \quad \text{Eq. 12}$$

This equation (Eq. 12) allowed to convert the HV values into SI units (GPa) for the hardness by multiplication with the numerical factor 0.009807. In order to get precise values, 10-20 indents (*Vickers* marks) were measured on one sample to obtain the average value of HV for each sample.

4.4 Preparation of nanoparticles

For nanoparticle separation, a Hettich EBA 20 S centrifuge (86 mm rotor radius) has been used.

4.4.1 Preparation of small ZrO₂ nanoparticles

Small ZrO₂ nanoparticles were synthesized following a literature known procedure^[122] via thermal decomposition of 58 mL of a 4 M solution of ZrOCl₂ in water in a stainless-steel-autoclave with a 90 mL poly(tetrafluoro ethylene) (PTFE)-inlay at 200°C. The reaction was carried out for 72 h and the particles were isolated by precipitation with acetone and centrifugation at 8000 rpm. Afterwards, they were washed with a mixture of water and ethanol (1:5) three times (centrifugation at 8000 rpm) and dried over P₂O₅ at 5 mbar to yield 17.4 g of a white powder.

Characterization:

pXRD: 100% crystalline ZrO₂, Baddeleyite-phase (monoclinic), crystallite size 4.5 nm.

DLS: hydrodynamic diameters in water: 17.8 ± 3.6 nm (n.w.), 22 ± 7 nm (m.w.).

TEM: crystals with aspect ratio of ~ 2 , spherical equivalent diameter of 6 ± 0.4 nm (n.w.).

S_{BET} = 140 ± 2 m²/g.

4.4.2 Preparation of large ZrO₂ nanoparticles

Larger ZrO₂ nanoparticles were prepared by a procedure described in literature,^[121] under hydrothermal conditions. A mixture of 14.5 mL (807 mmol) H₂O, 19.4 mL (322 mmol) acetic acid and 15.4 mL (9.2 mmol) zirconium acetate solution (16 wt% in acetic acid) was heated in a stainless steel autoclave with a 90 mL PTFE-inlay for 16 h at 170°C. The obtained stable particle-dispersion was then destabilized by removing 2/3 of the volume of the mixture by evaporation and adding 10 mL acetone. Afterwards, the product was separated (centrifugation at 8000 rpm) and washed three times (centrifugation at 8000 rpm) with a mixture of acetone and water (10:1). The final product was dried over P₂O₅ at 5 mbar, resulting in 4.4 g of a white powder.

Characterization:

pXRD: 100% crystalline ZrO₂, Baddeleyite-phase (monoclinic), crystallite size 2.9 nm.

DLS: hydrodynamic diameters in water: 54 ±11 nm (n.w.), 66 ±19 nm (m.w.).

TEM: irregular shaped polycrystalline particles, spherical equivalent diameter of 38 ±3 nm (n.w.).

S_{BET} = 171 ±2 m²/g.

4.4.3 Preparation of SiO₂ particles with various sizes

SiO₂ (nano)particle sols have been prepared by the *Stöber*-process.^[114] The nanoparticle preparations were carried out in 100 mL solvent by first adding water and NH₄OH to the solvent, followed by the dropwise addition of tetraethyl orthosilicate (TEOS). The reaction mixtures were stirred at room temperature with a magnetic stirrer (600 rpm). Then, the NH₃ was removed under oil-pump-vacuum and the amount of evaporated solvent was re-added to the mixture. The thus obtained nanoparticle dispersions were then directly used in the following *in situ* surface-modification step. The variation of synthetic parameters, such as solvent type, amount of water, TEOS, and concentrated aqueous ammonia solution (Table 30), resulted in different SiO₂ particle diameters.

Table 30. Synthetic parameters for preparation of SiO₂ particle samples with various sizes.

Sample	H ₂ O [mL]	TEOS [mL]	NH ₄ OH conc. [mL]	Solvent	Particle diam. (DLS) m.w. [nm]	reaction time [h]	literature
SiO ₂ small	2.00	10.5	0.05	methanol	9.4 ±2.7	72	[286]
SiO ₂ large	2.00	4.0	3.3	ethanol	72 ±19	20	[287]
SiO ₂ nano	2.00	4.0	3.0	ethanol	46 ±10	20	[287] adaption
SiO ₂ micron1	2.00	6.0	12.0	ethanol	390 ±80	20	[114] adaption
SiO ₂ micron2	0.00	6.0	12.0	ethanol	680 ±55	20	[114] adaption

To obtain dry nanopowders of unmodified SiO₂ nanoparticles, at this stage, the isolation of the nanoparticles from the prepared sol was carried out by the following procedure: The solvent was evaporated and the remaining product was washed three times with *n*-hexane, separated by centrifugation at 8000 rpm for 20 min and dried over P₂O₅ at 5 mbar to give dry, white nanopowders.

In case of the SiO₂ small sample, the yield was 2.17 g.

Characterization:

TEM: spherical particles with a mean diameter of 6.8 ±1.3 nm (n.w.).

S_{BET} = 711 m²/g.

In case of the SiO₂ large sample, the yield was 0.86 g.

Characterization:

TEM: spherical particles with a mean diameter of 60.8 ±1.6 (n.w.).

S_{BET} = 76 m²/g.

4.5 Syntheses of coupling agents

4.5.1 Preparation of alkyl spacer / no spacer based coupling agents

4.5.1.1 Preparation of dodecylphosphonic acid (DPPA)

The coupling agent dodecylphosphonic acid was synthesized via an *Arbuzov*-reaction and hydrolysis of the obtained phosphonate applying literature-known procedures.^[312, 313] 15.6 mL (64 mmol) 1-Bromododecane and 12.4 mL (74 mmol) triethylphosphite were stirred for 3.5 h in a 250 mL round-bottom flask under reflux. The excess of triethylphosphite was removed at 100°C / 12 mbar and the remaining intermediate-product (dodecylphosphonic acid diethyl ester) was afterwards refluxed with 70 mL HCl conc. for 22 h for hydrolysis. The crude product was obtained as a white solid after concentrating the reaction mixture to 20 mL. The product was washed several times with acetonitrile and dried in an oil-pump-vacuum. It was further recrystallized from hexane and dried in an oil-pump-vacuum. Yield: 9.5 g (38 mmol, 59%) colorless crystals.

Characterization:

¹H NMR(CDCl₃): δ(ppm) = 0.84 (t, J_{HH} = 6.7 Hz, 3H, CH₃); 1.26 (m, 18H, CH₂); 1.55-1.82 (m, 4H, CH₂-CH₂-P); 8.56 (s, 2H, P-OH).

¹³C NMR(DMSO-d₆): δ(ppm) = 31.83, 30.52, 29.68-29.62 (6C), 26.63, 22.99, 22.58 (CH₂); 14.22 (CH₃).

³¹P NMR(CDCl₃): δ(ppm) = 39.5.

IR(ATR): ν(cm⁻¹) = 2954 (CH₃); 2917 (ν_{as} C-H, CH₂); 2871 (CH₃); 2849 (ν_s C-H, CH₂); 1469 (C-H); 1212 (P=O); 1003 (P-O); 942 (P-OH).

4.5.1.2 Synthesis of 1-pyryl phosphonic acid (PhPPA)

The synthesis of 1-pyryl phosphonic acid^[448] was carried out using a metal catalyst as described in literature for the coupling of aryl-halides with triethylphosphite.^[314] 1.5 g (5.3 mmol) 1-Bromopyrene were mixed with 50 mg (0.53 mmol) anhydrous NiCl₂ and 3.4 g (15.9 mmol) triisopropylphosphite in a 50 mL round-bottom flask. The excess triisopropylphosphite was then removed in vacuum and the remaining solid was dissolved in toluene, washed twice with water and with conc. NaCl solution and dried over Na₂SO₄. After removal of the solvent, the remaining solid was washed with cold toluene and dried to give 1.8 g (4.9 mmol, 92%) brown crystals of 1-pyrylphosphonic acid isopropylester.

Characterization:

¹H NMR (CDCl₃): δ(ppm) = 1.45 (d, J_{HH} = 6.2 Hz, 12H, CH₃); 4.73-4.81 (m, 2H, CH); 8.11-8.25 (m, 11H, CH aromatic).

^{13}C NMR (CDCl_3): $\delta(\text{ppm}) = 128.7$ (C_{quart}); 127.3, 126.3, 126.1 (15C, CH arom.); 70.3 (CH, isopropyl); 24.7 (CH_3).

^{31}P NMR (CDCl_3): $\delta(\text{ppm}) = 29.4$.

IR(ATR): $\nu(\text{cm}^{-1}) = 3046, 2973, 2931$ (ν CH); 1247, 1237; 1041 (P=O); 992, 964 (P-O).

Elemental Analysis: found: 71.8%C, 6.2%H, 8.5%P; calculated: 71.72%C, 6.84%H, 8.41%P.

For the hydrolysis of the phosphonate to, 1.8 g (4.9 mmol) of the 1-pyrylphosphonic acid isopropylester were refluxed in 15 mL (180 mmol) HCl. conc. and 15 mL acetone for 1.5 days in a 50 mL round-bottom flask. Then, all liquid components were removed in vacuum. The brown residue was then washed with H_2O and dissolved in a mixture of ethyl acetate and THF (1:1). The residue was then again washed three times with water and with boiling cyclohexane. Recrystallization from ethanol gave 730 mg (1.9 mmol, 39%) pure product.

Characterization:

^1H NMR (MeOH-d_4): $\delta(\text{ppm}) = 8.03\text{-}8.40$ (m, 11H, CH aromatic).

^{13}C NMR (MeOH-d_4): $\delta(\text{ppm}) = 130.4$ (C_{quart}); 129.9, 129.8, 129.1, 126.9, 126.5, 126.2, 126.0, 125.8 (15C, CH aromatic).

^{31}P NMR(MeOH-d_4): $\delta(\text{ppm}) = 27.9$.

IR(ATR): $\nu(\text{cm}^{-1}) = 3041$ (ν CH); 1215, 1187, 1185, 1088, 1035, 970, 953, 919, 848.

Elemental Analysis: found: 66.5%C, 4.9%H, 11.2%P; calculated: 67.61%C, 4.61%H, 10.90%P.

4.5.1.3 Preparation of 3-(2,3,-dihydroxypropoxy) propylphosphonic acid (Diol-PPA)

Synthesis of dimethyl 3-(oxiran-2-ylmethoxy)propylphosphonate

The preparation of 3-(2,3,-dihydroxypropoxy) propylphosphonic acid dimethyl ester was carried out following a literature known procedure.^[203] The phosphonic acid ester was prepared by heating 35 mL dimethylphosphite (excess) in a 100 mL one neck round-bottom flask under argon-atmosphere to 120°C . Then, a mixture of 10 g allylglycidylether (87.6 mmol), 685 mg azo-bis-isobutyronitrile (4.17 mmol) and 15 mL dimethylphosphite was added dropwise under stirring. The reaction mixture was further stirred at 120°C for 2h. Then, the excess of dimethylphosphite was removed at 7 mbar / 90°C . The product was yielded as 12.76 g (56.90 mmol, 65%) slightly yellow colored oil.

Characterization:

^1H NMR(CDCl_3): $\delta(\text{ppm}) = 3.65\text{-}3.56$ (m, 1H, OCH_2 -epoxy); 3.62 (s, 6H, OCH_3); 3.40-3.30 (m, 1H, OCH_2 -epoxy); 3.27-3.16 (m, 2H, $\text{OCH}_2\text{CH}_2\text{CH}_2\text{P}$); 2.98 (m, CH epoxide ring); 2.63 (m, 1H, CH_2 epoxide ring); 2.45 (m, 1H, CH_2 epoxide ring); 1.72 (m, 2H, PCH_2); 1.69 (m, 2H, PCH_2CH_2).

^{13}C NMR(CDCl_3): $\delta(\text{ppm}) = 70.7$ ($\text{OCH}_2\text{CH}_2\text{CH}_2\text{P}$); 70.4 (OCH_2 -epoxy); 52.2 (OCH_3); 50.6 (CH epoxide); 43.9 (CH_2 epoxide); 22.6 (PCH_2); 19.8 (PCH_2CH_2).

^{31}P NMR(CDCl_3): $\delta(\text{ppm}) = 46.5$.

IR(ATR): $\nu(\text{cm}^{-1}) = 976, 1022$ (P-O); 1244 (P=O); 1461 (CH_2 scissoring); 2953 (νCH_2).

Synthesis of 3-(2,3-dihydroxypropoxy) propylphosphonic acid (Diol-PPA)

The hydrolysis step of previously prepared dimethyl 3-(oxiran-2-ylmethoxy)propyl phosphonate, to give the final diol moiety coupling agent by epoxy-ring opening and phosphonic acid ester hydrolysis, was carried out by refluxing 5 g (20.5 mmol) of the phosphonic acid ester with 40 mL HCl conc. for 16 h in a 100 mL one neck round bottom flask. The HCl was then removed in vacuum and the viscous, oily, crude product was recrystallized from chloroform to give 4.0 g (18.7 mmol, 91%) pure product.

Characterization:

^1H NMR(DMSO-d_6): $\delta(\text{ppm}) = 7.62$ (s, 2H, POH); 3.58 (m, 1H, CH_2OH); 3.56 - 3.20 (m, 7 H, CH_2 -O- CH_2 -CHOH CH_2OH); 1.65 - 1.35 (m, 4H, PCH_2CH_2).

^{13}C NMR(DMSO-d_6): $\delta(\text{ppm}) = 71.9$ ($\text{OCH}_2\text{CH}_2\text{CH}_2\text{P}$); 70.9 (OCH_2CHOH); 69.5 (OCH_2CHOH); 63.0 (CHOHCH_2OH); 25.5 (PCH_2); 23.4 (PCH_2CH_2).

^{31}P NMR(DMSO-d_6): $\delta(\text{ppm}) = 39.7$.

IR(ATR): $\nu(\text{cm}^{-1}) = 980, 1112$ (P-O); 1440 (CH_2 scissoring); 2871 (νCH_2).

4.5.1.4 Synthesis of oxiran-2-ylmethylphosphonic acid (Ep-PPA)

Preparation of 1-allyl phosphonic acid

The phosphonic acid ester hydrolysis procedure was carried out via the silyl ester method as described in literature for analogous products.^[203] Under argon-atmosphere 2.5 g (14.4 mmol) allylphosphonic acid diethylester were stirred in 10 mL abs. dichloromethane in a 50 mL one neck round bottom flask. Then, 3 mL (23 mmol) trimethylbromosilane were added and the mixture was stirred for 2 h at room temperature. The volatile components were then removed at 1 mbar and 4 mL methanol (99 mmol) mixed with 2 mL water (111 mmol) were added dropwise to the reaction vessel. After stirring for 16 h, again the volatile components were removed at 1 mbar to give 1.7 g (13.8 mmol, 96%) viscous, slightly yellow colored oil.

Characterization:

^1H NMR(CDCl_3): $\delta(\text{ppm}) = 10.84$ (s, 2H, POH); 5.77 (m, 1H, CH); 5.23 (m, 2H, $\text{CH}_2=\text{CH}$); 2.62 (dd, $J_{\text{HH}} = 7.3$ Hz, $J_{\text{HP}} = 22$ Hz, 2H, P- CH_2).

^{13}C NMR(CDCl_3): $\delta(\text{ppm}) = 126.7$ (CH); 120.5 ($\text{CH}_2=\text{CH}$); 62.1 (PCH_2).

^{31}P NMR(CDCl_3): $\delta(\text{ppm}) = 42.9$.

IR(ATR): $\nu(\text{cm}^{-1}) = 918, 983$ (P-O); 1134 (P=O); 1396, 1421 (CH); 1640 (alkene); 2908 (νCH_2); 2961, 2984 (CH).

Preparation of oxiran-2-ylmethylphosphonic acid (Ep-PPA)

In a 50 mL one neck round bottom flask 1 g of allylphosphonic acid (6.8 mmol) were dissolved in abs. methylenechloride and 10.2 mmol MCPBA (meta chloro perbenzoic acid) in 15 mL methylenechloride, previously dried over MgSO_4 , were added. The mixture was stirred at room temperature for 20 h. During this time, the product precipitated as white solid, which was then washed with chloroform and dried in vacuum to give 640 mg (68%) white solid.

Characterization:

^1H NMR(DMSO- d_6): $\delta(\text{ppm}) = 6.56$ (s, 2H, POH); 2.62-2.63 (m, 3H, epoxide ring); 2.05-1.55 (m, 2H, PCH_2).

^{13}C NMR(DMSO- d_6): $\delta(\text{ppm}) = 53.2$ (CH epoxide); 40.1 (CH_2 epoxide); 36.1 (P- CH_2).

^{31}P NMR(DMSO- d_6): $\delta(\text{ppm}) = 33.8$.

IR(ATR): $\nu(\text{cm}^{-1}) = 925, 979$ (P-O); 1156 (P=O); 2907(CH); 3083 (epoxide ring).

Elemental analysis: calculated C 26.1, H 5.1, P 22.4; found C 26.9, H 6.0, P 22.7.

4.5.1.5 Synthesis of 2-Methacryloyloxy-1-ethylphosphonic acid (MA-C2-PPA)

The educt diethyl-methacryloyloxyethylphosphonate was synthesized and kindly supported by *D. Francova* who describes the synthetic procedure and characterization of this product in a publication.^[203]

For the preparation of the coupling agent molecule, all preparation steps were carried out under argon atmosphere. Following a literature known procedure for the preparation of this molecule,^[449] 7.5 g (30 mmol) of diethyl-methacryloyloxyethylphosphonate were dissolved in 20 ml dry dichloromethane in a 50 mL round-bottom flask. After stirring for 10 minutes, 9.3 g (60 mmol) trimethylsilyl bromide was dissolved in 10 ml of dry dichloromethane and added dropwise at room temperature. The reaction mixture was then stirred additional 16 h at room temperature. The volatiles were removed at 1 mbar. Then, 10 ml methanol (MeOH) (230 mmol), mixed with 2 mL H_2O (111 mmol), were added and the mixture was stirred for 24 h. After hydrolysis, the solvent was evaporated and the product was dried at 40°C / 1 mbar. Thus, 4.4 g (23 mmol, 77 %) of a slightly yellow colored oil could be isolated.

Characterization:

^1H NMR (CDCl_3): $\delta(\text{ppm}) = 1.90$ (s, 3H, CH_3), 2.16-3.20 (m, 2H, $\text{CH}_2\text{-P}$), 4.31-4.41 (m, 2H, $\text{CH}_2\text{-O}$), 5.56 (s, 1H, $\text{C}=\text{CH}_2$), 6.11 (s, 1H, $\text{C}=\text{CH}_2$), 9.81 (s, 2H, OH).

^{13}C NMR (CDCl_3): $\delta(\text{ppm}) = 18.3$ (CH_3), 27.6 ($\text{CH}_2\text{-P}$), 51.8 ($\text{CH}_2\text{-O}$), 125.5 ($\text{C}=\underline{\text{C}}\text{H}_2$), 136.1 ($\underline{\text{C}}=\text{CH}_2$), 168.1 ($\text{-}\underline{\text{C}}\text{OO-CH}_2\text{-}$).

^{31}P NMR (CDCl_3): $\delta(\text{ppm}) = 29.5$ ppm.

IR(ATR): $\nu(\text{cm}^{-1}) = 1704$ ($\nu\text{C}=\text{O}$); 1635 ($\nu\text{C}=\text{C}$); 1456 (δ C-H); 1326 (δ =C-H); 1302 (δ =C-H); 1169 ($\nu\text{C}-\text{O}-\text{C}$); 1011 (P-O); 945 (P-O-H).

4.5.1.6 Synthesis of 1-Methacryloyloxy decyl-10-phosphoric acid monoester (MA-C10-PA)

The synthesis was performed following the adaption^[450] of a literature known procedure.^[451] Thereby, 9.3 g (61 mmol) POCl_3 were dissolved in 150 ml of dry THF in a 500 mL round-bottom flask and cooled with ethanol and liquid nitrogen to a bath temperature of -30 °C. Then, 6.2 g (61 mmol) triethylamine and 14.07 g (55 mmol) 10-hydroxy-decyl-1-methacrylate in 20 ml dry THF were added dropwise. The mixture was stirred for 3 h at -30 °C. Then, 10 mL (554 mmol) H_2O were added and the mixture was allowed to warm to room temperature after an additional 30 minutes stirring at 0 °C. After filtration, the filtrate mixture was washed three times with conc. NaCl solution and the aqueous phase was re-extracted with diethylether. The combined organic phases were then dried over MgSO_4 . The solvent was evaporated to give 16.3 g (50 mmol, 91 %) of a viscous oil.

Characterization:

^1H NMR (d^6 -DMSO): $\delta(\text{ppm}) = 1.15$ - 1.40 (m, 16H, CH_2 alkyl chain), 1.85 (s, 3H, CH_3) 3.82 (m, 2H, CH_2 -OP), 4.06 (m, 2H, CH_2 -O-COO-), 5.64 (s, 2H, $\text{C}=\text{CH}_2$), 5.98 (s, 2H, OH).

^{13}C NMR (d^6 -DMSO): $\delta(\text{ppm}) = 18.4$ (CH_3), 25.5, 25.6, 28.5 (CH_2); 29.0 (CH_2 - CH_2 -O); 29.4 (CH_2CH_2 -O-P); 64.6 (CH_2 -O-P); 65.6 (CH_2 -ester); 125.9 ($\text{C}=\text{CH}_2$); 136.5 ($\text{C}=\text{CH}_2$); 168.9 ($-\text{COO}-\text{CH}_2$ -).

^{31}P NMR (d^6 -DMSO): $\delta(\text{ppm}) = -1.1$.

IR(ATR): $\nu(\text{cm}^{-1}) = 2951$ ($\nu\text{C}-\text{H}$); 2875 ($\nu\text{C}-\text{H}$); 1690 ($\nu\text{C}=\text{O}$); 1631 ($\nu\text{C}=\text{C}$); 1456 (δ C-H); 1324 (δ =C-H); 1303 (δ =C-H); 1171 ($\nu\text{C}-\text{O}-\text{C}$); 1002 (P-O).

4.5.1.7 Synthesis of 2-bromoethylphosphonic acid (Br-C2-PPA)

Preparation of 2-bromoethylphosphonic acid diethylester

The synthesis of this molecule was carried out by adapting^[452] literature known procedures.^[327, 453] 36 mL 1,2-Dibromoethane (421.2 mmol) and 18 mL triethylphosphite (105.3 mmol) were heated at 160 °C for 16 h in a 50 mL round-bottom flask. The excess of dibromoethane was then removed via distillation and the product was purified via distillation at 85 °C / 2 mbar to give 23 g (92.7 mmol, 88%) clear, colorless liquid.

Characterization:

^1H NMR(CDCl_3): $\delta(\text{ppm}) = 1.23$ (t, $J_{\text{HH}} = 7.0$ Hz, 6H, OCH_2CH_3); 2.28 (m, 2H, P- CH_2); 3.43 (m, 2H, Br- CH_2); 4.02 (t, $J_{\text{HH}} = 6.9$ Hz, 4H, OCH_2CH_3).

^{13}C NMR(CDCl_3): $\delta(\text{ppm}) = 61.9$ (OCH_2); 30.6 (P-CH_2); 23.6 (Br-CH_2); 16.3 (CH_3).

^{31}P NMR(CDCl_3): $\delta(\text{ppm}) = 37.6$.

IR(ATR): $\nu(\text{cm}^{-1}) = 2981, 2908$ (C-H); 1443 (C-H); 1241 (P=O); $1053, 956$ (P-O); 818 .

Preparation of 2-bromoethylphosphonic acid (Br-C2-PPA)

The hydrolysis of 2-bromoethylphosphonic acid diethylester was carried out by the adaption of a procedure, described in literature.^[203] 2.4 g 2-bromoethylphosphonic acid diethylester (9.8 mmol) in 10 mL dry dichloromethane were stirred with 2.6 mL (19.6 mmol) trimethylsilylbromide at room temperature for 4 h in a 50 mL round-bottom flask. Then, the solvent and the excess trimethylsilylbromide were removed in oil pump vacuum at room temperature. 3 mL methanol (74.1 mmol) and 1.5 mL H_2O (83.3 mmol) were added, and the mixture was stirred for 16 h. Then, the product was dried at 1 mbar to give 1.8 g (9.7 mmol, 99%) clear, colorless, viscous oil which transformed into colorless needle-crystals within three days.

Characterization:

^1H NMR(CDCl_3): $\delta(\text{ppm}) = 2.46$ (m, 2H, P- CH_2); 3.53 (m, 2H, Br- CH_2); 11.00 (s, 2H, P-OH).

^{13}C NMR(CDCl_3): $\delta(\text{ppm}) = 30.6$ (P- CH_2); 22.9 (Br- CH_2).

^{31}P NMR(CDCl_3): $\delta(\text{ppm}) = 41.3$.

IR(ATR): $\nu(\text{cm}^{-1}) = 2804, 2271$ (O-H); 1441cm^{-1} (C-H); 1240 (P=O); 983cm (P-O), 934 (P-OH).

4.5.1.8 Preparation of 10-(trimethoxysilyl)decyl methacrylate (MA-C10-TMS)

Synthesis of dec-9-enyl methacrylate

Under argon-atmosphere, 5.00 g 9-decen-1-ol (32 mmol) were stirred in 20 mL dry diethylether at 0°C in a 50 mL round-bottom flask. Then, 3.34 g methacrylic acid chloride (32 mmol) were added dropwise at 0°C . The reaction mixture was then allowed to warm to room temperature and was stirred for 16 h. After this step, the reaction mixture was distributed between diethylether and H_2O in a separating funnel and the organic fraction was washed three times with H_2O and with conc. NaCl solution. The organic fraction was then dried over Na_2SO_4 and the solvent was evaporated to give 6.24 g (28 mmol, 88%) slightly yellow colored, clear, oily liquid.

Characterization: (MA...methyl methacrylate group)

^1H NMR(CDCl_3): $\delta(\text{ppm}) = 6.08$ (s, 1H, $\text{CH}_2=\text{MA}$); $5.83\text{-}5.74$ (m, 1H, $\text{CH}_2=\text{CH}$ - allyl); 5.52 (s, 1H, $\text{CH}_2=\text{MA}$); ; $5.00\text{-}4.89$ (m, 2H, $\text{CH}_2=\text{CH}$ - allyl); 4.11 (t, $J_{\text{HH}} = 7.0$ Hz, 2H, CH_2CH_2 -

O-); 2.01 (m, 2H, $\text{CH}_2\text{-CH=CH}_2$); 1.93 (s, 3H, CH_3); 1.70-1.51 (m, 4H, $\text{CH}_2\text{-CH}_2\text{-CH}_2\text{O-}$)
1.40-1.20 (m, 8H, CH_2).

^{13}C NMR(CDCl_3): $\delta(\text{ppm}) = 167.5$ (C=O); 139.1 (CH, allyl); 136.5 (C_{quart} , MA); 125.1 ($\text{CH}_2=\text{C}$, MA); 114.1 ($\text{CH}_2=\text{CH-}$, allyl); 64.8 (O- CH_2); 33.75 ($\text{CH}_2=\text{CH-CH}_2$) 29.2, 29.15, 28.9, 28.8, 28.6 (5C, CH_2); 25.92 ($\text{CH}_2\text{-CH}_2\text{-CH}_2\text{-O}$); 18.3 (CH_3).

IR(ATR): $\nu(\text{cm}^{-1}) = 2926, 2855$ (C-H); 1719 (C=O); 1638 (C=C); 1160.

Preparation of 10-(trimethoxysilyl)decyl methacrylate (MA-C10-TMS)

All steps were performed under argon-atmosphere. The hydrosilation reaction for the preparation of the product was carried out as described in literature for similar systems.^[140] 3.2 g dec-9-enyl methacrylate (14.3 mmol) was stirred together with 2.1 g trimethoxysilane (17.1 mmol) and 3 drops of the *Karstedt's* catalyst in 10 mL of toluene in a 50 mL round-bottom flask, at room temperature. After 5 days, a conversion of >98% was detected via ^1H NMR, and the volatile compounds were evaporated at 1 mbar / 40°C to give the product sample for characterization. As the product in its isolated form showed gelation after three days of storage, the product was further stored (at 4°C) and used as a 40 vol% solution in toluene to avoid the observed degradation of the product.

Characterization: (MA...methyl methacrylate group)

^1H NMR(CDCl_3): $\delta(\text{ppm}) = 6.08$ (s, 1H, $\text{CH}_2=\text{MA}$); 5.52 (s, 1H, $\text{CH}_2=\text{MA}$); 4.12 (t, $J_{\text{HH}} = 7.0$ Hz, 2H, $\text{CH}_2\text{CH}_2\text{-O-}$); 3.55 (s, 9H, O- CH_3); 1.93 (s, 3H, CH_3); 1.70-1.51 (m, 4H, $\text{CH}_2\text{-CH}_2\text{-CH}_2\text{O-}$) 1.40-1.20 (m, 10H, CH_2); 0.63 (t, 2H, CH_2Si).

^{13}C NMR(CDCl_3): $\delta(\text{ppm}) = 167.5$ (C=O); 136.5 (C_{quart} , MA); 125.1 ($\text{CH}_2=\text{C}$, MA); 64.8 (O- CH_2); 50.5 (O CH_3); 33.07 (Si- $\text{CH}_2=\text{CH}_2\text{-CH}_2$) 29.2, 29.15, 28.9, 28.8, 28.6 (5C, CH_2); 25.92 ($\text{CH}_2\text{-CH}_2\text{-CH}_2\text{-O}$); 18.3 (CH_3); 25.7 (Si CH_2CH_2); 9.1 (Si CH_2).

^{29}Si NMR(CDCl_3) : $\delta(\text{ppm}) = -41.0$.

IR(ATR): $\nu(\text{cm}^{-1}) = 2926, 2854$ (C-H); 1719 (C=O); 1638 (C=C, weak); 1161; 1082 (Si-O).

Elemental analysis: calculated C 58.9, H 9.8; found C 58.4, H 9.2; the relatively lower amount of found C and H can be explained by partial hydrolysis of the Si-O- CH_2CH_3 groups of the coupling agent molecule.

4.5.1.9 Synthesis of 3-(trimethoxysilyl)propyl 4-cyano-4-((2-cyanopropan-2-yl)diazonyl)pentanoate (Azo-TMS)

All synthetic steps have been carried out by the procedure, described by *Prucker and Ruhe*, working under argon-atmosphere.^[255]

Synthesis of 4-cyano-4-((2-cyanopropan-2-yl)diazenyl)pentanoic acid

50 g Laevulic acid (0.43 mol) were neutralized with 17.2 g NaOH (0.43 mol) by stirring the components in 150 mL water for 30 min in a 500 mL round-bottom flask to yield a solution with pH = 8. This solution was cooled to room temperature and 25 g acetone (0.43 mol) were added. The mixture was then added dropwise at 50°C under vigorous stirring to a solution of 56 g KCN (0.86 mol) and 56 g hydrazine sulfate (0.43 mol). After complete addition, the reaction solution was stirred for 3 h at 50°C. Then, the mixture was adjusted to pH = 4 with 1N HCl and cooled to 0°C. At this temperature, bromine was added (170 g, 1.06 mol) until it remained as excess, which was visible by a permanent red coloration of the reaction mixture. This mixture was then stirred for 30 min and then the excess of bromine was neutralized with saturated sodium bisulfite solution. The content of the reaction vessel was then filtered and the thus isolated white precipitate was then stirred in 250 mL of 1N NaOH for 30 minutes. Filtration yielded 25 g of the symmetric by-product (azo-bis-isobutyronitrile). The pH of the filtrate was then adjusted to 3 with 1 N HCl. Thus, a white precipitate could be yielded, which was then separated via filtration, washed with water and identified to be the product via ¹H NMR. The filtrate was then washed with dichloromethane to yield a second fraction of the product. A third fraction of the product was obtained from the original aqueous reaction solution: After 7 days, white crystals could be isolated and washed. ¹H NMR spectroscopy revealed that all three fractions contained the pure product and thus, they were combined to give a total yield of 5.83 g (26.3 mmol, 6.1%) white solid.

Characterization:

¹H NMR(CDCl₃): δ(ppm) = 10.54 (bs, 1H, COOH); 2.28-2.65 (m, 4H, CH₂); 1.70, 1.73 and 1.74 (s, 3H each, CH₃).

¹³C NMR(CDCl₃): δ(ppm) = 177.1 (COOH); 118.8 (CN); 117.6 (CN); 71.5 and 68.6 (C_{quart}); 32.9 and 28.9 (CH₂); 25.5 and 23.8 (CH₃).

IR(ATR): ν(cm⁻¹) = 2993, 2942 (C-H); 2242 (CN); 1699 (C=O).

DSC(10K/min): decomposition temperature 123.4°C (peak).

Preparation of 4-cyano-4-((2-cyanopropan-2-yl)diazenyl)pentanoic acid chloride

To a suspension of 18 g phosphorus pentachloride (90 mmol) in 20 mL dichloromethane in a 50 mL round-bottom flask, a solution of 4.0 g 4-cyano-4-((2-cyanopropan-2-yl)diazenyl)pentanoic acid (18.1 mmol) in 20 mL CH₂Cl₂ was added dropwise at 0°C under stirring. The stirring was then continued for 16 h at room temperature. Further, the orange colored suspension was filtered. The filtrate volume was reduced to 10 mL and was again filtered as precipitation occurred. Further, the solvent was removed in membrane pump vacuum. The remaining oily solution was then washed two times with 40 mL cold ⁿhexane and dried for 16 h at 5 mbar / 40°C to give 4.0 g (16.7 mmol, 92.5%) product in form of a yellow colored solid.

Characterization:

^1H NMR(CDCl_3): $\delta(\text{ppm}) = 2.90\text{-}3.10$ (m, 2H, CH_2COCl); $2.40\text{-}2.70$ (m, 2H, CH_2); 1.70, 1.73 and 1.74 (s, 3H each, CH_3).

^{13}C NMR(CDCl_3): $\delta(\text{ppm}) = 172.0$ (COCl); 118.8 (CN); 117.6 (CN); 71.5 and 68.6 (C_{quart}); 41.8 and 32.9 (CH_2); 25.3 and 23.8 (CH_3).

IR(ATR): $\nu(\text{cm}^{-1}) = 2992, 2942$ (C-H); 2242 (CN); 1795 (C=O).

Preparation of allyl 4-cyano-4-((2-cyanopropan-2-yl)diazenyl)pentanoate

To a solution of 2.9 g allyl alcohol (50 mmol) and 3.25 mL pyridine (40 mmol) in 25 mL dichloromethane in a 50 mL round-bottom flask, 4.0 g of 4-cyano-4-((2-cyanopropan-2-yl)diazenyl)pentanoic acid chloride (16.7 mmol) in 25 mL dichloromethane were added dropwise under stirring at 0°C . The reaction mixture was then allowed to warm to room temperature and stirred for 18 h. Then, the reaction mixture was washed two times with 2N H_2SO_4 , two times with saturated NaHCO_3 solution and with H_2O . The solution was then dried over Na_2SO_4 and the solvent was then removed in membrane pump vacuum. As a further purification step, the brownish colored, oily solution was washed with cold hexane, re-dissolved in 20 mL CH_2Cl_2 and filtered over neutral Al_2O_3 . After removal of the solvent in membrane pump vacuum, the product was dried over night at 5 mbar / 40°C . Yield: 1.5 g (5.8 mmol, 34.7%) red colored, viscous solid.

Characterization:

^1H NMR(CDCl_3): $\delta(\text{ppm}) = 5.80\text{-}6.00$ (m, 1H, =CH-); 5.18-5.35 (m, 2H, $\text{CH}_2=$); 4.51 (d, $J_{\text{HH}} = 6.9$ Hz, 2H, CH_2O); 2.25-2.70 (m, 4H, CH_2); 1.70, 1.68 and 1.66 (s, 3H each, CH_3).

^{13}C NMR(CDCl_3): $\delta(\text{ppm}) = 171.0$ (C=O); 131.7(=CH-); 118.8 (CN); 118.3 ($\text{CH}_2=$) 117.6 (CN); 71.5 and 68.6 (C_{quart}); 65.5 (CH_2O); 33.1, 29.0, 25.2, 23.8 (CH_2 and CH_3).

IR(ATR): $\nu(\text{cm}^{-1}) = 2990, 2942$ (C-H); 2242 (CN); 1735 (C=O).

Preparation of 3-(trimethoxysilyl)propyl 4-cyano-4-((2-cyanopropan-2-yl)diazenyl)pentanoate (Azo-TMS)

The hydrosilylation reaction for the preparation of the product was carried out adapting the synthetic conditions according to a literature known process for similar systems.^[140] 1.0 g allyl 4-cyano-4-((2-cyanopropan-2-yl)diazenyl)pentanoate (3.8 mmol) together with 3.0 g trimethoxysilane (25 mmol) and 3 drops of the *Karstedt's* catalyst in 10 mL abs. toluene were stirred for 4.5 days in a 50 mL round-bottom flask at 40°C until complete conversion of the C=C-bond could be detected via ^1H NMR-spectroscopy. After removal of the solvent, 1.46 g (3.8 mmol, 100%) product in form of an orange colored, viscous, liquid could be yielded. The product was then stored under argon atmosphere at 4°C .

Characterization:

^1H NMR(CDCl_3): $\delta(\text{ppm}) = 4.06$ (d, $J_{\text{HH}} = 6.4$ Hz, 2H, CH_2O); 3.59 (s, 9H, $\text{SiO}(\text{CH}_3)_2$); 2.25-2.70 (m, 6H, CH_2); 1.73, 1.71 and 1.69 (s, 3H each, CH_3), 0.68 (2H, SiCH_2).

^{13}C NMR(CDCl_3): $\delta(\text{ppm}) = 171.0$ (C=O); 118.8 (CN); 117.6 (CN); 68.5 and 68.0 (C_{quart}); 65.7 (CH_2O); 50.7 (CH_3O); 33.1, 29.0, 25.3, 23.8, 21.9 (CH_2 and CH_3).

IR(ATR): $\nu(\text{cm}^{-1}) = 2946, 2844; 2242$ (CN); 1735 (C=O); 1249; 1082 (Si-O).

DSC(10K/min): decomposition temperature 123.0°C (peak).

4.5.2 Preparation of diethylene glycol chain coupling agents

4.5.2.1 Preparation of the allyl ether of diethylene glycol monomethyl ether

The allyl ether of diethylene glycol monomethyl ether was prepared analogous to the described literature for similar oligomeric ethylene glycol systems.^[67] In a 100 mL three-necked round bottom flask, equipped with a reflux condenser and a dropping funnel, 10.0 g (83 mmol) diethylene glycol-monomethyl ether was dissolved in 30 mL THF abs. and 9.2 g (166 mmol) fine crunched KOH were added followed by stirring at room temperature for 30 min. Then 13.0 g of allyl bromide (107 mmol), dissolved in 10 mL THF abs. were added dropwise to the mixture. After the addition of allyl bromide the reaction mixture was heated to reflux overnight. Afterwards, the reaction mixture was cooled to room temperature, filtered and the filtrate was washed three times with 1 M NaOH. After drying over MgSO_4 , the solvent was removed at the rotary evaporator. The by-product (allyl alcohol) was removed by distillation at 50°C/30 mbar. Yield: 9.5 g (71%) slightly yellow liquid.

Characterization:

^1H NMR (CDCl_3): $\delta(\text{ppm}) = 3.35$ (s, 3H, CH_3); 3.52-3.68 (m, 8H, $\text{O-CH}_2\text{CH}_2\text{-O}$); 4.00 (d, $J_{\text{HH}} = 5.7$ Hz, 2H, $\text{O-CH}_2\text{-CH=CH}_2$); 5.17-5.22 (m, 2H, CH=CH_2); 5.87 (m, 1H, CH=CH_2).

^{13}C NMR (CDCl_3): $\delta(\text{ppm}) = 134.6$ ($\text{CH}_2=\text{CH}$); 116.8 ($\text{CH}_2=\text{CH}$); 71.9 ($\text{O-CH}_2\text{-CH=CH}_2$); 70.1-69.5 (4C, $\text{O-CH}_2\text{-CH}_2\text{-O}$); 58.4 ($\text{CH}_3\text{-O-CH}_2$).

IR(ATR): $\nu(\text{cm}^{-1}) = 850$ (νCO , rCH_2); 924 (νCO , rCH_2); 995 (νCO , rCH_2); 1029 (νCO , νCC , rCH_2); 1107 (νCO); 1200 (CH_2 twisting); 1248 (CH_2 twisting); 1290 (CH_2 twisting); 1351 (CH_2 wagging); 1452 (CH_2 scissoring); 1647 ($\text{CH}_2=\text{CH}$); 2871 (νsCH_2).

4.5.2.2 Synthesis of 1-(3-diethylene glycol monomethyl ether) propoxyphosphonic acid dimethyl ester

The synthesis of 1-(3-diethylene glycolmonomethylether) propoxyphosphonic acid dimethylester was performed via radical addition of the P-H-bond of dimethylphosphite to the olefinic functionality of the moiety as described in literature.^[203] The reaction was carried out under argon-atmosphere in a 100 mL round bottom flask. First, 20 mL of dimethylphosphite as reactant and solvent was heated to 120°C. While stirring vigorously, a mixture of 4.5 g

(28.1 mmol) diethylene glycol monomethyl ether allyl ether and 220 mg azo-bis-isobutyronitrile (1.34 mmol) in 6 mL dimethylphosphite were added dropwise. Thus a total amount of 286 mmol dimethylphosphite was used for the reaction. The reaction mixture was stirred for 2 h at 120°C. Afterwards the excess of dimethylphosphite was removed by distillation at 50°C/8 mbar. Yield: 5.3 g (70%) yellow liquid.

Characterization:

^1H NMR (CDCl_3): $\delta(\text{ppm}) = 1.46$ (m, 2H, $\text{CH}_2\text{-CH}_2\text{-CH}_2$); 1.76-1.84 (m, 2H, $\text{CH}_2\text{-CH}_2\text{-P}$); 3.30 (s, 3H, CH_3); 3.37-3.57 (m, 10H, $\text{O-CH}_2\text{CH}_2\text{-}$); 3.66 (s, 6H, P-O-CH_3).

^{31}P NMR (DMSO-d_6): $\delta(\text{ppm}) = 46.6$.

^{13}C NMR (DMSO-d_6): $\delta(\text{ppm}) = 71.7$ ($\text{O-CH}_2\text{-CH}_2\text{-CH}_2$); 70.1-69.5 (4C, $\text{O-CH}_2\text{-CH}_2\text{-O}$); 58.4 ($\text{CH}_3\text{-O-CH}_2$); 52.3 (2C, $\text{CH}_3\text{-O-P}$); 22.7 ($\text{CH}_2\text{-P}$); 19.3 ($\text{CH}_2\text{-CH}_2\text{-P}$).

IR(ATR): $\nu(\text{cm}^{-1}) = 1025$ (P-O); 1106 (νCO); 1198 (CH_2 twisting); 1246 (P=O); 1353 (CH_2 wagging); 1458 (CH_2 scissoring); 2872 (νsCH_2).

4.5.2.3 Synthesis of 1-(3-diethylene glycol monomethyl ether) propoxyphosphonic acid (DEG-PPA)

The coupling agent 1-(3-diethylene glycol monomethyl ether) propoxyphosphonic acid was prepared by the hydrolysis of the dimethyl phosphonate via its silylester.^[203] The reaction was performed in a 250 mL round bottom flask under an argon atmosphere avoiding the presence of moisture during the silylation step. 5.3 g (19.6 mmol) of 1-(3-diethylene glycol monomethyl ether) propoxyphosphonic acid dimethylester were dissolved in 50 mL absolute dichloromethane. 5 mL (38 mmol) bromotrimethylsilane were added and the reaction mixture was stirred for 16 h at room temperature. Afterwards, a mixture of 5 mL H_2O (280 mmol) and 10 mL MeOH (250 mmol) was added dropwise. The resulting reaction mixture was stirred for 16 h at room temperature. After removing the solvents and by-products at 70°C/oil pump vacuum, the product was finally dried under a membrane pump vacuum resulting in 4.0 g (83%) slightly yellow colored viscous oil.

Characterization:

^1H NMR (DMSO-d_6): δ (ppm) = 1.26-1.41 (m, 2H, $\text{CH}_2\text{-CH}_2\text{-CH}_2$); 1.41-1.58 (td, $J_{\text{HH}} = 8.6$ Hz, $J_{\text{HP}} = 15$ Hz, 2H, $\text{CH}_2\text{-CH}_2\text{-P}$); 3.21 (s, 3H, CH_3); 3.28-3.60 (m, 10H, $\text{O-CH}_2\text{CH}_2\text{-}$); 10.17 (s, 2H, P-OH).

^{31}P NMR (DMSO-d_6): $\delta(\text{ppm}) = 39.5$.

^{13}C NMR(DMSO-d_6): $\delta(\text{ppm}) = 71.7$ ($\text{O-CH}_2\text{-CH}_2\text{-CH}_2$); 70.5 ($\text{CH}_2\text{-O-CH}_3$); 70.3-70.0 (3C, $\text{O-CH}_2\text{-CH}_2\text{-O}$); 58.5 ($\text{CH}_3\text{-O-CH}_2$); 25.7 ($\text{CH}_2\text{-P}$); 23.5 ($\text{CH}_2\text{-CH}_2\text{-P}$).

IR(ATR): $\nu(\text{cm}^{-1}) = 932$ (P-OH); 984 (P-O); 1100 (P-O); 1198 (CH_2 twisting); 1220 (P=O); 1354 (CH_2 wagging); 1455 (CH_2 scissoring); 2873 (νsCH_2).

Elemental analysis: calculated C 39.7, H 7.9, P 12.8; found C 39.2, H 7.6, P 11.2.

4.5.2.4 Synthesis of 1-(3-diethylene glycol mono methylether) propoxy trimethoxysilane (DEG-TMS)

The coupling agent 1-(3-diethylene glycol monomethyl ether) propoxy triethoxysilane was synthesized via a hydrosilation reaction from the pre-synthesized diethylene glycol monomethyl ether using an approach described in literature for similar systems.^[140] All steps were carried out under an argon atmosphere due to the high moisture sensitivity of the educts and the product. In a 25 mL round bottom flask, equipped with a reflux condenser, 3.0 g (18.7 mmol) diethylene glycol monomethyl ether allylether was dissolved in 5 mL absolute toluene and 2 drops of the *Karstedt's* catalyst were added to the mixture. After the addition of 3.4 g (28.1 mmol) trimethoxysilane, the reaction mixture was stirred and heated to reflux for 7 h. Then the solvent and excess trimethoxysilane were removed in at 120°C/10 mbar for 5 h. Yield: 4.5 g (86%) colorless liquid.

Characterization:

¹H NMR(CDCl₃): δ(ppm)= 0.57 (t, J_{HH} = 7.8 Hz, 2H, CH₂-Si); 1.55-1.65 (m, 2H, CH₂-CH₂-Si); 3.29 (s, 3H, CH₃-O-CH₂); 3.35 (t, J_{HH} = 6.5 Hz, 2H, O-CH₂-CH₂-CH₂-); 3.41-3.54 (m, 17H, O-CH₂-CH₂-O, O-CH₂-CH₂-CH₂, O-CH₃).

²⁹Si NMR (CDCl₃): δ(ppm)= -43.3.

¹³C NMR(CDCl₃): δ(ppm)= 73.3 (O-CH₂-CH₂-CH₂); 71.9 (CH₂-O-CH₃); 70.6-69.9 (3C, O-CH₂-CH₂-O); 58.9 (CH₃-O-CH₂); 50.4 (3C, CH₃-Si); 22.6 (CH₂-CH₂-Si); 5.1 (CH₂-Si).

IR(ATR): ν(cm⁻¹) = 1080 (Si-OCH₃); 1194 (Si-OCH₃); 1352 (CH₂ wagging); 1458 (CH₂ scissoring); 2841 (νCH₂); 2940 (νCH₃).

Elemental analysis: calculated C 46.9, H 9.3; found C 48.2, H 9.6.

4.5.3 Syntheses of polysiloxane spacer chain coupling agents

4.5.3.1 Synthesis of α-(1-ethylphosphonic acid), ω-ⁿBu-poly(dimethyl siloxane) (ⁿBu-PDMS-PPA)

Synthesis of α-Si-H, ω-ⁿBu-poly(dimethyl siloxane)

The reaction was carried out, based on a literature known procedure.^[371] All steps were performed under argon atmosphere. 10.64 g Hexamethylcyclotrisiloxane (D₃) (48 mmol) were dissolved in 30 mL abs. THF. Then, 10 mL ⁿBuLi, 1.6 M in ⁿhexane, (16 mmol) were added and the reaction mixture was stirred at room temperature for 20 h in a *Schlenk* tube. The polymerization reaction was then quenched with 3.5 mL (32 mmol) dimethylchlorosilane and 3.9 mL (32 mmol) triethylamine while cooling at 0°C. Further, after 2 h of stirring, 100 mL water and 100 mL toluene were added to the reaction mixture and the organic phase was removed. The aqueous phase was extracted 3 times with toluene and the collected organic phases were dried over MgSO₄. The solvent was removed at the rotary evaporator at 45°C and

possible volatile impurities were removed under oil pump vacuum at 45°C to give 12.00 g (94%) clear colorless, oily, liquid.

Characterization:

^1H NMR(CDCl_3): $\delta(\text{ppm}) = 0.09$ (bs, $-\text{OSi}(\text{CH}_3)_2\text{O}-$); $0.19-0.20$ ($-\text{SiH}(\text{CH}_3)_2$, $-\text{CH}_2\text{Si}(\text{CH}_3)_2\text{O}-$); 0.54 (t, $J_{\text{HH}} = 7.3$ Hz, $-\text{CH}_2\text{Si}(\text{CH}_3)_2\text{O}-$); 0.89 (t, $J_{\text{HH}} = 6.5$ Hz, CH_3-CH_2-); $1.32-1.35$ (m, $\text{CH}_3-\text{CH}_2-\text{CH}_2-$); 4.72 (m, Si-H).

^{29}Si NMR(CDCl_3): $\delta(\text{ppm}) = -21.5$ ($-\text{OSi}(\text{CH}_3)_2\text{O}-$); -7.0 ($-\text{SiH}(\text{CH}_3)_2$); 7.5 ($-\text{CH}_2\text{Si}(\text{CH}_3)_2\text{O}-$).

^{13}C NMR(CDCl_3): $\delta(\text{ppm}) = 26.4$ (CH_3-CH_2-); 25.4 ($\text{CH}_3-\text{CH}_2-\text{CH}_2-$); 17.9 (Si- CH_2); 13.8 (CH_3-); $1.2-0.5$ (SiCH_3).

IR(ATR): $\nu(\text{cm}^{-1}) = 2961$ (νCH_3); 2128 (Si-H); 1258 (SiCH_3); 1018 (Si-O); 910 (Si-H); 789 (Si-C).

$M_n(\text{GPC}) = 800$ g/mol.

Synthesis of α -(1-propyl-3-(diethylphosphono)), ω - ^nBu -poly(dimethyl siloxane)

The reaction was carried out under argon atmosphere, by the adaption of a literature known procedure.^[140] 1.68 g α -Si-H, ω - ^nBu -poly(dimethyl siloxane) (2.8 mmol) were dissolved in 10 mL abs. toluene in a *Schlenk* tube. Then, 0.5 g (2.8 mmol) allylphosphonic acid diethylester and 2 drops of the *Karstedt's* catalyst were added. The reaction mixture was then stirred at 100°C for 7 h. The solvent was removed using a rotary evaporator and the product was then dried for 3 h at 65°C / 5 mbar to remove possible volatile impurities. Thus, the product, a clear oily liquid, could be isolated with a yield of 2.1 g (2.7 mmol, 96%).

Characterization:

^1H NMR(CDCl_3): $\delta(\text{ppm}) = 0.06$ (bs, SiCH_3); 0.52 (t, $J_{\text{HH}} = 7.3$ Hz, $-\text{CH}_2\text{Si}(\text{CH}_3)_2\text{O}-$); 0.63 (m, $-\text{P}-\text{CH}_2\text{CH}_2\text{CH}_2\text{Si}(\text{CH}_3)_2\text{O}-$); 0.86 (t, $J_{\text{HH}} = 6.5$ Hz, CH_3-CH_2-); $1.20-1.40$ (m, $\text{CH}_3-\text{CH}_2-\text{CH}_2-$, $\text{CH}_3-\text{CH}_2-\text{O}-$, $\text{CH}_2-\text{CH}_2-\text{P}$); $1.55-1.85$ (m, $\text{CH}_2-\text{CH}_2-\text{P}$); 4.08 (q, $\text{CH}_3\text{CH}_2\text{O}-$).

^{29}Si NMR(CDCl_3): $\delta(\text{ppm}) = -21.5$ ($-\text{OSi}(\text{CH}_3)_2\text{O}-$); 6.5 ($\text{PCH}_2\text{CH}_2\text{CH}_2\text{Si}(\text{CH}_3)_2\text{O}-$); 7.5 ($-\text{CH}_2\text{Si}(\text{CH}_3)_2\text{O}-$).

^{13}C NMR(CDCl_3): $\delta(\text{ppm}) = 61.3$ ($\text{CH}_3\text{CH}_2\text{O}-$); 30.4 (CH_2-P); 28.2 ($\text{CH}_2\text{CH}_2\text{P}$); 26.4 (CH_3-CH_2-); 25.4 ($\text{CH}_3-\text{CH}_2-\text{CH}_2-$); 16.7 ($\text{SiCH}_2\text{CH}_2\text{CH}_2\text{P}$); 17.9 (Si- CH_2); 16.4 ($\text{CH}_3\text{CH}_2\text{O}-$); 13.8 (CH_3-); $1.2-0.5$ (SiCH_3).

^{31}P NMR(CDCl_3): $\delta(\text{ppm}) = 31.9$.

IR(ATR): $\nu(\text{cm}^{-1}) = 2961$ (νCH_3); 2128 (Si-H); 1258 (SiCH_3); 1018 (Si-O); 960 (P-O); 789 (Si-C).

Synthesis of α -(1-propyl-3-phosphono), ω - ^nBu -poly(dimethyl siloxane) (^nBu -PDMS-PPA)

The reaction was performed under argon atmosphere applying a procedure, described in literature.^[203] 2.1 g of α -(1-ethylphosphonic acid diethylether), ω -ⁿBu-poly(dimethyl siloxane) (2.7 mmol) were dissolved in 10 mL abs. dichloromethane in a *Schlenk* tube and 1 mL trimethylsilylbromide (7.6 mmol) was added dropwise. Then, the reaction mixture was stirred for 5 h at room temperature. Afterwards, the solvent was removed in oil pump vacuum. After that, a mixture of 2 mL MeOH (49.4 mmol) and 1 mL H₂O (55.6 mmol) was added dropwise and the reaction mixture was stirred for 20 h at room temperature. Then, the volatiles were removed at 30°C under oil pump vacuum to give 1.9 g (2.6 mmol, 96%) colorless, clear liquid.

Characterization:

¹H NMR(CDCl₃): δ (ppm) = 0.06 (bs, SiCH₃); 0.52 (t, -CH₂Si(CH₃)₂O-); 0.63 (t, -P-CH₂CH₂CH₂Si(CH₃)₂O-); 0.86 (t, $J_{\text{HH}} = 6.5$ Hz, CH₃-CH₂-); 1.20-1.40 (m, CH₃-CH₂-CH₂-, CH₂-CH₂-P); 1.55-1.85 (m, CH₂-CH₂-P); 8.44 (P-OH).

²⁹Si NMR(CDCl₃): δ (ppm) = -21.5 (-OSi(CH₃)₂O-); 6.5 (PCH₂CH₂CH₂Si(CH₃)₂O-); 7.5 (-CH₂Si(CH₃)₂O-).

¹³C NMR(CDCl₃): δ (ppm) = 30.4 (CH₂-P); 28.2 (CH₂CH₂P); 26.4 (CH₃-CH₂-); 25.4 (CH₃-CH₂-CH₂-); 16.7 (SiCH₂CH₂CH₂P); 17.9 (Si-CH₂); 13.8 (CH₃CH₂-); 1.2-0.5 (SiCH₃).

³¹P NMR(CDCl₃): δ (ppm) = 25.1.

IR(ATR): ν (cm⁻¹) = 2961 (ν CH₃); 2128 (Si-H); 1258 (SiCH₃); 1018 (Si-O); 789 (Si-C) (unfortunately the P-O vibrational signals are strongly superposed with the Si-O and SiCH₃ modes).

4.5.3.2 Allyl-lithium initiated ring opening living anionic polymerization procedure using hexamethylcyclotrisiloxane as monomer

Preparation of tetraallyltin

Tetraallyltin has been prepared by a literature known procedure via *Grignard*-reaction.^[454] All steps have been carried out under argon-atmosphere and by stirring vigorously. 18.5 g magnesium powder (740 mmol) were put in a 2 L three-necked round bottom flask, together with 200 mL of dry diethylether. To initiate the reaction, 0.5 mL methyleneiodide were added, followed by the addition of further 500 mL dry diethylether. Then, 53 mL allylbromide (616 mmol) in 300 mL dry diethylether were added dropwise. This procedure was carried out to maintain a gentle reflux without any external heating. After the addition of allylbromide was completed, the reaction mixture was filtered and the filtrate was put into a 1 L round bottom flask. The mixture was then cooled to 0°C and 9 mL (72 mmol) of Sn(IV)-chloride were added dropwise over a 30 min time period. Then, the reaction mixture was heated to reflux for 16 h before it was cooled down to -10°C for the hydrolysis procedure. Therefor, 150 mL water were added dropwise over a 2 h period, followed by the dropwise addition of 300 mL 3.5% HCl. The mixture was then allowed to warm to room temperature and the

phases were separated utilizing a separating funnel. The aqueous phase was re-extracted with four portions of diethylether and the combined organic phases were washed three times with 5% aqueous KF-solution. Then, the organic phase was dried over MgSO₄ and the solvent was removed at the rotary evaporator. The product was then distilled at 65°C / 0.3 mbar. Thus, 12.6 g (44.5 mmol, 62%) product in form of a, slightly yellow colored, clear liquid could be isolated.

Characterization:

¹H NMR(CDCl₃): δ(ppm) = 1.92 (d, J_{HH} = 8.2 Hz, 2H, SnCH₂); 4.73-4.90 (m, 2H, CH=CH₂); 5.87-5.94 (m, 1H, CH=CH₂).

¹³C NMR(CDCl₃): δ(ppm) = 136.5 (-CH=CH₂); 114.8 (-CH=CH₂); 16.1 (SnCH₂).

¹¹⁹Sn NMR(CDCl₃): δ(ppm) = -46.8.

IR (ATR): ν(cm⁻¹) = 1622 (C=C stretching).

Preparation of allyl-lithium-solution in tetrahydrofuran

Allyl-Li in tetrahydrofuran (THF) has been freshly prepared before every polymerization experiment by a literature known procedure,^[454] via transmetallation reaction from tetraallyltin. All steps have been carried out under argon-atmosphere. To a solution of 2.0 g tetraallyltin (7.47 mmol) in 50 mL dry diethylether, 11.8 mL of ⁿbutyllithium in a *Schlenk* tube, 2.5 M in hexane, (29.88 mmol) were added dropwise at -10°C under stirring. While stirring for 1 h, the solution turned from green to yellow-orange. The mixture was then allowed to warm to room temperature. After this procedure, 30 mL dioxane were added slowly to give a white precipitate, which was washed three times with ⁿpentane and re-dissolved in 20 mL THF. The as prepared red solution was titrated with ^{sec}butanol to be of a 0.86 M (20 mL, 60% of theory) concentration and was directly used for the next reaction step.

Allyl-lithium initiated ring opening living anionic polymerization procedure using hexamethylcyclotrisiloxane as monomer: Preparation of α-trimethylsilyl, ω-allyl-poly(dimethyl siloxane) and α-(Si-H), ω-allyl-poly(dimethyl siloxane)

The preparation of the three different allyl-PDMS-products (A, B and C) have been performed using the following basic parameters: For the preparation of product A, a molar monomer/initiator ratio of 3 and for product B, a monomer/initiator ratio of 6 was used. Both polymerization reactions were quenched with trimethylchlorosilane. Product C was prepared using a monomer/initiator ratio of 3 and quenching with dimethylchlorosilane.

All steps have been carried out under argon-atmosphere at room temperature in *Schlenk* tubes. For each experiment, 5 mL of the freshly prepared 0.86 M (0.86 M for A and B, 0.76 M for C) allyl-Li-THF-solutions have been used (4 mmol). For product A, 2.66 g hexamethylcyclotrisiloxane (12 mmol), for product C, 2.00 g (9 mmol) of this monomer have been dissolved in 3 mL THF for and for product B, 5.32 g hexamethylcyclotrisiloxane (24

mmol) have been dissolved in 5 mL THF. Then, the initiator-solution was added to each experiment-flask, containing the monomer, and the reaction mixture was stirred at room temperature for 3 h. The polymerization reaction was then quenched with 1.1 mL (8 mmol) trimethylchlorosilane and 985 μ L (8 mmol) triethylamine for the products A and B and with 700 μ L (6 mmol) dimethylchlorosilane for product C. The thus formed white precipitate was allowed to set down overnight and was removed via filtration. The following workup procedure was the same for each experiment: 10 mL water were added to the reaction mixture and the organic phase was removed. The aqueous phase was then extracted three times with toluene and the collected organic phases were dried over MgSO_4 . The solvent and possible volatile impurities were removed under oil pump vacuum to give the products: Product A: 2.57g (91%) slightly yellow colored clear oily liquid, Product B: 5.37g (98%) colorless and clear oil, Product C: 1.90 g (~100%), clear oily liquid.

Characterization of product A and B: The identical chemical shifts in the NMR-spectra have been observed for both products:

^1H NMR(CDCl_3): $\delta(\text{ppm}) = 0.08$ (bs, $-\text{OSi}(\text{CH}_3)_2\text{O}-$); $0.20-0.50$ ($-\text{Si}(\text{CH}_3)_3$, $-\text{CH}_2\text{Si}(\text{CH}_3)_2\text{O}-$); 1.58 (d, $J_{\text{HH}} = 7.7$ Hz, $-\text{CH}_2\text{Si}(\text{CH}_3)_2\text{O}-$); 4.83 (m, $-\text{CH}=\text{CH}_2$); $5.74-5.84$ (m, $-\text{CH}=\text{CH}_2$).

^{29}Si NMR(CDCl_3): $\delta(\text{ppm}) = -21.7$ ($-\text{OSi}(\text{CH}_3)_2\text{O}-$); 4.6 ($-\text{CH}_2\text{Si}(\text{CH}_3)_2\text{O}-$); 7.3 ($-\text{Si}(\text{CH}_3)_3$).

^{13}C NMR(CDCl_3): $\delta(\text{ppm}) = 134.3$ ($-\text{CH}=\text{CH}_2$); 113.3 ($-\text{CH}=\text{CH}_2$); 26.2 ($-\text{CH}_2-\text{CH}=\text{CH}_2$); 1.9 ($-\text{Si}(\text{CH}_3)_3$); 1.1 ($-\text{OSi}(\text{CH}_3)_2\text{O}-$); 0.34 ($-\text{CH}_2\text{Si}(\text{CH}_3)_2\text{O}-$).

IR(ATR): $\nu(\text{cm}^{-1}) = 2962$ (νCH_3); 1632 (C=C stretching); 1258 (SiCH_3); 1015 (Si-O); 789 (Si-C).

GPC (toluene): Product A: $M_n = 810$ g/mol, PDI = 1.2; Product B: $M_n = 1230$ g/mol, PDI = 1.2.

Elemental Analysis: Product A: C 36.1, H 8.5.

Elemental Analysis: Product B: C 34.0, H 8.3.

Characterization of product C:

^1H NMR(CDCl_3): $\delta(\text{ppm}) = 0.08$ (bs, $-\text{OSi}(\text{CH}_3)_2\text{O}-$); $0.20-0.50$ ($-\text{SiH}(\text{CH}_3)_2$, $-\text{CH}_2\text{Si}(\text{CH}_3)_2\text{O}-$); 1.58 (d, $J_{\text{HH}} = 7.7$ Hz, $-\text{CH}_2\text{Si}(\text{CH}_3)_2\text{O}-$); $4.72-4.91$ (m, Si-H , $-\text{CH}=\text{CH}_2$); $5.76-5.86$ (m, $-\text{CH}=\text{CH}_2$).

^{29}Si NMR(CDCl_3): $\delta(\text{ppm}) = -21.7$ ($-\text{OSi}(\text{CH}_3)_2\text{O}-$); -6.5 ($\text{SiO}(\text{CH}_3)_2\text{H}$); 4.8 ($-\text{CH}_2\text{Si}(\text{CH}_3)_2\text{O}-$).

^{13}C NMR(CDCl_3): $\delta(\text{ppm}) = 134.3$ ($-\text{CH}=\text{CH}_2$); 113.3 ($-\text{CH}=\text{CH}_2$); 26.2 ($-\text{CH}_2-\text{CH}=\text{CH}_2$); $0.7-1.1$ ($-\text{Si}(\text{CH}_3)_2\text{O}-$); -0.3 ($(\text{CH}_3)_2\text{HSiO}$).

IR(ATR): $\nu(\text{cm}^{-1}) = 2962$ (νCH_3); 2127 (Si-H); 1632 (C=C stretching); 1258 (SiCH_3); 1017 (Si-O); 910 (Si-H); 789 (Si-C).

GPC (toluene): $M_n = 605$ g/mol; PDI = 1.2.

Elemental Analysis: 37.1%C, 8.7%H.

4.5.3.3 Preparation of α -(1-propyl-3-trimethoxysilyl), ω -trimethylsilyl-poly(dimethyl siloxane) (TMeS-PDMS-TMS)

The hydrosilation reaction for the capping agent preparation was carried out according to a procedure, described in literature for similar systems.^[140] All steps have been performed under argon-atmosphere. 1.0 g (1235 μ mol) Product A was dissolved in 5 mL abs. toluene in a *Schlenk* tube and 2 drops of the *Karstedt's* catalyst were added to the mixture. After the addition of 190 mg trimethoxysilane (28.1 mmol), the reaction-mixture was heated to reflux under stirring for 18 h. Then, the solvent and excess trimethoxysilane were removed in oil pump vacuum and the crude product was kept at 120°C / 10 mbar for 8 h, as an additional cleaning-step. The resulting 1.1 g of (1222 μ mol, 99%) slightly yellow colored, clear, oily liquid were then kept under argon atmosphere due to its moisture sensitivity.

Characterization:

¹H NMR(CDCl₃): δ (ppm) = 0.08 (bs, -OSi(CH₃)₂O-); 0.20-0.40 (-Si(CH₃)₃, -CH₂Si(CH₃)₂-); 0.50-0.80 (m, -CH₂-Si(OCH₃)₃); 0.95-1.00 (m, -CH₂Si(CH₃)₂-); 1.20-1.60 (m, -CH₂CH₂Si(CH₃)₂); 3.57 (s, Si(OCH₃)₃).

²⁹Si NMR(CDCl₃): δ (ppm) = -42.0 (-Si(OCH₃)₃) -21.6 (-OSi(CH₃)₂O-); 4.4 (-CH₂Si(CH₃)₂O-); 7.3 (-Si(CH₃)₃).

¹³C NMR(CDCl₃): δ (ppm) = 50.4 (Si(OCH₃)₃); 26.2 (-CH₂-Si-(CH₃)₂-O-); 22.3 (CH₂-Si(OCH₃)₃); 2.2 (-CH₂CH₂Si(CH₃)₂-); 2.0 (-CH₂Si(CH₃)₂-, -Si(CH₃)₃); 1.1 (-OSi(CH₃)₂O-).

IR(ATR): ν (cm⁻¹) = 2962 (ν CH₃); 1258 (SiCH₃); 1015 (Si-O); 789 (Si-C).

4.5.3.4 Preparation of α -(1-propyl-3-(phosphono)), ω -allyl-poly(dimethyl siloxane) (allyl-PDMS-PPA)

Synthesis of α -(1-propyl-3-(diethylphosphono)), ω -allyl-poly(dimethyl siloxane)

The hydrosilation reaction for the capping agent preparation was carried out according to a procedure, described in literature.^[140] The reaction was performed under argon-atmosphere. 1.5 g (2.48 mmol) Product C were dissolved in 2 mL abs. toluene in a *Schlenk* tube. Then, 540 mg allylphosphonic acid diethylester (3 mmol) and 2 drops of the *Karstedt's* catalyst were added. The reaction mixture was stirred for 48 h at room temperature until full conversion of the Si-H bond could be detected via IR-spectroscopy. Then, the educt excess and possible side-products were removed via distillation at 100°C / 1 mbar. The yield of the product was 1.64 g (2.26 mmol, 91%), colorless, clear liquid.

Characterization:

^1H NMR(CDCl_3): $\delta(\text{ppm}) = 0.06$ (bs, SiCH_3); 0.63 (m, $-\text{P}-\text{CH}_2\text{CH}_2\text{CH}_2\text{Si}(\text{CH}_3)_2\text{O}-$); 1.20-1.40 (m, $\text{CH}_3-\text{CH}_2-\text{O}-$, $\text{CH}_2-\text{CH}_2-\text{P}$); 1.55-1.85 (m, $\text{CH}_2-\text{CH}_2-\text{P}$, $-\text{CH}_2=\text{CH}-\text{CH}_2\text{Si}(\text{CH}_3)_2\text{O}-$); 4.07 (m, $\text{CH}_3\text{CH}_2\text{O}-$); 4.79 (m, $\text{CH}=\text{CH}_2-$); 5.76 (m, $\text{CH}=\text{CH}_2-$).

^{29}Si NMR(CDCl_3): $\delta(\text{ppm}) = -21.7$ ppm (D, $-\text{OSi}(\text{CH}_3)_2-$); 4.6 (M, $\text{CH}_2=\text{CH}-\text{CH}_2-\text{Si}-$), 7.3 (M, $\text{P}-\text{CH}_2-\text{CH}_2-\text{CH}_2-\text{Si}$).

^{13}C NMR(CDCl_3): $\delta(\text{ppm}) = 134.3$ ($\text{CH}=\text{CH}_2-$); 113.4 ($\text{CH}=\text{CH}_2-$); 61.3 ($\text{CH}_3\text{CH}_2\text{O}-$); 30.4 (CH_2-P); 28.2 ($\text{CH}_2\text{CH}_2\text{P}$); 26.1 ($\text{CH}=\text{CH}_2-\text{CH}_2-\text{Si}$) 17.9 ($\text{Si}-\text{CH}_2$); 16.7 ($\text{SiCH}_2\text{CH}_2\text{CH}_2\text{P}$); 16.4 ($\text{CH}_3\text{CH}_2\text{O}-$); 1.2-0.5 (SiCH_3).

^{31}P NMR(CDCl_3): $\delta(\text{ppm}) = 43.9$.

IR(ATR): $\nu(\text{cm}^{-1}) = 2961$ (νCH_3); 1632 ($\text{CH}=\text{CH}_2$); 1410 ($\text{CH}=\text{CH}_2$) 1257 (SiCH_3); 1017 ($\text{Si}-\text{O}$); 960 ($\text{P}-\text{O}$); 790 ($\text{Si}-\text{C}$).

GPC (toluene): $M_n = 867$ g/mol.

Synthesis of α -(1-propyl-3-(phosphono)), ω -allyl-poly(dimethyl siloxane) (allyl-PDMS-PPA)

The hydrolysis reaction of the phosphonic acid diethylester was performed under argon atmosphere, applying a literature known procedure.^[203] 1.64 g (2.26 mmol) of the α -(1-propyl-3-(diethylphosphono)), ω -allyl-poly(dimethyl siloxane) product were dissolved in 10 mL dry dichloromethane in a *Schlenk* tube and 1 mL trimethylsilylbromide (7.6 mmol) was added dropwise. Then, the reaction mixture was stirred for 2.5 h at room temperature. Afterwards, the solvent and excess of trimethylsilylbromide were removed in oil pump vacuum. After that, a mixture of 2 mL MeOH (49.4 mmol) and 1 mL H_2O (55.6 mmol) was added dropwise and the reaction mixture was stirred for 16 h at room temperature. Then, the reaction mixture was dried at 30°C at 1 mbar for 20 h to give 1.54 g (2.12 mmol, 94%) of a colorless, clear, viscous liquid.

Characterization:

^1H NMR(CDCl_3): $\delta(\text{ppm}) = 0.06$ (bs, SiCH_3); 0.65 (m, $-\text{P}-\text{CH}_2\text{CH}_2\text{CH}_2\text{Si}(\text{CH}_3)_2\text{O}-$); 1.20-1.40 (m, $\text{CH}_2-\text{CH}_2-\text{P}$); 1.55-1.85 (m, $\text{CH}_2-\text{CH}_2-\text{P}$, $-\text{CH}_2=\text{CH}-\text{CH}_2\text{Si}(\text{CH}_3)_2\text{O}-$); 4.87 (m, $\text{CH}=\text{CH}_2-$); 5.79 (m, $\text{CH}=\text{CH}_2-$); 8.51 (bs, $\text{P}-\text{OH}$).

^{29}Si NMR(CDCl_3): $\delta(\text{ppm}) = -21.7$ ppm (D, $-\text{OSi}(\text{CH}_3)_2-$); 4.7 (M, $\text{CH}_2=\text{CH}-\text{CH}_2-\text{Si}-$), 7.4 (M, $\text{P}-\text{CH}_2-\text{CH}_2-\text{CH}_2-\text{Si}$).

^{13}C NMR(CDCl_3): $\delta(\text{ppm}) = 134.3$ ($\text{CH}=\text{CH}_2-$); 113.4 ($\text{CH}=\text{CH}_2-$); 34.8 (CH_2-P); 29.5 ($\text{CH}_2\text{CH}_2\text{P}$); 26.1 ($\text{CH}=\text{CH}_2-\text{CH}_2-\text{Si}$) 17.9 ($\text{Si}-\text{CH}_2$); 16.7 ($\text{SiCH}_2\text{CH}_2\text{CH}_2\text{P}$); 1.2-0.5 (SiCH_3).

^{31}P NMR(CDCl_3): $\delta(\text{ppm}) = 37.0$.

IR(ATR): $\nu(\text{cm}^{-1}) = 2961$ (νCH_3); 1632 ($\text{CH}=\text{CH}_2$); 1413 ($\text{CH}=\text{CH}_2$) 1257 (SiCH_3); 789 ($\text{Si}-\text{C}$), ($\text{P}-\text{O}$ vibrational bands are superposed by $\text{Si}-\text{O}$ and SiCH_3 signals).

GPC (toluene): $M_n = 794$ g/mol.

Elemental Analysis: C 32.1, H 7.8, P 1.2.

4.6 Nanoparticle surface modification

In this chapter, for nanoparticle separation, a Hettich EBA 20 S centrifuge (86 mm rotor radius) has been applied for standard samples. For PDMS-grafting from experiments, a Hettich Rotanta 460R (180 mm rotor radius) has been used, giving the possibility to work under thermostatic conditions and under argon atmosphere. The latter was possible due to a special fixture, which allowed the use of *Schlenk*-tubes in the centrifuge.

4.6.1 ZrO₂ nanoparticle surface modification

ZrO₂ nanoparticles were surface modified with organophosphorus coupling agents using a *post*-modification approach as described in literature for titanium dioxide nanoparticles.^[149] A typical procedure is described here for the example of dodecylphosphonic acid @ ZrO₂ nanoparticles.

First, 5 mL of 10 g/L aqueous nanoparticle dispersion was prepared by dispersing the zirconia nanoparticle powder for 30 min in an ultrasonic bath. Afterwards, HCl conc. was added dropwise to the dispersion to adjust the pH to 2. The phosphonic acid, e.g. 18.7 mg dodecylphosphonic acid, to reach a 7.5 mM coupling agent concentration in the final mixture, was dissolved in 5 mL methanol, added to the particle dispersion and stirred for 2 days. The particles were then isolated via centrifugation at 6000 rpm, washed three times with ethanol (centrifugation at 6000 rpm), and dried over P₂O₅ at 5 mbar for 24h, resulting in 50 mg of a white powder.

The modification reaction parameters were linearly up-scaled when larger amount of modified nanoparticles had to be prepared.

Characterization: dodecylphosphonic acid@ZrO₂:

¹³C Solid State NMR: $\delta(\text{ppm}) = 30.0 - 19.5$ (11C, CH₂); 15.0 (CH₃).

³¹P Solid State NMR: $\delta(\text{ppm}) = 27.0$ (bs).

IR (ATR): $\nu(\text{cm}^{-1}) = 2921$ (ν_{as} C-H, CH₂); 2851 (ν_{s} C-H, CH₂); 1464 (C-H); 1034 (P-O broad).

Elemental Analysis: 12.95%C, 2.45%H, 2.3%P.

TGA: $\Delta m(200^\circ\text{C} - 800^\circ\text{C}) = 14.5\%$, Onset: 268°C.

4.6.2 SiO₂ nanoparticle surface modification

The SiO₂ nanoparticles were surface modified with organosilane coupling agents by utilizing a method described in literature,^[148] a quasi *in situ* modification. Thereby, the nanoparticle

sols, prepared in chapter 4.4.3, have been directly used. First, 0.1 mL NH₄OH conc. were added to the freshly prepared silica sol under stirring, followed by the addition of the trimethoxysilane coupling agent (e.g. dodecyltrimethoxysilane) to result in a 7.5 mM solution which was stirred for 48 h. The particles were then isolated by concentrating the dispersion via solvent removal and centrifugation at 8000 rpm. Afterwards, they were washed three times with ethanol (centrifugation at 8000 rpm) and dried over P₂O₅ at 5 mbar for 24 h.

Characterization, e.g.: dodecyltrimethoxysilane@SiO₂ small nanoparticles:

¹³C-Solid State NMR: $\delta(\text{ppm}) = 28.0\text{-}20.4$ (10C, CH₂); 17.0 (CH₃); 11.2 (Si-CH₂).

²⁹Si-Solid State NMR: $\delta(\text{ppm}) = -61.9$ (T); -69.6 (T); -97.3 (Q); -105.5 (Q); -114.3 (Q).

IR (ATR): $\nu(\text{cm}^{-1}) = 2929$ (ν_{as} C-H, CH₂); 2855 (ν_{s} C-H, CH₂); 1461 (C-H); 1091 (Si-O).

Elemental Analysis: 8.9%C, 3.4%H (the higher H/C ratio compared to the H/C ratio in the coupling agent originates from residual ethoxy-groups in the SiO₂ bulk material).

TGA: Δm (200°C-800°C) = 18.5%, Onset: 227°C.

4.6.3 PDMS grafting *from* experiments

All steps in this chapter have been carried out under argon atmosphere, including centrifugation, which was performed by utilization of a special fixture which allowed the use of *Schlenk* tubes in a centrifuge with a rotor radius of 180 mm, at 1200 rpm.

4.6.3.1 Model reaction: lithiation and trimethylsilyl-termination

100 mg Br-C2-PPA@ZrO₂ small nanoparticles (~200 μmol Br-groups, determined via TGA and nitrogen sorption measurements) were dried at 60°C and 0.1 mbar for 16 h in a *Schlenk* tube which could be fitted into the centrifuge fixture. Then, 5 mL of ⁿhexane were added and the mixture was treated for 5 min in an ultrasonic bath. The reaction mixture was then cooled to -78°C and vigorously stirred. Then, 0.5 mL ⁿBuLi, 2.5 M in ⁿhexane, (1.25 mmol, excess) were added and stirring was continued for 5 min. After that, the mixture was centrifuged (particles formed a white sediment) and washed with ⁿhexane to remove the excess of ⁿBuLi from the solution, and finally, 5 mL of abs. THF were added. Then, under stirring, 95 μL trimethylchlorosilane (703 μmol) and 85 μL triethylamine (614 μmol) were added and the mixture was allowed to warm to room temperature and then stirred for another 1 h. For the workup, 5 mL ⁿhexane were added and the particles were separated by centrifugation at 8000 rpm and washed three times with a mixture of THF : ⁿhexane = 1:1 (centrifugation at 8000 rpm). Then, the particles were washed two times with water and one time with ethanol. The product was then dried for 20 h at 1 mbar over P₂O₅ to give 70 mg of a white powder.

Characterization:

¹³C Solid State NMR: $\delta(\text{ppm}) = 19.3$ (CH₂-P); 8.7 (CH₂-CH₂-P); -2.6 (Si(CH₃)₃).

^{31}P Solid State NMR: $\delta(\text{ppm}) = 23.9$ (bs).

IR(ATR): $\nu(\text{cm}^{-1}) = 2962$ (ν C-H, CH_3); 1278 (SiCH_3); 1047 (P-O broad); 739 (Si-C).

4.6.3.2 PDMS grafting from Br-C2-PPA@ZrO₂ nanoparticles

Two different samples, sample "E" and sample "F" have been prepared with the only difference being the monomer concentration. The procedure for each grafting reaction was the same as described below:

200 mg Br-C2-PPA@ZrO₂ small nanoparticles (~400 μmol Br-groups, determined via TGA and nitrogen sorption measurements) were dried at 60°C and 0.1 mbar for 16 h in a *Schlenk* tube which was applicable in the centrifuge fixture. Then, 15 mL of $^n\text{hexane}$ were added and the mixture was treated for 5 min in an ultrasonic bath. The reaction mixture was then cooled to -78°C and vigorously stirred. Then, 0.5 mL $^n\text{BuLi}$, 2.5 M in $^n\text{hexane}$, (1.25 mmol, excess) were added and the mixture was stirred for 5 min. After that, the mixture was centrifuged (particles formed a white sediment) and washed with $^n\text{hexane}$ to remove the excess of $^n\text{BuLi}$ from the solution. Then, for the preparation of sample "E", 2.96 g (13.3 mmol) and for the preparation of sample "F", 8.87 g (40.0 mmol) hexamethylcyclotrisiloxane were dissolved in 10 mL abs. THF. This solution was then added to the particles in the reaction vessel and homogenized by 2 min of ultrasound treatment. The reaction mixture was then stirred and allowed to warm to room temperature.

During this period, to monitor the reaction with ^1H NMR, a kinetic experiment has been carried out. Therefore, after a certain time period, 0.2 mL of homogeneous reaction mixture have been taken from the reaction tube and quenched with 0.2 mL H₂O. The mixture was then dried at 45°C for 24 h and stirred for 15 h in 1 mL of CDCl₃ in a closed glass vessel. The mixture was then allowed to settle down and the liquid was filtered via a 200 nm mesh PTFE-syringe-filter. 0.5 mL of this solution were mixed with 0.5 mL of a diphenylether-standard-solution of a 0.36 M concentration and ^1H NMR-spectra were recorded. By comparing the integral from the resonance of aromatic ring of the diphenylether standard with the integrals from the resonance of the SiCH₃ group from the species in the reaction solution, the concentration of (OSi(CH₃)₂)₃ species, which is in solution during the grafting reaction, could be monitored.

After 5 days, the grafting reaction was quenched by the addition of 190 μL trimethylchlorosilane (1406 μmol) and 170 μL triethylamine (1228 μmol) and the mixture was stirred for 16 h at room temperature. For the workup, 10 mL THF were added and the particles were separated by centrifugation at 8000 rpm and washed three times with a mixture of THF : $^n\text{hexane} = 1:1$ (centrifugation at 8000 rpm). Then, the particles were washed two times with water and one time with ethanol (centrifugation at 8000 rpm). The product was then dried for 20 h at 1 mbar over P₂O₅ to give 350 mg of a white powder.

Characterization sample "F" (the identical shifts for the spectroscopy signals have been obtained for sample "E", but with lower intensities):

^{13}C Solid State NMR: $\delta(\text{ppm}) = 7.0 (\text{SiCH}_3)_2$; $-1.5 (\text{Si}(\text{CH}_3)_3)$.

^{29}Si Solid State NMR: $\delta(\text{ppm}) = -7.3 (\text{M})$; $-22.0 (\text{D})$.

IR (ATR): $\nu(\text{cm}^{-1}) = 2979 (\nu \text{ C-H, CH}_3)$; $1261 (\text{SiCH}_3)$; $1072, 1036 (\text{Si-O})$; $851, 806, 737 (\text{SiCH}_3)$; (P-O vibrations are superposed by Si-O bands).

Elemental Analysis: 32.0 C, 7.5 H.

4.6.4 Polystyrene grafted nanoparticles (PS@SiO₂)

The SiO₂ nanoparticles, modified with the radical initiating azo end group (Azo-TMS@SiO₂), were not dried after modification during the workup procedure, but kept as a swollen powder in toluene under argon atmosphere and stored at 4°C.

The grafting reaction was carried out according to a literature known procedure,^[255] under argon atmosphere, by dispersing 1 g wet (34 wt% solid content, swollen in toluene) Azo-TMS@SiO₂ small or large nanoparticle powder in 100 mL of a mixture of toluene : styrene = 2:1 (v/v), utilizing an ultrasonic bath. Then, three freeze-pump-thaw-cycles have been applied and the mixture was heated to 60°C for 63 h under vigorous stirring. The product was then separated by centrifugation (45 min at 8000 rpm) and washed with toluene until no free (untethered) polystyrene (which is a by-product within this procedure) remained in the supernatant. This was monitored by precipitation of free PS with MeOH in the supernatant solution. The product was stored and used for the further preparation steps, swollen in toluene. Parts of the product have been dried for characterization and thus also a total yield of 2.4 g could be calculated.

Characterization: (PS@SiO₂ small, PS@SiO₂ large)

^{13}C Solid State NMR: $\delta(\text{ppm}) = 143.1, 124.8 (6\text{C, aromatic})$; $51.0-25.0 (2\text{C, CH}_2)$; $17.4 (\text{CH}_3)$.

IR (ATR): $\nu(\text{cm}^{-1}) = 3026, 3085 (\nu \text{ C-H, aromatic ring})$; $2921 (\nu \text{ CH}_2)$; $1604 (\text{C}=\text{C, skeletal, aromatic ring})$; $1453, 1495 (\text{C-H, aromatic ring})$; $1052 (\text{Si-O-Si, broad})$; $727, 694 (\text{C-H, aromatic ring out of plane})$.

DSC(10K/min): $T_g = 97^\circ\text{C}$.

For the analysis of the molecular weight, the surface tethered PS was de-grafted from the nanoparticles by the following procedure. 250 mg wet PS@SiO₂ nanoparticles were dispersed in 50 mL toluene and 10 mL MeOH utilizing ultrasound. Then, 25 mg toluene-sulfonic acid monohydrate were added and the mixture was heated to reflux for 20 h under vigorous stirring. Then, the volume of the reaction mixture was reduced to 10 mL and the de-grafted polymer was precipitated the addition of MeOH, dried and analyzed via GPC.

Characterization of de-grafted polymer:

GPC(THF): $M_n = 220000$ g/mol, PDI = 1.4

4.7 Experiments using wafer substrates

All used solvents were filtered two times over a 200 μm mesh syringe filter. The wafer materials, $\text{ZrO}_2@\text{Si}$ and $\text{SiO}_2@\text{Si}$ were activated in 1N HCl for 5 min in an ultrasound cleaning bath and then washed neutral with water. The samples were then cleaned two times with MeOH and put into a 7.5 mM methanolic coupling agent solution. After 5 days, they were washed with MeOH in an ultrasound cleaning bath and stored under MeOH for 24 h. Then, they were washed another three times with MeOH and dried with pressurized synthetic air, directly before they were measured.

4.8 Preparation of nanocomposite materials

The bulk polymerization reactions (polystyrene and poly(methyl methacrylate)) were performed under argon atmosphere in sealed, cylindrical, flat bottom glass vessels with 24 mm inner diameter, 52 mm height and 15 mL volume. These reaction vessels have also been used for the compounding of the epoxy formulation.

For the stirring during polymerization reactions and epoxy resin compounding in these vessels, a magnetic stirrer was applied, utilizing cylindrical, PTFE coated stirring beads with 3 mm diameter and 8 mm length. All polymerization reactions were carried out by stirring at 250 rpm and all epoxy resin formulation were mixed at 500 rpm (a compromise between high shear force and less air bubble generation and thus foaming), in these systems of flat bottom vessel and stirring bead.

4.8.1 Polystyrene (PS) nanocomposites

4.8.1.1 PS materials via *in situ*-polymerization

For the preparation of polystyrene nanocomposites via *in situ* bulk polymerization, 3 mL styrene, for each sample, was mixed with 27 mg dibenzoyl peroxide (DBPO), to obtain a 1 wt% initiator containing solution. Then, the particles were added and stirred for 1 h for particle surface wetting. Afterwards, the mixtures were ultrasonicated for 5 min in an ultrasound cleaning bath and heated to 80°C for 16 h to obtain the nanocomposite materials. After removal from the glass vessel, nanocomposite material samples in form of disks with 2.4 cm diameter and 1.0-1.5 cm height could be yielded.

Characterization of the polymer matrix, average values for the whole series:

GPC (THF): $M_w = 66500 \pm 10000$ g/mol, PDI = 1.8-2.0.

DSC (10K/min): $T_g = 98-102^\circ\text{C}$.

4.8.1.2 PS materials via solution compounding

For solution compounding, polystyrene without nanofiller, prepared by the procedure as described in 4.8.1.1, has been used as polymer matrix. Therefore, for each sample, 6 g PS was dissolved in 25 mL THF and the nanoparticles in form of a toluene-wet powder were added. The mixture was then stirred at 300 rpm in 100 mL flat bottom glass beakers, with a magnetic stirrer, utilizing cylindrical PTFE coated stirring beads with 8 mm diameter and 40 mm length, for 16 h. After this procedure, homogeneous, stable dispersions could be obtained, see Figure 149. Then, the solvent was removed by stirring at 40°C for 24 h under and the product was finally dried at 5 mbar to give a dry, white powder.



Figure 149. Photograph of solution compounded sample containing 5 wt% polystyrene shell SiO_2 large nanoparticles, before evaporation of the solvent.

4.8.1.3 PS materials via melt extrusion

Melt extrusion experiments were performed on a Haake MiniLab 2 double screw laboratory extruder with a compounding volume of 7 cm^3 . The technical arrangement within this compounding volume is visualized in Figure 150. Thereby, the screws have been driven in a counter-rotating mode and a bypass allowed to drive the nanocomposite melt in circle to prolong the mixing period. Via the control of the valve, the melt compounded sample could be released through the outlet.

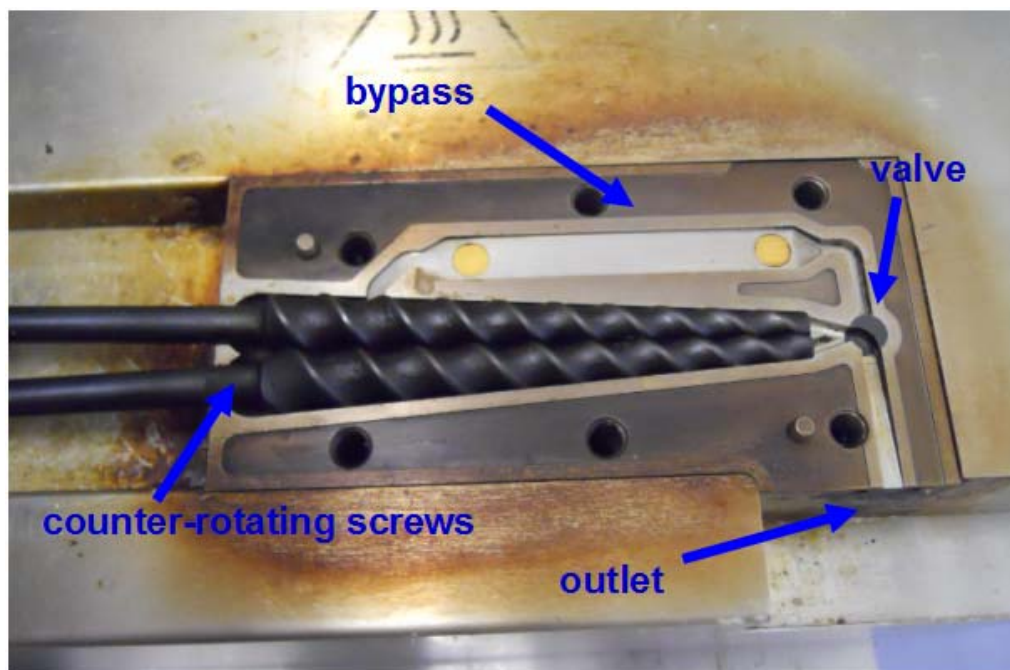


Figure 150. Photograph of the opened compounding arrangement of the laboratory extruder apparatus.

The extruder was either filled with a mixture of PS granulate containing no filler, prepared in 4.8.1.1, which was then mixed with the nanoparticle powder, or with the solution compounded samples from chapter 4.8.1.2. For each experiment, 6 g of material was used and heated at 220°C at a rotating speed of 100 rpm. After 10 min (a longer mixing time was not applied because of the sample degradation leading to brownish coloring of the material) of pumping the melt mixture in circle via the bypass, the outlet valve was opened and the compound was yielded in form of profiles with $\sim 5 \times 2$ mm dimensions of the cross section, after the melt solidified after a few seconds under the ambient conditions.

4.8.2 Poly(methyl methacrylate) (PMMA) nanocomposites

For the preparation of PMMA nanocomposites via *in situ* bulk polymerization, 2.5 mL methyl methacrylate, containing 0.05wt% of the initiator azo-bis-isobutyronitrile (AIBN) (from a freshly prepared stock solution) were put into the reaction vessels. Then, the particles were added to this solution and it was stirred for 1 h for surface wetting of the particles. Afterwards, the mixtures were ultrasonicated for 5 min in an ultrasound cleaning bath and heated to 55°C for 16 h as a pre-polymerization phase. Then, the reaction mixtures were heated at 80°C for 24h to obtain the final materials. After removal from the glass vessel, nanocomposite material samples in form of disks with 2.4 cm diameter and ~ 1.0 cm height could be yielded.

Characterization of the polymer matrix, average values for the whole series:

GPC (THF): $M_w = 298000 \pm 70000$ g/mol, PDI = 1.3-1.5.

DSC (10K/min): $T_g = 103-119^\circ\text{C}$.

4.8.3 Epoxy resin nanocomposites

Epoxy resin nanocomposites were prepared applying an *in situ*-curing approach. The amine cured bisphenol-F-based epoxy resin was prepared by a usual procedure, as it is described in literature for such formulations.^[269] 2.0 g (7.03 mmol) bisphenol-F-diglycidylether (BFDGE) was molten at 70°C and the particle powder was added, followed by magnetic stirring at 750 rpm for 2 h. The mixture was then further stirred at 500 rpm for 1 h to calm down the foaming and gas bubble formation. Then, by stirring at 500 rpm, 0.2 g (1.94 mmol) diethylenetriamine (DETA) were added to the reaction mixture. The thus obtained compound was immediately cast on a, high viscous silicone grease coated, stainless steel plate and allowed to calm down and spread on the metal plate for 5 min at 70°C to bring the curing mixtures into appropriate sample dimensions. The material was then cured at 120°C for 16 h to give sample plates of 1.4 mm thickness and 3-5 cm diameter.

Characterization of the polymer matrix:

DSC (10K/min): $T_g = 110^\circ\text{C}$.

5 Summary

The primary goal of this work was the systematic chemical surface tailoring of metal oxide nanoparticles and their use as fillers in polymer nanocomposites, epoxy resins, polystyrene and poly(methyl methacrylate). The influence of the nanoparticle surface modification on the dispersibility of the nanoparticles in organic media has been investigated and tuned in order to achieve an interfacial fit between the inorganic and organic compounds. Furthermore, polymer nanocomposites were prepared and the influence of chemical surface modification on dispersion structure, optical and mechanical properties was studied systematically. One goal was to obtain homogeneous nanocomposites that show enhanced mechanical properties. This was achieved via interfacial tuning, which made the application of a low shear force mixing procedure within nanocomposite preparation possible.

In the first part of the work, the chemical nanoparticle surface tailoring was investigated systematically as a tool to tune physical surface properties (hydrophobicity) of nanopowders. In the second part of this work, modified nanopowders were used for the preparation of polymer nanocomposites and structure-property-relationships were studied.

As metal oxide nanoparticle model systems, amorphous SiO_2 and crystalline ZrO_2 (Baddeleyite) nanoparticles were applied. The particles were prepared in different sizes, one size in the upper nanorange ("large") and one in the lower nanorange ("small"), where the nanorange is defined as 1-100 nm. SiO_2 nanoparticles were prepared by applying the *Stöber*-process, varying the particle size via the educt ratios. ZrO_2 nanoparticles were synthesized hydrothermally from different precursors to vary the particle size. Within the process of varying the particle size, different particle size determining methods were applied and compared. The compared methods were dynamic light scattering (DLS), transmission electron microscopy (TEM), powder-X-ray-diffraction (pXRD), nitrogen sorption and small angle X-ray-scattering (SAXS). TEM revealed a diameter of 6.8 ± 1.3 nm for small and 60.8 ± 1.6 nm for large SiO_2 nanoparticles, as well as diameters of 6.0 ± 0.4 nm for small ZrO_2 and 38.1 ± 2.8 for large ZrO_2 nanoparticles. The SiO_2 nanoparticles displayed a spherical shape, the small ZrO_2 nanoparticles were small single crystals and the large ZrO_2 nanoparticles were irregular shaped polycrystalline aggregates. A comparison of the different particle diameters, calculated from the different experimental methods, revealed that the measured particle size strongly depends on the measurement method, and thus, particle size values could only be compared within one method. Many reasons for these deviations were discussed in this work, such as the hydrodynamic shell of particles in dispersion resulting in higher particle size values when DLS is applied, but also the irregular shape and surface roughness of ZrO_2 nanoparticles which makes the system more complex to model and falsifies the results for particle diameters.

For the surface modification of SiO_2 nanoparticles the coupling agent molecules included trimethoxysilane anchor groups, and for the surface modification of ZrO_2 nanoparticles they

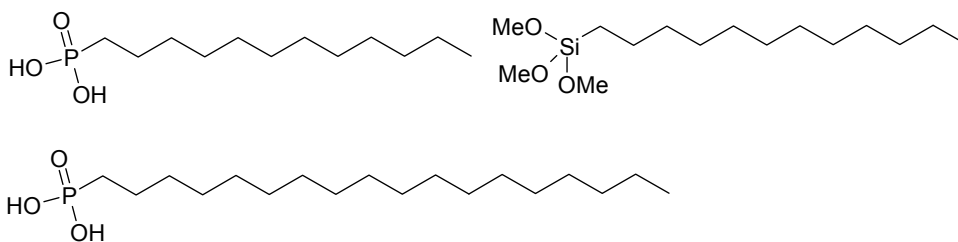
included organophosphorus anchor groups (phosphonic acids and phosphoric acid monoesters). Figure 151 gives an overview on the applied molecular coupling agents. The organic moiety of the coupling agents were varied basically within the scope of two larger studies within this work:

- i. To study the self-assembled-monolayer (SAM) formation on nanoparticle surfaces showing different curvature, long alkyl chain coupling agents were applied. To influence the SAM structure, co-coupling agents (which are systematically varied in their chemical structure) were applied in a mixed monolayer approach, to finally investigate on the effect of surface-SAM structure on powder agglomeration behavior.
- ii. To study the effect of nanoparticle surface tailoring on structural and macroscopic mechanical properties of polymer nanocomposite materials, various coupling agent molecules were applied. The variation of the alkyl spacer chain allows to tune the surface hydrophobicity. A functional end group allowed the variation of interaction strength between nanoparticle surface and polymer matrix. For example, for epoxy resins, the epoxide- end group allowed a covalent linkage to the particle during an *in situ* curing approach. Methacrylate- as well as styryl- end groups allow a covalent linkage between particle and matrix when *in situ* polymerization in an appropriate monomer is applied (grafting *through* the surface). Furthermore, alternative organic moieties, such as diethylene glycol chains were studied.

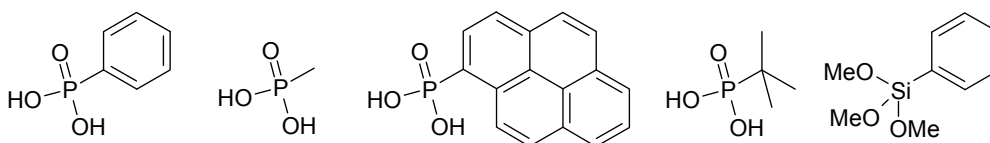
Besides these molecular coupling agents, also alternative polymeric and oligomeric surface modifications, poly(dimethyl siloxanes) (PDMS) as well as polystyrene-chains, were applied during the process of surface modification of the nanoparticles.

Via FT-IR and solid state NMR spectroscopic methods, a strong covalent attachment of all coupling agent molecules to the nanoparticle surface was verified. Via TGA and nitrogen sorption experiments, grafting densities of the coupling agent molecules could be calculated. For trimethoxysilanes@SiO₂, grafting densities between 0.4 and 3.4 molecules/nm² and for organophosphorus molecules@ZrO₂, grafting densities between 1.0 and 3.6 molecules/nm² were obtained. The resulting grafting density was strongly dependent on the particle and coupling agent nature. Strong nanoscopic curvature of the particles (e.g. small SiO₂ nanoparticles) and large steric demand of the coupling agent molecule reduced the maximum possible grafting density. Furthermore, if a molecule had a stronger tendency for SAM formation (e.g. octadecylphosphonic acid has a strong tendency to form dense packed chain structures on surfaces), the grafting density was higher. A dense SAM at ideal macroscopically planar surfaces showed a grafting density of ~4 molecules/nm² (long alkyl chains). The difference in grafting density from the systems described in the present work, can be explained by these geometrical effects and the fact that nanoparticle surfaces are non-ideal and contain many defect sites where the ability of strong attachment of coupling agent molecules can be decreased.

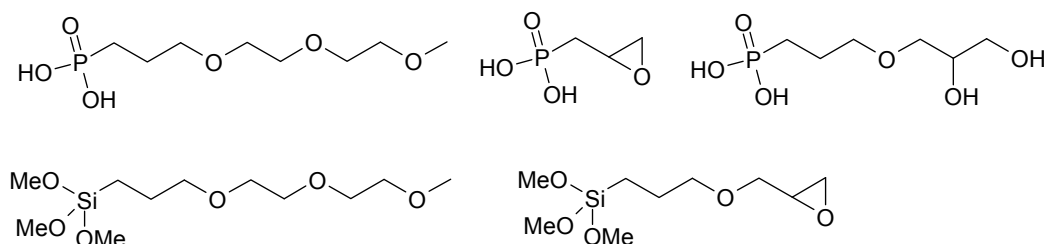
coupling agents used in self-assembled-monolayer studies



co-coupling agents used in self-assembled-monolayer studies



coupling agents used for epoxy resin nanocomposites



coupling agents used for polystyrene and poly (methyl methacrylate) nanocomposites

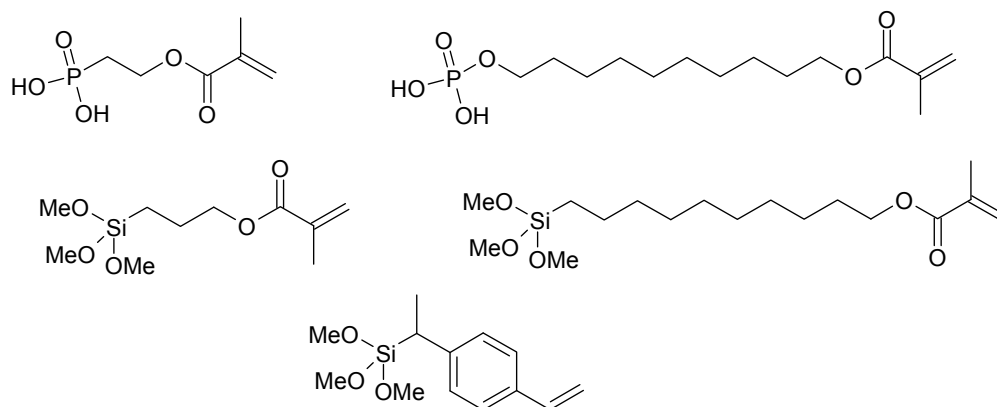


Figure 151. Molecular coupling agents which were applied for surface functionalization of metal oxide nanoparticles for studies on systematic surface and interface tailoring within this work.

The SAM-formation of long alkyl chains (C12 and C18) at different substrates (SiO₂ spheres and ZrO₂ nanocrystals) was investigated, as the effect of alkyl chain packing is important for the redispersibility behavior of thus hydrophobized nanopowders: Highly ordered inter-particle bilayers, formed via interaction of long alkyl chains between the nanoparticles

("zipper effect") can lead to strong agglomeration phenomena. The goal of this study was to correlate the molecular arrangement of the surface bond alkyl chains on the nanoscopic substrate with the resulting macroscopical properties (agglomeration and redispersibility).

The degree of ordering of the long alkyl chains on the nanoparticle substrates was monitored via FT-IR spectroscopy. Thereby, the wavenumber for the methylene C-H stretching vibration is lower for highly ordered systems ($\nu_{as} = 2917 \text{ cm}^{-1}$) and higher for more disordered structures ($\nu_{as} = 2930 \text{ cm}^{-1}$). The results of the performed studies on the substrate dependency of SAM ordering are summarized in Figure 152. In these studies it was found, by varying the curvature of SiO_2 nanoparticles, reaching from particles with 6 nm diameter (TEM) to plane wafer substrates that for flatter curvature a higher surface chain ordering could be obtained. For nanosized SiO_2 nanoparticles the SAM structure can be considered as highly disordered, whereas for the plane crystal shaped ZrO_2 nanoparticles, strong SAM ordering could be obtained. The reason for these observations is that the crystal facets represent plane areas which allow, even if these areas exhibit nanoscopic dimensions, a more dense chain packing and thus a higher SAM-ordering as compared to spherical curvatures. However, a method was found to tune the SAM ordering on these ZrO_2 facets via a mixed monolayer formation approach. While the surface coverage was kept constant, the ratio of long alkyl chain coupling agent and another, ordering disturbing, coupling agent (in the case of the results in Figure 152 a phenyl-moiety) was varied. The result was a precise tuning of long alkyl SAM ordering, where the chain ordering decreased with increasing amount of co-coupling agent.

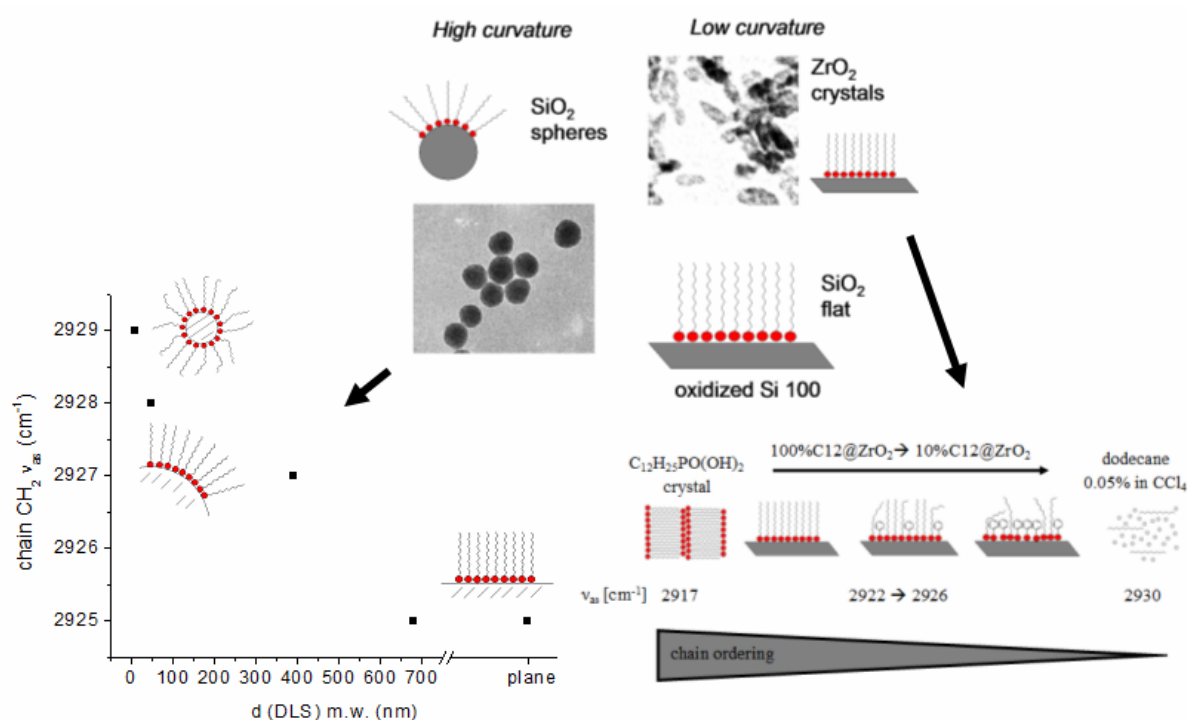


Figure 152. Schematic representation of the results obtained from FT-IR measurements for dodecyl-SAMs on spherical SiO_2 and crystal shaped ZrO_2 nanoparticles. Substrates with strong curvature show lower alkyl chain ordering. For substrates with high alkyl chain ordering, the latter can be tuned via mixed monolayer formation.

To extend the study on the tuning of SAM ordering via mixed modification on ZrO_2 nanofacets, various co-coupling agents with different steric demand have been used within this approach. Furthermore, different mixing ratios were applied. FT-IR measurements revealed that bulkier molecules show stronger disordering properties at same mixing ratios. Furthermore, the mixed modified nanopowders were measured with SAXS, applying a model to calculate a value which represents the agglomeration degree of the particles for each sample, the hard sphere volume fraction η . The lower the value of η the looser is the agglomeration.

The result of these studies was a correlation of alkyl chain ordering, derived from a spectroscopical method (FT-IR), with particle packing, derived from a scattering method (SAXS), Figure 153. With decreasing surface chain ordering the particle agglomerates in the powder became looser, thus the existence of the inter-particle "zipper-effect" could be directly demonstrated. Furthermore, DLS experiments showed that the more loose agglomerated systems could be more easily redispersed in organic solvents. Thus, the mixed SAM approach is a facile method to tune the redispersibility behavior of metal oxide nanopowders, which is of great technological relevance.

The generality of these assumptions was also proven for longer alkyl chain molecules (C18) on ZrO_2 nanocrystals and on macroscopical wafer substrates.

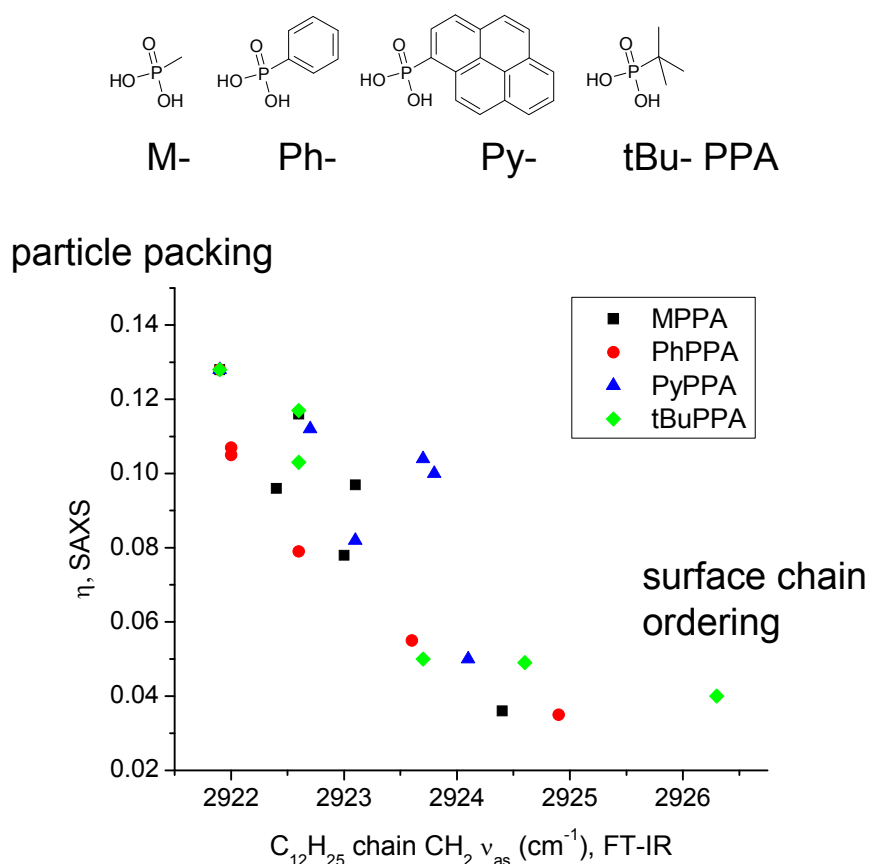


Figure 153. Correlation of surface chain ordering (FT-IR) with particle packing (SAXS) for mixed monolayer (dodecyl phosphonic acid and co-coupling agent) modified ZrO_2 nanocrystals.

Furthermore, in other studies on the systematic chemical surface tuning of nanoparticle surfaces poly(dimethylsiloxane) (PDMS) chains were introduced as an alternative to alkyl chain modified nanoparticles. To covalently attach PDMS chains of variable chain length with defined end groups to metal oxide nanoparticle surfaces, two fundamentally different methods were applied and compared in this work, see Figure 154.

A grafting-*onto* approach was applied, where a polymeric coupling agent of the type "anchor group-PDMS-functional end group" was directly attached to a metal oxide nanoparticle surface. This method had the advantage that a very well characterized and defined molecular system was adsorbed to the surface. A drawback of this method was the difficult synthesis of these molecules, especially if they contain polymerizable end groups. However, a synthetic pathway to such α, ω -heterotelechelic PDMS, as needed for the grafting *onto* approach, was developed in this work. The synthetic route was based on the anionic ring opening polymerization (ROP) of hexamethylcyclotrisiloxane (D_3) initiated by allyl-lithium. The thus prepared PDMS spacer coupling agent molecules have been used for the surface modification of ZrO_2 and SiO_2 nanoparticles. Thereby, the nanoparticles, modified with PDMS chains with $n = 5$ and $n = 12$ siloxane units, showed organophilic behavior and were dispersible in organic solvents and monomers (shown by DLS experiments). To study these systems in nanocomposites, nBu , and allyl- end groups were applied.

Furthermore, a grafting-*from* approach was applied, which had not been described in literature before in this way. This approach was successfully tested for the small ZrO_2 nanocrystal system. Thereby, initiator-molecules were attached to the nanoparticle surface. Then a ROP of D_3 was started from the particle surface and quenched to have a trimethylsilyl- end group. The initiating group was an alkyl-bromo moiety, surface bond via phosphonic acid anchor group, which was lithiated. It could be demonstrated via spectroscopic methods (FT-IR, NMR) that the surface attachment of the anchoring group is not affected by this process. The obtained material was highly hydrophobic and dispersible in organic solvents.

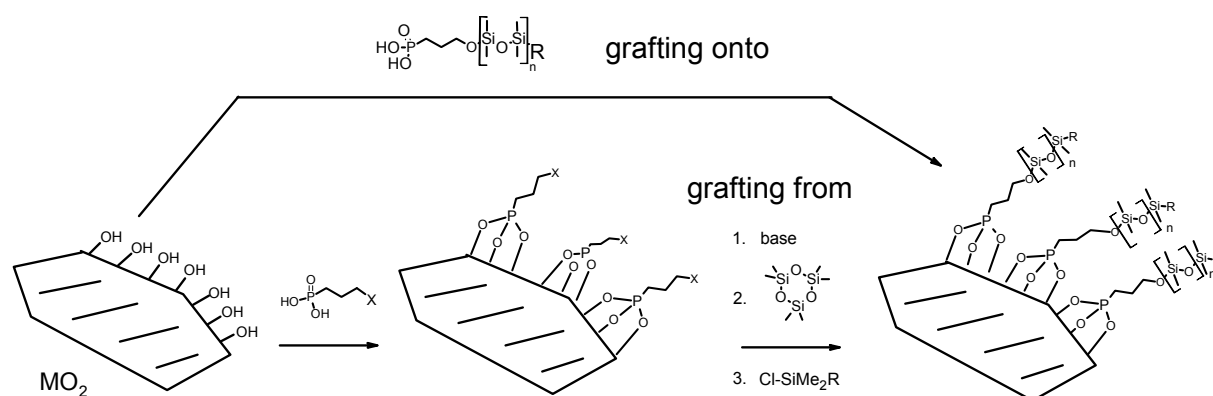


Figure 154. Applied strategies for the preparation of covalently attached PDMS chains on metal oxide nanoparticles. X = initiator generating end group (Br), reagent = nBuLi , R = optional functional end group or CH_3 group, M = Zr.

Comparing the results gained from these two approaches (PDMS with trimethylsilyl- terminus in each case), the grafting-*onto* approach showed lower grafting densities, 0.6 molecules/ nm^2

at a chain length of 850 g/mol (longer chains further decrease grafting density). The grafting-*from* approach thereby had the advantage that higher grafting densities of 1.0 molecules/nm² at higher chain length of 2600 g/mol, could be obtained. A further advantage of the grafting-*from*-approach was that the overall process of grafting is facile. However, the process was difficult to control because of the complex heterogeneous nature of the reaction mixture.

Furthermore, another type of surface modification which was applied within the preparation of PS nanocomposites was tested. A literature known approach of polystyrene grafting *from* the surface of Aerosil particles was adapted to the *Stöber* nanoparticles to produce PS-shell-SiO₂ nanoparticles. Via TEM and AFM measurements a thickness of the PS shell at 60 nm diameter SiO₂ nanoparticles (large) of ~50 nm could be observed. The grafted PS chains revealed a molecular weight of $M_n = 220000$. The PS@SiO₂ nanoparticles were very well-dispersible in toluene.

From the results of the the first part of the work the systematic tuning of nanoparticle surfaces with various organic moieties, the following points were concluded:

- Steric effects from the organic moiety can result in lower surface coverage values, namely when the moiety has more demand of space than the anchor group.
- Long alkyl chains result in dense monolayers which are responsible for an undesired inter-particle chain "zipper effect" resulting in stronger agglomeration, which can be overcome by applying mixed monolayers or using alternative spacers (PDMS).
- Oligo(ethylene glycol) chains form dense monolayers which do not show such a "zipper effect" behavior. These modifications result in hydrophilic, hygroscopic particle powders.
- PDMS chains do not form very dense monolayers when grafted *onto* nanoparticle surfaces. This effect can be positive when moderate polarity is required for the interfacial fit within polymer nanocomposites (e.g. poly(methyl methacrylate)).
- PDMS, grafted *from* nanoparticle surfaces, can give powders with higher grafting densities than for the corresponding grafted *onto* approach, however much lower as for long alkyl SAMs. Generally, the steric demand of the PDMS chains may limit the dense grafting of PDMS.
- Appropriate polystyrene shell nanoparticles are surface-tailored to provide an optimal interfacial fit with the bulk polymer PS.

By a systematic variation of spacer nature, length and chain end group, it was possible to tune the nanoparticle surface properties and thus their compatibility with their environment resulting e.g. in different dispersion behavior.

In the second part of this work the surface modified nanoparticles were incorporated into polymer matrices (polystyrene (PS), poly(methyl methacrylate) (PMMA), epoxy resins) with different filler degrees (3 wt%, 5 wt%, 10 wt%). The influence of chemical surface modification, particle nature and size, as well as filler percentage, on the structure and mechanical properties of the prepared nanocomposite materials was then investigated. The goal was to discover structure-property relations and to obtain homogeneous nanomaterials with enhanced mechanical properties via chemical interface tailoring.

SiO₂ nanoparticles (different sizes) were incorporated into a polystyrene matrix ($M_w = 66500 \pm 10000$ g/mol, PDI = 1.8 - 2.0) via *in situ* bulk polymerization, solution compounding and melt compounding in a laboratory-extruder. In all three cases homogeneous nanocomposites could be prepared by using PS-shell-nanoparticle, while unmodified nanoparticles led to strong phase separation of the compounds. The homogeneity of the materials was investigated via TEM of ultramicrotomy thin cuts and by SAXS measurements. Thus, it could further be shown that the homogeneity of the nanocomposites increases within the following row of applied coupling agents (*in situ* polymerized): Homogeneity dodecyl < phenyl < styryl. Reasons for this behavior are the proper interfacial fit of surface modifications which are structurally similar to the polymer matrix. Furthermore, the dispersion quality can be improved due to the ability of the functional end group to allow a surface grafting *through* during the *in situ* polymerization. It was shown via UV/VIS measurements that homogeneous nanocomposites exhibit high optical transparency.

PMMA ($M_w = 298000 \pm 70000$ g/mol, PDI 1.3 - 1.5) nanocomposites were prepared via *in situ* bulk polymerization, applying ZrO₂ and SiO₂ nanoparticles (different sizes) with different surface modification (dodecyl-, methacryloyl-C2/3-chain and methacryloyl-C10-chain). The best homogeneity (proved by SAXS, TEM) could also be achieved for systems with a surface modification, chemically similar to the surrounding matrix and allowing a copolymerization, methacryloyl groups. Unmodified nanoparticles showed poor dispersion properties. The results were thus qualitatively similar for the PS system, except for ZrO₂ systems, where a significant impact of particle size and shape on the dispersion behavior could be observed. Larger and irregular shaped nanoparticles were better dispersible than smaller regular nanocrystals. It was further shown that via the variation of the alkyl spacer chain length the dispersion behavior of the nanoparticles could be fine tuned. UV/VIS measurements revealed that homogeneous SiO₂ nanocomposites were transparent whereas ZrO₂ nanocomposites showed stronger *Rayleigh* scattering.

From the structural investigations on the prepared thermoplast nanocomposites, PS and PMMA (*in situ* polymerized), via SAXS and TEM the following conclusions on the relation between surface chemistry and dispersion quality of the nanoparticles in the polymer matrix could be made: If the basic requirement of a polymer matrix with a molecular weight in the appropriate range was fulfilled (gyration radius of polymer chains larger than nanoparticles), the dispersion quality of the final nanocomposites predominantly depends on the surface modification of the nanoparticles, which determines the interfacial match. First, it had to be guaranteed that the particles were dispersible in the monomer, which again depended on the

structural and chemical nature of the surface modification. Then, the following statements on the homogeneity of nanocomposites could be made:

- The functional end group is very important for the achievement of homogeneity, by its structural similarity to monomer and matrix and by allowing a polymer grafting *through* the nanoparticle surface.
- The variation of the spacer chain additionally allows a fine-tuning of the dispersion behavior.
- For the low complex system of SiO₂ nanospheres the conditions are optimal with respect to high homogeneity when a structurally similar polymerizable end group is present and a hydrophobicity providing long alkyl chain is applied as spacer.
- For the more complex ZrO₂ nanocrystal (crystals and irregular shaped) system, generally these statements are also true. Yet, due to other effects, like the zipper effect or effects related to structure and nature of these nanoparticles, the relations as described for the simple SiO₂ system must not be exactly the same in each case.

Epoxy resin nanocomposites were prepared to investigate a crosslinked resin system by applying ZrO₂ and SiO₂ nanoparticles (different sizes) with different surface modification. As a matrix system an aliphatic amine cured bisphenol-F based epoxy resin formulation was applied, utilizing an *in situ* curing approach.

For a systematic study of the influence of specific organic surface modification on dispersion structure and mechanical properties, selected coupling agents were applied and the SiO₂ as well as the ZrO₂ nanoparticle systems were studied. Thereby, three different chemical types of organic moieties, attached to the inorganic particle surface, for the chemical interface tailoring in the epoxy nanocomposites, were studied: Diethylene glycol (DEG) moieties, epoxide end groups, diol end groups. For comparison reasons, non modified metal oxide nanoparticles were also applied.

The influence of the type of chemical surface modification on the nanocomposite structure was investigated via TEM of ultramicrotomy thin cuts and by applying SAXS. Also, UV/VIS measurements revealed that homogeneous nanocomposites show good optical transparency.

Generally, it was found within these studies on the epoxy resin systems that the dispersion quality depends stronger on the filler percentage as compared to the PS or PMMA nanocomposites. The high viscosity of the curing mixture, and related effects were held responsible for this effect. For SiO₂ nanoparticles, the series of best homogeneity for a certain surface modification was found to be epoxy (best dispersion quality) > diol > DEG > unmodified (OH) (strongest agglomeration). For ZrO₂, the situation was *vice versa*: Agglomeration is highest for epoxy > diol > unmodified (OH) > DEG. As a reason for this effect, the influence of the nanoscopic structure (ZrO₂: crystal facets, SiO₂: spherical curvature) was discussed. Thereby, it was assumed that the crystal shape of the ZrO₂ nanoparticles promotes particle-particle interaction.

In conclusion, the dispersion quality within the epoxy resin nanocomposites is given by the interplay of several effects in this complex systems. On the one hand, surface groups like epoxides allow a covalent interaction with the matrix and thus a better dispersion of the particles is expected. On the other hand also homo-linkage between the particles can occur, resulting in strong aggregation. It is concluded that when tuning the nanoparticle surface to reach maximum homogeneity, chiefly the fact is important that the matrix-particle interaction has to be higher than the particle-particle interaction. Thereby, the surface group plays a crucial role, but also the nanoparticle nature and shape. Therefore, as in the case of ZrO_2 , the overall inter-particle interaction, can become very high. This is due to the high contact area between such nanocrystal facets, compared to the interaction between two spheres, as in the case of SiO_2 , where the contact theoretically is only on a point. This can lead to the effect that low matrix-interacting modifications such as DEG for ZrO_2 give an optimal homogeneity because the particle-matrix interaction is predominant whereas stronger interacting moieties such as the epoxide moiety lead to higher agglomeration because the particle-particle interaction dominates, as it was demonstrated. Additionally, suspension concentration effects can occur which can lower the agglomeration when the viscosity increases and thus the shear forces increase at the same stirring speed, but also raise the probability that two particles get together and agglomerate.

The investigations (SAXS, TEM, UV/VIS) of differently surface modified nanoparticles, incorporated in different matrix systems by applying an *in situ* polymerization process allowed the following conclusions on the dispersion quality:

- From the dispersion experiments liquid media using DLS, rough assumptions could be made: If the nanoparticles are poorly dispersible in monomer compounds one can expect nanocomposite materials with poor homogeneity. On the other side it is likely that when the particles are well-dispersible in the monomer, homogeneous nanocomposites are obtained.
- If the surface modification is similar to the matrix and monomer, as regards the chemical structure, the probability to gain homogeneous nanocomposites is high.
- Applying thermoplasts in a radical polymerization approach, the application of polymerizable surface groups lead to more homogeneous materials as in the case of similar, non polymerizable end groups. A surface grafting *through* effect of free polymer chains, dramatically enhancing the interfacial compatibility, is responsible for this.
- In the crosslinked epoxy resin system the situation was found to be rather complex. Various additional parameters strongly influence the dispersion quality, such as the particle nature itself. For instance, groups which can covalently link matrix and particles can also link the particles more likely with each other within this system. In specific cases, non polymerizable groups thus give optimal homogeneous materials. As a general rule, the matrix-particle interaction must exceed the particle-particle interaction to obtain homogeneous nanomaterials. Thus, not only the interfacial fit is important.

In consideration of these effects it was possible to tune the dispersion structure of the nanocomposites prepared within this work. Figure 155 gives an overview on how homogeneous nanocomposites could be obtained (PMMA, PS, epoxy resins) via systematic chemical surface tailoring of metal oxide nanoparticles. A comparison of TEM images from ultrathincuts is shown for the cases of appropriate and inappropriate interface tuning.

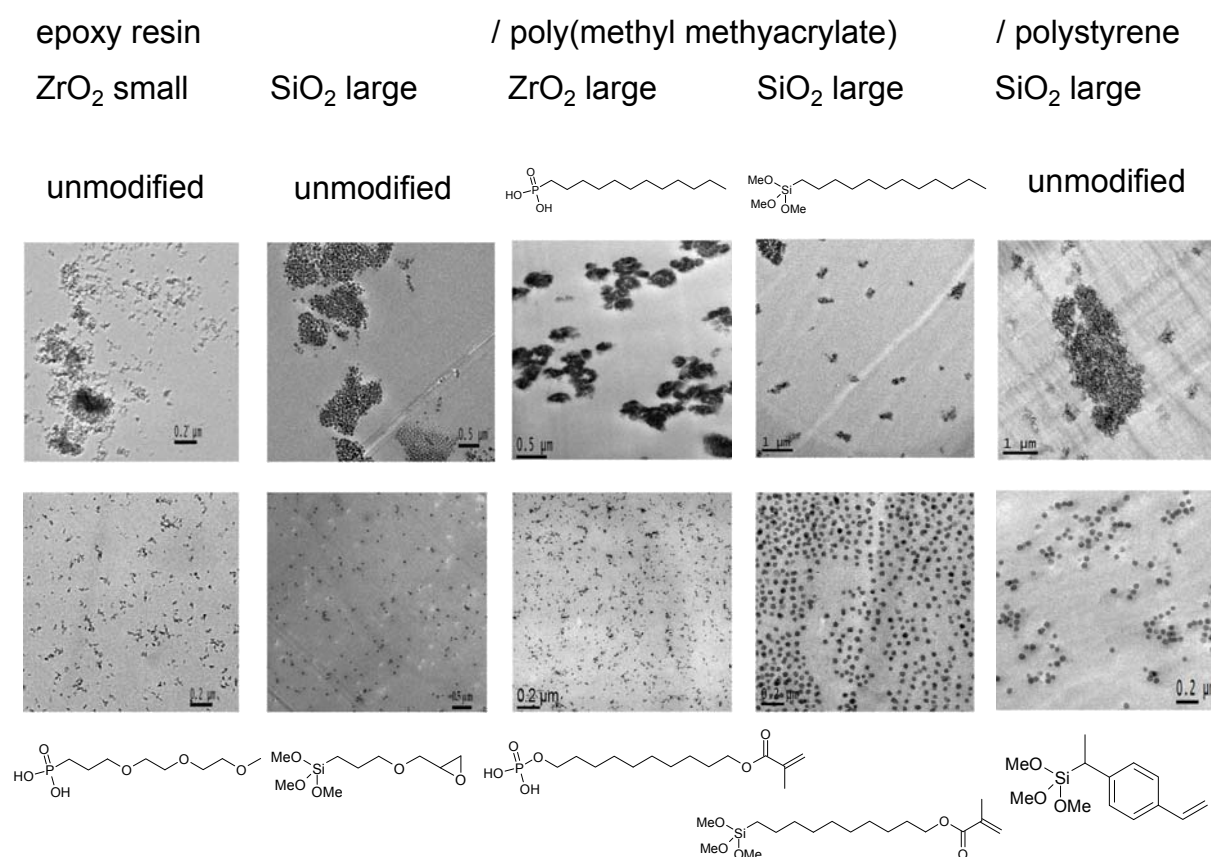


Figure 155. Overview on representative TEM images of ultrathincuts of various nanocomposites demonstrating how chemical surface tailoring can be used to produce homogeneous nanocomposites. The coupling agents used for the nanoparticle surface modification are depicted close to the corresponding TEM micrograph.

To correlate particle nature, particle size, and chemical surface modification with mechanical materials properties, dependent on the filler degree (reinforcement effect), the prepared nanocomposites were measured via *Vickers* hardness tests and dynamic mechanical thermoanalyses. For increasing filler percentage, usually increasing hardness of the materials could be observed, but with a different trend for the various applied nanoparticle systems. For example, high reinforcement could be obtained for PMMA by the incorporation of 10 wt % methacryloyl-group and C12 alkyl spacer modified ZrO₂ large nanoparticles, with an increase in hardness from 0.198 GPa (neat matrix) to 0.286 GPa. By the incorporation of diethylene glycol chain modified ZrO₂ large nanoparticles into the epoxy resin the hardness could be increased from 0.163 GPa (neat matrix) to 0.232 GPa. The hardness of PS could be increased from 0.16 GPa (neat matrix) to 0.23 GPa by incorporating styryl- modified SiO₂ small nanoparticles.

For PDMS chain modified ZrO₂ nanoparticles in PMMA an interesting effect could be observed: A decrease of hardness and glass transition temperature with increasing filler amount could be observed when polymerizable end groups were applied. This effect stands in contrast to the expected result of incorporating hard nanoparticles into an organic polymer matrix. It was concluded that the PDMS chains introduced a soft interface within the nanomaterial and the interfacial adhesion (the linkage via polymerizable end group gives strong matrix-particle adhesion) is of high importance for the observed macroscopic softening effect. It is considered to be an effect originating only from the interface properties within the material.

From these studies, conclusions on the relation between dispersion structure and mechanical properties could be drawn:

- Size of the nanoparticles: In general, smaller nanoparticles lead to stronger mechanical reinforcement effect (examples: SiO₂ in epoxy resin, SiO₂ in polystyrene), because they generate a larger interface region within the material which is able to absorb energy.
- Nature of the nanoparticles: Generally, ZrO₂ showed a higher reinforcement effect with same filler content than SiO₂.
- Morphology of nanoparticles: Rough, porous nanoparticles lead to stronger mechanical reinforcement (example: methacryloyl functionalized ZrO₂ in PMMA).
- Dispersion quality: Higher dispersion quality gives stronger reinforcement effects (general). The dispersion quality is strongly dependent on point 1 and 2 and the nature of chemical surface modification.
- The effects of point 1-3 are all considered to originate from one effect: The higher the interfacial region in the material the higher the reinforcement effect.
- Requirement for point 1-3 is an appropriate interfacial adhesion within the nanocomposite material.

As shown, the nanocomposite dispersion structure is related to the nature of the chemical surface modification, the nature of the nanoparticle and the inorganic filler content. Also the investigated mechanical parameters (hardness) were shown to be dependent of these three parameters. Thereby, it had to be considered that by tuning one parameter (e.g. the chemical surface modification), all other parameters were affected (e.g. interfacial adhesion can be improved, but agglomeration can be increased which can result in an overall lower reinforcement effect).

In this work, it was demonstrated how the surface of nanoparticles can be systematically tuned to enable the preparation of homogeneous nanocomposites. The application of a low shear-force-mixing approach (low energy effort) by (re)dispersing inorganic nanoparticle powders in organic matrices was thus possible. As a result, transparent nanocomposite materials with increased mechanical properties could be obtained.

6 Bibliography

- [1] G. Kickelbick in *Hybrid Materials: Synthesis, Characterization, and Applications*, (Ed. G. Kickelbick), Wiley-VCH, Weinheim, **2007**.
- [2] M. Ohring in *Engineering Materials Science*, Academic Press, San Diego, **1995**.
- [3] J. E. Carraher in *Polymer Chemistry*, CRC Press, Boca Raton, Florida, USA, **2006**, p. 722.
- [4] T. M. Cornsweet, *Science* **1970**, *168*, 433-438.
- [5] J. M. Hodgkinson, in *Mechanical testing of advanced fibre composites*, Woodhead Publishing, Cambridge, **2000**.
- [6] D. D. L. Chung in *Carbon Fiber Composites*, Butterworth-Heinemann, Boston, **1994**, p.
- [7] S. T. Peters in *Handbook of composites*, Chapman and Hall, London, **1998**, p. 242-253.
- [8] S. T. Peters in *Handbook of composites*, Chapman and Hall, London, **1998**.
- [9] A. B. Lloyd in *A companion to ancient Egypt, Vol. 1*, Blackwell Publishing, West Sussex, **2010**, p. 403.
- [10] P. Fratzl and R. Weinkamer, *Prog. Mater. Sci.* **2007**, *52*, 1263-1334.
- [11] H. Peterlik, P. Roschger, K. Klaushofer and P. Fratzl, *Nat. Mater.* **2006**, *5*, 52-55.
- [12] P. M. Ajayan, L. S. Schadler and P. V. Braun in *Nanocomposite Science and Technology*, Wiley-VCH, Weinheim, **2003**.
- [13] G. Kickelbick, *Prog. Polym. Sci.* **2003**, *28*, 83-114.
- [14] P. H. C. Camargo, K. G. Satyanarayana and F. Wypych, *Mater. Res.* **2009**, *12*, 1-39.
- [15] M. Harada, T. Miyamoto and M. Ochi, *J. Polym. Sci., Part B: Polym. Phys.* **2009**, *47*, 1753-1761.
- [16] M. Biswas and S. S. Ray, *Adv. Polym. Sci.* **2001**, *155*, 167-221.
- [17] D. Frihi, K. Masenelli-Varlot, G. Vigier and H. Satha, *J. Appl. Polym. Sci.* **2009**, *114*, 3097-3105.
- [18] X. Xia, X. Zeng, J. Liu and W. Xu, *J. Appl. Polym. Sci.* **2010**, *118*, 2461-2466.
- [19] T.-H. Hsieh, J.-K. Huang, K.-S. Ho, X. Bi, T.-H. Ho, S.-S. Yang and Y.-C. Chang, *J. Polym. Sci., Part B: Polym. Phys.* **2008**, *46*, 1214-1225.
- [20] I.-H. Kim and Y. G. Jeong, *J. Polym. Sci., Part B: Polym. Phys.* **2010**, *48*, 850-858.
- [21] Y. Fuse, Y. Ide and M. Ogawa, *Polym. Chem.* **2010**, *1*, 849-853.
- [22] R. Hiroi, S. S. Ray, M. Okamoto and T. Shiroi, *Macromol. Rapid Commun.* **2004**, *25*, 1359-1364.
- [23] S. Bal, *Bull. Mater. Sci.* **2010**, *33*, 27-31.
- [24] Y. Ye, H. Chen, J. Wu and L. Ye, *Polymer* **2007**, *48*, 6426-6433.

- [25] M. Bernabo, A. Pucci, H. H. Ramanitra and G. Ruggeri, *Materials* **2010**, *3*, 1461-1477.
- [26] J.-H. Choi, J. P. Kar, D.-Y. Khang and J.-M. Myoung, *J. Phys. Chem. C* **2009**, *113*, 5010-5013.
- [27] M. Chipara, J. R. Villarreal, M. D. Chipara, K. Lozano, A. C. Chipara and D. J. Sellmyer, *J. Polym. Sci., Part B: Polym. Phys.* **2009**, *47*, 1644-1652.
- [28] X. Huang, C. Kim, Z. Ma, P. Jiang, Y. Yin and Z. Li, *J. Polym. Sci., Part B: Polym. Phys.* **2008**, *46*, 2143-2154.
- [29] J.-F. Zhu and Y.-J. Zhu, *J. Phys. Chem. B* **2006**, *110*, 8593-8597.
- [30] P. S. Chinthamanipeta, S. Kobukata, H. Nakata and D. A. Shipp, *Polymer* **2008**, *49*, 5636-5642.
- [31] G. Filippone, G. Romeo and D. Acierno, *Langmuir* **2010**, *26*, 2714-2720.
- [32] H. Li, Z. Zhang, X. Ma, M. Hu, X. Wang and P. Fan, *Surf. Coat. Technol.* **2007**, *201*, 5269-5272.
- [33] R. Zhao and W. Luo, *Mater. Sci. Eng., A* **2008**, *A483-A484*, 313-315.
- [34] B. J. Ash, L. S. Schadler and R. W. Siegel, *Mater. Lett.* **2002**, *55*, 83-87.
- [35] A. Convertino, G. Leo, M. Tamborra, C. Sciancalepore, M. Striccoli, M. L. Curri and A. Agostiano, *Sens. Actuators, B* **2007**, *B126*, 138-143.
- [36] M. M. Demir, P. Castignolles, U. Akbey and G. Wegner, *Macromolecules* **2007**, *40*, 4190-4198.
- [37] E. Dzunuzovic, K. Jeremic and J. M. Nedeljkovic, *Eur. Polym. J.* **2007**, *43*, 3719-3726.
- [38] R. Medina, F. Hauptert and A. K. Schlarb, *J. Mater. Sci.* **2008**, *43*, 3245-3252.
- [39] M. Ochi, D. Nii, Y. Suzuki and M. Harada, *J. Mater. Sci.* **2010**, *45*, 2655-2661.
- [40] N. N. Mallikarjuna, A. Venkataraman and T. M. Aminabhavi, *J. Appl. Polym. Sci.* **2004**, *94*, 2551-2554.
- [41] A. Tocchio, D. Horak, M. Babic, M. Trchova, M. Veverka, M. J. Benes, M. Slouf and A. Fojtik, *J. Polym. Sci., Part A: Polym. Chem.* **2009**, *47*, 4982-4994.
- [42] N. Frickel, R. Messing, T. Gelbrich and A. M. Schmidt, *Langmuir* **2010**, *26*, 2839-2846.
- [43] M. M. Demir, K. Koynov, U. Akbey, C. Bubeck, I. Park, I. Lieberwirth and G. Wegner, *Macromolecules* **2007**, *40*, 1089-1100.
- [44] J. Huang, P. Lianos, Y. Yang and J. Shen, *Langmuir* **1998**, *14*, 4342-4344.
- [45] U. Kumar, K. Kumari, S. N. Sharma, M. Kumar, V. D. Vankar, R. Kakkar and V. Kumar, *Colloid Polym. Sci.* **2010**, *288*, 841-849.
- [46] X. Wang, L. Wu and J. Li, *J. Appl. Polym. Sci.* **2010**, *117*, 163-170.
- [47] R. Lach, G.-M. Kim, G. H. Michler, W. Grellmann and K. Albrecht, *Macromol. Mater.*

- Eng.* **2006**, *291*, 263-271.
- [48] O. Becker and G. P. Simon, *Adv. Polym. Sci.* **2005**, *179*, 29-82.
- [49] W. Shao, Q. Wang, F. Wang and Y. Chen, *J. Polym. Sci., Part B: Polym. Phys.* **2005**, *44*, 249-255.
- [50] A. J. Crosby and J.-Y. Lee, *Polym. Rev.* **2007**, *47*, 217-229.
- [51] H. Althues, J. Henle and S. Kaskel, *Chem. Soc. Rev.* **2007**, *36*, 1454-1465.
- [52] S. Kang, S. I. Hong, C. R. Choe, M. Park, S. Rim and J. Kim, *Polymer* **2000**, *42*, 879-887.
- [53] L. Mascia, L. Prezzi and B. Haworth, *J. Mater. Sci.* **2006**, *41*, 1145-1155.
- [54] J. Svehla, B. Feichtenschlager, T. Schmidt, D. Holzinger and G. Kickelbick, *J. Sol-Gel Sci. Technol.* **2011**, *57*, 287-298.
- [55] T. Koch, F. R. Kogler, U. Schubert and S. Seidler, *Monatsh. Chem.* **2007**, *138*, 293-299.
- [56] U. Schubert, *Chem. Soc. Rev.* **2011**, *40*, 575-582.
- [57] A. C. Balazs, T. Emrick and T. P. Russell, *Science* **2006**, *314*, 1107-1110.
- [58] M. E. Mackay, A. Tuteja, P. M. Duxbury, C. J. Hawker, B. Van Horn, Z. Guan, G. Chen and R. S. Krishnan, *Science* **2006**, *311*, 1740-1743.
- [59] H.-Y. Yu and D. L. Koch, *Langmuir* **2010**, *26*, 16801-16811.
- [60] X.-q. Gao, C. Deng, J. Xu, Z.-m. Li, J. Zhang and K.-z. Shen, *Polym. Bull.* **2010**, *65*, 59-68.
- [61] J. W. Gilman, S. Bourbigot, J. R. Shields, M. Nyden, T. Kashiwagi, R. D. Davis, D. L. Vanderhart, W. Demory, C. A. Wilkie, A. B. Morgan, J. Harris and R. E. Lyon, *J. Mater. Sci.* **2003**, *38*, 4451-4460.
- [62] C. Sanchez, B. Julian, P. Belleville and M. Popall, *J. Mater. Chem.* **2005**, *15*, 3559-3592.
- [63] S. I. Marras, I. Zuburtikudis and C. Panayiotou, *J. Mater. Sci.* **2010**, *45*, 6474-6480.
- [64] Z. Wu, H. Han, W. Han, B. Kim, H. Ahn Kyung and K. Lee, *Langmuir* **2007**, *23*, 7799-7803.
- [65] C. Chen and A. B. Morgan, *Polymer* **2009**, *50*, 6265-6273.
- [66] B. J. Lowes, A. G. Bohrer, T. Tran and D. A. Shipp, *Polym. Bull.* **2009**, *62*, 281-289.
- [67] C. Feldgitscher, H. Peterlik, M. Puchberger and G. Kickelbick, *Chem. Mater.* **2009**, *21*, 695-705.
- [68] J. Zhou, R. Li, S. Liu, Q. Li, L. Zhang, L. Zhang and J. Guan, *J. Appl. Polym. Sci.* **2009**, *111*, 2477-2484.
- [69] Z. Guo, H. T. Hahn, H. Lin, A. B. Karki and D. P. Young, *J. Appl. Phys.* **2008**, *104*, 014314/014311-014314-014315.

- [70] H. Althues, P. Simon and S. Kaskel, *J. Mater. Chem.* **2007**, *17*, 758-765.
- [71] F. N. Sayed, V. Grover, K. A. Dubey, V. Sudarsan and A. K. Tyagi, *J. Colloid Interface Sci.* **2010**, *353*, 445-453.
- [72] Y. Cui, J. Yang, Y. Zhan, Z. Zeng and Y. Chen, *Colloid Polym. Sci.* **2008**, *286*, 97-106.
- [73] Y. Kobayashi, A. Kurosawa, D. Nagao and M. Konno, *Polym. Compos.* **2010**, *31*, 1179-1183.
- [74] Y. Zheng, K. Chonung, G. Wang, P. Wei and P. Jiang, *J. Appl. Polym. Sci.* **2009**, *111*, 917-927.
- [75] Y. Hu, G. Gu, S. Zhou and L. Wu, *Polymer* **2011**, *52*, 122-129.
- [76] C. Nyambo, E. Kandare, D. Wang and C. A. Wilkie, *Polym. Degrad. Stab.* **2008**, *93*, 1656-1663.
- [77] M. J. Dumont, A. Reyna-Valencia, J. P. Emond and M. Bousmina, *J. Appl. Polym. Sci.* **2007**, *103*, 618-625.
- [78] C. E. Hoppe, F. Rivadulla, M. Arturo Lopez-Quintela, M. C. Bujan, J. Rivas, D. Serantes and D. Baldomir, *J. Phys. Chem. C* **2008**, *112*, 13099-13104.
- [79] M. Laus, O. Francescangeli and F. Sandrolini, *J. Mater. Res.* **1997**, *12*, 3134-3139.
- [80] D. Ciprari, K. Jacob and R. Tannenbaum, *Macromolecules* **2006**, *39*, 6565-6573.
- [81] A. S. Luyt, M. Messori, P. Fabbri, J. P. Mofokeng, R. Taurino, T. Zanasi and F. Pilati, *Polym. Bull.* **2011**, *66*, 991-1004.
- [82] H. Wang, Y. Bai, S. Liu, J. Wu and C. P. Wong, *Acta Mater.* **2002**, *50*, 4369-4377.
- [83] Y. Termonia, *J. Polym. Sci., Part B: Polym. Phys.* **2010**, *48*, 687-692.
- [84] J. Zhang, J. Lou, S. Ilias, P. Krishnamachari and J. Yan, *Polymer* **2008**, *49*, 2381-2386.
- [85] G. Nichols, S. Byard, M. J. Bloxham, J. Botterill, N. J. Dawson, A. Dennis, V. Diart, N. C. North and J. D. Sherwood, *J. Pharm. Sci.* **2002**, *91*, 2103-2109.
- [86] V. M. F. Evora and A. Shukla, *Mater. Sci. Eng., A* **2003**, *A361*, 358-366.
- [87] Q. L. Ji, M. Q. Zhang, M. Z. Rong, B. Wetzel and K. Friedrich, *Tribol. Lett.* **2005**, *20*, 115-123.
- [88] M. Avella, M. E. Errico and E. Martuscelli, *Nano Lett.* **2001**, *1*, 213-217.
- [89] W. K. Goertzen and M. R. Kessler, *Composites, Part A* **2008**, *39A*, 761-768.
- [90] S. Donthu, T. Sun and V. Dravid, *Adv. Mater.* **2007**, *19*, 125-128.
- [91] P. K. Giri, S. Bhattacharyya, D. K. Singh, R. Kesavamoorthy, B. K. Panigrahi and K. G. M. Nair, *J. Appl. Phys.* **2007**, *102*, 093515/093511-093515/093518.
- [92] J. G. Lee, S. M. Hong, J. J. Park, M. K. Lee, S. J. Hong, U. H. Joo and C. K. Rhee, *Mater. Charact.* **2010**, *61*, 1290-1293.

- [93] V. V. Dabhade, T. R. R. Mohan and P. Ramakrishnan, *Powder Technol.* **2007**, *171*, 177-183.
- [94] S. R. Tabaei, P. Joensson, M. Braenden and F. Hoeoek, *J. Struct. Biol.* **2009**, *168*, 200-206.
- [95] R. Liu, R. Rallo, S. George, Z. Ji, S. Nair, E. Nel Andre and Y. Cohen, *Small* **2011**, *7*, 1118-1126.
- [96] N. G. Sahoo, S. Rana, J. W. Cho, L. Li and S. H. Chan, *Prog. Polym. Sci.* **2010**, *35*, 837-867.
- [97] N. A. Kumar, H. S. Ganapathy, J. S. Kim, Y. S. Jeong and Y. T. Jeong, *Eur. Polym. J.* **2008**, *44*, 579-586.
- [98] A. Y. Fadeev, R. Helmy and S. Marcinko, *Langmuir* **2002**, *18*, 7521-7529.
- [99] P. H. Mutin, V. Lafond, A. F. Popa, M. Granier, L. Markey and A. Dereux, *Chem. Mater.* **2004**, *16*, 5670-5675.
- [100] M.-A. Neouze and U. Schubert, *Monatsh. Chem.* **2008**, *139*, 183-195.
- [101] S. Din and A. Kaleem, *Mater. Chem. Phys.* **1998**, *53*, 48-54.
- [102] J. A. Badenes March, M. L. Vicent, J. Calbo Paus, M. A. Tena Gomez and G. M. Tomas, *Solid State Sci.* **2005**, *7*, 1015-1024.
- [103] M. Asiltuerk, E. Burunkaya, F. Sayilkan, N. Kiraz and E. Arpac, *J. Non-Cryst. Solids* **2011**, *357*, 206-210.
- [104] H. Cao, X. Qiu, B. Luo, Y. Liang, Y. Zhang, R. Tan, M. Zhao and Q. Zhu, *Adv. Funct. Mater.* **2004**, *14*, 243-246.
- [105] D. A. Earl and D. E. Clark, *J. Am. Ceram. Soc.* **2000**, *83*, 2170-2176.
- [106] D. A. H. Hanaor and C. C. Sorrell, *J. Mater. Sci.* **2011**, *46*, 855-874.
- [107] P. Jutzi and U. Schubert in *Silicon Chemistry*, Wiley VCH, Weinheim, **2003**, p. 475-487.
- [108] K. P. Jayadevan and T. Y. Tseng in *Encycl. Nanosci. Nanotechnol.* **2004**, p. 333-376.
- [109] R. Mueller, L. Madler and S. E. Pratsinis, *Chem. Eng. Sci.* **2003**, *58*, 1969-1976.
- [110] H. Kloepfer in *Verfahren zur Herstellung hochdispenser Kieselsaeure, DE 893496 (C)* Germany, **1993**.
- [111] D. Boldridge, *Aerosol Sci. Technol.* **2010**, *44*, 182-186.
- [112] M. C. Heine, L. Madler, R. Jossen and S. E. Pratsinis, *Combust. Flame* **2006**, *144*, 809-820.
- [113] C. J. Brinker and G. W. Scherer in *Sol-Gel-Science - The Physics and Chemistry of Sol-Gel Processing*, San Diego, **1990**.

- [114] W. Stoeber, A. Fink and E. Bohn, *J. Colloid Interface Sci.* **1968**, *26*, 62-69.
- [115] I. A. Rahman, P. Vejayakumaran, C. S. Sipaut, J. Ismail, M. A. Bakar, R. Adnan and C. K. Chee, *Colloids Surf., A* **2007**, *294*, 102-110.
- [116] R. D. Badley, W. T. Ford, F. J. McEnroe and R. A. Assink, *Langmuir* **1990**, *6*, 792-801.
- [117] H. Nakabayashi, A. Yamada, M. Noba, Y. Kobayashi, M. Konno and D. Nagao, *Langmuir* **2010**, *26*, 7512-7515.
- [118] G. Garnweitner and M. Niederberger, *J. Am. Ceram. Soc.* **2006**, *89*, 1801-1808.
- [119] A. K. Ganguli, T. Ahmad, S. Vaidya and J. Ahmed, *Pure Appl. Chem.* **2008**, *80*, 2451-2477.
- [120] F. J. Arriagada and K. Osseo-Asare, *Colloids Surf., A* **1999**, *154*, 311-326.
- [121] D. Carriere, M. Moreau, P. Barboux, J.-P. Boilot and O. Spalla, *Langmuir* **2004**, *20*, 3449-3455.
- [122] Y. Murase and E. Kato, *J. Am. Ceram. Soc.* **2001**, *84*, 2705-2706.
- [123] F. Chen, Q. Hong, G.-Q. Xu, T. S. A. Hor and S. Shen, *J. Am. Ceram. Soc.* **2005**, *88*, 2649-2651.
- [124] D. Qin and H. Chen, *J. Mater. Sci.* **2006**, *41*, 7059-7063.
- [125] A. Snyder Mark, J. A. Lee, M. Davis Tracy, L. E. Scriven and M. Tsapatsis, *Langmuir* **2007**, *23*, 9924-9928.
- [126] K. S. Chan, D. P. Nicolella, B. R. Furman, S. T. Wellinghoff, H. R. Rawls and S. E. Pratsinis, *J. Mater. Sci.* **2009**, *44*, 6117-6124.
- [127] M. Ochi, D. Nii and M. Harada, *J. Mater. Sci.* **2010**, *45*, 6159-6165.
- [128] C. Chevigny, F. Dalmas, E. Di Cola, D. Gigmes, D. Bertin, F. Boue and J. Jestin, *Macromolecules* **2011**, *44*, 122-133.
- [129] N. Jouault, F. Dalmas, S. Said, E. Di Cola, R. Schweins, J. Jestin and F. Boue, *Macromolecules* **2010**, *43*, 9881-9891.
- [130] A. Bachinger in *Organophosphonates On Titanium Dioxide Photocatalysts: Isotropic and Anisotropic Modification and Photocatalytic Properties*, Vienna University of Technology, PhD Thesis, **2011**.
- [131] Y. Wang, J. Zhang, X. Shen, C. Shi, J. Wu and L. Sun, *Mater. Chem. Phys.* **2006**, *98*, 217-224.
- [132] Q. Chen, S. C. Bae and S. Granick, *Nature* **2011**, *469*, 381-384.
- [133] M. Szekeres, O. Kamalin, R. A. Schoonheydt, K. Wostyn, K. Clays, A. Persoons and I. Dekany, *J. Mater. Chem.* **2002**, *12*, 3268-3274.

- [134] A. Zabet-Khosousi and A.-A. Dhirani, *Chem. Rev.* **2008**, *108*, 4072-4124.
- [135] R. P. Bagwe, L. R. Hilliard and W. Tan, *Langmuir* **2006**, *22*, 4357-4362.
- [136] S. Laurent, D. Forge, M. Port, A. Roch, C. Robic, L. Vander Elst and R. N. Muller, *Chem. Rev.* **2008**, *108*, 2064-2110.
- [137] S. T. Peters in *Handbook of composites*, Chapman and Hall, London, **1998**, p. 148, 250-252.
- [138] A. Ulman, *Chem. Rev.* **1996**, *96*, 1533-1554.
- [139] G. Schmidt-Naake, L. Nothdurft and O. Töpfer, *Proceedings of European Congress of Chemical Engineering (ECCE-6)* **2007**.
- [140] D. Holzinger and G. Kickelbick, *J. Mater. Chem.* **2004**, *14*, 2017-2023.
- [141] I. O. Benitez, B. Bujoli, L. J. Camus, C. M. Lee, F. Odobel and D. R. Talham, *J. Am. Chem. Soc.* **2002**, *124*, 4363-4370.
- [142] S. E. Hunyadi and C. J. Murphy, *J. Phys. Chem. B* **2006**, *110*, 7226-7231.
- [143] S. A. Trammell, J. A. Moss, J. C. Yang, B. M. Nakhle, C. A. Slate, F. Odobel, M. Sykora, B. W. Erickson and T. J. Meyer, *Inorg. Chem.* **1999**, *38*, 3665-3669.
- [144] M. L. Hair and C. P. Tripp, *Colloids Surf., A* **1995**, *105*, 95-103.
- [145] M. Khayet, J. P. G. Villaluenga, J. L. Valentin, M. A. Lopez-Manchado, J. I. Mengual and B. Seoane, *Polymer* **2005**, *46*, 9881-9891.
- [146] L.-H. Lee, *J. Colloid Interface Sci.* **1968**, *27*, 751-760.
- [147] S. Onclin, B. J. Ravoo and D. N. Reinhoudt, *Angew. Chem., Int. Ed.* **2005**, *44*, 6282-6304.
- [148] A. P. Philipse and A. Vrij, *J. Colloid Interface Sci.* **1989**, *128*, 121-136.
- [149] G. Guerrero, P. H. Mutin and A. Vioux, *Chem. Mater.* **2001**, *13*, 4367-4373.
- [150] J. R. Miller and W. J. Koros, *Sep. Sci. Technol.* **1990**, *25*, 1257-1280.
- [151] N. R. Armstrong and V. R. Shepard, Jr., *J. Phys. Chem.* **1981**, *85*, 2965-2970.
- [152] F. Bellezza, A. Cipiciani and M. A. Quotadamo, *Langmuir* **2005**, *21*, 11099-11104.
- [153] K. Ikemura and T. Endo, *Dent Mater J* **2010**, *29*, 109-121.
- [154] D. Brovelli, G. Haehner, L. Ruiz, R. Hofer, G. Kraus, A. Waldner, J. Schloesser, P. Oroszlan, M. Ehrat and N. D. Spencer, *Langmuir* **1999**, *15*, 4324-4327.
- [155] C. A. Traina and J. Schwartz, *Langmuir* **2007**, *23*, 9158-9161.
- [156] Y. Sahoo, H. Pizem, T. Fried, D. Golodnitsky, L. Burstein, C. N. Sukenik and G. Markovich, *Langmuir* **2001**, *17*, 7907-7911.
- [157] T. Schulmeyer, S. A. Paniagua, P. A. Veneman, S. C. Jones, P. J. Hotchkiss, A. Mudalige, J. E. Pemberton, S. R. Marder and N. R. Armstrong, *J. Mater. Chem.* **2007**,

- 17, 4563-4570.
- [158] S. C. D'Andrea and A. Y. Fadeev, *Langmuir* **2003**, *19*, 7904-7910.
- [159] M. R. Alexander, G. Beamson, C. J. Blomfield, G. Leggett and T. M. Duc, *J. Electron Spectrosc. Relat. Phenom.* **2001**, *121*, 19-32.
- [160] C. Yee, G. Kataby, A. Ulman, T. Prozorov, H. White, A. King, M. Rafailovich, J. Sokolov and A. Gedanken, *Langmuir* **1999**, *15*, 7111-7115.
- [161] E. Ramirez, S. Jansat, K. Philippot, P. Lecante, M. Gomez, A. M. Masdeu-Bulto and B. Chaudret, *J. Organomet. Chem.* **2004**, *689*, 4601-4610.
- [162] R. L. Derosa and J. A. Trapasso, *J. Mater. Sci.* **2002**, *37*, 1079-1082.
- [163] A. Jozefczak and A. Skumiel, *J. Magn. Magn. Mater.* **2011**, *323*, 1509-1516.
- [164] C. D. Bain and G. M. Whitesides, *Angew. Chem.* **1989**, *101*, 522-528.
- [165] T.-Y. Dong, H.-H. Wu and M.-C. Lin, *Langmuir* **2006**, *22*, 6754-6756.
- [166] F. Bauer, H.-J. Glasel, U. Decker, H. Ernst, A. Freyer, E. Hartmann, V. Sauerland and R. Mehnert, *Prog. Org. Coat.* **2003**, *47*, 147-153.
- [167] Y. Xiang and D. Chen, *Eur. Polym. J.* **2007**, *43*, 4178-4187.
- [168] S. Li, S. P. Samuel, A. Mylonakis, A. Shah, A. Hsieh, A. Patel, E. Wei, G. Baran and Y. Wei, *J. Mater. Res.* **2008**, *23*, 66-71.
- [169] M. Pohl, S. Hogeckamp, N. Q. Hoffmann and H. P. Schuchmann, *Chem. Ing. Tech.* **2004**, *76*, 392-396.
- [170] M. Pohl, H. Schubert and H. P. Schuchmann, *Chem. Ing. Tech.* **2005**, *77*, 258-262.
- [171] F. Chi, B. Guan, B. Yang, Y. Liu and Q. Huo, *Langmuir* **2010**, *26*, 11421-11426.
- [172] C. J. Brinker and G. W. Scherer in *Sol-Gel-Science - The Physics and Chemistry of Sol-Gel Processing*, San Diego, **1990**, p. 235-284, 357-384.
- [173] S. Y. Kim, L. M. Hall, K. S. Schweizer and C. F. Zukoski, *Macromolecules* **2010**, *43*, 10123-10131.
- [174] A. Chandra, L.-S. Turng, P. Gopalan, R. M. Rowell and S. Gong, *Compos. Sci. Technol.* **2008**, *68*, 768-776.
- [175] K. Weissenbach and H. Mack, *Funct. Fillers Plast.* **2005**, 59-83.
- [176] R. Mueller, H. K. Kammler, K. Wegner and S. E. Pratsinis, *Langmuir* **2003**, *19*, 160-165.
- [177] J. D. Le Grange, J. L. Markham and C. R. Kurkjian, *Langmuir* **1993**, *9*, 1749-1753.
- [178] S. Altmann and J. Pfeiffer, *Monatsh. Chem.* **2003**, *134*, 1081-1092.
- [179] D. Brunel, A. Cauvel, F. Di Renzo, F. Fajula, B. Fubini, B. Onida and E. Garrone, *New J. Chem.* **2000**, *24*, 807-813.

- [180] S. Marcinko and A. Y. Fadeev, *Langmuir* **2004**, *20*, 2270-2273.
- [181] P. H. Mutin, G. Guerrero and A. Vioux, *J. Mater. Chem.* **2005**, *15*, 3761-3768.
- [182] R. Helmy and A. Y. Fadeev, *Langmuir* **2002**, *18*, 8924-8928.
- [183] C. Carraro, O. W. Yauw, M. M. Sung and R. Maboudian, *J. Phys. Chem. B* **1998**, *102*, 4441-4445.
- [184] B. Riegel, W. Kiefer, S. Hofacker and G. Schottner, *J. Sol-Gel Sci. Technol.* **2002**, *24*, 139-145.
- [185] R. Tian, O. Seitz, M. Li, W. Hu, Y. J. Chabal and J. Gao, *Langmuir* **2010**, *26*, 4563-4566.
- [186] H.-I. Hsiang and C.-Y. Chen, *J. Am. Ceram. Soc.* **2008**, *91*, 387-390.
- [187] F. Bauer, H. Ernst, U. Decker, M. Findeisen, H.-J. Flasel, H. Langguth, E. Hartmann, R. Mehnert and C. Peuker, *Macromol. Chem. Phys.* **2000**, *201*, 2654-2659.
- [188] Y.-C. Sheen, Y.-C. Huang, C.-S. Liao, H.-Y. Chou and F.-C. Chang, *J. Polym. Sci., Part B: Polym. Phys.* **2008**, *46*, 1984-1990.
- [189] A. Van Blaaderen and A. Vrij, *J. Colloid Interface Sci.* **1993**, *156*, 1-18.
- [190] F. Brodard-Severac, G. Guerrero, J. Maquet, P. Florian, C. Gervais and P. H. Mutin, *Chem. Mater.* **2008**, *20*, 5191-5196.
- [191] M. Textor, L. Ruiz, R. Hofer, A. Rossi, K. Feldman, G. Haehner and N. D. Spencer, *Langmuir* **2000**, *16*, 3257-3271.
- [192] R. Hofer, M. Textor and N. D. Spencer, *Langmuir* **2001**, *17*, 4014-4020.
- [193] A. Raman, R. Quinones, L. Barriger, R. Eastman, A. Parsi and E. S. Gawalt, *Langmuir* **2010**, *26*, 1747-1754.
- [194] W. H. Binder, M. Lomoschitz, R. Sachsenhofer and G. Friedbacher, *J. Nanomater.* **2009**.
- [195] P. Kohli and G. J. Blanchard, *Langmuir* **2000**, *16*, 695-701.
- [196] B. R. A. Neves, M. E. Salmon, P. E. Russell and E. B. Troughton, Jr., *Langmuir* **2001**, *17*, 8193-8198.
- [197] J. T. Woodward, A. Ulman and D. K. Schwartz, *Langmuir* **1996**, *12*, 3626-3629.
- [198] J. Soria, J. Sanz, I. Sobrados, J. M. Coronado, M. D. Hernandez-Alonso and F. Fresno, *J. Phys. Chem. C* **2010**, *114*, 16534-16540.
- [199] G. Guerrero, P. H. Mutin and A. Vioux, *Chem. Mater.* **2000**, *12*, 1268-1272.
- [200] K. Sasse in *Methoden der Organischen Chemie (Ed. Houben-Weyl)*, Thieme, Stuttgart, **1964**.

- [201] G. M. Kosolapoff, *J. Am. Chem. Soc.* **1945**, *67*, 1180-1182.
- [202] J. T. Kley, C. Unger and U. Massing, *Monatsh. Chem.* **1998**, *129*, 173-185.
- [203] D. Francova and G. Kickelbick, *Monatsh. Chem.* **2009**, *14*, 413-422.
- [204] M. D. Porter, T. B. Bright, D. L. Allara and C. E. D. Chidsey, *J. Am. Chem. Soc.* **1987**, *109*, 3559-3568.
- [205] W. Gao, L. Dickinson, C. Grozinger, F. G. Morin and L. Reven, *Langmuir* **1997**, *13*, 115-118.
- [206] D. L. Allara and R. G. Nuzzo, *Langmuir* **1985**, *1*, 52-66.
- [207] D. M. Spori, N. V. Venkataraman, S. G. P. Tosatti, F. Durmaz, N. D. Spencer and S. Zuercher, *Langmuir* **2007**, *23*, 8053-8060.
- [208] D. K. Schwartz, S. Steinberg, J. Israelachvili and J. A. N. Zasadzinski, *Phys. Rev. Lett.* **1992**, *69*, 3354-3357.
- [209] C. D. Bain, E. B. Troughton, Y. T. Tao, J. Evall, G. M. Whitesides and R. G. Nuzzo, *J. Am. Chem. Soc.* **1989**, *111*, 321-335.
- [210] M. K. Corbierre, N. S. Cameron and R. B. Lennox, *Langmuir* **2004**, *20*, 2867-2873.
- [211] P. Fiurasek and L. Reven, *Langmuir* **2007**, *23*, 2857-2866.
- [212] S. Kubowicz, J. Daillant, M. Dubois, M. Delsanti, J.-M. Verbavatz and H. Mohwald, *Langmuir* **2010**, *26*, 1642-1648.
- [213] A. O'Donnell, K. Yach and L. Reven, *Langmuir* **2008**, *24*, 2465-2471.
- [214] A. Badia, L. Demers, L. Dickinson, F. G. Morin, R. B. Lennox and L. Reven, *J. Am. Chem. Soc.* **1997**, *119*, 11104-11105.
- [215] M. Fukuto, R. K. Heilmann, P. S. Pershan, A. Badia and R. B. Lennox, *J. Chem. Phys.* **2004**, *120*, 3446-3459.
- [216] R. H. Terrill, T. A. Postlethwaite, C.-h. Chen, C.-D. Poon, A. Terzis, A. Chen, J. E. Hutchison, M. R. Clark, G. Wignall and et al., *J. Am. Chem. Soc.* **1995**, *117*, 12537-12548.
- [217] L. Chen, J. Xu, J. D. Holmes and M. A. Morris, *J. Phys. Chem. C* **2010**, *114*, 2003-2011.
- [218] Y. Min, M. Akbulut, K. Kristiansen, Y. Golan and J. Israelachvili, *Nat. Mater.* **2008**, *7*, 527-538.
- [219] E. M. Lambert, C. Viravaidya, M. Li and S. Mann, *Angew. Chem., Int. Ed.* **2010**, *49*, 4100-4103, S4100/4101-S4100/4111.
- [220] A. Badia, L. Cuccia, L. Demers, F. Morin and R. B. Lennox, *J. Am. Chem. Soc.* **1997**, *119*, 2682-2692.

- [221] K. P. Browne and B. A. Grzybowski, *Langmuir* **2011**, *27*, 1246-1250.
- [222] R. L. Jones, N. C. Pearsall and J. D. Batteas, *J. Phys. Chem. C* **2009**, *113*, 4507-4514.
- [223] S. A. Kulkarni, S. A. Mirji, A. B. Mandale and K. P. Vijayamohanan, *Thin Solid Films* **2006**, *496*, 420-425.
- [224] A. Badia, S. Singh, L. Demers, L. Cuccia, G. R. Brown and R. B. Lennox, *Chem.--Eur. J.* **1996**, *2*, 359-363.
- [225] C. D. Bain, J. Evall and G. M. Whitesides, *J. Am. Chem. Soc.* **1989**, *111*, 7155-7164.
- [226] C. D. Bain and G. M. Whitesides, *J. Am. Chem. Soc.* **1988**, *110*, 6560-6561.
- [227] C. D. Bain and G. M. Whitesides, *Science* **1988**, *240*, 62-63.
- [228] C. D. Bain and G. M. Whitesides, *J. Am. Chem. Soc.* **1988**, *110*, 3665-3666.
- [229] J. P. Folkers, P. E. Laibinis and G. M. Whitesides, *Langmuir* **1992**, *8*, 1330-1341.
- [230] P. E. Laibinis, R. G. Nuzzo and G. M. Whitesides, *J. Phys. Chem.* **1992**, *96*, 5097-5105.
- [231] M. C. Prado and B. R. A. Neves, *Langmuir* **2006**, *26*, 648-654.
- [232] E. Glogowski, J. He, T. P. Russell and T. Emrick, *Chem. Commun.* **2005**, 4050-4052.
- [233] A. Rezaee, L. C. Pavelka and S. Mittler, *Nanoscale Res. Lett.* **2009**, *4*, 1319-1323.
- [234] Y.-C. Lin, B.-Y. Yu, W.-C. Lin, S.-H. Lee, C.-H. Kuo and J.-J. Shyue, *J. Colloid Interface Sci.* **2009**, *340*, 126-130.
- [235] C. Gentilini and L. Pasquato, *J. Mater. Chem.* **2010**, *20*, 1403-1412.
- [236] W. Gao, L. Dickinson, C. Grozinger, F. G. Morin and L. Reven, *Langmuir* **1996**, *12*, 6429-6435.
- [237] J. Foisner, A. Glaser, T. Leitner, H. Hoffmann and G. Friedbacher, *Langmuir* **2004**, *20*, 2701-2706.
- [238] R. G. Nuzzo, L. H. Dubois and D. L. Allara, *J. Am. Chem. Soc.* **1990**, *112*, 558-569.
- [239] H. Schmitt, A. Badia, L. Dickinson, L. Reven and R. B. Lennox, *Adv. Mater.* **1998**, *10*, 475-480.
- [240] Y. Abe and T. Gunji, *Prog. Polym. Sci.* **2004**, *29*, 149-182.
- [241] Y.-T. Peng, K.-F. Lo and Y.-J. Juang, *Langmuir* **2010**, *26*, 5167-5171.
- [242] A. Arbe, M. Monkenbusch, J. Stellbrink, D. Richter, B. Farago, K. Almdal and R. Faust, *Macromolecules* **2001**, *34*, 1281-1290.
- [243] W. I. Patnode and D. F. Wilcock, *J. Am. Chem. Soc.* **1946**, *68*, 358-363.
- [244] V. Mittal, J. K. Kim and K. Pal in *Recent Advances in Elastomeric Nanocomposites*, Springer, Heidelberg, **2011**.
- [245] Q. Zhao and E. T. Samulski, *Polymer* **2006**, *47*, 663-671.
- [246] K. Rozga-Wijas, J. Chojnowski, W. Fortuniak, M. Scibiorek, Z. Michalska and L.

- Rogalski, *J. Mater. Chem.* **2003**, *13*, 2301-2310.
- [247] P.-L. Kuo, C.-C. Chen and S.-M. Yuen, *J. Phys. Chem. B* **2004**, *108*, 5541-5546.
- [248] N. Cinausero, N. Azema, M. Cochez, M. Ferriol, M. Essahli, F. Ganachaud and J.-M. Lopez-Cuesta, *Polym. Adv. Technol.* **2008**, *19*, 701-709.
- [249] N. Dutta and D. Green, *Langmuir* **2010**, *26*, 16737-16744.
- [250] D. Holzinger and G. Kickelbick, *Chem. Mater.* **2003**, *15*, 4944-4948.
- [251] G. Kickelbick, *Hybrid Materials: Synthesis, Characterization, and Applications*, (Ed. G. Kickelbick), Wiley-VCH, Weinheim, **2007**, p. 130.
- [252] E. Ruckenstein and Z. F. Li, *Adv. Colloid Interface Sci.* **2005**, *113*, 43-63.
- [253] M. N. Tchoul, S. P. Fillery, H. Koerner, L. F. Drummy, F. T. Oyerokun, P. A. Mirau, M. F. Durstock and R. A. Vaia, *Chem. Mater.* **2010**, *22*, 1749-1759.
- [254] H. Oh and P. F. Green, *Nat. Mater.* **2009**, *8*, 139-143.
- [255] O. Prucker and J. Ruehe, *Macromolecules* **1998**, *31*, 592-601.
- [256] O. Prucker and J. Ruehe, *Langmuir* **1998**, *14*, 6893-6898.
- [257] J. E. Mark in *Polymer Data Handbook*, Oxford Press, New York, **2006**.
- [258] C. Hub, S. E. Harton, M. A. Hunt, R. Fink and H. Ade, *J. Polym. Sci., Part B: Polym. Phys.* **2007**, *45*, 2270-2276.
- [259] V. M. Boucher, D. Cangialosi, A. Alegria, J. Colmenero, J. Gonzalez-Irun and L. M. Liz-Marzan, *J. Non-Cryst. Solids* **2011**, *357*, 605-609.
- [260] D. Stojanovic, A. Orlovic, S. Markovic, V. Radmilovic, P. S. Uskokovic and R. Aleksic, *J. Mater. Sci.* **2009**, *44*, 6223-6232.
- [261] J. E. Mark in *Polymer Data Handbook*, Oxford Press, New York, **2006**, p. 829-835.
- [262] S. Limpanart, S. Khunthon, P. Taepaiboon, P. Supaphol, T. Srihirin, W. Udomkichdecha and Y. Boontongkong, *Mater. Lett.* **2005**, *59*, 2292-2295.
- [263] R. Simons, G. G. Qiao, C. E. Powell and S. A. Bateman, *Langmuir* **2010**, *26*, 9023-9031.
- [264] B. Xu, Y. Q. Fu, M. Ahmad, J. K. Luo, W. M. Huang, A. Kraft, R. Reuben, Y. T. Pei, Z. G. Chen and J. T. M. De Hosson, *J. Mater. Chem.* **2010**, *20*, 3442-3448.
- [265] N. Jouault, P. Vallat, F. Dalmas, S. Said, J. Jestin and F. Boue, *Macromolecules* **2009**, *42*, 2031-2040.
- [266] A. Bansal, H. Yang, C. Li, K. Cho, B. C. Benicewicz, S. K. Kumar and L. S. Schadler, *Nat. Mater.* **2005**, *4*, 693-698.
- [267] E. Kontou and G. Anthonoulis, *J. Appl. Polym. Sci.* **2007**, *105*, 1723-1731.
- [268] T. H. Zhou, W. H. Ruan, M. Z. Rong, M. Q. Zhang and Y. L. Mai, *Adv. Mater.* **2007**,

- 19, 2667-2671.
- [269] P. F. Bruins in *Epoxy Resin Technology*, John Wiley and Sons, New York, **1968**.
- [270] J. E. Mark in *Polymer Data Handbook*, Oxford Press, New York, **2006**, p. 88-96.
- [271] S. L. Case in *Fundamental Importance of Fillers, Cure Conditions, and Crosslink Density on Model Epoxy Properties, Vol.* Virginia State University, Blacksburg, Virginia, **2003**.
- [272] W. Liu, S. V. Hoa and M. Pugh, *Compos. Sci. Technol.* **2005**, *65*, 2364-2373.
- [273] A. J. Kinloch, R. D. Mohammed, A. C. Taylor, C. Eger, S. Sprenger and D. Egan, *J. Mater. Sci.* **2005**, *40*, 5083-5086.
- [274] Y. Sun, Z. Zhang, K.-S. Moon and C. P. Wong, *J. Polym. Sci., Part B: Polym. Phys.* **2004**, *42*, 3849-3858.
- [275] Y. Imai, A. Terahara, Y. Hakuta, K. Matsui, H. Hayashi and N. Ueno, *Eur. Polym. J.* **2009**, *45*, 630-638.
- [276] Y.-C. Chiu, L. Riang, I. C. Chou, C.-C. M. Ma, C.-L. Chiang and C.-C. Yang, *J. Polym. Sci., Part B: Polym. Phys.* **2010**, *48*, 643-652.
- [277] S. Sulaiman, C. M. Brick, C. M. De Sana, J. M. Katzenstein, R. M. Laine and R. A. Basheer, *Macromolecules* **2006**, *39*, 5167-5169.
- [278] A. Bandyopadhyay, M. Sarkar and A. K. Bhowmick, *J. Mater. Sci.* **2006**, *41*, 5981-5993.
- [279] D. Wang, S. Fujinami, K. Nakajima, S. Inukai, H. Ueki, A. Magario, T. Noguchi, M. Endo and T. Nishi, *Polymer* **2010**, *51*, 2455-2459.
- [280] H. Peterlik and P. Fratzl, *Monatsh. Chem.* **2006**, *137*, 529-543.
- [281] C. Bitea, C. Walther, J. I. Kim, H. Geckeis, T. Rabung, F. J. Scherbaum and D. G. Cacuci, *Colloids Surf., A* **2003**, *215*, 55-66.
- [282] J. Cordelair and P. Greil, *J. Colloid Interface Sci.* **2003**, *265*, 359-371.
- [283] T. Moritz, S. Benfer, P. Arki and G. Tomandl, *Sep. Purif. Technol.* **2001**, *25*, 501-508.
- [284] K. S. W. Sing, D. H. Everett, R. A. W. Haul, L. Moscou, R. A. Pierotti, J. Rouquerol and T. Siemieniewska, *Pure Appl. Chem.* **1985**, *57*, 603-619.
- [285] S. Brunauer, P. H. Emmett and E. Teller, *J. Am. Chem. Soc.* **1938**, *60*, 309-319.
- [286] M. Litschauer and M.-A. Neouze, *J. Mater. Chem.* **2008**, *18*, 640-646.
- [287] A. M. Lipski, C. J. Pino, F. R. Haselton, I. W. Chen and V. P. Shastri, *Biomaterials* **2008**, *29*, 3836-3846.
- [288] M. Szekeres, J. Toth and I. Dekany, *Langmuir* **2002**, *18*, 2678-2685.

- [289] S. Pabisch, B. Feichtenschlager, H. Peterlik and G. Kickelbick, *Chem. Phys. Lett.* **2011**, *submitted*.
- [290] H. Peterlik and S. Pabisch, *private communication*, **2010**.
- [291] J. K. Percus and G. J. Yevick, *Phys. Rev.* **1958**, *110*, 1-13.
- [292] D. J. Kinning and E. L. Thomas, *Macromolecules* **1984**, *17*, 1712-1718.
- [293] J. S. Pedersen, *Adv. Colloid Interface Sci.* **1997**, *70*, 171-210.
- [294] G. Beaucage, *J. Appl. Crystallogr.* **1995**, *28*, 717-728.
- [295] G. Beaucage, *J. Appl. Crystallogr.* **1996**, *29*, 134-146.
- [296] G. Beaucage and D. W. Schaefer, *J. Non-Cryst. Solids* **1994**, *172-174*, 797-805.
- [297] S. Trabelsi, A. Janke, R. Haessler, N. E. Zafeiropoulos, G. Fornasieri, S. Bocchini, L. Rozes, M. Stamm, J.-F. Gerard and C. Sanchez, *Macromolecules* **2005**, *38*, 6068-6078.
- [298] G. Beaucage, H. K. Kammler and S. E. Pratsinis, *J. Appl. Crystallogr.* **2004**, *37*, 523-535.
- [299] D. J. Tobler, S. Shaw and L. G. Benning, *Geochim. Cosmochim. Acta* **2009**, *73*, 5377-5393.
- [300] M. Linsenbuehler, J. H. Werth, S. M. Dammer, H. A. Knudsen, H. Hinrichsen, K. E. Wirth and D. E. Wolf, *Powder Technol.* **2006**, *167*, 124-133.
- [301] C. J. Brinker and G. W. Scherer in *Sol-Gel-Science - The Physics and Chemistry of Sol-Gel Processing*, San Diego, **1990**, p. 21-58, 99-215, 518-562.
- [302] B. A. Korgel, S. Fullam, S. Connolly and D. Fitzmaurice, *J. Phys. Chem. B* **1998**, *102*, 8379-8388.
- [303] S. K. Park, K. D. Kim and H. T. Kim, *Colloids Surf., A* **2002**, *197*, 7-17.
- [304] S. Connolly, S. N. Rao and D. Fitzmaurice, *J. Phys. Chem. B* **2000**, *104*, 4765-4776.
- [305] D. L. Green, J. S. Lin, Y.-F. Lam, M. Z. C. Hu, D. W. Schaefer and M. T. Harris, *J. Colloid Interface Sci.* **2003**, *266*, 346-358.
- [306] A. H. Latham, M. J. Wilson, P. Schiffer and M. E. Williams, *J Am Chem Soc* **2006**, *128*, 12632-12633.
- [307] J. Wagner, *Chem.-Ing.-Tech.* **1986**, *58*, 578-583.
- [308] A. Aerts, L. R. A. Follens, M. Haouas, T. P. Caremans, M.-A. Delsuc, B. Loppinet, J. Vermant, B. Goderis, F. Taulelle, J. A. Martens and C. E. A. Kirschhock, *Chem. Mater.* **2007**, *19*, 3448-3454.
- [309] V. M. Gun'ko, V. I. Zarko, R. Leboda and E. Chibowski, *Adv. Colloid Interface Sci.* **2001**, *91*, 1-112.
- [310] J. L. Shi, C. W. Lu, C. L. Kuo, Z. X. Lin and T. S. Yen, *Ceram. Int.* **1992**, *18*, 155-159.

- [311] P. S. Haddad, T. R. Rocha, E. A. Souza, T. M. Martins, M. Knobel and D. Zanchet, *J. Colloid Interface Sci.* **2009**, *339*, 344-350.
- [312] G. M. Kosolapoff, *J. Am. Chem. Soc.* **1944**, *66*, 109-111.
- [313] T. Vallant, H. Brunner, U. Mayer and H. Hoffmann, *Langmuir* **1998**, *14*, 5826-5833.
- [314] D. Villemain, A. Elbilali, F. Simeon, P.-A. Jaffres, G. Maheut, M. Mosaddak and A. Hakiki, *J. Chem. Res., Synop.* **2003**, 436-437.
- [315] S. Pawsey, K. Yach and L. Reven, *Langmuir* **2002**, *18*, 5205-5212.
- [316] R. Quinones and E. S. Gawalt, *Langmuir* **2008**, *24*, 10858-10864.
- [317] Y. Jiang, S. Decker, C. Mohs and K. J. Klabunde, *J. Catal.* **1998**, *180*, 24-35.
- [318] V. Lafond, C. Gervais, J. Maquet, D. Prochnow, F. Babonneau and P. H. Mutin, *Chem. Mater.* **2003**, *15*, 4098-4103.
- [319] P. C. Crofts and G. M. Kosolapoff, *J. Am. Chem. Soc.* **1953**, *75*, 5738-5740.
- [320] D. Shamir, I. Zilbermann, E. Maimon, A. I. Shames, H. Cohen and D. Meyerstein, *Inorg. Chim. Acta* **2010**, *363*, 2819-2823.
- [321] W. A. Schafer, P. W. Carr, E. F. Funkenbusch and K. A. Parson, *J. Chromatogr.* **1991**, *587*, 137-147.
- [322] G. Cerrato, S. Bordiga, S. Barbera and C. Morterra, *Appl. Surf. Sci.* **1997**, *115*, 53-65.
- [323] T. J. Daou, J. M. Greneche, G. Pourroy, S. Buathong, A. Derory, C. Ulhaq-Bouillet, B. Donnio, D. Guillon and S. Begin-Colin, *Chem. Mater.* **2008**, *20*, 5869-5875.
- [324] N. Moszner, F. Zeuner, U. K. Fischer and V. Rheinberger, *Macromol. Chem. Phys.* **1999**, *200*, 1062-1067.
- [325] G. Busca, G. Ramis, V. Lorenzelli, P. F. Rossi, A. La Ginestra and P. Patrono, *Langmuir* **1989**, *5*, 911-916.
- [326] J. Randon, P. Blanc and R. Paterson, *J. Membr. Sci.* **1995**, *98*, 119-129.
- [327] A. Sonnauer and N. Stock, *J. Solid State Chem.* **2008**, *181*, 473-479.
- [328] C. A. R. Costa, L. F. Valadares and F. Galembeck, *Colloids Surf., A* **2007**, *302*, 371-376.
- [329] J. McElwee, R. Helmy and A. Y. Fadeev, *J. Colloid Interface Sci.* **2005**, *285*, 551-556.
- [330] C. J. Lomoschitz, B. Feichtenschlager, N. Moszner, M. Puchberger, K. Mueller, M. Abele and G. Kickelbick, *Langmuir* **2011**, *27*, 3534-3540.
- [331] C. Viornery, Y. Chevolut, D. Leonard, B.-O. Aronsson, P. Pechy, H. J. Mathieu, P. Descouts and M. Graetzel, *Langmuir* **2002**, *18*, 2582-2589.
- [332] V. V. Hoang, H. Zung and N. H. B. Trong, *Eur. Phys. J. D* **2007**, *44*, 515-524.
- [333] B. Zelakiewicz, S., A. de Dios, C. and Y. Tong, *J Am Chem Soc* **2003**, *125*, 18-19.

- [334] N. Subramanian, R. Schmidt, P. M. Wood-Adams and C. E. DeWolf, *Langmuir* **2010**, *26*, 18628-18630.
- [335] B. Feichtenschlager, C. J. Lomoschitz and G. Kickelbick, *J. Colloid Interface Sci.* **2011**, *360*, 15-25.
- [336] M. C. Prado and B. R. A. Neves, *Langmuir* **2010**, *26*, 648-654.
- [337] R. Bautista, N. Hartmann and E. Hasselbrink, *Langmuir* **2003**, *19*, 6590-6593.
- [338] W. G. Golden, C. D. Snyder and B. Smith, *J. Phys. Chem.* **1982**, *86*, 4675-4678.
- [339] R. G. Snyder, H. L. Strauss and C. A. Elliger, *J. Phys. Chem.* **1982**, *86*, 5145-5150.
- [340] S. Lifson and P. S. Stern, *J. Chem. Phys.* **1982**, *77*, 4542-4550.
- [341] R. G. Snyder, A. L. Aljibury, H. L. Strauss, H. L. Casal, K. M. Gough and W. F. Murphy, *J. Chem. Phys.* **1984**, *81*, 5352-5361.
- [342] P. Silberzan, L. Leger, D. Ausserre and J. J. Benattar, *Langmuir* **1991**, *7*, 1647-1651.
- [343] P. M. St. John and H. G. Craighead, *Appl. Phys. Lett.* **1996**, *68*, 1022-1024.
- [344] P. J. Davis, R. Deshpande, D. M. Smith, C. J. Brinker and R. A. Assink, *J. Non-Cryst. Solids* **1994**, *167*, 295-306.
- [345] K. Lee, A. N. Sathyagal and A. V. McCormick, *Colloids Surf., A* **1998**, *144*, 115-125.
- [346] D. A. Offord and J. H. Griffin, *Langmuir* **1993**, *9*, 3015-3025.
- [347] M. L. Schilling, H. E. Katz, S. M. Stein, S. F. Shane, W. L. Wilson, S. B. Ungashe, G. N. Taylor, T. M. Putvinski, C. E. D. Chidsey and S. Buratto, *Langmuir* **1993**, *9*, 2156-2160.
- [348] B. Vercelli, G. Zotti, G. Schiavon, S. Zecchin and A. Berlin, *Langmuir* **2003**, *19*, 9351-9356.
- [349] W. R. Caseri, *Mater. Sci. Technol.* **2006**, *22*, 807-817.
- [350] S. A. Kulinich and M. Farzaneh, *Appl. Surf. Sci.* **2004**, *230*, 232-240.
- [351] J. F. Kang, S. Liao, R. Jordan and A. Ulman, *J. Am. Chem. Soc.* **1998**, *120*, 9662-9667.
- [352] T. Manifar, A. Rezaee, M. Sheikhzadeh and S. Mittler, *Appl. Surf. Sci.* **2008**, *254*, 4611-4619.
- [353] N. Rozlosnik, M. C. Gerstenberg and N. B. Larsen, *Langmuir* **2003**, *19*, 1182-1188.
- [354] A. Y. Fadeev and T. J. McCarthy, *Langmuir* **2000**, *16*, 7268-7274.
- [355] S. Abermann, O. Bethge, C. Henkel and E. Bertagnolli, *Appl. Phys. Lett.* **2009**, *94*, 262904/262901-262904/262903.
- [356] S. F. Wang, F. Gu, M. K. Lu, S. W. Liu, D. Xu, D. R. Yuan and Y. X. Qi, *Inorg. Chem. Commun.* **2003**, *6*, 1275-1277.
- [357] L. Gao and J. McCarthy Thomas, *Langmuir* **2006**, *22*, 2966-2967.

- [358] A. Marmur, *Langmuir* **2004**, *20*, 3517-3519.
- [359] G. Wolansky and A. Marmur, *Langmuir* **1998**, *14*, 5292-5297.
- [360] S. Fotiadou, K. Chrissopoulou, B. Frick and S. H. Anastasiadis, *J. Polym. Sci., Part B: Polym. Phys.* **2010**, *48*, 1658-1667.
- [361] I. M. Kalogeras, A. Vassilikou-Dova, I. Christakis, D. Pietkiewicz and W. Brostow, *Macromol. Chem. Phys.* **2006**, *207*, 879-892.
- [362] C.-C. Su and Y.-H. Shen, *Colloids Surf., A* **2008**, *312*, 1-6.
- [363] C.-C. Su and Y.-H. Shen, *J. Colloid Interface Sci.* **2009**, *332*, 11-15.
- [364] V. Tsyalkovsky, V. Klep, K. Ramaratnam, R. Lupitsky, S. Minko and I. Luzinov, *Chem. Mater.* **2008**, *20*, 317-325.
- [365] M. Gnauck, E. Jaehne, T. Blaettler, S. Tosatti, M. Textor and H.-J. P. Adler, *Langmuir* **2007**, *23*, 377-381.
- [366] R. Valiokas, S. Svedhem, S. C. T. Svensson and B. Liedberg, *Langmuir* **1999**, *15*, 3390-3394.
- [367] J. T. Park, J. H. Koh, D. K. Roh, Y. G. Shul and J. H. Kim, *Int. J. Hydrogen Energy* **2010**, *36*, 1820-1827.
- [368] M. Nakade and M. Ogawa, *J. Mater. Sci.* **2007**, *42*, 4254-4259.
- [369] K. Prakashan, A. K. Gupta and S. N. Maiti, *J. Appl. Polym. Sci.* **2008**, *110*, 1457-1468.
- [370] J. Bauer, N. Husing and G. Kickelbick, *J. Polym. Sci., Part A: Polym. Chem.* **2002**, *40*, 1539-1551.
- [371] J. K. Paulasaari and W. P. Weber, *Macromolecules* **1999**, *32*, 6574-6577.
- [372] J. D. Jovanovic, M. N. Govedarica, P. R. Dvornic and I. G. Popovic, *Polym. Degrad. Stab.* **1998**, *61*, 87-93.
- [373] R. N. Jana, P. G. Mukunda and G. B. Nando, *Polym. Degrad. Stab.* **2003**, *80*, 75-82.
- [374] C. J. Lomoschitz in *Synthesis of Phosphorus Coupling Agents and Their Use in the Modification of ZrO₂ and Barium-Glass Surfaces*, Vienna University of Technology, PhD Thesis, **2011**.
- [375] M. Manca, B. Cortese, I. Viola, A. S. Arico, R. Cingolani and G. Gigli, *Langmuir* **2008**, *24*, 1833-1843.
- [376] C. Kim, C. Gurau Marc, S. Cremer Paul and H. Yu, *Langmuir* **2008**, *24*, 10155-10160.
- [377] L. Hartmann, F. Kremer, P. Pouret and L. Leger, *J. Chem. Phys.* **2003**, *118*, 6052-6058.
- [378] M. Zeghal, B. Deloche and P. Auroy, *Macromolecules* **1999**, *32*, 4947-4955.
- [379] C. Bernardini, S. D. Stoyanov, M. A. Cohen Stuart, L. N. Arnaudov and F. A. M. Leermakers, *Langmuir* **2011**, *27*, 2501-2508.

- [380] S. D. Smith, J. M. DeSimone, H. Huang, G. York, D. W. Dwight, G. L. Wilkes and J. E. McGrath, *Macromolecules* **1992**, *25*, 2575-2581.
- [381] R. Chakraborty and M. D. Soucek, *Eur. Polym. J.* **2008**, *44*, 3326-3334.
- [382] R. Chakraborty and M. D. Soucek, *Silicon* **2010**, *2*, 61-69.
- [383] E. Pouget, E. H. Garcia and F. Ganachaud, *Macromol. Rapid Commun.* **2008**, *29*, 425-430.
- [384] A. Ciolino, G. Sakellariou, D. Pantazis, M. A. Villar, E. Valles and N. Hadjichristidis, *J. Polym. Sci., Part A: Polym. Chem.* **2006**, *44*, 1579-1590.
- [385] R. Karunakaran and J. P. Kennedy, *J. Polym. Sci., Part A: Polym. Chem.* **2007**, *45*, 4284-4290.
- [386] J. Bauer, N. Huesing and G. Kickelbick, *J. Polym. Sci., Part A: Polym. Chem.* **2004**, *42*, 3975-3985.
- [387] M. Cypryk, B. Delczyk, A. Juhari and K. Koynov, *J. Polym. Sci., Part A: Polym. Chem.* **2009**, *47*, 1204-1216.
- [388] P. M. Lefebvre, R. Jerome and P. Teyssie, *Macromolecules* **1977**, *10*, 871-872.
- [389] L. Nothdurft, T. Glueck, W. Dempwolf and G. Schmidt-Naake, *Macromol. Mater. Eng.* **2008**, *293*, 132-139.
- [390] S. Boileau, L. Bouteiller and A. Kowalewska, *Polymer* **2003**, *44*, 6449-6455.
- [391] K. Matyjaszewski, P. J. Miller, E. Fossum and Y. Nakagawa, *Appl. Organomet. Chem.* **1998**, *12*, 667-673.
- [392] G. Fraenkel, A. F. Halasa, V. Mochel, R. Stumpe and D. Tate, *J. Org. Chem.* **1985**, *50*, 4563-4565.
- [393] A. M. Hawkrigde and J. A. Gardella, *J. Am. Soc. Mass Spectrom.* **2003**, *14*, 95-101.
- [394] L. Wilczek and J. P. Kennedy, *Polym. J.* **1987**, *19*, 531-538.
- [395] S. Sakai and T. Hikida, *J. Phys. Chem. A* **2008**, *112*, 10985-10992.
- [396] B. Ray, T. G. Neyroud, M. Kapon, Y. Eichen and M. S. Eisen, *Organometallics* **2001**, *20*, 3044-3055.
- [397] G. Fraenkel, J. Cabral, X. Chen and A. Chow, *J. Org. Chem.* **2009**, *74*, 2311-2320.
- [398] P. West, J. I. Purmort and S. V. McKinley, *J. Amer. Chem. Soc.* **1968**, *90*, 797-798.
- [399] S. A. Solomon, C. A. Muryn and R. A. Layfield, *Chem. Commun.* **2008**, 3142-3144.
- [400] S. M. Sieburth and W. Mu, *J. Org. Chem.* **1993**, *58*, 7584-7586.
- [401] J. Herzfeld and A. E. Berger, *J. Chem. Phys.* **1980**, *73*, 6021-6030.
- [402] L.-q. Wang, W. D. Samuels, G. J. Exarhos, B. I. Lee and Z. Cao, *J. Mater. Chem.* **1998**, *8*, 165-169.

- [403] F. Sinapi, I. Lejeune, J. Delhalle and Z. Mekhalif, *Electrochim. Acta* **2007**, *52*, 5182-5190.
- [404] M. Puchberger, *private communication*, **2010**.
- [405] A. Glisenti, *J. Mol. Catal. A: Chem.* **2000**, *153*, 169-190.
- [406] R. Richards, W. Li, S. Decker, C. Davidson, O. Koper, V. Zaikovski, A. Volodin, T. Rieker and K. J. Klabunde, *J. Am. Chem. Soc.* **2000**, *122*, 4921-4925.
- [407] W. D. Bascom, *J. Colloid Interface Sci.* **1968**, *26*, 89-94.
- [408] J. B. Conant and E. L. Jackson, *J. Am. Chem. Soc.* **1924**, *46*, 1003-1018.
- [409] T. S. Radhakrishnan, *J. Appl. Polym. Sci.* **1999**, *73*, 441-450.
- [410] B. Julian, R. Corberan, E. Cordoncillo, P. Escribano, B. Viana and C. Sanchez, *J. Mater. Chem.* **2004**, *14*, 3337-3343.
- [411] M. Russell, T., L. Pingree, S. C., M. Hersam, C. and T. Marks, J., *Langmuir* **2006**, *22*, 6712-6718.
- [412] D. Kaempfer, R. Thomann and R. Mulhaupt, *Polymer* **2002**, *43*, 2909-2916.
- [413] K. H. See, M. E. Mullins, O. P. Mills and P. A. Heiden, *Nanotechnology* **2005**, *16*, 1950-1959.
- [414] J. E. Carraher in *Polymer Chemistry*, CRC Press, Boca Raton, Florida, USA, **2006**, p. 194.
- [415] J. E. Mark, *Polymer Data Handbook*, Oxford Press, New York, **2006**, p. 830.
- [416] R. Contreras-Caceres, A. Sanchez-Iglesias, M. Karg, I. Pastoriza-Santos, J. Perez-Juste, J. Pacifico, T. Hellweg, A. Fernandez-Barbero and L. M. Liz-Marzan, *Adv. Mater.* **2008**, *20*, 1666-1670.
- [417] D. Amati and E. S. Kovats, *Langmuir* **1987**, *3*, 687-695.
- [418] S. Zorn, N. Martin, A. Gerlach and F. Schreiber, *Phys. Chem. Chem. Phys.* **2010**, *12*, 8985-8990.
- [419] S. Zorn, M. W. A. Skoda, A. Gerlach, R. M. J. Jacobs and F. Schreiber, *Langmuir* **2011**, *27*, 2237-2243.
- [420] L. H. Dubois, B. R. Zegarski and R. G. Nuzzo, *J. Am. Chem. Soc.* **1990**, *112*, 570-579.
- [421] W. Mar, J. Hautman and M. L. Klein, *Comput. Mater. Sci.* **1995**, *3*, 481-497.
- [422] H. Oikawa, T. Onodera, A. Masuhara, H. Kasai and H. Nakanishi, *Adv. Polym. Sci.* **2010**, *231*, 147-190.
- [423] H. J. Nam, J.-H. Kim, D.-Y. Jung, J. B. Park and H. S. Lee, *Appl. Surf. Sci.* **2008**, *254*, 5134-5140.
- [424] S. Choi, S. Stassi, A. P. Pisano and T. I. Zohdi, *Langmuir* **2010**, *26*, 11690-11698.

- [425] X. Shen, C.-M. Ho and T.-S. Wong, *J. Phys. Chem. B* **2010**, *114*, 5269-5274.
- [426] C.-K. Wu, K. L. Hultman, S. O'Brien and J. T. Koberstein, *J. Am. Chem. Soc.* **2008**, *130*, 3516-3520.
- [427] R. Shenhar, T. B. Norsten and V. M. Rotello, *Adv. Mater.* **2005**, *17*, 657-669.
- [428] A. J. Rahedi, J. F. Douglas and F. W. Starr, *J. Chem. Phys.* **2008**, *128*, 024902/024901-024902/024909.
- [429] J. E. Mark in *Polymer Data Handbook*, Oxford Press, New York, **2006**, p. 833.
- [430] A. P. Philipse and A. Vrij, *J. Chem. Phys.* **1988**, *88*, 6459-6470.
- [431] Y. Tu, L. Zhou, Y. Z. Jin, C. Gao, Z. Z. Ye, Y. F. Yang and Q. L. Wang, *J. Mater. Chem.* **2010**, *20*, 1594-1599.
- [432] K. Arisawa and R. S. Porter, *J. Appl. Polym. Sci.* **1970**, *14*, 879-896.
- [433] L. R. Whitlock and R. S. Porter, *J. Appl. Polym. Sci.* **1973**, *17*, 2761-2770.
- [434] T. Wu and Y. Ke, *Eur. Polym. J.* **2006**, *42*, 274-285.
- [435] J. E. Mark, *Polymer Data Handbook*, Oxford Press, New York, **2006**, p. 656.
- [436] P. Zhou, X. Chen, H. L. Frisch, Z. Zhu, J. Rider and G. E. Wnek, *Macromolecules* **1992**, *25*, 7334-7337.
- [437] G. Kickelbick, *J. Sol-Gel Sci. Technol.* **2008**, *46*, 281-290.
- [438] P. R. Cooper, *Appl. Opt.* **1982**, *21*, 3413-3415.
- [439] W.-F. Su, Y.-C. Fu and W.-P. Pan, *Thermochim. Acta* **2002**, *392-393*, 385-389.
- [440] J. E. Mark in *Polymer Data Handbook*, Oxford Press, New York, **2006**, p. 90.
- [441] M. Kamibayashi, H. Ogura and Y. Otsubo, *J. Colloid Interface Sci.* **2008**, *321*, 294-301.
- [442] R. Lach, L. Antonova Gyurova and W. Grellmann, *Polym. Test.* **2007**, *26*, 51-59.
- [443] R. Y. Kannan, H. J. Salacinski, P. E. Butler and A. M. Seifalian, *Acc. Chem. Res.* **2005**, *38*, 879-884.
- [444] M. Parvinzadeh, S. Moradian, A. Rashidi and M.-E. Yazdanshenas, *Appl. Surf. Sci.* **2010**, *256*, 2792-2802.
- [445] Y. Tang and M. Lewin, *Polym. Adv. Technol.* **2009**, *20*, 1-15.
- [446] D. D. Perrin, W. L. F. Armarego and D. R. Perrin, *Purification of Laboratory Chemicals*, **1966**, p.
- [447] F. L. McCrackin, E. Passaglia, R. R. Stromberg and H. L. Steinberg, *J. Res. Natl. Bur. Stand., Sect. A* **1963**, *A67*, 363-377.
- [448] C. Rill, *private communication*, **2010**.
- [449] N. Moszner, F. Zeuner, U. K. Fischer and V. Rheinberger, *Macromolecular Chemistry and Physics* **1999**, *200*, 1062-1067.

- [450] C. Lomoschitz in *private communication*, Vol. **2010**.
- [451] I. Omura, J. Yamauchi, Y. Nagase and F. Uemura in *Dental adhesive compositions containing acrylate phosphates*, Vol. EP0115410 (Kuraray Co., Ltd., Japan). Japan, **1984**, p. 44 pp.
- [452] M. Litschauer, *private communication*, **2010**.
- [453] L. Cauret, J.-C. Brosse, D. Derouet and H. De Livonniere, *Bull. Soc. Chim. Fr.* **1997**, *134*, 463-470.
- [454] K. S. Dunne, S. E. Lee and V. Gouverneur, *J. Organomet. Chem.* **2006**, *691*, 5246-5259.

Curriculum Vitae

Contact

Bernhard Feichtenschlager

Flurschützstraße 15/26, 1120 Wien, Austria

Phone Number: +43 650 400 9305

E-mail: feichtenschlager@gmx.net

Born: June, 7th 1983 in Braunau am Inn, Austria

Citizenship: Austrian

Education

- | | |
|-------------------|--|
| since 09/2008 | PhD studies at the Institute of Materials Chemistry, Vienna University of Technology, Supervisor: Prof. Kickelbick
Thesis: Chemical Tailoring of Metal Oxide Nanoparticle Surfaces to control Structure and Properties of Polymer Nanocomposites |
| since 10/2009 | Bachelor studies on business, economy and social sciences at the Vienna University of Economics and Business Administration |
| 02/2011 – 04/2011 | Research Stay at the Institute of Solid State Chemistry, Saarland University Saarbrücken, Germany |
| 10/2003 – 06/2008 | Master's degree (Diploma) in Technical Chemistry from the Vienna University of Technology
Diploma Thesis at the Institute of Materials Chemistry in cooperation with BASF AG, Topic: "Organically surface modified, anisotropically shaped, alumina and zirconia nanoparticles"
Graduation with Distinction |
| 09/1997 – 06/2002 | Graduation at the Technical High School for Electrical Engineering in Braunau am Inn |

Employment

- | | |
|-------------------|--|
| since 09/2008 | Project Assistant at the Institute of Materials Chemistry, Vienna University of Technology |
| 10/2007 – 04/2008 | Research Assistant (part-time) at the Institute of Materials Chemistry, Vienna University of Technology |
| 07/2007 – 09/2007 | Three month Internship at Boehringer Ingelheim Austria GmbH in Vienna, Austria, in the research department of medicinal chemistry |

08/2006 – 09/2006	Summer Intern at Wacker Chemie AG , Burghausen, Germany
08/2005 – 09/2005	at a production plant for polysiloxane compounds
08/2004 – 09/2004	at a production plant for polyvinylalcohol compounds
07/2003 – 08/2003	project at the department of central process analytics

Personal Skills and Interests

Languages

German: native speaker, **English:** excellent, **Russian:** basics

Interests

cooking, eastern european literature, mountains

Professional Activities, Honors and Grants

since 2007 Membership of the Austrian Chemical Society (GÖCh)

2004 – 2007 Scholarship for outstanding students from the Vienna University of Technology

04/2010 Prize for the best presentation at the conference "Topical Issues of Rational Use of Natural Resources" in St. Petersburg, Russia